

# UC Santa Cruz

## UC Santa Cruz Electronic Theses and Dissertations

### Title

Modeling the Early, Intermediate, and Late Stages of Planet Formation

### Permalink

<https://escholarship.org/uc/item/9fp6f1zb>

### Author

Rosenthal, Mickey Morley

### Publication Date

2020

Peer reviewed|Thesis/dissertation

UNIVERSITY OF CALIFORNIA  
SANTA CRUZ

**MODELING THE EARLY, INTERMEDIATE, AND LATE STAGES  
OF PLANET FORMATION**

A dissertation submitted in partial satisfaction of the  
requirements for the degree of

Doctor of Philosophy

in

ASTRONOMY AND ASTROPHYSICS

by

**Mickey M. Rosenthal**

September 2020

The Dissertation of Mickey M. Rosenthal is approved:

---

Ruth Murray-Clay, Chair

---

Jonathan Fortney

---

Andrew Skemer

---

Eugene Chiang

---

Quentin Williams  
Interim Vice Provost and Dean of Graduate Studies

Copyright © by

Mickey M. Rosenthal

2020

# Table of Contents

List of Figures	vii
List of Tables	xxv
Abstract	xxvi
Acknowledgments	xxix
Dedication	xxxiii
<b>1 Introduction</b>	<b>1</b>
1.1 The Protoplanetary Disk . . . . .	2
1.2 Early Solid Growth . . . . .	8
1.3 Growth from Planetesimals . . . . .	11
1.4 Growth of Gas Giants . . . . .	16
1.5 Ending Runaway Accretion . . . . .	17
1.6 Outline of Dissertation . . . . .	21
<b>2 Gas Assisted Growth of Planets in a Turbulent Medium</b>	<b>23</b>
2.1 Introduction . . . . .	23
2.2 Model Overview . . . . .	30
2.2.1 Accretion in the Presence of Gas . . . . .	30
2.2.2 Growth Timescale for Protoplanets . . . . .	38
2.3 Velocity of the Small Bodies through the Disk . . . . .	43
2.3.1 Gas Drag and Stopping Time . . . . .	44
2.3.2 Laminar Velocity of Small Particles . . . . .	46
2.3.3 Turbulent Velocity of Small Particles . . . . .	48
2.3.4 Combining Velocities and Changing Frames . . . . .	53
2.3.5 $v_{\text{shear}}$ . . . . .	54
2.3.6 $v_{\text{enc}}$ and Calculating Work . . . . .	55
2.4 Calculation of Accretion Cross Section . . . . .	59
2.4.1 Determining $R_{\text{acc}}$ . . . . .	59
2.4.2 Determining $H_{\text{acc}}$ . . . . .	67

2.5	Overview of Results . . . . .	73
2.5.1	Model Parameters . . . . .	73
2.5.2	Basic Model Output . . . . .	75
2.5.3	$t_{\text{Hill}}$ . . . . .	78
2.5.4	Gas Mitigated Growth . . . . .	82
2.5.5	Correspondence with Previous Models of Pebble Accretion . . . . .	83
2.5.6	Comparison to Xu et al. (2017) . . . . .	91
2.6	Exploration of Parameter Space . . . . .	102
2.6.1	Effects of Variation of Orbital Separation and Core Mass . . . . .	102
2.6.2	Effects of Varying $T_0$ . . . . .	106
2.6.3	Growth in a Gas Depleted Disk . . . . .	109
2.6.4	Effects of Varying Stellar Mass . . . . .	112
2.7	Flow Isolation Mass . . . . .	121
2.8	Summary and Conclusions . . . . .	130
<b>3</b>	<b>Restrictions on the Growth of Gas Giant Cores via Pebble Accretion</b>	<b>135</b>
3.1	Introduction . . . . .	135
3.2	Model Overview . . . . .	142
3.2.1	Basic Pebble Accretion Processes . . . . .	142
3.2.2	Pebble Accretion at Different Particle Radii . . . . .	146
3.2.3	Summary of Timescale Calculation . . . . .	149
3.2.4	Values of Parameters . . . . .	154
3.3	Gas-Assisted Growth Timescales at Wide Orbital Separation . . . . .	154
3.3.1	Growth at High Core Mass . . . . .	155
3.3.2	Growth Timescales for Low-Mass Protoplanets . . . . .	158
3.3.3	Size Distribution of Small Bodies . . . . .	162
3.3.4	Integrated Growth Timescales . . . . .	164
3.4	Restrictions on the Growth of Gas Giants . . . . .	170
3.4.1	Planetesimal Accretion Timescale . . . . .	170
3.4.2	Upper Limits on the Semi-Major axis of Gas Giant Growth . . . . .	172
3.4.3	Effect of Fixing Upper Particle Radius . . . . .	176
3.5	Final Mass of Gas Giants . . . . .	185
3.6	Summary/Conclusions . . . . .	192
<b>4</b>	<b>How Flow Isolation May Set the Mass Scale for Super-Earth Planets</b>	<b>195</b>
4.1	Introduction . . . . .	195
4.2	Model Overview . . . . .	199
4.3	Methods . . . . .	209
4.3.1	Fiducial Disk Model . . . . .	209
4.3.2	Summary of Pebble Accretion Model . . . . .	214
4.3.3	Calculation of the Flow Isolation Mass . . . . .	221
4.3.4	Structure of Planetary Atmospheres . . . . .	224
4.3.5	Pebble Isolation Mass . . . . .	228
4.4	Results . . . . .	230
4.4.1	Limiting Planet Mass for Fixed $St_{\text{max}}$ . . . . .	231

4.4.2	Flow Isolation Mass for Fragmentation-Limited Pebbles . . . . .	233
4.4.3	Variation with Stellar Mass . . . . .	237
4.5	Comparison to Observations of Close in Planets . . . . .	238
4.5.1	Weiss et al. (2018) and Millholland et al. (2017) . . . . .	238
4.5.2	Wu (2019) . . . . .	239
4.5.3	Zhu & Wu (2018) & Bryan et al. (2019) . . . . .	240
4.6	Summary and Conclusions . . . . .	241
<b>5</b>	<b>Ending Pebble Accretion Though Flow and Pebble Isolation</b>	<b>244</b>
5.1	Introduction . . . . .	244
5.2	Disk Model . . . . .	246
5.3	Pebble Isolation Mass . . . . .	251
5.4	Flow Isolation Mass . . . . .	258
5.5	Halting growth by flow and pebble isolation . . . . .	262
5.6	Summary and Conclusions . . . . .	264
<b>6</b>	<b>How Consumption and Repulsion Set Planetary Gap Depths and the Final Masses of Gas Giants</b>	<b>267</b>
6.1	Introduction . . . . .	267
6.2	Viscous discs: Surface Density Profiles at Fixed Planet Mass . . . . .	270
6.2.1	Order-of-magnitude scalings . . . . .	270
6.2.2	Numerical simulations . . . . .	278
6.3	Viscous discs: Gas Giant Growth . . . . .	289
6.3.1	Numerical calculation at $r_p = 10$ au . . . . .	289
6.3.2	Analytic estimates of the final planet mass . . . . .	291
6.4	Planets in Inviscid Wind-Driven Discs . . . . .	296
6.4.1	Wind-driven accretion discs . . . . .	296
6.4.2	Repulsion in inviscid discs . . . . .	298
6.4.3	Consumption and repulsion combined . . . . .	299
6.4.4	Numerical simulations . . . . .	302
6.5	Summary and Discussion . . . . .	308
6.5.1	Final planet masses . . . . .	309
6.5.2	Transitional discs . . . . .	315
<b>7</b>	<b>Measuring the Orbital Parameters of Radial Velocity Systems in Mean Motion Resonance—a Case Study of HD 200964</b>	<b>318</b>
7.1	Introduction . . . . .	318
7.2	Observations . . . . .	322
7.3	Previous Analysis . . . . .	330
7.4	Methods . . . . .	331
7.4.1	Fits Incorporating Planet-Planet Interactions . . . . .	332
7.4.2	Rejection Sampling . . . . .	342
7.4.3	Likelihood Function Conditioned on Stability . . . . .	346
7.4.4	Final Posterior Distribution . . . . .	349
7.4.5	Stable Regions of Period-Period Space . . . . .	356

7.5	Analysis of Underlying Mean-Motion Resonance . . . . .	359
7.6	Reanalysis of Early Data . . . . .	367
7.7	Possibility of a Third Planet . . . . .	369
7.8	Summary and Conclusions . . . . .	372
<b>Bibliography</b>		<b>374</b>
<b>A Calculation of Gas-Assisted Growth Timescale</b>		<b>388</b>
A.1	Summary of Calculation Algorithm . . . . .	388
A.2	Derivation of Velocity Formulae in Different Frames . . . . .	394
A.3	Canonical Core Accretion Timescale . . . . .	397
A.4	Details of Turbulent Velocity Calculation . . . . .	399
<b>B Appendices for Consumption Calculation</b>		<b>403</b>
B.1	Analytic Steady-State Solution for $\Sigma$ and $\dot{M}$ For Viscous Disc with Planet	403
B.2	Magnetized winds and disc accretion . . . . .	408
<b>C Additional Plots for analysis of the planetary system around HD 200964</b>		<b>412</b>
C.1	Full Posterior Distributions . . . . .	412
C.2	Plots of the evolution of $\phi$ for the 3:2 and 4:3 MMR . . . . .	417

# List of Figures

1.1	Cartoon sketch of the force on a gas parcel in a protoplanetary disk. . .	3
1.2	Problem setup for estimation of the gravitational focusing radius. . . . .	12
1.3	Setup for the calculation of the torque from a gas giant on the surrounding disk. . . . .	18
2.1	A graphical illustration the energy regimes used to determine whether small bodies are able to accrete. <i>Upper Left Panel:</i> Here $R_{\text{stab}} > R_b$ , so particles can inspiral onto the core in a region where the gas flow is not substantially altered by the core's gravity. Particles that deplete their kinetic energy relative to the core via gas drag will inspiral onto the core and be captured. <i>Upper Right Panel:</i> If the particle is unable to deplete its kinetic energy during the interaction then it will simply have its trajectory deflected before exiting $R_{\text{stab}}$ , and will not accrete. <i>Lower Left Panel:</i> Here $R_b > R_{\text{stab}}$ , so the gas flow is altered substantially when the small body is accreting. The gas will tend to flow around the atmospheric radius, so particles that have $KE < W$ , i.e. particles that deplete their kinetic energy, will couple to the gas and flow around the core without accreting. <i>Lower Right Panel:</i> Larger particles which do not deplete their kinetic energy and instead penetrate into the atmospheric radius will experience a rapid increase in gas density as they enter the atmosphere of the nascent planet. This increased density may rapidly deplete the kinetic energy of the small body, which will then inspiral and accrete, similar to what occurs in the upper left panel. . . . .	40

- 2.2 A cartoon illustration of the typical manner in which pebble accretion operates as the small body size is increased. The black circle represents the planet, while the blue circles depict incoming particles. The extent of the planet's atmosphere is denoted by the grey shaded region, and the yellow shaded region shows the region where incoming particles can be accreted. *Left Panel:* For small particles,  $R'_{WS} = R_{stab} < R_b$ , so the core's gravitational sphere of influences lies inside its atmosphere. In this regime particles couple to the local gas flow and flow around the core without being accreted. *Middle Panel:* For intermediate sizes of particles,  $R'_{WS} > R_b$ , meaning particles can be bound to the core in a region outside the core's atmosphere. For these intermediate sizes of particles the work done by gas drag exceeds the incoming kinetic energy of these small bodies, meaning that particles that pass interior to  $R_{stab}$  will be accreted. Particles with impact parameters  $> R_{stab}$  will be sheared off the core by gas drag. *Right Panel:* Finally, large particles will be so massive that their incoming kinetic energy is too large to be depleted by gas drag. These particles will not be accreted via pebble accretion, regardless of impact parameter. For the case shown here  $R'_{WS}$  has grown so much that  $R_{stab} = R_H$ , but this is not always the case for particles with  $KE > W$ . . . . . 41
- 2.3 A graphical illustration of the quantities used to determine the growth timescale for the planetary core. . . . . 42
- 2.4 An illustration of the effects of the gravitational interactions between the small body and the core on the velocity between the two bodies during their encounter,  $v_{enc}$ . *Left Panel:* Both particles enter from the lower left, as indicated by the arrow. The upper particle (dashed curve) has  $v_{\infty} < v_{orbit}$  while the lower particle (solid curve) has  $v_{\infty} > v_{orbit}$ . The upper, slow moving particle has the direction of its velocity substantially changed during the interaction, while the lower, fast moving particle only receives a small perturbation to its velocity in the direction perpendicular to its motion. *Lower Right Panel:* The slow moving particle is excited to a velocity comparable to  $v_{orbit}(r) = \sqrt{GM/r}$  during its interaction with the core. *Upper Right Panel:* The fast moving particle receives a small perturbation to its velocity, of order  $v_{kick} = GM/(R_{acc}v_{\infty})$ . As can be seen in the figure, the actual perturbation is approximately a factor of 2 larger than  $v_{kick}$ . Including this factor of 2 does not have a substantial effect on our results. . . . . 58

- 2.5 A plot of the timescale for growth of the protoplanetary core as a function of small body radius, plotted for various values of  $\alpha$ , which measures the strength of turbulence. The values shown are for  $a = 1$  AU and  $M = 10^{-1}M_{\oplus}$ . Also shown are the Stokes numbers for the plotted values of small body radius. Note that in a non-linear drag regime there is no longer a velocity independent relationship between radius and Stokes number; in this case the given values are calculated for drift velocities in the laminar ( $\alpha = 0$ ) case. The timescale is set to  $\infty$  for particles that are unable to accrete according to the energy criteria discussed in section 2.2.1, i.e. the range of radii plotted shows the range of particle sizes the core is able to accrete via pebble accretion. . . . . 94
- 2.6 A plot of the timescale for growth of the protoplanetary core as a function of  $\alpha$ , along with plots of the four quantities used to determine  $t_{\text{grow}}$  (c.f. Equation 2.6), which are also plotted as a function of  $\alpha$ . The values shown are for  $a = 1$  AU,  $M_* = M_{\odot}$ ,  $M = 10^{-1}M_{\oplus}$  and  $r_s = 35$  cm. The minimum timescale  $t_{\text{Hill}}$  is also shown (red dashed line). . . . . 95
- 2.7 A plot of  $P_{\text{col}} \equiv 2R_{\text{acc}}v_{\infty}$  as a function of  $r_s$  and  $M$  for a core at  $a = 30$  AU with  $\alpha = 0$ . Several important features along with their formulae are marked on the plot. See the text for a discussion of what causes these features to emerge. . . . . 96
- 2.8 Comparison of results from our model in the laminar regime ( $\alpha = 0$ ) with analytic models of [Ormel & Klahr \(2010\)](#) and [Johansen & Lambrechts \(2017\)](#). The upper row plots  $P_{\text{col}} = 2R_{\text{acc}}v_{\infty}$  for a core at  $a = 30$  AU as a function of small body radius and core mass, while the lower panels instead plot the growth timescale,  $t_{\text{grow}}$ . The red hatched region denotes where growth is completely shut off in our modeling, whereas the white regions show places where gas-assisted growth will not operate, but the core can still grow by other means (e.g. gravitational focusing). The upper panels show agreement to order of magnitude between the three models, with exceptions in a few regions (see text for more details). The bottom panels highlight the effect of particle scale height, which is included in our model even in the laminar regime, but not in the other two analytic models. . . . . 97
- 2.9 Comparison of results from our model with turbulence included ( $\alpha = 10^{-3}$ ) with modeling of pebble accretion by [Chambers \(2014\)](#). The upper row plots  $P_{\text{col}} = 2R_{\text{acc}}v_{\infty}$  for a core at  $a = 30$  AU as a function of small body radius and core mass, while the lower panels instead plot the growth timescale,  $t_{\text{grow}}$ . The red hatched region denotes where growth is completely shut off in our modeling, whereas the white regions show places where gas-assisted growth will not operate, but the core can still grow by other means (e.g. gravitational focusing). . . . . 98

2.10	A comparison of the growth rate $k_{\text{abs}}$ from our model and the MHD simulations of Xu et al. (2017), plotted as a function of the Stokes number of the particles the cores are accreting. Here $k_{\text{abs}} \equiv \dot{M}/\dot{M}_{\text{Hill}}$ , where $\dot{M} = M/t_{\text{grow}}$ , and $\dot{M}_{\text{Hill}} = M/t_{\text{Hill}}$ , i.e. $k_{\text{abs}}$ represents the growth rate of the core in units of the accretion rate for growth at $t_{\text{Hill}}$ . The two panels depict growth for two different values of core mass – $\mu_c \equiv M/M_T = 3 \times 10^{-3}$ and $\mu_c = 3 \times 10^{-2}$ , where $M_T$ is the thermal mass, defined in Equation (2.75). Each panel shows the growth rate for three different levels of turbulence, which are listed in the legend. The solid lines show the output from our model, while the data points show the Xu et al. results. . . . .	99
2.11	The growth timescale as a function of core mass, for $a = 5$ AU. The red hatched region denotes where growth is completely shut off in our modeling, whereas the white regions show places where gas-assisted growth will not operate, but the core can still grow by other means (e.g. gravitational focusing). The feature in the upper right emerges for $R_b > R_H$ (see Section 2.7). . . . .	100
2.12	The growth timescale as a function of core mass, for $a = 50$ AU. The red hatched region denotes where growth is completely shut off in our modeling, whereas the white regions show places where gas-assisted growth will not operate, but the core can still grow by other means (e.g. gravitational focusing). . . . .	101
2.13	The range of small body radii which can accrete within a factor of two of $t_{\text{Hill}}$ for a given semi-major axis and core mass. As indicated in the legend, different hatching styles indicate different levels of turbulence. If a given region is accessible for different levels of turbulence the various hatching styles are overlaid. . . . .	116
2.14	The ratio of kinetic energy relative to the core to work done by the gas on an incoming particle assuming $\alpha = 0$ , plotted as a function of small body radius $r_s$ . Curves are shown for a range of core masses. The left panel shows the situation at $a = 1$ AU, while the right panel is for $a = 50$ AU. . . . .	117
2.15	The growth timescale as a function of semi-major axis for two different values of the prefactor of the temperature profile, $T_0$ . Both panels use the values $r_s = 0.25$ cm, $M = 10^{-1}M_{\oplus}$ . The panel on the top is for $\alpha = 0$ , while the panel on the bottom is for $\alpha = 10^{-2}$ . The effect of increasing $T_0$ is more substantial in the laminar case, since $H_p$ and $v_{pk}$ both scale as $c_s^2$ in this regime, as opposed to $c_s$ in the turbulent case. . . . .	118

- 2.16 The gas-assisted growth timescale for a disk with its gas surface density depleted by a factor of 100. The values shown are for  $a = 30$  AU, and  $M = 1.5 \times 10^{-2} M_{\oplus}$ . Both a laminar ( $\alpha = 0$ ) and a strongly turbulent ( $\alpha = 10^{-2}$ ) case are shown. The solid lines shown the values for the surface density used in the paper, while the dashed lines depict the effect of changing the surface density. . . . . 119
- 2.17 The effect of varying the mass of the central star. The values shown here are at a distance of  $a = 70$  AU, and  $M = 0.5 M_{\oplus}$ . The panels show the grow timescale as a function of small body size for a laminar ( $\alpha = 0$ ) and strongly turbulent ( $\alpha = 10^{-2}$ ) disk. Each panel shows the timescale for five different stellar masses. *Top Panel:* In the laminar case the small particles which accrete at  $R_{\text{acc}} = R_{\text{WS}}$  are accreted more rapidly around higher mass stars, as more massive stars have higher rates of shear and reduced small body scale height. As particle size increases the particles will begin accreting at  $R_{\text{acc}} = R_H$  – the effect of stellar mass in this regime depends on the size of  $H_{KH}$  relative to  $R_H$  (see text). *Bottom Panel:* The inclusion of turbulence allows the scale height of smaller particles to be set by turbulent diffusion instead of the Kelvin-Helmholtz shear instability, making the scale height independent of  $M_*$  in this regime. In this case the increase in shear rate is balanced by the decrease in  $R_{\text{WS}}$ , causing the growth curves to merge for low values of  $r_s$ . For higher values of  $r_s$  where  $R_{\text{acc}} = R_H$  the situation is the same as in the top panel. . . 120
- 2.18 A schematic illustration of the trajectories of particles with  $KE < W$  for  $M > M_{\text{flow}}$ . The particle (blue circle), comes in from the left. Since the particle is able to dissipate its kinetic energy relative the core, it begins to follow the local gas flow. The core’s atmosphere extends up to  $R_H$ , and the nebular gas flows around this obstacle. The particle is pulled along with the gas, causing it to flow around the core without being accreted. 123
- 2.19 The value of the flow isolation mass (solid line), as well as the flow isolation mass scaled down by a factor of four (dashed line), both plotted as a function of semi-major axis. Also shown are the masses of the cores of the solar system planets. Values for the four giant planets are taken from [Guillot \(2005\)](#). For the terrestrial planets the total mass is shown. For the gas giant the mass of the core is used, whereas for the ice giants the total mass in solids is plotted. . . . . 129

3.1	Colored lines show the dust surface density in 0.1 mm – 1 mm sized particles taken from 870 $\mu\text{m}$ continuum emission observations of protoplanetary disks done by <a href="#">Andrews et al. (2009)</a> . See text for details. Also shown for reference is the value of the solid surface density in the minimum-mass solar nebula (MMSN), appropriate for the outer disk, $30 (a/\text{AU})^{-3/2} \text{ g cm}^{-2}$ ( <a href="#">Weidenschilling 1977b</a> , <a href="#">Hayashi 1981</a> ), as well as the fiducial surface density used in this work to match the observations. In the gray shaded region the values of the curves are extrapolations to scales smaller than the observations can resolve. . . . .	139
3.2	The growth timescale for a protoplanet as a function of the small-body radius the core is accreting. The timescale is plotted for several values of $\alpha$ , which measures the strength of turbulence in the disk. The values shown are for a $5 M_{\oplus}$ core at 30 AU. The lines are cut off for particles that are unable to accrete according to the energy criteria discussed in Section 3.2.3. . . . .	157
3.3	The growth timescale as a function of core mass, for $a = 30 \text{ AU}$ . The red hatched region indicates where no accretion is possible. In the white regions particles can still accrete via other processes, e.g. gravitational focusing. . . . .	159
3.4	Integrated growth timescale for a core at $a = 20 \text{ AU}$ as a function of core mass. The growth timescale is integrated over sizes using a Dohnanyi distribution with a maximum size corresponding to $St = 10^{-1}$ , as discussed in Section 3.3.3. The approximate $e$ -folding time of the gaseous component of the disk, $\tau_{\text{disk}}$ , is marked as a dashed horizontal line. As the core grows, it can accrete a larger fraction of the available small-body sizes, causing the growth timescale to drop rapidly. Eventually, the core’s mass becomes large enough that it can accrete all available particle sizes, causing it to enter into a regime where growth timescale is independent of $M$ . We also note that once the core becomes massive enough that the growth timescale drops below $\tau_{\text{disk}}$ , subsequent growth at higher core masses proceeds on timescales well below the disk lifetime. . . . .	169

3.5	Graphical illustration of how gas giant core growth is limited for different semi major axes. The monotonically increasing line (black) shows the <i>minimum</i> mass needed for gas-assisted growth to produce a gas giant core; for masses higher than the plotted mass, the growth timescale for the core is less than the disk lifetime. The monotonically decreasing line (blue) shows the <i>maximum</i> mass it is possible to achieve via planetesimal accretion. Values lower than the indicated mass can be reached within the disk lifetime, but for larger masses the disk will dissipate before the mass is reached. The vertical line denotes the semi-major axis upper limit on where growth of gas giant cores can occur; interior to this region, planetesimal accretion can build a massive enough core rapidly enough that pebble accretion becomes efficient and dominates growth at higher masses. The green shaded region indicates where growth of gas giants is ruled out, as both planetesimal accretion and pebble accretion are too slow. . . . .	180
3.6	Minimum mass for which the growth timescale is shorter than $\tau_{\text{disk}} = 2.5 \text{ Myr}$ , shown for various values of $\alpha$ . Masses smaller than the values depicted have growth timescales larger than $\tau_{\text{disk}}$ , so if the core can exceed this mass by other means, it should be able to reach $M_{\text{crit}}$ , but growth by pebble accretion will be unable to exceed this mass within $\tau_{\text{disk}}$ . A mass for growth by planetesimal accretion is also shown, but this mass has a different interpretation: it is the <i>largest</i> mass a core can grow to via gravitational focusing within $\tau_{\text{disk}}$ . . . . .	181
3.7	Maximum semi-major axis at which growth to critical core mass is possible as a function of $\alpha$ . Curves are shown for a Dohnanyi distribution with a maximum-sized particle corresponding to $St = 10^{-1}$ (solid line) and $St = 1$ (dashed line). . . . .	182
3.8	A comparison of our analytic expression for the maximal semi-major axis where gas giant growth is possible (Equation 3.34), with the numerical solution. Results are presented for two different planetesimal surface densities, $\Sigma_{\text{pla}} = \Sigma_p$ and $\Sigma_{\text{pla}} = \Sigma_p/2$ . . . . .	183
3.9	The blue region shows where growth of gas giant cores is possible for a size distribution with maximal pebble size of $r_s = 1 \text{ mm}$ , plotted as a function of the strength of turbulence. In contrast to the size distributions which used a fixed Stokes number as the upper limit, this distribution has a lower limit on where core growth can occur as well as an upper limit. The lower limit is the maximum of a fixed semi-major axis limit, and a limit for a given $\alpha$ – an analytic expression for the latter (c.f. Equation 3.37) is also shown (black dashed line). . . . .	184

3.10	<p>“Starvation” mass, past which growth of a gas giant halts, plotted as a function of semi-major axis. <i>Panel a</i>): In this panel, the mass is obtained by assuming that growth shuts off when the planet opens up a gap of width <math>\Delta = 5R_H</math> (see text for more details). Inside the gray region, the <math>\alpha</math> value required to prevent gap opening before the core reaches the given mass is so large that a core will not be able to form within the lifetime of the gas disk (see Section 3.4.2). The shape of this region is determined using our upper limits on <math>\alpha</math> taken from the <math>St_{\max} = 0.1</math> in Figure 3.7. The labeled curves show maximum masses for constant values of <math>\alpha</math>. <i>Panel b</i>): Here the starvation mass is determined numerically using fitting formulae to numerical results for the gas accretion rate from 3D hydrodynamical simulations by <a href="#">Lissauer et al. (2009)</a>. The starvation mass is determined by solving for the mass at which <math>M_{\text{starve}}/\dot{M} = \tau_{\text{disk}}</math>. The dashed lines again indicate the semi-major axes where turbulence prevents a gas giant core from forming via pebble accretion. . . . .</p>	191
4.1	<p>A plot of the growth timescale of a planet at <math>a = 0.5</math> AU undergoing pebble accretion as a function of planet mass and small body radius. The disk parameters used are described in Section 4.3.1. The two panels show the growth timescale for two different levels of turbulence in the disk. In the lefthand side of both panels, the red hatched region indicates where growth cannot occur because pebbles flow around the core (see Section 4.2). The white regions indicate where particles do not dissipate their kinetic energy relative to the core, and therefore cannot be accreted by pebble accretion. Pebbles in this region could still be accreted by other processes however (e.g. gravitational focusing). . . . .</p>	201
4.2	<p>The mass of a protoplanet undergoing pebble accretion as a function of time, for three different values of initial mass. All particles are assumed to have Stokes number of <math>10^{-2}</math>. The disk parameters used are given in Section 4.3.1. In all cases the protoplanet’s solid mass runs away to extremely large masses on timescales shorter than the lifetime of the protoplanetary disk (<math>\sim 3</math> Myr). . . . .</p>	203
4.3	<p>A cartoon illustrating schematically how flow isolation operates. The planet’s (black dot) atmosphere is shown by the gray shaded region, and extends up to <math>R_B</math>. The gas flows around the atmosphere, as shown by the dashed blue lines. The larger, green particle, has maximal impact parameter for accretion <math>R_{\text{stab}} &gt; R_B</math>, and thus can be captured at scales of <math>R_{\text{stab}}</math> before encountering the modified gas flow. The smaller red particle has <math>R_{\text{stab}} &lt; R_B</math>, and is diverted by the atmosphere’s modification to the flow instead of being captured. . . . .</p>	208

4.4	The atmospheric mass of a planet accreting at the maximal pebble accretion rate as a function of semi-major axis, using mixing length theory to calculate the temperature gradient. While the atmospheric mass is slightly reduced from the fully convective value, the decrease is relatively modest. . . . .	225
4.5	A plot of the maximal mass a planet accreting pebbles can reach as a function of semi-major axis, accretion rate, and maximum Stokes number present. . . . .	231
4.6	A plot of the maximal Stokes number pebbles can reach as a function of semi-major axis and particle fragmentation velocity. The maximal particle size at a given semi-major axis is given by Equation (4.59). . . . .	234
4.7	A plot of the maximal mass a planet accreting pebbles can reach as a function of semi-major axis and particle fragmentation velocity. The maximal particle size at a given semi-major axis is given by Equation (4.59). . . . .	235
5.1	The particle size dependence of pebble and flow isolation differs. Pebble isolation (left) cuts off accretion of large particles more easily; in the presence of a distribution of particle sizes, small particles can contribute substantially to growth even when the largest particles have been cut off. In contrast, flow isolation (right) blocks small particles first, halting growth once the largest particles are blocked. The range of particle sizes that can be accreted for each mechanism (top, green region), and the resulting growth timescales (bottom, solid black lines) are shown for a core located at $r = 0.278$ au. The disk has $\alpha = 10^{-3}$ , and the maximum particle size at the planet's semi-major axis is $St_{\max} = 10^{-1}$ (dashdot blue line). In the upper panels, the particle sizes that can accrete are bounded by $St_{\text{peb}}$ (left) and $St_{\text{flow}}$ (right) (solid black lines). The mass at which the gas is excited to super-Keplerian velocities is $M_{\text{peb,iso}}^{\dagger}$ (vertical gray dashed line), and is calculated using the formula of Bitsch et al. (2018). The planet's final mass, $M_{\text{peb}}$ , determined by the point at which $t_{\text{grow}} = t_{\text{disk}} = 3$ Myr (dashed red line), is indicated by the dashed black vertical line. For flow isolation, the planet's final mass is well approximated as the mass at which particles of size $St_{\max}$ are blocked. For pebble isolation this is not the case, and calculation of the core's integrated growth timescale is required to determine the planet's final mass. . . . .	250

- 5.2 Comparison between the analytic expressions of Bitsch et al. (2018) for the pebble isolation mass ( $M_{\text{peb,iso}}^\dagger$  and  $M_{\text{peb,iso}}$ ) and numerically calculated final masses ( $M_{\text{peb}}$ ) determined by solving for the mass such that  $t_{\text{grow}} = t_{\text{disk}} = 3 \text{ Myr}$ . Each panel displays these masses as a function of semi-major axis for a distinct value of the  $\alpha$  parameter. Blue, orange, and green refer to  $St_{\text{max}} = 10^{-2}$ ,  $10^{-1}$ , and  $10^0$  respectively. The solid gray line shows the value of  $M_{\text{peb,iso}}^\dagger$  (Equation 5.14), i.e. the mass needed to excite the gas to super-Keplerian velocities, the dashdot lines show the value of  $M_{\text{peb,iso}}(St_{\text{max}})$  (Equation 5.15), i.e. the mass necessary to block particles of size  $St_{\text{max}}$ , and the symbols show the value of  $M_{\text{peb}}(St_{\text{max}})$  for a pebble size distribution given by Equation (5.8). . . . . 257
- 5.3 The value of the flow isolation mass (dashed lines, Equation 5.22 with  $f = 1.75$ ) as a function of semi-major axis, level of turbulence, and maximum particle size. Colors refer to the same values of  $St_{\text{max}}$  as in Figure 5.2. The final planet masses from pebble isolation alone (see Figure 5.2) are shown for reference. . . . . 260
- 5.4 Halting planetary growth by a combination of pebble and flow isolation. Repeated style choices are the same as in Figure 5.1. The core is located at  $r = 0.278 \text{ au}$ , and the disk has  $\alpha = 10^{-3}$ , again as in Figure 5.1. *Upper Panel:* The range of particle sizes available for accretion as a function of planet mass. The hatched regions correspond to flow isolation (negatively sloped hatching) and pebble isolation (positively sloped hatching). The two patterns are overlaid when flow and pebble isolation act simultaneously. *Lower Panel:* Growth timescale of a core for the range of particle sizes depicted in the upper panel. Two different maximum particle sizes are considered:  $St_{\text{max}} = 10^{-2}$  (upper solid line and dotted magenta line) and  $St_{\text{max}} = 10^{-1}$  (lower solid line and dashdot blue line). For  $St_{\text{max}} = 10^{-2}$ , flow isolation blocks all available particle sizes before pebble isolation kicks in, causing growth to rapidly slow as  $St_{\text{flow}} \rightarrow 10^{-2}$ , i.e. as the planet approaches the mass necessary to block particles of size  $St = 10^{-2}$ . The planet's final mass is extremely well approximated by Equation (5.22), i.e. the situation is essentially the same as if flow isolation acted alone. For  $St_{\text{max}} = 10^{-1}$ , pebble isolation begins blocking particles of size  $St_{\text{max}}$  before flow isolation can. Because the allowed range of particle sizes is also being blocked from the bottom by flow isolation, growth rapidly slows once this occurs, with the planet ending its growth very close to  $M_{\text{peb,iso}}^\dagger$ . . . . . 261

- 5.5 Final planet masses when pebble and flow isolation act in tandem, determined by numerically calculating the mass for which  $t_{\text{grow}} = t_{\text{disk}} = 3 \text{ Myr}$ . Blue, orange, and green refer to  $St_{\text{max}} = 10^{-2}$ ,  $10^{-1}$ , and  $10^0$  respectively. The solid gray line shows the value of  $M_{\text{peb,iso}}^\dagger$  (Equation 5.14), i.e. the mass needed to excite the gas to super-Keplerian velocities, the dashed lines show the value of  $M_{\text{flow}}(St_{\text{max}})$  (Equation 5.22 with  $f = 1.75$ ), and the symbols show the value of  $M_{\text{final}}(St_{\text{max}})$ , the numerically calculated final planet mass when pebble and flow isolation both operate, for a pebble size distribution given by Equation (5.8). . . . . 262
- 6.1 Sketch of the disc surface density and accretion flow in the vicinity of a planet. The planet is located at orbital radius  $r_p$ , inside a gap having surface density  $\Sigma_p$ . At  $r > r_p$ , the disc surface density is  $\Sigma_+$  and mass accretes inward at rate  $\dot{M}_+$ . Downstream of the planet, at  $r < r_p$ , the corresponding surface density and accretion rate are  $\Sigma_-$  and  $\dot{M}_-$ , respectively. The difference  $\dot{M}_+ - \dot{M}_-$  is the accretion rate onto the planet  $\dot{M}_p$ . . . . . 275
- 6.2 How the surface density profile of a viscous disc responds to a planet that both consumes disc gas, and repels gas away by Lindblad torques. Surface densities are calculated from our 1D numerical simulation of a planet of fixed mass, either  $M_p = 0.3 M_J$  (top panel) or  $M_p = 10 M_J$  (bottom panel), at  $t = 3t_{\nu,p}$  when the disc near the planet at  $r_p = 10 \text{ au}$  has viscously relaxed. When computing the planetary accretion rate  $\dot{M}_p$ , the gap is modeled as a single cell whose “true” surface density equals the grid-level  $\Sigma$  lowered by a factor of  $(1 + B/\nu) \simeq B/\nu$ ; plotted here are the true sub-grid values  $\Sigma_p$ . Accordingly, the planet’s gap is not spatially resolved and its width should not be taken literally from this figure. Red double-tipped arrows have lengths equal to their associated variables in dex, and demonstrate good agreement between numerics and analytics. The planet of mass  $M_p = 0.3 M_J$ , accreting at the Bondi rate, creates an asymmetric gap, with the inner disc surface density  $\Sigma_-$  lower than the outer  $\Sigma_+$  by  $A_{\text{Bondi}}/(3\pi B) > 1$ ; conditions are always consumption-dominated for Bondi accretion and  $B$  as given by (6.27). The planet of mass  $M_p = 10 M_J$ , accreting at the Hill rate, creates a symmetric gap where  $\Sigma_-/\Sigma_+ \sim 1$ ; conditions here are repulsion-dominated as  $M_p > M_{\text{repulsion,visc}}$  (equation 6.31). . . . . 286
- 6.3 Same as Figure 6.2 for the case  $M_p = 0.3 M_J$ , but for different choices of  $B$  scaled to  $A_{\text{Bondi}}$ . As long as  $A_{\text{Bondi}}/(3\pi) > B$ , the planet’s gap is consumption-dominated and its surface density  $\Sigma_p$  is independent of the repulsion coefficient  $B$ . The depression of the inner disc relative to the outer disc is, however, sensitive to  $B$  for  $B > \nu$ ;  $\Sigma_-/\Sigma_+ \simeq (1 + B/\nu)/[A_{\text{Bondi}}/(3\pi\nu)]$ . . . . . 288

- 6.4 Snapshots of the surface density profile  $\Sigma(r)$  and disc accretion rate  $\dot{M}_{\text{disc}}(r) = -2\pi\Sigma u_r r$  ( $> 0$  for accretion toward the star) for a planet embedded at  $r_p = 10$  au in a viscous  $\alpha = 10^{-3}$  disc. The planet mass is allowed to freely grow starting from  $M_p(0) = 0.1M_J$ . At  $t = 0.3t_{\nu,p}$ , the planet resides in a consumption-dominated, asymmetric gap (top panel, dashed curve) and accretes from regions both exterior and interior to its orbit which have not yet viscously relaxed (bottom panel, dashed curve). At the later time  $t = 3t_{\nu,p}$ , the planet has grown sufficiently (see also Figure 6.5) that its gap is now repulsion-dominated and more symmetric (top panel, solid curve); the planet now accretes only from the outer disc, reducing the flow of mass into the inner disc by less than a factor of 2 (bottom panel, solid curve. At this time we have multiplied  $\dot{M}_{\text{disc}}$  by a factor of 5 for easier viewing). . . . . 294
- 6.5 Accretion history of a planet of initial mass  $M_p(0) = 0.1M_J$  embedded at  $r_p = 10$  au (where  $h = 0.054$ ) in a viscous disc of initial mass  $M_{\text{disc}} = 15.5M_J$ . Transitions from Bondi accretion to Hill accretion ( $M_{\text{thermal}}$ , equations 6.25–6.26 and 6.28), and from consumption to repulsion-dominated gaps ( $M_{\text{repulsion,visc}}$ , equation 6.31), are indicated. An analytic estimate of the final planet mass is plotted as  $M_{\text{final,visc}}$  (equation 6.39), computed assuming repulsion-dominated conditions (at  $r_p = 10$  au for this disc mass, conditions are actually intermediate between the repulsion and consumption limits, and so plotting equation 6.42 which assumes consumption-dominated conditions would give a similar result as equation 6.39; see also Figure 6.9). . . . . 295
- 6.6 How the surface density profile of an inviscid disc responds to a planet that consumes disc gas and repels gas away by Lindblad torques. The planet, located at  $r_p = 10$  au, freely accretes starting from a seed mass of  $0.1M_J$ ; the  $\Sigma$  profile shown here is taken at a time  $t = t_{\text{adv}} = 3$  Myr, when the planet has grown to  $\sim 0.3M_J$  (see also Figure 6.8). As is the case throughout this paper, the planet’s gap is not spatially resolved, but is modeled as a single cell. The “true” surface density inside this cell equals the grid-level  $\Sigma$  lowered by a factor of  $\tilde{B}_{\text{inv}}$ , whose magnitude is given by the red double-tipped arrow. The gap is repulsion and not consumption dominated ( $\tilde{B}_{\text{inv}} > A/(2\pi r|c|)$ , equation 6.52); as such, the gap is symmetric in the sense that the surface density contrast with the outer disc is practically the same as with the inner disc. This figure is the inviscid counterpart to Figure 6.2 which was made for a viscous disc. 305

- 6.7 Snapshots of the surface density profile  $\Sigma(r)$  and disc accretion rate  $\dot{M}_{\text{disc}}(r) = -2\pi\Sigma u_r r$  ( $> 0$  for accretion toward the star) for a planet embedded in an inviscid, wind-driven disc. The planet mass is allowed to freely grow starting from  $M_p(0) = 0.1 M_J$ ; the masses corresponding to the plotted times are  $0.27 M_J$  ( $t = 0.1 t_{\text{adv}} = 0.3$  Myr) and  $0.34 M_J$  ( $t = 3 t_{\text{adv}} = 9$  Myr; see also Figure 6.8). At  $t = 3 t_{\text{adv}}$ , the disc has relaxed into a quasi-steady state in the presence of the planetary mass sink, and  $\dot{M}_{\text{disc}}(r)$  looks essentially the same as it would without the planet; the accretion rate onto the planet is negligible compared to the disc accretion rate—the gap is repulsion-dominated—and so the disc is not materially affected. Even at  $t = 0.1 t_{\text{adv}}$ , the interior surface density  $\Sigma_-$  and  $\dot{M}_{\text{disc}}$  depress by only  $\sim 15\%$  because of consumption. . . . . 306
- 6.8 Mass evolution of a planet embedded at  $r_p = 10$  au in an inviscid but still accreting disc of initial mass  $M_{\text{disc}} = 15.5 M_J$ . Within  $\sim 1$  disc advection time  $t_{\text{adv}}$ , the planet, whose gap is repulsion-dominated ( $\tilde{B}_{\text{inv}} > A_{\text{Bondi}}/(2\pi r_p |c|)$ ), grows to a mass of  $\sim 0.35 M_J$ . The final planet mass varies by only  $\sim 10\%$  when the initial seed mass  $M_p(0)$  varies by a factor of 10. This figure is the inviscid counterpart to Figure 6.5 which was made for a viscous disc. . . . . 307
- 6.9 Final planet masses grown from viscous discs having  $\alpha = 10^{-3}$  and varying total mass (top vs. bottom panels). Planet masses are initialized at  $0.1 M_J$  and grown using the 1D numerical code of section 6.3, which utilizes the repulsive gap contrast of Kanagawa et al. (2015; see also Duffell & MacFadyen 2013 and Fung et al. 2014) and gas accretion that switches from Bondi to Hill at the thermal mass. Points are plotted at  $t = 50 t_1 = 85$  Myr, where  $t_1 = r_1^2/[3\nu(r_1)]$  is the viscous diffusion time at  $r_1 = 30$  au. Analytic curves are given by equation (6.38) for the repulsion limit (dashed blue), and equations (6.42)–(6.43) for the consumption limit (dotted orange), also evaluated at  $t = 50 t_1$ . At most orbital distances, planet mass growth is limited by repulsion-dominated gaps; only at the largest distances, where the disc aspect ratio is large, are gaps relatively harder to open and conditions remain consumption-limited. The analytics, which are derived assuming the planet mass is small compared to the disc mass, are a better guide for the more massive disc in the bottom panel. . . . . 310

6.10	Final planet masses in an inviscid, wind-driven disc of varying mass (top vs. bottom panels). Planet masses are initialized at $0.01M_J$ and grown using the 1D numerical code of section 6.4.4, which uses the time-dependent gap contrast of <a href="#">Ginzburg &amp; Chiang (2019a)</a> to model repulsion, in a purely advective disc whose height-averaged radial accretion velocity is $c = -4$ cm/s and exponential drain-out time is $t_{\text{adv}} = 3$ Myr. Points are plotted after $5t_{\text{adv}} = 15$ Myr. They mostly respect equation (6.56), which gives final planet masses grown in repulsion-limited and deep ( $\tilde{B}_{\text{inv}} > 1$ ) gaps (dashed curve not including the drop-off at the largest distances). At $r_p \sim 100$ au, the disc has such low density that the planet's initial growth timescale $M_p/\dot{M}_p$ is comparable to $t_{\text{adv}}$ ; here there are not many doublings before the disc drains away. In this regime the planet does not open a substantial gap ( $\tilde{B}_{\text{inv}} < 1$ ) and its final mass can be estimated analytically by integrating $\dot{M}_p = A_{\text{Bondi}}\Sigma$ with $\Sigma$ given by the no-planet solution (6.46); the dashed curve is the minimum of the resulting expression (not shown) and (6.56). . . . .	314
7.1	The four data sets for the radial velocity of HD 200964, along with the theoretical radial velocity curve obtained using the parameters given in Table 7.5. The data sets are: Lick (pink points), Keck11 (green points), Keck (red points), and APF (blue points). Note that, as discussed in Section 7.4.1, each data set has a constant offset that we fit separately. Furthermore, the jitter term given in Table 7.5 is added in quadrature to the quoted error bars to obtain the error bars shown in the figure. The residuals between the theoretical velocity and the data are shown in the bottom panel. . . . .	325
7.2	A generalized Lomb-Scargle periodogram for the RV data of HD 200964. Note the two strong peaks at $\sim 600$ and $\sim 900$ days, demonstrating that the system likely features two closely-packed planets. The full width at half maximum of each peak is indicated by the gray rectangle. . . . .	333
7.3	A comparison of the radial velocity determined by numerically integrating the motions of the planets and by advancing the planets forward on Keplerian orbits. The orbital parameters used are our best-fit long-term stable solution, as discussed in Section 7.4.3. The top panel shows the stellar radial velocity determined by the two methods, while the bottom shows the difference in the two curves. There is substantial disagreement between the integrated and Keplerian radial velocities due to the strong planet-planet interactions present. . . . .	334

7.4	2D histograms of the posterior distributions for the planets' periods, using $N$ -body integration to calculate the radial velocity but without long-term stability (black points, see Section 7.4.1) and advancing the planets on Keplerian orbits (red points). Lines denoting exact ratios of $P_c/P_b$ are shown for ratios of 3:2 (blue), 7:5 (gray) and 4:3 (orange). . . . .	340
7.5	2D histograms of the posterior distributions for the planets' periods, using $N$ -body integration to calculate the radial velocity but without long-term stability. The black points show the posterior produced by using the full dataset, while the red points show the posterior obtained by analyzing only the <a href="#">JPH11</a> data. Lines denoting exact ratios of $P_c/P_b$ are shown for ratios of 3:2 (blue), 7:5 (gray), 4:3 (orange), and 5:4 (green). . . . .	341
7.6	Distance between planet b (black line) and planet c (blue line), and the host star for our best-fit solution without long-term stability (see Section 7.4.1). The planets experience large, non-periodic fluctuations in distance from the star due to their strong mutual perturbations. The short timescale of these fluctuations relative to the age of the host star makes it unlikely, if the proposed best fit solution were correct, that the system would be observed in the original orbital configuration. Furthermore, these fluctuations are a strong indication that the system will become unstable on timescales much less than the age of the system. This is indeed the case—planet c is eventually scattered to a distance $> 100$ AU on $10^5$ year timescales. . . . .	343
7.7	Comparison of the theoretical radial velocity curves for our best-fit, long-term stable solutions with different period ratios. <i>Top Panel:</i> Our overall maximum likelihood solution, which has $P_c/P_b \sim 7/5$ . <i>Middle Panel:</i> An example solution which shows clear libration of the 4:3 resonant angle. <i>Bottom Panel:</i> Our maximum likelihood solution that also shows libration of the 3:2 resonant angle. . . . .	352
7.8	2D histograms of the posterior distributions for the planets' periods without long-term stability (black points, see Section 7.4.1) and the three modes identified for fits conditioned on stability for $10^6 P_c$ (pink, purple, and red points, see Section 7.4.3). Note that the plotted values refer to the periods at JD 2453213.895. Lines denoting exact ratios of $P_c/P_b$ are shown for ratios of 3:2 (blue), 7:5 (gray) and 4:3 (orange). . . . .	353

7.9	Posterior probability distributions shown in Figure 7.8, with the points hexagonally binned and averaged. The points are colored by $\log P(D \theta)$ . The plotted values refer to the periods at JD 2453213.895. Note that the probability has not been properly marginalized over the other parameters, and is only meant to give a rough idea of the relative probability between the peaks (see text). Lines denoting exact ratios of $P_c/P_b$ are shown for ratios of 3:2 (blue), 7:5 (gray) and 4:3 (orange). . . . .	355
7.10	Osculating period values averaged over $500P_c$ for 1000 draws from the three modes of the posterior distribution identified by our MCMC search. Each mode lies close to a different fixed value of $P_c/P_b$ . Colors are the same as those in Figure 7.9. Lines denoting exact ratios of $P_c/P_b$ are shown for ratios of 3:2 (blue), 7:5 (gray) and 4:3 (orange). See Section 7.4.4 for a discussion. . . . .	357
7.11	2D histogram of results from a Monte Carlo simulation of stable planetary systems. Orbital parameters for the two planets are randomly drawn, and systems that pass the stability criteria described in the text are recorded. The non-stable posterior distribution of the planetary periods is shown in red, and the three long-term stable modes are shown in pink. . . . .	359
7.12	Value of the inner and outer 3:2 resonant angles for our best-fit 3:2 solution. Both angles clearly librate. . . . .	361
7.13	Value of the inner and outer 7:5 resonant angles for our best-fit solution, which are defined in Equation (7.3). The angles do appear to show libration, but the large masses of both planets involved in the resonance complicate the libration pattern, as discussed in the text and demonstrated in Figure 7.14 . . . . .	362
7.14	Evolution of $\phi_{\text{inner}}$ for the 7:5 MMR as the masses of the planets involved in the resonance are increased. For low mass planets, libration of $\phi_{\text{inner}}$ is easily discerned (middle left panel). As the mass of the perturbing planet is increased, kicks on a synodic timescale distort the libration pattern (bottom left panel; blue dashed lines denote conjunctions between the planets). If both planets have comparable mass, the center of the libration begins to circulate on the secular timescale (upper right panel). Finally, for large, comparably massive planets, both these effects serve to “wash out” the libration of $\phi_{\text{inner}}$ (lower right panel). . . . .	364
7.15	Value of the outer 4:3 resonant angle for two orbital configurations drawn from our posterior distribution. In the upper panel, we plot $\phi_{\text{outer}}$ for a case where the period ratio of the planets is close to 4:3, and $\phi_{\text{outer}}$ appears to librate. In the lower panel we plot the 4:3 outer resonant angle for our maximum solution; the angle appears to circulate in this case. . . . .	366

7.16	2D histograms of the posterior distributions for our planetary parameters from analysis of just the datasets used in <a href="#">JPH11</a> . The black points show the distribution without long-term stability, while the orange and green points show our posterior conditioned on stability for $10^6 P_c$ . Lines denoting exact ratios of $P_c/P_b$ are shown for ratios of 3:2 (blue), 7:5 (gray), 4:3 (orange), and 5:4 (green). . . . .	368
7.17	Radial velocity of the best-fitting third planet as a function of orbital phase. The radial velocity of planets b and c has been removed. . . . .	371
A.1	The Reynolds number of a small body as a function of Stokes number and semi-major axis, for the case $\alpha = 10^{-1}$ . The region where $Re > 25$ and the assumptions made in our model begin to be violated is indicated, as is the region where $r_s < 9\lambda/4$ and the particle enters the diffuse regime. For lower values of $\alpha$ the region where $Re > 25$ shrinks rapidly. . . . .	401
B.1	Analytic solution (black solid curve) for the surface density profile of a viscous disc perturbed by a planet, as given by equations (B.5), (B.6) and (B.11), using parameters as close as possible to those used in the top panel of Figure 6.2, whose numerical result is overlaid here for comparison (orange dashed curve). For our analytic unperturbed “no planet” disc (blue dashed curve) we use a power law of slope -1 and normalization at 1 au equal to the corresponding “no planet” curve in Figure 6.2. The $A$ and $B$ coefficients are taken from equations (6.25) and (6.27) for $M_p = 0.3 M_J$ . The differences between the analytic and numeric curves mainly arise from the behaviour of the outermost disc near the turn-around “transition radius” ( <a href="#">Lynden-Bell &amp; Pringle 1974</a> ; <a href="#">Hartmann et al. 1998</a> ). This transition radius, which varies with time, does not appear in our steady-state solution. . . . .	407
C.1	A corner plot showing the posterior distribution of the planetary parameters for the two planets orbiting HD 200964, without long term stability taken into account. All values for the orbital elements refer to the values at JD 2453213.895. The red lines indicate the location of the maximum likelihood parameters. . . . .	413
C.2	Corner plot showing the posterior distribution of parameters obtained by conditioning the likelihood function on stability for $10^6 P_c$ . This posterior contains our best-fit, long-term stable solution. All values for the orbital elements refer to the values at JD 2453213.895. The red lines indicate the location of the maximum likelihood parameters. . . . .	414

C.3	Corner plot showing the posterior distribution of parameters for period ratios $P_c/P_b \sim 3/2$ , obtained by conditioning the likelihood function on stability for $10^6 P_c$ . This posterior was obtained by initializing the search close to the 3:2 MMR. As can be seen in Figure 7.9, the points in this posterior have an overall lower value of log likelihood than the posterior distribution shown in Figure C.2. . . . .	415
C.4	Corner plot showing the posterior distribution of parameters for period ratios $P_c/P_b \sim 4/3$ , obtained by conditioning the likelihood function on stability for $10^6 P_c$ . This posterior was obtained by initializing the search near previously published orbital solutions. This search identifies two clear modes in $P_c$ vs. $P_b$ . Though the walkers spend more time at the lower period ratio mode, reinitializing the search at the higher period mode reveals that these solutions are a better fit to the data. See Section 7.4.3 for more detail. . . . .	416
C.5	Evolution of $\phi_{\text{inner}}$ for the 3:2 MMR as the masses of the planets involved in the resonance are increased. The panels are analogous to Figure 7.14	417
C.6	Evolution of $\phi_{\text{inner}}$ for the 4:3 MMR as the masses of the planets involved in the resonance are increased. The panels are analogous to Figure 7.14	418

# List of Tables

2.1	Summary of Symbols Used in Text . . . . .	72
2.1	Summary of Symbols Used in Text . . . . .	73
2.2	Fiducial Disk Parameters . . . . .	75
7.1	Stellar parameters for HD 200964, taken from <a href="#">Brewer et al. (2016)</a> . . . . .	322
7.2	Keck Radial Velocities for HD 200964 . . . . .	326
7.2	Keck Radial Velocities for HD 200964 . . . . .	327
7.2	Keck Radial Velocities for HD 200964 . . . . .	328
7.3	APF Radial velocities for HD 200964 . . . . .	329
7.4	Median orbital parameters, no long term stability . . . . .	339
7.5	Maximum likelihood orbital parameters, no long term stability . . . . .	340
7.6	Median orbital parameters, $10^6 P_c$ stability, 7:5 MMR . . . . .	350
7.7	Median orbital parameters, $10^6 P_c$ stability, 4:3 MMR . . . . .	351
7.8	Median orbital parameters, $10^6 P_c$ stability, 3:2 MMR . . . . .	351
7.9	Maximum Likelihood orbital parameters, $10^6 P_c$ stability, 7:5 MMR . . . . .	351
7.10	Maximum Likelihood orbital parameters, $10^6 P_c$ stability, 4:3 MMR . . . . .	354
7.11	Maximum Likelihood orbital parameters, $10^6 P_c$ stability, 3:2 MMR . . . . .	354

## Abstract

Modeling the Early, Intermediate, and Late Stages of Planet Formation

by

Mickey M. Rosenthal

With the rapid increase in our ability to observe exoplanets and exoplanetary systems over the past two decades, the amount of data available to planet formation theorists has grown considerably. This in turn has spurred development in our understanding of the physics of planet formation. In this dissertation, I discuss the work I have done to understand the physical processes that shape the architectures of the planetary systems we observe. This work can broadly be broken down into studies that cover three distinct epochs of planet formation, which I roughly term the “early,” “middle,” and “late” stages.

Chapters 2 - 5 discuss a new paradigm for the early stages of planetary growth generally referred to as “pebble accretion.” In Chapter 2, I discuss in detail an analytic model I developed to calculate how planets grow through pebble accretion, with a focus on how this process varies as a function of planetary mass, particle size, and the level of turbulence in the protoplanetary disk. I demonstrate that over a wide range of parameter space turbulence can greatly reduce the efficiency of pebble accretion. In Chapter 3 I apply these considerations to the growth of gas giant planets at wide orbital separations. I derive an inverse relationship between the level of turbulence in a protoplanetary disk and the semi-major axis at which the core of giant planet can form. In Chapter 4 I discuss how our modeling of pebble accretion naturally predicts an upper

mass limit that planets can reach, which I term the “flow isolation mass.” I discuss the characteristics of this mass scale, and discuss predictions for the architectures of planetary systems that reach the flow isolation mass in the context of new observations. Finally, in Chapter 5 I contrast growth limited by flow isolation to another limiting mass scale known as the “pebble isolation mass.” I demonstrate that because of the top-down manner in which pebble isolation inhibits particle accretion, analytic estimates of the pebble isolation mass can be off by factors as large as  $\sim 5$ , and analytic estimation of the planet’s final mass is considerably more difficult. I also show that if pebble accretion is simultaneously inhibited by pebble and flow isolation, growth generally stops at observed super-Earth mass scales over a wide range of disk parameters, and final planet masses can once again be estimated analytically in a straightforward manner.

Chapter 6 discusses the intermediate stage of planet formation, where the cores of giant planets have reached sufficient size to undergo runaway gas accretion. I discuss the two-way feedback process between the growing planet and the protoplanetary disk it feeds from. I derive analytic expressions for the planet’s perturbation to the surface density, which I broadly classify into the “consumption” and “repulsion” regimes. These analytic expressions are vetted against 1D numerical simulations, both for viscous disks that accrete due to local kinematic viscosity, and inviscid disks which accrete via magnetized winds.

Chapter 7 is concerned with the late stages of planet formation, where giant planets interact under their mutual gravity. I develop a method to fit radial velocity signals of planets where the mutual gravitational interaction is strong and the system

must be tested for long-term stability, and apply this method to the planetary system around the star HD 200964. I demonstrate that the increased time baseline from additional observations moves the best-fit period ratio from 4:3 closer to 7:5, with the 3:2 also providing plausible fits that exhibit long-term stability. I discuss these different period ratios in the context of different formation pathways.

## Acknowledgments

I want to thank my advisor Ruth Murray-Clay, for her unwavering support and guidance during the six years of my PhD. Ruth is not only one of the most brilliant scientists that I have ever had the pleasure of knowing, but is one of the most compassionate and generous as well. Her conviction to incite change and to make the world around her better is something that I continually admire and hope to emulate. I ended up working for Ruth mainly through good old-fashioned luck, and I am incredibly grateful that I did.

I was extremely fortunate during my PhD to get to meet two wonderful groups of graduate students, both at UC Santa Barbara and at UC Santa Cruz. I have met some of the most brilliant, kindest, and most fascinating people I have ever had the pleasure to interact with during my time in graduate school. Thank you to these friends for making my time in graduate school some of my best years, and for continually being sources of support and levity, both for me and for each other.

Thanks to Jenna for being my partner and confidante through the end of this journey. Having you to come home to during the long times away and being able to travel the world with you made it all worth it. Your amazing care and kindness are a continual inspiration for me.

Thank you to my family, both immediate and extended, for believing in me even when I sometimes did not. Thanks to my mother for her wisdom and guidance, thanks to my dad for his humor (and excellent music recommendations), and thanks to my sister for continually teaching me how to be a better person.

## Published Material

The text of this dissertation includes reprints of the following previously published material, led by myself, with the permission of the listed coauthors. Minor edits have been made where appropriate to enable these initially disparate manuscripts to read as one cohesive work.

Chapter 2 was published in the literature as [Rosenthal et al. \(2018\)](#). I was responsible for developing the model, building off previously unpublished work by Hagai Perets, Ruth Murray-Clay, and Natania Wolanasky. Ruth Murray-Clay supervised the work throughout its development. All of the figures and text are my own, with feedback and edits from the listed coauthors, particularly Ruth Murray-Clay.

Chapter 3 was published in the literature as [Rosenthal & Murray-Clay \(2018\)](#). This work builds off the model discussed in Chapter 2; the analysis is my own, supervised by Ruth Murray-Clay. All the figures and text are my own, again with feedback and editing by Ruth Murray-Clay.

Chapter 4 was published in the literature as [Rosenthal & Murray-Clay \(2019\)](#). This work again builds off the model discussed in Chapter 2; the analysis is my own, supervised by Ruth Murray-Clay. All the figures and text are my own, again with feedback and editing by Ruth Murray-Clay.

Chapter 6 was published in the literature as [Rosenthal et al. \(2020\)](#). This model was a collaborative effort between myself and the listed coauthors. All of the code used in the project is my own. I created all of the figures used in the project, with substantial feedback from my coauthors, particularly Eugene Chiang. The text of this chapter

represents a collaborative effort between myself and the listed coauthors, particularly Eugene Chiang, with the exception of Section B.2, which was written primarily by Eugene Chiang.

Chapter 7 was published in the literature as [Rosenthal et al. \(2019\)](#). All of the observations used for this project were performed by Jenn Burt, Bradford Holden, R. Paul Butler, and Steve Vogt. I developed the code used to fit general radial velocity signals used in this project. This code was then applied to the system HD 200964 by Wynn Jacobson-Galan, Brett Nelson, Eonho Chang, Nicholas Kaaz, and Jackson Yant. I took the initial results produced by these coauthors and used them to perform the final analysis seen in the paper. All figures used in this project are my own, with feedback from the listed coauthors, particularly Ruth Murray-Clay. All of the text is my own, again with feedback from my coauthors, particularly Ruth Murray-Clay, except for Section 7.2, which was written by Jennifer Burt.

### **Scientific Acknowledgments**

This work was supported by NSF CAREER grant number AST-1555385. Thanks to the Heising-Simons foundation for funding the undergraduate researchers with whom I was privileged to work. Chapter 7 is based on observations obtained at the W. M. Keck Observatory, which is operated jointly by the University of California and the California Institute of Technology, and we thank the UC-Keck and NASA-Keck Time Assignment Committees for their support. We also wish to extend special thanks to those of Hawaiian ancestry on whose sacred mountain of Mauna Kea we are privileged to be guests. Without their generous hospitality, the Keck observations presented

herein would not have been possible. The work herein was also based on observations obtained at the Automated Planet Finder (APF) facility and its Levy Spectrometer at Lick Observatory. Computations were carried out using the Hummingbird computational cluster at UC Santa Cruz. Simulations in this paper made use of the REBOUND code which is freely available at <http://github.com/hannorein/rebound>.

Thanks to the professors at UC Santa Barbara, particularly Peng Oh and Lars Bildsten, for being my teachers and mentors during the early stages of time as a graduate student.

Thanks as well to Hagai Perets for his help on completing my first paper, and for all his time discussing the interesting physics of planet formation, which has led to many avenues of future inquiry. Thanks very much to Eugene Chiang and Sivan Ginzburg for their guidance and help completing our consumption paper. I learned an incredible amount working on this paper and it was invaluable for my growth as a scientist. My sincerest thanks to the other members of my research group: Diana, John, Renata, and Tyler. I am extraordinarily thankful that I got to embark on the journey of grad school with peers who were not only such gifted scientists, but amazing friends as well.

*Dropping science like Galileo dropped the orange*

*-The Beastie Boys*

# Chapter 1

## Introduction

Planet formation theory has the distinction of being perhaps the only scientific theory that, for a good deal of its life, grew out of analysis of a single data point, namely our solar system. There is obviously a sense in which this statement is simplistic, as there is a large and diverse set of data to be gained from analysis of the solar system. Indeed, [Lissauer \(1993\)](#) begins his review of planet formation theory, written before the discovery of the first exoplanet, by listing a huge number of observations that theories of planet formation must explain. Furthermore this data is far more precise than what can currently be obtained from exoplanetary systems, and will be for the foreseeable future. However, for astrophysicists who wish to compare theoretical predictions for the architectures of planetary systems with observations, the solar system was the only point of comparison for a great deal of the growth of planet formation theory. Nonetheless, prior to the discovery of exoplanetary systems, a great deal of work had been done in understanding the physics of planet formation. Much of this work is still relevant today,

and is used in our analysis of exoplanetary systems. In this introduction, I will briefly discuss some basic idea in the theory of planet formation, all of which were developed before the rapid discovery of exoplanets began in the 2000s. This discussion will be supplemented by order of magnitude derivations of some of the relevant physics.

## 1.1 The Protoplanetary Disk

The first proposals that planetary systems form from disks which are the left-over products of star formation are generally attributed to [Kant \(1755\)](#) and [Laplace \(1796\)](#). While over the centuries this theory went in and out of favor, formation from a protoplanetary disk is the currently favored paradigm for planet formation, partially because modern day observational techniques allow us to not only verify that young stars host disks of gas and dust, but to perform detailed observations of these disks as well (see [Andrews 2020](#) for a review).

Early observations suggested that lifetime of these protoplanetary disks were short,  $\lesssim 3 \times 10^7$  years ([Walter et al. 1988](#)); this result is held up by modern observations, which suggest protoplanetary disk lifetimes of order  $\lesssim 10$  Myr ([Mamajek 2009](#), [Andrews 2020](#)). If protoplanetary disks act as viscous accretion disks, then the evolution timescale of the disk is roughly  $t \sim r^2/\nu$ , where  $r$  is the semi-major axis and  $\nu$  is the kinematic viscosity. For these lifetimes to be produced by disk evolution, we would therefore require viscosities of order

$$\nu \sim \frac{r^2}{t} \sim \frac{(1 \text{ au})^2}{1 \text{ Myr}} \sim 10^{13} \text{ cm}^2\text{s}^{-1} \quad (1.1)$$

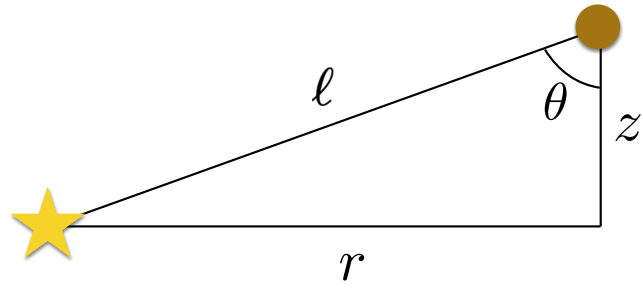


Figure 1.1: Cartoon sketch of the force on a gas parcel in a protoplanetary disk.

These viscosities are far too large to be produced by molecular viscosity  $\nu_{\text{mol}}$ , and it thus common to parameterize the gas viscosity using the Shakura-Sunyaev  $\alpha$  parameter (Shakura & Sunyaev 1973)

$$\nu = \alpha c_s H \tag{1.2}$$

where  $c_s = \sqrt{kT/\mu}$  is the local isothermal sound speed,  $k$  is Boltzmann's constant,  $\mu$  is the mean molecular weight of the gas, and  $H$  is the scale height of the gas. An estimate of  $c_s$  and  $H$  would allow us to estimate  $\alpha$ .

Due to the low overall temperatures in protoplanetary disks, the disk is thin ( $H/r \ll 1$ ), which allows a simple estimation of gas scale height as follows: writing down pressure balance for a gas parcel yields (see Figure 1.1)

$$\frac{GM_*}{\ell^2} \cos \theta = \frac{1}{\rho} \frac{dP}{dz} \tag{1.3}$$

where  $P$  is the local pressure and  $\rho$  is the local density. Assuming the disk is thin so that  $\ell \approx r$ , and using an order of magnitude derivative, we have

$$\frac{GM_*}{r^2} \frac{z}{r} = \frac{1}{\rho} \frac{P}{z} \tag{1.4}$$

Replacing  $P/\rho$  with the isothermal sound speed,  $c_s = \sqrt{kT/\mu} = \sqrt{P/\rho}$ , and using the

fact that  $GM_*/r^3 = \Omega^2$ , we have

$$z = \frac{c_s}{\Omega} \quad (1.5)$$

that is, the height of the disk is roughly  $H = c_s/\Omega$ . We can get a better sense of the vertical density structure by solving the differential equation in (1.3)

$$\frac{GM_*}{r^2} \frac{z}{r} = -\frac{1}{\rho} \frac{dP}{dz} \quad (1.6)$$

$$c_s^2 \frac{d\rho}{\rho} = -\Omega^2 z dz \quad (1.7)$$

$$\ln\left(\frac{\rho}{\rho_0}\right) = -\frac{z^2}{2c_s^2/\Omega^2} \quad (1.8)$$

or

$$\rho(z) = \rho_0 e^{-\frac{z^2}{2H^2}} \quad (1.9)$$

so  $H = c_s/\Omega$  is the  $e$ -folding length of the vertical density profile.

The disk temperature profile is generally set by either viscous accretion or passive irradiation (Chiang & Goldreich 1997). The profile from viscous heating can be obtained by first noting that the rate of energy dissipation from shear per unit area is

$$J_{\text{in}} \sim \Sigma \nu (\text{Rate of shear})^2 = \Sigma \nu \left( r \frac{\partial \Omega}{\partial r} \right)^2 \sim \Sigma \nu \Omega^2 \quad (1.10)$$

The rate that the disk can radiate out this energy is roughly

$$J_{\text{out}} \sim \sigma_{\text{SB}} T^4 \quad (1.11)$$

where  $\sigma_{\text{SB}}$  is the Stefan-Boltzmann constant. Equating these quantities, and using the usual expression  $\dot{M} \sim \Sigma \nu$  for a steady state accretion disk yields

$$T \propto \dot{M} r^{-3/4} \quad (1.12)$$

For passive irradiation, the disk receives a stellar flux of  $L_*/(4\pi r^2)$  over some area  $A$ . Because the disk flares, the flux is absorbed at an angle  $\varphi \sim H/r$ . Equating the heating and cooling rates gives

$$\frac{L_*}{4\pi r^2} A \frac{H}{r} \sim \sigma_{\text{SB}} A T^4 \quad (1.13)$$

$$T^{7/2} \propto \frac{1}{\Omega r^3} \quad (1.14)$$

so

$$T \propto r^{-3/7} \quad (1.15)$$

Note that the profile from viscous heating falls off much more sharply with semi-major axis than the profile from passive irradiation. Thus, the inner regions of protoplanetary disks are likely dominated by viscous heating, with the outer regions dominated by passive irradiation.

Early analyses of the structure of the protoplanetary disk from which the solar system formed suggest that the inner regions of disks contain far less mass than the outer regions, which is an important component for predicting the architectures of general planetary systems. [Weidenschilling \(1977b\)](#) and [Hayashi \(1981\)](#) discuss the idea of a “minimum-mass solar nebula” (MMSN), which, as the name implies, is a minimum mass estimate for the solar nebula. This estimate is obtained by enhancing the composition of each planet to solar, and taking the resulting mass and spreading it over non-overlapping annuli spanning the orbit of each planet. The resulting disk has a mass of  $1 - 2 \times 10^{-2} M_{\odot}$ , and a surface density profile that scales as  $\Sigma \propto r^{-3/2}$ . This  $r^{-3/2}$  scaling implies that the mass of the disk is an increasing function of semi-major axis, as

$$M_{\text{disk}} \sim \int 2\pi r \Sigma(r) dr \propto r^{1/2} \quad (1.16)$$

Another estimate of the structure of the proto-solar disk can be obtained by modeling the disk as a viscous accretion disk. Neglecting the self-gravity of the disk, the governing equation for the time evolution of the disk is given by

$$\frac{\partial \Sigma}{\partial t} = \frac{3}{r} \frac{\partial}{\partial r} \left[ r^{1/2} \frac{\partial}{\partial r} \left( r^{1/2} \nu \Sigma \right) \right] \quad (1.17)$$

If the viscosity can be written as a simple power law in  $r$ , independent of  $t$ , i.e.  $\nu \propto r^{\gamma}$

this admits a similarity solution

$$\Sigma(r, t) = \frac{M_{\text{disk},0}(2 - \gamma)}{2\pi r_1^2} \left(\frac{r_1}{r}\right)^\gamma (1 + t/t_s)^{\frac{-5/2-\gamma}{2-\gamma}} \exp\left[-\frac{(r/r_1)^{2-\gamma}}{1 + t/t_s}\right] \quad (1.18)$$

where  $r_1$  is a characteristic disk radius,  $M_{\text{disk},0}$  is the initial disk mass and  $t_s = [3(2 - \gamma)]^{-1} r_1^2 / \nu(r_1)$  is the viscous timescale at  $r_1$  (Lynden-Bell & Pringle 1974). If we use the Shakura-Sunyaev  $\alpha$  parameterization of the viscosity,  $\nu = \alpha H^2 \Omega$ , where  $H$  is the gas scale height and  $\Omega$  is the local Keplerian orbital frequency, then for usual protoplanetary disk conditions  $\nu$  scales approximately as  $r^1$  (e.g. for a passively irradiated disk  $\nu \propto T/\Omega \propto r^{-3/7} r^{3/2} \propto r^{15/14}$ ). This in turn implies that the surface density scales as approximately  $\Sigma \propto r^{-1}$  and the mass profile scales as  $M \propto r^1$ , again implying that most of the mass is the in outer regions of the disk.

## 1.2 Early Solid Growth

The early stages of solid growth, up to  $\lesssim$  km sized objects, dubbed “planetesimals,” was not given as much attention in early studies of planet formation theory as the later stages. It was generally thought that particles grew collisionally from  $\mu\text{m}$  sized grains inherited from the ISM up to planetesimal sizes. There are serious problems with this scenario however. A chief issue is the radial drift of solids due to the sub-Keplerian rotation of the gaseous component of the disk (Weidenschilling 1977a, Nakagawa et al. 1986). This issue is straightforward to demonstrate using order of magnitude calculations: due to the pressure gradient in the disk, the net force on gas parcel on a circular

orbit is

$$\frac{GM_*}{r^2} = \frac{1}{\rho} \frac{dP}{dr} + \frac{v_{\text{gas}}^2}{r} \quad (1.19)$$

where  $P$  is the local pressure,  $\rho$  is the local gas density and  $M_*$  is the mass of the central star. Approximating  $dP/d\rho \sim P/\rho$  and solving for  $v_{\text{gas}}$  gives

$$v_{\text{gas}} \sim \sqrt{v_k^2 - c_s^2} \quad (1.20)$$

$$= v_k \sqrt{1 - \left(\frac{H}{r}\right)^2} \quad (1.21)$$

$$\approx v_k \left(1 - \frac{H^2}{2r^2}\right) \quad (1.22)$$

where we've performed a binomial expansion assuming  $H/r \ll 1$ . This is generally written as

$$v_{\text{gas}} = v_k (1 - \eta) \quad (1.23)$$

where  $\eta \equiv H^2 / (2r^2) = c_s^2 / (2v_k^2)$ .

Because of the gas' sub-Keplerian velocity, particles will experience a headwind, which will cause them to drift inwards. For this derivation, we assume that particles are well coupled to the gas, in the sense that their azimuthal velocity relative to Keplerian is  $\sim \eta v_k$ . We write the drag force on the small body as  $F_d/m = v_{\text{rel}}/t_s$ , where  $t_s$  is the "stopping time" of the small body, defined as  $t_s \equiv mv_{\text{rel}}/F_D$  and  $v_{\text{rel}}$  is the relative velocity between the small body and the gas. Note that we can always

write the gas drag force in this manner, but for drag laws which are linear in  $v_{\text{rel}}$ ,  $t_s$  is a function only of the disk and particle properties, making this form much more convenient. Assuming this is the case for our small body, we can write down force balance in the radial direction and simplify. Noting that for radial drift  $v_{\text{rel}} = \dot{R}$ , where  $R$  is the radial distance from the star, we have:

$$\frac{GM_*}{R^2} = -\frac{\dot{R}}{t_s} + \frac{v_\phi^2}{R} \quad (1.24)$$

$$\frac{GM_*}{R^2} = -\frac{\dot{R}}{t_s} + \frac{v_k^2}{R} (1 - \eta)^2 \quad (1.25)$$

$$\frac{\dot{R}}{t_s} = \frac{v_k^2}{R} (1 - \eta)^2 - \frac{v_k^2}{R} \quad (1.26)$$

$$\frac{\dot{R}}{t_s} \approx -2 \frac{\eta v_k^2}{R} \quad (1.27)$$

where in going from the penultimate line to the last we've performed a binomial expansion on  $\eta$ . Solving for  $\dot{R}$  gives:

$$\dot{R} = -2\eta v_k \tau_s \quad (1.28)$$

where  $\tau_s \equiv t_s \Omega$ .

Noting that  $\eta \sim 10^{-2} - 10^{-3}$  we therefore predict that solids with  $\tau_s \sim 1$  will inspiral into the star on timescales of  $\sim 10^3 \Omega^{-1}$ , which is much shorter than the lifetime of the disk. This is clearly an issue if we wish to collisionally grow particles, as it implies that particles must rapidly grow past  $\tau_s = 1$  in order to save themselves from being lost in the central star.

Because of this and other issues with collisional growth, a competing theory is

direct collapse of particles to sizes large enough to prevent this inspiral. One mechanism for this collapse was proposed by [Goldreich & Ward \(1973\)](#), who proposed that particles settling to the disk midplane could reach high enough densities to trigger gravitational collapse. While it was later pointed out that fluid instabilities such as the Kelvin-Helmholtz instability would prevent this mechanism from reaching large enough densities to trigger gravitational collapse, the idea of directly collapsing solids to planetesimal sizes continues to be well studied today, with the streaming instability ([Youdin & Goodman 2005](#)) being a particularly promising mechanism to produce planetesimals.

### 1.3 Growth from Planetesimals

A good deal of early planet formation research focused on the formation of planets via accretion of planetesimal sized objects (e.g. [Safronov 1972](#), [Petit & Henon 1986](#), [Dones & Tremaine 1993](#), see [Goldreich et al. 2004](#) for a review). For objects of this size, gravitational interactions become extremely important. The approximate gravitational sphere of influence between bodies can be estimated as follows (see Figure 1.2):

Imagine a small body entering from  $\infty$  with velocity  $v_\infty$  towards a large body of mass  $M_p$ . What is the impact parameter  $b$  needed so that the small body will just graze the surface of the large body? From conservation of angular momentum, we have

$$bv_\infty = R_p v_{\text{surf}} \tag{1.29}$$

where  $R_p$  is the radius of the large body and  $v_{\text{surf}}$  is the velocity of the small body when

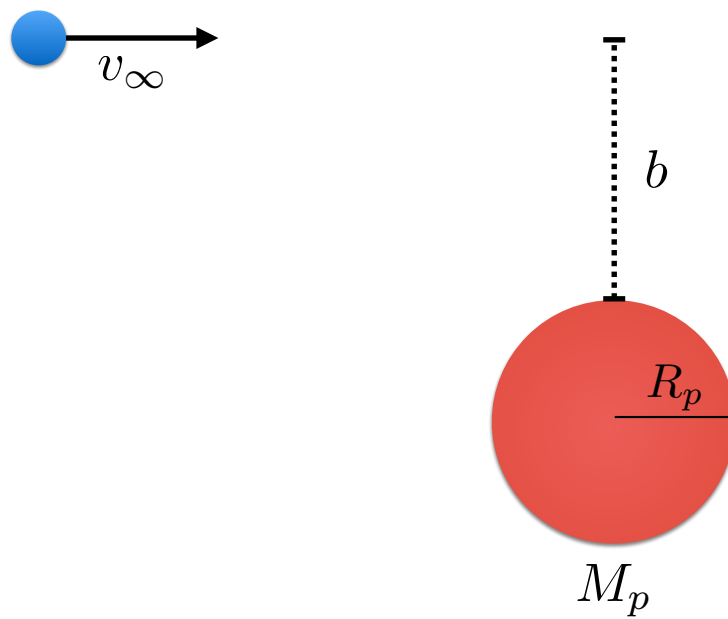


Figure 1.2: Problem setup for estimation of the gravitational focusing radius.

it grazes the surface. Using conservation of energy, we have

$$\frac{1}{2}v_\infty^2 = \frac{1}{2}v_{\text{surf}}^2 - \frac{GM_p}{R_p} \quad (1.30)$$

$$v_{\text{surf}} = v_\infty \sqrt{1 + \frac{v_{\text{esc}}^2}{v_\infty^2}} \quad (1.31)$$

where we've used the fact that  $2GM_p/R_p$  is the escape velocity from the large body.

Thus, the impact parameter  $b$  for grazing the large body is

$$b = R_p \sqrt{1 + \frac{v_{\text{esc}}^2}{v_\infty^2}} \quad (1.32)$$

This is minimal impact parameter needed to “gravitationally focus” small bodies into a collision with a larger one. If the velocity dispersion ( $v_\infty$ ) of the small bodies is comparable to the escape velocity from the large body, the large body can only accrete small bodies that are within its geometric cross section. As the velocity dispersion of the small bodies decreases the cross section for accretion can be much larger than the physical radius of the large body.

Because the largest bodies grow the fastest, if we begin with distribution of planetesimal sizes the largest ones will quickly run away, dominating their local region. These large bodies are referred to as “oligarchs”, with different oligarchs dominating their respective feeding zones. We can get a sense of how large these feeding zones are by calculating these protoplanets’ gravitational sphere of influence, also known as the “Hill radius.” This radius is determined by equating the stellar tidal gravity with the

planet’s gravity:

$$\frac{GM_*}{a^2} \frac{R_H}{a} = \frac{GM_p}{R_H^2} \quad (1.33)$$

$$R_H = a \left( \frac{M_p}{M_*} \right)^{1/3} \quad (1.34)$$

A more careful derivation would give a factor of  $3^{1/3}$  in the denominator.

Planetesimals that undergo close encounters with an oligarch have their random velocity excited to  $\sim R_H \Omega \equiv v_H$  (Petit & Henon 1986), which is known as the “Hill velocity.” This velocity provides a lower bound for the velocity dispersion of the planetesimals, and therefore provides an upper bound for the protoplanet’s growth rate. If we assume that planetesimals’ vertical velocity is roughly  $v_H$  as well, leading to scale height of  $H_p \sim v_H/\Omega = R_H$ , then the protoplanet’s growth rate is roughly

$$\dot{M}_p \sim \rho \sigma v_\infty \sim \frac{\Sigma_p}{R_H} R_p^2 \left( 1 + \frac{v_{\text{esc}}^2}{v_H^2} \right) v_H \quad (1.35)$$

where  $\rho$  is the mass density of planetesimals,  $\sigma$  is the accretion cross section, and  $\Sigma_p$  is the surface density of planetesimals. Noting that  $v_{\text{esc}}^2/v_H^2 \sim r M_p^{1/3}/(R_p M_*^{1/3}) \sim (r/R_*) (\rho_p/\rho_*) \gg 1$ , where  $\rho_p$  and  $\rho_*$  are the densities of the protoplanet and the star, we have

$$\dot{M}_p \sim \Sigma_p R_p R_H \Omega \quad (1.36)$$

Note that because  $R_H \Omega \propto r^{-1/2}$ , and  $\Sigma_p$  very likely decreases as we move outwards in

the disk, growth rates are faster closer to the star, and slow down as we move to larger semi-major axes.

Eventually the oligarchs will consume all of the material in their local feeding zone, ending their growth at the “isolation mass.” Assuming that each embryo can feed on scales  $\sim R_H$ , the isolation mass is roughly

$$M_{\text{iso}} \sim \Sigma_{\text{p}} r \Delta r \sim \Sigma_{\text{p}} r^2 \left( \frac{M_{\text{iso}}}{M_*} \right)^{1/3} \quad (1.37)$$

or

$$M_{\text{iso}} \sim \frac{(\Sigma_{\text{p}} r^2)^{3/2}}{M_*^{1/2}} \quad (1.38)$$

Note that unless the scaling on  $\Sigma_{\text{p}}$  is steeper than  $r^{-2}$ , the isolation mass will increase as we move outwards in the disk.

The spacing between isolation mass embryos is not expected to be large enough that the isolation mass embryos are dynamically isolated. These embryos will eventually excite each other onto crossing orbits, where they will eventually collide and merge. This phase of growth is known as the “giant impact” phase, and proceeds on timescales much longer than the lifetime of the gaseous component of the protoplanetary disk ( $\sim 10^8$  years, e.g. [Lissauer 1993](#)).

## 1.4 Growth of Gas Giants

In the early stages of the protoplanetary disk, while the gaseous component is still present, solid protoplanets that reach sufficient mass will be able to gravitationally bind local gas and accrete an atmosphere. The distance interior to which the planet can gravitationally bind gas, i.e. the extent of the planet’s atmosphere, can be roughly estimated by equating the escape velocity from the planet with the local isothermal sound speed

$$c_s \sim \sqrt{\frac{GM_p}{R_B^2}} \Rightarrow R_B = \frac{GM_p}{c_s^2} \quad (1.39)$$

which defines the planets’ “Bondi radius.” The planet will be able to accrete an atmosphere if  $R_B \gtrsim R_p$ .

As the planet grows the mass of its atmosphere will increase. As early as the 1970s, it was recognized that if the atmosphere reaches sufficient mass, then a hydrostatic solution is no longer possible, and the atmosphere will collapse onto the planet, triggering rapid accretion (Cameron 1973, Perri & Cameron 1974). Early estimates of the critical core mass required to trigger this runaway accretion were around  $M_{\text{crit}} \sim 10 - 15 M_{\oplus}$  (Mizuno 1980, Pollack et al. 1996), though the value of  $M_{\text{crit}}$  remains an open question (see e.g. Piso et al. 2015, Lee & Chiang 2015).

This mechanism for forming gas giant planets is known as the “core accretion” scenario. Note that the idea that a gas giant can form only if a sufficient mass in solids is accumulated, combined with the short lifetime of the gas disk and the long

timescales for embryos to grow past isolation mass, is in qualitative agreement with the architecture of the solar system: in the inner solar system, isolation masses are low (Equation 1.38), but growth rates are fast (Equation 1.36). Planets therefore rapidly become stuck at their isolation mass, resulting in lower mass rocky planets with little mass in gas. In the outer solar system, isolation masses are large but growth is slow. Thus we end up with the ice giants – massive embryos that grew too slowly to reach  $M_{\text{crit}}$  within the lifetime of the gas disk but still accreted some mass in gas from the nebula. It is only at intermediate semi-major axes that growth rates are fast enough and isolation masses large enough that isolation mass embryos can reach  $M_{\text{crit}}$  while the gas disk is still present and trigger runaway gas accretion.

An alternative to core accretion, where giant planets directly collapse from the gas disk due to gravitational instability, has been proposed as well, and continues to be studied today (see [Kratter & Lodato 2016](#) for a review).

## 1.5 Ending Runaway Accretion

What halts the stage of runaway gas accretion once it starts? The possibility of giant planets opening gaps in disks has long been considered a possible way to cut off runaway accretion ([Goldreich & Tremaine 1980](#), [Lin & Papaloizou 1993](#)). With more modern studies showing that protoplanetary disks may be quite massive (e.g. [Tripathi et al. 2017](#), [Powell et al. 2017](#)), and observations showing annular gaps in protoplanetary disks ([Zhang et al. 2018](#)), research into the details of the gap opening process continues to be important.

At its core, the process of gap opening stems from the torque imparted to the protoplanetary disk. The magnitude of this torque can be estimated to order of magnitude as follows: consider a planet embedded in a gas disk, with semi-major axis  $r$ . A gas parcel comes by and encounters planet, so that its velocity is deflected by an angle  $\beta$ , as shown in the figure.

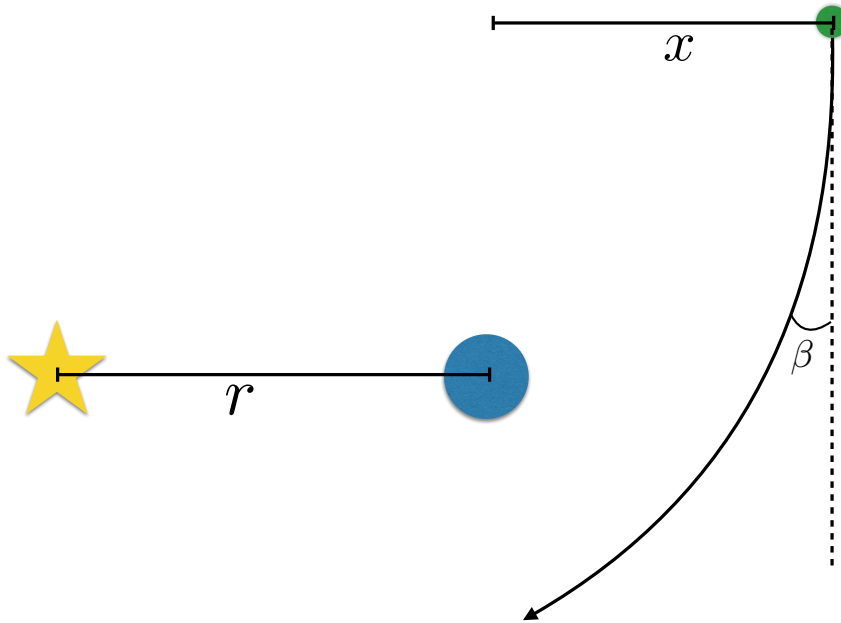


Figure 1.3: Setup for the calculation of the torque from a gas giant on the surrounding disk.

We want to calculate the angle  $\beta$ , and then use this angle to calculate the torque exerted on the parcel. We use an impulse approximation to calculate the angle,

that is

$$\Delta p = F \Delta t \quad (1.40)$$

$$m \Delta v = \frac{GM_p m}{x^2} \frac{x}{\Omega x} \quad (1.41)$$

$$\Delta v = \frac{GM_p}{x^2 \Omega} \quad (1.42)$$

where we've used the Keplerian shear  $v_0 = \Omega x$  to calculate the parcels velocity relative to the planet, and  $\Omega$  is, as usual, the local orbital frequency. Assuming that this perturbation to velocity is small, we have

$$\tan \beta \sim \beta \sim \frac{\Delta v}{\Omega x} = \frac{GM_p}{x^3 \Omega^2} \quad (1.43)$$

so

$$\beta \sim \frac{M_p r^3}{M_* x^3} \quad (1.44)$$

where we've used Kepler's 3rd law,  $GM_* = \Omega^2 r^3$ . The change in the particle's  $\hat{y}$  velocity is therefore

$$\Delta v_y = v - v \cos \beta \approx v \beta^2 \quad (1.45)$$

where we've used the second order Taylor expansion of cosine,  $\cos \beta = 1 - \beta^2/2 + O(\beta^4)$ , and dropped the factor of 1/2.

The change in angular momentum from the encounter is therefore

$$\Delta J = mr\Delta v_y \sim mr\Omega x\beta^2 \quad (1.46)$$

This is the torque on a single parcel. If we want the total torque on the disk, which will also be the torque on the planet, we need to include the encounter rate of the planet with the gas parcels.

$$T = \Delta J \times \left( \frac{\text{Encounters}}{\text{Time}} \right) = \Delta J \left( \frac{\Sigma}{m} \right) x (\Omega x) \quad (1.47)$$

Thus

$$T = mr\Omega x \left( \frac{M_p}{M_*} \right)^2 \frac{r^6}{x^6} \left( \frac{\Sigma}{m} \right) \Omega x^2 \quad (1.48)$$

Rearranging this equation

$$T = q^2 \left( \frac{r}{x} \right)^3 \Sigma \Omega^2 r^4 \quad (1.49)$$

where  $q \equiv M_p/M_*$ . To complete this calculation, we'd need to integrate over all values of  $x$ . The way this is often done is to note that the torque is larger at smaller  $x$ , and that the smallest location where the torques from different orbital phases add coherently is on the scale of the disk scale height  $H$ . The torque is then

$$T = \frac{q^2}{h^3} \Sigma \Omega^2 r^4 \quad (1.50)$$

where  $h \equiv H/r$ .

Calculation of the surface density local to the planet, i.e. the surface density available for accretion, is complex, and generally must be done with hydrodynamical simulations. However, it turns out, as demonstrated by [Fung et al. \(2014\)](#), that a good approximation for the local surface density can be found by equating the planetary torque, evaluated inside the gap, with the viscous torque evaluated outside the gap,  $T_\nu \sim \Sigma_0 \nu \Omega r^2$ . That is

$$\frac{q^2}{h^3} \Sigma_{\text{gap}} \Omega^2 r^4 \sim \Sigma_0 \nu \Omega r^2 \quad (1.51)$$

Using an  $\alpha$  disk model, i.e.  $\nu = \alpha h^2 r^2 \Omega$ , gives

$$\frac{\Sigma_{\text{gap}}}{\Sigma_0} \sim \frac{\alpha h^5}{q^2} \quad (1.52)$$

which agrees well with simulations for sub-thermal planets, i.e.  $M_p < 3h^3 M_*$ .

Modern research into gap opening focuses on the exact mechanisms by which gaps are opened (e.g. [Goodman & Rafikov 2001](#), [Ginzburg & Sari 2018](#)), the depths of gaps opened by planets (e.g. [Tanigawa & Tanaka 2016](#)) and final planet masses of planets.

## 1.6 Outline of Dissertation

In this dissertation, I will discuss work I have done investigating how planets form, which builds off the ideas presented in this introduction. In Chapters 2 - 5 I

discuss modeling of a theory for forming rocky planets known as “pebble accretion.” These pebble sized objects interact strongly with the nebular gas, allowing them to be captured on far shorter timescales than the timescales for planetesimals discussed above. In Chapter 6 I discuss how an accreting planet affects the structure of the gas disk from which it accretes, and how this two-way feedback process can be used to determine the final mass that gas giant planets are able to reach. Finally, in Chapter 7 I discuss work I have done modeling the radial velocity signals of gas giant planets in mean-motion resonances. Giant planets in such resonances provide evidence of the dynamical interactions these bodies underwent after they finished growing, in the late stages of the planet formation process.

## Chapter 2

# Gas Assisted Growth of Planets in a Turbulent Medium

### 2.1 Introduction

In the core accretion model of gas giant formation, the growth of a gas giant is constrained by two main factors: the growth timescale of the planet relative to the lifetime of the gas disk, and the amount of solid material available for a growing planet to accrete. Because early stages of formation were not well understood, many classic models of planet formation focus on later stages of growth, beginning with solid “planetesimals” of size  $\gtrsim$  km. In these models, growth is too slow to produce gas giants at wide orbital separations. In contrast, close to the host star there is insufficient material locally available to produce a solid core massive enough to grow a gas giant. While these processes can produce architectures similar to the solar system, they are not suf-

ficient to explain the diverse system architectures that are observed around other stars. In particular, recent theoretical work has pointed to the possibility that accretion of “pebble” sized bodies may be important in both determining the growth timescale of cores and providing a reservoir of solid material through radial drift (Ormel & Klahr 2010, Perets & Murray-Clay 2011, Ormel & Kobayashi 2012, Lambrechts & Johansen 2012, Lambrechts et al. 2014, Levison et al. 2015a, Morbidelli et al. 2015, Visser & Ormel 2016, Ida et al. 2016, Xu et al. 2017). In this paper we will introduce an order of magnitude model of protoplanetary growth by pebble accretion, focusing on the regime in which the core is sufficiently massive that the gravity of the core is non-negligible. In what follows we will use the term “protoplanet” to refer to cores in this regime. We will focus on incorporating the effects of local disk turbulence into the various length and velocity scales that set the growth timescale.

Before proceeding, we briefly define a number of standard terms that will be used throughout this work. Within the context of a bottom up formation model, the growth of gas giant planets proceeds by “core accretion” – a gas giant core grows until it reaches a large enough mass,  $M_{\text{crit}}$ , that its atmospheric mass is comparable to its core mass. At this point the core rapidly accretes gas from the nebula, culminating in a gas giant (see e.g. Pollack et al. 1996). In this work we will not address the physics that set  $M_{\text{crit}}$  (see e.g. Rafikov 2006, Piso et al. 2015), and will instead consider growth timescales as a function of core mass. In the absence of some dissipative mechanism, the largest enhancement to the collision cross section comes from “gravitational focusing” by the large cores. Gravitational focusing refers to the effect where large bodies can accrete

material with impact parameters far outside their physical radius through the influence of gravity. This effect is significant for particles with velocity dispersions smaller than the large body escape velocity. In what follows we will refer to models of core accretion where gravitational focusing is the largest enhancement to the accretion cross section as “canonical core accretion” or “planetesimal accretion.”

Two particular challenges to planetesimal accretion stem from the existence of directly imaged planets at wide orbital separations and “Super Earths” close in to their host stars. The star HR8799 has a system of four gas giants orbiting at  $a \approx 15 - 70$  AU (Marois et al. 2008, Marois et al. 2010).  $N$ -body integrations show that it is unlikely that this system was formed by scattering (Dodson-Robinson et al. 2009), indicating that these planets likely formed *in situ*. Gravitational instability may be an alternative way to form the HR8799 planets, as reviewed by Kratter & Lodato (2016). However, Kratter et al. (2010) argue that, if formed by gravitational instability, the wide orbital separation gas giants should represent the low-mass tail of a distribution of stellar companions. Thus far, observations do not clearly connect the population of wide orbital separation gas giants to the Brown Dwarf population (Bowler 2016). There exist a number of other wide separation gas giants, but whether they formed *in situ* is less well constrained. Super Earths are difficult to explain through local isolation mass due to their large masses and proximity to the central star. At such small orbital separations, there is not enough material locally to grow such massive planets without causing the protoplanetary disk to become unstable to collapse (Schlichting 2014), indicating that radial drift of particles may be an important factor in planet formation. More massive

particles can also move radially due to Type I migration and/or gas dynamical friction (e.g. [Grishin & Perets 2015](#)).

These difficulties can be amended through a more detailed consideration of the interaction between the gas present in the disk and the material accreted by the growing cores. While the effect of gas drag on smaller ( $\lesssim 0.1 - 1$  km) planetesimals can be substantial ([Rafikov 2004](#)), even more striking is the effect of drag on smaller, mm–cm sized particles. For these bodies gas drag can enhance accretion rates by dissipating the relative kinetic energy between the small bodies and growing cores during their interaction. Due to the sizes of bodies for which this is possible, this process is commonly referred to as “pebble accretion.” We will alternatively refer to this process as “gas-assisted growth,” to highlight the idea that enhancements to growth come from the constructive effect of collisions between the small bodies being accreted and the gas particles, and to avoid confusion with the geological use of the term “pebble.” We also note that “pebbles” need not necessarily be particles of small sizes, but could also include “fluffy” aggregates of low density that have similar aerodynamic properties to rocky mm–cm sized particles. Because the term “pebble accretion” is well established, we use these two terms interchangeably.

Models of gas-assisted growth in the context of planet formation find that gas drag acting on pebble sized particles can lead to substantially higher growth rates than models that rely on growth by planetesimal accretion. For a wide range of disk parameters, massive ( $M \gtrsim 10^{-3} M_{\oplus}$ ) cores can accrete pebble sized particles at impact parameters comparable to the core’s Hill radius ([Ormel & Klahr 2010](#); [Lambrechts &](#)

Johansen 2012). If particles of these sizes are present, cores accreting at these rates can easily grow a gas giant at wide orbital separation, as opposed to cores undergoing planetesimal accretion. The presence of these smaller pebbles is supported by observations of protoplanetary disks. Matching observations of the spectral energy distribution of disks requires a dust size distribution where most of the mass is in  $\sim 1$  mm sized particles (D'Alessio et al. 2001), while sub-mm images of disks find solid surface densities in this size range which are comparable to the minimum mass solar nebula (Andrews et al. 2009, Andrews 2015).

While these rapid growth timescales can solve some of the issues present in growing wide orbital separation gas giants, they present issues of their own. Chief among these is that pebble accretion is, in some respects, *too* efficient. Because the growth rate at large masses is so fast, the last doubling timescale to  $M_{\text{crit}}$  is extremely short in pebble accretion. Thus gas-assisted growth seems to predict that growth of gas giants should be a ubiquitous phenomenon. Direct imaging surveys, however, place severe constraints on the existence of gas giants at wide orbital separation (e.g. Brandt et al. 2014, Chauvin et al. 2015, Bowler 2016, Galicher et al. 2016). Pebble accretion must therefore be inhibited in some manner from what current models naively predict.

One commonly neglected effect in models of the pebble accretion is the effect of turbulent gas velocities on planetary accretion efficiency. Turbulence can increase the velocity of the gaseous component of the disk. This in turn has a number of ramifications for gas-assisted growth: pebble velocities are now higher as well, accretion cross sections can shrink substantially, and the scale height of particles can increase. These effects

can greatly decrease the efficiency of accretion.

The effects of turbulence on pebble accretion have been discussed in a number of different regimes. The majority of works including turbulence discuss the growth of lower mass planetesimals – in these models the growing body is assumed to be of low enough mass that its gravity is negligible, i.e. these models discuss the effect of turbulence for accretion where the cross section is comparable to the body’s geometric cross section (e.g. [Homann et al. 2016](#)). Previous models of pebble accretion for higher mass protoplanets generally neglect the effects of turbulence, or include it only by modifying the scale height of small bodies. A few works do modify the particle velocities or impact parameters due to the influence of turbulence. [Ormel & Kobayashi \(2012\)](#) examine growth over a large range of large body sizes, and include a turbulent component to the velocity through “turbulent stirring” on the random velocities of small bodies ([Ormel & Kobayashi 2012](#)). [Guillot et al. \(2014\)](#) include the effect of turbulence on the radial motion of small bodies. [Chambers \(2014\)](#) employ a methodology more similar to our own, using asymptotic expressions from [Ormel & Cuzzi \(2007\)](#) for the relative velocity between the small bodies and gas due to turbulence, and extending the [Ormel & Klahr \(2010\)](#) expressions for impact parameter and accreted particle sizes to include this turbulent component. In this formulation however, the impact parameter, as well as the sizes of small bodies that can be accreted, are functions solely of the relative velocity between the small body and the core at infinity. Our approach, which separately calculates the parameters relevant to growth, as well as the velocity preceding and during the encounter between the small body and the core, can be more naturally extended

to include turbulence, and captures facets of the problem not covered by the [Chambers](#) results. Furthermore, the focus of our study is distinct from those described above: these papers are concerned with holistically studying growth of planets at a few points in parameter space by including a wide variety of processes and modeling the problem numerically. Our methodology instead focuses on studying the effects of turbulence over a broad parameter space, and understanding the conditions under which turbulence is important to pebble accretion.

With these considerations in mind, in this paper we present an order of magnitude model of pebble accretion. We approach the problem in a different manner than past theories have, allowing separate changes to the different parameters that set the growth timescale, as opposed to grouping growth timescales into a few regimes. This allows us to more fully take into account the effects of turbulence than previous studies, including the effects of turbulence on not just the particle scale height, but also the velocity dispersion of the small bodies as well as the impact parameters for accretion. This model can be applied over a wide range of parameter space to give results accurate to order of magnitude, and can accurately describe the trends present in gas-assisted growth. We use this model to discuss the overarching features of pebble accretion, as well as to investigate how turbulence modifies these features. We also discuss how pebble accretion operates in different regions of parameter space, particularly at wide orbital separations and low core masses. In these regimes growth at intermediate masses may dominate the timescales for gas giant growth, which we will discuss in more detail in Chapter 3.

In Section 2.2 we give an overview of how growth operates in the presence of nebular gas, and discuss broadly how we calculate the growth timescale in our model. In Section 2.3 we discuss our choices for modeling the velocities that enter into our calculation. Section 2.4 details how the length scales relevant to the accretion cross section are calculated. In Section 2.5, we give an overview of the output from our model, in particular discussing the broad features of pebble accretion as well as the effects of turbulence. We also give a detailed comparison between our modeling and other works on pebble accretion. Readers that are not concerned with the details of our model can find a summary of our algorithm in Appendix A.1, and may skip directly to Section 2.5 for our results. In Section 2.6 we discuss how gas-assisted growth operates when various parameters are adjusted. In Section 2.7 we note how the relatively simple assumptions on which our model is based lead naturally to a “Flow Isolation Mass,” past which accretion of pebbles ceases. Finally in Section 3.6 we summarize our results and discuss future extensions of our model.

## **2.2 Model Overview**

### **2.2.1 Accretion in the Presence of Gas**

We begin by discussing generally how we model growth of planets in the presence of nebular gas. The details of how specific quantities are calculated are deferred to subsequent sections.

Our calculation proceeds in an order of magnitude manner – i.e. the approximations made and the neglected effects mean that quoted values should be correct to

within an order of magnitude. In what follows, we consider two types of bodies. The large bodies, or protoplanetary cores, are assumed to be massive enough that they are unaffected by gas drag and thus move at the local Keplerian orbital velocity. This constrains our cores to have radii  $\gtrsim 10$  km, in which case their velocity will deviate from Keplerian by at most  $10^{-3}$  of the gas velocity, with a weak dependence on stellocentric distance for fiducial disk parameters. In practice we rarely consider cores of such small size. We note also that while these cores are insensitive to aerodynamical gas drag, large bodies with masses in the range  $10^{21} \text{ g} < M < 10^{25} \text{ g}$  can still be affected by gas dynamical friction (Grishin & Perets 2016). We do not include these effects here. The second type of particles considered are “small” bodies, which can be substantially affected by gas drag. The growth timescale in pebble accretion is strongly dependent on the size of small body under consideration, unlike canonical core accretion where the size of the planetesimals enters only through its effect on the small body velocity dispersion. Thus, all calculations are performed as a function of small body radius,  $r_s$ . Quantities of interest can later be averaged over size by assuming a size distribution for the small bodies. Note that quoted values of the growth timescale  $t_{\text{grow}}$  implicitly assume that all of the surface density is contained in particles of the given value of  $r_s$ . For a size distribution where most of the mass is in the largest sizes of particles present (e.g. a Dohnanyi size distribution, Dohnanyi 1969), this value of  $t_{\text{grow}}$  is approximately equal to the growth timescale for a distribution of small body sizes where the maximum size present is the given value of  $r_s$ . In this paper we will not perform integrations over small body size explicitly; see our Chapter 3 for examples of this process as well as a

discussion of the effects of altering the size distribution.

In gas-assisted growth, the interaction between the small body and the nebular gas modifies the accretion process substantially. As the small body approaches the core, gas drag will dissipate the kinetic energy of the small body relative to the large body. This loss of energy can cause small bodies on non-collisional trajectories to become bound to the core and eventually be accreted. This process is similar to the  $L^2s$  mechanism identified by Goldreich et al. (2002) for formation of Kuiper Belt binaries, with gas drag as the source of dissipation in the place of dynamical friction. Gas drag can also stop small bodies from accreting – if particles couple strongly to the gas as they flow around the core then they will be unable to accrete.

Which of these processes occur depends on the relative size of two different length scales: the stability radius,  $R_{\text{stab}}$  and the Bondi radius,  $R_b$ . The stability radius is the smallest radius at which stable orbits by the small body about the large body are possible: outside of  $R_{\text{stab}}$  interactions between the small body and either the nebular gas or the central star will shear the small body away from the large body’s gravity. Inside of  $R_{\text{stab}}$  the small body can safely inspiral onto the core. The details of how  $R_{\text{stab}}$  is calculated are discussed in Section 2.4.1. The Bondi radius, on the other hand, is approximately the radius at which the escape velocity from the core is equal to the speed of sound in the gas:

$$R_b = \frac{GM}{c_s^2}, \quad (2.1)$$

where  $M$  is the mass of the core and  $c_s = \sqrt{kT/\mu}$  is the isothermal sound speed of the gas. Here  $k$  is Boltzmann’s constant and  $\mu$  is the mean molecular weight of the nebular

gas. We consider the Bondi radius because it roughly tells us the length scale interior to which the the core can have a stable atmosphere, which has substantial effects on the flow pattern. For the lowest mass cores we consider, the Bondi radius may be less than the physical radius of the core,  $R$ . This occurs roughly at a core mass of:

$$M_a \equiv \frac{c_s^3}{G} \left( \frac{3}{4\pi G \rho_p} \right)^{1/2} \quad (2.2)$$

$$\approx 2 \times 10^{-4} M_\oplus \left( \frac{a}{30 \text{ AU}} \right)^{-9/14} \left( \frac{\rho_p}{2 \text{ g cm}^{-3}} \right)^{-1/2},$$

where  $\rho_p$  is the density of the protoplanet (e.g. Rafikov 2006), and for the expression in the second line we've used our fiducial disk parameters (see Section 2.5.1). If  $R_b < R$ , then the effects discussed below are unchanged, with  $R$  taking the place of  $R_b$ . In what follows, we will discuss accretion for  $R_b < R_H$ , where  $R_H$  is the core's Hill radius (see Section 2.4.1). We discuss accretion in the regime  $R_b > R_H$  in Section 2.7.

Given these considerations, we center our model around two main ideas about accretion in the presence of gas, which are summarized in Figure 2.1:

1. If the radius for stable orbits exceeds the Bondi radius, i.e.  $R_{\text{stab}} > R_b$ , then the flow pattern of gas is not substantially altered in the region where particles can stably orbit the core. In this case any small bodies that deplete their kinetic energy relative to the core within  $R_{\text{stab}}$  will inspiral onto the core and be accreted. On the other hand any particles that are unable to dissipate their kinetic energy in this regime will pass out of  $R_{\text{stab}}$  and will not be accreted.
2. If instead the Bondi radius exceeds the stable orbit radius, i.e.  $R_b > R_{\text{stab}}$ , then

particles which *are* able to deplete their kinetic energy relative to the core *will not* accrete. This is due to the fact that in this regime, well coupled particles will tend to flow around the core’s atmosphere, which extends up to  $R_b$ . If instead particles are *unable* to dissipate their kinetic energy, so that they penetrate into the atmospheric radius, the increase in density as the particle enters the growing planet’s atmosphere is taken to be so substantial that the particle will now be able to dissipate its kinetic energy and will accrete onto the core.

The first point is supported not only by order of magnitude considerations, but also by detailed numerical simulations of growth of protoplanets in the presence of gas (e.g. [Ormel & Klahr 2010](#), [Lambrechts & Johansen 2012](#)). Analytic calculations also show that even for small bodies several orders of magnitude larger than the sizes we will be concerned with, small bodies inspiral on times shorter than the disk lifetime. Thus we are justified in neglecting this part of the accretion process ([Perets & Murray-Clay 2011](#)). We also neglect the possibility that the core’s envelope is periodically replenished by the protoplanetary disk; see [Ormel et al. \(2015\)](#) for a discussion of this possibility, and [Alibert \(2017\)](#) for an application of this replenishment to pebble accretion.

Our second point invokes the classical solution of flow around an obstacle: for  $R_b < R_H$  the flow of the nebular gas is subsonic, meaning the core’s atmosphere is approximately incompressible. See [Ormel \(2013\)](#) Figure 5A for an example of this flow pattern in the context of a planet embedded in a protoplanetary disk. We note here that more detailed simulations of the flow show structure that may produce circulation into  $R_b$  ([Ormel 2013](#), [Fung et al. 2015](#)), which we assume we can neglect for the level of

accuracy we desire in this model. In addition, we do not explicitly calculate the work done on particles interior to  $R_b$  – our assumption that particles with  $KE > W$  will always be accreted for  $R_{\text{stab}} < R_b$  will eventually be violated for large enough particle sizes. See [Inaba & Ikoma \(2003\)](#) for an in depth discussion of accretion in this regime.

While the criteria above are used throughout parameter space, in order to better illustrate how we model gas-assisted growth we also provide a simplified “sketch” of how accretion in our model operates, which accurately describes pebble accretion over a large amount of parameter space.<sup>1</sup> Figure 2.2 shows a “cartoon” of gas-assisted growth for a fixed core mass and semi-major axis in the disk, with small body radius increasing from left to right. Each panel shows the core’s Bondi radius,  $R_b$  as well as the two radii that are used to determine  $R_{\text{stab}}$  – the Hill radius  $R_H$  (see Section 2.4.1), which is the distance past which the stellar gravity will pull particles off the core, and the radius  $R'_{WS}$  (see Section 2.4.1) beyond which gas drag pulls particles off the core. Since smaller particles have a higher surface area to volume ratio and therefore experience larger gas drag accelerations,  $R'_{WS}$  is smaller for smaller particles. In the far left panel, the particles are low mass, meaning gas drag can easily pull them off of the core, and  $R'_{WS}$  lies inside the core’s atmosphere. Because these particles have low mass they easily dissipate their kinetic energy during the encounter with the core, meaning they are in

---

<sup>1</sup>The main assumption in this description is that particles that have  $R_b > R_{\text{stab}}$  will always have  $KE < W$ . To see this, note that  $R_{\text{stab}} < R_b$  implies that  $F_D(v_{cg}) > GMm/R_b^2$ , where  $v_{cg} = \max(v_{\text{gas}}, v_{\text{shear}})$  is the relative velocity of the gas and the core at the Bondi radius (see Section 2.3 and Equation 2.39). This can be rewritten as  $m/R_b < F_d(v_{cg})/c_s^2$ . Taking the ratio  $KE/W = mv_{\infty}^2/(4F_d(v_{\text{enc}})R_b)$  (see Equations 3.17 and 3.18) and inserting this inequality implies that  $KE/W < (v_{\infty}^2/c_s^2) F_d(v_{cg})/F_d(v_{\text{enc}}) < 1$ . For the case  $R_b < R$ ,  $c_s \rightarrow v_{\infty}$  in the last inequality, which still implies  $KE/W < 1$  as long as the escape velocity from the planet’s surface is larger than the velocity of the gas flow at the planet’s surface, which is typically satisfied for planetary radii  $R \gtrsim 10 - 100$  km.

the regime in the lower righthand panel of Figure 2.1 and do not accrete. As particle size grows,  $R'_{WS}$  increases as well, until it exceeds  $R_b$ , the scale of the core's atmosphere, i.e. there now exists a region exterior to the core's atmosphere where particles can stably orbit the core. Because these particles are still of relatively low mass they are able to dissipate their kinetic energy through gas drag. We therefore fall into the upper lefthand panel of Figure 2.1, which signals the onset of pebble accretion (middle panel of Figure 2.2). Finally, as particle size continues to increase we eventually reach a point where the particles are so massive that they no longer dissipate their kinetic energy. As particle size increases,  $R'_{WS}$  will continue to increase, meaning we clearly still have  $R_{\text{stab}} > R_b$ . These particles are therefore in the upper righthand panel of Figure 2.14 and will not accrete (righthand panel of Figure 2.2).

Given this formalism, for the purposes of discussing whether a given small body will accrete, we simply need to compare the magnitude of the kinetic energy of the particle relative to the core and the work done on the particle during its encounter with the core. The kinetic energy of the particle relative to the core before the encounter is

$$KE = \frac{1}{2}mv_{\infty}^2, \quad (2.3)$$

while we take the work done by gas drag to be simply

$$W = 2R_{\text{acc}}F_D(v_{\text{enc}}), \quad (2.4)$$

where  $R_{\text{acc}} = \max(R_{\text{stab}}, R_b)$ , and  $F_D(v_{\text{enc}})$  is the drag force on a small body moving at a velocity  $v_{\text{enc}}$ , which is the relative velocity between the small body and the large body during the encounter. Calculation of  $v_{\text{enc}}$  and discussion why  $R_{\text{acc}}$  is used for determining the work done by gas drag are located in section 2.3.6.

Our consideration of the ranges of particle sizes that can be accreted is an important aspect to our modeling that is often not present in other works. See section 2.5.5 for a detailed discussion.

Given the uncertainties in the size distribution of small bodies present in protoplanetary disks, understanding the extent of particle radii for which gas-assisted growth is possible is an important facet to studying the role of pebble accretion in planet formation. Furthermore, an important effect of nebular turbulence is to change the range of small body sizes that can be accreted (see Section 2.6.1), which makes a detailed consideration of the small body sizes where pebble accretion can operation an important facet of our model.

In summary, a particle will be able to accrete if one of the following criteria are met:

1.  $R_{\text{stab}} > R_b$  and  $2F_D(v_{\text{enc}})R_{\text{acc}} > \frac{1}{2}mv_{\infty}^2$
2.  $R_{\text{stab}} < R_b$  and  $2F_D(v_{\text{enc}})R_{\text{acc}} < \frac{1}{2}mv_{\infty}^2$

Small bodies which do not satisfy either of these criteria will not be able to accrete, that is we set  $t_{\text{grow}} = \infty$  for these particles. We emphasize that setting  $t_{\text{grow}} = \infty$  refers *only* to the timescale for growth by pebble accretion: it is possible these particles could still be accreted via less efficient processes, such as capture by

gravitational focusing unassisted by gas drag or by collisions unaffected by gravity (see Equation A.42). In particular, having  $t_{\text{grow}} = \infty$  does not imply that growth literally halts. See Section 2.5.5 for further discussion. While in principle our model could be extended to include these effects, in this work we are concerned primarily with gas-assisted growth, and therefore we do not explicitly include these other timescales.

### 2.2.2 Growth Timescale for Protoplanets

We now discuss in more detail how the growth timescales for cores are computed. In order to calculate the growth timescale for the large bodies for a given core mass  $M$ , we use the usual expression (see e.g. [Goldreich et al. 2004](#), hereafter GLS)

$$t_{\text{grow}} \equiv \left( \frac{1}{M} \frac{dM}{dt} \right)^{-1}. \quad (2.5)$$

The rate that small bodies encounter the core is given by  $n\sigma_{\text{acc}}v_{\infty}$ , where  $n$  is the volumetric number density of small bodies of a given size,  $\sigma_{\text{acc}}$  is the cross section for accretion of the small body by the large body, and  $v_{\infty}$  is the velocity at which small bodies encounter the large body. Note that  $v_{\infty}$  is not necessarily the velocity of the small body during its encounter with the core, since this encounter can change the relative velocity;  $v_{\infty}$  is the relative velocity between the two bodies at large separations. The number density of solids is simply  $n = \rho_s/m = f_s\Sigma/(2mH_p)$  where  $\rho_s$  is the mass density of the small bodies,  $\Sigma$  is the surface density of the gaseous component of the disk,  $f_s$  is the solid to gas mass ratio,  $m$  is the mass of the small body, and  $H_p$  is the scale height of solids in the disk. Since each accretion of a small body increases the

mass of the large body by  $m$ , the growth timescale is given by

$$t_{\text{grow}} = \frac{MH_p}{2f_s \Sigma v_\infty R_{\text{acc}} H_{\text{acc}}} , \quad (2.6)$$

where we've decomposed  $\sigma_{\text{acc}}$  into the product of lengthscales in the plane of the disk and perpendicular to it:  $\sigma_{\text{acc}} = (2R_{\text{acc}})(2H_{\text{acc}})$ . Thus, the aim of our calculation is to determine the quantities  $R_{\text{acc}}$ ,  $H_{\text{acc}}$ ,  $H_p$ , and  $v_\infty$ . Once these quantities are known we can immediately determine the growth timescale. The role each of these quantities plays in the growth timescale is illustrated graphically in Figure 2.3.

In the next few sections we will discuss in detail how each of the above quantities are calculated in the context of pebble accretion. Our algorithm is summarized in Appendix A.1.

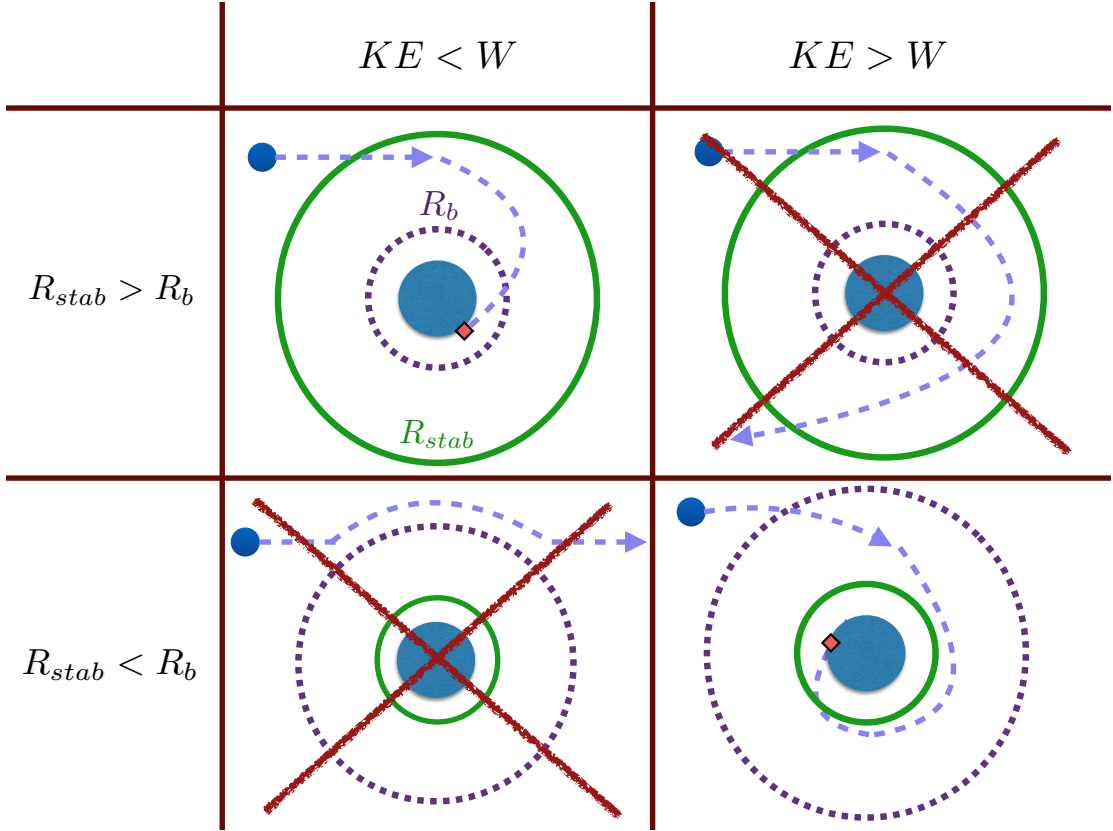


Figure 2.1: A graphical illustration the energy regimes used to determine whether small bodies are able to accrete. *Upper Left Panel:* Here  $R_{stab} > R_b$ , so particles can inspiral onto the core in a region where the gas flow is not substantially altered by the core's gravity. Particles that deplete their kinetic energy relative to the core via gas drag will inspiral onto the core and be captured. *Upper Right Panel:* If the particle is unable to deplete its kinetic energy during the interaction then it will simply have its trajectory deflected before exiting  $R_{stab}$ , and will not accrete. *Lower Left Panel:* Here  $R_b > R_{stab}$ , so the gas flow is altered substantially when the small body is accreting. The gas will tend to flow around the atmospheric radius, so particles that have  $KE < W$ , i.e. particles that deplete their kinetic energy, will couple to the gas and flow around the core without accreting. *Lower Right Panel:* Larger particles which do not deplete their kinetic energy and instead penetrate into the atmospheric radius will experience a rapid increase in gas density as they enter the atmosphere of the nascent planet. This increased density may rapidly deplete the kinetic energy of the small body, which will then inspiral and accrete, similar to what occurs in the upper left panel.

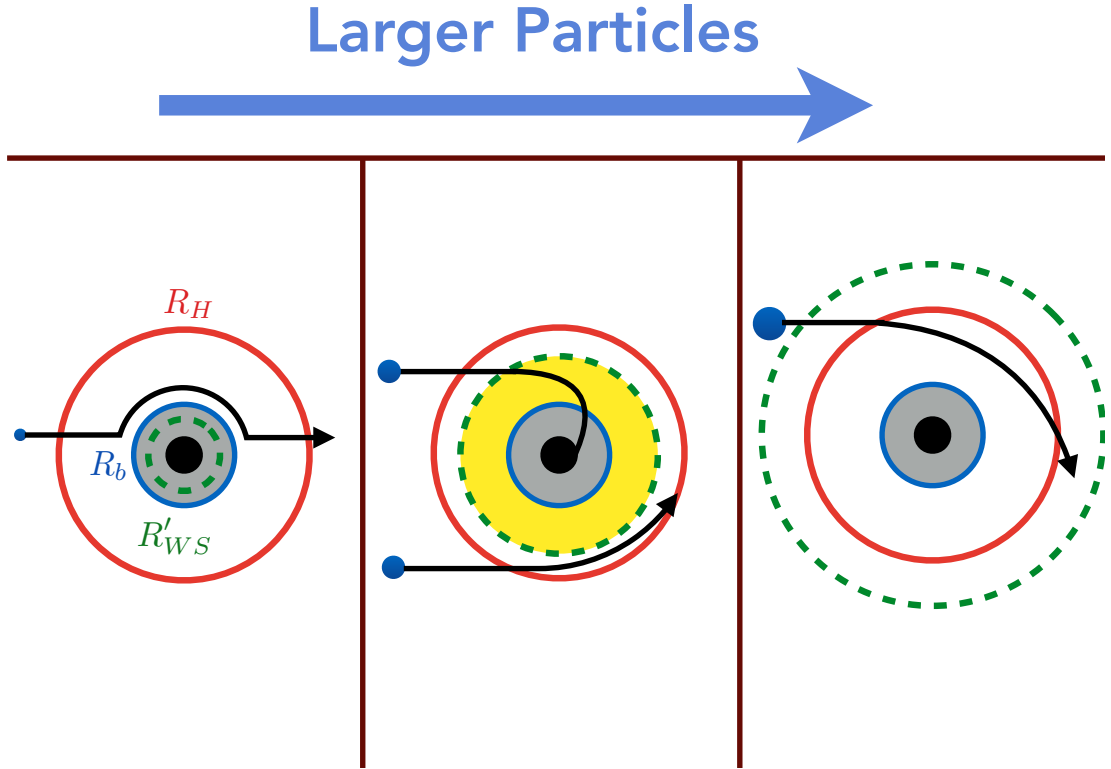


Figure 2.2: A cartoon illustration of the typical manner in which pebble accretion operates as the small body size is increased. The black circle represents the planet, while the blue circles depict incoming particles. The extent of the planet’s atmosphere is denoted by the grey shaded region, and the yellow shaded region shows the region where incoming particles can be accreted. *Left Panel:* For small particles,  $R'_{WS} = R_{\text{stab}} < R_b$ , so the core’s gravitational sphere of influences lies inside its atmosphere. In this regime particles couple to the local gas flow and flow around the core without being accreted. *Middle Panel:* For intermediate sizes of particles,  $R'_{WS} > R_b$ , meaning particles can be bound to the core in a region outside the core’s atmosphere. For these intermediate sizes of particles the work done by gas drag exceeds the incoming kinetic energy of these small bodies, meaning that particles that pass interior to  $R_{\text{stab}}$  will be accreted. Particles with impact parameters  $> R_{\text{stab}}$  will be sheared off the core by gas drag. *Right Panel:* Finally, large particles will be so massive that their incoming kinetic energy is too large to be depleted by gas drag. These particles will not be accreted via pebble accretion, regardless of impact parameter. For the case shown here  $R'_{WS}$  has grown so much that  $R_{\text{stab}} = R_H$ , but this is not always the case for particles with  $KE > W$ .

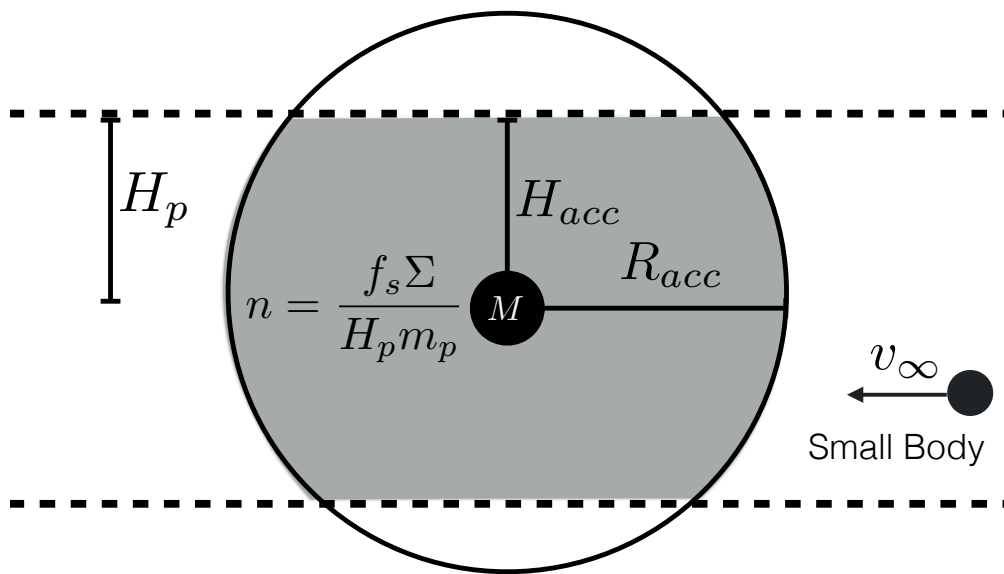


Figure 2.3: A graphical illustration of the quantities used to determine the growth timescale for the planetary core.

## 2.3 Velocity of the Small Bodies through the Disk

As small bodies move through the disk their velocities are affected by drag from the nebular gas as well as gravitational interactions with both the central star and the core. In order to calculate  $t_{\text{grow}}$  we need to understand what sets  $v_{\infty}$ , the velocity of a small body relative to the big body, and  $v_{\text{enc}}$ , the velocity of the small body during its encounter with the core. Calculating these velocities requires us to treat not only the gas drag force on the small bodies, but also to understand how drag from the laminar and turbulent components of the gas velocity each contribute to the velocity of the small bodies. Furthermore the gas velocity influences the size of both  $R_{\text{acc}}$  and  $H_{\text{acc}}$ , in ways that can have substantial impact on  $t_{\text{grow}}$ .

We begin by reviewing our choices for modeling gas drag regimes and introduce the stopping time to parameterize the coupling between the small bodies and the gas (Section 2.3.1). The gas is taken have both a bulk, laminar component that is independent of time, and a fluctuating, turbulent component that time averages to zero. Both of these components can have an effect on the small bodies' velocity, and we discuss each separately (Sections 2.3.2 and 2.3.3). These two components can be combined to give the average velocity between the small body and the large one due to gas drag,  $v_{pk}$ . (Section 2.3.4). Gas drag is not the only source of relative velocity in the disk – the shear present in the disk due to the dependence of the Keplerian orbital frequency on semi-major axis can also affect these relative velocities (Section 2.3.5). Gas drag can also have a strong effect on the relative velocity between the small body and the core during their encounter,  $v_{\text{enc}}$ , as can the gravitational force from the core (Section 2.3.6).

These sections synthesize results from many works, which we present in detail so that the framework and assumptions our model is based on are clearly laid out. Readers who only wish to review our choices for modeling the velocity may consult the summary of our calculation in Appendix A.1.

### 2.3.1 Gas Drag and Stopping Time

Gas drag is generally treated by breaking the drag force,  $F_D$ , into a number of different regimes. We summarize our choices below; for a more in depth discussion, see [Batchelor \(2000\)](#). First, we distinguish between the “diffuse regime,” which applies for particles with  $r_s < 9\lambda/4$ , and the “fluid regime,”  $r_s > 9\lambda/4$ . Here  $r_s$  is the radius of the small body and  $\lambda$  is the mean free path of the gas particles. In the diffuse, non-supersonic,<sup>2</sup> regime, the drag force on the particle is given by the Epstein drag law

$$F_D = \frac{4}{3}\pi\rho_g v_{th} v_{rel} r_s^2, \quad (2.7)$$

where  $\rho_g = \Sigma/(2H_g)$  is the density of the gas,  $v_{th} = \sqrt{8/\pi} c_s$  is the thermal velocity of the gas, and  $v_{rel}$  is the relative velocity between the gas and the object. For a particle in the fluid regime, we must consider an additional parameter – the Reynolds number of the particle, given by  $Re = 2r_s v_{rel}/(0.5 v_{th} \lambda)$ . For  $Re < 1$  the particle is in the Stokes

---

<sup>2</sup>It is easy to see we can in general neglect the super-sonic regime ( $v_{rel} > c_s$ ): since  $v_{rel} \lesssim v_{gas} \approx \eta v_k$  (see section 2.3.2 for a discussion of the notation), we have  $c_s < \eta v_k \Rightarrow H_g/a > 1$ , where  $H_g \sim c_s/\Omega$  is the gas scale height, and  $\Omega$  is the local Keplerian orbital frequency. Thus for the super-sonic case the protoplanetary disk has an aspect ratio greater than 1, in strong opposition to observations of protoplanetary disks.

drag regime, and the drag force is given by

$$F_D = 3\pi\rho_g v_{th} v_{\text{rel}} \lambda r_s , \quad (2.8)$$

where  $\lambda$  is the mean free path of the gas particles. For  $Re > 1$ , the particle is in the Ram pressure regime, and

$$F_D = \frac{1}{2}\rho_g \pi r_s^2 v_{\text{rel}}^2 . \quad (2.9)$$

To mitigate discontinuities in the drag force we use a smoothed drag force law in the fluid regime given by [Cheng \(2009\)](#):

$$F_D = \frac{1}{2}C_D(Re)\pi r_s^2 \rho_g v_{\text{rel}}^2 , \quad (2.10)$$

where

$$C_D(Re) = \frac{24}{Re} (1 + 0.27Re)^{0.43} + 0.47 [1 - \exp(-0.04Re^{0.38})] . \quad (2.11)$$

As  $Re \rightarrow 0$  we have  $C_D \rightarrow 24/Re$ , so  $F_D$  reduces to the Stokes drag law given in (2.8).

As  $Re \rightarrow \infty$ ,  $C_D \rightarrow 0.47$ , in which case  $F_D$  becomes the Ram drag force given in (2.9) (with a slightly different prefactor).

We can define a timescale from the drag force, known as the “stopping time”

of the particle

$$t_s \equiv \frac{mv_{\text{rel}}}{F_D}. \quad (2.12)$$

The Epstein and Stokes drag laws are both linear in velocity – in these linear drag regimes, it is straightforward to show from Equations (2.7) and (2.8) that for spherical particles of uniform density  $\rho_s$ :

$$t_s = \begin{cases} \frac{\rho_s r_s}{\rho_g v_{th}}, & \text{Epstein} \\ \frac{4 \rho_s r_s^2}{9 \rho_g v_{th} \lambda}, & \text{Stokes} \end{cases} \quad (2.13)$$

In these regimes the stopping time of the particle is a function only of the properties of the particle and the gas, and in particular is independent of the particle’s velocity. Hence  $t_s$  is often used as a parameterization of the particle’s size,  $r_s$ , in terms of how well the small body is coupled to the gas flow (e.g. [Chiang & Youdin 2010](#)). If the drag law is instead quadratic in velocity, as in Equation (2.10), we numerically solve for the stopping time using Equations (2.18), (2.23) and (2.25). In practice we solve these equations iteratively to calculate a self-consistent solution.

### 2.3.2 Laminar Velocity of Small Particles

Due to the internal pressure of the gas, the gas component of the protoplanetary disk will move at a sub-Keplerian orbital velocity. [Weidenschilling \(1977a\)](#) gives

the difference in velocity  $\Delta v$  as  $\Delta v \approx \eta v_k$ , where  $v_k$  is local Keplerian orbital velocity,  $v_k = a\Omega$ , and  $\eta$  is a measure of the local gas pressure support, with approximate value  $\eta \approx c_s^2 / (2v_k^2)$ . Due to this sub-Keplerian rotation, small bodies experience a “head-wind” from the gas, which produces a drag force on the small bodies. If we use a polar coordinate system such that  $\hat{r}$  denotes the direction pointing away from the central star and  $\hat{\phi}$  denotes the direction of the disk’s rotation, then the drag force causes the small bodies to move with a sub-Keplerian velocity in the  $\hat{\phi}$  direction, and to drift in the  $-\hat{r}$  direction. In the above notation, the particle acquires a laminar velocity relative to the gas given by

$$v_{r,\text{gas}} = -2\eta v_k \left[ \frac{\tau_s}{1 + \tau_s^2} \right], \quad (2.14)$$

$$v_{\phi,\text{gas}} = -\eta v_k \left[ \frac{1}{1 + \tau_s^2} - 1 \right], \quad (2.15)$$

where  $\tau_s = t_s \Omega$ . See [Nakagawa et al. \(1986\)](#) for further details. <sup>3</sup>

Since the laminar gas velocity relative to Keplerian is simply  $v_{gas,k} = -\eta v_k \hat{\phi}$ ,

---

<sup>3</sup>There will also be turbulent component to  $v_r$ , which stems from the inward diffusion of the gas due to the turbulent viscosity  $\nu = \alpha c_s H_g$  (see Section 2.3.3 for a discussion of the notation.) [Guillot et al. \(2014\)](#) give this velocity as  $v_{r,\text{turb}} = v_\nu / (1 + \tau_s^2)$ , where  $v_\nu \sim \alpha c_s H_g / a$  is the radial velocity of the gas due to turbulence. Following [Guillot et al.](#), the turbulent component  $v_r$  dominates for  $\tau_s < \tau_{s,\nu} = \alpha c_s^2 / (2\eta v_k) \approx \alpha$ . [Lambrechts & Johansen \(2014\)](#) show that, for the parameters they consider, this velocity is negligible compared to  $v_{r,k}$  because the diffusive lengthscale  $\ell$  is always less than the global scale of the disk  $a$ . However, their expression for  $\ell$  can be rewritten as  $\ell/r \approx \alpha (H_g/a)^2 / (2\tau_s \eta) \approx \alpha / \tau_s$ , which leads to the same conclusion as above for the size at which turbulence dominates. For our purposes we neglect this effect, since the small particles for which  $v_\nu > v_{r,k}$  move at velocities comparable to the fluctuating turbulent velocity  $v_t$ , which dominates:  $v_\nu / v_t \sim \sqrt{\alpha} H_g / a \ll 1$ .

the velocity of the particle relative to Keplerian is

$$v_{r,k} = -2\eta v_k \left[ \frac{\tau_s}{1 + \tau_s^2} \right], \quad (2.16)$$

$$v_{\phi,k} = -\eta v_k \left[ \frac{1}{1 + \tau_s^2} \right]. \quad (2.17)$$

It is straightforward to show that the magnitude of the laminar component of the particle's velocity is

$$v_{pg,\ell} = \eta v_k \tau_s \frac{\sqrt{4 + \tau_s^2}}{1 + \tau_s^2}, \quad (2.18)$$

relative to the gas, and

$$v_{pk,\ell} = \eta v_k \frac{\sqrt{1 + 4\tau_s^2}}{1 + \tau_s^2}, \quad (2.19)$$

relative to Keplerian.

### 2.3.3 Turbulent Velocity of Small Particles

In order to describe the strength of the turbulence in the disk, we use the standard Shakura-Sunyaev  $\alpha$  parameterization of the effective kinematic viscosity. We employ  $\alpha$  simply as a convenient parameterization of the strength of turbulence; for our purposes  $\alpha$  is fundamentally a local quantity, and is not necessarily connected with the accretion rate onto the star. In terms of  $\alpha$ , the effective kinematic viscosity of the turbulent gas,  $\nu_t$ , is given by (Shakura & Sunyaev 1973):

$$\nu_t = \alpha c_s H_g , \quad (2.20)$$

where  $H_g = c_s/\Omega$  is the scale height of the gas. If we write the viscosity as the product of the local turbulent velocity and the largest scale turbulent eddies,  $\nu_t = v_t \ell_t$ , and have  $\ell_t \approx v_t/\Omega$ , then  $v_t = \sqrt{\alpha} c_s$ .

We use the Kolmogorov theory of turbulence to determine the turbulent energy spectrum. As described in [Cuzzi & Hogan \(2003\)](#), in the Kolmogorov theory turbulence exists over a range of scales or “eddies,” which are characterized by their wave number  $k_\ell = 1/\ell$ . The largest scale eddies, which occur on the lengthscale  $l_t$ , are the scale on which energy is supplied by the turbulence; these large scale eddies “turn over” and transfer their energy to smaller scale eddies, until energy is finally dissipated by kinematic viscosity on some smallest scale  $\tilde{\eta}$ . If we assume that the rate of energy transfer between scales is independent of eddy size, we can show that the energy spectrum of the turbulence is given by  $E(k) \propto k^{-5/3}$ , where  $E(k)$  has units of energy per mass per wavenumber. The velocity associated with  $k$  is then  $v(k) = (2kE(k))^{1/2} \propto k^{-1/3}$ , and the overturn time for an eddy of wavenumber  $k$  is  $t_k = 1/(kv(k)) \propto k^{-2/3}$ . Thus the larger scale eddies overturn more slowly and contain more of the turbulent kinetic energy. The size of the smallest scale eddies can be determined by setting the rate of energy loss from molecular viscosity equal to the eddy turnover time, which gives  $\tilde{\eta} = (\nu^3/\epsilon)^{1/4}$ , where  $\nu \sim v_{th}\lambda$  is the molecular viscosity and  $\epsilon$  the rate of energy dissipation. The length  $\tilde{\eta}$  is known as the “Kolmogorov microscale” of length. We can

determine the relation between the smallest and largest scale eddies by setting the rate that energy is supplied at the largest scales,  $v_t^2/t_L \sim v_t^3/l_t$  equal to  $\epsilon$ , the rate that energy is dissipated at small scales. Plugging in our expression for  $\epsilon$  in terms of  $\tilde{\eta}$  and  $\nu$  gives  $\tilde{\eta}/l_t \sim (v_t l_t/\nu)^{-3/4} = Re_t^{-3/4}$ , where we've defined the Reynolds number of the turbulence,  $Re_t \equiv \nu_t/\nu$ . In terms of  $\alpha$  we have  $Re_t = \alpha c_s H_g/(v_{th}\lambda)$ .

Qualitatively, the behavior of a small body in response to an eddy of wavenumber  $k$  depends on the ratio of the particle's stopping time to the eddy turnover time  $t_k$ . Particles with  $t_s < t_k$  will come to equilibrium with the eddy before it turns over, and will follow the large scale motion of the eddy. On the other hand particles with  $t_s > t_k$  will not come to equilibrium with the eddy before it turns over, and will therefore only receive a small perturbative kick from the eddy. To characterize the small body's response to the turbulence, most authors use the Stokes number,  $St \equiv t_s/t_L$ , where  $t_L$  is the overturn time of the largest eddies. We make the usual assumption that  $t_L = \Omega^{-1}$ , in which case  $St = \tau_s$ , the parameter used in describing the particle's interaction with the laminar gas flow. This permits the use of one parameter, which we will hereafter refer to as  $St$ , to characterize the particle's interaction with both the laminar and turbulent components of the nebular gas flow. See [Youdin & Lithwick \(2007\)](#) for a more in depth discussion of the effect of varying  $t_L$ .

Due to their interaction with the turbulent gas, small bodies will move relative to inertial space with some non-zero root-mean-square (RMS) velocity,  $v_{pi,t}$ . The RMS velocity can be calculated through order of magnitude means as follows ([Youdin & Lithwick 2007](#)): For  $St \gg 1$  we have  $t_s \gg t_L$ ; in this regime particles receive many

uncorrelated “kicks” from the largest scale eddies over a single stopping time, causing the particle to random walk in velocity. Since the particles’ velocity damps out over a time  $t_s$ , the particle receives approximately  $N \sim t_s/t_L \sim St$  kicks of amplitude  $v \sim v_t t_L/t_s = v_t/St$  resulting in a velocity  $v_{pi,t} \sim v_t/\sqrt{St}$ . On the other hand, for  $St \ll 1$ , we expect  $v_{pi,t} \sim v_t$ . The simplest expression that has the correct behavior in each of these limits is given by

$$v_{pi,t} = \frac{v_t}{\sqrt{1 + St}}. \quad (2.21)$$

In order to better calculate the velocities of smaller particles, i.e. particles with  $St < 1$ , we employ expressions from [Ormel & Cuzzi \(2007\)](#) (hereafter OC07), who give closed form equations for the RMS velocity of solid particles suspended in a turbulent medium. By following the methodology of [Voelk et al. \(1980\)](#), but also using results which take into account the finite inner scale of eddies at  $k_\eta = 1/\tilde{\eta}$ ,<sup>4</sup> OC07 arrive at an analytic expression for the RMS inertial space velocity of particles suspended in a turbulent medium

$$v_{pi,t}^2 = v_t^2 \left( 1 - \frac{St^2(1 - Re_t^{-\frac{1}{2}})}{(St + 1)(St + Re_t^{-\frac{1}{2}})} \right). \quad (2.22)$$

---

<sup>4</sup>The OC07 results also use a different auto-correlation function (ACF) for the gas velocity of an eddy with turnover time  $t_k$ . [Markiewicz et al. \(1991\)](#) encapsulate the [Voelk et al. \(1980\)](#) ACF in the more general form

$$R(t, t'; k) = \frac{E(k)}{2\pi k^2} \left( 1 + \frac{|t - t'|}{t_k} \right)^n e^{-|t - t'|/t_k},$$

The [Voelk et al.](#) results use  $n = 0$ , but [Markiewicz et al.](#) instead use  $n = 1$  because of the zero slope behavior at  $t = t'$ . Fits to the results of numerical simulations by [Cuzzi & Hogan \(2003\)](#) further validate the choice of  $n = 1$  over  $n = 0$ .

Relative to the gas, the velocity is:

$$v_{pg,t}^2 = v_t^2 \left( \frac{St^2(1 - Re_t^{-\frac{1}{2}})}{(St + 1)(St + Re_t^{-\frac{1}{2}})} \right). \quad (2.23)$$

Equation (2.23) was originally derived by [Cuzzi & Hogan \(2003\)](#) for particles with  $St \ll 1$ . OC07 however, argue from the results of numerical calculations and comparison with simulations, that Equations (2.22) and (2.23) hold to order unity for particles of arbitrary Stokes number. We are therefore justified in applying this equation to determine the RMS turbulent velocity of arbitrary sized accreting particles, with one caveat. We first note that, for large Stokes numbers, we have  $v_{pi,t} \rightarrow v_t/Re_t^{1/4}$  which cannot be completely correct, as in the limit as  $St \rightarrow \infty$  we expect for the particles to be so massive that they are completely unaffected by turbulence, and thus  $v_{pi,t} \rightarrow 0$ . In addition, we note that, for  $St \ll Re_t$ , as long as we do not have  $St \ll 1$ , Equation (2.22) reduces to (2.21). Thus we can use (2.21) to determine the velocity of larger  $St$  particles; in practice we use (2.21) for  $St \geq 10$ . This form should connect smoothly to the more precise form given in equation (2.22) as long as  $Re_t \gg 10$ . Using the fiducial values given in Section 2.5.1, the Reynolds number of the turbulence is given by

$$Re_t = 4.07 \times 10^{10} \alpha \left( \frac{a}{\text{AU}} \right)^{-1}. \quad (2.24)$$

Thus, unless we are at extremely large orbital separations with weak turbulence, we can model the full range of Stokes numbers in this manner with little error.

### 2.3.4 Combining Velocities and Changing Frames

We have previously discussed how to calculate the laminar and turbulent components of the particle's velocity. However, in order to calculate the total RMS velocity we need to understand how to combine these two components. Furthermore, calculation of drag forces requires knowledge of the velocity of the particle relative to the gas, whereas calculation of  $v_\infty$  will require the velocity of the particle relative to the local Keplerian velocity, since this is the velocity at which small bodies approach the core. We therefore also need to understand how to convert our velocities from one frame to another. The methodology necessary for our calculation is summarized here; for a more detailed derivation see Appendix A.

We let  $\delta\mathbf{v}$  represent the “fluctuating” or turbulent component of the gas velocity and  $\bar{\mathbf{v}}$  represent the laminar component – i.e. if we write  $\mathbf{v} = \bar{\mathbf{v}} + \delta\mathbf{v}$  then  $\langle\mathbf{v}\rangle = \bar{\mathbf{v}}$ . We can then show that

$$v^2 = \bar{v}^2 + \langle\delta v^2\rangle, \quad (2.25)$$

i.e. the turbulent and laminar components combine in quadrature.

If the subscripts  $p, g$ , and  $k$  denoted the velocity of the small bodies, the gas, and the local Keplerian velocity respectively, then

$$\bar{v}_{pk} = \bar{v}_{pg} + \bar{v}_{gk} . \quad (2.26)$$

So the laminar component of the particle's velocity can be changed from one frame to another in the usual manner (i.e. the  $\hat{\phi}$  component is altered by  $\eta v_k$  while the  $\hat{r}$  component is unchanged) independent of the turbulent velocity.

For the turbulent component of the velocity, one can show

$$\langle \delta v_{gk}^2 \rangle = \langle \delta v_{pk}^2 \rangle + \langle \delta v_{pg}^2 \rangle , \quad (2.27)$$

which is given in a number of works (e.g. [Csanady 1963](#), [Cuzzi et al. 1993](#), and [OC07](#)), and is usually derived by considering the Fourier components of the turbulent velocities in frequency space. An alternate derivation is given in Appendix A.

Neglecting the effects from the fact that the Keplerian velocity is not truly an inertial reference frame (see [Youdin & Lithwick 2007](#) for a discussion of non-inertial effects), Equations (2.25), (2.26) and (2.27) fully specify how to calculate all the velocities relevant to the problem from the input given by Equations (2.14), (2.15) and (2.22).

### 2.3.5 $v_{\text{shear}}$

Because the Keplerian velocity of the disk varies as  $v_k \propto a^{-1/2}$ , bodies that are separated substantially in the radial direction will move relative to one another in the azimuthal direction even in the absence of other effects. For our purposes we

approximate this “shear” velocity as

$$v_{\text{shear}} = \Omega r , \quad (2.28)$$

where  $r$  is the separation between the two bodies in the radial direction. For small bodies encountering growing protoplanets we have  $r \approx R_{\text{acc}}$ . If this velocity is larger than the drift-dispersion velocity of small bodies,  $v_{pk}$ , then  $v_{\text{shear}}$  will set  $v_{\infty}$ , the velocity at which small bodies encounter cores. That is, we set

$$v_{\infty} = \max(v_{pk}, v_{\text{shear}}) . \quad (2.29)$$

We will refer to particles with  $v_{\infty} = v_{pk}$  as begin “drift-dispersion” dominated, and particles with  $v_{\infty} = v_{\text{shear}}$  as being “shear dominated.”

### 2.3.6 $v_{\text{enc}}$ and Calculating Work

It remains to determine the relevant velocity for calculating the drag force. Note that this velocity is relative to the gas (in contrast to  $v_{\infty}$ , which is relative to the local Keplerian velocity) and cannot be set by shear, since the gas and the particles will have the same shear velocity.<sup>5</sup> For particles that approach the core with velocities

---

<sup>5</sup>Particles that are in the regime depicted in the lower lefthand panel of Figure 2.1 may experience the full shear velocity over an extended distance as they are turned relative to the core. Because these particles already deplete their kinetic energy this effect does not affect our conclusions about the relative size of  $KE$  and  $W$ .

faster than the local circular orbit velocity about the large body, i.e. for particles with  $v_\infty > v_{\text{orbit}} = \sqrt{GM/R_{\text{acc}}}$ , the dominant effect of the gravitational force from the core will be to give the particle a small “kick” in the direction perpendicular to its motion. By using the impulse approximation, one can show that the magnitude of the resultant perpendicular velocity is of order  $v_{\text{kick}} = GM/(R_{\text{acc}}v_\infty)$  (see e.g. [Binney & Tremaine 2008](#)). This effect is illustrated in Figure 2.4 (solid curve). As also shown in Figure 2.4, particles that approach the core with velocities such that  $v_\infty < v_{\text{orbit}}$  will experience a substantial change in their total velocity during their interaction with the core (dashed curve). During the encounter, the magnitude of the particle’s velocity when the particle is a distance  $r$  from the core is approximately  $|v| \approx \sqrt{GM/r}$  (see the lower righthand panel of Figure 2.4). If the magnitude of the work done on the particle can be expressed as  $W(r) = F_D(r)r$ , then for a particle in a linear drag regime we have  $W(r) \propto r^{1/2}$ , i.e. the majority of the work done during encounter occurs when the particle is at the largest scales. If the particle is in a quadratic (Ram) drag regime, then  $F_D$  is independent of  $r$ , so the work done at all scales is approximately equal. In either regime we are therefore justified in approximating the work done during the encounter as  $W = 2F_D(v_{\text{enc}})R_{\text{acc}}$ , where  $v_{\text{enc}} = v_{\text{orbit}}(R_{\text{acc}}) = \sqrt{GM/R_{\text{acc}}}$ .

Finally, if the particle’s drift velocity relative to the gas,  $v_{pg}$ , is larger than the velocity from the gravitational influence of the core, then  $v_{pg}$  will set the velocity during the encounter.

In summary, we define the relevant velocity for the work calculation,  $v_{\text{enc}}$  to

be

$$v_{\text{enc}} = \begin{cases} \max(v_{\text{orbit}}, v_{pg}), & v_{\infty} < v_{\text{orbit}} \\ \max(v_{\text{kick}}, v_{pg}), & v_{\infty} > v_{\text{orbit}} \end{cases} \quad (2.30)$$

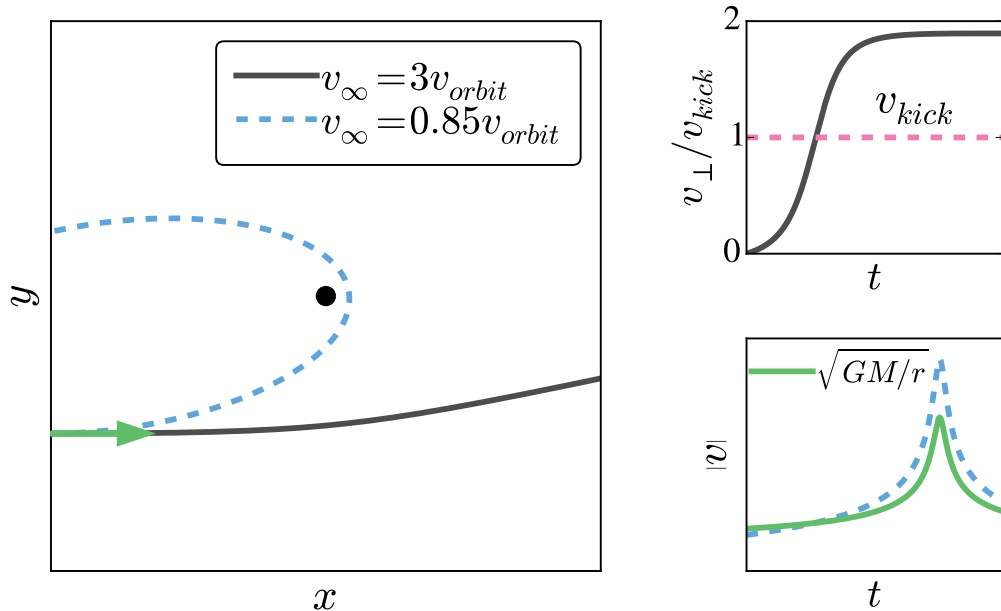


Figure 2.4: An illustration of the effects of the gravitational interactions between the small body and the core on the velocity between the two bodies during their encounter,  $v_{enc}$ . *Left Panel:* Both particles enter from the lower left, as indicated by the arrow. The upper particle (dashed curve) has  $v_\infty < v_{orbit}$  while the lower particle (solid curve) has  $v_\infty > v_{orbit}$ . The upper, slow moving particle has the direction of its velocity substantially changed during the interaction, while the lower, fast moving particle only receives a small perturbation to its velocity in the direction perpendicular to its motion. *Lower Right Panel:* The slow moving particle is excited to a velocity comparable to  $v_{orbit}(r) = \sqrt{GM/r}$  during its interaction with the core. *Upper Right Panel:* The fast moving particle receives a small perturbation to its velocity, of order  $v_{kick} = GM/(R_{acc}v_\infty)$ . As can be seen in the figure, the actual perturbation is approximately a factor of 2 larger than  $v_{kick}$ . Including this factor of 2 does not have a substantial effect on our results.

## 2.4 Calculation of Accretion Cross Section

We now turn to how the particle velocities discussed in the previous section are used to calculate the growth timescale of the core. We discuss how the length and width of the accretion cross section,  $R_{\text{acc}}$  and  $H_{\text{acc}}$ , are calculated, as well as how the scale height of the small bodies,  $H_p$ , is determined.

### 2.4.1 Determining $R_{\text{acc}}$

The capture radius,  $R_{\text{acc}}$ , is the radius interior to which a small body will accrete if certain energy criteria are met, as discussed in Section 2.2.1. The scale  $R_{\text{acc}}$  is also used to determine both the incoming kinetic energy of a small body and the work done by gas drag during the encounter. In this work we assume that particles that cannot dissipate their kinetic energy at  $R_{\text{acc}}$  will not be able to accrete on a smaller length scale. To see this, we note that, for a general impact parameter  $b$ , we have

$$\frac{KE}{W} = \frac{mv_{\infty}^2}{4F_D(v_{\text{enc}})b}. \quad (2.31)$$

If the small body's velocity is shear dominated, so that  $v_{\infty} = v_{\text{shear}}$ , then it can be shown analytically that the only particles that may have  $KE/W > 1$  are those shearing into  $R_H$ . In this case particles with substantially smaller impact parameters will not penetrate into  $R_H$  due to the nature of three-body trajectories (see e.g. [Petit & Henon](#)

1986). If instead  $v_\infty = v_{pk}$ , then we have

$$\frac{KE}{W} \propto \frac{1}{F_D(v_{\text{enc}})b} \propto \begin{cases} (v_{\text{enc}}b)^{-1}, & \text{Epstein, Stokes} \\ (v_{\text{enc}}^2b)^{-1}, & \text{Ram} \end{cases} \quad (2.32)$$

The maximal possible scaling of  $v_{\text{enc}}$  with impact parameter is  $v_{\text{enc}} = v_{\text{kick}} \propto b^{-1}$ . Therefore, Equation (2.32) implies that  $KE/W$  is always minimized at large  $b$  when gas drag is in the Epstein or Stokes regime, and our calculation of the energy criterion at the largest possible accretion scale is sufficient. The only case for which gas-assisted growth may be ruled out by the energy criterion at a large scale and yet possible at a smaller impact parameter is in the Ram pressure drag regime. We do not include this possibility in our calculation of the accretion rate. This cases holds over small amount of parameter space, as it requires particles to have both  $r_s > 9\lambda/4$  and  $Re \gg 1$ . Our modeling may rule out accretion of large particles in the inner disk (where the Ram regime is most important) that would be able to accrete at smaller scales.

To determine  $R_{\text{acc}}$ , we note that capture is in principle possible either within the planet's atmosphere, where the gas density increases substantially, or within the radius at which a small body can stably orbit the core. Thus the capture radius is set by the relative size of the atmospheric radius, which extends up to  $R_b$  (for  $R_b < R_H$ ; see Section 2.7 for  $R_b > R_H$ ), and the stability radius,  $R_{\text{stab}}$ :

$$R_{\text{acc}} = \max(R_{\text{stab}}, R_b) . \quad (2.33)$$

The stability radius is determined by requiring the that the force on the small body is

dominated by the gravity of the core. We consider two other forces that can disrupt accretion, which leads to two different length scales that can set  $R_{\text{stab}}$ .

### The Hill Radius

The first scale is set by demanding that the small body not be sheared off by the gravity from the host star; this leads to the traditional measure of stability, the Hill radius, where the gravitational acceleration from the core is balanced by the tidal gravity from the star (Hill 1878). For  $M_* \gg M$ , where  $M_*$  is the mass of the central star,

$$R_H \approx a \left( \frac{M}{3M_*} \right)^{1/3}, \quad (2.34)$$

where  $a$  is the semi-major axis of the core's orbit.

The fact that accretion can occur for impact parameters of order  $R_H$  is one of the main enhancements to growth rate that comes from pebble accretion. In the absence of gas, the maximal impact parameter for accretion is smaller than  $R_H$  by a factor  $(R/R_H)^{1/2}$ , where  $R$  is the radius of the planet (see Appendix A.3). Both Lambrechts & Johansen (2012) (hereafter LJ12) and Ormel & Klahr (2010) (hereafter OK10) and ) find regimes where  $R_{\text{acc}} \sim R_H$  in their numerical calculations of pebble accretion. In LJ12's framework, accretion at  $R_H$  occurs for core masses greater than  $M_t = \sqrt{1/3} v_{\text{gas}}^3 / (G\Omega)$  and particle sizes  $St \gtrsim 1$ .<sup>6</sup>

---

<sup>6</sup>LJ12 do not explicitly detail the Stokes number range where accretion at  $R_H$  occurs – because they run their simulations only for particles of size  $St = 10^{-2}, 10^{-1}, 10^0$ , they merely note that only particles with  $St = 10^{-2}$  appear to accrete at an impact parameter less than the Hill radius (see below). Following Xu et al. (2017), we take their regime where  $R_{\text{acc}} = R_H$  to hold only for  $St \gtrsim 1$ .

In OK10’s framework, impact parameters comparable to  $R_H$  occur in what they refer to as the “three body regime”, which occurs for  $St > 1$ , and  $St > \zeta_w \equiv \eta v_k/v_H$ , where  $v_H \equiv R_H\Omega$  is the Hill velocity. In this regime, OK10 give the impact parameter as  $b_{3b}/R_H = 1.7p^{1/2} + 1.0/St$ , where  $p \equiv R/R_H$ . This agrees generally with our results that  $R_{acc} \approx R_H$  in the Hill accretion regime.

The  $1/St$  dependence given by OK10 appears to encapsulate the chaotic nature of trajectories for particles that shear into the Hill sphere: often particles will orbit the core many times before exiting the Hill sphere. This effect can cause particles that would not accrete according to our energy criterion to be captured, since in our modeling we only include particles that dissipate their energy over one orbital crossing. If we use the result from [Goldreich et al. \(2002\)](#), who studied binary capture of Kuiper Belt objects by dynamical friction, that the probability of capture,  $P_{cap}$ , for a particle that shears into the Hill radius is equal to the fraction of energy it dissipates over one orbit, then this leads to an effective accretion rate of

$$\frac{dM}{dt} \sim R_H v_H \Sigma_p \frac{W}{KE}. \quad (2.35)$$

For high mass cores, the gravitational force from the core dominates the velocity of the small body during the encounter, and the encounter velocity is  $v_{enc} \sim v_H$ . This in turn implies that  $W/KE \propto 1/St$ . For 2D accretion ( $H_p < R_{acc}$ ), which is the regime modeled by OK10, our expression therefore agrees with their results. For low mass cores however, the particle-gas relative velocity will instead dominate the velocity during the encounter, which will lead to scaling that differs from  $1/St$  in this regime.

In summary, particles that have  $R_{\text{stab}} = R_H$  and  $v_\infty = v_H$  accrete with timescales given by

$$t'_{\text{grow}} = \frac{t_{\text{grow}}}{\min(1, W/KE)} \quad (2.36)$$

where  $t_{\text{grow}}$  is given by Equation (2.6). In what follows Equation (2.36) is used to modify  $t_{\text{grow}}$  for particles that shear into  $R_H$ .

### The WISH Radius and Shearing Radius

In the presence of gas, even if the gravity from the core dominates over the tidal gravity from the star, it is possible that the relative acceleration of the core and the small body will be strong enough to strip the small body away from the core. In this regime,  $R_{\text{stab}}$  is set not by the Hill radius, but by what [Perets & Murray-Clay](#) refer to as the wind-shearing (WISH) radius ([Perets & Murray-Clay 2011](#)). At the WISH radius, the differential acceleration between the large and the small body due to gas drag is balanced by the gravitational acceleration. That is

$$R'_{WS} = \sqrt{\frac{G(M+m)}{\Delta a_{WS}}}, \quad (2.37)$$

where  $m$  is the mass of the small body, and  $\Delta a_{WS}$  is the differential acceleration between the small and the big body, given by

$$\Delta a_{WS} = \left| \frac{F_D(M)}{M} - \frac{F_D(m)}{m} \right|, \quad (2.38)$$

where  $F_D$  is the force exerted on the particle due to gas drag. For the mass ratios considered here the first term in Equation (2.38) is generally negligible. To determine the relevant velocity for calculating the drag force  $F_D$ , we note that particles that are accreted by the core will have their velocity modified by the core's gravity, increasing their velocity relative to the gas during the encounter. The most extreme case occurs when the velocity of particles match the local Keplerian velocity at which the core is moving. These particles temporarily experience the full gas velocity with respect to the core, which is a combination of the sub-Keplerian and turbulent velocities, as well as the Keplerian shear in the disk. We can encompass this behavior, in the limit  $M \gg m$  by writing  $R'_{WS}$  as

$$R'_{WS} \approx \sqrt{\frac{GMm}{F_d(\max[v_{\text{gas}}, v_{\text{shear}}])}} \quad (2.39)$$

where  $v_{\text{gas}} = \sqrt{\eta^2 v_k^2 + \alpha c_s^2}$  is the RMS velocity of the nebular gas, and we use the prime to differentiate this radius from the definition of  $R_{WS}$  used below. The case  $v_{\text{gas}} > v_{\text{shear}}$  is discussed in detail by [Perets & Murray-Clay \(2011\)](#). In the three drag regimes discussed in Section 2.3.1, [Perets & Murray-Clay \(2011\)](#) give  $R_{WS}$  as

$$R_{WS} = (GM\rho_s)^{1/2} \times \begin{cases} \left(\frac{1}{\rho_g v_{th} v_{\text{gas}}}\right)^{1/2} r_s^{1/2}, & \text{Epstein} \\ \left(\frac{4}{9} \frac{\sigma}{\mu v_{th} v_{\text{gas}}}\right)^{1/2} r_s, & \text{Stokes} \\ \left(\frac{1}{0.165} \frac{1}{\rho_g v_{\text{gas}}^2}\right)^{1/2} r_s^{1/2}, & \text{Ram} \end{cases} \quad (2.40)$$

where  $\rho_s$  is the internal density of the small body. We will use the term WISH radius and the symbol  $R_{WS}$  to refer solely to the case  $v_{\text{gas}} > v_{\text{shear}}$ . For the case  $v_{\text{shear}} > v_{\text{gas}}$  on the other hand, the righthand side of Equation (2.39) now depends on impact parameter. In this regime we will refer to the impact parameter as the “shearing radius”,  $R_{\text{shear}}$ . In general,  $R_{\text{shear}}$  is determined by numerically solving the equation

$$R_{\text{shear}} = \sqrt{\frac{GMm}{F_d(R_{\text{shear}}\Omega)}} \quad (2.41)$$

For a particle in a linear drag regime, the particle’s Stokes number is independent of velocity, which allows us to solve for  $R_{\text{shear}}$  analytically:

$$R_{\text{shear}} = (3St)^{1/3} R_H . \quad (2.42)$$

In Section 2.5.5 we will compare our results to OK10 and LJ12 in the laminar regime – for now we translate their impact parameters into our notation.

The WISH radius is equivalent, in the laminar regime, to the effective accretion radius,  $r_d$ , used by LJ12, as well as to the settling radius  $b_{\text{set}}$ , used by OK10. LJ12 give the effective accretion radius as  $r_d = (t_B/t_s)^{-1/2} r_B$ . Here  $t_B = r_B/v_\infty$  is the drift time across the “Bondi radius” –  $r_B = GM/v_\infty^2$ .<sup>7</sup> As LJ12 note,  $r_d$  is equal to the WISH radius, as can be seen from that fact that

$$r_d = \sqrt{t_s \eta v_k \frac{GM}{(\eta v_k)^2}} = R_{WS} . \quad (2.43)$$

---

<sup>7</sup>As LJ12 note, their definition of the Bondi radius differs from the definition used in other works (including this one), which uses  $c_s$  in the place of  $v_\infty$ .

LJ12 also give a radius equal to  $R_{\text{shear}}$  (up to a factor of  $3^{1/3}$ ) for particles with  $St = 10^{-2}$  and  $M > M_t$ .

In their “settling” regime, OK10 determine the impact parameter  $b_{\text{set}} = R_{\text{acc}}/R_H$  by solving the cubic equation

$$b_{\text{set}}^3 + \frac{2\zeta_w}{3}b_{\text{set}}^2 - 8St = 0 \quad (2.44)$$

If the cubic term in the above equation is negligible, then we get the solution

$$b_{\text{set}} = \sqrt{12St/\zeta_w} . \quad (2.45)$$

In terms of  $\zeta_w$ , we can rewrite  $R_{WS}$  as

$$R_{WS} = \sqrt{3} \left( \frac{St}{\zeta_w} \right)^{1/2} R_H , \quad (2.46)$$

so  $b_{\text{set}} = 2R_{WS}$  in the laminar regime. If the middle term is negligible on the other hand, the solution is

$$b_{\text{set}} = 2St^{1/3} \quad (2.47)$$

which is  $\sim R_{\text{shear}}$ . One can verify by inspection that the solution to Equation (2.44) is approximately the minimum of Equations (2.45) and (2.47).

## Combining Length Scales

Once  $R_H$ ,  $R_{WS}$ , and  $R_{\text{shear}}$  are calculated, we take the stability radius to simply be the smallest of these three radii:

$$R_{\text{stab}} = \min(R_{WS}, R_{\text{shear}}, R_H) \quad (2.48)$$

We now have the pieces necessary to determine  $R_{\text{acc}}$  – we first compute  $R_{WS}$  and  $R_{\text{shear}}$  – the minimum of these two length scales determines the scale on which gas drag will pull small bodies off the core before they can be accreted. We then calculate  $R_H$  – the scale on which the stellar gravity disrupts accretion – and calculate  $R_{\text{stab}}$  by taking in the minimum of these scales. Finally, we take  $R_{\text{acc}}$  to be:

$$R_{\text{acc}} = \max(R_{\text{stab}}, R_b) . \quad (2.49)$$

Note that accretion within  $R_{\text{acc}}$  only occurs when additional energy criterion are met, as discussed in Section 2.2.1.

### 2.4.2 Determining $H_{\text{acc}}$

We now turn to the height of the accretion rectangle. The height of this rectangle will be the minimum of the dust scale height and the capture radius, since any particle outside the capture radius will not be able to accrete on to the core:

$$H_{\text{acc}} = \min(R_{\text{acc}}, H_p) . \quad (2.50)$$

In general, the solid particles will tend to settle to the midplane of the disk due to the vertical influence of gravity and the lack of pressure support. However, several processes will tend to oppose this settling, giving the particles some finite vertical extent. In our model, we include two different processes that drive particles vertically – the first is turbulent diffusion due to the isotropy of the small body’s turbulent velocities.

For  $St > \alpha$ , the scale height of the particles due to their interaction with turbulence is given by (Youdin & Lithwick 2007):

$$H_t = \sqrt{\frac{\alpha}{St}} H_g . \quad (2.51)$$

We can understand this expression by separately considering larger particles with  $St \gg 1$  and small, well coupled particles with  $St \ll 1$ . For the larger particles, as discussed in Section 2.3.3, we can think of the particle’s velocity as resulting from the large number of uncorrelated kicks it receives from the eddies. In this case we have  $v_{pk,t} \sim v_t/\sqrt{St}$ , which gives a scale height of

$$H_t \sim \frac{v_t}{\Omega\sqrt{St}} \sim \sqrt{\frac{\alpha}{St}} H_g , \quad (2.52)$$

since  $v_t = \sqrt{\alpha} H_g \Omega$ .

As described in the Youdin & Lithwick (2007), for  $St \ll 1$  we expect the particles to be well coupled to the gas, and thus expect the particles’ diffusion coefficient to be approximately equal to the gas value. We can express the turbulent diffusion

coefficient of the gas as  $D_g = \alpha_z c_s H_g$ . In what follows we take  $\alpha_z \approx \alpha$  unless otherwise stated. While  $\alpha$  and  $\alpha_z$  can differ, since  $\alpha$  enters our calculation mainly as a parameterization of the turbulent gas velocity, we are more interested in the relative size of  $\alpha_z$  and  $v_z$ , the vertical turbulent gas velocity. Magnetohydrodynamic simulations find that these two values are similar to order of magnitude (e.g. [Xu et al. 2017](#)). Tightly coupled particles should settle to the midplane at approximately their terminal velocity, so their time to settle to the midplane from a height  $z$  is approximately  $t_{\text{set}} \sim z/v_{\text{term}}$ . At terminal velocity the drag force balances the vertical component of gravity,  $F_{g,z} \sim (GMm/r^2)(z/r) \sim m\Omega^2 z$ . Setting  $F_d \sim m\Omega^2 z$  implies that  $v_{\text{term}} \sim St\Omega z$ , which gives  $t_{\text{set}} \sim 1/(St\Omega)$ . Finally, setting  $t_{\text{set}}$  equal to the particle diffusion time  $H_t^2/D_p$  gives Equation (2.51). [Carballido et al. \(2006\)](#) derive (2.51) for  $St \gg 1$  by more rigorous means, whereas [Dubrulle et al. \(1995\)](#) do the same for  $St \ll 1$ .

Note that for  $St > \alpha$  we have  $H_t > H_g$  which is clearly incorrect; turbulence cannot drive particles to heights larger than the extent of the gas disk. We therefore cap  $H_t$  at  $H_g$ . [Dubrulle et al. \(1995\)](#) derive (2.51) as the scale height of the dust to gas ratio  $\rho_s/\rho_g$ , and note that this height  $h$  is related to the dust scale height by the equation

$$H_t = h \left[ 1 + \left( \frac{h}{H_g} \right)^2 \right]^{-1/2}, \quad (2.53)$$

which has the expected behavior that  $H_t \rightarrow H_g$  as  $St \rightarrow \infty$ . Equation (2.53) can be used in the place of equation (2.51), though this does not substantially change the results. We employ (2.51) in order to maintain relative simplicity in our analytic results.

Turbulence’s modification to the particle scale height is discussed in a number of works, including OK10 and LJ12, though it is often not explicitly included in calculations of growth rate; instead, authors generally note that for  $H_t > R_{\text{acc}}$ , the growth timescale is increased by a factor of  $H_t/R_{\text{acc}}$ . We also note that equation (2.53) can be written as

$$H_t = H_g \sqrt{\frac{\alpha}{\alpha + St}}, \quad (2.54)$$

which is employed by [Ormel & Kobayashi \(2012\)](#) for the dust scale height in the presence of turbulence. Equation (2.54) agrees with [Youdin & Lithwick \(2007\)](#), Equation (28) without their factor of  $\xi^{-1/2}$ , where  $\xi \equiv 1 + St/(1 + St)$  for the values chosen in this paper.

Even in the absence of strong turbulence, the Kelvin-Helmholtz shear instability prevents small bodies from settling too close to the midplane. For small particles, which are well-coupled to the gas flow, this leads to a scale height of

$$H'_{KH} = \frac{H_g^2}{a} = \frac{2\eta v_k}{\Omega}, \quad (2.55)$$

(see for example [Lee et al. 2010](#)). In order to extend this scale height to include larger particles, we assume that even when large bodies dominate the mass distribution, a population of small bodies exists that is substantial enough to drive the Kelvin-Helmholtz shear instability, and therefore turbulence, close to the midplane. We expect the turbulent velocity in this case to be comparable to the vertical shear rate, which is  $\sim \eta v_k$ .

In this case, we can make arguments analogous to the ones preceding Equation (2.52), which leads to a scale height  $H_p \sim \eta v_k / (\Omega \sqrt{St})$ . Thus, we can describe  $H_{KH}$  over the full range of particle sizes using the expression

$$H_{KH} = \frac{H_g^2}{a} \min(1, St^{-1/2}) . \quad (2.56)$$

If only large bodies are present, they may need to settle further in order to excite the Kelvin-Helmholtz instability, which would change the dependence on  $St$ . We leave a self-consistent calculation to another work. Furthermore, by employing this expression for larger particle sizes, we are neglecting the possibility of dynamical stirring of the large bodies. Mutual scatterings and/or the gravitational force of the core can drive small particles vertically, and may be more important than interactions with the gas for determining the scale height of larger particles, which are decoupled from the gas.

Finally, we take the solid scale height to simply be the maximum of these two heights

$$H_p = \max(H_t, H_{KH}) . \quad (2.57)$$

The possibility of 3D accretion ( $H_p > R_{\text{acc}}$ ) in the non-turbulent regime is generally neglected in works on pebble accretion, but we find that it has non-trivial effects on the growth timescale.

Table 2.1: Summary of Symbols Used in Text

Parameter	Symbol	Formula/Value
Mass of large body	$M$	–
Mass of central star	$M_*$	–
Keplerian orbital frequency	$\Omega$	$\sqrt{\frac{GM_*}{a^3}}$
Radius of small bodies	$r_s$	–
Density of solid bodies	$\rho_s$	$2 \text{ g cm}^{-3}$
Mass of small bodies	$m$	$\frac{4}{3}\pi\rho_s r_s^3$
Stopping time of small bodies	$t_s$	$\frac{m v_{\text{rel}}}{F_D}$
Small body Stokes number/dimensionless stopping time	$St$	$t_s \Omega$
Shakura-Sunyaev $\alpha$ parameter	$\alpha$	–
Large body Hill radius	$R_H$	$a \left( \frac{M}{3M_*} \right)^{1/3}$
Wind-shearing (WISH) radius	$R_{WS}$	$\approx \sqrt{\frac{GM t_s}{v_{\text{gas}}}}$
Shearing radius	$R_{\text{shear}}$	$\approx R_H (3St)^{1/3}$
Large body Bondi radius	$R_b$	$\frac{GM}{c_s^2}$
Largest radius for stable orbits about large body	$R_{\text{stab}}$	$\min(R_{WS}, R_{\text{shear}}, R_H)$
Extent of large body's atmosphere	$R_{\text{atm}}$	$\min(R_b, R_H)$
Impact parameter for accretion	$R_{\text{acc}}$	$\max(R_{\text{stab}}, R_{\text{atm}})$
Scale height of small bodies due to turbulence	$H_t$	$\sqrt{\frac{\alpha}{St}} H_g$
Scale height due to Kelvin-Helmholtz shear instability	$H_{KH}$	$\frac{H_g^2}{a} \min(1, St^{-1/2})$
Scale height of small bodies	$H_p$	$\max(H_t, H_{KH})$
Vertical extent of accretion cross section	$H_{\text{acc}}$	$\min(R_{\text{acc}}, H_p)$
Velocity of small bodies relative to nebular gas	$v_{pg}$	See Appendix A

Table 2.1 (cont'd): Summary of Symbols Used in Text

Parameter	Symbol	Formula/Value
Velocity of small bodies relative to Keplerian	$v_{pk}$	See Appendix A
Keplerian shear velocity	$v_{\text{shear}}$	$R_{\text{acc}}\Omega$
Approach velocity of small bodies	$v_{\infty}$	$\max(v_{pk}, v_{\text{shear}})$
Orbital velocity about large body	$v_{\text{orbit}}$	$\sqrt{\frac{GM}{R_{\text{acc}}}}$
Impulse approximation velocity perturbation by large body	$v_{\text{kick}}$	$\frac{GM}{R_{\text{acc}}v_{\infty}}$
Velocity of small body during encounter with large body	$v_{\text{enc}}$	See Appendix A

## 2.5 Overview of Results

Having discussed in detail how our model operates, we can now present the output from our model. For reference, we also provide a table detailing the symbols we use (Table 2.1). In this section we discuss our results broadly in order to introduce how gas-assisted growth operates in the presence of turbulence.

### 2.5.1 Model Parameters

We begin by providing the values of the fiducial parameters used for describing the protoplanetary disk, which are necessary to provide concrete numerical results. A discussion of the effects of varying some of these parameters is given in Section 2.6.

We assume a surface density profile of

$$\Sigma(a) = 500 \left( \frac{a}{\text{AU}} \right)^{-1} \text{ g cm}^{-2}, \quad (2.58)$$

where  $a$  is the semi-major axis in the disk. This profile is chosen to be consistent with measurements of the surface density in solids of size 0.1-1 mm, taken from sub-mm observations of protoplanetary disks ([Andrews et al. 2009](#), [Andrews 2015](#)), which probe

these particle sizes. In order to calculate the surface density profile of solid bodies,  $\Sigma_p$ , we assume a constant dust to gas ratio of  $f_s \equiv \Sigma_p/\Sigma = 1/100$ . The semi-major axis dependence of the temperature profile is taken from [Chiang & Youdin \(2010\)](#)

$$T = T_0 \left( \frac{a}{\text{AU}} \right)^{-3/7}. \quad (2.59)$$

For most purposes we will take the prefactor to be  $T_0 = 200 \text{ K}$ , which would place the Earth outside of the water ice line during its formation (e.g. [Powell et al. 2017](#)). We also note this prefactor is consistent with assuming the disk is heated primarily by irradiation from a central star with luminosity  $L_* \sim 3L_\odot$  (e.g. [Ida et al. 2016](#)), which is appropriate for a solar mass star of age 1 Myr ([Tognelli et al. 2011](#)). The effects of varying  $T_0$  are discussed in Section 2.6.2.

From here we can then calculate the isothermal sound speed and scale height of the disk in the usual manner:  $c_s = \sqrt{kT/\mu}$  and  $H_g = c_s/\Omega$ . Here  $\mu$  is the mean molecular weight of particles in the disk; we take  $\mu = 2.35m_H \approx 3.93 \times 10^{-24} \text{ g}$ , which assumes a disk composed of 70%  $\text{H}_2$  and 30% He by mass. We can also calculate the gas density  $\rho_g = \Sigma/(2H)$ , and the mean free path of gas particles,  $\lambda = \mu/(\rho_g\sigma)$ , where  $\sigma$  is the neutral collision cross section, which we take to be  $\sigma \sim (3\text{\AA})^2 \sim 10^{-15} \text{ cm}^2$ . In order to convert from Stokes number, which is the relevant parameter for calculating  $t_{\text{grow}}$ , to physical size, we need to specify the internal density of the pebbles,  $\rho_s$ . We take this density to be  $\rho_s = 2 \text{ g/cm}^3$  unless stated otherwise, which is appropriate for rocky bodies. Note however, that the solids in protoplanetary disks may be fluffy, i.e. their densities may be low, which can have important ramifications for planet formation

Table 2.2: Fiducial Disk Parameters

Parameter	Symbol	Formula/Value
Solid to gas ratio	$f_s$	0.01
Mean molecular weight of gas particles	$\mu$	$2.35 m_H \approx 3.93 \times 10^{-24} \text{ g}$
Neutral collision cross section	$\sigma$	$10^{-15} \text{ cm}^2$
Gas surface density	$\Sigma$	$\Sigma(a) = 500 \left(\frac{a}{\text{AU}}\right)^{-1} \text{ g cm}^{-2}$
Protoplanetary disk temperature	$T$	$T(a) = 200 \left(\frac{a}{\text{AU}}\right)^{-3/7} \text{ K}$
Isothermal sound speed	$c_s$	$c_s = \sqrt{\frac{kT}{\mu}}$
Average thermal velocity	$v_{th}$	$v_{th} = \sqrt{\frac{8}{\pi}} c_s$
Gas scale height	$H_g$	$H_g = \frac{c_s}{\Omega}$
Gas density	$\rho_g$	$\rho_g = \frac{\Sigma}{2H_g}$
Gas mean free path	$\lambda$	$\lambda = \frac{\mu}{\rho_g \sigma}$

(see e.g. [Kataoka et al. 2013](#)). While we consider the effect of varying  $M_*$  in Section 2.6.4, unless otherwise noted all values quoted in the paper are for a solar mass star,  $M_* = M_\odot$ . As noted in Section 2.2.1, the radius of the large body needs to be  $\gtrsim 10 \text{ km}$ , which corresponds to  $M \sim 10^{-9} M_\oplus$  for a density of  $2 \text{ g/cm}^3$ . In practice we do not consider cores that are close to this lower limit.

A summary of our fiducial disk parameters is given in Table 2.2.

## 2.5.2 Basic Model Output

For the purposes of understanding the broad features of pebble accretion, we present a typical output of our model in Figure 2.5. Figure 2.5 plots the growth timescale (Equation 2.6) as a function of the small body radius,  $r_s$ , for a core of mass  $M = 10^{-1} M_\oplus$  at  $a = 1 \text{ AU}$ . The growth timescales for several  $\alpha$  values, ranging from purely laminar flow to extremely strong turbulence, are shown. The timescale is set to  $\infty$  for particles that do not satisfy the energy criteria discussed in Section 2.2.1, so the plotted range for each value of  $\alpha$  indicates the range of small body radii the core can accrete via pebble

accretion. The Stokes numbers corresponding to the given values of radius are shown for reference (the laminar drift velocity is used to calculate  $St$  for particles not in a linear drag regime).

We begin by examining the laminar case, where  $\alpha = 0$ . For large values of  $r_s$ , particles shear into the Hill radius. However, growth is slow because particles are large and cannot fully dissipate their kinetic energy relative to the gas, which increases  $t_{\text{grow}}$  by a factor  $KE/W$ . Once particles are small enough that  $KE \sim W$  they can accrete on rapid timescales. In terms of the small body's Stokes number, we can in general write the criterion for particles to be able to deplete their kinetic energy as

$$St < \frac{4v_{\text{enc}}R_{\text{acc}}\Omega}{v_{\infty}^2}. \quad (2.60)$$

For particles of this size, gravity dominates over gas drag effects – therefore  $R_H$  determines  $R_{\text{acc}}$ , as opposed to  $R_{WS}$ . The large size of these particles also means that their velocity dispersion and drift velocity are low, so the approach velocity is set by shear, i.e.  $v_{\infty} = v_H$ . Using these values to calculate  $v_{\text{enc}}$  and plugging the result into Equation (2.60) gives

$$St < 4\sqrt{3}, \quad (2.61)$$

which will be a general upper limit on Stokes numbers that the core is able to accrete rapidly. Note that if the small body is not in a linear drag regime then the Stokes number is no longer independent of velocity. In this case the Stokes number calculated

for the small body moving through the disk (which is relative to  $v_{pk}$ ) will not necessarily be the same as the Stokes number during the encounter with the core (which is relative to  $v_{enc}$ ).

Growth for  $R_{acc} = R_H$  and  $v_\infty = v_H$  is extremely rapid in comparison to the planetesimal accretion timescale. As small body size continues to decrease however, eventually gas drag considerations overtake three body effects, and the shear radius shrinks below the Hill radius. This causes the growth timescale to increase for  $r_s \lesssim 20$  cm. From this point the shear radius continues to shrink with small body size, slowing accretion. The first kink in the slope around  $r_s \sim 15$  cm comes from small bodies changing from the fluid regime to the diffuse regime, while the second kink around  $r_s \sim 0.2$  cm stems from  $R_{shear}$  shrinking below  $H_p$ , which dilutes the density of small bodies, in turn slowing accretion. Eventually, the shear radius shrinks below the Bondi radius, which signals the point at which particles are so small that they will couple to the gas and flow around  $R_b$ . This causes growth to cut off for small values of  $r_s$ .

As increasingly strong turbulence is taken into account, the picture becomes more complicated. For the  $\alpha = 10^{-1}$  case, growth for large particle sizes is quite similar to the laminar case, since the growth parameters are solely determined by the core's mass for high  $St$ . As the particle size shrinks, we still find a small range of radii where growth occurs at  $R_{acc} = R_H$ ,  $v_\infty = v_H$ . Rather rapidly however, several new features emerge that were not previously present. First, the strong turbulence greatly increases the particle scale height. As particle size decreases this scale height increases until it

becomes larger than  $R_H$ , slowing down growth. As particle size decreases, for  $St < 1$  the drift-dispersion velocity of particles increases as they couple more strongly to the gas. Due to the rapid turbulent velocity of the gas,  $v_{pk}$  actually overtakes  $v_H$  around  $r_s = 100$  cm, slightly mitigating the increase in growth timescale. The WISH radius is also decreased due to the strong turbulence, which makes it easier to pull particles off of the core. Because of this the radius at which  $R_{WS} < R_H$  is much higher than in the laminar case, and around  $r_s = 50$  cm growth is again inhibited as the WISH radius begins determining  $R_{acc}$ . Another kink in the slope appears around  $r_s = 20$  cm as the scale height of particles becomes so large that  $H_p = H_g$ , at which point the particle scale height stops increasing. The final kink occurs at  $r_s \approx 15$  cm, and is again due to the particles switching from the fluid to the diffuse regime. Growth again stops when  $R_{WS} < R_b$ , but because of the decreased values of WISH radius relative to the laminar case, this occurs at a larger value of  $r_s$ . Similar features occur for the smaller values of  $\alpha$ , but due to the weaker turbulence these features occur at smaller values of  $r_s$ . The only exception is the domination of the turbulent RMS velocity over  $v_H$ , which for these values of parameters only occurs for the  $\alpha = 10^{-1}$  case. As can be seen in the figure, for lower values of  $\alpha$  wider ranges of small body sizes can accrete at what appears to be a minimal value of timescale, which we discuss in the next section.

### 2.5.3 $t_{\text{Hill}}$

The floor to the growth timescale in Figure 2.5 corresponds to a minimum value of  $t_{\text{grow}}$ , which cores reach when they can accrete over their entire Hill sphere. The

appearance of this minimum growth timescale, or maximal growth rate, is a consistent thread throughout the parameter space probed by our model.

We refer to this timescale as the “Hill timescale,” or  $t_{\text{Hill}}$ . This timescale is reached when all aspects of the accretion processes are set by the core’s gravity – that is when we have  $R_{\text{acc}} = R_H > H_p$ , and  $v_\infty = v_H$ . From Equations (2.6) and (2.50) it is easy to see that if  $H_p < R_{\text{acc}}$  then  $t_{\text{grow}}$  is independent of  $H_p$ . Using these values for our timescale parameters in (2.6) gives the value of  $t_{\text{Hill}}$  as

$$t_{\text{Hill}} = \frac{M}{2f_s \Sigma R_H^2 \Omega} . \quad (2.62)$$

A similar regime is identified by [Lambrechts & Johansen \(2012\)](#), Section 3.2, who refer to it as “Hill Accretion.” They however, only use this term to differentiate between the drift dominated and shear dominated regimes, which roughly corresponds to where  $R_{\text{acc}} = R_H$  for their model. Within their Hill regime, the growth timescale is not necessarily equal to  $t_{\text{Hill}}$ . See Section 2.5.5 for a more in depth comparison of the two models.

In general,  $t_{\text{Hill}}$  represents an extremely rapid timescale for growth. Scaled to fiducial values, the minimum timescale can be expressed as

$$t_{\text{Hill}} \approx 4300 \left( \frac{a}{\text{AU}} \right)^{1/2} \left( \frac{M}{M_\oplus} \right)^{1/3} \text{ years} . \quad (2.63)$$

This represents a significant enhancement over the timescale achievable via canonical core accretion, as can be seen by comparing equation (2.63) to (A.44).

This is the substantial decrease in growth timescale promised by gas-assisted growth. The source of this decrease can be mostly attributed to an increase in  $R_{\text{acc}}$ . As previously stated, the minimum timescale indicates accretion in a regime such that essentially all particles that encounter the Hill radius of the growing planet are accreted. In contrast, in the absence of gas the trajectories of particles that enter the Hill radius are chaotic, and whether a collision occurs is extremely sensitive to the value of the small body’s impact parameter. See for example [Petit & Henon \(1986\)](#). For this reason encounters with the core in this regime are often treated probabilistically, with the collision rate of small bodies equal to the product of the rate at which small bodies encounter radius and the probability that a particle inside the Hill radius will accrete. Performing such a calculation leads to an effective impact parameter for accretion in the so called “3-body regime” that is to order of magnitude equal to the geometric mean of the Hill radius and the planetary radius -  $b \sim \sqrt{RR_H}$ . See GLS and [Ormel & Klahr \(2010\)](#) Equation (5). From comparison with Equation (A.43) we see that the maximal increase in accretion rate that can be provided by pebble accretion is of order  $R_H/R$ .

To see why  $t_{\text{Hill}}$  is in general the fastest rate of growth possible, we first note that since  $R_{\text{stab}} = \min(R_H, R_{WS}, R_{\text{shear}})$ , it is clear that the maximal accretion cross section is of order  $\sigma_{\text{gas,max}} \sim R_H^2$ . Since turbulence can increase the RMS velocity of small bodies to values substantially larger than  $v_H$  however, it is conceivable that strong turbulence could increase the growth rate by increasing  $v_\infty$ , i.e. by increase the rate at which small bodies encounter the core. However, increasing the velocity of small bodies drives them vertically as well as horizontally, which decreases the density of small bodies

and slows accretion. This trade off rules out accretion on timescales faster than  $t_{\text{Hill}}$ , which we demonstrate to order of magnitude below. We first note that

$$H_{KH} = \frac{2\eta v_k}{\Omega} \max(1, St^{-1/2}) \gtrsim \frac{v_{pk,\ell}}{\Omega}, \quad (2.64)$$

$$H_t \approx \frac{v_{pk,t}}{\Omega}, \quad (2.65)$$

we also make the approximation that

$$v_{pk} = \max(v_{pk,\ell}, v_{pk,t}). \quad (2.66)$$

rather than the quadrature of  $v_{pk,\ell}$  and  $v_{pk,t}$ . We separately consider “2D accretion,” defined by  $H_p < R_{\text{acc}}$ , and “3D accretion,” where  $H_p > R_{\text{acc}}$ .

For 2D accretion, we can write  $t_{\text{grow}}$  as

$$t_{\text{grow}} = \frac{M}{2\Sigma_p R_H v_\infty} \quad (2.67)$$

$$= t_{\text{Hill}} \left( \frac{R_H \Omega}{v_\infty} \right), \quad (2.68)$$

where  $t_{\text{Hill}} \equiv M / (2\Sigma_p R_H^2 \Omega)$  and  $\Sigma_p \equiv f_s \Sigma$ . Thus  $t_{\text{grow}} < t_{\text{Hill}}$  requires  $v_\infty > v_H$  while still having  $R_H > H_p$ . But from Equations (2.64) - (2.66) we see that  $R_H > H_p$  implies that  $v_H > v_{pk}$ , so  $v_\infty = v_H$ . Thus the timescale for growth cannot drop below  $t_{\text{Hill}}$  for 2D accretion.

We now consider the 3D accretion regime when the Hill radius sets the geometry, that is  $H_p > R_{\text{acc}} = R_H$ . In this case, we can write the growth timescale

as

$$t_{\text{grow}} = \frac{MH_p}{2\Sigma_p R_H^2 v_\infty} = t_{\text{Hill}} \left( \frac{H_p \Omega}{v_\infty} \right) \quad (2.69)$$

If the particle is shear dominated, then  $t_{\text{grow}} > t_{\text{Hill}}$  since  $R_H < H_p$ . Furthermore, since Equations (2.64) - (2.66) imply that  $H_p \Omega \gtrsim v_{pk}$ , if the particle is drift-dispersion dominated we again have  $t_{\text{grow}} > t_{\text{Hill}}$ . Thus, in the 3D accretion regime  $t_{\text{Hill}}$  also represents the smallest possible timescale.

#### 2.5.4 Gas Mitigated Growth

While growth at  $t_{\text{Hill}}$  is extremely rapid, it is important to realize that in practice the minimum timescale can only be achieved for a certain range of small body sizes. Maximal accretion efficiency occurs for particles where the dominant effect of the gas is to dissipate particles' kinetic energy as they encounter the growing core, and all other aspects of the accretion process are set by the gravitational influence of the core. When the mass of small or large bodies is low enough that gas determines aspects of the accretion process, the timescale for growth will increase, in many cases quite substantially.

To examine in more detail what causes the timescale to increase above  $t_{\text{Hill}}$  as the interaction between the gas and the small bodies increases in importance, we plot the four quantities that go into the calculation of  $t_{\text{grow}}$  along with timescale itself in Figure 2.6. As  $\alpha$  increases, the gas-particle interaction will dominate over the gravitational interaction between the small body and the core. For low values of  $\alpha$  we have  $R_{WS} >$

$R_H > H_p$  and  $v_\infty = v_{\text{shear}}$  (as expected for  $R_H > H_t$ ), so the particle is in the 2D accretion regime and is able to accrete at  $t_{\text{Hill}}$ . As  $\alpha$  increases, the particle scale height begins to increase, until eventually  $H_p > R_H$ . At this point accretion becomes less efficient, and the timescale correspondingly increases. There are several other kinks in the timescale graph, which are caused by, in order of increasing  $\alpha$ :

1.  $R_{WS}$  decreasing to the point that  $R_{WS} < R_H$ .
2.  $v_\infty$  being set by dispersion instead of shear, i.e. switching to the drift-dispersion dominated regime.
3. Reaching  $H_p = H_g$ , at which point  $H_p$  stops increasing.

For large  $\alpha$  values, the growth timescale is almost an order of magnitude larger than  $t_{\text{Hill}}$ , indicating a substantial slow down in growth rate.

### 2.5.5 Correspondence with Previous Models of Pebble Accretion

In this Section we compare our model to the analytic results from OK10 and [Johansen & Lambrechts \(2017\)](#) (hereafter JL17)<sup>8</sup> in the laminar ( $\alpha = 0$  regime) as well as the extension of the OK10 model by [Chambers \(2014\)](#) to include turbulence. We discuss why our framework is more useful for incorporating the results of turbulence.

In order to facilitate comparison between the various models, we begin by highlighting some important features that emerge in our modeling of the growth rate.

Figure 2.7 shows a plot of  $P_{col} \equiv 2R_{acc}v_\infty$  for  $\alpha = 0$  in our model as a function of  $r_s$  and

---

<sup>8</sup>We compare to JL17 as opposed to LJ12 because the JL17 expressions are extensions of LJ12's analytic model, but their framework is more clearly laid out. In generating the comparison we use their Equations (30) and (31) to determine  $R_{acc}$  for  $M < M_t$  and  $M > M_t$  respectively.

$M$ . Several features, along with their analytic formulae, are marked on the plot. We discuss these features in detail below. Note that in calculating the analytic expressions for these features we implicitly assume a linear drag regime so that we can employ the analytic expressions for  $R_{WS}$  and  $R_{\text{shear}}$  (see Appendix A.1).

In the upper lefthand corner of the plot, we see that accretion is cut off once  $R_b > R_{\text{stab}}$ . At low core mass,  $R_{\text{stab}} = R_{WS}$  when this cutoff occurs, but at high core masses  $R_{\text{shear}}$  dominates, which causes the kink in the slope seen in the figure. The combination of these two scales causes a cutoff in accretion for

$$St < \min \left( 3 \frac{v_H^3 v_{\text{gas}}}{c_s^4}, 9 \frac{v_H^6}{c_s^6} \right). \quad (2.70)$$

In the bottom of the plot, we see that, at low core masses, accretion shuts off for particles that pass a certain maximum size. In this regime we have  $R_{\text{acc}} = R_{WS}$ ,  $v_\infty \approx v_{\text{gas}}$ , and  $v_{\text{enc}} = v_{\text{kick}}$ , which leads to a maximum size of

$$St = 12 \left( \frac{v_H}{v_{\text{gas}}} \right)^3. \quad (2.71)$$

However, as particle size continues to increase, we see that accretion actually resumes once particles become large enough. This is caused by these large particles decoupling from the gas, which lowers  $v_\infty = v_{pk}$  and raises  $v_{\text{enc}} = v_{pg}$  enough to overcome the increased mass of these particles. If we set  $R_{\text{acc}} = R_H$ ,  $v_{pg} \approx v_{\text{gas}}$  and approximate  $v_{pk}$  by its Taylor Expansion at  $\infty$  in the laminar regime,  $v_{pk} \approx 2v_{\text{gas}}/St$ , then we can derive

an approximate expression for the Stokes number at which accretion commences again:

$$St = \frac{v_{\text{gas}}}{v_H} . \quad (2.72)$$

Note that as particle size continues to increase, the energy criteria are only satisfied for a small range of particle sizes. However accretion continues probabilistically in this regime in accordance with Equation (2.36).

The gap in particle size where accretion is not possible disappears once the core surpasses a certain mass. If particles that have their encounter velocity dominated by the particle-gas relative velocity,  $v_{\text{enc}} = v_{pg}$ , become available for accretion, then the range of particle sizes the core can accrete will be extended, since these particles can dissipate more of their kinetic energy due to their larger encounter velocities. See Section 2.6.1 for more discussion of this effect. For these particles to be available, the previously derived upper limit on particle size,  $St = 12v_H^3/v_{\text{gas}}^3$ , must occur after the transition where  $v_{pg} = v_{\text{kick}}$ . Using the Taylor expansion of  $v_{pg}$  about 0 in the laminar regime,  $v_{pg} \approx 2v_{\text{gas}}St$ , we see that the latter transition occurs at  $St \approx (3/4)^{1/3} (v_H/v_{\text{gas}})$ . Therefore, the mass scale where this transition occurs is given by

$$\frac{v_H}{v_{\text{gas}}} = 48^{-1/3} . \quad (2.73)$$

Finally, as discussed in Section 2.5.2, at high core masses the transition where  $KE = W$

occurs at a fixed Stokes number of

$$St = 4\sqrt{3}, \quad (2.74)$$

which is noted on the plot as well.

We now contrast the output from our model in the laminar regime with the analytic models of OK10 and JL17. Figure 2.8 below shows plots of both  $P_{col} \equiv 2R_{acc}v_{\infty}$  and  $t_{grow}$  for a core at 30 AU, using our model, OK10’s, and JL17’s<sup>9</sup> (for a discussion of how the parameters of the protoplanetary disk are modeled, see Section 2.5.1). We plot  $P_{col}$  to disentangle the effects of particle scale height on the growth timescale, as we discuss below.

In all three figures, we see the same broad features: while pebble accretion operates for a broad range of particle sizes, there exists an “optimal” range near  $St = 1$  ( $r_s \approx 10$  cm) at which accretion reaches its maximal possible rate, and the growth timescale becomes comparable to  $t_{Hill} = M/(2R_H^2\Omega\Sigma_p)$ . In all three models, optimum accretion at  $St \approx 1$  does not begin until the core has reached a “large enough” mass. Furthermore, as the core mass increases, the core’s growth rate grows as well, in large part due to the increasing size of the core’s Hill radius. The growth timescale, however, increases as the core grows, because the core’s growth rate scales with  $M$  to a power

---

<sup>9</sup>OK10 include a “Hyperbolic” regime in their modeling, which uses the gravitational focusing cross section for accretion but the laminar terminal small body velocity (our Equation 2.19) for  $v_{\infty}$ . Because we explicitly do not include gravitational focusing in our model, we similarly do not include this regime when comparing with OK10. We therefore also neglect their exponential term for  $R_{acc}$  (OK10 Equation 32), which is included in their model to smooth between the settling and hyperbolic regimes, and instead solve their Equation (27) to determine  $R_{acc}$ . JL17 use a similar exponential smoothing term to smooth  $R_{acc}$  for all Stokes numbers larger than a given value (for fixed core mass). For the same reasons as above, we neglect this term in our comparison.

less than one.

In our and OK10's modeling, we see two other notable features as well: firstly, there exists a gap in the range of particle sizes that can be accreted for low core masses, which in our framework cannot accrete because their incoming kinetic energies are too high. Secondly, in the righthand side of the plots ( $r_s \gtrsim 100$  m) particles have  $R_H < R_{WS}, R_{\text{shear}}$  (i.e.  $R_{\text{acc}} = R_H$ ), but accretion is inefficient. This is due to the fact that these particles cannot fully dissipate their kinetic energy during a single orbital crossing; but because of the chaotic nature of trajectories for particles with impact parameter  $\sim R_H$  their growth timescale is increased by a factor of  $KE/W$  (see Section 2.4.1 for more detail.)

As can be verified from the plots, in the regions of parameter space where our model predicts that pebble accretion should operate, our results agree within factors of a few with both of these analytic models. This main disagreements are:

1. The mass scale above which accretion occurs on timescales comparable to  $t_{\text{Hill}}$  is not exactly the same in the models. As discussed previously, in our model there is a transition in behavior past  $v_H/v_{\text{gas}} \approx 48^{-1/3}$ . In JL17's model, the parameters that set  $t_{\text{grow}}$  change for a mass  $M > M_t$ , where  $M_t = \sqrt{1/3}v_{\text{gas}}^3/(G\Omega)$ . This is equivalent to  $v_H/v_{\text{gas}} = \sqrt{1/3}$ , which is clearly comparable to the cut in our model. In OK10's modeling, the size of the gap progressively narrows, as the borders between the two regimes –  $St = 12v_H^3/v_{\text{gas}}^3$ , and  $St = v_{\text{gas}}/v_H$  – become comparable. Eventually the gap disappears for  $v_H/v_{\text{gas}} = 1$ .
2. As discussed above, in our modeling accretion shuts off for particles below a certain

radius, which stems from the fact that once  $R_{\text{stab}}$  shrinks below  $R_b$  we expect particles to flow around the core’s atmosphere (see Figure 2.1, in particular the lower righthand panel). The regions where this effect occurs are denoted by red hatching. We note that in these regions we expect growth by all mechanisms to be inhibited, e.g. capture by gravitational focusing or even physical collisions with the core will not occur. (In contrast, in the white regions of the plot we still expect capture mechanisms other than gas-assisted growth to operate.) Because this process is set by the modification of the flow by the core’s gravity, we would not expect OK10’s integrations to capture it, since they assume a constant headwind velocity in their integrations. LJ12’s simulations do not appear to go to high enough core masses with small enough particle sizes to capture this effect.<sup>10</sup> This effect does appear to be consistent with the results of Ormel (2013), who find minimal accretion for small particle sizes at high core masses (see their Figure 12)

11

3. JL17 define a “weak coupling” regime, where the stopping time of the particle exceeds the time to pass the protoplanet,  $t_p = GM/(v_{\text{gas}} + v_H)^3$ . For  $v_{\text{gas}} \gg v_H$  this criterion is equivalent to  $St > 3v_H^3/v_{\text{gas}}^3$ , which is line with our and OK10’s criterion  $St > 12v_H^3/v_{\text{gas}}^3$ . For  $v_H \gg v_{\text{gas}}$ , the passing time criterion reduces to

<sup>10</sup>LJ12’s 1e-1.0.01 simulation, which is the highest core mass and smallest particle size they simulate, is actually marginal in the sense that  $R_{\text{shear}} = R_b$  in our notation. While there is a reduction in accretion in this run, it is unclear whether accretion is actually substantially reduced in the way we would expect in our modeling. It is also unclear whether LJ12’s resolution is fine enough to resolve the core’s atmosphere and therefore the modification of the flow pattern.

<sup>11</sup>In the bottom panel of Figure 12, Ormel (2013) almost all particle streamlines are unable to accrete for  $St = 10^{-4}$  (in our notation). For  $St = 10^{-3}$  however, particles over a range of impact parameters are able to accrete. For the parameters used by Ormel (2013) the particle size where  $R_{\text{stab}} (= R_{WS})$  in this region of parameter space) is less than  $R_b$  is  $St < 5 \times 10^{-4}$ .

$St > 3$ , which is again similar to our  $St > 4\sqrt{3}$  limit. For particle sizes exceeding this critical Stokes number, JL17 exponentially smooth  $R_{\text{acc}}$  to zero, which differs from our and OK10's modeling.

4. In the lower righthand region, OK10's results and our diverge. In this regime, particles that shear into  $R_H$  cannot fully dissipate their kinetic energy over one orbital crossing. This makes them accrete probabilistically, in accordance with Equation (2.36), i.e., instead of shutting off accretion because  $W < KE$  in this regime, we increase the growth timescale by a factor  $KE/W$ . For particles with  $v_{\text{enc}} \sim v_H$ , which holds for larger cores, this increases the growth timescale by a factor of  $St$ , which agrees with OK10's expression for  $R_{\text{acc}}$  in this regime –  $R_{\text{acc}} = R_H/St$ . However, for the low mass cores in the bottom righthand corner of the plot, the particle gas relative velocity dominates over the core's gravity, changing the Stokes number dependence.

Thus while our results are generally in order of magnitude agreement with other modeling in the laminar regime, there are few notable regions where our results diverge. It can be shown analytically that the agreement between our model and the other two essentially stems from the fact that, to order of magnitude, many of the transitions between length and velocity regimes occur in the same region of parameter space. For example, the transitions where  $R_H = R_{WS}$  and where  $v_{pk,\ell} = v_H$  both occur for  $St \sim \zeta_w$ . In the laminar case, there are therefore essentially fewer regimes that need to be covered.

When turbulence is included however, this is no longer the case. As an example,

in Figure 2.9 we compare our modeling to the pebble accretion modeling of [Chambers \(2014\)](#). The expressions used in [Chambers \(2014\)](#) are analogous to the OK10 expressions, with the replacement of OK10’s  $\zeta_w \equiv \eta v_k / v_H$  parameter with  $v_{\text{gas}} / v_H$ , where  $v_{\text{gas}} = \max(\eta v_k, \sqrt{\alpha} c_s)$ . In our comparison, we neglect the exponential smoothing term they carry over from OK10, as well as terms involving eccentricity and inclination, as they are not included in our model.<sup>12</sup> As can be seen from the figure, for low core masses and small body sizes, our models are in order of magnitude agreement. Again, analytic calculations can be used to demonstrate that for low core masses and small particle sizes, the expressions between the two models agree to order of magnitude. For example, the cutoff in Stokes number employed by [Chambers](#) –  $St_{\text{crit}} = 12(v_H / v_{\text{gas}})^3$  is replicated in our model for small cores and small particle radii. However, as can also be seen in the figure, there are numerous regimes covered in our modeling that aren’t captured by extending the OK10 expressions. A prominent example is the feature in the lower righthand corner, where low mass core can accrete “large” particles ( $\sim 10^2 - 10^3$  cm) on rapid timescales. This features results from the fact that, for low core masses, the velocities of these larger particles are set by their interactions with the nebular gas. Because these large particles are not well coupled to the gas flow, they have low kinetic energies relative to the core, but high velocities relative to the gas, allowing a certain

---

<sup>12</sup>The [Chambers \(2014\)](#) modeling of the velocity of small bodies induced by turbulence appears to use expressions for the RMS particle-particle relative velocity, as opposed to the velocity of small bodies relative to the local Keplerian orbital velocity. This may be an error in the text, as other expressions used by these authors to model the relative velocity between a small body and an embryo (e.g. their Equation 8), are expressions for a particle relative to the local Keplerian velocity. In particular, their expression tends toward 0 for small Stokes number particles, whereas we would expect that small, well-coupled particles move relative to the embryos at velocities comparable to the RMS turbulent gas velocity (assuming the embryos are decoupled from the gas, which is a good approximation since  $M_{\text{emb}} \geq 5 \times 10^{-6} M_{\oplus}$  in their work). This appears to underestimate the incoming velocities of small bodies for strong turbulence ( $\alpha \gtrsim \eta$ ). In our comparison with [Chambers \(2014\)](#) we therefore use the expression  $v_{\text{turb}}^2 = \alpha c_s^2 / (1 + St)$  in place of their Equation (9).

range of particle radii to dissipate energy during the encounter that is comparable to their kinetic energy. The shape of this feature depends on the transitions where  $KE \sim W$  as well as where  $R_{WS} \sim R_H$  and  $v_{pk} \sim v_H$ . In the presence of turbulence these transitions no longer need occur at similar regions of parameter space, leading to a more complex model of pebble accretion that is not well captured by extending the OK10 expressions.

### 2.5.6 Comparison to Xu et al. (2017)

We close this section by comparing the results of our model to numerical simulations of pebble accretion in the presence of turbulence. Xu et al. (2017) performed magnetohydrodynamic (MHD) simulations of gas-assisted growth of turbulence due to the magnetorotational instability (MRI). These simulations provide an excellent point of comparison for our order of magnitude model, since they use much more detailed physics but apply over a narrower range of parameter space. As we will show below, our model agrees with the Xu et al. results to order of magnitude, as we would expect.

Xu et al. perform six sets of simulations; they use two different values of core mass, at three different levels of turbulence for each core. The core masses are parameterized in terms of the “thermal mass,” which Xu et al. give as

$$M_T \approx 160M_{\oplus} \left( \frac{a}{30 \text{ AU}} \right)^{3/4}. \quad (2.75)$$

Note that this is the same as the flow isolation mass (see Section 2.7) for the values used in their work. The simulations are performed at core masses of  $\mu_c \equiv$

$M/M_T = 3 \times 10^{-3}$  and  $\mu_c = 3 \times 10^{-2}$ . The three levels of turbulence are achieved by performing a pure hydrodynamic simulation, a non-ideal MHD simulation with ambipolar diffusion, and an ideal MHD simulation. While thus far in our work we have assumed that  $\alpha \approx \alpha_z$ , where  $\alpha_z$  is the diffusion coefficient for the particle scale height, Xu et al. are able to separately calculate  $\alpha$  and  $\alpha_z$ . We also use their value for  $v_z$  to calculate our  $\alpha$  value, as we use  $\alpha$  to parameterize the turbulent gas velocity. For the pure hydrodynamic run they have  $v_z = \alpha_z = 0$ . For the ambipolar diffusion run the authors give  $\langle v_z^2/c_s^2 \rangle = 3.0 \times 10^{-4}$ ,  $\alpha_z = 7.8 \times 10^{-4}$ , while for the ideal MHD simulation they give  $\langle v_z^2/c_s^2 \rangle = 1.21 \times 10^{-2}$ , and  $\alpha_z = 4.4 \times 10^{-3}$ .

A comparison between our analytic model and their simulations is shown in Figure 2.10. This figure plots  $k_{\text{abs}} \equiv \dot{M}/\dot{M}_{\text{Hill}}$  as a function of the particle Stokes number  $St$ . Here  $\dot{M} = M/t_{\text{grow}}$  is the growth rate of the core, and  $\dot{M}_{\text{Hill}} = M/t_{\text{Hill}}$  is the growth rate for Hill accretion. The solid lines depict the model presented in this paper, while the data points show the results from the Xu et al. paper. For the purposes of matching their model, we've used a temperature profile consistent with their results, used their values of  $\alpha_z$  for the calculation of  $H_p$  (as opposed to using  $\alpha$ ), and set the scale height in the laminar case to be  $H_{p,\text{lam}} = 0.01H$  to be consistent with these authors' choice.

As can be seen in Figure 2.10, our model nicely achieves the intended goal of reproducing the trends found by the numeric results, as well as being accurate to within a factor of 2 for all of the values found in the numeric simulations. It is worth noting here that the simulations are carried out at quite large values of core mass, and serve mostly

to confirm our prediction that the efficiency of pebble accretion is not hugely reduced by increasing turbulence. It would be interesting to investigate in future simulations whether the drop off in efficiency for lower core masses predicted in our model (see Section 2.6.1) is reproduced in the numeric simulations.

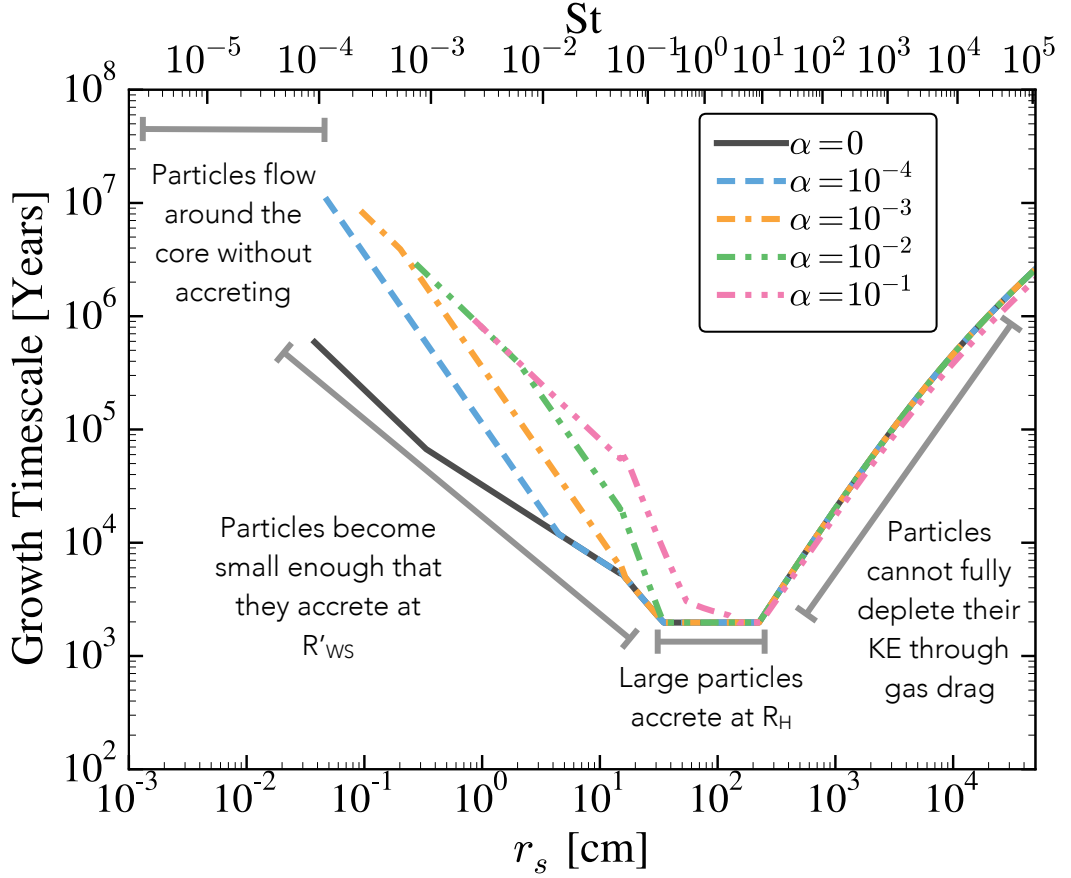


Figure 2.5: A plot of the timescale for growth of the protoplanetary core as a function of small body radius, plotted for various values of  $\alpha$ , which measures the strength of turbulence. The values shown are for  $a = 1 \text{ AU}$  and  $M = 10^{-1} M_{\oplus}$ . Also shown are the Stokes numbers for the plotted values of small body radius. Note that in a non-linear drag regime there is no longer a velocity independent relationship between radius and Stokes number; in this case the given values are calculated for drift velocities in the laminar ( $\alpha = 0$ ) case. The timescale is set to  $\infty$  for particles that are unable to accrete according to the energy criteria discussed in section 2.2.1, i.e. the range of radii plotted shows the range of particle sizes the core is able to accrete via pebble accretion.

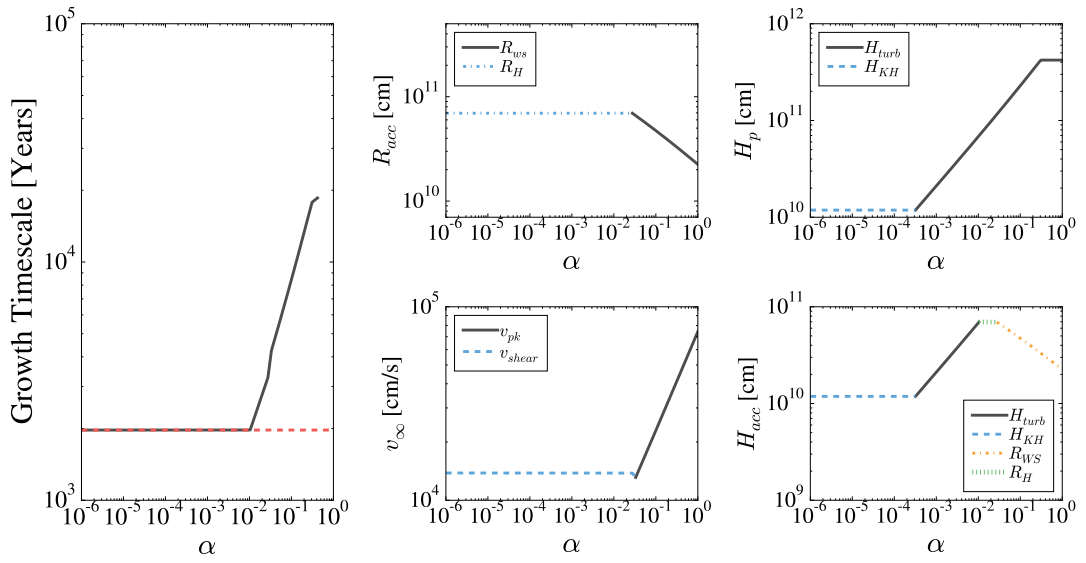


Figure 2.6: A plot of the timescale for growth of the protoplanetary core as a function of  $\alpha$ , along with plots of the four quantities used to determine  $t_{\text{grow}}$  (c.f. Equation 2.6), which are also plotted as a function of  $\alpha$ . The values shown are for  $a = 1 \text{ AU}$ ,  $M_* = M_\odot$ ,  $M = 10^{-1} M_\oplus$  and  $r_s = 35 \text{ cm}$ . The minimum timescale  $t_{\text{Hill}}$  is also shown (red dashed line).

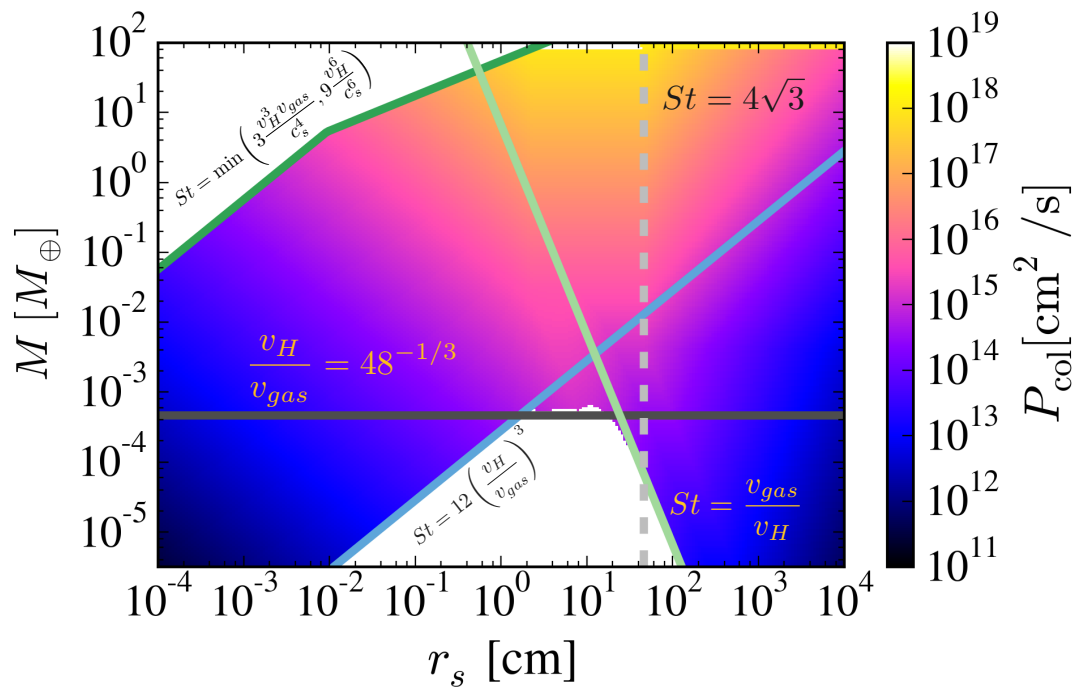


Figure 2.7: A plot of  $P_{col} \equiv 2R_{acc}v_{\infty}$  as a function of  $r_s$  and  $M$  for a core at  $a = 30$  AU with  $\alpha = 0$ . Several important features along with their formulae are marked on the plot. See the text for a discussion of what causes these features to emerge.

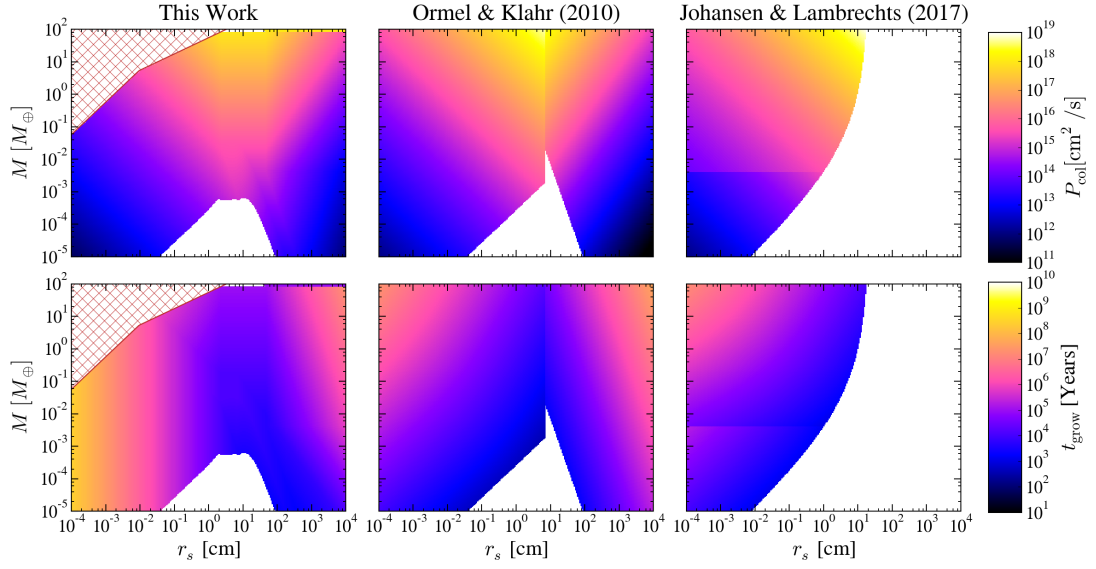


Figure 2.8: Comparison of results from our model in the laminar regime ( $\alpha = 0$ ) with analytic models of [Ormel & Klahr \(2010\)](#) and [Johansen & Lambrechts \(2017\)](#). The upper row plots  $P_{col} = 2R_{acc}v_{\infty}$  for a core at  $a = 30$  AU as a function of small body radius and core mass, while the lower panels instead plot the growth timescale,  $t_{grow}$ . The red hatched region denotes where growth is completely shut off in our modeling, whereas the white regions show places where gas-assisted growth will not operate, but the core can still grow by other means (e.g. gravitational focusing). The upper panels show agreement to order of magnitude between the three models, with exceptions in a few regions (see text for more details). The bottom panels highlight the effect of particle scale height, which is included in our model even in the laminar regime, but not in the other two analytic models.

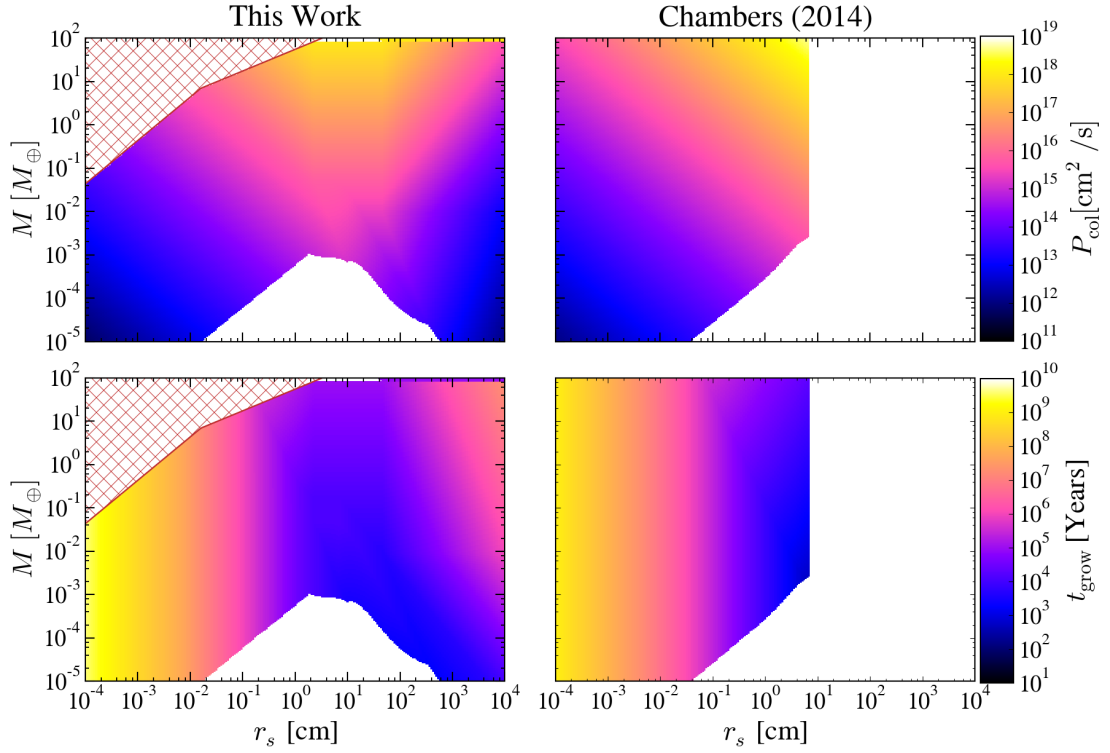


Figure 2.9: Comparison of results from our model with turbulence included ( $\alpha = 10^{-3}$ ) with modeling of pebble accretion by [Chambers \(2014\)](#). The upper row plots  $P_{col} = 2R_{acc}v_{\infty}$  for a core at  $a = 30$  AU as a function of small body radius and core mass, while the lower panels instead plot the growth timescale,  $t_{grow}$ . The red hatched region denotes where growth is completely shut off in our modeling, whereas the white regions show places where gas-assisted growth will not operate, but the core can still grow by other means (e.g. gravitational focusing).

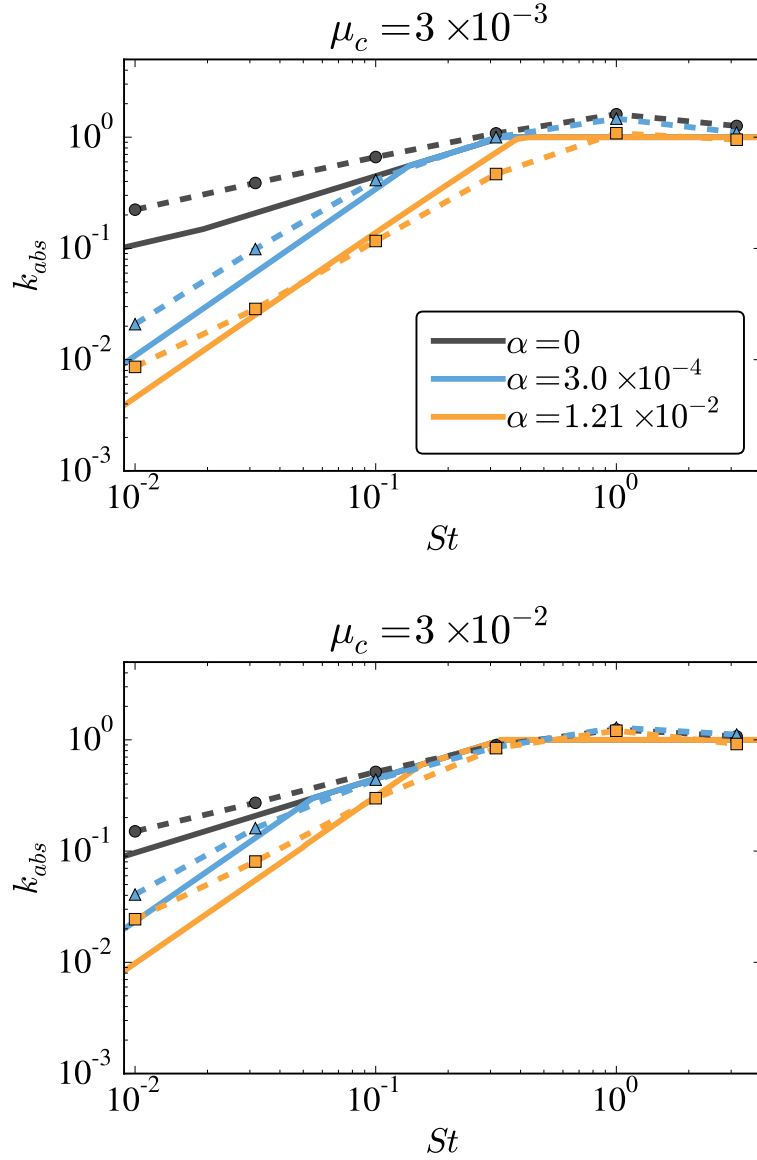


Figure 2.10: A comparison of the growth rate  $k_{\text{abs}}$  from our model and the MHD simulations of Xu et al. (2017), plotted as a function of the Stokes number of the particles the cores are accreting. Here  $k_{\text{abs}} \equiv \dot{M}/\dot{M}_{\text{Hill}}$ , where  $\dot{M} = M/t_{\text{grow}}$ , and  $\dot{M}_{\text{Hill}} = M/t_{\text{Hill}}$ , i.e.  $k_{\text{abs}}$  represents the growth rate of the core in units of the accretion rate for growth at  $t_{\text{Hill}}$ . The two panels depict growth for two different values of core mass –  $\mu_c \equiv M/M_T = 3 \times 10^{-3}$  and  $\mu_c = 3 \times 10^{-2}$ , where  $M_T$  is the thermal mass, defined in Equation (2.75). Each panel shows the growth rate for three different levels of turbulence, which are listed in the legend. The solid lines show the output from our model, while the data points show the Xu et al. results.

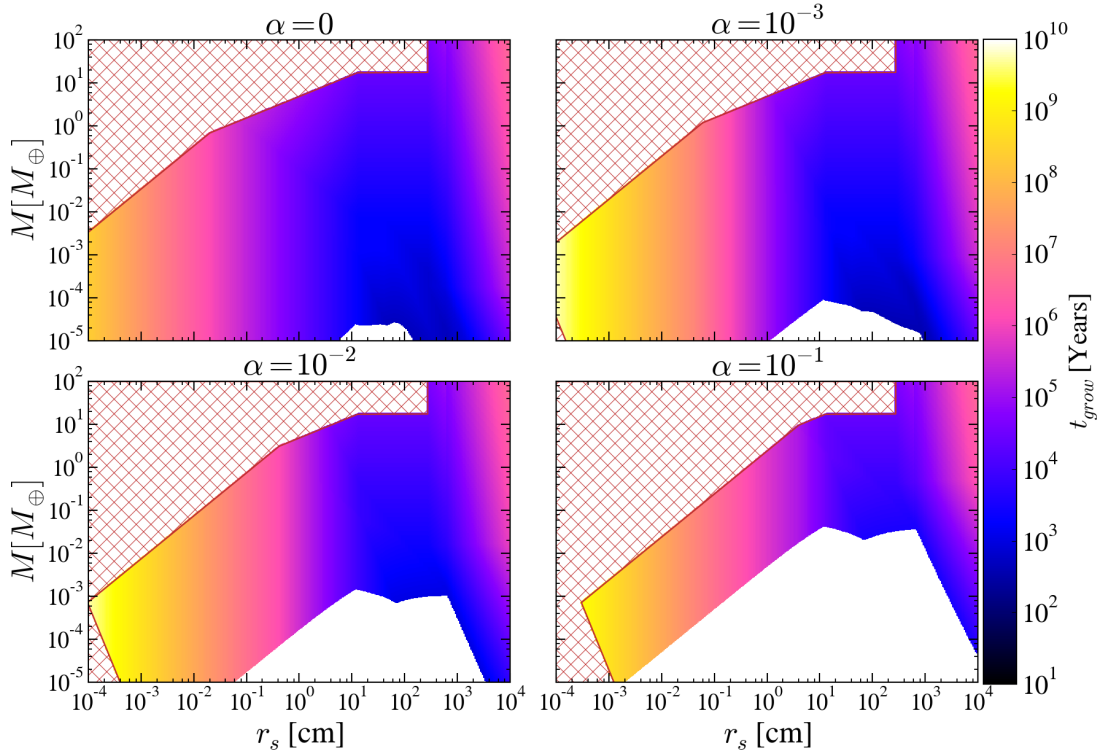


Figure 2.11: The growth timescale as a function of core mass, for  $a = 5$  AU. The red hatched region denotes where growth is completely shut off in our modeling, whereas the white regions show places where gas-assisted growth will not operate, but the core can still grow by other means (e.g. gravitational focusing). The feature in the upper right emerges for  $R_b > R_H$  (see Section 2.7).

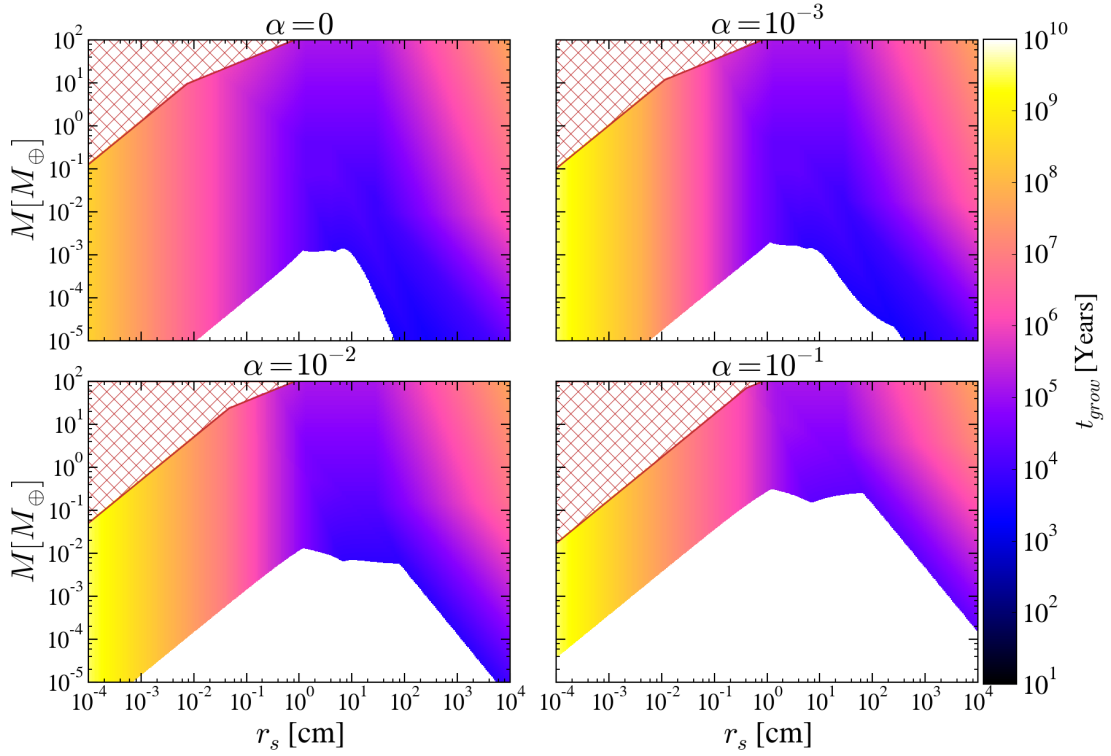


Figure 2.12: The growth timescale as a function of core mass, for  $a = 50$  AU. The red hatched region denotes where growth is completely shut off in our modeling, whereas the white regions show places where gas-assisted growth will not operate, but the core can still grow by other means (e.g. gravitational focusing).

## 2.6 Exploration of Parameter Space

In this section we give an overview of the effects of varying a few of the most important parameters in our model. In the first three sections we discuss varying parameters related to the disk in which growth is occurring. We begin by discussing the combined effects of varying the semi-major axis,  $a$ , and the core mass,  $M$ , both of which determine the importance of interactions between the small body and the gas relative to gravitational effects between the small body, growing core, and central star. We then investigate the effects of varying  $T_0$ , prefactor which sets the temperature profile,  $\Sigma_g$ , the local gas surface density, and  $M_*$ , the mass of the central star.

### 2.6.1 Effects of Variation of Orbital Separation and Core Mass

In Section 2.5.3, we identified the minimal timescale  $t_{\text{Hill}}$  that pebble accretion can operate on. We also emphasized, however, that pebble accretion can operate on timescales that are substantially slower – in many cases these timescales can exceed the lifetime of the disk,  $\tau_{\text{disk}} \sim 2.5$  Myr, which implies that pebble accretion essentially won't occur. In this section we highlight how at low core masses at wide orbital separations only a small range of particle sizes, if any, accrete on timescales comparable to  $t_{\text{Hill}}$ .

To illustrate how core mass and orbital separation effect the growth timescale, we plot  $t_{\text{grow}}$  as a function of both  $r_s$  and  $M$  for a core at  $a = 5$  AU in Figure 2.11, and for a core at  $a = 50$  AU in Figure 2.12. To begin, we note that growth is generally slower at wide orbital separation, since the dynamical time  $t_{\text{dyn}} \sim \Omega^{-1}$  is larger and the solid surface density is smaller. For low core mass there is also a gap in the particle sizes that

can be accreted. For low turbulence this gap is small, but as  $\alpha$  increases, the width of this gap increases as well. This effect is enhanced at wide orbital separation, where the gap extends to higher core masses and is overall wider. Thus, low mass cores can often only accrete small pebble radii. These small particles are accreted on slow timescales which are  $\gtrsim \tau_{disk}$ , as small pebbles can only be captured at low impact parameters, and have low densities since they can be easily lofted by turbulence. Thus we see that growth is much slower at low core mass and wide orbital separation, particularly as the strength of turbulence is increased. If there exists a population of  $\gtrsim 10$  m “boulders,” then we see from the figure that there exists a narrow range of these larger particle sizes for which accretion can proceed on rapid timescales, even if accretion of pebble sized particles is slow.

Once the core exceeds a certain critical mass, the gap disappears and accretion proceeds much more rapidly, allowing pebbles to accrete on timescales comparable to  $t_{\text{Hill}}$ . To emphasize this effect in Figure 2.13 we plot the range of particle sizes that can accrete on timescales within a factor of two of  $t_{\text{Hill}}$ . Each panel depicts a different core mass, while different hatching patterns depict different levels of turbulence. As expected from the above discussion, for low core mass only close in cores with low levels of nebular turbulence can accrete particles on timescales comparable to  $t_{\text{Hill}}$ . As core mass increases however, particles farther out in the disk can be accreted with growth timescales  $\sim t_{\text{Hill}}$ , even when turbulence is strong.

We now discuss more quantitatively what sets the range of particle sizes that can be accreted, and how that range is affected by changing the core mass and orbital

separation. For low mass cores accreting small particles, we expect  $R_{WS}$  to set the impact parameter. Because the particles are so small, and therefore well coupled to the gas, we will have  $v_{pk} \approx v_{\text{gas}}$ , and  $v_{pg} \ll v_{\text{kick}}$ . Thus, in this regime we expect  $v_{\infty} \approx v_{\text{gas}}$  (since shear is negligible for low mass cores), and  $v_{\text{enc}} = v_{\text{kick}}$  (since  $v_{\text{gas}} < v_{\text{orbit}}$  in this regime). Plugging these values into our expressions for  $KE$  and  $W$  we can show that having  $KE < W$  requires

$$St < 12 \frac{v_H^3}{v_{\text{gas}}^3}, \quad (2.76)$$

which was given previously in Equation (2.71). This is one facet that makes accretion less efficient for low mass cores, high turbulence, and wide orbital separation – since  $v_H/v_{\text{gas}} \propto M^{1/3}a^{-4/7}$  in the laminar regime (i.e. approximating  $v_{\text{gas}} \approx \eta v_k$ ) and  $\propto M^{1/3}a^{-2/7}\alpha^{-1/2}$  in the turbulent regime ( $v_{\text{gas}} \approx \sqrt{\alpha}c_s$ ), decreasing core mass, increasing  $\alpha$  or increasing orbital distance will all make the limit on  $St$  more stringent.

As small body radius increases,  $v_{\text{kick}}$  decreases due to the increasing size of the core’s WISH radius, while  $v_{pg}$  rises as particles decouple from the gas. Eventually we reach the point that  $v_{pg} > v_{\text{kick}}$ , meaning that now  $v_{\text{enc}} = v_{pg}$ . In this regime the dependence of the energy on small body radius becomes more complex: throughout a large amount of parameter space  $KE/W$  increases with particle size, which encapsulates the fact that it is more difficult for heavier particles to dissipate their kinetic energy. If  $v_{\text{enc}} = v_{pg}$  however, the work done during the encounter increases strongly with small body radius, which actually make it *easier* for large particles to be accreted. Furthermore, if  $v_{\infty} = v_{pk}$  then the incoming  $KE$  of particles can also decrease with

small body radius, making it even easier for heavier particles to be accreted.

This effect is illustrated in Figure 2.14, which plots the ratio  $KE/W$  as a function of  $r_s$  for different core masses. The two different panels show cores at different orbital separations. For the low mass cores in the righthand panel, we see that once  $r_s$  increases past a certain value the qualitative behavior of  $KE/W$  changes – instead of monotonically increasing, the slope flattens out or even decreases. However, for the very low mass cores this behavior is inconsequential, since particles are ruled out from accreting before we reach a large enough particle size that  $v_{\text{enc}} = v_{pg}$  and this more complex behavior starts. For larger core masses however this is no longer the case, and the range of particle sizes that can be accreted is greatly extended. This what causes the gap seen in the range of accreted particle sizes to disappear – once particles with  $v_{\text{enc}} = v_{pg}$  become available accretion generally continues until the limit  $St = 4\sqrt{3}$  discussed in Equation (2.61) is reached. From comparison of the two panels we also see that this effect is much more prominent at wide orbital separations – at 1 AU none of the cores exhibit the change in slope seen at 50 AU.

Thus, we see that growth changes qualitatively once particles with  $v_{pg} > v_{\text{kick}}$  can be accreted. The critical value of mass where this occurs can be approximated by calculating the mass at which  $v_{pg} > v_{\text{kick}}$  is reached before the critical Stokes number given in Equation (2.76) is reached. If we keep the approximations that led to Equation (2.76) but take  $v_{pg} \approx 2v_{\text{gas}}St$  in the laminar regime and  $v_{pg} \approx v_{\text{gas}}\sqrt{St}$  in the turbulent regime, we can solve for the Stokes number past which  $v_{pg} > v_{\text{kick}}$ . Doing so, and setting the resulting Stokes number equal to (2.76) yields a mass limit, which, in both regimes,

may be approximated by

$$\frac{v_H}{v_{\text{gas}}} \approx 48^{-1/3} \quad (2.77)$$

This inefficiency of pebble accretion at lower core masses is also identified by [Visser & Ormel \(2016\)](#), who calculate the growth timescale of planetesimals by numerically integrating the pebble equation of motion in the presence of two different laminar gas flow patterns. [Visser & Ormel](#) find that pebble accretion is only faster than gravitational focusing (which they refer to as the ‘‘Safronov regime’’) once the growing planetesimal exceeds a certain radius,  $R_{PA}$ . They also find that this critical radius increases further out in the disk, which is again consistent with our results. It can be seen from our analytic expressions however, that while these effects are present in our model even in the laminar case, they are strongly amplified by the presence of turbulence.

### 2.6.2 Effects of Varying $T_0$

In this section we consider the effects of varying the prefactor to the temperature profile,  $T_0$ . While changing the disk temperature will affect the properties of the small bodies, such as number density and composition, by changing what volatile species are present in solids at a given location, we neglect such effects in what follows. The consequences of changing the temperature profile are complex and depend on the local disk parameters as well as the core mass and strength of turbulence. Nevertheless, in general increasing the temperature is detrimental to the accretion rate when gas domi-

nated processes set the scales relevant to growth. For growth at  $t_{\text{Hill}}$ , however, none of the scales depend on temperature, so the most rapid growth timescales are unaffected by increasing the disk temperature.

The primary effect of varying  $T_0$  on growth timescales is due to the dependence of  $c_s$  on  $T$ :  $c_s \propto T^{1/2}$ . Since  $H_{KH} \propto c_s^2$ , and  $H_t \propto c_s$ , increasing  $T_0$  will increase  $H_p$ . Similarly,  $v_{pk,\ell} \propto c_s^2$  and  $v_{pk,t} \propto c_s$ , so increasing  $T_0$  will also increase  $v_\infty$  in the drift dominated regime. Finally, from inspection of Equation (2.40), we see that  $T_0$  affects  $R_{WS}$  by changing  $\rho_g (\propto c_s^{-1})$ ,  $v_{th}$ , and  $v_{\text{gas}}$ . By inspecting the scaling of  $R_{WS}$  one can show that  $R_{WS}$  is a decreasing function of  $T_0$ .

While some the above effects increase  $t_{\text{grow}}$ , while other decrease it, the general effect of increasing  $T_0$  is to slow down growth. To see this, we can make the same approximations described in Equations (2.64) - (2.66). As in Section 2.5.3 we consider in the 2D and 3D regimes separately.

In the 2D regime where  $H_p < R_{\text{acc}}$ ,  $H_{\text{acc}} = R_{\text{acc}}$ , so we have  $t_{\text{grow}} \propto (R_{\text{acc}} v_\infty)^{-1}$ . Having  $R_{\text{acc}} > H_p$  implies that  $v_{\text{shear}} = R_{\text{acc}} \Omega > v_{pk}$ , which in turn implies that  $R_{\text{shear}} < R_{WS}$ . Thus we expect that  $t_{\text{grow}}$  is independent of  $T_0$  in this regime.

For 3D accretion, we have  $H_p > R_{\text{acc}}$ , which implies that  $v_\infty = v_{pk}$ . Therefore we have  $t_{\text{grow}} \propto (R_{WS}^2 \Omega)^{-1}$ , which is an increasing function of  $T_0$ . We therefore expect that (approximately) higher  $T_0$  should lead to slower growth. An example of the difference caused by increasing  $T_0$  is shown in Figure 2.15.

A secondary effect of increasing  $T_0$  is that  $t_s$  and  $St$ , which depend on  $\rho_g$ ,  $v_{th}$ , and  $\lambda$ , are also affected. However, inspection of Equation (2.13) shows that in the

Epstein regime the effects of  $T_0$  on  $t_s$  cancel out. Therefore  $T_0$  only affects  $St$  in the fluid regime. This substantially diminishes the importance of this dependence, since for a large amount of parameter space the small body sizes which grow the most efficiently are in the Epstein regime. For particles that are in the fluid regime, higher values of  $T_0$  will shift values of  $St$  to lower values of  $r_s$ .

Because of the approximate cancellation between  $v_\infty$  and  $H_p$  in the 3D regime, in general the maximal increase in timescale that can be provided by increasing  $T_0$  is of order  $t_{\text{hot}}/t_{\text{cold}} \sim R_{\text{acc,cold}}^2/R_{\text{acc,hot}}^2$ , where hot and cold denote the higher and lower values of  $T_0$  respectively. Since  $R_H$  generally represents an upper limit on  $R_{\text{acc}}$  (ignoring accretion in the  $R_{\text{acc}} = R_b$  regime), the maximal increase is of order  $(R_{WS,\text{cold}}/R_{WS,\text{hot}})^2$ , which in the laminar Stokes and Ram regimes can be of order  $\left(\frac{c_{s,\text{hot}}}{c_{s,\text{cold}}}\right)^3 = \left(\frac{T_{0,\text{hot}}}{T_{0,\text{cold}}}\right)^{3/2}$ . In practice, this maximal value is rarely reached, since it requires simultaneously satisfying  $r > 9\lambda/4$  to be in the fluid regime, while also having  $St < v_{\text{gas}}^3/(3v_H^3)$  in order to have  $R_{WS} < R_{\text{shear}}$ . In practice therefore, the increases increase growth timescale generally goes as  $T_{0,\text{hot}}/T_{0,\text{cold}}$ . Because accretion timescales at  $t_{\text{Hill}}$  are not dependent on temperature, increasing  $T_0$  does not affect the rapid growth rates supplied by gas-assisted growth.

Changing  $T_0$  will also have an effect on the range of particle sizes that the growing core is able to accrete. For small particle sizes, the accretion cut off is determined by the point where  $R_b = R_{WS}$ . Since  $R_b \propto c_s^{-2}$ , which is stronger than the dependence of  $R_{WS}$  on  $c_s$  regardless of drag regime, increasing  $T_0$  will decrease the size of the Bondi radius relative to the WISH radius. This in turn will allow the core to

accrete smaller sized bodies. For larger particle sizes, the effect of increasing  $T_0$  is not as clear cut. For particles accreting at  $t_{\text{Hill}}$ , the only effect of increasing  $T_0$  is to increase the drag force on accreting small bodies, which allow the core to accrete larger sizes. In other regimes however, increasing  $T_0$  can also increase the approach velocity of small bodies. In these cases the increase in kinetic energy of accreting particles outweighs the larger amount of work done, and the maximal size of small bodies accreted is reduced.

### 2.6.3 Growth in a Gas Depleted Disk

In this section, we explore growth in a disk where the gas density has been reduced by a factor of 100, but the solid surface density is unchanged; i.e we have  $\Sigma = \Sigma_{g,0}(a/\text{AU})^{-1}$ , where  $\Sigma_{g,0} = \Sigma_0/100$ , and  $\Sigma_0 = 500 \text{ g cm}^{-2}$  is the prefactor employed elsewhere in this paper for the gas surface density. However we keep  $\Sigma_{p,0} = 5 \text{ g cm}^{-2}$ . We note that this may affect some of the expressions used in this work, which implicitly assume  $\rho_g \gg \rho_p$ , where  $\rho_p$  is the volumetric mass density of the small bodies. We neglect in any such effects in what follows. These choices for gas and solid densities are made to emulate the conditions in the disk when the gas component of the disk is in the process of photoevaporating, which is an important stage in some theories of planet formation (e.g. [Lee & Chiang 2016](#), [Frelikh & Murray-Clay 2017](#)). As we shall show below, the predominant effect of reducing the gas surface density is to shift the range of small body sizes where accretion occurs to lower values.

An example of growth in a depleted disk is shown in Figure 2.16. As can be seen in the figure, the predominant effect of changing  $\Sigma$  is to shift growth down to lower values of  $r_s$ . This is due to the fact that the quantities that go into calculating

$t_{\text{grow}}$ , even the energy criteria, are functions of  $r_s$  through their dependence on  $St$  alone. Since in the Epstein regime  $t_s \propto r_s/\rho_g$  and in the Stokes regime  $t_s \propto r_s^2/\rho_g$ , the radius corresponding to a given Stokes number decreases when the surface density, and correspondingly the volumetric density, are decreased. This is what causes the shift to lower radii seen in Figure 2.16. Other than this shift however, there is essentially no change in the growth timescale. Said another way, when the timescale is viewed as a function of Stokes number, i.e. if we consider  $t_{\text{grow}}(St)$  as opposed to  $t_{\text{grow}}(r_s)$ , then this function is independent of  $\Sigma$ .

The sole caveat is that for particles not in a linear drag regime, the Stokes number of a particle is now dependent on the particle's velocity, which means that the Stokes numbers used for calculating different quantities might not be the same. For example we can express the WISH radius as  $R_{WS} = \sqrt{GMSt/(v_{\text{gas}}\Omega)}$ , but the  $St$  value in that expression is defined with respect to  $v_{\text{rel}} = v_{\text{gas}}$ , meaning it will not be the same as the Stokes number for e.g.  $v_{pk}$ , which assumes of course that  $v_{\text{rel}} = v_{pk}$ . In this case the simple argument that all quantities are solely dependent on  $St$  breaks down. In practice if we use e.g. the Stokes number defined with respect to laminar drift velocities for comparison purposes, the discrepancy between the two surface densities is minor. Furthermore, if we write the critical radius dividing the fluid and diffuse drag regimes,  $r_s = 9\lambda/4$ , in terms of Stokes number, it is straightforward to show the particle is in the fluid regime for

$$St_{\text{crit}} > 7.4 \times 10^{-2} \left( \frac{a}{\text{AU}} \right)^{23/7} \left( \frac{\Sigma_{g,0}}{500 \text{ g cm}^{-2}} \right)^{-2}. \quad (2.78)$$

Because of the strong scaling of  $St_{\text{crit}}$  with  $a$ , for  $a \gtrsim 5$  AU the differences between the two surface densities disappear entirely.

Thus, in general the range of small body sizes where accretion is effective will shift to lower values as the gaseous component of the disk dissipates. The subsequent effects of such a shift are quite sensitive to the underlying size distribution of the small bodies. A particularly salient issue here is whether radius or Stokes number controls the processes that produce the size distribution, as could be the case if e.g fragmentation near  $St \sim 0.1$  generates an upper cutoff to growth (Blum & Wurm 2008). If the Stokes number is what matters, then the effects of dissipating the surface density would be rather minimal, provided the surface density of the disk evolves faster than the disk dissipation timescale. If the size distribution is determined by radius however, and there exists a small range of sizes where most of the mass of the disk is located, then the shift in effective accretion range could have substantial effects, either positive or negative, on the accretion rate of small bodies. In the outer disk, for example, the combination of growth and radial drift may set an important particle scale (e.g. Birnstiel et al. 2012, Powell et al. 2017). The combination of these effects merits further investigation. See Lambrechts & Johansen (2014) for an example of pebble accretion in the presence of particle sizes determined by the interplay of growth and drift (note these authors use a full gas disk, not one depleted in gas surface density).

#### 2.6.4 Effects of Varying Stellar Mass

In this section we discuss the dynamical effect of varying  $M_*$ . Clearly, higher mass stars will have a higher overall temperature, should on average have higher surface densities as well. Since we have discussed those effects in previous sections, in this section we consider only the effect of varying  $M_*$ , leaving the other properties of the disk unchanged.

Changing  $M_*$  has an effect on the growth process solely through its effect on the local Keplerian orbital frequency  $\Omega$  and the size of the Hill radius  $R_H$ . Higher mass stars have lower dynamical times, which tends to speed up growth. On the other hand, in the presence of more massive stars the Hill radius of a growing planet will shrink as it becomes more difficult to hold on to accreting material, which clearly inhibits growth. The interplay between these two factors will determine the net effect of varying the stellar mass – which effect dominates, and therefore whether changing stellar mass is beneficial or detrimental to growth, depends on the other input parameters.

An example is shown in Figure 2.17. The Figure shows a plot of  $t_{\text{grow}}$  vs.  $r_s$  for five different stellar masses; the panels show the growth timescale for two different levels of turbulence. Many of the main features of varying  $M_*$  are visible in the figure. For the  $\alpha = 0$  case, small particles ( $r_s \lesssim 0.1$  mm) are accreted much more rapidly by the more massive stars. In this regime particles have  $R_{\text{acc}} = R_{WS}$  and accrete in 3D, with scale height  $H_p = H_{KH}$ . Thus the primary effect here of varying stellar mass is to change  $\eta v_k$  and  $\rho_g$  along with  $\Omega$ . In the Epstein regime however, these effects on both  $R_{WS}$  and  $St$  cancel out, and because  $H_{KH} \sim 2\eta v_k/\Omega$ , the increase in growth rate in

this regime scales roughly as  $\Omega \propto M_*^{1/2}$ . Eventually, the particle size increases to the point that  $R_{\text{shear}} < R_{WS}$ , which also implies that particles are now shear dominated. Because, in the laminar regime, this change roughly corresponds to where we shift from 3D to 2D accretion, the effect of increasing stellar mass in this regime is actually to *increase* the growth timescale –  $t_{\text{grow}} \propto (R_{\text{shear}}^2 \Omega)^{-1} \propto St^{-2/3} R_H^{-2} \Omega^{-1} \propto M_*^{1/6}$ , since  $St$  is independent of  $M_*$  in the Epstein regime. This is what causes the overlap in  $t_{\text{grow}}$  curves as  $r_s$  increases. Due to the fact that changing  $M_*$  can switch the regime that determines one of our growth parameters (e.g. shear vs. dispersion dominated) the maximal change in growth rate for two stellar masses  $M_{*,1}$  and  $M_{*,2}$  in this regime can be complicated. In general, however, the change is of order  $\Omega_1/\Omega_2 = (M_{*,1}/M_{*,2})^{1/2}$ , as can be seen in Figure 2.17.

As we increase in particle size, the cores reach the point where they can accrete particles at  $R_{\text{acc}} = R_H$ . As can be seen in Figure 2.17, the value of  $r_s$  where this transition occurs is a decreasing function of  $M_*$  due to the decreased size of the Hill radius at higher stellar mass. Figure 2.17 also shows that increasing stellar mass initially decreases the growth timescale, but for higher  $M_*$  further increasing the mass of the star actually increases the growth timescale. This is due to the fact that decreasing  $M_*$  increases  $H_{KH}$ , affecting whether the largest size particles are accreting in the 2D or 3D regime. Low mass stars will accrete in 3D, in which case increasing  $M_*$  will decrease the growth timescale by bringing the particle density down and the rate of shear up. Once the stellar mass becomes sufficiently large however, we will have  $R_H > H_{KH}$ , and the core will accrete in 2D. In this case increasing  $M_*$  will slow down growth by decreasing

the size of the Hill radius.

As turbulence increases, the difference between the various stellar masses for small particle size disappears. This effect occurs due to a balance between the decreased growth rate from decreasing encounter rate and an increased growth rate due to an increased particle density, since we generally accrete in 3D in this regime. If particles are drift-dispersion dominated, then  $v_\infty = v_{pk} \approx v_{\text{gas}}$  and  $R_{\text{acc}} = R_{WS}$ . When  $\alpha \neq 0$ ,  $R_{WS}$  is no longer independent of  $M_*$ . If  $\alpha > \eta$ , then  $v_{\text{gas}}$  is approximately constant with respect to varying  $\Omega$ , meaning that the quantity in the denominator of  $t_{\text{grow}} - R_{WS}^2 v_{pk} \propto M_*^{-1/2}$ . Furthermore, if  $v_{\text{shear}} > v_{pk}$ , then  $R_{\text{acc}} = R_{\text{shear}}$ , and the denominator of  $t_{\text{grow}}$  is  $\propto R_{\text{shear}}^3 \Omega \propto M_*^{-1/2}$ . For sufficiently strong turbulence that  $H_{\text{turb}} > H_{KH}$ , we have  $H_p \propto \Omega^{-1} \propto M_*^{-1/2}$ . Thus for 3D accretion in the strong turbulence regime these effects approximately cancel out, causing the growth curves to merge.

For high core masses, the transition on the right side of the graphs where  $t_{\text{grow}}$  increases as a function of  $r_s$  occurs at essentially the same value of small body radius, independent of  $M_*$ . As noted in Equation (2.61), the energy criteria  $KE < W$  can be rewritten as  $St < 4\sqrt{3}$  for particles in this growth regime. For particles in the Epstein regime the Stokes number is independent of  $M_*$ , causing the cutoff radius to be approximately the same for all stellar masses. The timescale in this regime is weakly dependent on  $M_{\text{star}}$  – these large particles accrete at  $t_{\text{Hill}}$ , with an increase in growth timescale  $\propto St$ , which again is essentially independent of  $M_*$ . Thus the growth timescale goes as  $t_{\text{grow}} \propto (R_H v_H)^{-1} \propto M_*^{1/6}$ .

In the laminar regime the cutoff at small radii is also independent of  $r_s$ . This

cutoff occurs when  $R_{WS} < R_b$ , and since, as previously noted,  $R_{WS}$  is independent of  $M_*$  in the laminar regime, this cutoff is independent of  $M_*$  as well. As turbulence increases  $R_{WS}$  becomes a decreasing function of  $M_*$ , causing the cutoff in growth to shift to higher values of  $r_s$ .

For low core masses, the low end cutoff still has the same dependence on  $M_*$ . However, growth will now cut off at the limit given by Equation (2.76), which is an increasing function of  $M_*$  in both the laminar and turbulent regimes.



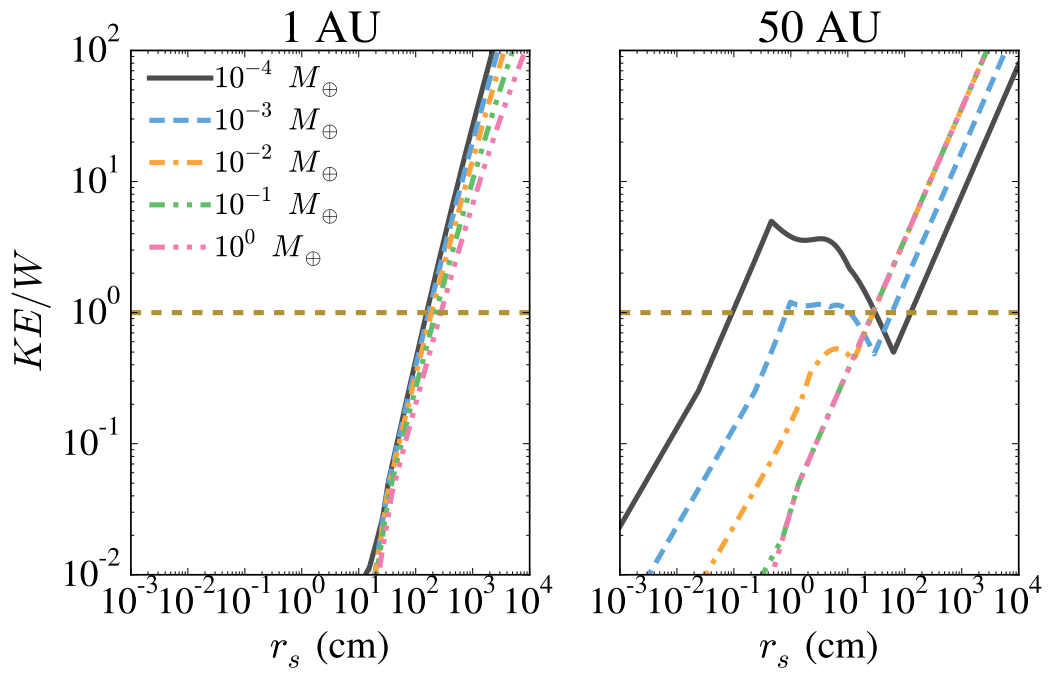


Figure 2.14: The ratio of kinetic energy relative to the core to work done by the gas on an incoming particle assuming  $\alpha = 0$ , plotted as a function of small body radius  $r_s$ . Curves are shown for a range of core masses. The left panel shows the situation at  $a = 1$  AU, while the right panel is for  $a = 50$  AU.

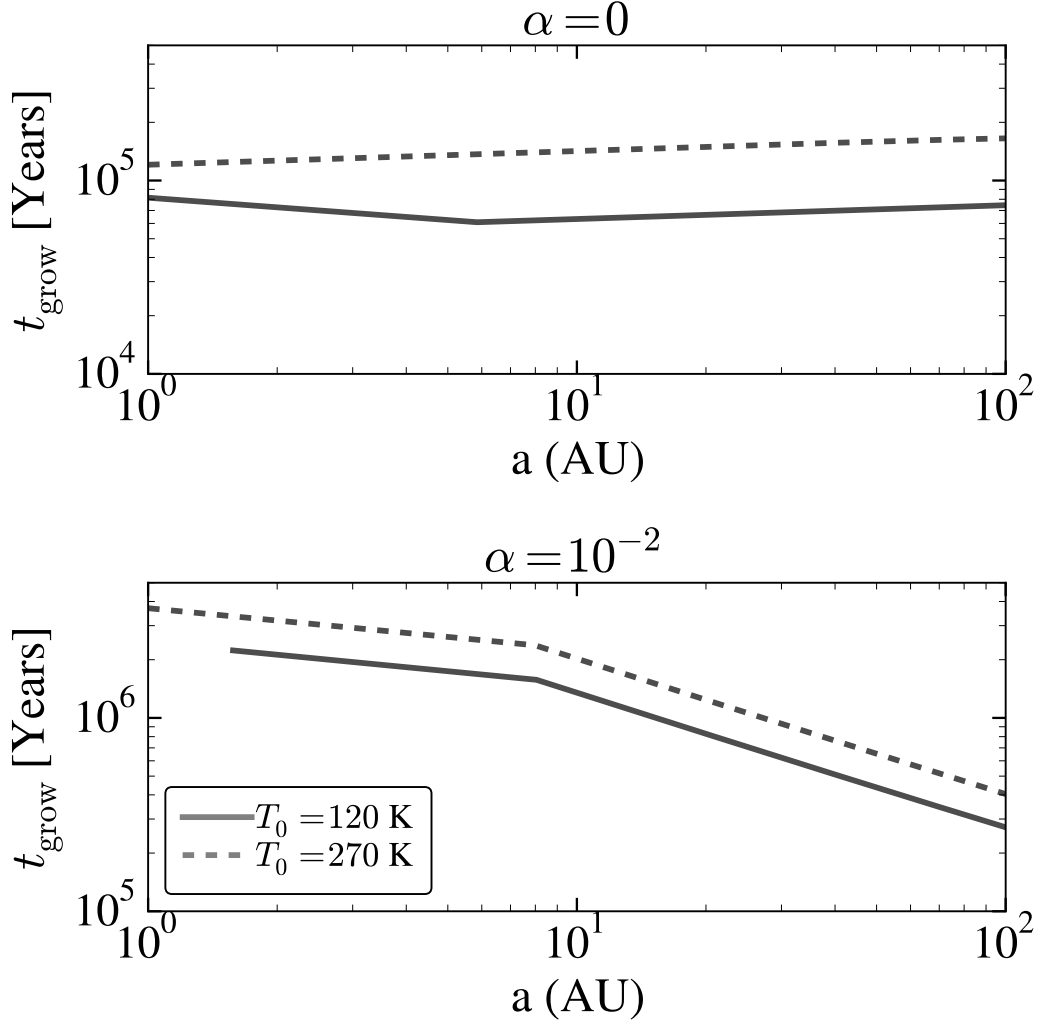


Figure 2.15: The growth timescale as a function of semi-major axis for two different values of the prefactor of the temperature profile,  $T_0$ . Both panels use the values  $r_s = 0.25$  cm,  $M = 10^{-1}M_{\oplus}$ . The panel on the top is for  $\alpha = 0$ , while the panel on the bottom is for  $\alpha = 10^{-2}$ . The effect of increasing  $T_0$  is more substantial in the laminar case, since  $H_p$  and  $v_{pk}$  both scale as  $c_s^2$  in this regime, as opposed to  $c_s$  in the turbulent case.

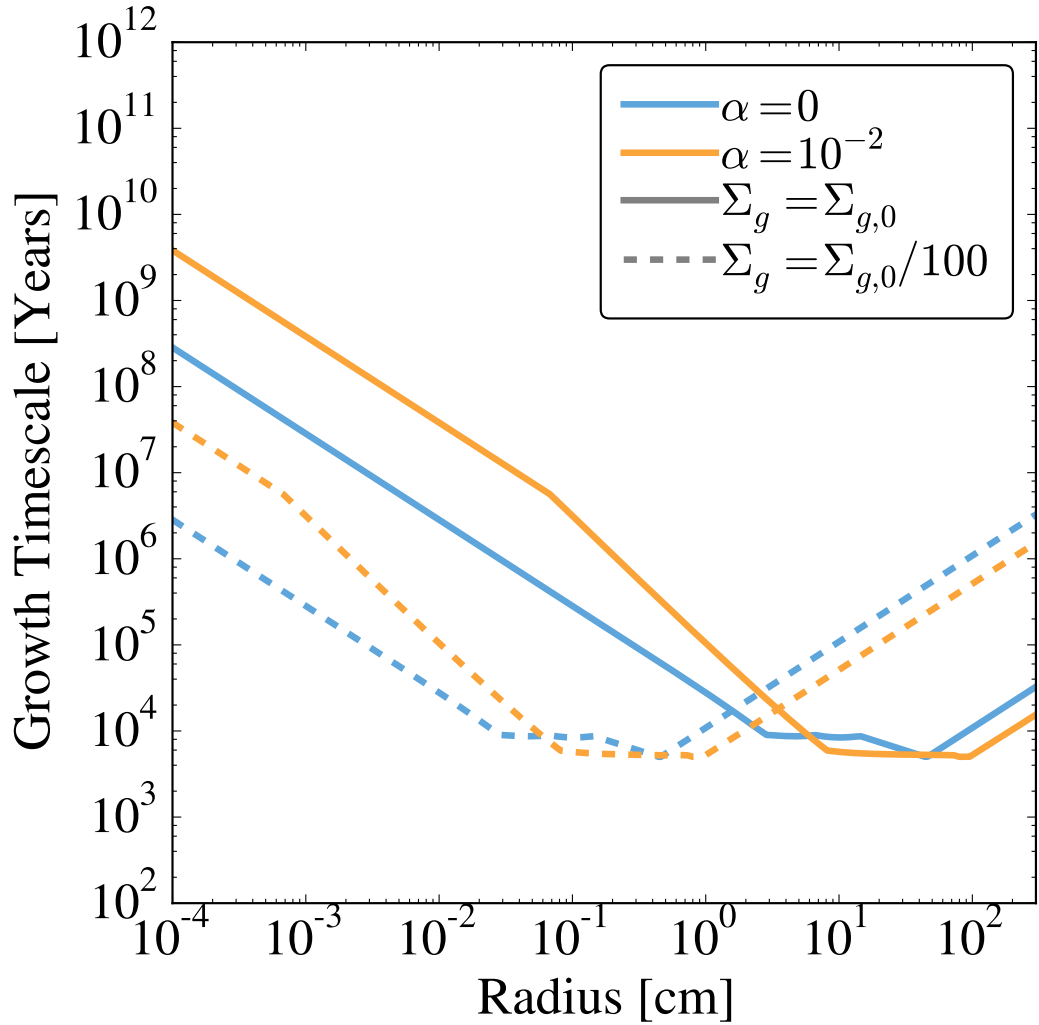


Figure 2.16: The gas-assisted growth timescale for a disk with its gas surface density depleted by a factor of 100. The values shown are for  $a = 30$  AU, and  $M = 1.5 \times 10^{-2} M_{\oplus}$ . Both a laminar ( $\alpha = 0$ ) and a strongly turbulent ( $\alpha = 10^{-2}$ ) case are shown. The solid lines shown the values for the surface density used in the paper, while the dashed lines depict the effect of changing the surface density.

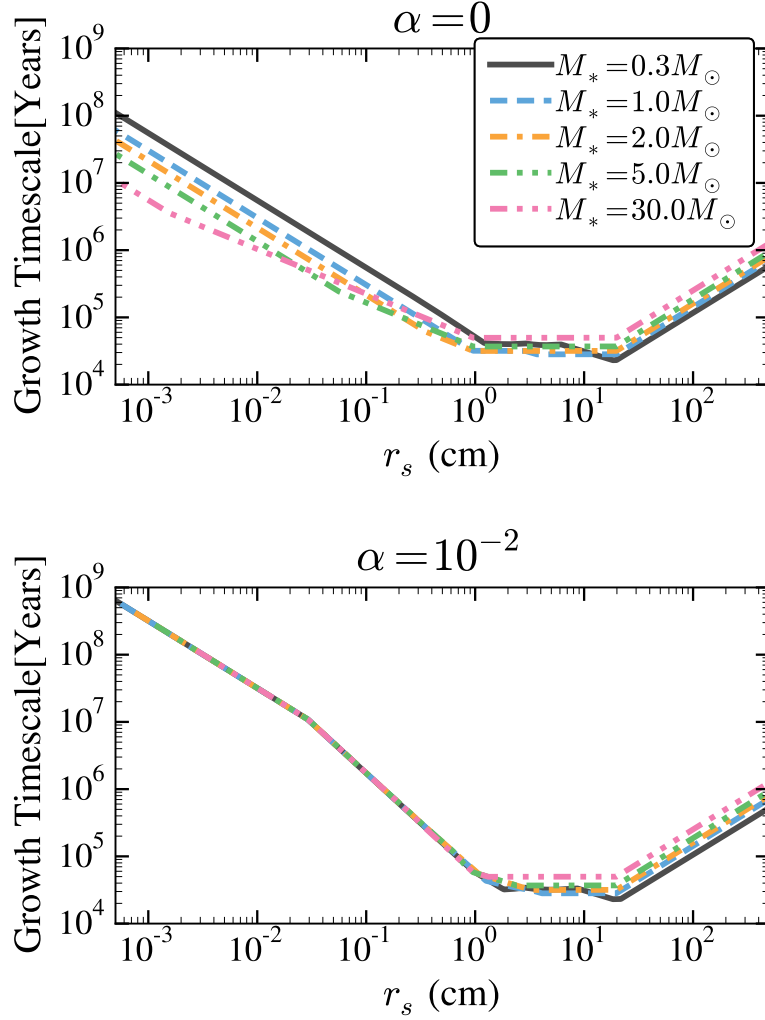


Figure 2.17: The effect of varying the mass of the central star. The values shown here are at a distance of  $a = 70$  AU, and  $M = 0.5 M_{\oplus}$ . The panels show the growth timescale as a function of small body size for a laminar ( $\alpha = 0$ ) and strongly turbulent ( $\alpha = 10^{-2}$ ) disk. Each panel shows the timescale for five different stellar masses. *Top Panel:* In the laminar case the small particles which accrete at  $R_{\text{acc}} = R_{WS}$  are accreted more rapidly around higher mass stars, as more massive stars have higher rates of shear and reduced small body scale height. As particle size increases the particles will begin accreting at  $R_{\text{acc}} = R_H$  – the effect of stellar mass in this regime depends on the size of  $H_{KH}$  relative to  $R_H$  (see text). *Bottom Panel:* The inclusion of turbulence allows the scale height of smaller particles to be set by turbulent diffusion instead of the Kelvin-Helmholtz shear instability, making the scale height independent of  $M_*$  in this regime. In this case the increase in shear rate is balanced by the decrease in  $R_{WS}$ , causing the growth curves to merge for low values of  $r_s$ . For higher values of  $r_s$  where  $R_{\text{acc}} = R_H$  the situation is the same as in the top panel.

## 2.7 Flow Isolation Mass

In this section we discuss accretion in the regime  $R_b > R_H$ . In general, the core's atmosphere extends up to a scale  $R_{\text{atm}} = \min(R_b, R_H)$ , as once  $R_b > R_H$   $R_{\text{atm}}$  is limited by gravitational effects from the central star, as opposed to the core's ability to bind nebular gas. Thus for core masses large enough that  $R_b > R_H$  the energy criteria discussed in Section 2.2.1 are the same with  $R_b \rightarrow R_H$ .

Figure 2.11 shows the emergence of a feature for high core masses where only larger sizes of particles can accrete. This occurs when the core reaches a mass  $M_{\text{flow}}$  such that  $R_b = R_H$ . As discussed in Section 2.2.1, in the regime  $R_H > R_b$ , small bodies with  $R_{\text{stab}} < R_b$  will not be able to accrete if they dissipate their kinetic energy during their interaction with the core – since the gas will flow around the core's approximately incompressible static atmosphere, particles that couple to the gas flow near the core will be pulled around without accreting. For lower mass cores, only particles that are small enough that  $R_{WS} < R_b$  are restricted from accreting in this manner, i.e. this consideration dictates the lower limit on the particle size that can be accreted. Once the core's mass is large enough that  $R_b > R_H$  however, we now have  $R_{\text{atm}} = R_H$ , and therefore  $R_{\text{stab}} \lesssim R_{\text{atm}}$  for all particle sizes. Thus, any particles that dissipate their kinetic energy relative to the core will be pulled around by the gas flow without accreting. Because  $R_{\text{atm}} = R_H$ , we expect the gas flow to be around  $R_H$ , instead of  $R_b$  as it was in the lower mass case. See Figure 4.3 for an illustration.

We note that the gas will be accelerated by the core's gravity as it passes through  $R_b$ ; interior to  $R_b$  the local orbital velocity exceeds the sound speed, which

means the flow can accelerate to supersonic velocities. In this case, it is less clear that the core's atmosphere will act as an incompressible obstacle. However, there still should exist a scale  $r$  past which the flow can no longer penetrate the core's atmosphere. To see this, we can compare the incoming kinetic energy of the flow to the binding energy of the core's atmosphere. In a time  $\Delta t$  the mass of gas entering into the length scale  $r$  is of order  $\rho_{\text{neb}} v_{\text{app}} \Delta t r^2$ , where  $\rho_{\text{neb}}$  is the volumetric mass density of the nebular gas and  $v_{\text{app}}$  is the velocity of the incoming gas relative to the core. Since  $R_b \gtrsim R_H$  implies that  $v_H \gtrsim c_s > v_{\text{gas}}$  we have  $v_{\text{app}} \lesssim v_H$ . The timescale for gas to enter  $r$  is  $\Delta t \sim r/v_{\text{app}}$ . The binding energy of the atmosphere at scale  $r$  is  $\sim GM^2/r \sim \rho_{\text{atm}} v_{\text{esc}}^2 r^3$ . Thus, the ratio of the incoming kinetic energy to the binding energy is

$$\frac{\rho_{\text{neb}} v_{\text{app}}^2 r^3}{\rho_{\text{atm}} v_{\text{esc}}^2 r^3} \leq \frac{\rho_{\text{neb}} r}{3\rho_{\text{atm}} R_H}, \quad (2.79)$$

where we've used the fact that  $v_{\text{app}} \leq v_H$  and that  $v_H^2/v_{\text{esc}}^2 = r/(3R_H)$ . The quantity above is clearly  $\ll 1$  for  $r \lesssim R_H$ , particularly since close to the planet we expect  $\rho_{\text{atm}} \gg \rho_{\text{neb}}$ . Thus there exists a scale  $r \lesssim R_H$  where the incoming kinetic energy of the gas is much less than the binding energy of the core's atmosphere.

The core reaching  $M_{\text{flow}}$  signals a rapid cutoff in the accretion of pebbles: for masses just below  $M_{\text{flow}}$  there will always exist a wide range of particle sizes that dissipate their kinetic energy during the interaction with the core. Once  $M > M_{\text{flow}}$  accretion of these particle sizes, which generally represent the most rapid accretion rates, suddenly shuts off. We can demonstrate analytically that a broad range of particle sizes satisfying  $KE < W$  will be present for  $M = M_{\text{flow}}$ . To begin, we first show that at this

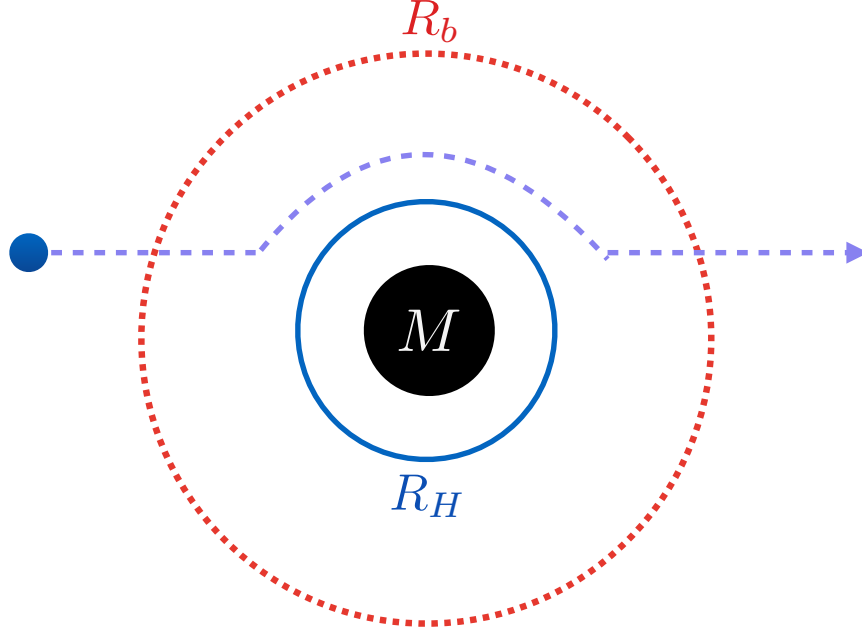


Figure 2.18: A schematic illustration of the trajectories of particles with  $KE < W$  for  $M > M_{\text{flow}}$ . The particle (blue circle), comes in from the left. Since the particle is able to dissipate its kinetic energy relative the core, it begins to follow the local gas flow. The core's atmosphere extends up to  $R_H$ , and the nebular gas flows around this obstacle. The particle is pulled along with the gas, causing it to flow around the core without being accreted.

mass scale, we never have  $R_{\text{stab}} = R_{WS}$ . Firstly,  $R_b = R_H$  implies that  $v_H = c_s/\sqrt{3}$ .

The analytic criterion for the relative sizes of  $R_b$ ,  $R_{WS}$ , and  $R_{\text{shear}}$  for  $R_b = R_H$  can therefore be summarized as:

$$R_{\text{shear}} < R_{WS} : St > \sqrt{3} \left( \frac{v_{\text{gas}}}{c_s} \right)^3$$

$$R_{WS} > R_b : St > \frac{1}{\sqrt{3}} \left( \frac{v_{\text{gas}}}{c_s} \right)$$

Since  $v_{\text{gas}}/c_s \ll 1$ , the above implies that  $R_{\text{stab}} = R_{\text{shear}}$  occurs prior to accretion commencing for  $R_{WS} > R_b$ . Thus, accretion commences for  $R_{\text{shear}} > R_b$ , which occurs at a Stokes number of

$$St > 9 \left( \frac{v_H}{c_s} \right)^6 = \frac{1}{3}. \quad (2.80)$$

On the other hand, accretion will cease when  $KE > W$ . Since these particles are clearly shear dominated, we will simply have our criterion given in Equation (2.61) for particles which shear into  $R_H$

$$St < 4\sqrt{3}. \quad (2.81)$$

Thus, any particle in the range  $1/3 < St < 4\sqrt{3}$  will be accreted for masses just below  $M_{\text{flow}}$ , but for  $M > M_{\text{flow}}$  all particles in this range will no longer be accreted, i.e.  $M > M_{\text{flow}}$  represents a general point throughout parameter space where accretion of small bodies through pebble accretion cuts off.

Solving  $R_b = R_H$  for  $M$  gives  $M_{\text{flow}}$  as

$$M_{\text{flow}} = \frac{1}{\sqrt{3}} \frac{c_s^3}{G\Omega}. \quad (2.82)$$

Plugging in fiducial values of our parameters gives

$$M_{\text{flow}} = 4.4 \left( \frac{T_0}{200 \text{ K}} \right)^{3/2} \left( \frac{a}{\text{AU}} \right)^{6/7} \left( \frac{M_*}{M_\odot} \right)^{-1/2} M_\oplus. \quad (2.83)$$

For the temperature profile used in this work, the value of flow isolation mass is markedly similar to the distribution of solar system cores. Figure 2.19 shows the flow isolation mass scaled down by a factor of 4 as a function of semi-major axis. This corresponds to a cutoff in accretion for  $R_b = 4^{-2/3} R_H \approx 0.4 R_H$ , as opposed to  $R_b = R_H$ . For the terrestrial planets we have plotted the total mass of the planet. For the gas giants the bars indicate the range of possible masses, since these values are not as well constrained. For the gas giants the mass of the cores, as opposed to the total mass in solids, are shown, as once runaway gas accretion begins the amount of solids in the planet will not be set by the flow isolation mass. The values plotted are taken from Figures 7 and 8 of [Guillot \(2005\)](#), with the maximal range of core masses shown. For the ice giants we use the total mass in solids, since the flow isolation mass will more directly influence this number if runaway gas accretion does not occur. Again, these values are taken from [Guillot \(2005\)](#) (Section 3.4). The correspondence between the flow isolation mass and the masses of the solar system cores may indicate that the flow isolation mass played a role in influencing the final masses of the solar system planets.

We stress that this figure should not be over interpreted, as there a variety of factors that complicate the formation of the solar system planets. In particular, meteoritic dating (e.g. [Yin et al. 2002](#), [Kleine et al. 2009](#)) and dating of the Moon-forming impact (e.g. [Bottke et al. 2015](#)) provide strong evidence that the final assembly

of the terrestrial planets occurred on timescales  $\gtrsim 10$  Myr and that a period of “giant impacts” was important for setting the final masses of these planets. Because protoplanetary disks do not last longer than 10 Myr, nebular gas would not be present and gas-assisted growth would not occur during this phase. It is possible that the flow isolation mass played a role in setting in the initial embryo masses that underwent this phase of giant impacts. Any such scenario however, would have to explain the low masses of Mercury, Mars, and the inferred mass of the Moon-forming impactor (Canup 2012). It is conceivable that some cores reached flow isolation, while others stalled at low core mass due to the inefficiency of growth at low core masses described in Section 2.6.1. If all cores reached flow isolation, giant impacts could in principle remove mass from some, as has been proposed to explain the anomalously high density of Mercury (e.g. Benz et al. 1988). Modeling by Leinhardt & Stewart (2012) demonstrates that, for collision events typical of the final stages of terrestrial planet formation, the outcomes span the range from perfect accretion to erosion of the more massive target. Note that any scenario invoking flow isolation in the inner solar system is contrary to standard models of terrestrial planet formation, which rely on the giant impacts phase to increase the masses of the terrestrial planets above their isolation mass (e.g. Agnor et al. 1999).

The flow isolation mass may be most relevant in the context of the ice giant planets, which were previously thought to form by growing to their local isolation mass, though note that the ice giants are thought to have migrated substantially from the location of their initial formation (reviewed e.g. in Morbidelli et al. 2008). In the context of pebble accretion however, planets are not limited by locally available material due

to radial drift of solids. The flow isolation mass could provide a plausible mechanism that sets the mass of these planets in the context of pebble accretion (see [Frelikh & Murray-Clay 2017](#) for a more in depth discussion).

We note here that a similar mass is identified by [Lambrechts & Johansen \(2014\)](#), who refer to it as the “Pebble Isolation Mass.” We strongly emphasize, however, that the existence of the pebble isolation mass is based on different physics than our flow isolation mass: the pebble isolation mass is based on the gravity of the planet opening a gap in the pebble disk, as opposed to the planet altering the local flow of nebular gas. [Lambrechts & Johansen \(2014\)](#) calculate the pebble isolation mass by identifying the point where gravitational perturbations from the growing core’s gravity render the gas velocity immediately outside of the planet’s orbit “super-Keplerian,” which tends to push pebbles outwards rather than bring them in. [Lambrechts & Johansen](#) perform numerical simulations at 5 AU in order to determine the pebble isolation mass at this orbital separation. They then calculate the dependence of  $M_{\text{flow}}$  on the disk aspect ratio,  $H/a$ , analytically, and determine that  $M_{\text{flow}} \propto (H/a)^3$ . Combining these results, [Lambrechts & Johansen](#) give the pebble isolation mass as

$$M_{\text{flow}} \approx 20 \left( \frac{a}{5 \text{ AU}} \right)^{3/4} M_{\oplus} . \quad (2.84)$$

Despite the different physics used to calculate these mass scales, the flow isolation mass and the pebble isolation mass occur at roughly the same value – to see this, we first note that since  $H/a \propto c_s/(\Omega a)$ , we have  $(H/a)^3 \propto T^{3/2} a^{3/2}$ . Thus our scaling agrees with

the [Lambrechts & Johansen](#) result. Furthermore, if we use a temperature in agreement with these authors' choice,  $T \approx 270 \text{ K } (a/\text{AU})^{-1/2}$ , then our criterion for pebble isolation mass, i.e. that  $R_b = R_H$ , gives

$$M_{\text{flow}} = 23.2 \left( \frac{a}{5 \text{ AU}} \right)^{3/4} M_{\oplus}, \quad (2.85)$$

in rough agreement with the [Lambrechts & Johansen](#) result. Finally, we note that the flow isolation mass is similar in scale to the “Thermal mass” discussed in Section 2.5.6, past which the core’s Hill radius exceeds the disk scale height ([Lin & Papaloizou 1993](#)).

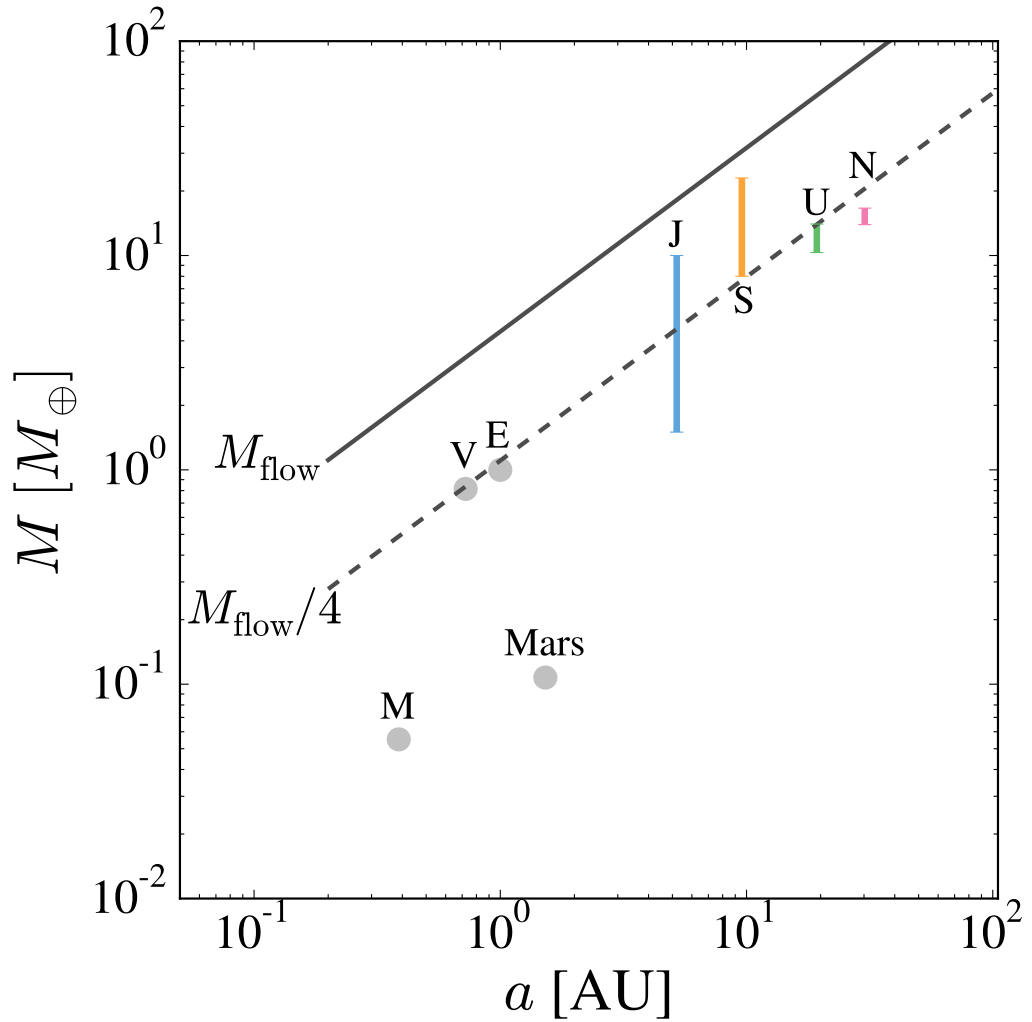


Figure 2.19: The value of the flow isolation mass (solid line), as well as the flow isolation mass scaled down by a factor of four (dashed line), both plotted as a function of semi-major axis. Also shown are the masses of the cores of the solar system planets. Values for the four giant planets are taken from [Guillot \(2005\)](#). For the terrestrial planets the total mass is shown. For the gas giant the mass of the core is used, whereas for the ice giants the total mass in solids is plotted.

## 2.8 Summary and Conclusions

In this paper we have presented an order of magnitude model of pebble accretion, which accounts for the effects of turbulence on a variety of the timescale parameters. We calculate the growth timescale for a planet as

$$t_{\text{grow}} = \frac{MH_p}{2f_s \Sigma v_\infty R_{\text{acc}} H_{\text{acc}}} . \quad (2.86)$$

We calculate  $v_\infty$ ,  $R_{\text{acc}}$ ,  $H_{\text{acc}}$ , and  $H_p$  separately, allowing a number of different physical processes to set each of these velocity and length scales. Our model uses the wind-shearing radius of [Perets & Murray-Clay \(2011\)](#) to take into account the effects of gas drag on the stability of small bodies during the accretion process, which can set  $R_{\text{acc}}$  instead of  $R_H$  or  $R_b$ . We also use the approximate formulae presented by [Ormel & Cuzzi \(2007\)](#) for the RMS turbulent velocity of small bodies in a turbulent medium to incorporate the effects of turbulence into  $v_\infty$ . An incoming small body has its incoming kinetic energy compared to the work done by gas drag during the encounter, which determines the range of small body sizes that the core can accrete. The resulting model gives the growth timescale as well as a variety of other important parameters ( $v_{pk}$ ,  $H_p$ ,  $F_D$ , ...). Due to its relative simplicity, our model can be applied over a large range of parameter space, and can be coupled with other physical processes, such as planetary migration.

Studying the output of our model reveals many important aspects of protoplanetary growth via pebble accretion in the presence of turbulence. Once protoplanets

reach a large enough size (ranging from  $10^{-4} - 10^{-1}M_{\oplus}$ , depending on the strength of turbulence, as well as the location in the disk and the sizes of pebbles available), growth timescales become far shorter than the lifetime of the gaseous protoplanetary disk. This results remains true even for extremely strong ( $\alpha \gtrsim 10^{-2}$ ) turbulence. These enhanced growth rates are more than substantial enough to allow the formation of gas giants at wide orbital separations, where planetesimal accretion is inefficient, provided the cores can first reach this high mass.

Of equal importance however, are the regions where pebble accretion is not as efficient. We find that turbulence can substantially lower the growth rate at low core masses. For lower core masses and stronger turbulence, a smaller range of particle sizes are able to accrete at  $t_{\text{Hill}}$ , and it becomes easier for turbulence to cut off gas-assisted growth for more massive particles entirely. These effects are exacerbated at wide orbital separations, where the detrimental effects of the gas on the accretion process are more substantial. Thus when studying the growth in pebble accretion it is important to consider not just the maximal accretion efficiency where the core accretes over its Hill radius, but to consider what sizes of small bodies are available and how these small bodies are affected by their interactions with the gas. These effects can have considerable ramifications for the predictions of any theory of planet formation by pebble accretion.

While we have used fiducial values of disk parameter in order to provide concrete numeric results in this paper, our model is quite flexible with regards to the disk parameters used. We briefly discussed the effects of modifying a few of these parameters, namely the temperature and surface density profiles and the stellar mass. While

these effects are complicated, we can briefly summarize them as follows:

- For higher temperatures, accretion generally slows down. The timescale for the most rapid accretion, where particles accrete over the entirety of the core’s Hill sphere, is unaffected by disk temperature, though the range of particle sizes that can accrete at this rate may shrink in hotter disks.
- Depleting the gas surface density shifts the correspondence between Stokes number and small body radius, essentially shifting the curve of  $t_{\text{grow}}(r_s)$  to smaller values of particle size. The scale of  $t_{\text{grow}}$  is unchanged.
- In a laminar disk, increasing stellar mass makes accretion of smaller particle radii, which accrete at  $R_{\text{acc}} = R_{WS}$ , more efficient due to the increased gas density and shear rate. In a turbulence disk the growth rate for small particle radii is insensitive to stellar mass. For larger particle sizes where  $R_{\text{acc}} = R_H$  the effect of increasing stellar mass is not as clear cut, but the overall effect is much less significant than in the small radius case.

Finally, we identified a natural upper limit to core mass in the context of pebble accretion, the “Flow Isolation Mass.” Past this mass the Bondi radius of the core will exceed its Hill radius, in which case the region where the core’s gravity alters the gas flow exceeds the radius for stable orbits about the core, regardless of the small body size being accreted. In this regime the normal mechanism for pebble accretion will not be able to operate, since particles that dissipate their kinetic energy relative to the core will follow the flow of gas and be pulled around the core without accreting.

This upper limit may set the critical mass that triggers run away gas accretion, since once cores reach this limit their accretion luminosity will drop, allowing them to accrete substantially more gas from the surrounding nebula. We note that the value of the flow isolation mass as a function of semi-major axis is quite similar to the distribution of the cores of the solar system planets. While this is an intriguing possibility, further study is needed to determine the importance of this mass scale.

An interesting and important extension to our model would be to consider lower mass cores, for which the effects of gas are more pronounced. This would require modeling not just the effects of the RMS random velocity of the small bodies, but also the particle-particle relative velocity between the small body and the core. Expressions for the turbulence induced relative velocity are given in e.g. OC07, but these formulae are much more complex than Equation (2.22). Another effect that may be more important for lower masses is consideration of the full probability density function of the particle-particle relative velocity. In this work we have used only the RMS value for velocity, but considering particles in the low and high velocity tails of the distribution can have important effects, as has been noted for early stages of growth ([Windmark et al. 2012](#)). Our preliminary investigations of gas-assisted growth at planetesimal sizes show that many novel features appear in this regime that are not present in the higher mass case – for example the range of particle sizes that planetesimals can accrete efficiently can be much narrower than the range for protoplanets. This effect could lead to stratification in the composition of planetesimals, which could be observed in our solar system. Furthermore, for low masses the actual collision velocity between the core and

small body can be smaller than their initial relative velocity, due to the inspiral of the particle, which can have important ramifications for whether a given collision results in growth, bouncing, or fragmentation.

There are a large number of applications for our model to address issues in planet formation. In Chapter 3 we present one such application: we apply our theory to the question of formation of gas giants at wide orbital separation. We are particularly interested in how the strength of turbulence can help place restrictions on when gas giant formation is possible, which may help us understand why wide orbital separation gas giants are so uncommon even though pebble accretion timescales are so rapid.

## Chapter 3

# Restrictions on the Growth of Gas Giant Cores via Pebble Accretion

### 3.1 Introduction

In the traditional “core accretion” model of planet formation, growth of planets proceeds in a bottom-up manner. Planets begin their growth as rocky cores, or protoplanets. If these protoplanets reach sufficient size within the lifetime of the gas disk, they will be able to trigger runaway gas accretion, resulting in a gas giant ([Pollack et al. 1996](#)). This runaway occurs when  $M_{\text{atm}} \sim M_{\text{core}}$ , where  $M_{\text{atm}}$  is the mass of the planet’s atmosphere and  $M_{\text{core}}$  is the mass of the planet in solids. The critical core mass,  $M_{\text{crit}}$ , where this occurs is usually quoted as  $M_{\text{crit}} \sim 10M_{\oplus}$ , though the actual mass

depends on the disk parameters, especially the opacity and the core’s accretion rate (see, e.g. [Rafikov 2006](#), [Piso et al. 2015](#)). A gas giant will not form if the planet cannot reach  $M_{\text{crit}}$  within the lifetime of the gas disk,  $\tau_{\text{disk}}$ , which is  $\sim 2.5$  Myr for G stars ([Mamajek 2009](#), [Ribas et al. 2014](#)). Traditional models rely on gravitational focusing to increase the effective radius for collisions. These models, which we will refer to as “canonical core accretion” or “planetesimal accretion” models, give growth timescales that are generally fast enough to reach critical core mass for  $a \lesssim 10$  AU, but become longer than the disk dispersal timescale past this distance. (See [Goldreich et al. 2004](#), hereafter GLS, for a review of gas-free regimes.)

Observations of exoplanetary systems have challenged this canonical core accretion model in a number of ways. Here we focus on the existence of systems that feature gas giants at wide orbital separations (see, e.g. [Bowler 2016](#) for a review). Of particular note is the planetary system surrounding the star HR 8799, which exhibits a nonhierarchical, multiplanet structure: HR 8799 consists of four gas giant planets ( $M \sim 10 M_J$ ) at extremely wide projected separations: 14, 24, 38, and 68 AU ([Marois et al. 2008](#), [Marois et al. 2010](#)). HR 8799 poses a serious challenge to canonical core accretion models because the last doubling timescale for growth at these distances is far too long for a core to reach the critical mass necessary to trigger runaway growth within  $\tau_{\text{disk}}$ . Additional effects, such as gas drag from the planet’s atmosphere ([Inaba & Ikoma 2003](#)) or damping of the planetesimals’ random motions by the nebular gas ([Rafikov 2004](#)), can increase the cross section for collisions further. Neither of these effects, however, are sufficient to allow the *in situ* formation of gas giants at 70 AU.

A number of alternative formation scenarios have been proposed to explain the formation of HR 8799. One commonly suggested explanation is that HR 8799 is evidence of an alternative formation scenario known as “gravitational instability,” wherein the gaseous component of the protoplanetary disk becomes unstable to gravitational collapse and subsequently fragments into the observed gas giant planets (Boss 1997; see also Kratter & Lodato 2016 for a more recent review). However, Kratter et al. (2010) pointed out that it is difficult to form fragments of the sizes seen in HR 8799 without having these “planets” grow to brown dwarf or even M-star masses. The lack of observed brown dwarfs at wide orbital separations provides some evidence against this hypothesis, but additional statistical work is needed (Bowler 2016). Outward scattering after formation at smaller orbital separations is another possibility, but  $N$ -body simulations by Dodson-Robinson et al. (2009) find that scattering is unlikely to produce systems with the multiplanet architecture of HR 8799.

In recent years, a third possibility has emerged: a modification to the theory of core accretion commonly referred to as “pebble accretion,” which we will also refer to as “gas-assisted growth” (Ormel & Klahr 2010, Perets & Murray-Clay 2011, Ormel & Kobayashi 2012, Lambrechts & Johansen 2012, Lambrechts & Johansen 2014, Levison et al. 2015a, Morbidelli et al. 2015, Visser & Ormel 2016, Ida et al. 2016, Xu et al. 2017, Rosenthal et al. 2018). In pebble accretion, the interaction between solid bodies and the gas disk is considered in detail when determining the growth rates of planets. In particular, gas drag can enhance growth rates by removing energy from small bodies. Particles that deplete their kinetic energy within the gravitational sphere of influence

of a larger body can become bound to this parent body, which will eventually lead to accretion of the particle by the growing protoplanet. This process can occur at larger impact parameters than are required for the particle to collide with the core, which in turn increases the accretion cross section. This interaction often affects mm-cm-sized bodies the most strongly. Note, however, that for low-density, “fluffy” aggregates, the radius of bodies most substantially affected by gas drag can be substantially larger.

For gas-assisted growth to operate, a reservoir of pebble-sized objects must exist in the protoplanetary disk. Because the sizes of these pebbles are comparable to the  $\sim$  mm wavelengths used to measure dust surface densities in the outer regions of protoplanetary disks, observations can directly probe the surface densities in the small solids that fuel gas-assisted growth. These observations find large reservoirs of small, pebble-sized solids (Andrews et al. 2009, Andrews 2015). An example is shown in Figure 3.1, which presents disk surface densities measured by Andrews et al. (2009). The figure shows the surface density in particles of radius 0.1 mm – 1 mm, which is inferred by integrating the size distribution used in the paper ( $dN/dr_s \propto r_s^{-3.5}$ ) from 0.1 to 1 mm. Performing the integration gives the fraction of the measured solid surface density contained in this size range ( $\sim 70\%$ ).

Given this observed reservoir of small solids, pebble accretion dramatically increases the expected growth rate of large cores. Under fiducial conditions, the timescale for a core’s last doubling to canonical values of  $M_{\text{crit}}$  is below the disk lifetime, even at many tens of AU separations. Though fast accretion of solids deposits enough energy to delay the onset of runaway accretion of a gas envelope, once a core has reached

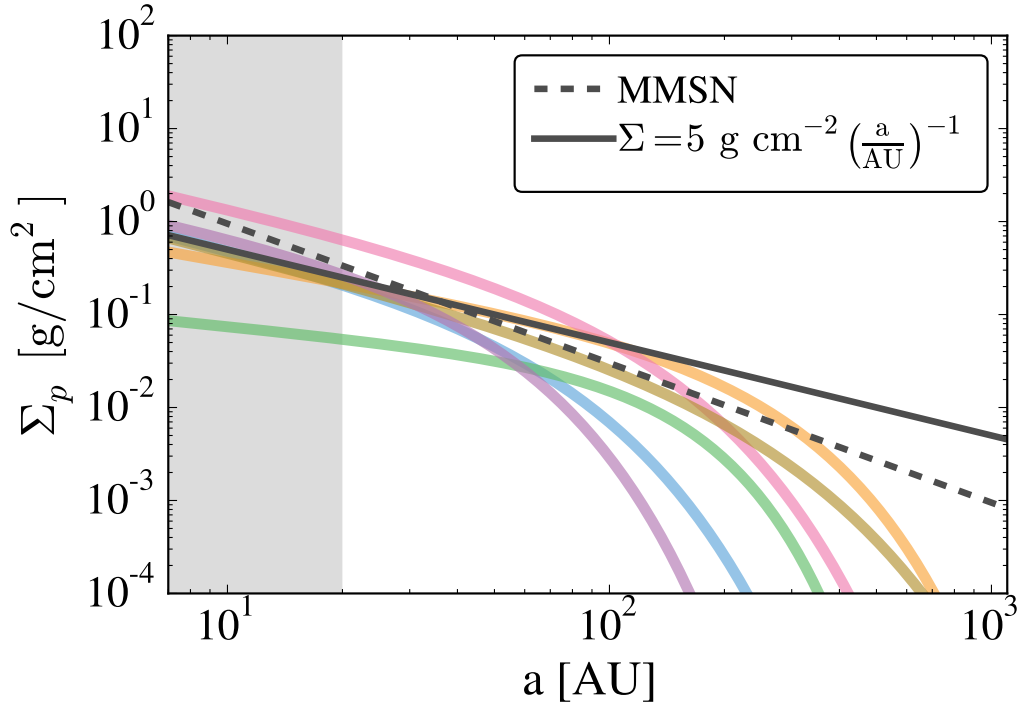


Figure 3.1: Colored lines show the dust surface density in 0.1 mm – 1 mm sized particles taken from 870  $\mu\text{m}$  continuum emission observations of protoplanetary disks done by [Andrews et al. \(2009\)](#). See text for details. Also shown for reference is the value of the solid surface density in the minimum-mass solar nebula (MMSN), appropriate for the outer disk,  $30 (a/\text{AU})^{-3/2} \text{ g cm}^{-2}$  ([Weidenschilling 1977b](#), [Hayashi 1981](#)), as well as the fiducial surface density used in this work to match the observations. In the gray shaded region the values of the curves are extrapolations to scales smaller than the observations can resolve.

several Earth masses, finely tuned disk conditions are required to slow atmospheric growth enough to prevent runaway from ultimately occurring. Thus, growth via pebble accretion seems to predict that wide orbital separation gas giants should be common. However, direct imaging surveys show that planets  $\gtrsim 2 - 5 M_J$  are rare at distances  $> 30 \text{ AU}$  ([Brandt et al. 2014](#), [Chauvin et al. 2015](#), [Bowler 2016](#), [Galicher et al. 2016](#)).

One possibility for solving this problem is the presence of turbulence in the

nebular gas. In this work, by “turbulence,” we generally mean any anomalous root mean square (RMS) velocity of the nebular gas that is not due to the laminar velocity that arises from radial pressure support in the disk. The main effect of turbulence on pebble accretion is to increase the velocity dispersion of the pebbles due to their coupling with the gas; it is only in Section 3.5 that we connect our parameterization of the turbulent RMS velocity to the transport of angular momentum in the disk. Turbulence can both increase the kinetic energy of an incoming particle and decrease the core’s gravitational sphere of influence. Turbulence also drives particles vertically, reducing the overall densities of small bodies and slowing accretion. Turbulence is usually only included in models of protoplanetary growth by pebble accretion by increasing the particle scale height and hence reducing the mass density of solids. Some models of the early stages of planetesimal growth discuss the effects of turbulence (e.g. [Guillot et al. 2014](#), [Homann et al. 2016](#)), but these models are concerned with accretion at cross sections comparable to the core’s geometric cross section; i.e. they neglect the effects of the core’s gravity.

In this paper, we use an order-of-magnitude model of pebble accretion ([Rosenthal et al. 2018](#), hereafter R18) to propose a criterion for the formation of gas giants via gas-assisted growth. In particular, R18 investigated how turbulence affects the growth of gas giant cores as a function of core mass. High-mass cores ( $\gtrsim 10^{-2} - 10^{-1} M_{\oplus}$ ) can grow on timescales less than the lifetime of the gas disk, even in strong turbulence. However, for lower-mass cores and stronger turbulence, the range of pebble sizes available for growth is restricted. In this case, the pebble sizes for which growth is most efficient often cannot be accreted, and growth can “stall” at low core masses.

In effect, a core must first achieve a minimum mass before it can quickly grow to  $M_{\text{crit}}$  via gas-assisted growth. In this paper, for our fiducial calculation, we assume that growth to this minimum mass happens by canonical core accretion, which allows us to place semi-major axis limits on where gas giant growth is possible. We also calculate values for the core mass needed at a given semi-major axis for pebble accretion to be rapid, which apply regardless of how the early stages of growth proceed. The assumption that low-mass growth is fueled by planetesimal accretion requires that, in addition to the reservoir of small pebbles, a substantial population of larger planetesimals has formed. We discuss the ramifications of varying the mass in planetesimals in Section 3.4.2. Close to the central star, planetesimal accretion can dominate the early growth of planets, with pebble accretion setting the growth timescale for high-mass cores. Far from the central star, however, planetesimal accretion is less efficient, limiting its ability to grow cores to high enough masses that pebble accretion kicks in. Thus, turbulence can set the maximum distance at which gas giant formation is possible via pebble accretion. We find that for quiescent disks, gas giants can form far out in the disk ( $a \lesssim 70$  AU), but for stronger turbulence, this maximum distance is smaller (e.g.  $a \lesssim 40$  AU for  $\alpha \gtrsim 10^{-2}$ ). Furthermore, while disks with weaker turbulence can have gas giants at wider orbital separation, the weaker viscosities in these disks mean that the masses of the gas giants formed are likely lower ( $\lesssim 2 M_J$ ), which would preclude them from being detected by the current generation of direct-imaging surveys. Therefore, there may exist a population of wide orbital separation gas giants that have yet to be found due to their low luminosities.

In Section 4.2, we review our model, which is discussed in detail in R18. In Section 3.3, we discuss how gas-assisted growth operates at wide orbital separation, contrasting the rapid growth at high core mass with the slower growth for low-mass cores. In Section 3.4, we explore how turbulence can place limits on the semi-major axes where gas giants can form. In Section 3.5, we investigate the implications for the final masses of gas giants if turbulence plays a role in gap opening in addition to early core growth. Finally, in Section 3.6, we summarize our results and give our conclusions.

## 3.2 Model Overview

In this section, we will give a brief summary of the ideas behind pebble accretion and how they are implemented in our model. We will focus on pebble accretion at the mass scales relevant to limiting gas giant growth – i.e. masses in the range  $10^{-4}M_{\oplus} \lesssim M \lesssim 10^{-2}M_{\oplus}$  (see Figure 3.6). A more general and in-depth discussion can be found in Chapter 2, and in R18.

### 3.2.1 Basic Pebble Accretion Processes

In this section, we discuss the basic parameters that go into calculating the growth timescale and contrast gas-assisted growth with growth via planetesimal accretion.

The setup for our model consists of a large body, or protoplanetary “core,” growing by accreting a population of small bodies. Our calculation is performed for a given size of small body, expressed either in terms of the small body’s mass,  $m$ , or its

radius  $r_s$ . Note that, practically speaking, the important parameter for our calculation is the particle's Stokes number,  $St$  (see Section 3.2.3). We can convert from Stokes number to radius or mass by assuming a density for the small bodies. In what follows, we will assume a density of  $\rho_s = 2 \text{ g cm}^{-3}$ , which is appropriate for rocky or icy bodies. We note, however, that lower density, fluffy aggregates will have higher radii at a given Stokes number.

In general, the growth timescale for the large body of mass  $M$  is given by

$$t_{\text{grow}} = \left( \frac{1}{M} \frac{dM}{dt} \right)^{-1}, \quad (3.1)$$

while the growth rate,  $dM/dt$  can be expressed as

$$\frac{dM}{dt} = m(n\sigma_{\text{acc}}v_{\infty}) = m \left( \frac{f_s \Sigma}{2H_p m} \right) (2R_{\text{acc}})(2H_{\text{acc}})v_{\infty}. \quad (3.2)$$

Here  $n$  is the volumetric number density of small bodies,  $\sigma_{\text{acc}}$  is the accretion cross section, and  $v_{\infty}$  is the velocity at which small bodies approach the large body. In the second equality, we have set  $n = f_s \Sigma / (2H_p m)$ , where  $H_p$  is the scale height of the small bodies,  $\Sigma$  is the surface density of the gas, and  $f_s \equiv \Sigma_p / \Sigma$  is the solid-to-gas mass ratio in the disk. We have also decomposed  $\sigma_{\text{acc}}$  into the product of length scales parallel and perpendicular to the disk plane,  $2R_{\text{acc}}$  and  $2H_{\text{acc}}$ , respectively. Combining these two expressions gives

$$t_{\text{grow}} = \frac{MH_p}{2f_s \Sigma v_\infty R_{\text{acc}} H_{\text{acc}}} . \quad (3.3)$$

Thus, once  $H_p$ ,  $v_\infty$ ,  $R_{\text{acc}}$ , and  $H_{\text{acc}}$  are determined,  $t_{\text{grow}}$  can be calculated.

For growth that proceeds by accretion of massive planetesimals, the effects of gas drag are generally negligible (though see [Rafikov 2004](#) for a discussion of the effects of gas drag on smaller planetesimals of size  $\lesssim 1$  km). In this case, the value of  $R_{\text{acc}}$  is determined by the maximum impact parameter at which a small body will be gravitationally focused into a collision with the core,

$$R_{\text{focus}} = R \left( 1 + \frac{v_{\text{esc}}^2}{v_\infty^2} \right)^{1/2} , \quad (3.4)$$

where  $R$  is the physical radius of the core, and  $v_{\text{esc}} = \sqrt{2GM/R}$  is the escape velocity from the core.

An important parameter for calculating  $R_{\text{focus}}$  is the core's ‘‘Hill radius,’’ which is the characteristic radius at which the large body's gravity strongly influences the trajectories of the small bodies. For a big body of mass  $M$  orbiting a star of mass  $M_*$  at a semi major axis  $a$ , the Hill radius,  $R_H$  is given by ([Hill 1878](#)),

$$R_H = a \left( \frac{M}{3M_*} \right)^{1/3} , \quad (3.5)$$

which can be obtained by determining the length at which the gravity of the large body is equal to the tidal gravity from the central star. Particles that pass within distances  $\sim R_H$  of the core move on complex trajectories that cannot be expressed as a simple function of impact parameter (Petit & Henon 1986). Particles that emerge from the Hill radius without colliding with the large body will generally have their velocities relative to the core excited up to  $v_\infty \sim R_H \Omega \equiv v_H$  in a random direction (GLS), where  $\Omega = \sqrt{GM_*/a^3}$  is the Keplerian angular frequency and  $a$  is the semi-major axis of the core’s orbit. The quantity  $v_H$  is known as the “Hill velocity.” If  $v_\infty \sim v_H \ll v_{\text{esc}}$ , it is straightforward to show that

$$R_{\text{focus}} \sim \sqrt{RR_H} . \quad (3.6)$$

Since interactions with the core excite planetesimals to a random velocity  $v_\infty \sim v_H$ , this is the largest capture radius possible for planetesimal accretion without invoking some damping mechanism to lower the planetesimal velocity below  $v_H$ . Note, however that since  $R \ll R_H$ ,  $R_{\text{focus}} < R_H$ .

In gas-assisted growth, on the other hand, the value of  $R_{\text{acc}}$  can be much larger than  $R_{\text{focus}}$ . For “pebble-sized” small bodies, the interaction between the small bodies and the gas is important when calculating the accretion rate. In particular, gas drag can remove kinetic energy from the small body as it interacts with the growing core. If the work done by gas drag is sufficiently large, small bodies that otherwise would have merely been deflected by the core’s gravity can become gravitationally bound to the core, further reducing their energy and causing them to inspiral and eventually be

accreted by the core. This can dramatically increase the impact parameters at which accretion will occur. As discussed by, e.g. R18, in certain regions of parameter space, the core can accrete over the entirety of its Hill sphere, i.e. accretion proceeds with  $R_{\text{acc}} = R_H \gg R_{\text{focus}}$ .

### 3.2.2 Pebble Accretion at Different Particle Radii

The Hill radius represents the largest distance at which particles can be captured. However, not all sizes of particles can be captured at  $R_H$ . To fully characterize the scale at which pebbles are captured, we need to introduce two additional radii.

The first radius is the wind shearing (WISH) radius, which is the radius interior to which the core's gravity dominates over the differential acceleration between the small body and the core due to gas drag,

$$R'_{WS} = \sqrt{\frac{G(M+m)}{\Delta a_{WS}}}, \quad (3.7)$$

where  $\Delta a_{WS}$  is the differential acceleration between the two bodies due to gas drag (Perets & Murray-Clay 2011). Particles that approach the core at impact parameters  $> R'_{WS}$  will be pulled off the core by gas drag even if they are inside of  $R_H$ . Thus, the value of  $R_{\text{acc}}$  is given by

$$R_{\text{acc}} = \min(R_H, R'_{WS}). \quad (3.8)$$

However, the value of  $R'_{WS}$  depends on the size of the small body being accreted, unlike

$R_H$ . To see this, we note that if  $M \gg m$ , we can rewrite  $R'_{WS}$  as

$$R'_{WS} \approx \sqrt{\frac{GMt_s}{v_{\text{rel}}}}. \quad (3.9)$$

Here  $t_s$  is the stopping time of the small body,

$$t_s \equiv \frac{mv_{\text{rel}}}{F_D(m)}, \quad (3.10)$$

$v_{\text{rel}}$  is the relative velocity between the small body and the gas, and  $F_D(m)$  is the drag force on the small body (see the Appendix for a discussion of how the correct  $v_{\text{rel}}$  for calculating  $R'_{WS}$  is determined). The stopping time parameterizes the size of the particle in terms of its interaction with the gas. Qualitatively, for large core masses only the stopping time of the smaller body is relevant because the core is essentially unaffected by gas drag. The largest particles that can deplete their kinetic energy will have  $R'_{WS} > R_H$ , and will be able to accrete over the entirety of the core's Hill sphere, while smaller particles will have  $R'_{WS} < R_H$  and will only be accreted at more modest values of impact parameter. See the right two panels of Figure 2.1.

Pebble accretion will not continue down to arbitrary sizes of small bodies. As  $R'_{WS}$  decreases with decreasing particle size, we will eventually reach the scale of the core's atmosphere. Because the atmosphere is essentially static, and the flow velocity is subsonic, the local gas flow will not be able to penetrate into the core's atmosphere. Gas will instead flow around the static atmosphere held by the core. See, e.g. [Ormel \(2013\)](#) for an example of this behavior in the context of a planet embedded in a protoplanetary

disk.

We take the scale of the core’s atmosphere to be determined by the Bondi radius,  $R_b$ , which is the scale at which the escape velocity from the core is equal to the local isothermal sound speed  $c_s = \sqrt{kT/\mu}$ , where  $k$  is Boltzmann’s constant,  $T$  is the temperature, and  $\mu$  is the mean molecular weight of the gas molecules. Thus,  $R_b$  is given by

$$R_b = \frac{GM}{c_s^2}. \quad (3.11)$$

Once particles are small enough that  $R'_{WS} < R_b$ , they need to penetrate into the core’s atmosphere to become bound to the core. However, these small particles will couple strongly to the gas, which will flow around  $R_b$ , stopping the particles from accreting. Thus, we take  $R'_{WS} = R_b$  to set the smallest size of particles that can be accreted; see the left panel of Figure 2.1. We note here that we are neglecting any effects from potential “recycling” of the core’s atmosphere by the protoplanetary disk, but see, e.g. [Ormel et al. \(2015\)](#) and [Lambrechts & Lega \(2017\)](#) for discussions of this effect. If the gas flow is able to penetrate into the core’s atmosphere (e.g. [Fung et al. 2015](#)), or if the core’s atmospheric mass is small due to the high accretion luminosity, the core may be able to accrete the small particle sizes that we exclude. However, the accretion timescales for these particles are extremely long (see Section 3.3.1), so even if these particles can indeed accrete, their inclusion makes a negligible contribution to the total growth rate.

Cores that have  $R_b < R$  will not be able to accrete a substantial amount of

gas from the nebula, which occurs for planetary masses  $M < M_a$ , where

$$M_a \equiv \frac{c_s^3}{G} \left( \frac{3}{4\pi G \rho_p} \right)^{1/2} \quad (3.12)$$

$$\approx 2 \times 10^{-4} M_\oplus \left( \frac{a}{30 \text{ AU}} \right)^{-9/14} \left( \frac{\rho_p}{2 \text{ g cm}^{-3}} \right)^{-1/2} \quad (3.13)$$

where  $\rho_p$  is the density of the protoplanet (e.g. Rafikov 2006). The lowest core masses considered in this work are below this threshold. In this case, the considerations discussed above will still apply with the protoplanet's radius  $R$  in place of its Bondi radius (i.e. accretion will cease for  $R'_{WS} < R$ ).

In summary, the largest sizes of particles that can deplete their kinetic energy can be captured at the core's Hill radius  $R_H$ . For smaller sizes of particles, the WISH radius will eventually become smaller than  $R_H$ , which limits the impact parameters where accretion can occur. Finally, the smallest sizes of particles will have  $R'_{WS} < R_b$ . These particles will not be able to penetrate into distances  $< R'_{WS}$ , and therefore will not be able to accrete via pebble accretion.

### 3.2.3 Summary of Timescale Calculation

In this section, we briefly discuss how  $t_{\text{grow}}$ , as well as the parameters necessary for calculating the growth timescale ( $R_{\text{acc}}$ ,  $H_{\text{acc}}$ ,  $H_p$ , and  $v_\infty$ , see Equation 3.3), are determined. We also define symbols that will be used in the rest of the paper. For a summary of how these parameters are calculated, see the Appendix. For a more detailed discussion of how the calculation is performed, see R18.

Besides the orbital separation,  $a$ , the mass of the planet,  $M$ , and the stellar

mass,  $M_*$ , the other input parameters needed to calculate the growth timescale are the radius of the small bodies being accreted,  $r_s$ , and the strength of the turbulence, which is parameterized by the Shakura-Sunyaev  $\alpha$  parameter (Shakura & Sunyaev 1973).

Using the value of  $r_s$ , we can calculate the stopping time of the particle,  $t_s$ , and the particle's Stokes number,

$$St \equiv t_s \Omega . \quad (3.14)$$

The Stokes number is a dimensionless measurement of the particle's size in terms of how well coupled the particle is to the gas and is the directly relevant parameter for calculating the effects of gas drag on the particle. We also note that using this form of the Stokes number for expressions involving turbulence implicitly assumes that the turnover time of the largest-scale turbulent eddies is equal to the local orbital period.

The value of  $\alpha$  parameterizes the strength of the local turbulence in terms of the turbulent viscosity:  $\nu_t = \alpha c_s H_g$ , where  $H_g = c_s/\Omega$  is the scale height of the gas disk. In terms of  $\alpha$ , the local turbulent gas velocity is given by

$$v_{\text{gas,t}} = \sqrt{\alpha} c_s . \quad (3.15)$$

We use  $\alpha$  mainly to parameterize the magnitude of the turbulent gas velocity, which is the quantity that affects the pebble accretion process. It is only in Section 3.5 that we explicitly use  $\alpha$  to parameterize the viscosity. While the  $\alpha$  model of accretion disks is generally invoked to transport angular momentum inward and explain measured accre-

tion rates in protoplanetary disks (see, e.g. [Muzerolle et al. 2005](#)), for our purposes,  $\alpha$  is fundamentally a local parameter and is not necessarily connected with the accretion rate onto the central star. The most commonly cited mechanism for generating turbulence in protoplanetary disks is the magnetorotational instability (MRI; for a review, see [Balbus 2009](#)). Simulations of MRI under ideal magnetohydrodynamical (MHD) conditions find effective  $\alpha$  values of  $10^{-2} - 10^{-1}$  (e.g. [Hawley et al. 1995](#)), while MHD simulations that include nonideal MHD effects such as ambipolar diffusion find lower  $\alpha$  values, in the range  $10^{-4} - 10^{-3}$  (e.g. [Bai & Stone 2011](#)). In these simulations, the RMS turbulent gas velocity can be approximated to order of magnitude by taking  $v_{gas} = \sqrt{\alpha}c_s$ , as in Equation (4.37) (e.g. [Xu et al. 2017](#)). More recent works argue that magnetically driven winds can generate observed accretion rates, in which case protoplanetary disks could be quite inviscid (see, e.g. [Bai 2016](#), [Suzuki et al. 2016](#)). Even in this case, however, pure fluid instabilities, such as convective overstability (see, e.g. [Lyra 2014](#)) or the zombie vortex instability (see, e.g. [Marcus et al. 2015](#)), spiral density waves raised by giant planets (see, e.g. [Bae et al. 2016](#)), and hydrodynamical turbulence (see, e.g. [Flock et al. 2017](#)), can all generate large RMS velocities for which the effective  $\alpha$  value in Equation (4.37) is not equal to the  $\alpha$  value characterizing angular momentum transport.

Once  $a$ ,  $M$ ,  $M_*$ ,  $r_s$ , and  $\alpha$  are specified, we can calculate the quantities needed to determine  $t_{\text{grow}}$ . To begin, in order to determine the rate that particles encounter the core, as well as the kinetic energy of the small body relative to the protoplanet, we need to calculate the small body's velocity far from the core. Because we take the core to move at the local Keplerian velocity, we take  $v_\infty$  to be set by the larger of the

particle's shear velocity,  $v_{\text{shear}} = R_{\text{acc}}\Omega$ , and its velocity relative to the local Keplerian velocity, which is due to the particle's interaction with both the laminar and turbulent components of the gas velocity. We use  $v_{pk}$  to denote the value of this velocity relative to the Keplerian orbital velocity. Thus,  $v_{\infty}$  is given by

$$v_{\infty} = \max(v_{pk}, v_{\text{shear}}). \quad (3.16)$$

For every particle size, we calculate both the kinetic energy of the particle before the encounter,

$$KE = \frac{1}{2}mv_{\infty}^2, \quad (3.17)$$

and the work done by gas drag during the encounter,

$$W = 2F_D(v_{\text{enc}})R_{\text{acc}}, \quad (3.18)$$

where  $v_{\text{enc}}$  is the velocity of the small body relative to the gas during its encounter with the core. For a discussion of how  $F_D$  and  $v_{\text{enc}}$  are calculated, see the Appendix. Particles that have  $KE > W$  cannot accrete; i.e. we set  $t_{\text{grow}} = \infty$  for such particles, regardless of the values of the parameters in Equation (3.3).<sup>13</sup> In practice, this sets the upper limit on the particle sizes that can be accreted via gas-assisted growth.

In addition to determining the work done on the particle during its encounter,

---

<sup>13</sup>Particles with  $R_{\text{acc}} = R_H$  and  $v_{\infty} = v_H$  merely have their growth timescale enhanced by a factor  $KE/W$  for  $KE > W$ , see the appendix for more details.

the impact parameter for accretion  $R_{\text{acc}}$  is used to determine the width of the accretion cross section. As stated in Section 3.2.2,  $R_{\text{acc}}$  is given by

$$R_{\text{acc}} = \min(R_H, R'_{WS}) . \quad (3.19)$$

For more details on how  $R'_{WS}$  is calculated, see the Appendix.

The height of the accretion rectangle  $H_{\text{acc}}$  is the minimum of the particle scale height  $H_p$  and the impact parameter for accretion  $R_{\text{acc}}$ :

$$H_{\text{acc}} = \min(R_{\text{acc}}, H_p) , \quad (3.20)$$

as particles with a vertical extent larger than  $R_{\text{acc}}$  will not be accreted. The particle scale height is also needed because it sets the density of the small bodies; it can be set by the Kelvin-Helmholtz shear instability or by turbulent diffusion,

$$\begin{aligned} H_p &= \max(H_{KH}, H_t) \\ &= \max \left[ \frac{2\eta v_k}{\Omega} \min \left( 1, St^{-1/2} \right), H_g \min \left( 1, \sqrt{\frac{\alpha}{St}} \right) \right] , \end{aligned} \quad (3.21)$$

where  $v_k$  is the local Keplerian orbital velocity,  $\eta \equiv c_s^2 / (2v_k^2)$  is a measure of the pressure support in the protoplanetary disk, and  $\eta v_k$  is the velocity of the nebular gas relative to  $v_k$  due to radial pressure support (i.e. the non-turbulent velocity of the gas).

### 3.2.4 Values of Parameters

For the purposes of reporting numerical values in what follows, we use a fiducial set of parameters that specify the properties of the protoplanetary disk at a given semi-major axis. The effect of varying some of the parameters is discussed in R18.

We take the central star to be a solar mass,  $M_* = M_\odot$ . The small bodies and the core are taken to be spherical, with density  $\rho_s = 2 \text{ g cm}^{-3}$ . We assume the gas disk is 70%  $\text{H}_2$  and 30 % He by mass, leading to a mean molecular weight of  $\mu \approx 2.35 m_H \approx 3.93 \times 10^{-24} \text{ g}$ , with a neutral collision cross section  $\sigma \approx 10^{-15} \text{ cm}^2$ . The temperature and gas surface density profiles are taken to be power laws in the semi-major axis. For the temperature profile we take  $T = T_0(a/\text{AU})^{-3/7} \text{ K}$  (Chiang & Goldreich 1997), where  $T_0 = 200 \text{ K}$ , which is appropriate for a disk irradiated by star of luminosity  $L \sim 3L_\odot$  (e.g. Ida et al. 2016). For the gas surface density we use  $\Sigma = 500(a/\text{AU})^{-1} \text{ g cm}^{-2}$ , and we assume a constant solid-to-gas mass ratio of  $f_s = 1/100$ . These choices are made to match solid surface densities found in observations of protoplanetary disks (see Figure 3.1).

## 3.3 Gas-Assisted Growth Timescales at Wide Orbital Separation

In this section, we discuss the timescales for growth via pebble accretion at wide orbital separation ( $\gtrsim 10 \text{ AU}$ ), where canonical core accretion models are slow. We find that even in the presence of strong ( $\alpha \gtrsim 10^{-2}$ ) turbulence, the growth timescales for high-mass cores are far shorter for pebble accretion than for planetesimal accretion.

Indeed, the doubling timescale is so fast at these orbital separations that it begs the question of what inhibits this rapid growth. To investigate this question, we also show that, unlike for planetesimal accretion, gas-assisted growth is generally slower for low core masses, particularly when turbulence is strong.

### 3.3.1 Growth at High Core Mass

In the case of planetesimal accretion, the growth timescale for a core to reach  $M_{\text{crit}}$  is dominated by the last doubling timescale of the core; i.e. the slowest growth occurs for the highest core masses. Thus, when considering whether growth of wide orbital separation gas giants is possible, most authors examine the growth timescales at large core masses, which limit growth in canonical core accretion.

The modification to the core accretion model presented by gas-assisted growth, on the other hand, substantially decreases the last doubling time at  $M_{\text{crit}}$  to well below the disk lifetime, even at wide orbital separations (e.g. [Lambrechts & Johansen 2012](#)). While turbulence can reduce the rapid growth rates provided by pebble accretion, our modeling reveals that, at high core mass, growth remains efficient even in the presence of strong turbulence. This agrees with results from MHD simulations by [Xu et al. \(2017\)](#), who numerically explore the growth rates of high-mass planetary cores in the presence of MRI turbulence.

An example of our results is shown in Figure 3.2, which shows the growth timescale for a  $5 M_{\oplus}$  planet located at 30 AU. For particle sizes  $r_s \gtrsim 50$  cm, the growth timescale increases  $\propto St$ , as these particles require many orbital crossings to fully dissipate their kinetic energy (see the appendix and R18). As we decrease the small-body

radius, we encounter small-body sizes ( $1 \text{ cm} \lesssim r_s \lesssim 50 \text{ cm}$ ) that are large enough that wind-shearing and scale height considerations are unimportant, allowing them to accrete over the entire Hill sphere at a rapid rate that is independent of  $r_s$ . As we continue to move to smaller pebble radii, eventually the particle size becomes small enough that the WISH radius and the particle scale height become important, decreasing the accretion rate. Finally, we reach the point where  $R'_{WS} < R_b$ , which marks the pebble size at which particles couple so strongly to the gas that they flow around  $R_b$  without accreting. This causes the cutoff in the graph seen on the left. For all values of  $\alpha$  shown in Figure 3.2, there exists a broad range of small-body sizes,  $r_s$ , for which gas-assisted growth is able to operate, and the growth timescale of the core is less than the disk lifetime. Though turbulence erodes accretion of the smallest pebbles that were available in the laminar case, there still exists a range of particle sizes where rapid growth is possible.

Figure 3.2 shows the emergence of a regime where the core can accrete larger particles at a minimal timescale that is independent of  $r_s$  and  $\alpha$ . This timescale is reached for cores accreting in 2D (i.e.  $H_{\text{acc}} = H_p$ ) over the entirety of their Hill radius. As discussed in, e.g. R18, the maximal possible approach velocity in the 2D regime occurs when particles shear into  $R_H$ , i.e. when  $v_\infty = v_H$ ; larger velocities will excite pebbles vertically, causing the core to accrete in 3D. Setting  $H_{\text{acc}} = H_p$ ,  $R_{\text{acc}} = R_H$  and  $v_\infty = v_H$  in Equation (3.3), we that see this timescale is given by

$$t_{\text{Hill}} = \frac{M}{2f_s \Sigma R_H^2 \Omega} . \quad (3.22)$$

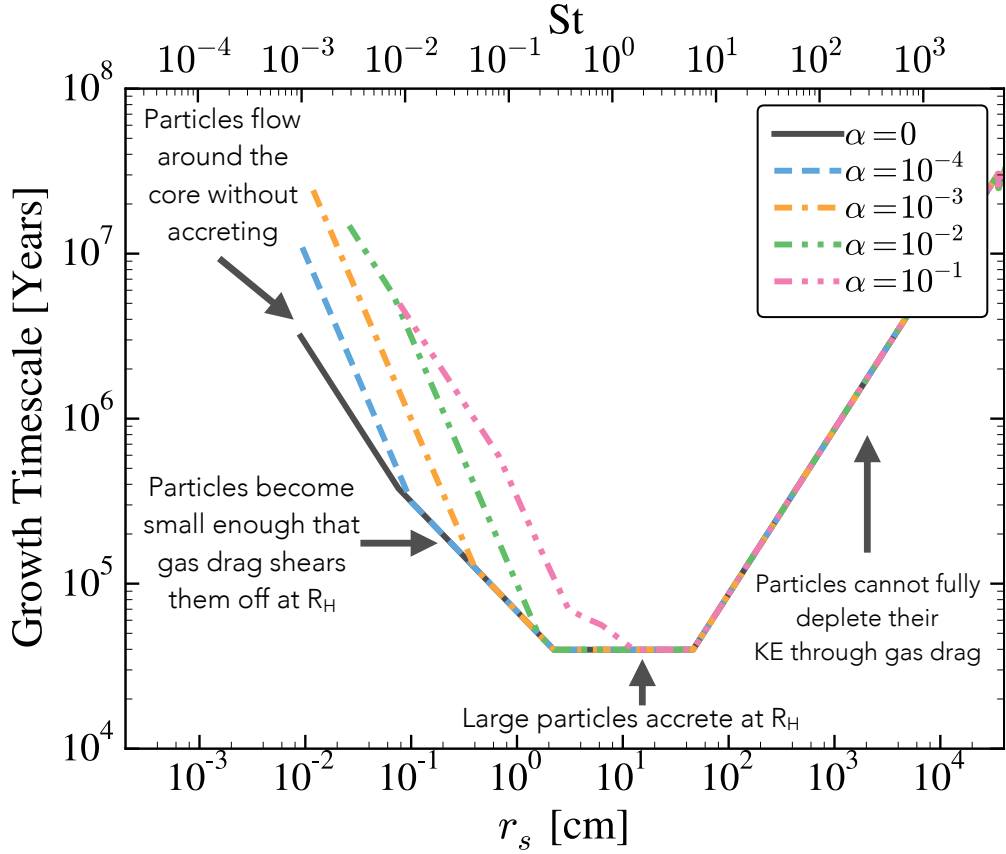


Figure 3.2: The growth timescale for a protoplanet as a function of the small-body radius the core is accreting. The timescale is plotted for several values of  $\alpha$ , which measures the strength of turbulence in the disk. The values shown are for a  $5 M_{\oplus}$  core at 30 AU. The lines are cut off for particles that are unable to accrete according to the energy criteria discussed in Section 3.2.3.

In terms of fiducial parameters,  $t_{\text{Hill}}$  can be expressed as

$$t_{\text{Hill}} \approx 4 \times 10^4 \left( \frac{a}{30 \text{ AU}} \right)^{1/2} \left( \frac{M}{5 M_{\oplus}} \right)^{1/3} \text{ years.} \quad (3.23)$$

This timescale, which we will refer to as the “Hill timescale,” is faster than gravitational focusing by a factor  $R_H^2/R_{\text{focus}}^2 \approx R_H/R$ . If we approximate the star and the planet as uniform density spheres and take  $\rho_* \sim \rho_p$ , we have  $R_H/R \sim a/R_*$ . Thus,

not only is the enhancement in growth rate substantial, the enhancement of pebble accretion relative to gravitational focusing is an increasing function of semi-major axis.

The qualitative features of growth discussed above apply over a wide range of core masses. This can be seen from examination of Figure 3.3, which shows the growth timescale for protoplanets as a function of both core mass and small-body radius. The four panels show the growth timescale for four different values of  $\alpha$ , while each individual panel shows the growth rate plotted as a function of both  $r_s$  and  $M$ . As can be seen in Figure 3.3, growth at “high” core masses ( $\gtrsim 10^{-3} - 10^{-2} M_{\oplus}$ ) proceeds in a similar manner to what is shown in Figure 3.2: the largest pebbles accrete on the rapid Hill timescale, independent of the small-body radius  $r_s$ , while smaller pebbles accrete less efficiently. Thus, as long as there exists a reservoir of particles that are able to accrete at  $t_{\text{Hill}}$ , growth at higher core mass proceeds rapidly, even in the presence of strong turbulence.

However, it is also clear from examination of Figure 3.3 that below some “minimum” mass, growth operates in a qualitatively different manner. We discuss the reasons for this change, as well as the ramifications for planetary growth, in the next section.

### 3.3.2 Growth Timescales for Low-Mass Protoplanets

In the last section, we showed that growth at large core masses is quite fast in gas-assisted growth, even in the presence of strong turbulence. This efficiency brings another issue, however, as we now need to understand why wide orbital separation gas giants are not ubiquitous given these rapid growth rates. As we will show below, at wide orbital separations and low core masses, growth timescales can be substantially

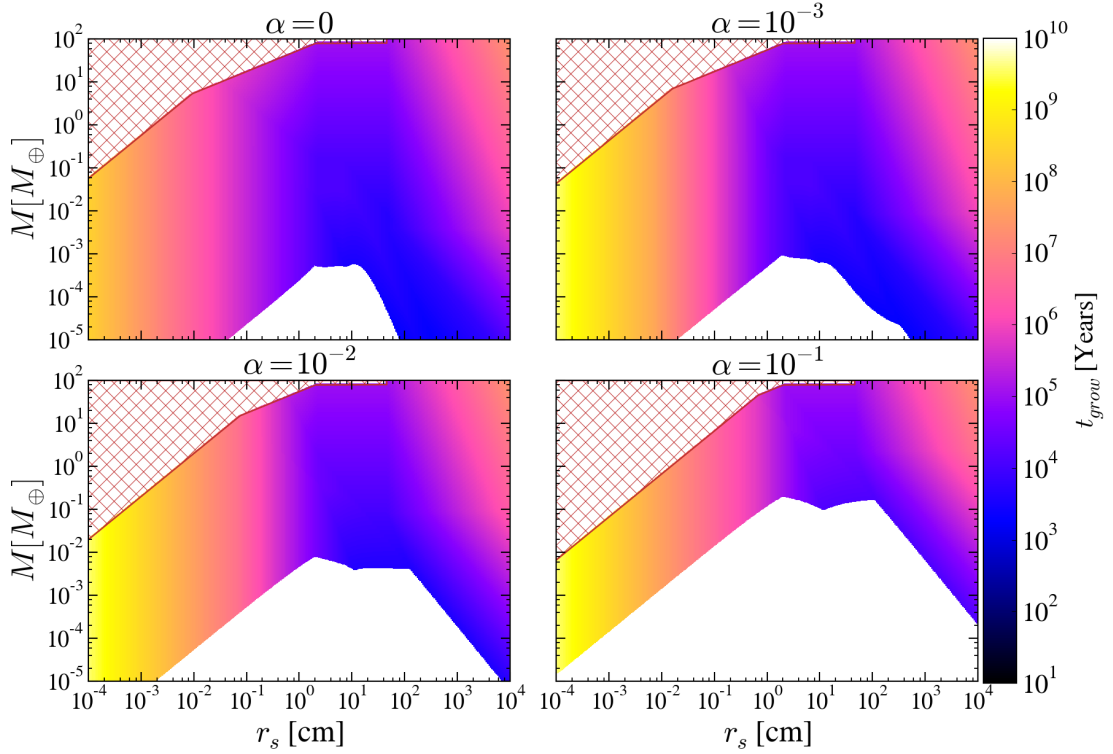


Figure 3.3: The growth timescale as a function of core mass, for  $a = 30$  AU. The red hatched region indicates where no accretion is possible. In the white regions particles can still accrete via other processes, e.g. gravitational focusing.

longer than  $t_{\text{Hill}}$ .

Figure 3.3 illustrates the difference in growth at low core masses. One feature of particular note in this figure is how the range of particle sizes available for accretion is restricted both at low core masses ( $M \lesssim 10^{-3} - 10^{-2} M_{\oplus}$  in the figure) and as the strength of turbulence increases. The limited range of sizes where pebble accretion can operate is often neglected in other works on pebble accretion, e.g. [Lambrechts & Johansen \(2012\)](#). While some works, such as [Ormel & Klahr \(2010\)](#), discuss an upper limit on particle size that agrees with our work in the laminar regime, this upper limit

shrinks rapidly as the strength of turbulence is increased, as can be seen in the figure. For a more in-depth comparison of these models, see R18.

In all four panels, we see that, for low core masses, it is primarily small particles with high accretion timescales that are available for growth. It is only when the core reaches a sufficiently “large” mass <sup>14</sup> that the features discussed in the previous section emerge and cores are able to rapidly accrete pebbles. Thus, there is in some sense a “minimum” mass, above which pebble accretion becomes efficient and proceeds on timescales less than the lifetime of the disk. This trend is more pronounced as the strength of turbulence is increased, in the sense that the mass required for accretion to be faster than the disk lifetime increases rapidly as  $\alpha$  increases.

We note here that in the “weak” turbulence regime (top panels of Figure 3.3), there is a feature where the cores can accrete a limited range of sizes (with  $r_s \sim 1$  m) on short timescales. This is caused by the fact that the heaviest particles can actually have low kinetic energies relative to the core, since they drift at speeds close to the Keplerian velocity. This effect is eroded by the presence of turbulence, since it excites the random velocity of even the largest particles. In what follows, this effect is unimportant, since our choice of size distribution means that such large particles are not present (see Section 3.3.3), though it is an interesting area for future inquiry.

The difficulty in accreting larger pebbles at low core mass is due to the weaker gravitational influence of the core. Gravitational perturbations from the core on the incoming pebbles can greatly increase the drag force on the small body during the encounter, since they increase the velocity of the particle relative to the local gas flow.

---

<sup>14</sup>The mass scale where this change occurs is well approximated by  $v_H/v_{\text{gas}} = 48^{-1/3}$ , see R18.

The strength of this perturbation increases with increasing core mass. Thus, as core mass decreases, the work done by gas drag is reduced, limiting the range of small-body sizes that can be accreted. Furthermore, the size of  $R_{\text{acc}}$  also decreases with core mass, which means incoming particles have a smaller distance over which they can dissipate their kinetic energy relative to the core. Increasing the strength of the turbulence in the disk amplifies the difficulty in accreting particles, as incoming pebbles now have substantially higher kinetic energies.

Not only can a smaller range of particles be accreted at low core mass, the smaller particle sizes that are available for growth have long growth timescales. One reason for this is that smaller particles can be more easily pulled off the core by gas drag, meaning that their maximum impact parameter for accretion is  $R_{\text{acc}} = R'_{WS}$ , which can be quite small in comparison to  $R_H$ . Furthermore, these particles are more easily excited vertically by the turbulent gas velocity (see Equation 3.21). Thus, smaller particles have larger scale heights, reducing their number density and further slowing growth.

Thus, at lower core masses, we expect growth via pebble accretion in high turbulence to be quite slow, as the only particles that the smaller cores can accrete have large growth timescales. These timescales can be several orders of magnitude slower than the growth timescale at  $M_{\text{crit}}$ , meaning that growth at low core masses can often be the time-limiting step in gas giant formation via gas-assisted growth.

### 3.3.3 Size Distribution of Small Bodies

Because the growth timescale is generally much slower for smaller particle sizes than it is for larger ones, the timescale for growth will also be dependent on the size distribution of small bodies that are available for accretion. Thus, in order to facilitate a more quantitative discussion of where growth of gas giants is possible in our model, we will integrate quantities of interest over an assumed size distribution, a process we now discuss in more detail.

If the size distribution of small bodies is specified, i.e. if we know  $dN/dr_s$ , we can integrate the accretion rate of the large body over small body radius and obtain a total accretion rate. This integrated timescale is sensitive to the actual form of size distribution employed; thus, while integrating over size distribution can be quite illustrative, the results are less general.

For our purposes, we employ the power-law distribution from [Dohnanyi \(1969\)](#), who calculated the steady-state size distribution from a collisional cascade. This gives a distribution of sizes such that  $dN/dr_s \propto r_s^{-3.5}$ . For a power-law size distribution  $dN/dr_s \propto r^{-q}$ , most of the mass is in the largest particle sizes for  $q < 4$ . Thus, our results are insensitive to the lower cutoff radius but highly dependent on the upper radius, since for an  $r_s^{-3.5}$  power-law, most of the mass is in the larger particles. This is the most important feature of the size distribution we employ: for any size distribution with most of the mass in the largest particle radii, the qualitative picture discussed below is unchanged, though the quantitative results will change by order unity factors.

Unless otherwise stated, we use an upper radius such that the largest Stokes

number present is  $St_{\max} = 10^{-1}$ , and a lower radius such that the smallest bodies present correspond to  $St_{\min} = 10^{-4}$ . This constant Stokes number upper limit is most appropriate for the case when particle growth is limited by collisions, and the relative velocity is dominated by laminar drift. The value of  $St_{\max} = 10^{-1}$  comes from [Blum & Wurm \(2008\)](#), who gave  $r_s = 10$  cm as the size past which collisions become destructive for a particular set of disk parameters. This radius corresponds to  $St \sim 10^{-1}$  for the disk they considered. If bodies are held together mainly by chemical forces, then the relative velocity between particles is the main determinant of the outcome of a collision. This relative velocity in turn depends on the particle Stokes number and the amplitude of the gas velocity. Because the laminar drift velocity  $\eta v_k$  is approximately constant throughout the disk, if laminar drift sets the collision velocity, the particle Stokes number is the only parameter relevant to determining when collisions become destructive.

This simple description of the size distribution neglects the effects of increased turbulence, which would increase the particle-particle relative velocities during a collision, in turn lowering the critical Stokes number for destructive collisions. This also neglects the importance of radial drift in the outer regions of protoplanetary disks, which can proceed on shorter timescales than particle-particle collisions. In general, the size distribution of pebbles in disks is more complex than the simple prescription given here. We use this as our fiducial size distribution in order to reduce the number of input parameters our results depend on while still describing the general features of gas-assisted growth.

### 3.3.4 Integrated Growth Timescales

In this section, we discuss how integrated growth timescales change as the core grows. We also discuss how we can analytically calculate the integrated growth timescale, which is used later on to calculate analytic expressions for both the minimum mass for pebble accretion to be rapid and the semi-major axes where gas giant growth can occur.

An example of the results from integrating over small-body size is shown in Figure 3.4, which plots the integrated growth timescale at  $a = 20$  AU as a function of core mass for several different levels of turbulence. An estimate for the  $e$ -folding time for the dissipation of the gaseous component of the disk,  $\tau_{\text{disk}} \approx 2.5$  Myr, is also shown. The disk dissipation timescale  $\tau_{\text{disk}}$  represents an approximate cutoff for gas giant formation; cores that are unable to reach the critical core mass within  $\tau_{\text{disk}}$  will not be able to trigger runaway accretion before the gas is substantially depleted.

At low core masses, the growth timescale drops quickly as the core mass increases. This is due to the fact that these larger cores can accrete more massive pebbles. For the lower-mass cores, the largest pebbles that the core can accrete are smaller than the maximal size of the particles present. Therefore, as the core grows, it can accrete a larger fraction of the available solids, increasing the growth rate.

If the growth timescale has only a simple power-law dependence on  $r_s$  for the whole range of sizes, we can explicitly integrate the growth timescale over size and calculate an analytic expression for  $t_{\text{grow}}$ . This requires that none of the parameters that go into calculating  $t_{\text{grow}}$  change regimes over the range of sizes considered: for

example, if  $R_{\text{acc}} = R_H$  for the largest sizes present but  $R_{\text{acc}} = R'_{WS}$  for the smaller sizes, our integrand is now a piecewise function of  $r_s$ , and a simple analytic solution is no longer possible. In practice, if we make the approximation that the regimes that apply for the maximal particle size present hold throughout the integral, the resultant errors are generally small.

In what follows, we will be particularly interested in the mass at which the growth timescale becomes shorter than the lifetime of the gas disk, since subsequent growth will proceed on even shorter timescales. From Figure 3.4, we can see that, at the point where  $t_{\text{grow}}$  becomes shorter than  $\tau_{\text{disk}}$ , cores are small enough that  $R_{\text{acc}} = R'_{WS}$  (i.e. the core's WISH radius is smaller than its Hill radius for all of the small-body sizes it accretes)<sup>15</sup>. We also assume that  $R'_{WS}$  is small enough that the core accretes in 3D, i.e.  $R'_{WS} < H_p$ . Additionally, for the small-body radii the core is accreting  $v_\infty = v_{pk} \approx v_{\text{gas}}$  (i.e. the small body's random velocity dominates over shear, and these particles are well coupled to the gas). Due to the wide orbital separations and small particle sizes we are interested in, the particles are expected to be in the Epstein drag regime. Using these values throughout the integration over size allows us to compute  $t_{\text{grow}}$  analytically, and comparison of the resultant analytic expressions with the numerical calculations presented below shows that these approximations are robust. Finally, when calculating the work done on the particle, we set  $v_{\text{enc}} = v_{\text{kick}} = GM / (R_{\text{acc}} v_\infty)$  (see the appendix for more details). It can be shown that particles with the Stokes number given by Equation (3.24) are in this regime.

---

<sup>15</sup>As discussed in the appendix,  $R'_{WS}$  is really the smaller of two radii:  $R'_{WS} = \min(R_{WS}, R_{\text{shear}})$ . In making our analytic approximations, we assume that the cores we are concerned with are low enough mass that  $R_{WS} < R_{\text{shear}}$ . This assumption can be shown to be generally valid by comparing the analytic approximations we derive to our numerical results

Using the considerations above, we can now calculate closed-form expressions for  $t_{\text{grow}}$ . To begin, we determine the largest size of particle these low-mass cores can accrete. Using Equations (3.10), (3.17), and (3.18) and the values of parameters discussed in the preceding paragraph, we see that the maximal size of particle the core can accrete is given by<sup>16</sup>

$$St_\ell = 12 \frac{v_H^3}{v_{\text{gas}}^3} . \quad (3.24)$$

Because our size distribution is dominated by the largest particle sizes, we can use the Stokes number limit from Equation (3.24) to determine the growth rate. If we neglect the lower bounds on integrations over particle size, it is straightforward to demonstrate that the growth rate is, to order-of-magnitude, given by the product of the growth rate for the largest sizes of particles the core can accrete,  $\dot{M}(St_\ell)$ , and the fraction of the surface density contained in solids up to size  $St_\ell$ ,  $f(St_\ell)$ :

$$\dot{M} \sim \dot{M}(St_\ell) f(St_\ell) . \quad (3.25)$$

Plugging in our assumed values for the parameters into Equation (3.3) for  $t_{\text{grow}}$ , we see that in this regime,

$$t_{\text{grow}} = \frac{H_p}{2\Sigma_p G t_s} . \quad (3.26)$$

---

<sup>16</sup>We note that this is similar to the barrier between the ‘‘Hyperbolic’’ and ‘‘Full Settling’’ regimes identified by [Ormel & Klahr \(2010\)](#), except that our value for  $v_{\text{gas}}$  includes a contribution from the turbulent gas velocity, which dominates for  $\alpha > \eta$ .

Thus, there are two possible growth regimes, depending on whether  $H_p = H_{KH}$  or  $H_p = H_t$ . For  $St < 1$ , we have  $H_t > H_{KH}$  (i.e.  $H_p = H_t$ ) for  $\alpha > 2\eta St$ . This limit on  $St$  divides our analytic expressions into two piecewise regimes.

Explicitly performing the integration over size, the growth timescale is given by

$$t_{\text{grow}} \approx \begin{cases} 9 \times 10^7 \text{ years} \left( \frac{M}{10^{-5} M_{\oplus}} \right)^{-2} \left( \frac{a}{30 \text{ AU}} \right)^{5/2} St_{\text{max}}^{1/2} \left( \frac{\alpha}{10^{-3}} \right)^{7/2}, & \alpha > 2\eta St_{\ell} \\ 3 \times 10^7 \text{ years} \left( \frac{M}{10^{-5} M_{\oplus}} \right)^{-3/2} \left( \frac{a}{30 \text{ AU}} \right)^{51/14} St_{\text{max}}^{1/2}, & \alpha < 2\eta St_{\ell} \end{cases} \quad (3.27)$$

Eventually, the core becomes massive enough that it can accrete all sizes of particles available, i.e.  $St_{\ell} > St_{\text{max}}$ . This causes the growth timescale to become independent of  $M$ , since  $\dot{M} \propto R_{WS}^2 \propto M$ . In this regime, the growth timescale is given by

$$t_{\text{grow}} \approx \begin{cases} 7 \times 10^3 \text{ years} \left( \frac{a}{30 \text{ AU}} \right)^{11/14} St_{\text{max}}^{-3/2} \left( \frac{\alpha}{10^{-3}} \right)^{1/2}, & \alpha > 2\eta St_{\text{max}} \\ 1 \times 10^4 \text{ years} \left( \frac{a}{30 \text{ AU}} \right)^{15/14} St_{\text{max}}^{-1}, & \alpha < 2\eta St_{\text{max}} \end{cases} \quad (3.28)$$

Thus, the low-mass growth of the core, where the growth timescale decreases for increasing core mass, is the time-limiting step in gas-assisted growth. As can be seen in Figure 3.4 and verified by the analytic expressions above, once the core reaches

a mass such that  $t_{\text{grow}} < \tau_{\text{disk}}$ , all subsequent growth should proceed on timescales that are faster than the disk lifetime. Therefore, the early stages of core growth, where gravitational focusing of planetesimals may be faster than gas-assisted growth, will play a key role in whether a planet can grow to be a gas giant.

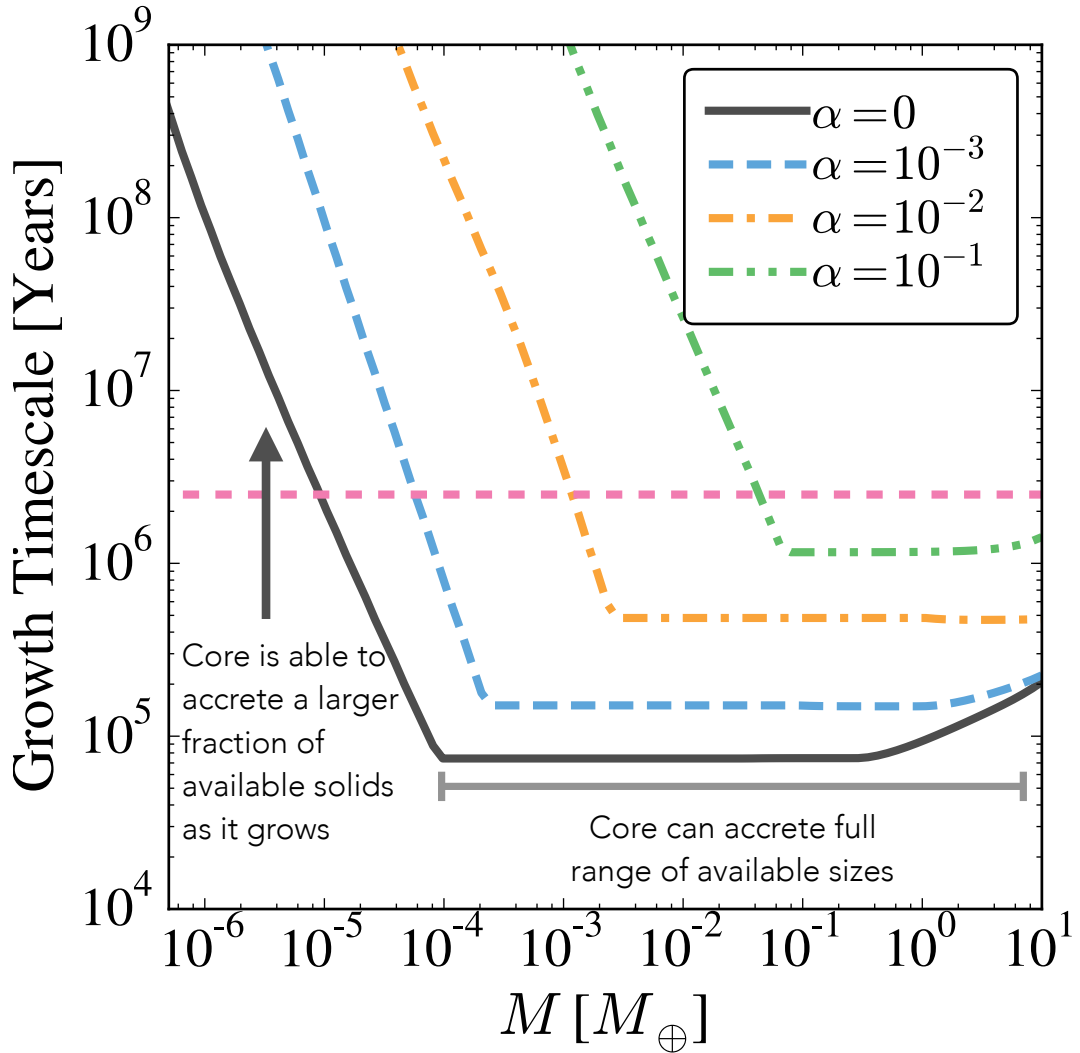


Figure 3.4: Integrated growth timescale for a core at  $a = 20$  AU as a function of core mass. The growth timescale is integrated over sizes using a Dohnanyi distribution with a maximum size corresponding to  $St = 10^{-1}$ , as discussed in Section 3.3.3. The approximate  $e$ -folding time of the gaseous component of the disk,  $\tau_{\text{disk}}$ , is marked as a dashed horizontal line. As the core grows, it can accrete a larger fraction of the available small-body sizes, causing the growth timescale to drop rapidly. Eventually, the core’s mass becomes large enough that it can accrete all available particle sizes, causing it to enter into a regime where growth timescale is independent of  $M$ . We also note that once the core becomes massive enough that the growth timescale drops below  $\tau_{\text{disk}}$ , subsequent growth at higher core masses proceeds on timescales well below the disk lifetime.

## 3.4 Restrictions on the Growth of Gas Giants

The effects of the previous sections imply that to understand under what conditions gas giant formation is possible via pebble accretion, we must examine lower-mass cores, for which the gas-assisted growth timescale can be quite long. If these cores were to grow by gas-assisted growth alone, then growth would always stall at sufficiently small core mass such that turbulence dominates over the core's gravity. For low core masses, however, planetesimal accretion can be quite rapid. Therefore, the final fate of a protoplanet depends on whether canonical core accretion can provide sufficiently rapid growth at small core masses such that the core can reach a size where pebble accretion becomes efficient, which will in turn allow the core to grow rapidly to the critical core mass needed for runaway growth.

### 3.4.1 Planetesimal Accretion Timescale

In order to calculate the semi-major axis where gas giants form, we consider early growth by planetesimal accretion and subsequent growth by pebble accretion. This requires us to calculate the timescale for growth by planetesimal accretion for a given core mass. In general, the scale height of particles is given by  $H_p = v_z/\Omega$ , where  $v_z$  is the vertical component of the small body's velocity. As stated previously, the fastest growth possible via planetesimal accretion (without some external damping mechanism) occurs when the planetesimal velocity dispersion is equal to the Hill velocity. We use this regime for our fiducial value of the growth timescale via planetesimal accretion. If we take  $v_z \sim v_\infty = v_H$ , and use Equations (3.2) and (A.42), then the growth rate of the

core is proportional to

$$\dot{M} \propto R_H R \Sigma_{\text{pla}} \Omega , \quad (3.29)$$

where  $\Sigma_{\text{pla}}$  is the surface density of planetesimals. The prefactor in the above equation is not well constrained by analytic considerations; in a more detailed treatment, it should be taken from  $N$ -body simulations of the interactions between the planetesimals. For our purposes, we take the prefactor from [Johansen & Lambrechts \(2017\)](#); this gives

$$\dot{M} = 6\pi R_H R \Sigma_{\text{pla}} \Omega . \quad (3.30)$$

For our fiducial value of the growth timescale, we set  $\Sigma_{\text{pla}} = \Sigma_p$ , which gives a timescale of

$$t_{\text{pla}} \approx 2 \times 10^7 \text{ years} \left( \frac{a}{30 \text{ AU}} \right)^{3/2} \left( \frac{M}{5 M_{\oplus}} \right)^{1/3} . \quad (3.31)$$

Solving for the mass where  $t_{\text{pla}} = \tau_{\text{disk}}$  gives an expression for the maximum mass a planet can reach via planetesimal accretion,

$$M_{\text{pla}} = 8 \times 10^{-3} M_{\oplus} \left( \frac{a}{30 \text{ AU}} \right)^{-9/2} \left( \frac{\Sigma_{\text{pla},0}}{5 \text{ g cm}^{-2}} \right)^3 , \quad (3.32)$$

where  $\Sigma_{\text{pla},0}$  is the prefactor of the planetesimal surface density profile, i.e.  $\Sigma_{\text{pla}} = \Sigma_{\text{pla},0} (a/\text{AU})^{-1}$ . Our choice of  $\Sigma_{\text{pla}} = \Sigma_p$  gives reasonable values of the masses planets can reach within the gas disk lifetime at the semi-major axes of the solar system gas giants (see Figure 3.6). Some of the effects of varying the surface density of planetesimals are discussed in Section 3.4.2.

### 3.4.2 Upper Limits on the Semi-Major axis of Gas Giant Growth

In order to place constraints on the semi-major axis at which gas giant growth is possible, we begin by determining the minimal mass below which pebble accretion is too slow to grow a core within  $\tau_{\text{disk}}$ . In order to do this, we make the approximation that once the core becomes massive enough that  $t_{\text{grow}} < \tau_{\text{disk}}$ , the growth timescale of the core will remain below  $\tau_{\text{disk}}$  as the core continues to grow to  $M_{\text{crit}}$ . Thus, once the core becomes massive enough, its subsequent growth time is small compared to the disk lifetime. As can be seen in Figure 3.4, and from Equations (3.27) and (3.28), this approximation is quite robust. An exploration of  $t_{\text{grow}}$  vs.  $M$  over a large amount of parameter space shows that this is generally true throughout the disk. We note, however, that if the sizes of the available particles are not set by Stokes number but rather by absolute particle size, there can exist regions of the disk where this approximation breaks down, as the particle sizes where growth is efficient are essentially determined by Stokes number. We consider this possibility in more detail below.

Because the growth timescale is dominated by growth at low core masses, we can determine an approximate minimum mass for gas giant growth through pebble accretion by solving for the mass at which  $t_{\text{grow}} = \tau_{\text{disk}}$ . This is the mass below which

growth will stall, and the core will be unable to grow to  $M_{\text{crit}}$  within  $\tau_{\text{disk}}$ . This idea is shown graphically in Figure 3.5.

The mass where growth stalls as a function of semi-major axis, calculated numerically using our full expressions, is shown in Figure 3.6. Again, the effects of turbulence on growth rate are clearly visible in the figure: in the laminar case, even extremely wide orbital separation cores can grow faster than  $\tau_{\text{disk}}$  down to a very low core mass. At high turbulence ( $\alpha \gtrsim 10^{-2}$ ), however, the core needs to reach masses  $\gtrsim 10^{-3}M_{\oplus}$  before pebble accretion becomes fast enough for these cores to reach  $M_{\text{crit}}$  within the disk lifetime. Also shown in the plot is the *maximum* mass that a core can grow to using gravitational focusing of planetesimals. We emphasize here that the interpretation of this line is the opposite of the gas-assisted growth values; for gravitational focusing, all values *lower* than the given mass are approximately obtainable within the disk lifetime.

We can also obtain an analytic approximation for  $M_{\text{peb}}$ , the mass where the pebble accretion timescale drops below the disk lifetime. Setting (3.27) equal to  $\tau_{\text{disk}}$  gives

$$M_{\text{peb}} = \begin{cases} 6 \times 10^{-5} M_{\oplus} \left(\frac{a}{30 \text{ AU}}\right)^{5/4} \left(\frac{\alpha}{10^{-3}}\right)^{7/4} \left(\frac{\tau_{\text{disk}}}{2.5 \text{ Myr}}\right)^{-1/2} St_{\text{max}}^{1/4}, & \alpha > 2\eta St_{\text{max}} \\ 5.6 \times 10^{-5} M_{\oplus} \left(\frac{a}{30 \text{ AU}}\right)^{17/7} \left(\frac{\tau_{\text{disk}}}{2.5 \text{ Myr}}\right)^{-2/3} St_{\text{max}}^{1/3}, & \alpha < 2\eta St_{\text{max}} \end{cases} \quad (3.33)$$

which demonstrates analytically the strong dependence that the efficiency of pebble accretion has on both semi-major axis and strength of turbulence.

Figure 3.5 shows how we can use Figure 3.6 to determine where the interplay between canonical core accretion and gas-assisted growth will allow a gas giant to grow. The intersection between the pebble accretion and planetesimal accretion values represents the approximate semi-major axis upper limit on gas giant growth. For values higher than this semi-major axis, planetesimal accretion is too slow to bring the core to the minimum mass needed such that gas-assisted growth can subsequently grow the core to  $M_{\text{crit}}$  within the disk lifetime. For values smaller than this semi-major axis, however, planetesimal accretion can grow the core to a sufficiently massive size rapidly enough that gas-assisted growth can take over. This semi-major axis also represents an upper limit on where a core can form, as for smaller orbital separations, the growth timescale decreases (see Equations 3.27 and 3.28). This is not the case if the size distribution is determined by particle radius instead of Stokes number, as we discuss in Section 3.4.3. We also note that if a core larger than the pebble accretion mass were present past this semi-major axis limit (e.g. if it were scattered outward), then the core could grow sufficiently rapidly to trigger gas giant formation.

Figure 3.7 plots the maximum distance obtained by solving numerically for the mass at which  $M_{\text{pla}} = M_{\text{peb}}$  using our full expressions. In order to illustrate the effect of changing the upper limit on the size distribution, two different size distributions are shown – one in which the maximum Stokes number is  $St_{\text{max}} = 0.1$ , and one in which  $St_{\text{max}} = 1$ . From the plot, it is clear that as turbulence increases, the semi-major axis at which gas giant growth is possible drops substantially. Growth is also slightly more inhibited for the  $St = 1$  distribution; this is due to the fact that cores need to

reach higher masses in order to accrete  $St = 1$  particles as opposed to  $St = 0.1$  particles. However, because  $St = 1$  particles accrete more rapidly, this effect is attenuated, causing the overall dependence on  $St_{\max}$  to be rather weak.

Using Equation (3.33), we can derive analytic approximations to the curve shown in Figure 3.7. Setting  $M_{\text{peb}} = M_{\text{pla}}$ , we obtain,

$$a_{\text{upper}} \approx \begin{cases} 70 \text{ AU} \left( \frac{\alpha}{10^{-3}} \right)^{-7/23} \left( \frac{\Sigma_{\text{pla}}}{5 \text{ g cm}^{-2}} \right)^{12/23} \left( \frac{\tau_{\text{disk}}}{2.5 \text{ Myr}} \right)^{14/23} St_{\max}^{-1/23}, & \alpha > 2\eta St_{\max} \\ 60 \text{ AU} \left( \frac{\Sigma_{\text{pla}}}{5 \text{ g cm}^{-2}} \right)^{42/97} \left( \frac{\tau_{\text{disk}}}{2.5 \text{ Myr}} \right)^{154/291} St_{\max}^{-14/291}, & \alpha < 2\eta St_{\max} \end{cases} \quad (3.34)$$

These analytic expressions are overplotted on the numerical results in Figure 3.8. Curves for two different planetesimal surface densities, one where we use our fiducial value of  $\Sigma_{\text{pla}} = \Sigma_p$  and one where we have reduced the surface density by a factor of 2, are shown. As expected, our analytic results agree well with the full numerical calculation in the limits of small and large  $\alpha$ . Figure 3.8 also demonstrates that reducing the planetesimal surface density can have a marked effect on the semi-major axis where gas giant growth is possible.

The considerations discussed above can provide a plausible mechanism by which the growth of gas giants is suppressed: higher values of turbulence inhibit core growth at lower masses and make it so rapid growth via pebble accretion can only proceed once higher values of mass are reached. Because planetesimal accretion is slow at these wide orbital separations, cores will stall in their growth at low mass and be unable to reach the high masses needed for gas giant growth to proceed. In our order-

of-magnitude model, the actual values quoted are of less import than the scalings and overall behavior predicted by the model. Thus, while we would not expect the quoted limit of e.g.  $a \lesssim 30\text{AU}$  for gas giant growth at  $\alpha \approx 10^{-2}$ , to be precise, we would argue that we should expect the general inhibiting of pebble accretion, and therefore gas giant growth, for stronger values of turbulence.

### 3.4.3 Effect of Fixing Upper Particle Radius

Thus far, we have fixed the upper limit of our size distribution in terms of particle Stokes number. In contrast, disk models that are used to fit to observations of protoplanetary disks tend to use size distributions with fixed maximum particle radius instead of Stokes number. Size distributions fixed by particle radius can also emerge naturally if drift limits particle size as opposed to collisions. For example, [Powell et al. \(2017\)](#) derived an expression for the gas surface density determined by particle drift, which can be rewritten as an expression for particle radius (see their Equation 8):

$$r_s = \frac{\Sigma a}{t_{\text{disk}} \eta v_k \rho_s}, \quad (3.35)$$

where  $t_{\text{disk}}$  is the age of the disk. If  $\Sigma_g \propto a^{-1}$ , then the only semi-major axis dependence in the above equation comes from  $\eta v_k$ , which has extremely shallow radial dependence (e.g.  $\eta v_k \propto a^{1/14}$  for the temperature profile we employ). Therefore, we also present results that use a size distribution where the upper size limit is fixed by particle radius. We follow the disk models of [Andrews et al. \(2009\)](#), who used a Dohnanyi ( $dN/ds \propto r_s^{-3.5}$ ) distribution, with  $r_{s,\text{min}} = 0.005 \mu\text{m}$  and  $r_{s,\text{max}} = 1 \text{mm}$ . This 1 mm maximum

size is consistent with fitting of disk spectral energy distributions (D'Alessio et al. 2001).

A plot of the numerical solution for the semi-major axes where gas giant growth is possible for a distribution with fixed size limits is shown in Figure 3.9. The blue region indicates where growth is possible. As can be seen from the figure, using  $r_s = 1$  mm as an upper size limit throughout the disk has pronounced effects on the semi major axes available for gas giant growth. For  $\alpha \gtrsim 10^{-4}$ , the region where gas giants can grow shrinks rapidly, causing a complete cutoff in gas giant growth for  $\alpha \gtrsim 10^{-3}$ . In this regime, we therefore expect turbulence to completely inhibit gas giant growth, instead of restricting growth to smaller values of semi-major axis.

Using an upper limit fixed by particle size leads to a lower limit on semi-major axis in addition to an upper limit. This lower limit stems from the fact that fixing a maximum particle radius means that even the largest sizes of particles present may have low Stokes numbers, causing them to be accreted inefficiently or not accreted at all. This introduces two additional processes that we need to consider when calculating where gas giants can form, one that gives a fixed semi-major axis limit independent of  $\alpha$ , and another that gives a lower limit on  $a$  for a given  $\alpha$ .

Firstly, cores accreting the maximum size of particle may not be able to grow to  $M_{\text{crit}}$  and trigger runaway gas accretion, as the Bondi radius may grow larger than  $R'_{WS}$  for the maximal particle size (and therefore for all smaller values of  $r_s$ ) before  $M = M_{\text{crit}}$ . This means that all available particle sizes will be in the regime where they flow around the core's atmosphere without being accreted (see the left panel of Figure 2.1), which will halt growth via pebble accretion. A core will have  $R'_{WS} = R_b$  when it

reaches a mass of

$$M_{R_{WS}=R_b} \approx 10M_{\oplus} \left( \frac{a}{10 \text{ AU}} \right)^{11/7} \left( \frac{r_s}{1 \text{ mm}} \right), \quad (3.36)$$

where we have assumed the particle is in the Epstein drag regime in converting from  $t_s$  to  $r_s$ . Since the mass where this equality occurs is an increasing function of semi-major axis, these considerations imply that, close in to the star, the core may not be able to reach sufficient mass through pebble accretion to trigger runaway gas accretion. Using  $M_{\text{crit}} = 10M_{\oplus}$  as a conservative upper limit for runaway accretion to occur requires  $a \gtrsim 10 \text{ AU}$  before cores can reach  $M_{\text{crit}}$ .

A second complication that can also serve to place a lower limit on semi-major axis is that, unlike for the fixed Stokes number size distribution, growth timescale can be a *decreasing* function of semi-major axis when particle radii are instead fixed. In particular, the mass-independent growth timescales for accretion of the full range of sizes given by Equation (3.28) can decrease as we move outwards in the disk. This stems from the fact that the Stokes number of  $r_s = 1 \text{ mm}$  particles will increase further out in the disk, and particles with higher values of  $St$  (for  $St < 1$ ) are generally accreted more rapidly. Thus, even if we find an upper limit on semi-major axis in the manner described above, we also have to check whether the growth timescale again becomes longer than the disk lifetime closer in to the central star. Because the low- $\alpha$  regime shown in Figure 3.9 occurs for small values of semi-major axis, where the Stokes number of an  $r_s = 1 \text{ mm}$  particle is quite low ( $\sim 5 \times 10^{-4}$ ), the  $\alpha > 2\eta St_{\text{max}}$  regime of Equation (3.28) applies everywhere when calculating our semi-major axis lower limit. We can therefore

determine our lower limit on growth analytically by setting this timescale equal to  $\tau_{\text{disk}}$ .

Doing so yields

$$a_{\text{low}} \approx 58 \text{ AU} \left( \frac{\alpha}{10^{-3}} \right)^{7/10} \left( \frac{r_{s,\text{max}}}{1 \text{ mm}} \right)^{-21/10} \left( \frac{\tau_{\text{disk}}}{2.5 \text{ Myr}} \right)^{-7/5}, \quad (3.37)$$

which is plotted in Figure 3.9 (black dashed line).

These two processes are what yields the lower limit seen in Figure 3.9; regardless of the value of  $\alpha$ , core growth cannot proceed for  $a \lesssim 10 \text{ AU}$ , as the core will be isolated from accretion of all available pebble sizes before it can trigger runaway gas accretion. As  $\alpha$  increases, the growth timescale for accretion of the full range of particle sizes may become longer than the disk lifetime close in to the central star, requiring the core to be at larger values of semi-major axes before gas giant growth is possible.

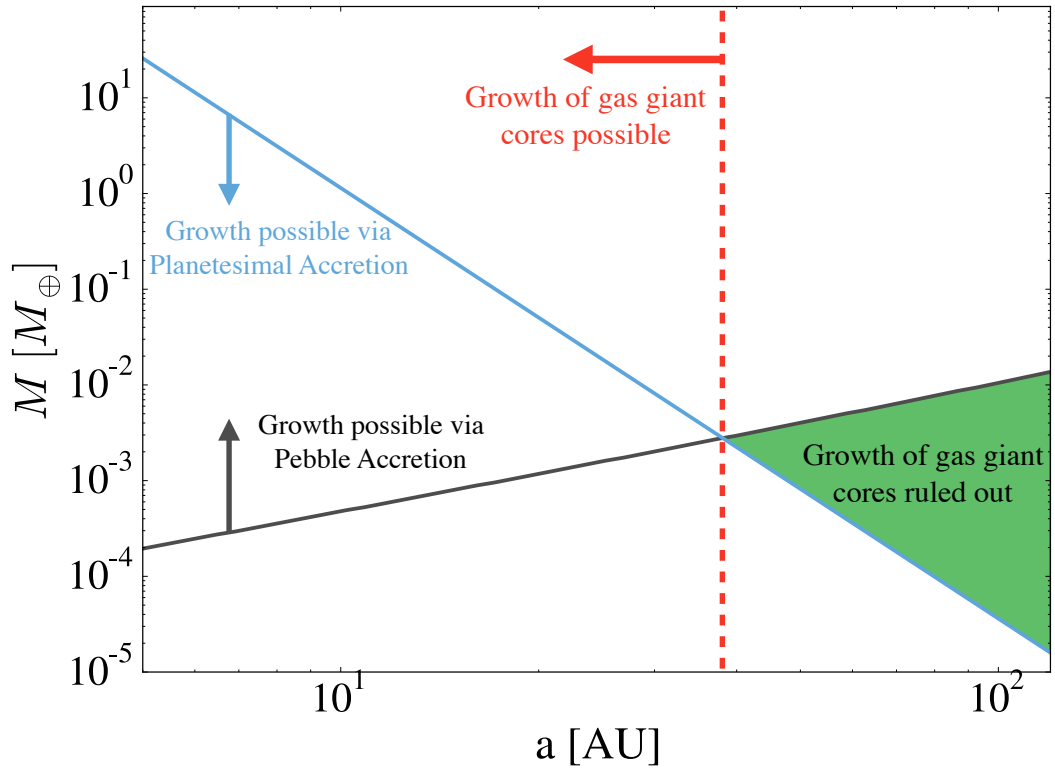


Figure 3.5: Graphical illustration of how gas giant core growth is limited for different semi major axes. The monotonically increasing line (black) shows the *minimum* mass needed for gas-assisted growth to produce a gas giant core; for masses higher than the plotted mass, the growth timescale for the core is less than the disk lifetime. The monotonically decreasing line (blue) shows the *maximum* mass it is possible to achieve via planetesimal accretion. Values lower than the indicated mass can be reached within the disk lifetime, but for larger masses the disk will dissipate before the mass is reached. The vertical line denotes the semi-major axis upper limit on where growth of gas giant cores can occur; interior to this region, planetesimal accretion can build a massive enough core rapidly enough that pebble accretion becomes efficient and dominates growth at higher masses. The green shaded region indicates where growth of gas giants is ruled out, as both planetesimal accretion and pebble accretion are too slow.

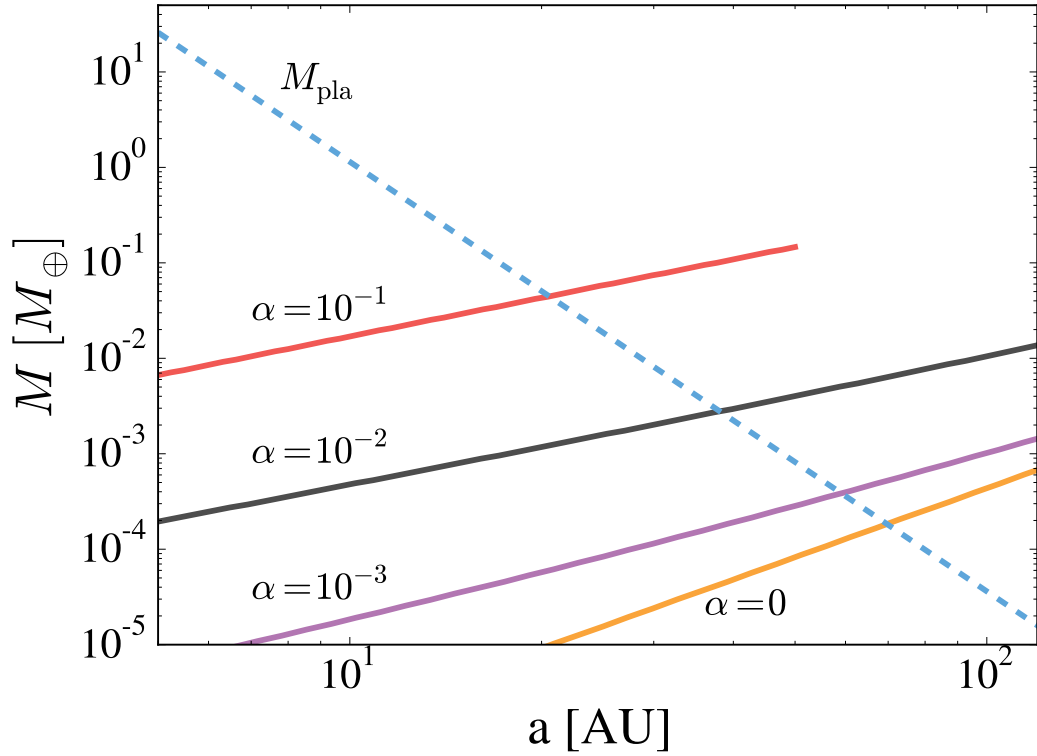


Figure 3.6: Minimum mass for which the growth timescale is shorter than  $\tau_{\text{disk}} = 2.5 \text{ Myr}$ , shown for various values of  $\alpha$ . Masses smaller than the values depicted have growth timescales larger than  $\tau_{\text{disk}}$ , so if the core can exceed this mass by other means, it should be able to reach  $M_{\text{crit}}$ , but growth by pebble accretion will be unable to exceed this mass within  $\tau_{\text{disk}}$ . A mass for growth by planetesimal accretion is also shown, but this mass has a different interpretation: it is the *largest* mass a core can grow to via gravitational focusing within  $\tau_{\text{disk}}$ .

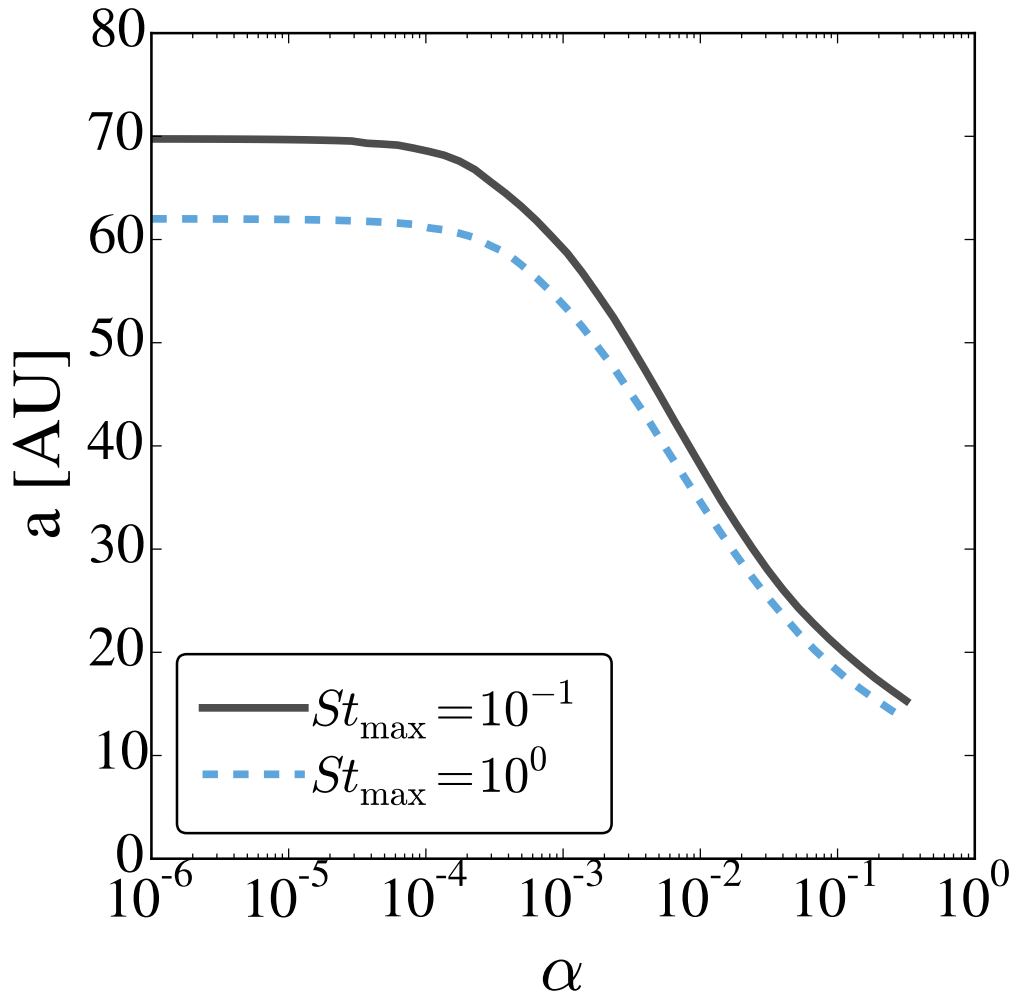


Figure 3.7: Maximum semi-major axis at which growth to critical core mass is possible as a function of  $\alpha$ . Curves are shown for a Dohnanyi distribution with a maximum-sized particle corresponding to  $St = 10^{-1}$  (solid line) and  $St = 1$  (dashed line).

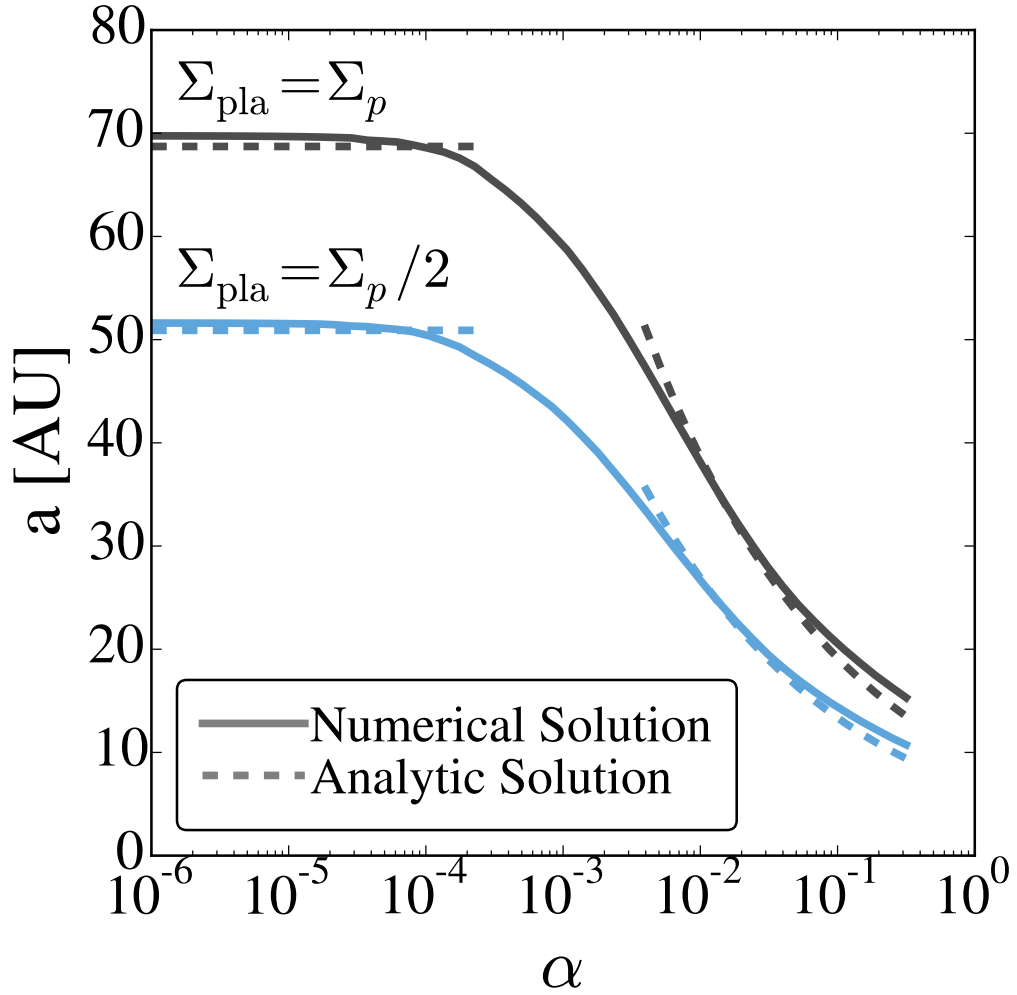


Figure 3.8: A comparison of our analytic expression for the maximal semi-major axis where gas giant growth is possible (Equation 3.34), with the numerical solution. Results are presented for two different planetesimal surface densities,  $\Sigma_{\text{pla}} = \Sigma_p$  and  $\Sigma_{\text{pla}} = \Sigma_p/2$ .

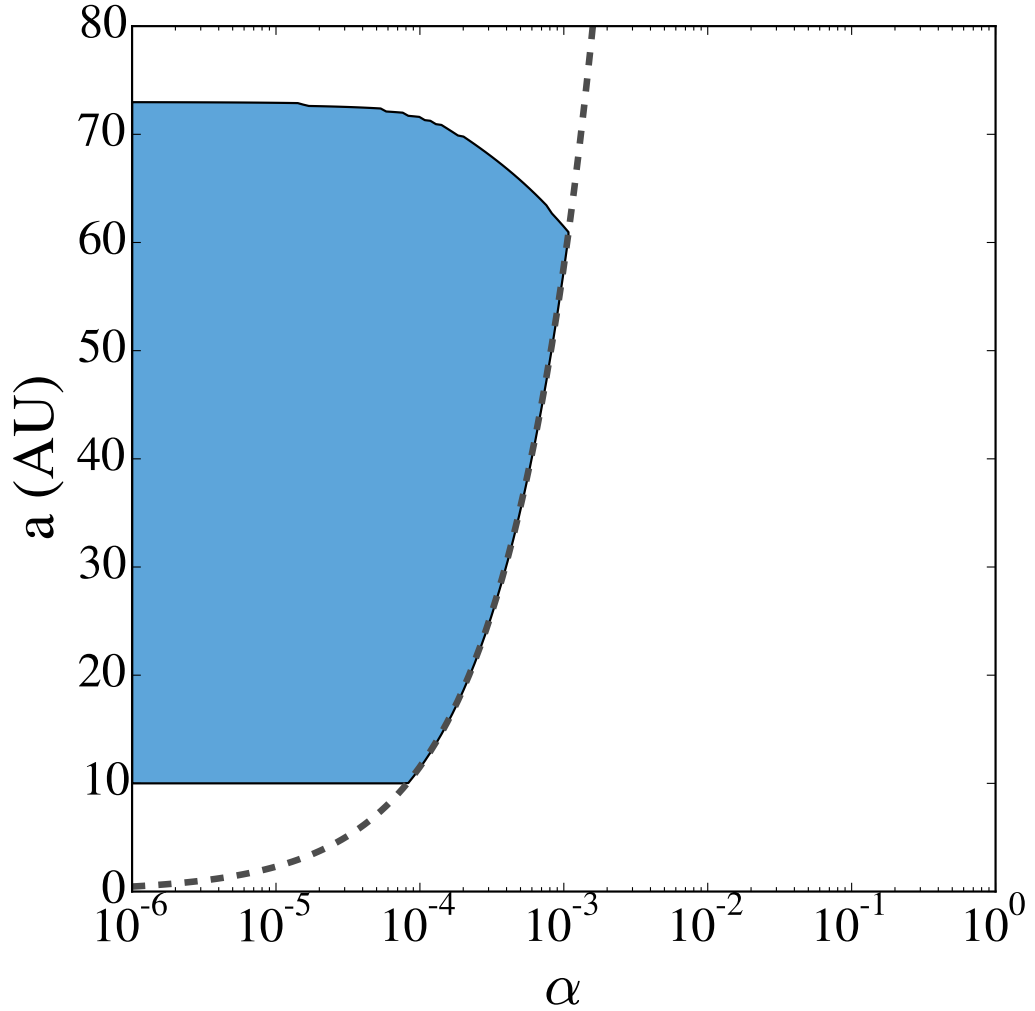


Figure 3.9: The blue region shows where growth of gas giant cores is possible for a size distribution with maximal pebble size of  $r_s = 1$  mm, plotted as a function of the strength of turbulence. In contrast to the size distributions which used a fixed Stokes number as the upper limit, this distribution has a lower limit on where core growth can occur as well as an upper limit. The lower limit is the maximum of a fixed semi-major axis limit, and a limit for a given  $\alpha$  – an analytic expression for the latter (c.f. Equation 3.37) is also shown (black dashed line).

### 3.5 Final Mass of Gas Giants

In this section, we consider the effect of  $\alpha$  on the final mass that gas giants can reach and tie these considerations to our previous discussions on how turbulence affects the early stages of gas giant growth. Note that in this section, we take the  $\alpha$  value to affect the viscosity of the disk, as opposed to merely using  $\alpha$  to parameterize the RMS gas velocity, as was done in the previous sections.

Once a core begins runaway gas accretion, the accretion rate for nebular gas is initially extremely rapid (e.g. [Pollack et al. 1996](#)). If accretion proceeded unhindered at this rate, gas giants would easily be able to accrete all of the gas in their local feeding zones before the gas disk dissipated. However, the observed masses of gas giants are well below their local gas isolation mass; what, then, stops gas giants from growing? This is usually explained by appealing to gap opening by the growing planet: as the planet grows, it will gravitationally torque the local nebular gas, pushing it away. If gas is torqued away more rapidly than it is transported inward by viscosity, the planet can clear a gap in the disk, reducing the gas surface density near the growing planet. This reduction in surface density can starve the planet of material for growth and can eventually shut off growth entirely. If this process sets the final mass that gas giants can reach, then, in general, gas giants will be able to reach larger masses in disks that have higher viscosities. Thus, if we translate our  $\alpha$  values into viscosities (as opposed to just parameterizations of the local turbulent gas velocity), then turbulence can play a role in *both* whether a gas giant core can form and in the final mass of the planet.

The physical processes that determine the final mass of gas giants remain an

open question meriting further inquiry. In order to provide concrete numerical results, in what follows, we consider two possible criteria from the literature for determining the mass that gas giants reach, and we discuss the implications for the population of wide orbital separation gas giants when these criteria are coupled with growth via pebble accretion. Thus, while the expressions we use may not capture the final masses of gas giants, the results below will still hold qualitatively as long as disks with higher viscosity produce higher-mass gas giants.

For our first criterion from the literature, we determine the width of the gap opened by the planet and shut off accretion when the gap has reached a certain size. The width of the gap opened can be obtained by equating the rate of angular momentum transport due to viscosity,  $\dot{H}_\nu = 3\pi\Sigma\nu a^2\Omega$ , with the rate that the planet delivers angular momentum to the disk (Lin & Papaloizou 1993):

$$\dot{H}_T = f_g q^2 \Sigma a^4 \Omega^2 \left(\frac{a}{\Delta}\right)^3. \quad (3.38)$$

Here  $q \equiv M/M_*$  is the planet-to-star mass ratio,  $\Delta$  is the width of the gap opened, and  $f_g$  is an order unity factor. Equating these two expressions gives the gap width in units of the Hill radius as

$$\frac{\Delta}{R_H} = \left(\frac{f_g q a^2}{\pi \alpha H_g^2}\right)^{1/3}. \quad (3.39)$$

From comparison with the results of numerical simulations of the growth of Jupiter by [Lissauer et al. \(2009\)](#), [Kratter et al. \(2010\)](#) adopted  $\Delta/R_H \sim 5$  as their criterion for starvation, which we adopt as well. Scaled to fiducial parameters, [Kratter et al.](#) gave the starvation mass as

$$M_{\text{starve}} \approx 8M_J \left( \frac{\alpha}{4 \times 10^{-4}} \right) \left( \frac{T}{40 \text{ K}} \right) \left( \frac{a}{70 \text{ AU}} \right) \left( \frac{\Delta}{5R_H} \right)^3. \quad (3.40)$$

Using this expression for the starvation mass, we can calculate the final mass of gas giant planets in our model as a function of the strength of turbulence in the disk. An example is shown in the upper panel of Figure 3.10.

The gray region shows limits on gas giant mass, which are obtained by using our values for the  $St_{\text{max}} = 0.1$  curve in Figure 3.7. For points inside the gray region, in order to grow a gas giant up to the given mass, the viscosity needs to be so large that early stages of growth are too slow for a core to reach  $M_{\text{crit}}$  within the lifetime of the gas disk. Said another way, for semi-major axes and masses inside the gray region, growth of gas giants is ruled out using the criteria described in Section 3.4.2. Also plotted in Figure 3.10 are the upper mass limits for several constant  $\alpha$  values. When these curves enter the gray region, growth of gas giants is ruled out in our model. For low levels of turbulence, growth of gas giants can proceed out to large semi-major axes, but the final masses of these planets are low. As turbulence increases, opening a gap in the disk becomes harder, allowing the gas giant planets to reach higher masses, but the semi-major axes at which growth can occur become more restricted. We stress that

this is a general feature of gas giant growth via pebble accretion and, in particular, is independent of the criterion used to determine the final mass of gas giants. Because viscous torques oppose the torque from the growing planet, the final mass the gas giant reaches will increase with the viscosity in the disk. Thus, if growth of gas giants proceeds by pebble accretion, we expect disks with higher viscosities to host more massive gas giants at smaller orbital separations.

While the torques from the growing planet can increase the width of the gap as the planet grows, material can still flow through the gap opened by the planet (e.g. [Fung et al. 2014](#)). For example, [Morbidelli et al. \(2014\)](#) showed that meridional circulation can still transport material from the top layer of the disk, which may imply that consideration of gap opening alone is insufficient to determine the final mass of gas giants. Thus, we present an alternate criterion for gap opening that takes into account gas accretion rates taken directly from the 3D hydrodynamical simulations performed by [Lissauer et al. \(2009\)](#). [Lissauer et al.](#) provided numerical results for the upper limit on the planet’s gas accretion rate as a function of planetary mass for  $\alpha = 4 \times 10^{-3}$  and  $4 \times 10^{-4}$ . Using these accretion rates, we can determine the mass past which  $t_{\text{grow}} = M/\dot{M} > \tau_{\text{disk}}$ . This scale represents another way of determining the starvation mass, since planets larger than this value will not grow substantially before the nebular gas dissipates. In practice, we can use the fitting formula given in Equation (2) of [Lissauer et al. \(2009\)](#) for  $\alpha = 4 \times 10^{-3}$  to determine this mass numerically as a function of semi-major axis. For  $\alpha = 4 \times 10^{-4}$  the authors did not provide a closed-form expression; we instead interpolate between the values plotted in their Figure 2 to obtain  $\dot{M}$  as a

function of  $M$ .

The result of this calculation is shown in the lower panel of Figure 3.10. As can be seen from the figure, this criterion leads to lower starvation masses in comparison with halting growth at a fixed value of gap width. As in the upper panel, the dashed sections of the lines indicate where the timescale to form the core exceeds the lifetime of the gas disk. Unlike the upper panel however, it is not possible to indicate the overall region where this occurs, as [Lissauer et al. \(2009\)](#) did explicitly calculate  $\dot{M}$  as a function of  $\alpha$ .

These considerations could provide an explanation for the proposed correlation between stellar mass and gas giant frequency. While the dynamical changes due to increasing stellar mass have a relatively minor effect on core growth rates (R18), these higher-mass stars are expected to have substantially higher luminosities with moderately higher amounts of ionizing radiation (e.g., [Preibisch & Feigelson 2005](#), [Winston et al. 2010](#)). Disks with higher ionization fractions should have higher levels of MHD turbulence (e.g. [Armitage 2011](#)), leading to higher effective  $\alpha$  values. Thus, from the above considerations, we should expect that higher-mass stars will yield higher-mass planets. Furthermore, if disk mass is correlated with stellar mass ([Pascucci et al. 2016](#)) and the final mass of gas giants is set by accretion rate (as opposed to gap width, where the disk surface density cancels out), then we would expect planets around more massive stars to accrete at higher rates and therefore reach higher masses before their growth timescale becomes lower than the disk lifetime. Thus, the gas giant planets found around more massive stars may represent the high-mass tail of a distribution of

gas giants formed at large distances via gas-assisted growth, which have their final mass dictated by gap-opening criteria. If this is the case, then we would expect that there exists a population of gas giants around these stars as well that are simply lower mass than can be detected with the current generation of imaging instruments. This is easily accomplished if these planets are  $\lesssim 2M_J$ ; see, e.g. [Bowler \(2016\)](#).

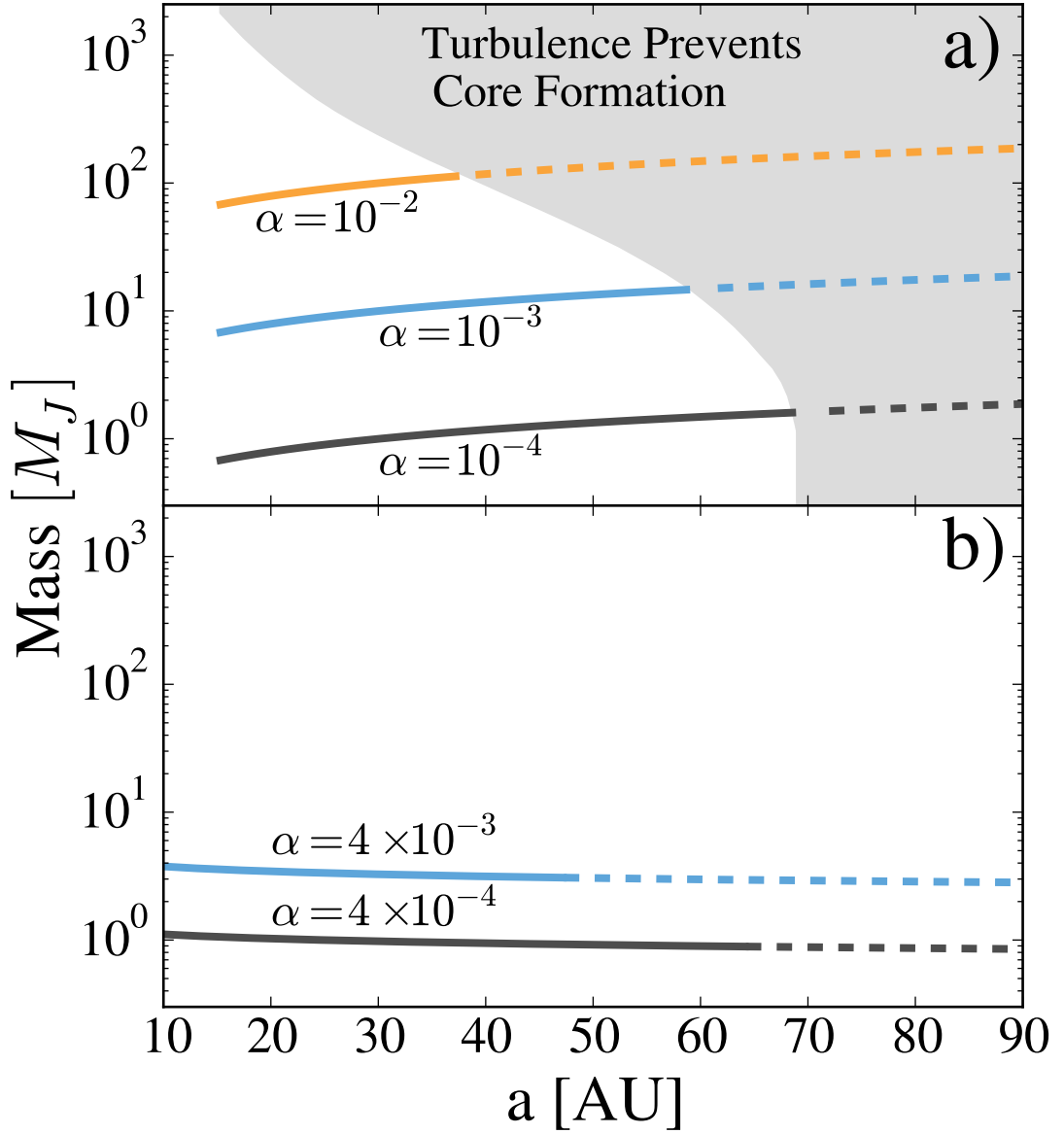


Figure 3.10: “Starvation” mass, past which growth of a gas giant halts, plotted as a function of semi-major axis. *Panel a)*: In this panel, the mass is obtained by assuming that growth shuts off when the planet opens up a gap of width  $\Delta = 5R_H$  (see text for more details). Inside the gray region, the  $\alpha$  value required to prevent gap opening before the core reaches the given mass is so large that a core will not be able to form within the lifetime of the gas disk (see Section 3.4.2). The shape of this region is determined using our upper limits on  $\alpha$  taken from the  $St_{\max} = 0.1$  in Figure 3.7. The labeled curves show maximum masses for constant values of  $\alpha$ . *Panel b)*: Here the starvation mass is determined numerically using fitting formulae to numerical results for the gas accretion rate from 3D hydrodynamical simulations by [Lissauer et al. \(2009\)](#). The starvation mass is determined by solving for the mass at which  $M_{\text{starve}}/\dot{M} = \tau_{\text{disk}}$ . The dashed lines again indicate the semi-major axes where turbulence prevents a gas giant core from forming via pebble accretion.

### 3.6 Summary/Conclusions

In this paper, we have used our previously discussed model of gas-assisted growth in a turbulent disk to study the problem of growth of gas giants at wide orbital separations. At these large distances, last doubling timescales for growth by planetesimal accretion are far longer than the disk dispersal timescale of the gas, making growth of gas giants by canonical core accretion extremely difficult.

Gas-assisted growth allows cores to easily complete their last doubling time to critical core mass, even in strong turbulence. The maximal growth rate provided by pebble accretion,  $t_{\text{Hill}}$ , is extremely rapid, even in the outer disk. For massive cores, even strong turbulence does not substantially inhibit growth.

The same is not true for smaller core masses. however. Growth of gas giants at large distances can easily stall at smaller core masses. By integrating our growth rates over small-body size we obtained the minimum mass past which pebble accretion timescales drop below the lifetime of the gas disk,  $M_{\text{peb}}$ . By assuming that the early stages of growth are set by gravitational focusing of planetesimals, we were able to translate these minimum masses into limits on the semi-major axes where gas giant growth is possible. We demonstrated that as the disk becomes more turbulent, the range of semi-major axes where gas giants can grow is sharply reduced. These effects may play a large role in the paucity of gas giants at wide orbital separations found by direct-imaging surveys; if disks are not quiescent enough, then pebble accretion may simply produce smaller planets that are unable to accrete sufficient mass in small bodies to go critical. In addition, our mass limits are relevant regardless of how early growth

proceeds – for example, if a body were scattered from the inner disk and it exceeded our minimum mass, it could grow to  $M_{\text{crit}}$  and trigger runaway gas accretion. We also presented approximate analytic expressions for both  $M_{\text{peb}}$  and the upper distance limit where gas giants can form,  $a_{\text{upper}}$ .

In addition to the strength of turbulence, we find that the available particle sizes and abundance of planetesimals are major factors in where gas giants can form. Gas-assisted growth is sensitive to the Stokes numbers of the pebbles, as opposed to their absolute size. Thus, if particles of the “correct” range of Stokes numbers are not available, then gas-assisted growth timescales can be quite slow. Furthermore, if planetesimals are not abundant enough, then the early stages of growth via planetesimal accretion can take too long for subsequent growth via pebble accretion to occur on rapid timescales.

Finally, we examined the role that viscosity plays in determining the final mass that gas giants reach, in addition to setting where a critical mass core can form. We find that, regardless of the quantitative metric used to determine the final gas giant mass, higher-viscosity disks should feature higher-mass gas giants but at smaller orbital separations. More quantitatively, at the lower  $\alpha$  values needed to produce gas giants out to  $a \gtrsim 70$  AU, the gas giants formed will be too low-mass to have been observed by direct-imaging surveys. Thus, there may lurk a population of wide orbital separation gas giants that the current generation of imaging surveys has yet to detect.

Thus, if growth of gas giants at wide orbital separations proceeds by gas-assisted growth, and if gap opening sets the final masses of gas giants, we can make

qualitative predictions about the observed population of gas giant planets. For a given stellar mass, we would expect that higher-mass gas giants should be observed closer in to the central star, as the disks with higher levels of turbulence will produce higher-mass gas giants at smaller orbital separations. We note that this conclusion may be altered if final planet masses depend on disk surface density, which is not the case for the gap-opening criterion we use. For different stellar masses, we expect higher-mass stars to exhibit higher levels of ionizing radiation. Thus, larger stars may have disks with higher  $\alpha$  values and consequently host more massive gas giants. In addition, the larger disk masses exhibited by more massive stars could push the limits for growth past the distances given here for our fiducial surface density, allowing planets to form at larger distances in high- $\alpha$  disks. We suggest that this propensity to produce massive planets in high-turbulence disks may be the reason that most currently observed directly imaged gas giants have been found orbiting A stars.

## Chapter 4

# How Flow Isolation May Set the Mass Scale for Super-Earth Planets

### 4.1 Introduction

The *Kepler* mission has provided a wealth of data about the architectures of close-in planetary systems. Chief among these results is the fact that “Super-Earths,” planets in the mass range between the Earth and the solar system ice giants, are extremely common in the innermost 1 au of planetary systems (e.g. [Borucki et al. 2010](#); [Batalha et al. 2013](#)). *Kepler* data indicates that these planets not only far outnumber gas giants in this inner region of planetary systems—they are also an extremely common outcome of star formation, appearing around approximately one third of FGK

stars (Fressin et al. 2013). A key question in theories of planet formation is how these planets formed, particularly due to the notable absence of any super-Earth planets in our own solar system.

Overall trends in the *Kepler* data may contain clues to the mechanisms that cause systems to preferentially form super-Earths. For example, recent analysis by Weiss et al. (2018) has shown that not only are super-Earths abundant, but within a given multi-planet system super-Earths tend to be of similar size. In addition, Wu (2019) has discussed the existence of a characteristic planetary mass present in the *Kepler* data, which scales approximately linearly with the stellar mass  $M_*$ .

In this paper, we propose that these observations may be explained by the combined processes of “pebble accretion”—rapid gas-assisted accretion of small nebular solids (e.g. Ormel & Klahr 2010; Johansen & Lacerda 2010; Perets & Murray-Clay 2011; Lambrechts & Johansen 2012; Ormel & Kobayashi 2012; Guillot et al. 2014; Lambrechts & Johansen 2014; Levison et al. 2015b; Morbidelli et al. 2015; Ida et al. 2016; Visser & Ormel 2016; Chambers 2016; ?; Xu et al. 2017; Rosenthal et al. 2018; Rosenthal & Murray-Clay 2018; Bitsch et al. 2019)—and flow isolation (Rosenthal et al. 2018, hereafter R18), a process by which coupling of these small solids to the gas flow around a planet cuts off pebble accretion at a characteristic planetary mass. Pebble accretion requires a sufficiently massive seed to begin operating (Ormel & Klahr 2010, Lambrechts & Johansen 2012, Rosenthal et al. 2018), but once this seed mass is produced by classic planet formation processes, pebble accretion proceeds on timescales that are negligible in comparison to the evolution timescale of the gas disk (e.g. Ormel & Klahr 2010,

[Lambrechts & Johansen 2012](#), [Rosenthal & Murray-Clay 2018](#)), which is  $\sim$ Myr (e.g. [Mamajek 2009](#)). This rapid growth would naturally erase initial differences between planet masses, forcing all planets that enter this stage of accretion to halt their growth at the characteristic mass scale produced by flow isolation. Furthermore, if this mass scale is not strongly dependent on semi-major axis, this effect would lead to similarly sized planets within a given system.

The existence of a characteristic mass scale limiting planet formation is not surprising. In classical models of planet formation, planetary growth via accretion of planetesimal sized objects is initially limited by the “isolation mass” – the total mass in solids located inside a planet’s feeding zone. A planet grows until it has accreted all locally available material, at which point growth halts and the planet has reached its isolation mass. An isolation mass based on accretion of local solids was a key part of early theories of planet formation made to explain our solar system (see e.g. [Lissauer 1993](#), [Goldreich et al. 2004](#) for a review) and numerous works looking at a giant impacts stage of isolation mass embryos find agreement between the resultant architectures and the demographics of super-Earth systems (e.g. [Schlichting 2014](#), [Dawson et al. 2016](#), [Ogihara et al. 2018](#)).

However, the importance of an isolation mass based on local solid mass can be circumvented if pebble accretion operates, allowing planets to grow by accretion of small, mm-cm sized particles instead of  $\sim$ km sized “planetesimals.” Grains of these sizes drift radially inwards at rates much faster than the lifetime of the gas disk (e.g. [Weidenschilling 1977a](#)), ensuring that there is more mass available for accretion than just

the local isolation mass. Furthermore, because they are captured on such fast timescales, accretion of these grains dominates over accretion of locally available planetesimals, allowing planets to grow far beyond their isolation mass.

However, the rapid timescales predicted by pebble accretion bring in their own challenge. Pebble accretion timescales become extremely rapid compared to the disk lifetime as planets reach terrestrial mass scales (e.g., [R18](#)). If a limiting mass scale for pebble accretion is not included, these rapid growth rates imply that the final masses of planets either stall at sub-Earth masses or run away to form gas giants, with few planets finishing their growth in the super-Earth sub-Neptune mass range ([Lin et al. 2018](#)), which is clearly in conflict with observations of close-in planetary systems. If pebbles are present, forming planets in this mass range thus requires some other physical process to halt growth via pebble accretion before runaway gas accretion can occur.

Thus, both analysis of the observed *Kepler* planets and theoretical considerations stemming from the efficiency of pebble accretion point to the existence of a characteristic mass scale that sets the final mass that close-in planets can reach. Several recent works (e.g. [Bitsch et al. 2015](#), [Izidoro et al. 2019](#), [Lambrechts et al. 2019](#)) have looked at the architectures of systems where growth is limited by the “pebble isolation mass,” a limiting mass scale for pebble accretion first identified by [Lambrechts et al. \(2014\)](#), which can limit growth by pebble accretion to super-Earth masses in the inner disk. In this paper we discuss a different candidate for setting the upper mass of planets formed through pebble accretion – the “flow isolation mass.” For planets growing by accreting pebbles, once planets reach a sufficient mass such that the extent

of their atmosphere overtakes the impact parameter for accretion, pebbles flow around the atmosphere without being accreted, causing growth to halt. This is in contrast to the pebble isolation mass, which halts growth by raising a pressure perturbation in the gas disk, trapping pebbles exterior to the planet’s orbit, as opposed to allowing them to flow past the planet (see Section 4.3.5 for more discussion of the pebble isolation mass). Flow isolation naturally stops growth at terrestrial to super-Earth mass scales for reasonable fiducial disk parameters. We discuss how this mass scale emerges and is calculated, and compare predictions of the flow isolation mass with the observed population of super-Earth planets from *Kepler*. In Section 4.2 we discuss how flow isolation operates. In Section 7.4 we present the details of our model, in particular how gas drag is modeled and how the impact parameter for accretion is calculated. In Section 4.4 we present scalings and numerical results for the flow isolation mass using our fiducial disk model. In Section 7.2 we compare expected signatures of the flow isolation mass in the architectures of planetary system with results from the *Kepler* data. Finally, in Section 4.6 we summarize our results and conclusions.

## 4.2 Model Overview

In this section we discuss broadly how pebble accretion timescales vary as a function of mass, which leads naturally to either sub-Earth or Jupiter mass planets in the absence of a limiting mass scale. We then introduce the idea of flow isolation and explain how it modifies the planetary growth processes.

In pebble accretion, a process first reported by [Ormel & Klahr \(2010\)](#), [Johansen](#)

& Lacerda 2010, and Lambrechts & Johansen (2012), protoplanetary cores grow by accretion of solids that are marginally coupled to the local nebular gas. These solids are both massive enough that they are not completely coupled to the gas, but not so massive that they are unaffected by gas drag. When these particles encounter growing cores, gas drag can have a substantial effect on the outcome of the interaction. In particular, gas drag can remove the relative kinetic energy between the particle and the protoplanet, gravitationally binding the particle at impact parameters where the particle would otherwise have been only deflected by the core’s gravity. This increase in impact parameter can lead to dramatically faster growth rates in certain parts of parameter space.

While pebble accretion can operate at extremely fast rates, in general the timescale for growth by pebble accretion is sensitive to both the mass of the growing protoplanet and the small body size the core is accreting. An example of the pebble accretion timescale at  $r = 0.5$  AU, using the model of R18, with the disk parameters described in Section 4.3.1, is shown in Figure 4.1. The figure shows the growth timescale as a function of protoplanetary mass  $M_p$  and small body radius  $s$ . The two panels illustrate how growth changes in the presence of nebular turbulence, which is given in terms of the Shakura-Sunyaev  $\alpha$  parameter (Shakura & Sunyaev 1973). As can be seen from Figure 4.1, for large protoplanet masses ( $M_p \gtrsim 10^{-6} M_\oplus$  for the  $\alpha = 6.5 \times 10^{-5}$  case, and  $M_p \gtrsim 10^{-3} M_\oplus$  for  $\alpha = 1.3 \times 10^{-2}$ ) and marginally coupled particle radii ( $s \sim 10^1 - 10^3$  cm), accretion occurs at an extremely rapid rate. At lower masses, however, the particle sizes that accrete on these rapid timescales are unavailable for growth,

meaning the core will grow substantially more slowly.

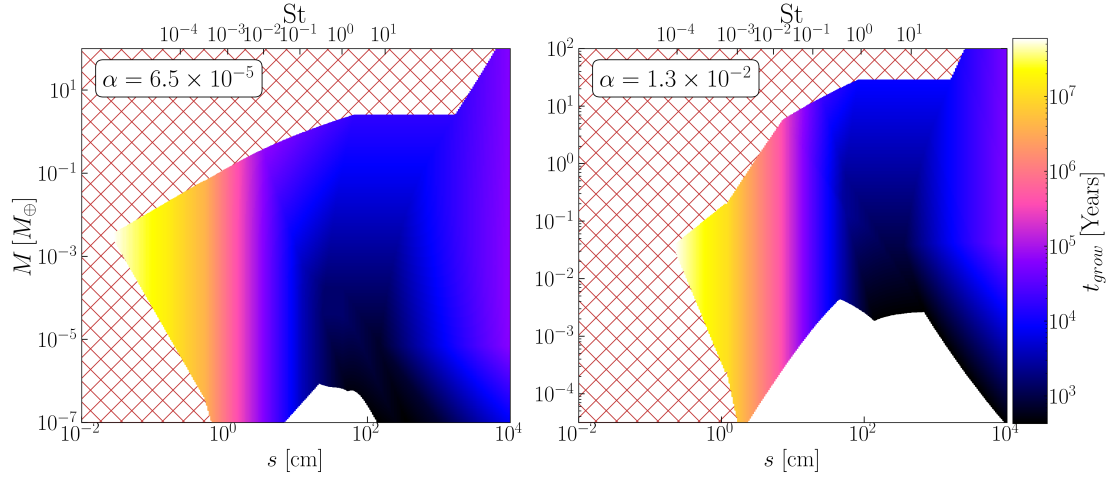


Figure 4.1: A plot of the growth timescale of a planet at  $a = 0.5$  AU undergoing pebble accretion as a function of planet mass and small body radius. The disk parameters used are described in Section 4.3.1. The two panels show the growth timescale for two different levels of turbulence in the disk. In the lefthand side of both panels, the red hatched region indicates where growth cannot occur because pebbles flow around the core (see Section 4.2). The white regions indicate where particles do not dissipate their kinetic energy relative to the core, and therefore cannot be accreted by pebble accretion. Pebbles in this region could still be accreted by other processes however (e.g. gravitational focusing).

Because of the slower growth timescales at low core mass, these growth timescales appear to lead to binary outcomes in terms of the final planet mass. Either planets become stuck below the masses where planet formation is efficient, or they surpass this mass and grow on such rapid timescales that they easily reach  $M_{crit}$ , the critical core mass needed to trigger runaway gas accretion, if growth is not halted in some manner. An example of the rapid growth timescales from pebble accretion are shown in Figure 4.2, which plots the mass of a protoplanet as a function of time for three different initial masses. The core grows both by gravitational focusing of pebbles (i.e. what [Ormel & Klahr 2010](#) term the “hyperbolic” regime) and by pebble accretion once it becomes

massive enough, with the pebbles all assumed to have size  $St = 10^{-2}$ . Here  $St$  is a dimensionless measure of particle size

$$St = t_s \Omega \tag{4.1}$$

where  $t_s \equiv mv_{\text{rel}}/F_{\text{D}}$  is the particle’s stopping time,  $m$  is the particle’s mass,  $v_{\text{rel}}$  is the relative velocity between the particle and the gas,  $F_{\text{D}}$  is the drag force on the particle, and  $\Omega$  is the local Keplerian angular frequency.

If the core is able to reach a mass such that  $St = 10^{-2}$  particles can be captured through pebble accretion processes, growth becomes extremely fast and the planet reaches masses that are more than sufficient to trigger runaway gas accretion. If the planet is unable to reach this point, however, planetary growth stalls at low mass. We note that in the inner regions of planetary systems, once planetesimals with  $St \gg 1$  are present (see e.g. [Chiang & Youdin 2010](#) for a review of the “meter-size barrier”), growth via gravitational focusing even without the assistance by gas may prevent protoplanets from stalling at masses low enough to avoid pebble accretion (see e.g. [Goldreich et al. 2004](#)).

This discussion, however, neglects the effect of the growing planet’s atmosphere on accretion. As discussed in [R18](#), as the planet grows it will accrete an atmosphere from the protoplanetary disk. Interior to the planet’s atmosphere, the gas is static <sup>17</sup>,

---

<sup>17</sup>Note that recent work by [Ormel et al. \(2015\)](#) and [Cimerman et al. \(2017\)](#) has shown that protoplanetary atmospheres may actually interact with the gas disk down to some scale, causing the atmosphere of planet’s to be “recycled”. In Section 4.3.4 we give an order of magnitude calculate that demonstrates that the atmospheres of sub-thermal planets undergoing pebble accretion should be able to repel atmospheric flows at a scale comparable to  $R_{\text{B}}$

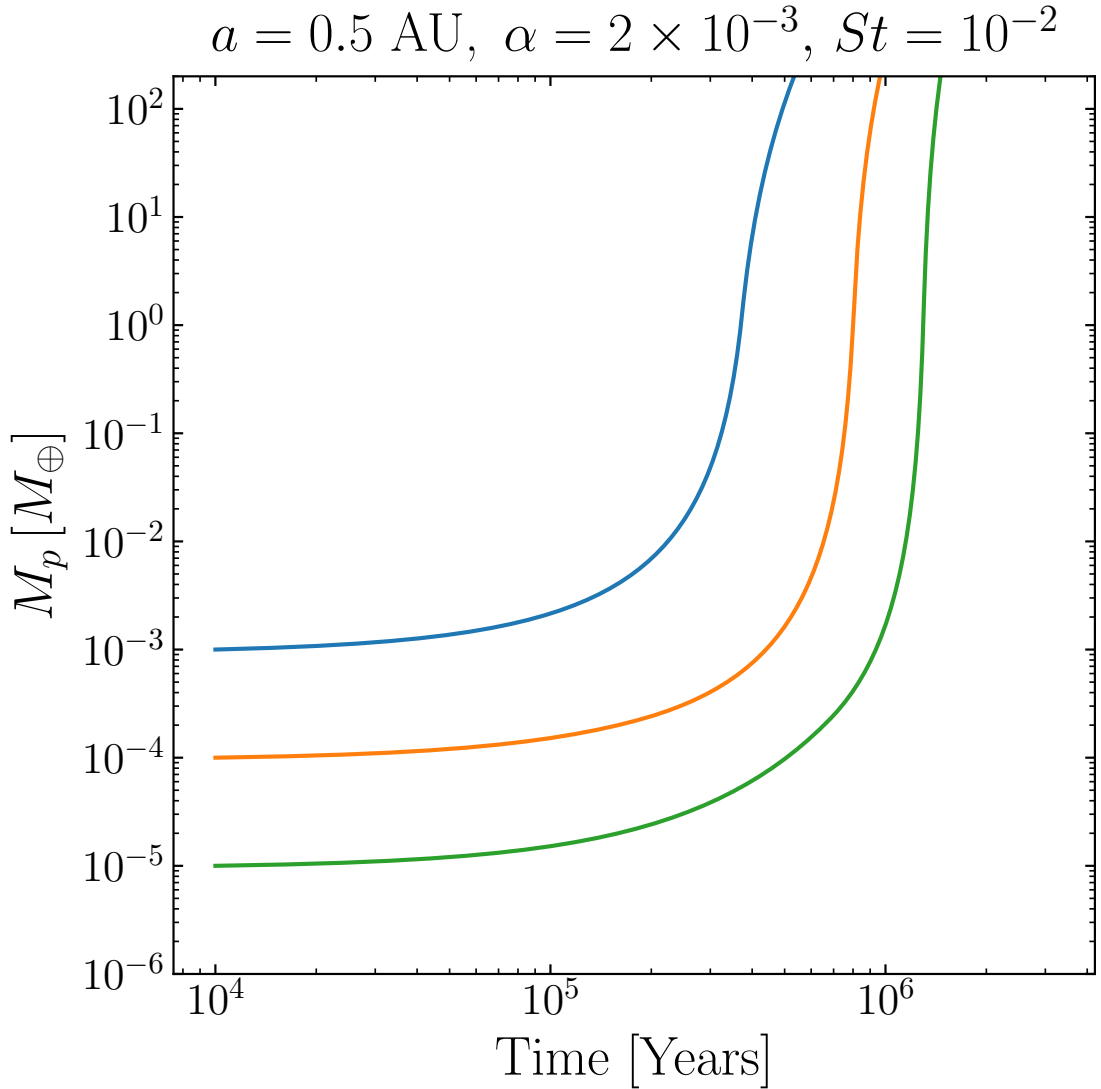


Figure 4.2: The mass of a protoplanet undergoing pebble accretion as a function of time, for three different values of initial mass. All particles are assumed to have Stokes number of  $10^{-2}$ . The disk parameters used are given in Section 4.3.1. In all cases the protoplanet’s solid mass runs away to extremely large masses on timescales shorter than the lifetime of the protoplanetary disk ( $\sim 3 \text{ Myr}$ ).

with a density profile that rises steeply from its nebular value. Because of this, the planet’s atmosphere will block the flow of nebular gas, causing the gas to flow around the planet’s atmosphere (e.g. [Ormel 2013](#)). Because of this alteration in flow pattern, particles that couple strongly to the nebular gas may flow around the core’s atmosphere without being accreted. In order to determine whether particles of a given size will be diverted by the core’s alteration of the gas flow, there are two criteria that must be met: 1. the maximum pebble accretion impact parameter for particles of this size must be smaller than the scale of the core’s alteration of the gas flow, and 2. the time for the particle to respond to change in gas direction must be shorter than the interaction timescale between the particle and the core. The scale of the core’s alteration of the gas flow is given by the core’s Bondi radius, which is roughly the length scale at which the escape velocity from the planet is equal to the local sound speed  $c_s$

$$R_B = \frac{GM_p}{c_s^2} \tag{4.2}$$

where  $M_p$  is the mass of the planet.<sup>18</sup> The timescale for the particle to respond to the gas flow is the particle’s stopping time,  $t_s$ .

The maximum impact parameter at which pebble accretion could conceivably operate,  $R_{\text{stab}}$  is given by the scale at which gas drag balances the gravitational accel-

---

<sup>18</sup>Note that because we are primarily interested in planets with masses less than or equal to the thermal mass—see Equation (4.44)—we assume for this discussion that the planet’s atmosphere is limited by the Bondi radius.

eration of the core<sup>19</sup>, that is

$$R_{\text{stab}} = \sqrt{\frac{GM_{\text{p}}m}{F_{\text{D}}}} . \quad (4.3)$$

Beyond this radius, even a particle that started gravitationally bound to the core would not be accreted because it would be stripped off by the gas flow. In evaluating Equation (4.3),  $F_{\text{D}}$  should be calculated using the relative velocity between the gas and the core at the impact parameter  $R_{\text{stab}}$ . This relative velocity results from either a combination of the sub-Keplerian orbital velocity of the gas and turbulent motion, which we refer to as  $v_{\text{gas}}$ , or from Keplerian shear.

For particles to be pulled around the core by the gas, the two relevant criteria are therefore

$$R_{\text{stab}} < R_{\text{B}} \quad (4.4)$$

$$t_{\text{s}} < \frac{R_{\text{B}}}{v_{\infty}} \equiv t_{\text{cross}} \quad (4.5)$$

where  $v_{\infty}$  is the velocity of the incoming particle relative to the core. We now show that the former criterion is sufficient, as the latter is always satisfied for  $R_{\text{stab}} < R_{\text{B}}$ .

There are two regimes for  $v_{\infty}$ : either the particle comes in with a velocity relative to the core,  $v_{\text{pc}} \leq v_{\text{gas}}$  resulting from drift and turbulent excitation by the gas, or the Keplerian shear in the disk sets the incoming velocity, in which case  $v_{\infty} \sim R_{\text{B}}\Omega$ , where

---

<sup>19</sup>For sufficiently large  $St$  and  $M_{\text{p}}$  we instead expect  $R_{\text{stab}} = R_{\text{H}}$ . Once  $R_{\text{H}} < R_{\text{B}}$  the process of flow isolation is slightly modified, as the scale of the core's atmosphere is now  $R_{\text{H}}$  rather than  $R_{\text{B}}$ . See [Rosenthal et al. \(2018\)](#) for a discussion of flow isolation in this regime. The full expression for  $R_{\text{stab}}$  is given in Equation (4.41).

$\Omega = \sqrt{GM_*/r^3}$  is the local Keplerian orbital frequency,  $r$  is the semi-major axis of the planet, and  $M_*$  is the mass of the host star. In the latter regime we have

$$t_{\text{cross}} = \frac{R_{\text{B}}}{\Omega R_{\text{B}}} = \Omega^{-1} \quad (4.6)$$

and so  $t_{\text{s}} < t_{\text{cross}}$  is equivalent to taking  $St \equiv t_{\text{s}}\Omega < 1$ , which is the regime we confine our attention to in the remainder of this work. In the former regime, we have

$$t_{\text{cross}} = \frac{R_{\text{B}}}{v_{\text{pc}}} > \frac{R_{\text{B}}}{v_{\text{gas}}} \quad (4.7)$$

since the incoming velocity of the particle is at most the gas velocity. Rearranging Equation (4.3) and using the definition of the stopping time gives

$$t_{\text{s}} = \frac{R_{\text{stab}}^2 v_{\text{gas}}}{GM_{\text{p}}} = \frac{R_{\text{stab}}^2}{R_{\text{B}}^2} \frac{v_{\text{gas}}^2}{c_{\text{s}}^2} \frac{R_{\text{B}}}{v_{\text{gas}}} < \frac{R_{\text{B}}}{v_{\text{gas}}} < t_{\text{cross}} \quad (4.8)$$

since  $R_{\text{stab}} < R_{\text{B}}$  by assumption and  $v_{\text{gas}} < c_{\text{s}}$  since all gas flows are subsonic for planetary masses less than the thermal mass (see Equations 4.37 and 4.44).

In summary, the only criterion that is necessary to determine whether particles will be pulled around the core's atmosphere is

$$R_{\text{stab}} < R_{\text{B}} \quad (\text{pebble accretion cannot operate}). \quad (4.9)$$

In practice, this process sets the lower limit on particle sizes that can be accreted, as  $R_{\text{stab}}$  decreases with decreasing particle size. This process is illustrated schematically in

Figure 4.3. We also note here that this cutoff in accretion is distinct from the decrease in accretion rate that occurs for smaller particle sizes, which has been discussed in other works on pebble accretion, e.g. [Lambrechts & Johansen \(2012\)](#), [Visser & Ormel \(2016\)](#), [R18](#), and can be seen in Figure 4.1. As an example, a  $10 M_{\oplus}$  core growing by accreting pebbles around a solar mass star has a growth timescale of roughly

$$t_{\text{grow}} \sim 6500 \text{ years} \left( \frac{r}{0.5 \text{ au}} \right)^{1/2} \left( \frac{\Sigma_{\text{p}}}{5 \text{ g cm}^{-2}} \right)^{-1} St^{-2/3} \quad (4.10)$$

where  $\Sigma_{\text{p}}$  is the local pebble surface density and  $r$  is the planet's semi-major axis (e.g. [Lambrechts & Johansen 2012](#)). This would require the maximal pebble size to be below  $St \lesssim 10^{-4}$  for the growth timescale to exceed 3 Myr. Flow isolation, on the other hand, cuts off growth for much larger Stokes numbers; for example, in the righthand panel of Figure 4.1, growth is shut off for all particles with  $St \lesssim 10^{-1}$ .

Because of the decreasing value of  $R_{\text{stab}}$  with decreasing particle radius, this process effectively sets a lower limit on the particle size that can be captured by pebble accretion. However, if this lower limit on particle size exceeds the maximal size of particle present in the disk, then growth of the planet will halt completely. A maximal pebble size is expected from a number of physical processes, such as a fragmentation barrier (e.g. [Birnstiel et al. 2012](#)), or from radial drift in the outer disk (e.g. [Brauer et al. 2008](#), [Birnstiel et al. 2012](#)). For a given maximum particle size, we then have an upper limit on the mass a planet can grow to via pebble accretion, which is set by

$$R_{\text{stab}}(St_{\text{max}}) < R_{\text{B}} \quad (\text{flow isolation mass}) . \quad (4.11)$$

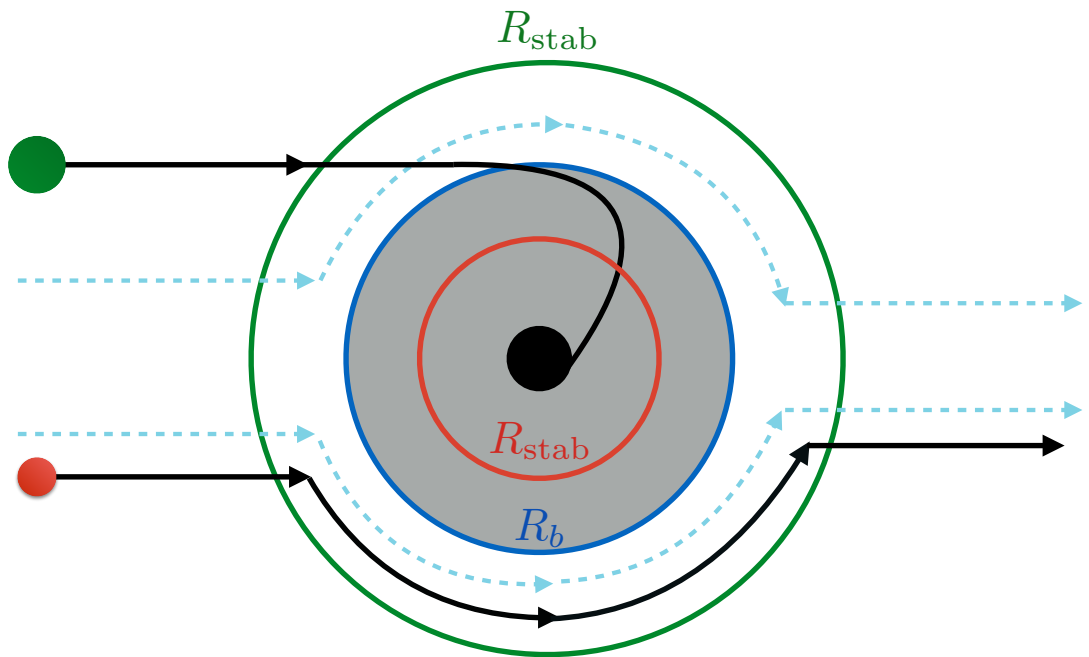


Figure 4.3: A cartoon illustrating schematically how flow isolation operates. The planet's (black dot) atmosphere is shown by the gray shaded region, and extends up to  $R_B$ . The gas flows around the atmosphere, as shown by the dashed blue lines. The larger, green particle, has maximal impact parameter for accretion  $R_{stab} > R_B$ , and thus can be captured at scales of  $R_{stab}$  before encountering the modified gas flow. The smaller red particle has  $R_{stab} < R_B$ , and is diverted by the atmosphere's modification to the flow instead of being captured.

In practice, we may require the impact parameter for accretion to become a factor of a few smaller than  $R_{\text{B}}$  before accretion is completely inhibited, i.e. while Equation (4.11) does give the scaling of the flow isolation mass, there is still some undetermined coefficient  $f > 1$  on the lefthand side of the equation. This constant depends on the details of the atmospheric dynamics in the vicinity of the planet, and can be determined by comparison with numerical simulations. We leave this comparison for future work. In what follows, we determine the flow isolation by determining the mass such that

$$fR_{\text{stab}}(St_{\text{max}}) = R_{\text{B}} \quad (4.12)$$

and pick  $f = 1.75$  for presenting our results.

Thus Equation (4.12) defines a “flow isolation mass,” which is a function of the properties of the protoplanetary disk and the maximum particle size present (which may itself be a simple function of the disk parameters). The presence of this mass scale can halt pebble accretion at masses below the critical mass for runaway accretion of a gas envelope, allowing a super-Earth or terrestrial mass planet to remain.

## 4.3 Methods

### 4.3.1 Fiducial Disk Model

To evaluate the flow isolation mass, we use a fiducial protoplanetary disk, described by the following expressions.

Given the small semi-major axes at which super-Earths are observed, an im-

portant component of our protoplanetary disk model is viscous heating, which sets the temperature in the inner regions of protoplanetary disks. The midplane temperature from viscous heating can be determined by equating the rate of heating from accretion with radiative cooling from the midplane

$$\frac{GM_*\dot{M}}{r} = \frac{64\pi}{9} \frac{\sigma_{\text{SB}}T_c^4 r^2}{\tau_c} \quad (4.13)$$

(e.g. [Oka et al. 2011](#), [Kratte & Murray-Clay 2011](#)). Here  $\sigma_{\text{SB}}$  is the Stefan-Boltzmann constant,  $\tau_c$  is the vertical optical depth for thermal radiation escaping from the midplane, and  $\dot{M}$  is the rate of mass flow through the disk. Setting  $\tau_c = \kappa\Sigma/2$ , where  $\kappa$  is the Rosseland mean opacity, the midplane temperature is given by

$$T_c = \left[ \frac{9}{128\pi} \frac{GM_*\dot{M}\kappa\Sigma}{\sigma_{\text{SB}}r^3} \right]^{1/4} \quad (4.14)$$

If we assume a steady-state accretion disk, the disk surface density,  $\Sigma$ ,  $\dot{M}$ , and  $\alpha$  can be related using the equation

$$\dot{M} = 3\pi\Sigma\nu = 3\pi\Sigma\alpha c_s H \quad (4.15)$$

where  $\nu$  is the local kinematic viscosity. This gives us the freedom to fix two of  $\dot{M}$ ,  $\Sigma$ , or  $\alpha$ ; the remaining parameter can be calculated from the other two quantities using Equation (4.15). It is common to fix  $\dot{M}$  and  $\alpha$ , and derive the surface density from these two quantities. Doing so, however, leads to extremely large surface densities when  $\alpha$  is decreased. For example, for  $\alpha = 10^{-4}$ , and  $\dot{M} = 10^{-8}M_{\odot}\text{yr}^{-1}$ , the surface density

at 1 au is  $\Sigma \approx 12000 \text{ g cm}^{-2}$ , and the disk is Toomre  $Q$  unstable for  $r \gtrsim 10\text{AU}$ . Thus, in this work we choose to fix  $\Sigma$  in addition to  $\dot{M}$ , meaning that  $\alpha$  is no longer constant.

For ease of notation, we now define the quantities

$$M_{*,\odot} \equiv \frac{M_*}{M_\odot}, \quad L_{*,\odot} \equiv \frac{L_*}{L_\odot} \quad (4.16)$$

$$r_{\text{AU}} = \frac{r}{\text{AU}}, \quad \dot{M}_8 \equiv \frac{\dot{M}}{10^{-8} M_\odot \text{yr}^{-1}}, \quad \Sigma_{3000} = \frac{\Sigma_0}{3000 \text{ g cm}^{-2}}$$

where  $L_*$  is the stellar luminosity, and  $\Sigma_0$  is the surface density at 1 au.

We choose our surface density normalization of  $\Sigma_0 = 3000 \text{ g cm}^{-2}$  from comparison with [Powell et al. \(2019\)](#) who compute disk surface densities through particle drift rates. From comparison with measured dust surface density profiles as found in e.g. [Andrews et al. \(2009\)](#), we also choose a power law exponent of  $\gamma = 1$ . Thus, our fiducial surface density profile is

$$\Sigma = 3000 \text{ g cm}^{-2} r_{\text{AU}}^{-1} \quad (4.17)$$

Setting  $\kappa = 0.1 \text{ cm}^2 \text{ g}^{-1}$ , the fiducial temperature from viscous heating is then

$$T_{\text{visc}} = 230 \text{ K } M_{*,\odot}^{1/4} \dot{M}_8^{1/4} \Sigma_{3000}^{1/4} r_{\text{AU}}^{-1} \quad (4.18)$$

Farther out in the disk, the disk temperature will be set by passive irradiation from the

central star. We take our fiducial profile from [Ida et al. \(2016\)](#)

$$T_{\text{irr}} = 150 \text{ K } M_{*,\odot}^{-1/7} L_{*,\odot}^{2/7} r_{\text{AU}}^{-3/7} \quad (4.19)$$

(see [Chiang & Goldreich 1997](#) for more detail).

The temperature as a function of semi-major axis is then  $T = \max(T_{\text{visc}}, T_{\text{irr}})$ , where  $T_{\text{visc}}$  and  $T_{\text{irr}}$  are given by Equation (4.18) and (4.19) respectively. The disk changes from being heated by viscous accretion to passive irradiation at a fiducial semi-major axis of

$$r_{\text{vis-irr}} = 2.2 \text{ AU } \dot{M}_8^{7/16} M_{*,\odot}^{11/16} \Sigma_{3000}^{7/16} L_{*,\odot}^{-1/2} \quad (4.20)$$

In each region, the value of  $\alpha$  can be calculated using Equation (4.15)

$$\alpha = \begin{cases} 5.3 \times 10^{-4} r_{\text{AU}}^{1/2} \dot{M}_8^{3/4} M_{*,\odot}^{1/4} \Sigma_{3000}^{-5/4} & r < r_{\text{vis-irr}} \\ 8.2 \times 10^{-4} r_{\text{AU}}^{-1/14} \dot{M}_8 M_{*,\odot}^{9/14} \Sigma_{3000}^{-1} L_{*,\odot}^{-2/7} & r > r_{\text{vis-irr}} \end{cases} \quad (4.21)$$

We also note that if global disk evolution is governed by magnetic winds, as opposed to viscous evolution, as discussed by e.g. [Bai \(2016\)](#), then accretion heating would be reduced in the inner regions of disks. In this case, our model of a viscously heated inner disk would not be appropriate. Instead, our expressions for a passively irradiated disk would apply throughout most of the extent of the disk (as opposed to just  $r > r_{\text{vis-irr}}$ ), with a different regime, where the finite angular size of the star sets the irradiation, applying for  $r \lesssim 0.2 \text{ au}$ . See [Wu \(2019\)](#) for a discussion of this scaling.

For our fiducial disk we take the star to have solar mass,  $M_* = M_\odot$ , with luminosity  $L_* = 3L_\odot$ , which corresponds to a solar mass star of age  $\sim 1$  Myr (Tognelli et al. 2011). The gas has a mean molecular weight  $\mu = 2.35 m_{\text{H}} \approx 3.93 \times 10^{-24}$  g. The neutral collision cross section in the disk is  $\sigma \approx 10^{-15}$  cm<sup>2</sup>. The pebbles are taken to have density  $\rho_s = 2$  g cm<sup>-3</sup>.

We note that the flow isolation mass is not sensitive to the solid surface density. For the calculations in this work that do require a surface density be specified (i.e Figures 4.1, 4.2 and 4.4), we used

$$\Sigma_{\text{p}} = 5 \text{ g cm}^{-2} \left( \frac{r}{\text{AU}} \right)^{-1} \quad (4.22)$$

which is taken to match observations of the solid surface density in protoplanetary disks (Andrews et al. 2009, Andrews 2015). We further note that if this surface density is converted to a mass flux using the relation  $F_{\text{peb}} = 2\pi r v_r \Sigma_{\text{p}}$  (e.g. Lambrechts & Johansen 2014), where  $v_r \sim 2\eta v_{\text{k}} St$  is the radial drift velocity of pebbles, then, for the  $St = 10^{-2}$  particles used in producing Figure 4.2, this corresponds to a pebble mass flux of roughly  $70 M_\oplus \text{ Myr}^{-1}$  in the inner, viscously heated region of the disk.

Finally, we note that we are neglecting Type I migration effects in our discussion, and instead considering expected planet masses if planets form in-situ at their observed locations.

We now quantitatively discuss how to calculate the mass scale where flow isolation occurs. We also discuss the properties of the atmospheres of cores undergoing pebble accretion.

### 4.3.2 Summary of Pebble Accretion Model

In Section 4.3.1 and 4.3.2 we briefly summarize how the maximum impact parameter for pebble accretion,  $R_{\text{stab}}$  is calculated in the model of [Rosenthal et al. \(2018\)](#); see [R18](#) for more detail.

#### Stokes number and Gas Drag Regimes

The relevant parameter for measuring particle size in pebble accretion is the particle’s Stokes number,  $St$ . The Stokes number measures particle size in terms of how well coupled the particle is to the gas, and is given by

$$St \equiv t_s \Omega . \tag{4.23}$$

Here  $t_s$  is the particle’s stopping time, and  $\Omega$  is the local Keplerian angular frequency. Particles with  $St \sim 1$  are maximally affected by gas drag, while particles with  $St \ll 1$  are strongly coupled to the gas, and particles with  $St \gg 1$  are decoupled from the gas flow. Calculation of the particle radius  $s$  for which  $St \sim 1$  yields radii in the eponymous “pebble” size range of mm-cm, particularly in the outer disk.

Thus, in order to calculate the particle’s Stokes number we first need to determine the drag force on the particle. The gas drag force on the pebbles is split into two regimes – a “diffuse regime,” which applies for  $s < 9\lambda/4$ , and a “fluid regime,” which holds for  $s > 9\lambda/4$ . Here  $s$  is the radius of the pebble,  $\lambda = \mu/(\rho_g \sigma)$  is the mean free path of the gas molecules,  $\rho_g = H/(2\Sigma)$  is the volumetric mass density of the gas, and

$H = c_s/\Omega$  is the scale height of the gas disk. The particle is in the fluid regime for

$$St \gtrsim \begin{cases} 3.4 \times 10^{-3} r_{\text{AU}}^3 M_8^{1/8} M_{*,\odot}^{-3/8} \Sigma_{3000}^{-15/8} & r < r_{\text{vis-irr}} \\ 2.8 \times 10^{-3} r_{\text{AU}}^{23/7} L_{*,\odot}^{2/7} M_{*,\odot}^{-4/7} \Sigma_{3000}^{-2} & r > r_{\text{vis-irr}} \end{cases} \quad (4.24)$$

In the diffuse regime, the drag force is given by the Epstein drag law

$$F_{\text{D,eps}} = \frac{4}{3} \pi \rho_g v_{\text{th}} v_{\text{rel}} s^2, \quad (4.25)$$

where  $v_{\text{th}} = \sqrt{8/\pi} c_s$  is the average thermal velocity of the gas particles, and  $v_{\text{rel}}$  is the relative velocity between the particle and the gas. Assuming spherically symmetric particles of uniform density  $\rho_s$ , the stopping time of a particle in the Epstein regime is

$$t_{s,\text{Eps}} = \frac{\rho_s}{\rho_g} \frac{s}{v_{\text{th}}} \quad (4.26)$$

which is independent of the small body's velocity.

In the fluid regime, the drag force depends on the Reynolds number of the particle,  $Re = 2sv_{\text{rel}}/(0.5v_{\text{th}}\lambda)$ , and can be approximated by

$$F_{\text{D}} = \begin{cases} 3\pi\rho_g v_{\text{th}} v_{\text{rel}} \lambda s & Re < 1, \text{ Stokes} \\ 0.22\pi\rho_g v_{\text{rel}}^2 s^2 & Re \gtrsim 800, \text{ Ram} \end{cases} \quad (4.27)$$

Note that the Stokes regime is a linear drag regime, and the stopping time of a particle

in the Stokes regime is given by

$$t_{s,\text{Stokes}} = \frac{4}{9} \frac{\rho_s}{\rho_g} \frac{s^2}{v_{\text{th}} \lambda} \quad (4.28)$$

Generally a smoothing function is employed to transition cleanly between the Stokes and Ram regimes (e.g. [Cheng 2009](#)). In order to make the effect of various drag regimes clear in our results, we instead choose to use a piecewise drag function that transitions between the Stokes and Ram regimes at the Reynolds number for which the drag forces are equal. That is, we take the drag force in the fluid regime to be given by

$$F_{\text{D}} = \begin{cases} \frac{3\pi}{4} \rho_g v_{\text{th}}^2 \lambda^2 Re & Re \leq \frac{12}{0.22}, \text{ Stokes} \\ \frac{0.22\pi}{16} \rho_g v_{\text{th}}^2 \lambda^2 Re^2 & Re > \frac{12}{0.22}, \text{ Ram} \end{cases} \quad (4.29)$$

This slightly underestimates the drag force on the particle at intermediate Reynolds numbers, which increases the calculated impact parameter for accretion (see Equation 4.35) and therefore slightly increases the flow isolation mass, as the core must get to larger masses before the Bondi radius exceeds the impact parameter for accretion.

In the ram regime, the stopping time is dependent on velocity, meaning that, for a given particle size  $s$ ,  $t_s$  must be solved for numerically, using  $v_{\text{rel}}(t_s)$ . The relevant equations for the laminar and turbulent components of the relative velocity between the particle and the gas respectively are

$$v_{\text{pg},\ell} = \eta v_{\text{k}} St \frac{\sqrt{4 + St^2}}{1 + St^2} \quad (4.30)$$

(Nakagawa et al. 1986), and

$$v_{\text{pg},t}^2 = v_{\text{gas},t}^2 \left( \frac{St^2(1 - Re_t^{-\frac{1}{2}})}{(St + 1)(St + Re_t^{-\frac{1}{2}})} \right) \quad (4.31)$$

(Ormel & Cuzzi 2007). Here  $\eta \equiv c_s^2/(2v_k)$  is a measure of pressure support in the gas disk,  $v_k = r\Omega$  is the local Keplerian orbital velocity, and  $Re_t \equiv \alpha c_s H/(v_{\text{th}}\lambda)$  is the Reynolds number of the turbulence, given in terms of the Shakura-Sunyaev  $\alpha$  parameter, which we use to parameterize the strength of turbulence in the disk. In terms of  $\alpha$ , the root-mean-square (RMS) turbulent gas velocity is given by

$$v_{\text{gas},t} = \sqrt{\alpha} c_s . \quad (4.32)$$

Finally, the total RMS velocity between the particle and the gas is given by

$$v_{\text{pg}} = \sqrt{v_{\text{pg},\ell}^2 + v_{\text{pg},t}^2} . \quad (4.33)$$

### Calculation of Impact Parameter for Pebble Accretion

Flow isolation occurs when the impact parameter for accretion,  $R_{\text{stab}}$ , shrinks below the core's Bondi radius. In this section, we discuss in detail how  $R_{\text{stab}}$  is calculated.

The scale at which a growing planet's gravity dominates over the stellar gravity

is the planet’s Hill radius, which is given by

$$R_{\text{H}} = r \left( \frac{M_{\text{p}}}{3M_{*}} \right)^{1/3}, \quad (4.34)$$

and  $M_{\text{p}}$  is the mass of the planet (Hill 1878). In the most favorable cases, pebble accretion allows cores to accrete over the entirety of their Hill radii (e.g. Lambrechts & Johansen 2012, R18), resulting in extremely rapid growth timescales relative to gravitational focusing of planetesimals.<sup>20</sup> However, in order for pebble accretion to operate, the core’s gravitational force needs to dominate over the force on the particle due to gas drag, in addition to the stellar tidal gravity (e.g. Perets & Murray-Clay 2011). Balancing the core’s gravity with the differential acceleration due to gas drag leads to a scale is known as the wind-shearing (WISH) radius, which is given by

$$R'_{\text{WS}} = \sqrt{\frac{G(M_{\text{p}} + m)}{\Delta a_{\text{WS}}}} \approx \sqrt{\frac{GM_{\text{p}}t_{\text{s}}}{v_{\text{rel}}}} \quad (4.35)$$

(Perets & Murray-Clay 2011). Here  $m$  is the mass of the small body,  $\Delta a_{\text{WS}}$  is the relative acceleration between the protoplanet and the small body due to gas drag, and  $v_{\text{rel}}$  is the relative velocity between the small body and the nebular gas. In the second equality we’ve assumed that  $M_{\text{p}} \gg m$ .

In order to calculate  $R'_{\text{WS}}$ , we need to determine the relevant velocity for determining the drag force. As the particle approaches the core, the particle will be

---

<sup>20</sup>Accretion at  $R_{\text{H}}$  is faster than gravitationally focusing a population of small bodies with velocity dispersion  $v_{\text{H}} \equiv R_{\text{H}}\Omega$  (which leads to the fastest growth rate in the absence of a mechanism to damp planetesimal velocities) by a factor of  $R_{\text{H}}/R_{\text{p}} \sim r/R_{*}$ , where  $R_{\text{p}}$  is the planet’s radius,  $r$  is the semi-major axis of the planet, and  $R_{*}$  is the stellar radius.

slowed relative to the gas flow, increasing the drag force it feels. In the most restrictive case, the particle will feel the full velocity of the gas relative to the core, which is assumed to be massive enough that it moves at the local Keplerian orbital velocity. The local gas velocity is a combination of two factors: motion of the gas relative to the Keplerian velocity, and shear in the disk.

The motion of the gas relative to the local Keplerian velocity has both a laminar component and a turbulent component. The laminar component arises from pressure support in the disk, which causes the gas disk to rotate at a slightly sub-Keplerian orbital velocity

$$v_{\text{gas,lam}} = \frac{c_s^2}{2v_k} = \eta v_k \quad (4.36)$$

As discussed previously, the amount of turbulence in the disk is parameterized by the Shakura-Sunyaev  $\alpha$  parameter (see Equation 4.32). The total RMS velocity of the gas relative to the local Keplerian velocity is

$$v_{\text{gas}} = \sqrt{\eta^2 v_k^2 + \alpha c_s^2} \quad (4.37)$$

(e.g. [R18](#)).

The second factor contributing to the relative velocity between the gas and the local Keplerian velocity is shear in the disk. Because orbital velocity decreases as we move outwards in the disk, particles separated in the radial direction move relative

to one another in the azimuthal direction. This shear velocity is of order

$$v_{\text{shear}} = R\Omega \quad (4.38)$$

where  $R$  is the separation between the particles.

If we set  $v_{\text{rel}} = \max(v_{\text{gas}}, v_{\text{shear}})$ , then we have two measures of the impact parameter for accretion. In the former case, where  $v_{\text{rel}} = v_{\text{gas}}$ , we refer to the impact parameter as  $R_{\text{WS}}$  (i.e. unprimed); in the latter case we refer to the impact parameter as  $R_{\text{shear}}$ . For a particle in a linear drag regime, there are simple analytic forms for  $R_{\text{WS}}$  and  $R_{\text{shear}}$ :

$$R_{\text{WS}} = R_{\text{H}} \sqrt{3St \left( \frac{v_{\text{H}}}{v_{\text{gas}}} \right)} \quad (4.39)$$

$$R_{\text{shear}} = R_{\text{H}} (3St)^{1/3} \quad (4.40)$$

For a particle in a nonlinear drag regime, the values of these parameters are calculated numerically. See [R18](#) for a comparison of this method of modeling of impact parameter with other works. In general, the impact parameter for accretion is given by

$$R_{\text{stab}} = \min(R_{\text{WS}}, R_{\text{shear}}, R_{\text{H}}) \quad (4.41)$$

### 4.3.3 Calculation of the Flow Isolation Mass

#### Analytic Calculation for Linear Drag Regimes

As can be seen from Equations (4.39) and (4.40), the impact parameter for pebble accretion decreases as small body radius is decreased. Thus, the requirement that pebble accretion can only operate for  $fR_{\text{stab}} > R_{\text{B}}$  translates into an lower limit on the small body radius that can captured via pebble accretion. In a linear drag regime, where a particle's Stokes number is independent of velocity and depends only upon particle and disk properties, we can substitute equations (4.39) and (4.40) into Equation (4.12) and solve for  $St$ . Doing so yields

$$St_{\text{min}} = \max \left[ f^{-2} \left( \frac{H}{r} \right)^{-3} \left( \frac{v_{\text{gas}}}{c_{\text{s}}} \right) \left( \frac{M_{\text{p}}}{M_{*}} \right), f^{-3} \left( \frac{H}{r} \right)^{-6} \left( \frac{M_{\text{p}}}{M_{*}} \right)^2 \right]. \quad (4.42)$$

where  $f$  is the undetermined coefficient introduced in Equation (4.12). Thus, if particles only exist up to some maximum size  $St_{\text{max}}$ , then we can translate Equation (5.21) to an upper limit on planet mass

$$\frac{M_{\text{flow}}}{M_{*}} = \min \left[ f^2 \frac{c_{\text{s}}}{v_{\text{gas}}} \left( \frac{H}{r} \right)^3 St_{\text{max}}, f^{3/2} \left( \frac{H}{r} \right)^3 \sqrt{St_{\text{max}}} \right] \quad (4.43)$$

We note again that this analytic expression is only valid if the particle is in a linear drag regime; the general numerical procedure for calculating  $M_{\text{flow}}$  is discussed in the next section. Once the core grows to a mass such that  $R_{\text{B}} > R_{\text{H}}$ , the core's atmosphere will begin to be limited by tidal effects. In this regime the extent of the core's atmosphere,  $R_{\text{atm}}$  will now extend to  $R_{\text{H}}$  as opposed to  $R_{\text{B}}$ , and we will have  $R_{\text{stab}} \leq R_{\text{atm}}$  regardless

of small body size. In this regime, [Rosenthal et al. \(2018\)](#) argue that growth by pebble accretion is completely halted. Given the order of magnitude nature of this argument, we again introduce an order unity factor when solving for the mass scale, which should be calibrated from numerical simulations. Because the physical processes important in this regime differ from those that dominate at lower masses (for example, the velocity difference between the planetary atmosphere and the background gas becomes supersonic), we use a different order unity constant,  $f'$ , when determining this mass scale. Solving  $R_B = f' R_H$  for planet mass gives

$$\frac{M_{\text{p,max}}}{M_*} = \left(\frac{f'^3}{3}\right)^{1/2} \frac{c_s^3}{G\Omega} = \left(\frac{f'^3}{3}\right)^{1/2} (H/r)^3 \quad (4.44)$$

This is similar in scale to the thermal mass, an often cited scale at which a growing planet is able to open a gap in the gas disk ([Lin & Papaloizou 1993](#)). At the thermal mass,  $R_H \sim R_B \sim H$ , though the exact form of the expression for the thermal mass depends on which of these two length scales are set equal. For the purposes of this work we define the thermal mass as the scale at which  $R_B = H$ , in which case the thermal mass is given by

$$M_{\text{th}} = 3 \left(\frac{H}{r}\right)^3 M_* \quad (4.45)$$

Note that while we use this definition of thermal mass when expressing our results in terms of  $M_p/M_{\text{th}}$ , this definition of thermal mass makes no difference in the calculated value of the flow isolation mass, which is more fundamentally given by Equation (4.43).

A different definition of the thermal mass would simply introduce additional prefactors into equations such as (5.22).

In terms of the thermal mass, we can write the full expression for the flow isolation mass as

$$\frac{M_{\text{flow}}}{M_{\text{th}}} = \min \left[ f^2 \frac{c_s}{3v_{\text{gas}}} St_{\text{max}}, \frac{f^{3/2}}{3} \sqrt{St_{\text{max}}}, \left( \frac{f'}{3} \right)^{3/2} \right] \quad (4.46)$$

To maintain simplicity in presenting our results we set  $f' = f = 1.75$  in what follows.

R18 previously used the term “Flow Isolation Mass” to refer to scenario where  $R_B > R_H$ , indicating that pebbles of all sizes were inhibited from accreting. However, if pebbles exist up to some maximum size, then growth can halt because pebbles of the maximal size are inhibited from accreting from the constraint in Equation (5.21). This limits planetary growth to masses lower than the thermal mass. In this work we expand the term “Flow Isolation Mass” to include this case as well.

## General Numerical Procedure

In this section we sketch the general procedure to calculate  $M_{\text{flow}}$  numerically.

If the particle is not in a linear drag regime then  $St$  can no longer be defined without reference to the relative velocity between the particle and gas. In this work, we define the particle’s Stokes number in a non-linear drag regime with respect to  $v_{\text{pg}}$  as defined by Equation (4.33). Thus for a given maximum Stokes number, the algorithm to calculate  $M_{\text{flow}}$  is as follows

1. Use  $St_{\text{max}}$  to calculate  $v_{\text{pg}}$ , using Equations (4.30)–(4.33).

2. Use the calculated value of  $v_{\text{pg}}$  to solve the equation  $F_{\text{D}} = mv_{\text{pg}}/t_{\text{s}}$  for particle size  $s$ , using Equation (4.29) to relate  $F_{\text{D}}$  and  $s$ .
3. Solve for the masses such that  $R_{\text{B}} = fR'_{\text{WS}}$ , where  $R'_{\text{WS}}$  refers to the two solutions to the equation  $F_{\text{D}} = GM_{\text{p}}/R'^2_{\text{WS}}$  (Equation 4.35), when the drag force is calculated using a)  $v_{\text{gas}} = \sqrt{\eta^2 v_{\text{k}}^2 + \alpha c_{\text{s}}^2}$  (Equation 4.37) and b)  $v_{\text{shear}} = R'_{\text{WS}}\Omega$  (Equation 4.38). Note that in the latter case the velocity, and therefore the drag force, is also function of impact parameter.
4. Finally, the flow isolation mass is the minimum of three mass scales: the two masses calculated in 3. above, and the mass scale where  $f'R_{\text{H}} = R_{\text{B}}$  defined in Equation (4.44).

We remind the reader that we use  $f' = f = 1.75$  for presenting our results. Note that several, if not all, of the solutions described above need to be performed numerically, particularly if a more complicated drag law is used (e.g. the previously discussed [Cheng 2009](#) smoothed drag law) instead of our simpler, piecewise prescription.

#### 4.3.4 Structure of Planetary Atmospheres

Equation (5.22) is the key result of our paper. In deriving this expression, we have assumed that the atmosphere of the growing core is able to repel the flow of nebular gas. In this section, we discuss the atmospheric properties of planets undergoing pebble accretion, in particular to ensure that the mass of the atmosphere is still substantial enough to act as an effective obstacle.

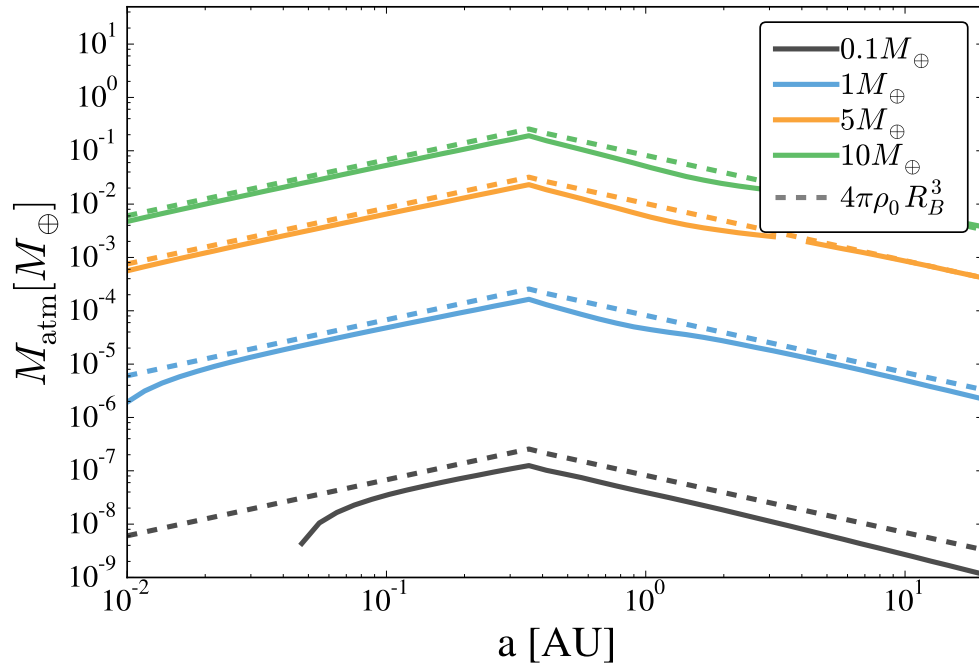


Figure 4.4: The atmospheric mass of a planet accreting at the maximal pebble accretion rate as a function of semi-major axis, using mixing length theory to calculate the temperature gradient. While the atmospheric mass is slightly reduced from the fully convective value, the decrease is relatively modest.

As planets approach the flow isolation mass, pebble accretion rates are generally extremely rapid (see Figure 4.1). At these masses, a large fraction of the available pebble sizes will be accreted over the extent of the planet’s Hill radius (e.g. [Ormel & Klahr 2010](#), [Lambrechts & Johansen 2012](#)). This leads to a growth timescale that is independent of small body radius

$$t_{\text{Hill}} = \frac{M_{\text{p}}}{2\Sigma_{\text{p}}R_{\text{H}}^2\Omega} \sim 4 \times 10^3 \text{ years} \left(\frac{r}{\text{AU}}\right)^{1/2} \left(\frac{M_{\text{p}}}{M_{\oplus}}\right)^{1/3}. \quad (4.47)$$

where  $\Sigma_{\text{p}}$  is the pebble surface density, and we have used our fiducial disk model in the second expression (see Section 4.3.1). Assuming that all of the energy of the pebbles is deposited at the surface of the planet, this corresponds to a luminosity of

$$\frac{GM_{\text{p}}\dot{M}_{\text{Hill}}}{R_{\text{p}}} = \Sigma_{\text{p}}R_{\text{H}}^2v_{\text{esc}}^2\Omega \quad (4.48)$$

$$\approx 2.7 \times 10^{28} \text{ erg/s} \left(\frac{M_{\text{p}}}{M_{\oplus}}\right)^{4/3} \left(\frac{r}{\text{AU}}\right)^{-1/2} \quad (4.49)$$

where we have again used our fiducial disk parameters, and assumed a density of  $\rho_{\text{p}} = 5.5 \text{ g/cm}^3$  for the planet. Because of this extremely high accretion luminosity, planets undergoing pebble accretion will generally transport energy by convection through the entirety of their atmosphere. However, convection cannot transport an arbitrary amount of energy; for high enough luminosities convection will become inefficient, limiting the mass of the planet’s atmosphere.

In order to ensure that the atmospheric masses of planets undergoing pebble accretion were not too limited by pebble accretion, we numerically calculate steady state

atmospheric masses following the methods of Rafikov (2006). The nebular parameters were calculated using the fiducial disk model discussed in Section 4.3.1. We assume a simple power law opacity,  $\kappa = \kappa_0 (T/T_0)$ , where  $T_0$  is the temperature of the nebula at the given semi-major axis and  $\kappa_0 = 0.1 \text{ cm}^2 \text{ g}^{-1}$ . The temperature gradient  $\nabla \equiv d \ln T / d \ln P$  was calculated using mixing length theory following Appendix D of Rafikov (2006).

The results of this calculation are shown in Figure 4.4 for  $\alpha = 10^{-2}$ . An analytic estimate of the mass of a fully convective atmosphere,  $M_{\text{atm}} \approx 4\pi\rho_0 R_{\text{B}}^3$ , where  $\rho_0$  is the nebular density, is also plotted. The solid lines are truncated on the left when  $R_p > R_{\text{B}}$ . As can be seen in the figure, the atmospheric masses of these planets are generally very close to the fully convective value, with efficiency of convection only being important for the  $M_p = 10^{-1} M_{\oplus}$  planet past  $a \sim 1 \text{ au}$ .

A simple order of magnitude argument shows that the mass of a fully convective atmosphere is sufficient to repel the flow of nebular gas. Consider a core of mass such that  $R_{\text{B}} < R_{\text{H}}$  with a fully convective atmosphere of mass  $M_{\text{atm}} \sim \rho_{\text{neb}} R_{\text{B}}^3$ . The gas moves relative to the core's atmosphere with a velocity  $v_{\text{app}} \sim \max(\eta v_{\text{k}}, \Omega R_{\text{B}})$ . In a time  $\Delta t \sim R_{\text{B}} / v_{\text{app}}$  the core encounters a mass in gas of  $M_{\text{gas}} \sim \rho_{\text{neb}} R_{\text{B}}^2 v_{\text{app}} \Delta t$ , which therefore has kinetic energy  $KE \sim \rho_{\text{neb}} v_{\text{app}}^2 R_{\text{B}}^3$ . The binding energy of the atmosphere is of order  $E_{\text{bind}} \sim GM_{\text{p}} M_{\text{atm}} / R_{\text{B}}$ . The ratio of these two quantities is therefore

$$\frac{KE}{E_{\text{bind}}} \sim \frac{\rho_{\text{neb}} v_{\text{app}}^2 R_{\text{B}}^3}{\rho_{\text{neb}} G M_{\text{p}} R_{\text{B}}^2} \sim \frac{v_{\text{app}}^2 R_{\text{B}}}{v_{\text{H}}^2 R_{\text{H}}} \quad (4.50)$$

If  $v_{\text{app}} = \Omega R_{\text{B}}$  then the quantity on the right is  $< 1$  since  $R_{\text{B}} < R_{\text{H}}$  by assumption.

Otherwise  $v_{\text{app}} = \eta v_{\text{k}}$ , in which case the quantity on the right is of order  $c_{\text{s}}^2/v_{\text{k}}^2 = (H/r)^2 \ll 1$ . In both cases the incoming kinetic energy of the gas is much less than the binding energy of the atmosphere, meaning the nebular gas will not ablate the stationary atmosphere. In particular, the “recycling” effects identified by e.g. [Ormel et al. \(2015\)](#) are unlikely to result in an unbound atmosphere during this phase of planetary growth.

We also note that a similar conclusion can be reached by comparing the pressure from the incoming gas, which is of order  $\rho_{\text{neb}}v_{\text{app}}^2$ , to the atmosphere’s hydrostatic pressure, which is of order  $\rho_{\text{neb}}c_{\text{s}}^2$  (neglecting any enhancement to the atmospheric density). The ratio of incoming gas pressure to hydrostatic pressure is therefore  $\sim v_{\text{app}}^2/c_{\text{s}}^2 \sim v_{\text{app}}^2 R_{\text{B}}/(v_{\text{H}}^2 R_{\text{H}})$ , which is the same ratio given in the righthand side of Equation (4.50). The ratio of pressures is therefore  $< 1$  by the same argument given above.

#### 4.3.5 Pebble Isolation Mass

In this section we discuss another candidate for limiting the growth of planets via pebble accretion, the “pebble isolation mass,” first identified by [Lambrechts et al. \(2014\)](#). Once a planet reaches this mass scale, perturbations from the planet on the local gas disk raise pressure bumps in the disk that trap pebbles, preventing them from being accreted by the planet. From the results of their hydrodynamical simulations, [Lambrechts et al.](#) give the pebble isolation mass as

$$M_{\text{iso}} = 20M_{\oplus} \left( \frac{H/r}{0.05} \right)^3 . \quad (4.51)$$

Though it is not noted in [Lambrechts & Johansen \(2014\)](#), this mass scale is similar in scale to the mass scale where  $R_B = R_H$ ; specifically using the mass scale given in Equation (4.44) without the factor  $f$  and using the temperature profile used in [Lambrechts et al. \(2014\)](#) gives the semi-major axis scaling as in Equation (4.51) with a prefactor of  $\sim 23M_\oplus$ .

[Bitsch et al. \(2018\)](#) followed up on the work of ([Lambrechts et al. 2014](#)) by exploring the variation of pebble isolation mass with the level of nebular turbulence and radial pressure gradient, and also accounted for how different pebble sizes are able to diffuse through the pressure bump raised by the planet. Their results confirm that the pebble isolation mass is of the scale of the thermal mass, with a variation of a factor of 2-3 as  $\alpha$  is increased, and smaller effect from the radial pressure gradient. They also found that the mass of the planet must be increased an additional factor to block smaller particles; while the overall functional form of this increase is complicated, it is inversely proportional to the particle Stokes number.

Thus, in general the pebble isolation mass is of order the scale where  $R_B = R_H$ . From our purely analytic arguments, i.e. without the unknown order unity factor  $f$ , we expect the flow isolation mass to be of order this scale or smaller, (e.g.  $\approx 30\%$  of this scale when  $St_{\max} = 10^{-1}$ ) which would indicate that  $M_{\text{flow}} \lesssim M_{\text{peb}}$  for small values of  $St_{\max}$ , with  $M_{\text{flow}} \sim M_{\text{peb}}$  within a factor of 2-3 for  $St_{\max} \sim 1$ . A precise comparison is complicated by the dependence of the mass scales on the value of  $f$ , the value of  $\alpha$ , and to a lesser extent  $\partial \ln P / \partial \ln r$ . A more difficult to overcome complication stems from the dependence of  $M_{\text{peb}}$  on the *smallest* Stokes numbers present: in contrast to the

flow isolation mass, the pebble isolation mass more readily blocks large particles than small particles, meaning that the pebble isolation mass increases as the particle size that is required to be blocked is decreased. Because particles in protoplanetary disks do not exist at a single size, but instead have a distribution of sizes, in order to halt growth the planet must block not just the largest particles, but also sufficiently small particles such that the planet grows on timescales longer than the dissipation timescale of the protoplanetary disk. One could attempt to estimate this smallest particle size by assuming a size distribution for the small particles, and then calculating the smallest particle size below which the growth timescale for the core exceeded the lifetime of the gas disk. While we initially attempted this approach, we found that in many cases the calculated mass exceeded the regime where the analytic expressions of [Bitsch et al. \(2018\)](#) hold. We therefore leave a detailed comparison between these two mass scales at high  $St_{\max}$  to future work.

## 4.4 Results

In this section we present values for the limiting mass that a growing planet can reach via pebble accretion by taking into account the flow isolation mass. We present results both fixed maximum Stokes number (Section 4.4.1), and for a simple fragmentation limited model of particle size (Section 4.4.2). In Section 4.4.3 we discuss how the flow isolation mass scales as a function of stellar mass.

#### 4.4.1 Limiting Planet Mass for Fixed $St_{\max}$

In this section we give limits on planet mass as a function of the maximum Stokes number present in the disk. Results for the flow isolation mass for fixed  $St_{\max}$

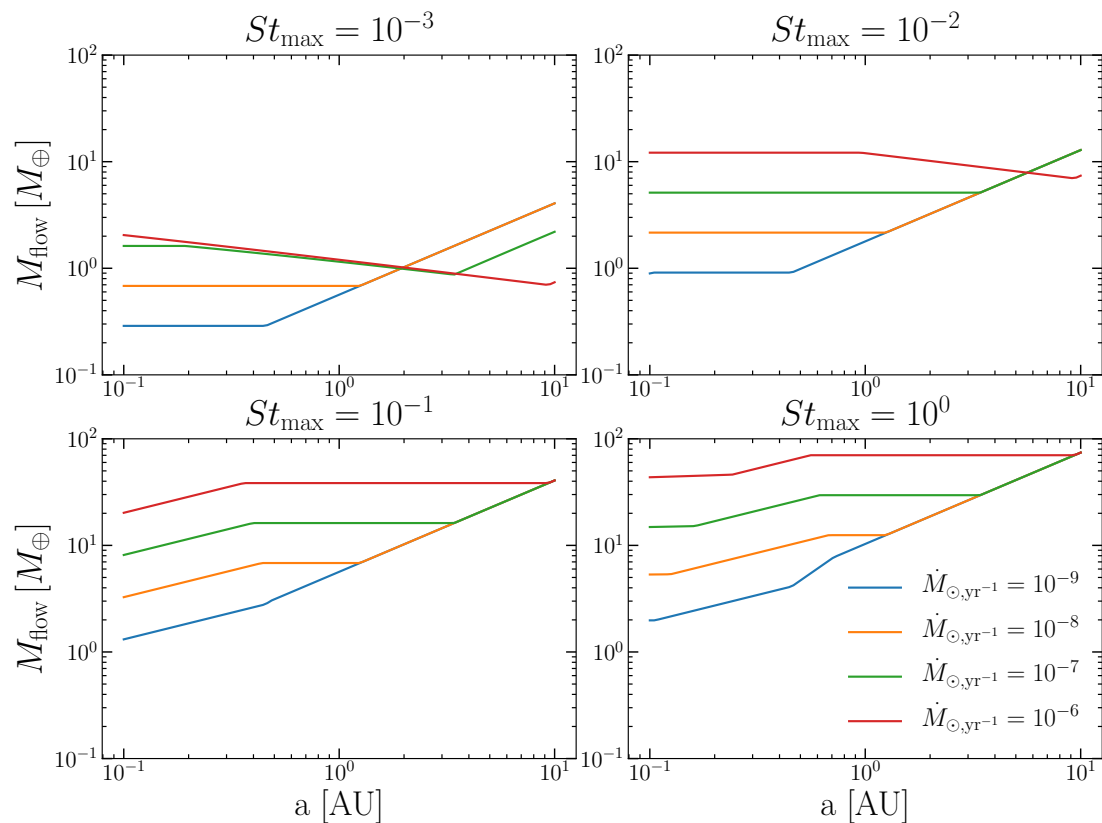


Figure 4.5: A plot of the maximal mass a planet accreting pebbles can reach as a function of semi-major axis, accretion rate, and maximum Stokes number present.

are shown in Figure 4.5.

Several features are apparent in Figure 4.5. Firstly, the limiting mass increases as a function of semi-major axis. However, the dependence is relatively shallow, particularly in the inner disk, where the mass can become independent of semi-major axis. In the inner region of the disk viscous heating dominates over irradiation; for planets

at this mass scale the second of the three analytic expressions given in Equation (5.22) dominates, i.e., the flow isolation mass is given by

$$\frac{M_{\text{flow}}}{M_{\text{th}}} = \frac{f^{3/2}}{3} \sqrt{St_{\text{max}}} \quad (4.52)$$

Defining

$$St_1 = \frac{St_{\text{max}}}{10^{-1}} \quad (4.53)$$

then, scaled to our fiducial disk profile, this mass is given by

$$M_{\text{flow}} = \begin{cases} 6.8M_{\oplus} St_1^{1/2} r_{\text{AU}}^0 M_8^{3/8} M_{*,\odot}^{-1/8} \Sigma_{3000}^{3/8} & r < r_{\text{vis-irr}} \\ 3.5M_{\oplus} St_1^{1/2} r_{\text{AU}}^{6/7} M_{*,\odot}^{-5/7} L_{*,\odot}^{3/7} & r > r_{\text{vis-irr}} \end{cases} \quad (4.54)$$

i.e. the flow isolation mass is independent of semi-major axis in the inner disk, which is what causes the flattening of the lines seen in Figure 4.5. We stress that Equation (4.54) is approximate: it is one of the three possible regimes that can set the flow isolation mass, as seen in Equation (5.22), which is itself an analytic approximation to the flow isolation mass in a linear drag regime, as described in Section 6.2.2. Indeed, the scaling in Equation (4.54) may be complicated by several effects. When the Stokes number is low and the accretion rate is high (e.g., Figure 4.5 top left, red line), the WISH radius can set the flow isolation mass rather than the shearing radius. This causes  $M_{\text{flow}}$  to decrease with semi-major axis. Furthermore, close in to the star non-linear drag effects become important, causing  $M_{\text{flow}}$  to deviate from the simple scaling predicted by

Equation (4.54), as seen in the bottom two panels of Figure 4.5.

Finally, as can be seen in Figure 4.5, increasing the maximum Stokes number present in the disk increases the maximal mass planets can achieve. This is because larger particles can be captured at greater impact parameters, requiring the planet to reach higher masses before  $R_B$  overtakes  $R_{\text{stab}}$ . In the next section, we consider how this maximal particle size might scale with semi-major axis.

#### 4.4.2 Flow Isolation Mass for Fragmentation-Limited Pebbles

In the previous section we described the limiting planet mass as a function of Stokes number. There exist however, models for the maximal particle size present in the disk, which we can employ to remove the dependence on  $St_{\text{max}}$ . In particular, in the inner regions of protoplanetary disks it is thought that fragmentation between particles limits the sizes that small bodies can reach, due to high collision velocities and frequent collisions. In this section we use a relatively simple model in which collision velocities above a threshold velocity  $u_{\text{frag}}$  result in fragmentation (e.g. [Birnstiel et al. 2009](#)). This would be expected if the binding energy of the particle scales as the particle's mass, which is an acceptable approximation for small solids held together by chemical bonds. Lab experiments suggest that  $u_{\text{frag}}$  in the range 1-10 m/s may apply, though the (unknown) material properties of the colliding pebbles affect this number significantly ([Stewart & Leinhardt 2009](#); [Blum & Wurm 2008](#)).

If turbulent motions dominate the relative velocity between particles, then the

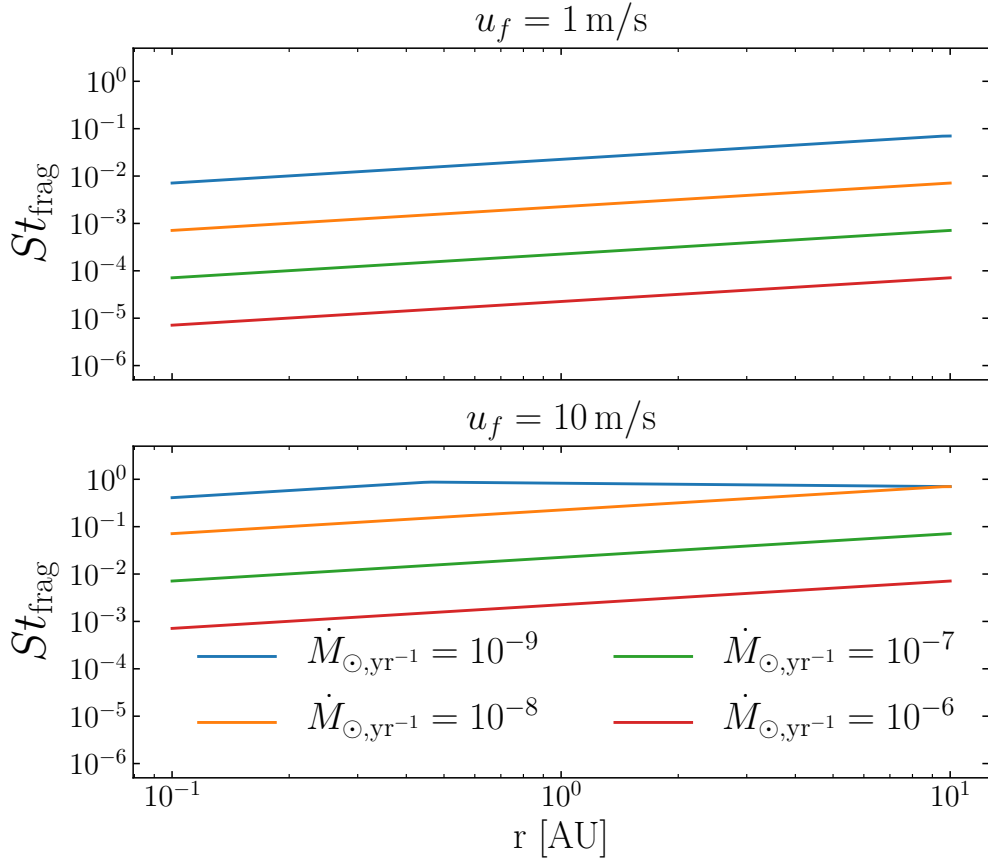


Figure 4.6: A plot of the maximal Stokes number pebbles can reach as a function of semi-major axis and particle fragmentation velocity. The maximal particle size at a given semi-major axis is given by Equation (4.59).

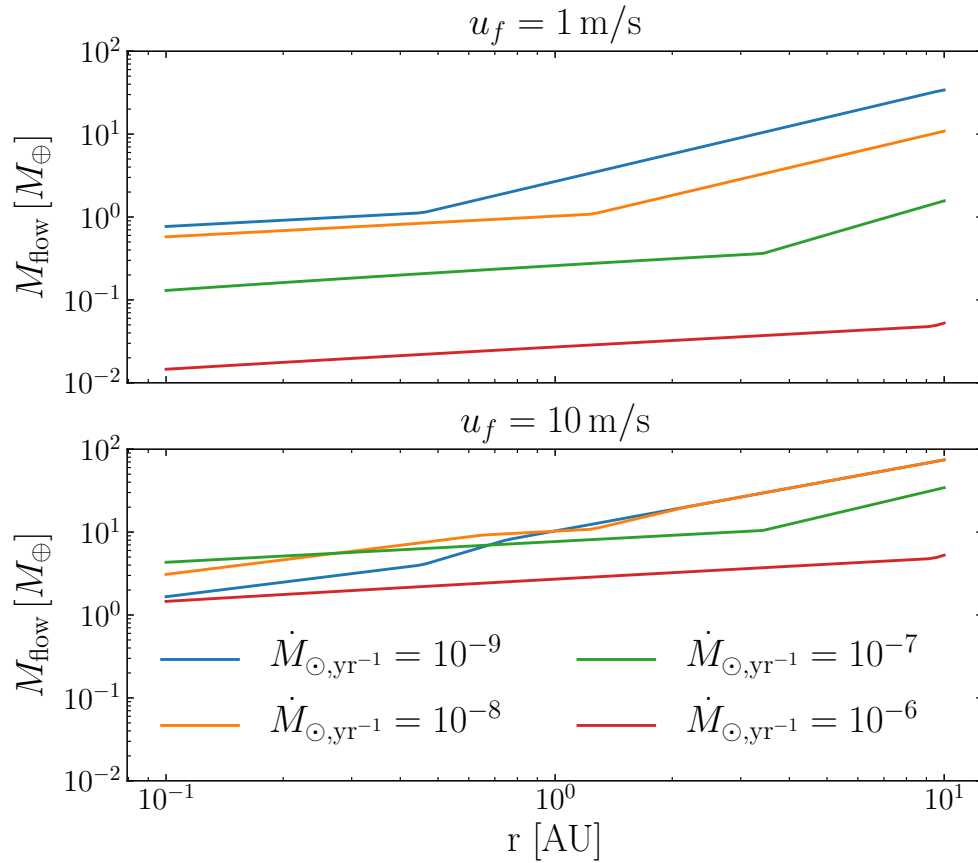


Figure 4.7: A plot of the maximal mass a planet accreting pebbles can reach as a function of semi-major axis and particle fragmentation velocity. The maximal particle size at a given semi-major axis is given by Equation (4.59).

relative velocity between two particles of with Stokes number  $St$  is of order

$$v_{\text{coll}} = v_{\text{gas,t}} \sqrt{St} \quad (4.55)$$

assuming the particles have stopping times such that  $t_\eta < t_s < t_L$ , where  $t_\eta$  and  $t_L$  are the turnover times of the smallest and largest scale eddies respectively (Ormel & Cuzzi 2007). This leads to a maximum Stokes number of

$$St_{\text{max}} = \frac{u_{\text{frag}}^2}{\alpha c_s^2} \quad (4.56)$$

Birnstiel et al. (2009). In what follows, we also consider collisions stemming from the laminar gas velocity. For particles with  $St < 1$ , the particle's laminar velocity relative to Keplerian is well approximated by  $v_\ell = 2\eta v_k St$ , leading to a relative velocity of

$$v_{\text{rel},\ell} = 2\eta v_k (St_1 - St_2) \sim \eta v_k St_1 \quad (4.57)$$

where  $St_1$  and  $St_2$  are the Stokes numbers of the larger and smaller particles, respectively. This leads to a maximum Stokes number of roughly

$$St_{\text{max}} = \frac{u_{\text{frag}}}{\eta v_k} . \quad (4.58)$$

Combining Equations (4.56) and (4.58) gives

$$St_{\text{max}} = \min \left( \frac{u_{\text{frag}}^2}{\alpha c_s^2}, \frac{u_{\text{frag}}}{\eta v_k} \right) \quad (4.59)$$

The maximum Stokes number for fragmentation velocities of  $u_{\text{frag}} = 1 \text{ m/s}$  and  $10 \text{ m/s}$  are shown in Figure 4.6.

In Figure 4.7 we plot the value of the flow isolation mass for fragmentation velocities of  $u_{\text{frag}} = 1 \text{ m/s}$  and  $10 \text{ m/s}$ . For a fragmentation velocity of  $u_{\text{frag}} = 1 \text{ m/s}$  (upper panel), only the colder disks, i.e. those with lower  $\dot{M}$ , are able to produce super-Earth masses. For  $u_{\text{frag}} = 10 \text{ m/s}$  (lower panel), however, the mass scale is much less sensitive to the temperature. This is because there are two competing effects that tend to cancel one another out as the temperature is increased: higher temperatures increase the thermal mass, increasing the flow isolation mass as well. However, higher temperatures lead to larger collision velocities between particles, which decreases the maximum Stokes number and correspondingly lowers the flow isolation mass.

We comment that a given protoplanetary disk likely evolves at different accretion rates during its lifetime. This implies that the final mass a planet reaches depends on when the initial protoplanet forms, as was also identified by [Bitsch et al. \(2019\)](#).

We emphasize that because both pebble accretion timescales for growing cores and collisional growth/destruction timescales for source pebbles are very fast, particularly in the inner disk, planets are likely able to reach the maximum flow isolation masses shown in Figure 4.7.

#### 4.4.3 Variation with Stellar Mass

In Equation (4.54), we gave the scaling of the flow isolation mass with fiducial disk parameters. However, two of these quantities,  $M_8$  and  $\Sigma_{3000}$  likely scale with stellar mass. A number of observational works point to  $\dot{M}$  scaling with  $M_*^2$  (e.g. [Natta et al.](#)

2006, Alcalá et al. 2014), and recent work points to a linear or steeper than linear scaling of disk mass with stellar mass (Andrews et al. 2013, Pascucci et al. 2016). If we neglect variation in the outer disk radius, then this implies that the surface density also scales linearly with stellar mass. Inserting these scalings into the inner, viscously heated regime of Equation (4.54) (and assuming that our fiducial value of  $\Sigma_0 = 3000 \text{ g cm}^{-2}$  applies for  $M_{*,\odot} = 1$ ) gives

$$M_{\text{flow}} = 6.8 M_{\oplus} St_1^{1/2} M_{*,\odot}^1 \quad (4.60)$$

i.e. the flow isolation mass scales approximately linearly with the host star mass.

## 4.5 Comparison to Observations of Close in Planets

In this section we compare predictions made if planet mass is limited by the flow isolation mass to trends identified in the population of close in planets. We point out that these trends are readily explained if planet mass is limited by flow isolation. For a discussion of super-Earth observations in the context of pebble isolation, see Bitsch et al. (2019).

### 4.5.1 Weiss et al. (2018) and Millholland et al. (2017)

Weiss et al. (2018) investigated the characteristics of the multi-planet systems found in the *Kepler* sample. These authors found a correlation between the sizes of planets within a given multi-planet system, i.e. planets in the same system are likely to be similar in size. Millholland et al. (2017) further showed through analysis of the

Kepler planets that also have masses measured through transit timing variations that this similarity applies to mass as well as radius. Note however, that some authors have attributed this effect to detection bias (Zhu 2019).

Similarity between sizes of planets emerges naturally if planet mass is limited by flow isolation. Looking at Equation (4.54), we see that in the inner regions of protoplanetary disks the flow isolation mass is roughly independent of semi-major axis, which stems from viscous heating dominating the temperature structure in this region. Thus, if flow isolation limits planetary growth, super-Earths in the same system would be similar in mass. Excluding atmospheric loss effects, they would also be similar in size.

#### 4.5.2 Wu (2019)

Using updated radius values for planets found from the Kepler mission in concert with Gaia DR2 stellar radii, Wu (2019) explored the effects of photoevaporation in sculpting the observed super-Earth population. Wu found that this population could be explained as stemming from a single characteristic mass scale, of roughly  $M_p \sim 8M_\oplus$ . Furthermore, Wu demonstrated that this mass scale varies with stellar mass and radius with a power law indices in the range

$$M_p = 8M_\oplus M_*^{0.95-1.4} r_{\text{AU}}^{0-0.5} \quad (4.61)$$

Note that this mass scale refers to the bare core mass of these planets; planets that do not undergo photoevaporation will accrete some amount of nebular gas, changing their

observed radius (and, to a lesser extent, mass).

Comparison between Equations (4.60) and (4.61) shows that the scaling of this characteristic mass scale is exactly what we would expect if pebble accretion fuels the growth of these planets, only to be shut off by flow isolation. We note that [Wu \(2019\)](#) argues the characteristic mass scale identified in that work could be the thermal mass, whereas we have argued that this mass scale could be the flow isolation mass, which is generally less than or equal to the thermal mass. This difference stems from how the temperature profile in the inner regions of the protoplanetary disk and the scaling of various disk parameters with stellar mass are modeled.

#### 4.5.3 [Zhu & Wu \(2018\)](#) & [Bryan et al. \(2019\)](#)

Using previously published planetary systems, [Zhu & Wu \(2018\)](#) calculated the correlation between systems with “cold” Jupiters and inner super-Earths. They found that 90% of systems that host an outer cold Jupiter contain inner super-Earths. [Bryan et al. \(2019\)](#) further investigated the occurrence rate of such outer gas giant companions in systems that contain super-Earths by taking radial velocity data on systems containing super-Earths and looking for trends in the radial velocity signals. They found an occurrence rate of  $39\% \pm 7\%$  for planets  $0.5\text{-}20 M_{\text{jup}}$  at 1-20 au, and also demonstrated that systems that host super-Earths are more likely to contain an outer gas giant planet.

This effect would follow naturally for systems of super-Earths where the mass of the planets is limited by flow isolation. In such systems, solid surface densities and pebble sizes were clearly conducive to formation of planets via pebble accretion in the

inner disk. At larger semi-major axes, the disk temperature is set by passive irradiation instead of viscous heating, indicating a weaker scaling of temperature with semi-major axis. This weaker scaling leads to larger values of thermal mass in the outer disk, and correspondingly larger flow isolation masses. Thus, in the outer regions of these disks the flow isolation mass can reach values large enough to trigger runaway gas accretion, allowing gas giants to form at larger semi-major axes (c.f. Figures 4.5 and 4.7, upward trends at righthand sides of plots). Therefore, in systems which produced inner super-Earths via flow isolation, we would expect outer gas giants to be more likely, in line with the results of [Zhu & Wu \(2018\)](#) and [Bryan et al. \(2019\)](#). We note that at very large semi-major axes, drift limits the sizes of available pebbles (e.g., [Powell et al. 2019](#)), meaning that the trend toward larger flow isolation masses will likely reverse at large separations. We also point out that this correlation between inner super-Earth and outer gas giants is not unique to the flow isolation mass, but is a natural prediction of theories where a limiting mass scale increases in the outer disk, as is true for the pebble isolation mass, e.g. [Brügger et al. \(2018\)](#), [Bitsch et al. \(2019\)](#), or the local isolation mass used in classic models of the solar system (e.g. [Lissauer 1993](#)).

## 4.6 Summary and Conclusions

We discussed how pebble accretion timescales vary as a function of core mass, and pointed out that at super-Earth masses growth timescales for pebble accretion are extremely rapid for a large range of pebble sizes. These rapid growth rates make it difficult to form super-Earths via pebble accretion unless something halts growth once

planets reach this mass scale.

We further demonstrated that modification of the gas flow pattern by the planet's atmosphere limits accretion of the smallest pebble sizes. The Stokes number of the smallest pebble size a planet can accrete can be determined by finding the size for which the maximal impact parameter for accretion,  $R_{\text{stab}}$ , is equal to the scale of the core's atmosphere,  $R_{\text{B}}$ . If the solids present in the protoplanetary disk are limited to sizes smaller than a maximum size, then this process naturally predicts that growth of planet will cease once the minimum-sized particles a planet can accrete is larger than the maximal size present in the disk. For a reasonable fiducial disk profile and particle sizes, we showed that the resulting mass scale where growth ceases is around super-Earth masses.

Furthermore, we showed that several trends present in the demographics of the super-Earth population follow naturally if the masses of these planets are limited by flow isolation: super-Earths in the same system would be correlated in mass and radius, as reported by [Weiss et al. \(2018\)](#), due to the shallow scaling of the flow isolation mass with semi-major axis in the inner disk. We would also expect a characteristic mass scale, i.e. the flow isolation mass, to be present in the super-Earth population, and to scale approximately linearly with stellar mass and weakly with semi-major axis, as reported by [Wu \(2019\)](#). Finally, we would expect systems that have inner super-Earths to be more likely to host an outer gas giant, as the the flow isolation mass is larger at these larger orbital separations, a trend which was detected by [Zhu & Wu \(2018\)](#) and [Bryan et al. \(2019\)](#).

While the trends in the super-Earth population seem consistent with being limited to the local flow isolation mass, there remain other regimes where the importance of the flow isolation mass could be tested, particularly in contrast with the pebble isolation mass. One such regime would be planet formation in the outer regions of protoplanetary disks – in these regions maximal Stokes numbers are likely set by drift (e.g. [Birnstiel et al. 2012](#)), which leads to maximal Stokes number of  $St \sim 10^{-1} - 10^{-2}$ . On the other hand, the thermal mass is quite large in the outer disk, as the aspect ratio of the disk generally increases as a function of semi-major axis. Thus, in this region we would expect the predictions of flow isolation and pebble isolation to be quite different, with flow isolation predicting substantially lower planetary masses.

## Chapter 5

# Ending Pebble Accretion Through Flow and Pebble Isolation

### 5.1 Introduction

The final masses of planets produced by pebble accretion are not determined by pebble accretion growth rates alone. Once a planetary core is massive enough that pebble accretion sets in, it generally grows on timescales much shorter than the lifetime of the gas disk ([Ormel & Klahr 2010](#), [Lambrechts & Johansen 2012](#), [Rosenthal et al. 2018](#)). On its own, this would seem to predict that planets either stall at low mass before they undergo pebble accretion, or grow to such large masses that they trigger runaway gas accretion ([Pollack et al. 1996](#)) and become gas giants (e.g., [Lin et al. 2018](#)). However, several authors have investigated the possibility of a limiting mass scale for pebble accretion, where the growth process qualitatively changes, and accretion of

pebbles halts.

[Lambrechts et al. \(2014\)](#) proposed the idea of a “pebble isolation mass,” resulting from the planet’s perturbation of the local gas pressure gradient. These authors argue that once the planet has reached sufficient mass, it excites the gas to super-Keplerian velocities exterior to its orbit, which blocks the inward radial drift of pebbles and ends pebble accretion. [Bitsch et al. \(2018\)](#) followed up on this work, both by using hydrodynamical simulations to study how the mass needed to excite super-Keplerian velocities changed as a function of disk parameters, and also by studying how the pebble isolation mass changes as a function of particle size. [Bitsch et al.](#) find that increasing levels of turbulence not only make it more difficult for the planet to raise a pressure perturbation, but can also allow smaller particles to drift through the pressure bump while still blocking larger particles from accreting.

[Rosenthal et al. \(2018\)](#) argued that pebbles below a certain size would not be captured through pebble accretion because they are too strongly coupled to the gas, and thus flow with the gas around the planetary atmosphere. This argument implies that planetary growth by pebble accretion should halt if this “minimum” pebble size for accretion is larger than the maximal particle size available, a process [Rosenthal & Murray-Clay \(2019\)](#) dubbed “flow isolation.” In contrast to pebble isolation, flow isolation blocks particles in a “bottom-up” manner – the smallest particle sizes are the first to be cut off, with the largest particles only being blocked when the planet achieves “large enough” masses.

Both the pebble isolation mass and the flow isolation mass are independent of

solid surface density, instead depending only on local disk parameters and particle size. Both scales are primarily dependent on temperature, and scale roughly as the thermal mass, i.e.  $M_{\text{iso}} \sim h^3 M_*$ , where  $h$  is the disk aspect ratio and  $M_*$  is the mass of the central star. The pebble isolation mass is generally within factors of 2-3 of the thermal mass, while the flow isolation is comparable to the thermal mass or lower.

In this letter, we discuss the interplay between these two mass scales. In particular, we first show that the top-down blocking of particles seen in pebble isolation means that the actual final mass the planet reaches can be larger than the mass at which the gas velocity in the perturbed becomes super-Keplerian. In contrast, for flow isolation we demonstrate that because particles are blocked in a bottom-up manner, only the largest particle sizes need to be considered. Finally, we show that if these two processes operate simultaneously, then the final planet mass from pebble accretion is well approximated by taking the minimum of the flow isolation mass and the pebble isolation mass calculated in the absence of diffusion.

## 5.2 Disk Model

In this section we briefly discuss the disk model used to generate our numerical results. Our disk is broken into two regions, depending on whether the temperature is set by viscous heating or by passive irradiation. We choose our disk parameters such that  $\alpha$  and  $\dot{M} = 3\pi\Sigma\nu$  are radially constant, where  $\Sigma$  is the gas surface density,  $\nu = \alpha H^2 \Omega$  is the kinematic viscosity (Shakura & Sunyaev 1973),  $H$  is the local gas scale height and  $\Omega$  is local Keplerian angular frequency. We do not prescribe the value of  $\dot{M}$  directly. Instead

we choose a fixed surface density profile for the viscously-heated inner region of the disk. This profile is scaled such that the surface density at 1 au is  $\Sigma_{0,\text{visc}} = 2000 \text{ g cm}^{-2}$ . The resulting disk has the feature that increasing  $\alpha$  increases both  $\dot{M}$  and temperature, which we feel provides useful intuition. In particular, models that fix  $\dot{M}$  and  $\alpha$  have the slightly counter-intuitive feature that increasing  $\alpha$  decreases  $T$ , which we wished to avoid. In the viscously heated inner region of the disk, balancing accretion heating with radiative cooling gives (e.g. [Oka et al. 2011](#), [Kratter & Murray-Clay 2011](#))

$$T_c = \left[ \frac{9}{128\pi} \frac{GM_* \dot{M} \kappa \Sigma}{\sigma_{\text{SB}} r^3} \right]^{1/4} \quad (5.1)$$

Here  $r$  is the semi-major axis,  $M_*$  is the mass of the central star,  $\sigma_{\text{SB}}$  is the Stefan-Boltzmann constant, and  $\kappa$  is the Rosseland mean opacity. Eliminating  $\dot{M}$  in favor of  $\Sigma$  and  $\nu$ , setting  $\kappa = 0.1 \text{ g}^{-1} \text{ cm}^2$ , and choosing a radial dependence such that  $\dot{M}$  is constant with  $r$  gives

$$T_{\text{visc}} = 220 \text{ K} \left( \frac{r}{\text{au}} \right)^{-9/10} \left( \frac{M_*}{M_\odot} \right)^{1/6} \left( \frac{\alpha}{10^{-3}} \right)^{1/3} \left( \frac{\Sigma_{0,\text{visc}}}{2000 \text{ g cm}^{-2}} \right)^{2/3} \quad (5.2)$$

At larger orbital separations, the disk temperature is set by passive irradiation. We take our fiducial profile from [Ida et al. \(2016\)](#) (see [Chiang & Goldreich 1997](#) for details)

$$T_{\text{irr}} = 205 \text{ K} \left( \frac{r}{\text{au}} \right)^{-3/7} \left( \frac{M_*}{M_\odot} \right)^{-1/7} \left( \frac{L_*}{3L_\odot} \right)^{2/7} \quad (5.3)$$

where  $L_*$  is the luminosity of the central star. We set  $M_* = M_\odot$  in what follows, and set  $L_* = 3L_\odot$ , which is appropriate for a solar mass star of age  $\sim 1 \text{ Myr}$  ([Tognelli et al.](#)

2011).

The temperature at a given semi-major axis is  $T = \max(T_{\text{visc}}, T_{\text{irr}})$ . The disk switches from being dominated by viscous heating to passive irradiation at a semi-major axis of

$$r_{\text{vis-irr}} = 1.16 \text{ au} \left( \frac{M_*}{M_\odot} \right)^{65/99} \left( \frac{L_*}{3L_\odot} \right)^{-20/33} \left( \frac{\alpha}{10^{-3}} \right)^{70/99} \quad (5.4)$$

In the viscously heated region, the surface density is given by

$$\Sigma_{\text{visc}} = 2000 \text{ g cm}^{-2} \left( \frac{r}{\text{au}} \right)^{-3/5} \quad (5.5)$$

where the  $\Sigma_{\text{visc}} \propto r^{-3/5}$  dependence derives from requiring  $\alpha$  and  $\dot{M}$  to be radially constant. In the passively irradiated region, requiring that  $\dot{M}$  be radially constant for constant  $\alpha$  implies that  $\Sigma_{\text{irr}} \propto r^{-15/14}$ . Enforcing continuity in  $\Sigma$  at  $r_{\text{vis-irr}}$  gives

$$\Sigma_{\text{irr}} = 2150 \text{ g cm}^{-2} \left( \frac{r}{\text{au}} \right)^{-15/14} \left( \frac{M_*}{M_\odot} \right)^{13/42} \left( \frac{\alpha}{10^{-3}} \right)^{1/3} \left( \frac{L_*}{3L_\odot} \right)^{-2/7} \quad (5.6)$$

The overall surface density is given by  $\Sigma = \min(\Sigma_{\text{visc}}, \Sigma_{\text{irr}})$ , which is equivalent to choosing the surface density corresponding to the dominant heating mechanism. The available pebble surface density is fixed at

$$\Sigma_{\text{p}} = 5 \text{ g cm}^{-2} \left( \frac{r}{\text{au}} \right)^{-1} \quad (5.7)$$

which is chosen to be consistent with measurements in the outer disk of the surface

density in solids of size 0.1-1 mm, taken from sub-mm observations of protoplanetary disks ([Andrews et al. 2009](#), [Andrews 2015](#)).

For the purposes of calculating growth timescales, we assume that the solid surface density at a given semi-major axis is distributed over particle size  $s$  such that

$$\frac{dN}{ds} \propto s^{-3.5} \quad (5.8)$$

where  $N$  is the number of particles as a function of size at a given semi-major axis. We assume smallest particles have Stokes number  $St = 10^{-6}$ . Because this size distribution has most of the mass in the largest particle sizes the smallest particle size is relatively unimportant. The largest particle size is varied in this work (see below).

While the global disk accretion rate is not strictly needed for our calculations, we note that our choices above imply

$$\dot{M} = 1.2 \times 10^{-8} M_{\odot} \text{ yr}^{-1} \left( \frac{\alpha}{10^{-3}} \right)^{4/3} \left( \frac{M_*}{M_{\odot}} \right)^{-1/3} \left( \frac{\Sigma_{0,\text{visc}}}{2000 \text{ g cm}^{-2}} \right)^1 \quad (5.9)$$

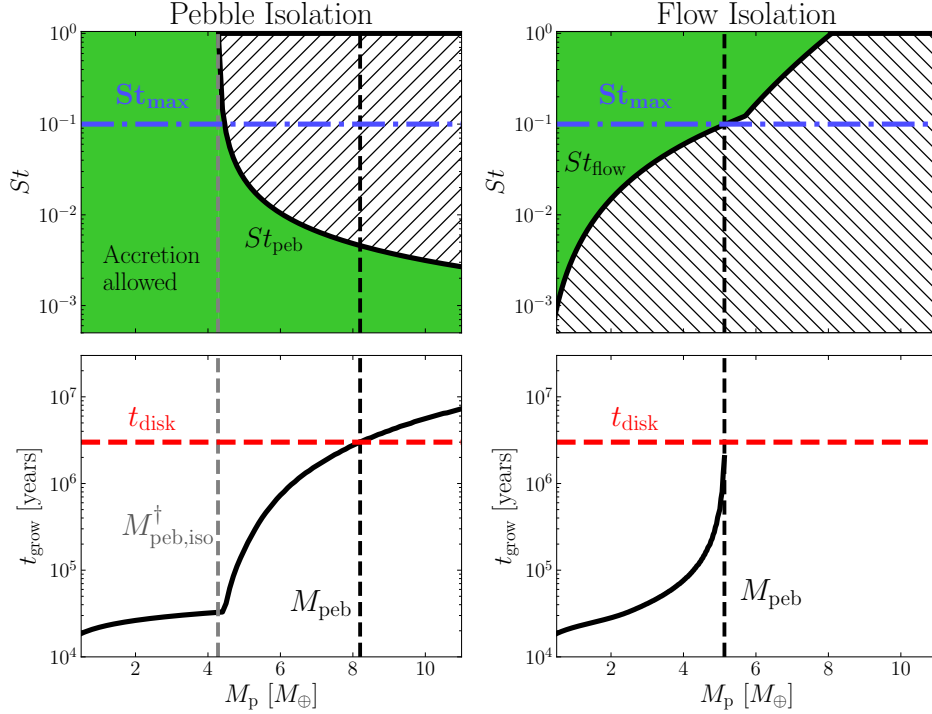


Figure 5.1: The particle size dependence of pebble and flow isolation differs. Pebble isolation (left) cuts off accretion of large particles more easily; in the presence of a distribution of particle sizes, small particles can contribute substantially to growth even when the largest particles have been cut off. In contrast, flow isolation (right) blocks small particles first, halting growth once the largest particles are blocked. The range of particle sizes that can be accreted for each mechanism (top, green region), and the resulting growth timescales (bottom, solid black lines) are shown for a core located at  $r = 0.278$  au. The disk has  $\alpha = 10^{-3}$ , and the maximum particle size at the planet’s semi-major axis is  $St_{\max} = 10^{-1}$  (dashdot blue line). In the upper panels, the particle sizes that can accrete are bounded by  $St_{\text{peb}}$  (left) and  $St_{\text{flow}}$  (right) (solid black lines). The mass at which the gas is excited to super-Keplerian velocities is  $M_{\text{peb,iso}}^\dagger$  (vertical gray dashed line), and is calculated using the formula of Bitsch et al. (2018). The planet’s final mass,  $M_{\text{peb}}$ , determined by the point at which  $t_{\text{grow}} = t_{\text{disk}} = 3$  Myr (dashed red line), is indicated by the dashed black vertical line. For flow isolation, the planet’s final mass is well approximated as the mass at which particles of size  $St_{\max}$  are blocked. For pebble isolation this is not the case, and calculation of the core’s integrated growth timescale is required to determine the planet’s final mass.

### 5.3 Pebble Isolation Mass

The concept of the ‘‘Pebble isolation mass’’ was first introduced in [Lambrechts et al. \(2014\)](#). In this work, the authors investigate how the planet alters the local pressure gradient through 3D hydrodynamical simulations. In the absence of planets, protoplanetary disks orbit at a rate slightly slower than the local Keplerian velocity,  $v_k$ ,

$$v_{\text{orb}} = (1 - \eta)v_k \quad (5.10)$$

where  $\eta$  is given by

$$\eta = -\frac{1}{2}h^2 \frac{\partial \ln P}{\partial \ln r} \quad (5.11)$$

(e.g. [Weidenschilling 1977a](#)). Here  $h \equiv H/r$  is the disk aspect ratio, and  $P$  is the local pressure. This sub-Keplerian rotation causes pebble sized particles to drift radially at a velocity

$$v_r \approx -2\eta v_k St \quad (5.12)$$

(e.g. [Nakagawa et al. 1986](#)). Above,  $St \equiv t_s \Omega$  is particle’s Stokes number,  $t_s$  is the particle’s characteristic gas drag timescale, and  $\Omega$  is the local Keplerian orbital frequency. Equation (5.12) applies for  $St \lesssim 1$ . We restrict our attention to  $St \leq 1$  for the remainder of this work.

For usual protoplanetary disk conditions  $\partial \ln P / \partial \ln r$  is negative, leading to

a sub-Keplerian orbital velocity. However, planets can gravitationally excite local gas, changing the local pressure profile and in some cases exciting local material to super-Keplerian velocities. [Lambrechts et al. \(2014\)](#) argue that when a planet reaches sufficient mass, pebble drift velocities should reverse direction, trapping particles and halting growth of planets through pebble accretion. [Lambrechts et al.](#) performed hydrodynamical simulations to determine the mass threshold above which gas is excited to super-Keplerian velocities. They found that this occurred for planetary masses larger than

$$M_{\text{peb,simp}} \approx 20 M_{\oplus} \left( \frac{h}{0.05} \right)^3 \quad (5.13)$$

which they termed the “pebble isolation mass.”

Following up on the work of [Lambrechts et al. \(2014\)](#), [Bitsch et al. \(2018\)](#) performed additional hydrodynamic simulations to determine how the pebble isolation mass changed as a function of disk properties. Specifically, [Bitsch et al. \(2018\)](#) varied both the disk viscosity and pressure gradient, and then determined the mass above which super-Keplerian velocities were excited. They find that the pebble isolation mass is well described by the formula

$$M_{\text{peb,iso}}^{\dagger} = 25 f M_{\oplus} \quad (5.14)$$

$$f = \left( \frac{h}{0.05} \right)^3 \left[ 0.34 \left( \frac{\log_{10} \alpha}{-3} \right)^{-4} + 0.66 \right] \left( 1 - \frac{\frac{\partial \ln P}{\partial \ln r} + 2.5}{6} \right)$$

As discussed previously,  $M_{\text{peb}}^{\dagger}$  is mostly dependent on  $h^3$ , with the additional terms

varying the mass by factors of 2-3.

However, this mass scale only tells us where the planet raises a large enough pressure perturbation to accelerate neighboring gas to super-Keplerian velocities. Because of turbulent diffusion, particles may still be able to diffuse through the pressure bump. Smaller particles will be more well-coupled to the gas, which makes it easier for them to diffuse through the pressure bump. Thus, the mass needed to block particles of a given size increases as particle size decreases. [Bitsch et al. \(2018\)](#) add an additional term to the pebble isolation mass to account for this effect. The full pebble isolation mass is then given by

$$M_{\text{peb,iso}} = M_{\text{peb,iso}}^{\dagger} + \frac{\Pi_{\text{crit}}}{\lambda} M_{\oplus} \quad (5.15)$$

where

$$\Pi_{\text{crit}} = \frac{\alpha}{2St} \quad (5.16)$$

$$\lambda = \frac{0.00476}{f} \quad (5.17)$$

We can invert this expression to determine the smallest particle blocked by a core of mass  $M_p$

$$St_{\text{peb}} = \left( \frac{\alpha}{2\lambda} \right) \left( \frac{M_p - M_{\text{peb,iso}}^{\dagger}}{M_{\oplus}} \right)^{-1} \quad (5.18)$$

This expression is plotted for a core at 1 au in the upper left panel of Figure 5.1. The

shaded region indicates the range of particle sizes that the core can accrete at a given mass.

In general, pebbles are not expected to exist up to arbitrary sizes in protoplanetary disks. Processes such as drift of large solids, or fragmentation of particles are expected to inhibit growth past a certain limiting size (e.g. [Birnstiel et al. 2012](#)). If particles exist up to a maximum size  $St_{\max}$  in the disk, Equation (5.18) implies that planetary growth will be unaffected unless  $St_{\text{peb}} \leq St_{\max}$ .

As a core grows,  $St_{\text{peb}}$  will decrease. Once  $St_{\text{peb}} \leq St_{\max}$ , the planet is able to block progressively smaller solids from being captured as it grows. This slows the planet’s growth for two reasons: first, smaller particles lead to core growth on longer timescales (e.g. [Lambrechts & Johansen 2012](#), [Rosenthal et al. 2018](#)). Second, these higher mass particles generally represent a large fraction of the total local solid mass. The size distribution of dust particles in protoplanetary disks is a complex topic, as all particle sizes interact via the processes of growth, drift, and fragmentation (see e.g. [Birnstiel et al. 2010](#)). However, in the inner regions of protoplanetary disks, where particle sizes are limited by fragmentation, it is generally expected that the size distribution will be “top-heavy,” in the sense that most of the mass will be contained in the largest particle sizes (e.g. [Birnstiel et al. 2011](#)). If the size distribution is instead “bottom-heavy,” i.e. if most of the mass in the smallest size particles, the growth timescale will increase more slowly with increasing planet mass.

Thus, as the planet grows past  $M_{\text{peb,iso}}(St_{\max})$  its growth timescale will increase due to a variety of effects. Eventually, the planet’s growth will slow to such a

degree that the gaseous component of the protoplanetary disk will dissipate before the planet can further increase its mass. We can therefore estimate the final mass of the planet by determining the mass at which the growth timescale of the planet is equal to the lifetime of the gas disk, that is

$$t_{\text{grow}}(St_{\text{peb}}, M_{\text{peb}}) = t_{\text{disk}} \quad (5.19)$$

Note that we have written the growth timescale as a function of both the largest particle size the core can accrete ( $St_{\text{peb}}$ ), and the core's mass, since the growth timescale for pebble accretion is sensitive to both of these quantities. The growth timescale of the core (at a fixed distance from the star) is determined by integrating the planet's accretion rate over particle size

$$\dot{M}_{\text{p}} = \int_{s_{\text{min}}}^{s_{\text{peb}}} \sigma(s) \frac{Av_{\infty}}{2H_{\text{p}}} d \ln s \quad (5.20)$$

where  $\sigma$  is the surface density of particles per logarithmic size bin,  $A$  is the accretion cross section for pebbles,  $v_{\infty}$  is the relative velocity between the pebbles and the growing core, and  $H_{\text{p}}$  is the pebble scale height. Here  $s_{\text{peb}}$  is the particle size corresponding to a particle with Stokes number  $St_{\text{peb}}$ . In general,  $A$ ,  $v_{\infty}$ , and  $H_{\text{p}}$  are functions of  $M_{\text{p}}$  and  $s$ , as well as the disk parameters. The planet's growth timescale is then calculated as  $t_{\text{grow}} = M_{\text{p}}/\dot{M}_{\text{p}}$ .

By specifying a model for the particle's growth timescale, i.e. a model for  $A$ ,  $v_{\infty}$ , and  $H_{\text{p}}$ , as well as  $\sigma(s)$ , we can find  $M_{\text{peb}}$  by simultaneously solving Equations

(5.18) and (5.19). Even if a simple model for pebble accretion is used (e.g. forcing the core to grow in only a single pebble accretion “regime”), these equations do not have an analytic solution and must be solved numerically. In the bottom left panel of Figure 5.1 we show an example of the growth timescale of the core as the function of mass including the effects of pebble isolation. As discussed in Section 5.2,  $\sigma$  is calculated by assuming a Dohnanyi distribution of particle sizes,  $dN/ds \propto s^{-3.5}$  (Dohnanyi 1969). We assume that the maximum size of particles at the planet’s location in the protoplanetary disk have  $St_{\max} = 10^{-1}$ . We use the pebble accretion model of Rosenthal et al. (2018) to determine  $A$ ,  $v_{\infty}$ , and  $H_p$ .

Note that while the core excites the gas to super-Keplerian velocities at  $M_{\text{peb,iso}}^{\dagger} \approx 4.1M_{\oplus}$ , growth does not halt until the planet is approximately a factor of 2 larger,  $M_{\text{peb}} \approx 8.1M_{\oplus}$ . Note that we refer to this mass scale, where the growth timescale exceeds the lifetime of the disk, as  $M_{\text{peb}}$ . We also stress that  $M_{\text{peb}}$  is larger than  $M_{\text{peb,iso}}$ , the mass necessary to block particles of size  $St_{\max} = 10^{-1}$ . Thus, accounting for the growth rate of the planet via particles that drift through the pressure bump increases the pebble isolation mass substantially.

In Figure 5.2 we calculate  $M_{\text{peb}}$  over a grid of values in  $r$ ,  $\alpha$ , and  $St_{\max}$ , and compare with both  $M_{\text{peb,iso}}^{\dagger}$  (Equation 5.14) and  $M_{\text{peb,iso}}$  (Equation 5.15). The difference between these mass scales increases at larger  $\alpha$  and at smaller semi-major axis. Larger values of  $\alpha$  increase the particle sizes that can drift through the pressure bump for a given planet mass, meaning that the planet has to reach larger masses to cut off growth. Growth rates via pebble accretion are also faster in the inner regions of

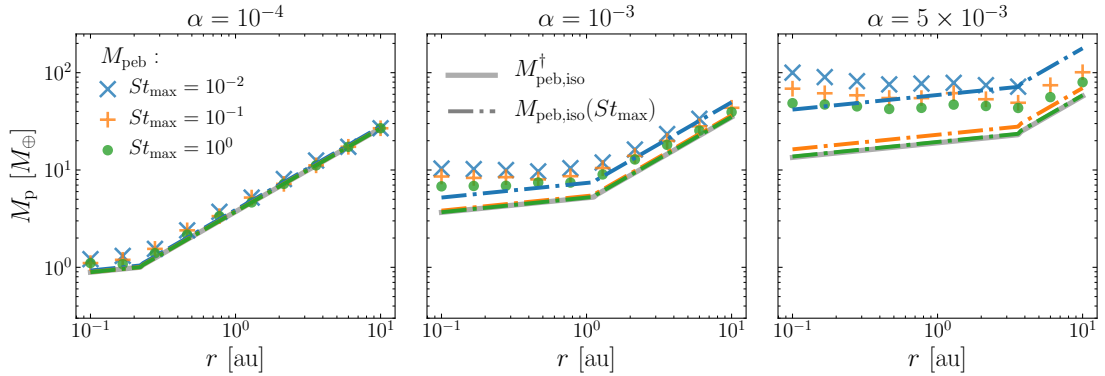


Figure 5.2: Comparison between the analytic expressions of Bitsch et al. (2018) for the pebble isolation mass ( $M_{\text{peb,iso}}^\dagger$  and  $M_{\text{peb,iso}}$ ) and numerically calculated final masses ( $M_{\text{peb}}$ ) determined by solving for the mass such that  $t_{\text{grow}} = t_{\text{disk}} = 3 \text{ Myr}$ . Each panel displays these masses as a function of semi-major axis for a distinct value of the  $\alpha$  parameter. Blue, orange, and green refer to  $St_{\text{max}} = 10^{-2}$ ,  $10^{-1}$ , and  $10^0$  respectively. The solid gray line shows the value of  $M_{\text{peb,iso}}^\dagger$  (Equation 5.14), i.e. the mass needed to excite the gas to super-Keplerian velocities, the dashdot lines show the value of  $M_{\text{peb,iso}}(St_{\text{max}})$  (Equation 5.15), i.e. the mass necessary to block particles of size  $St_{\text{max}}$ , and the symbols show the value of  $M_{\text{peb}}(St_{\text{max}})$  for a pebble size distribution given by Equation (5.8).

the disk, allowing the planet to reach larger masses before growth is halted. We note that smaller particle sizes also increase the contrast between  $M_{\text{peb,iso}}^\dagger$  (solid gray line) and  $M_{\text{peb}}$  (symbols), due to the fact that the planet must reach larger masses before it can block these particles. The lines for  $St_{\text{max}} = 10^{-2}$  are truncated for large values of  $r$  because the growth timescale at  $M_{\text{peb,iso}}^\dagger$  exceeds  $t_{\text{disk}}$ , i.e.  $t_{\text{grow}} > t_{\text{disk}}$  before pebble isolation restricts any particle size.

For  $St_{\text{max}} = 10^{-2}$ , using  $M_{\text{peb,iso}}$  (dot-dashed lines) in place of  $M_{\text{peb,iso}}^\dagger$  mitigates a good deal of the discrepancy between our numerically calculated  $M_{\text{peb}}$  and the analytic expressions, particularly in the outer disk. This is not surprising, as at these orbital separations the planet's growth timescale is comparable to  $t_{\text{disk}}$  even before pebble isolation blocks any particles. In the inner disk, these two mass scales are different

by factors  $\sim 2$ . For the other values of  $St_{\max}$ ,  $M_{\text{peb,iso}}^\dagger$  is not substantially different from  $M_{\text{peb,iso}}$ .

Thus, we have shown that if growth is limited by pebble isolation, it is important to consider the diffusion of pebbles through the pressure bump before we can determine the planet’s final mass. This stems from the fact that small particles will still diffuse through the bump even though larger particles are blocked. In the next section we consider halting growth through a different process, flow isolation, where the smallest particles are the easiest to block.

## 5.4 Flow Isolation Mass

The flow isolation mass was first proposed as mass scale at which pebble accretion should stop by [Rosenthal et al. \(2018\)](#). [Rosenthal & Murray-Clay \(2019\)](#) then followed up on this work, focusing on the limiting mass scale as function of  $St_{\max}$ , the largest local particle size.

The idea behind the flow isolation mass is that particles below a certain minimum size should not be able to accrete, as they are too strongly coupled to the nebular gas. [Rosenthal & Murray-Clay \(2019\)](#) argue that the nebular gas will flow around the core on scales comparable to  $\sim R_{\text{atm}}$ , the size of the core’s atmosphere. Because of this modification to the gas flow, particles that are well coupled to the gas on this scale and encounter the atmosphere before becoming gravitationally bound to the core will be pulled around the growing planet without accreting. Equivalently, “pebbles” (particles of size  $St \leq 1$ ) whose impact parameter for pebble accretion,  $R_{\text{acc}}$ , is less than the scale

of the core’s atmosphere,  $R_{\text{atm}}$ , will not accrete. Solving the equation  $R_{\text{acc}} = R_{\text{atm}}$  for  $St$  gives the minimum particle size,  $St_{\text{flow}}$ , that a core can accrete. Using the model of [Rosenthal & Murray-Clay \(2019\)](#) to solve for  $St_{\text{flow}}$  gives

$$St_{\text{flow}} = \max \left[ f^{-2} \left( \frac{H}{r} \right)^{-3} \left( \frac{v_{\text{gas}}}{c_s} \right) \left( \frac{M_p}{M_*} \right), f^{-3} \left( \frac{H}{r} \right)^{-6} \left( \frac{M_p}{M_*} \right)^2 \right] \quad (5.21)$$

where  $v_{\text{gas}}$  is the local gas velocity relative to Keplerian,  $c_s$  is the local isothermal sound speed, and  $f$  is an order unity factor discussed in [Rosenthal & Murray-Clay \(2019\)](#). We take  $f = 1.75$  in what follows. In both regimes, we see that  $St_{\text{flow}}$  increases with planet mass, meaning that particles are blocked in a “bottom-up” manner, as opposed to the top-down manner in which particles are blocked by pebble isolation. An example of the range of sizes a core can block by flow isolation grows is shown in the upper righthand panel of Figure 5.1.

If particles exist only up to some maximum size  $St_{\text{max}}$ , then, assuming the particle size distribution is top-heavy, once  $St_{\text{flow}}$  approaches this maximum size growth will rapidly slow. [Rosenthal & Murray-Clay \(2019\)](#) asserted that final planet mass could be determined by calculating the mass such that  $St_{\text{flow}} = St_{\text{max}}$ . While a more rigorous criteria would be to calculate the mass such that the growth timescale of the planet exceeds the disk lifetime, for a top-heavy size distribution requiring  $St_{\text{flow}} = St_{\text{max}}$  is a very good approximation. This is verified in the two righthand panels of Figure 5.1. [Rosenthal & Murray-Clay \(2019\)](#) refer to the mass scale where particles of size  $St_{\text{max}}$  are blocked as the “flow isolation mass.” We can get an analytic approximation for the flow isolation mass by inverting (5.21). Doing so, and accounting for the case in which

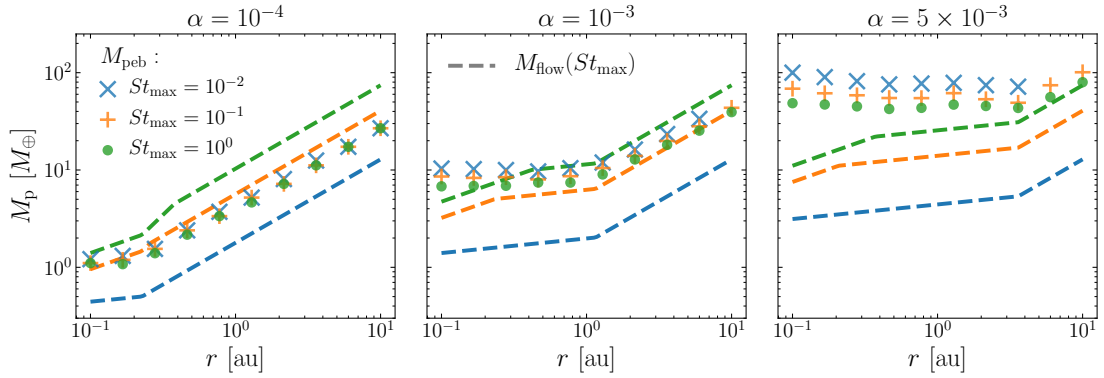


Figure 5.3: The value of the flow isolation mass (dashed lines, Equation 5.22 with  $f = 1.75$ ) as a function of semi-major axis, level of turbulence, and maximum particle size. Colors refer to the same values of  $St_{\max}$  as in Figure 5.2. The final planet masses from pebble isolation alone (see Figure 5.2) are shown for reference.

particles accrete at the planet’s Hill radius gives

$$\frac{M_{\text{flow}}}{M_{\text{th}}} = \min \left[ f^2 \frac{c_s}{3v_{\text{gas}}} St_{\max}, \frac{f^{3/2}}{3} \sqrt{St_{\max}}, \left( \frac{f'}{3} \right)^{3/2} \right] \quad (5.22)$$

where  $M_{\text{th}} \equiv 3h^3 M_*$  is the thermal mass and  $f' = 1.75$  is an additional order unity factor (see Rosenthal & Murray-Clay 2019 for details). Our previous claim that  $M_{\text{flow}} \lesssim M_{\text{th}}$  can be seen from inspection of Equation (5.22). The value of the flow isolation mass for our grid of  $r$ ,  $\alpha$ , and  $St_{\max}$  is shown in Figure 5.3. We note that because our order unity coefficient  $f$  appears to reasonably large powers in Equation (5.22) (as discussed in Rosenthal & Murray-Clay 2019, the second regime with  $M_{\text{flow}} \propto f^{3/2}$  is the most relevant for growth of super-Earths), the choice of  $f$  can change the value of  $M_{\text{flow}}$  by factors of a few. The numerically calculated values of  $M_{\text{peb}}$  are shown for reference.

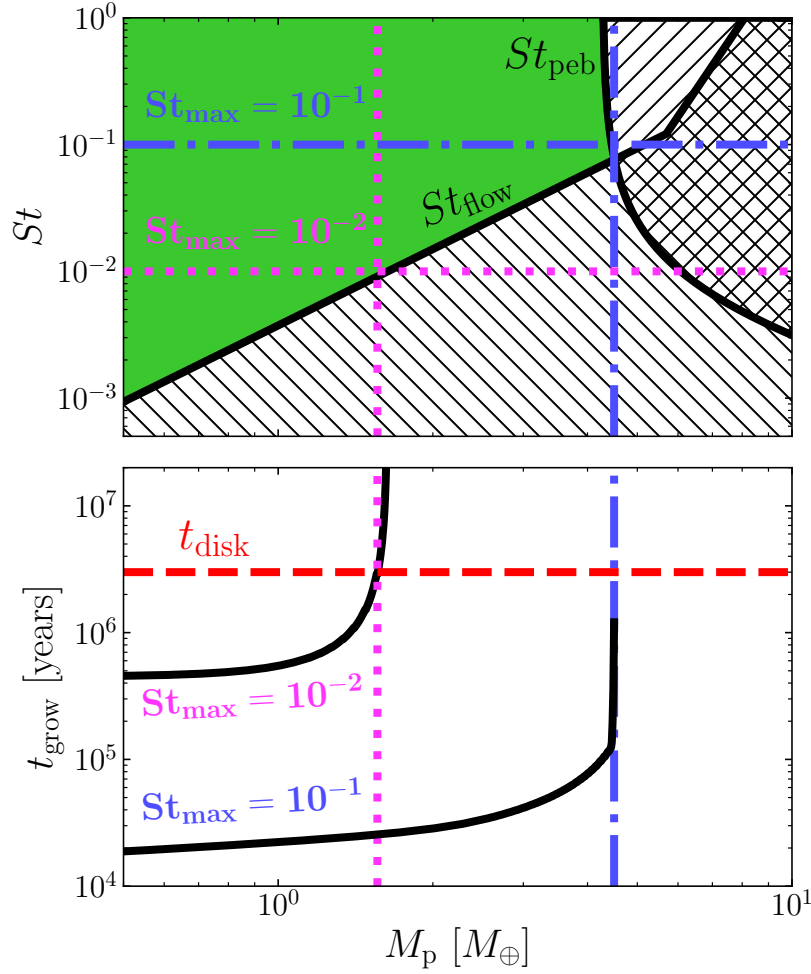


Figure 5.4: Halting planetary growth by a combination of pebble and flow isolation. Repeated style choices are the same as in Figure 5.1. The core is located at  $r = 0.278$  au, and the disk has  $\alpha = 10^{-3}$ , again as in Figure 5.1. *Upper Panel:* The range of particle sizes available for accretion as a function of planet mass. The hatched regions correspond to flow isolation (negatively sloped hatching) and pebble isolation (positively sloped hatching). The two patterns are overlaid when flow and pebble isolation act simultaneously. *Lower Panel:* Growth timescale of a core for the range of particle sizes depicted in the upper panel. Two different maximum particle sizes are considered:  $St_{\max} = 10^{-2}$  (upper solid line and dotted magenta line) and  $St_{\max} = 10^{-1}$  (lower solid line and dashdot blue line). For  $St_{\max} = 10^{-2}$ , flow isolation blocks all available particle sizes before pebble isolation kicks in, causing growth to rapidly slow as  $St_{\text{flow}} \rightarrow 10^{-2}$ , i.e. as the planet approaches the mass necessary to block particles of size  $St = 10^{-2}$ . The planet’s final mass is extremely well approximated by Equation (5.22), i.e. the situation is essentially the same as if flow isolation acted alone. For  $St_{\max} = 10^{-1}$ , pebble isolation begins blocking particles of size  $St_{\max}$  before flow isolation can. Because the allowed range of particle sizes is also being blocked from the bottom by flow isolation, growth rapidly slows once this occurs, with the planet ending its growth very close to  $M_{\text{peb,iso}}^{\dagger}$ .

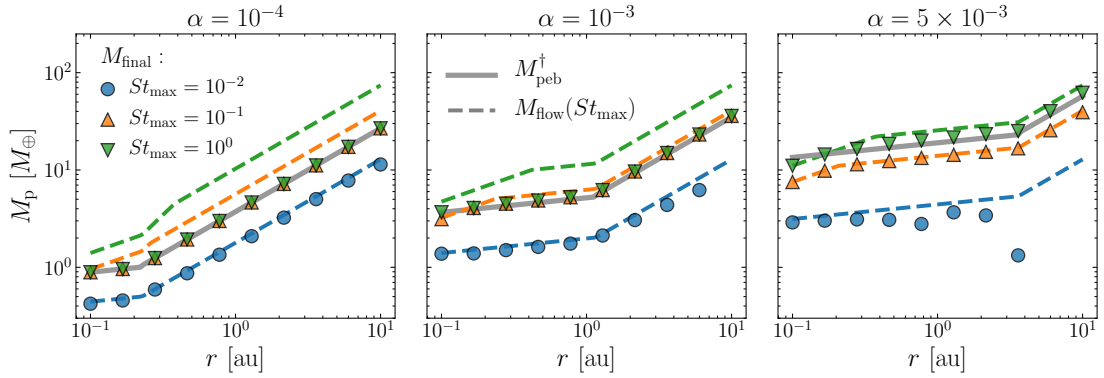


Figure 5.5: Final planet masses when pebble and flow isolation act in tandem, determined by numerically calculating the mass for which  $t_{\text{grow}} = t_{\text{disk}} = 3 \text{ Myr}$ . Blue, orange, and green refer to  $St_{\text{max}} = 10^{-2}$ ,  $10^{-1}$ , and  $10^0$  respectively. The solid gray line shows the value of  $M_{\text{peb,iso}}^{\dagger}$  (Equation 5.14), i.e. the mass needed to excite the gas to super-Keplerian velocities, the dashed lines show the value of  $M_{\text{flow}}(St_{\text{max}})$  (Equation 5.22 with  $f = 1.75$ ), and the symbols show the value of  $M_{\text{final}}(St_{\text{max}})$ , the numerically calculated final planet mass when pebble and flow isolation both operate, for a pebble size distribution given by Equation (5.8).

## 5.5 Halting growth by flow and pebble isolation

In this section we consider the planet’s final mass,  $M_{\text{final}}$ , if pebble accretion is halted by a combination of flow and pebble isolation. There are two cases to consider. If  $M_{\text{flow}} < M_{\text{peb,iso}}^{\dagger}$ , then all available particle sizes are cut off before pebble isolation kicks in. This case is essentially the same as just flow isolation acting alone, and  $M_{\text{final}} \approx M_{\text{flow}}$ . This case is illustrated Figure 5.4, for  $St_{\text{max}} = 10^{-2}$  (dotted magenta lines). On the other hand, if  $M_{\text{peb,iso}}^{\dagger} > M_{\text{flow}}$ , then pebble isolation will begin limiting the upper end of particle sizes while flow isolation limits accretion from the bottom. In this case, once  $M_{\text{p}} > M_{\text{peb,iso}}^{\dagger}$ , the upper end of the size distribution, containing the majority of the total pebble mass, as well as the most rapidly accreted particles, will be cut off. Because flow isolation is simultaneously limiting the lower end of the size

distribution, the planet’s growth will slow much more rapidly than in case where pebble isolation acts alone, generally resulting in a final mass that is close to  $M_{\text{peb,iso}}^\dagger$ . An example of this process is again shown in Figure 5.4, for  $St_{\text{max}} = 10^{-1}$  (dashdot blue line).

Thus, for planets undergoing pebble and flow isolation, the planet’s final mass is well approximated by

$$M_{\text{final}} \approx \min \left( M_{\text{peb,iso}}^\dagger, M_{\text{flow}} \right) \quad (5.23)$$

This approximation would break down if  $M_{\text{peb,iso}}^\dagger \ll M_{\text{flow}}$ , in which case large particles would be inhibited from accreting by pebble isolation before flow isolation had a substantial effect. However, as previously noted, the flow isolation mass cannot attain values much larger than the thermal mass, and the pebble isolation mass is within factors of 2-3 of the thermal mass as well. Thus, there does not exist a regime where  $M_{\text{peb,iso}} \ll M_{\text{flow}}$ , and Equation (5.23) should hold throughout parameter space.

In Figure 5.5 we plot the final planet mass for planets undergoing simultaneous pebble and flow isolation over our grid in  $r$ ,  $\alpha$ , and  $St_{\text{max}}$ . As can be seen in the figure, our numerically calculated results strongly validate our analytic approximation given in Equation (5.23). Note that this statement only applies generally when flow and pebble isolation work in tandem.

We could in principle improve on Equation (5.23) by using  $M_{\text{peb,iso}}(St_{\text{max}})$ , as given by Equation (5.15), as opposed to  $M_{\text{peb,iso}}^\dagger$ . From inspection of Figure 5.2 however, we see that the difference between  $M_{\text{peb,iso}}^\dagger$  and  $M_{\text{peb,iso}}$  is most pronounced for high  $\alpha$

and low  $St_{\max}$ , which is precisely where  $M_{\text{flow}}$  is small, and therefore tends to set the planet’s final mass. Thus, use of  $M_{\text{peb,iso}}^\dagger$  in Equation (5.23) as opposed to  $M_{\text{peb,iso}}$ , is still quite accurate, while also being a good deal simpler.

## 5.6 Summary and Conclusions

In this work, we contrasted the final masses of close-in, rocky planets undergoing pebble and flow isolation. For pebble isolation, we demonstrated that for a top-heavy pebble size distribution, the top-down manner in which the pressure bump blocks particles implies that the mass scale at which a growing core excites a super-Keplerian gas velocity can be a poor approximation for the planet’s final mass. The difference between the mass scale authors generally refer to as the “pebble isolation mass,” i.e. Equation (5.14), and the planet’s actual final mass is particularly pronounced for  $\alpha \gtrsim 10^{-3}$  and  $r \lesssim 1$  au. Unfortunately calculation of  $M_{\text{final}}$  in this regime does not admit a simple analytic solution, and thus must be done numerically when pebble isolation acts alone. We also comment that one needs to calculate whether a core undergoing pebble isolation is required to block a larger mass in pebbles than the core’s own mass. Because pebble isolation requires sequestering blocked pebbles in a pressure bump raised by the planet, this is likely an unstable situation.

In contrast, for flow isolation particles are blocked in a bottom-up manner. In this regime, we demonstrated that the planet’s final mass is well approximated by determining the mass such that  $St_{\text{flow}} = St_{\max}$ , which is typically referred to as the “flow isolation mass.” Finally, we showed that if flow and pebble isolation operate in tandem,

then we now have a simple analytic approximation for the planet’s final mass, namely  $M_{\text{final}} \approx \min \left( M_{\text{peb,iso}}^\dagger, M_{\text{flow}} \right)$ .

We have restricted our attention in this work to a simple power law size distribution for pebbles such that  $dN/ds \propto s^{-3.5}$ . While the detailed effect of changing the size distribution is complex, is not difficult to get a qualitative understanding of such a change. Modifying the size distribution to be more “bottom-heavy,” so that more of the mass is in the smaller size particles, would increase the importance of the growth effects discussed in Section 5.3. That is, the difference between  $M_{\text{final}}$  and  $M_{\text{peb,iso}}^\dagger$  would be enhanced, as the effect of blocking the largest size particles on the core’s growth timescale would be reduced. Conversely, a more top-heavy size distribution would lead to these growth effects having less importance, as the effect of blocking the largest particle sizes would be enhanced.

While in this work we have simply taken maximum particle sizes to be fixed, in reality there is interplay between the maximum particle size and the disk conditions. In particular, for the inner regions of disks, where particle sizes are likely set by fragmentation, hotter disks likely lead to smaller particle sizes due to increased collision velocities. In this case, the predictions between pebble isolation and flow isolation would be quite different – pebble isolation would lead to hot disks hosting much more massive planets, as higher temperatures both increase the thermal mass and decrease the particle size. Flow isolation, however, would lead to planets being more uniform in mass across different temperatures, as hotter disks increase the flow isolation mass, but smaller particles decrease it. This would also be expected if these two processes were working tandem.

A detailed analysis of these trends merits future work.

We further comment that flow and pebble isolation mass scales are also close to commonly quoted critical core masses for runaway gas accretion, particularly for low opacities (see e.g. [Lee et al. 2014](#)). Formation of systems of super-Earths via pebble accretion requires that any limiting mass scale for pebble accretion be lower than this critical core mass, otherwise pebble accretion will lead to gas giants instead of super-Earths. While a full discussion of this effect is beyond the scope of this work, we do comment that this interplay between the flow/pebble isolation mass and the critical core mass is likely an “all or nothing effect,” in the following sense: in the viscously heated inner regions of disks the flow and pebble isolation masses vary weakly with semi-major axis (e.g. for  $T \propto r^{-1}$ ,  $(H/r)$  is independent of  $r$ ), resulting in some systems forming multiple super-Earths (for  $M_{\text{iso}} < M_{\text{crit}}$ ), while others form multiple Jupiters (for  $M_{\text{iso}} > M_{\text{crit}}$ ). The latter configuration is likely unstable, causing dynamical upheaval and leading to some of the gas giants being ejected or scattered into the central star. This scenario of planet-planet scattering amongst multiple Jupiters has been shown to be consistent with the observed eccentricity distribution of extrasolar gas giants ([Frelikh et al. 2019](#), [Anderson et al. 2020](#)). Furthermore, initial studies show that this scenario can reproduce the observed ratio of super-Earth to gas giant systems for  $M_{\text{crit}} \approx 8.5 M_{\oplus}$  (Anderson et al., in prep). The simple arguments made here should be tested in the future by more sophisticated models that include e.g. time dependent evolution of the small body surface density and size distribution.

## Chapter 6

# How Consumption and Repulsion Set Planetary Gap Depths and the Final Masses of Gas Giants

### 6.1 Introduction

Annular gaps in protoplanetary discs are often attributed to embedded planets. The interpretation stems from the theory of satellite-disc interactions that successfully predicted the existence of shepherd moons in planetary rings (e.g., [Goldreich & Tremaine 1982](#)). Satellites in rings, and by analogy planets in discs, repel material away from their orbits as the waves they excite at Lindblad resonances dissipate and impart angular momentum to the ambient medium (see also [Goodman & Rafikov 2001](#); [Ginzburg & Sari 2018](#)). The repulsive, gap-forming planetary Lindblad torque competes against the

disc’s viscous torque which diffuses material back into the gap.

Most studies of protoplanetary disc gaps concentrate exclusively on the Lindblad and viscous torques (e.g., [Fung et al. 2014](#); [Kanagawa et al. 2015](#); [Zhang et al. 2018](#)) and neglect how gaps can also deepen because embedded planets consume local disc gas. Exceptions include, e.g., [Zhu et al. \(2011\)](#), [Dürmann & Kley \(2015, 2017\)](#), and [Muley et al. \(2019\)](#), whose numerical simulations of planet-disc interactions allow for both planetary accretion and planetary torques. Our aim here is to give an elementary and analytic accounting of both effects: to understand, for planets on fixed circular orbits, how Lindblad repulsion and planetary consumption combine to set gap depths. This is a two-way feedback problem—planetary accretion affects the gas density inside the gap, but the density inside the gap determines the rate of planetary accretion ([Ginzburg & Chiang 2019a, 2019b](#)). Accordingly we will calculate how gas giants grow in tandem with their deepening gaps. Much of our analytic framework is the same as that of [Tanigawa & Tanaka \(2016\)](#) and [Tanaka et al. \(2020\)](#), who used it to study nascent planets in viscous discs; we will explore both viscous and inviscid discs.

The problem of planetary accretion within disc gaps is also a global one insofar as a planet can accrete gas that is brought to it from afar, from regions outside the gap. Thus we will stage our calculations within circumstellar discs that transport mass across decades in radius. This opens up another form of feedback: in feeding the planet, the disc can have its entire surface density profile changed (e.g., [Lubow & D’Angelo 2006](#); [Zhu et al. 2011](#); [Owen 2016](#)).

Our work is organized as follows. In section 6.2 we describe how Lindblad

repulsion and planetary accretion of disc gas (“consumption”) work together to determine gap depths and surface density profiles of viscous circumstellar accretion discs. Our largely analytic considerations are supplemented with simple numerical experiments modeling planet-disc interactions and disc evolution in 1D (orbital radius). In section 6.2 we fix, for simplicity, the planet mass; in section 6.3, we allow the planet mass to grow freely and solve the full two-way feedback problem. In section 6.4, motivated by recent theoretical and observational developments, we consider discs that transport their mass not by viscous diffusion but rather by angular momentum losses from magnetized winds. For such inviscid, wind-driven discs, accretion is not diffusive but purely advective, and embedded planets carve out especially deep gaps in the absence of viscous backflow. We summarize and discuss the implications of our findings on gas giant masses and disc structure, including the structure of transitional discs, in section 6.5.

A simplified study such as ours will not capture important (and sometimes poorly understood) effects, among them planetary migration (e.g., [Kley & Nelson 2012](#); [Duffell et al. 2014](#); [Dürmann & Kley 2015, 2017](#); [Fung & Chiang 2017](#); [Kanagawa et al. 2018](#); [McNally et al. 2020](#)), eccentricity evolution (both of the planet and the disc; e.g., [Papaloizou et al. 2001](#); [Goldreich & Sari 2003](#); [Kley & Dirksen 2006](#); [Duffell & Chiang 2015](#); [Muley et al. 2019](#)), and the 3D dynamics of circumplanetary discs (e.g., [Fung et al. 2019](#)). Our goal is not so much to be realistic but to acquire some intuition about the interplay of Lindblad repulsion and planetary accretion, and to provide a baseline understanding that can guide the development and interpretation of more sophisticated

models. Where possible, we place our results in context with state-of-the-art numerical experiments in the literature (see in particular section 6.5).

## 6.2 Viscous discs: Surface Density Profiles at Fixed Planet Mass

We study how the surface densities of viscous accretion discs are shaped by repulsive planetary Lindblad torques in addition to planetary accretion of disc gas (“consumption”). Section 6.2.1 contains analytic considerations which are tested numerically in section 6.2.2. In these sections, while we allow the disc surface density to deplete by consumption, we do not simultaneously allow the planet’s mass to increase. This fixing of the planet’s mass is done for simplicity, to see how the planet affects the disc but not vice versa. In section 6.3, we free up the planet’s mass and allow two-way feedback between planet and disc.

### 6.2.1 Order-of-magnitude scalings

Consider an accreting planet embedded in a viscous disc. From Figure 6.1 we identify three disc surface densities:  $\Sigma_p$  at the orbital radius of the planet ( $r = r_p$ ),  $\Sigma_+$  exterior to the planet, and  $\Sigma_-$  interior to the planet. The planet depresses the local surface density because it is both consuming disc gas and repelling disc gas away by Lindblad torques. Our goal is to estimate the depth of the planet’s gap in relation to the inner and outer discs:  $\Sigma_p/\Sigma_-$  and  $\Sigma_p/\Sigma_+$ . We assume a steady state where the disc has viscously relaxed: given a viscosity  $\nu$ , the system age  $t$  is at least as long as the

diffusion time  $r^2/\nu$  across the disc. In addition,  $t$  is at most the planet growth timescale  $M_p/\dot{M}_p$ , so that we may consider the planet mass fixed at any given moment.

Mass flows steadily inward at rate  $\dot{M}_+$  from the outer disc. Part of this flow is accreted by the planet at rate  $\dot{M}_p$ , with the rest feeding the inner disc which accretes onto the star at rate  $\dot{M}_-$ . Dropping numerical pre-factors (these will be restored in later sections), we have

$$\begin{aligned}\dot{M}_+ &= \dot{M}_- + \dot{M}_p \\ \Sigma_+ \nu &\sim \Sigma_- \nu + \dot{M}_p \\ &\sim \Sigma_- \nu + A \Sigma_p.\end{aligned}\tag{6.1}$$

There are a number of assumptions embedded in these order-of-magnitude statements. For  $\dot{M}_+$  and  $\dot{M}_-$  we have substituted standard steady-state expressions for a disc of shear viscosity  $\nu$  (e.g., [Frank et al. 2002](#)), valid asymptotically at locations far from any mass sink ( $|r - r_p| \gtrsim r_p$ ). At the same time, the locations we are considering in the outer and inner discs are not so far from the planet that we need to account for spatial variations in  $\nu$ , which may change by order-unity factors over length scale  $r$ .

For the planet's accretion rate, we have assumed in (6.1) that it scales linearly with the local surface density  $\Sigma_p$  with proportionality constant  $A$ :

$$\dot{M}_p = A \Sigma_p.\tag{6.2}$$

This assumption is satisfied, e.g., by a planet accreting at the Bondi rate (e.g., [Frank](#)

et al. 2002):

$$\begin{aligned} \dot{M}_{\text{p,Bondi}} &\sim \rho_{\text{p}} c_{\text{s}} R_{\text{B}}^2 \\ &\sim \frac{\Sigma_{\text{p}}}{H} c_{\text{s}} \left( \frac{GM_{\text{p}}}{c_{\text{s}}^2} \right)^2 \end{aligned} \quad (6.3)$$

where  $\rho_{\text{p}}$  is the disc midplane mass density near the planet,  $c_{\text{s}}$  is the disc sound speed,  $R_{\text{B}} = GM_{\text{p}}/c_{\text{s}}^2$  is the Bondi radius,  $H = c_{\text{s}}/\Omega$  is the disc scale height,  $\Omega$  is the orbital angular frequency, and  $G$  is the gravitational constant. Then

$$A_{\text{Bondi}} \sim \frac{m^2}{h^4} \Omega r^2 \quad (6.4)$$

where  $m \equiv M_{\text{p}}/M_{\star}$  is the planet-to-star mass ratio, and  $h \equiv H/r$  is the disc aspect ratio. Ginzburg & Chiang (2019a, their section 1.1) discusses how Bondi accretion may be valid for “sub-thermal” planets whose masses are less than

$$M_{\text{thermal}} \sim h^3 M_{\star} \quad (6.5)$$

the mass for which the Bondi radius  $R_{\text{B}}$ , the Hill radius  $R_{\text{H}} \sim m^{1/3}r$ , and the disc scale height  $H$  are all equal. A sub-thermal planet has  $R_{\text{B}} < R_{\text{H}} < H$ —its gravitational sphere of influence has radius  $R_{\text{B}}$ , set by gravity and thermal pressure—and should accrete at the Bondi rate, isotropically from the all-surrounding disc (Ginzburg & Chiang 2019a; see also fig. 1 of Tanigawa & Tanaka 2016 for evidence supporting the Bondi  $m^2$  scaling, taken from the 3D simulations of D’Angelo et al. 2003). For a

super-thermal planet having  $M > M_{\text{thermal}}$ , the hierarchy of length scales reverses so that  $R_{\text{B}} > R_{\text{H}} > H$ —the planet’s sphere of influence, now set by gravitational tides at radius  $R_{\text{H}}$ , “pops out” of the disc—and arguably the planet accretes in a more 2D fashion, presenting a cross-section of order  $R_{\text{H}}H$  to disc gas that shears by at a velocity  $\Omega R_{\text{H}}$ . The corresponding “Hill rate” for consumption is then

$$\dot{M}_{\text{p,Hill}} \sim \rho_{\text{p}} \times R_{\text{H}}H \times \Omega R_{\text{H}} \sim \Sigma_{\text{p}} R_{\text{H}}^2 \Omega \quad (6.6)$$

whence

$$A_{\text{Hill}} \sim m^{2/3} \Omega r^2. \quad (6.7)$$

A Hill-based scaling for consumption is commonly used in 2D disc-planet hydrodynamical simulations (e.g., [Zhu et al. 2011](#); [Dürmann & Kley 2015, 2017](#); [Muley et al. 2019](#)). We have assumed in writing the above that the planet masses are large enough for accretion to be hydrodynamically-limited as opposed to cooling-limited ([Ginzburg & Chiang 2019a](#), cf. their fig. 1).

In this paper we will calculate the growth of planets from sub-thermal to super-thermal masses, so will have occasion to use both  $A_{\text{Bondi}}$  and  $A_{\text{Hill}}$ . We recognize that the 2D picture motivating our Hill scaling may not be correct; in 3D, meridional flows from gap walls can feed the planet along its poles ([Szulágyi et al. 2014](#); [Morbidelli et al. 2014](#); [Fung & Chiang 2016](#)). Relatedly, the disc density scales with height  $z$  above the midplane as  $\exp[-z^2/(2H^2)]$  (for an isothermal atmosphere), which implies that a considerable fraction of the disc mass resides between  $|z| = H$  and  $2H$ ; accordingly, the

planet does not pop out of the disc until it is strongly super-thermal, i.e., until  $m$  is a large multiple of  $h^3$  (cf. equation 6.5). An isotropic version of super-thermal accretion controlled by the Hill sphere gives  $\dot{M}_{\text{p,Hill,iso}} \sim \rho_{\text{p}} \times R_{\text{H}}^2 \times \Omega R_{\text{H}}$  or  $A_{\text{Hill,iso}} \sim m\Omega r^2/h$ . Yet another prescription for accretion is given by [Tanigawa & Watanabe \(2002\)](#):  $A_{\text{TW}} \sim m^{4/3}\Omega r^2/h^2$ , an empirical relation based on their 2D numerical simulations (see also [Tanigawa & Tanaka 2016](#)). To the extent that these alternative scalings increase with  $m$  more steeply than our nominal  $A_{\text{Hill}} \propto m^{2/3}$ , whatever final super-thermal planet masses we derive should be lower limits (see sections 6.2.2 and 6.5).

Momentum conservation provides another relation between the surface densities. It is easiest to write down downstream of the planet in the accretion flow (in the inner disc), as the flow of momentum upstream (in the outer disc) is complicated by the mass sink presented by the planet. In the inner disc there are no sinks of mass or momentum, only a steady transmission of mass inward and angular momentum outward (assuming, as we do throughout this paper, a non-migrating planet; see section 6.5 for pointers to the migrating case). The rate at which angular momentum is carried viscously outward by the inner disc equals the viscous transport rate local to the planet, plus the repulsive Lindblad torque exerted by the planet on the disc:<sup>21</sup>

$$\Sigma_{-}\nu\Omega r^2 \sim \Sigma_{\text{p}}\nu\Omega r^2 + B\Sigma_{\text{p}}\Omega r^2 \quad (6.8)$$

with

$$B \sim \frac{m^2}{h^3}\Omega r^2 \quad (6.9)$$

---

<sup>21</sup>The planet excites waves in the inner disc which carry negative angular momentum inward. This is equivalent to transmitting positive angular momentum outward.

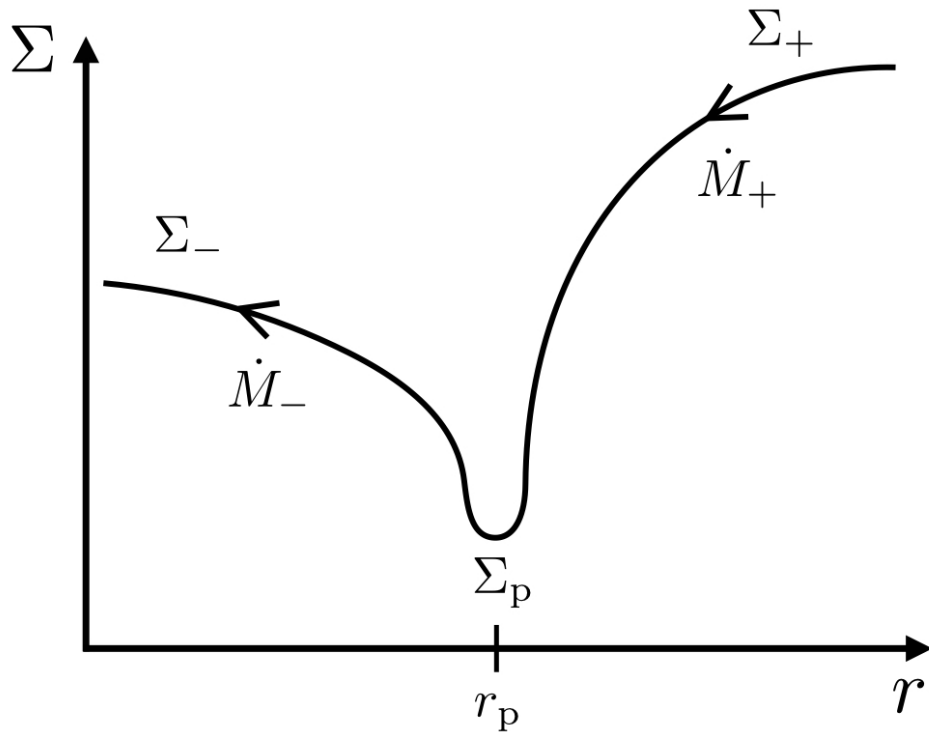


Figure 6.1: Sketch of the disc surface density and accretion flow in the vicinity of a planet. The planet is located at orbital radius  $r_p$ , inside a gap having surface density  $\Sigma_p$ . At  $r > r_p$ , the disc surface density is  $\Sigma_+$  and mass accretes inward at rate  $\dot{M}_+$ . Downstream of the planet, at  $r < r_p$ , the corresponding surface density and accretion rate are  $\Sigma_-$  and  $\dot{M}_-$ , respectively. The difference  $\dot{M}_+ - \dot{M}_-$  is the accretion rate onto the planet  $\dot{M}_p$ .

given by the standard [Goldreich & Tremaine \(1980\)](#) linear Lindblad torque, integrating the effects of all Lindblad resonances up to the torque cutoff. A similar statement to (6.8), dropping the viscous term local to the planet, was made by [Fung et al. \(2014\)](#). Given  $B$ , (6.8) can be solved for the gap contrast with the inner disc:

$$\frac{\Sigma_p}{\Sigma_-} \sim \frac{1}{1 + B/\nu} \quad (6.10)$$

(see also [Duffell & MacFadyen 2013](#); [Kanagawa et al. 2015](#); [Ginzburg & Sari 2018](#)). Combining mass conservation (6.1) with momentum conservation (6.8) yields the gap contrast with the outer disc:

$$\frac{\Sigma_p}{\Sigma_+} \sim \frac{1}{1 + (A + B)/\nu}. \quad (6.11)$$

An equivalent equation is derived by [Tanigawa & Tanaka \(2016, their appendix B\)](#) and [Tanaka et al. \(2020, their equation 26\)](#). Equations (6.10) and (6.11) inform us that planetary consumption ( $A \neq 0$ ) leads to asymmetric gap contrasts: a deeper gap relative to the outer disc than to the inner disc. The outer gap contrast is the more important insofar as the outer disc controls surface densities everywhere downstream; in other words,  $\Sigma_+$  is the independent variable while  $\Sigma_p$  and  $\Sigma_-$  are dependent variables. Equation (6.11) states that, given  $\Sigma_+$ , the effects of accretion ( $A$ ) and repulsion ( $B$ ) in setting the gap depth  $\Sigma_p$  are additive (not multiplicative). If  $A > B$ , then consumption dominates.

For  $A = A_{\text{Bondi}}$  and  $B$  given by (6.9),

$$A_{\text{Bondi}}/B \sim 1/h > 1 \quad (6.12)$$

and consumption dominates repulsion in setting the gap depth, independent of planet mass in the sub-thermal regime. On the other hand, for  $A = A_{\text{Hill}}$ ,

$$A_{\text{Hill}}/B \sim m^{-4/3}h^3 \quad (6.13)$$

which says that for super-thermal planets that are massive enough, repulsion dominates consumption ( $A_{\text{Hill}}/B < 1$ ).

We may also solve for the relative accretion rates:

$$\frac{\dot{M}_p}{\dot{M}_+} \sim \frac{A\Sigma_p}{\Sigma_+\nu} \sim \frac{A/\nu}{1 + (A+B)/\nu} \quad (6.14)$$

$$\frac{\dot{M}_-}{\dot{M}_+} \sim \frac{\Sigma_-}{\Sigma_+} \sim \frac{1 + B/\nu}{1 + (A+B)/\nu}. \quad (6.15)$$

A couple example limiting cases of (6.14) and (6.15) are as follows. If we take  $A/B = A_{\text{Bondi}}/B \sim 1/h > 1$  and further assume that  $B/\nu > 1$  so that the inner gap contrast is significant (equation 6.10), we find

$$\frac{\dot{M}_p}{\dot{M}_+} \sim 1 - B/A_{\text{Bondi}} \sim 1 - h \quad (6.16)$$

$$\frac{\dot{M}_-}{\dot{M}_+} \sim B/A_{\text{Bondi}} \sim h \quad (6.17)$$

which says that the planet consumes nearly all of the mass supplied to it by the outer disc, leaving behind a fraction  $h$  to feed the inner disc. If instead we take  $A/B = A_{\text{Hill}}/B$  and further assume  $B > A_{\text{Hill}} > \nu$  (repulsion-limited and deep gap), then

$$\frac{\dot{M}_{\text{p}}}{\dot{M}_{+}} \sim A_{\text{Hill}}/B \sim m^{-4/3}h^3 < 1 \quad (6.18)$$

$$\frac{\dot{M}_{-}}{\dot{M}_{+}} \sim 1 - A_{\text{Hill}}/B \sim 1 - m^{-4/3}h^3 \quad (6.19)$$

and the planet diverts only a small fraction,  $A_{\text{Hill}}/B$ , of the disc accretion flow onto itself.

The order-of-magnitude considerations presented here are firmed up in subsequent sections, including in Appendix B.1, where we derive in greater analytic detail the surface density profile and mass accretion rates, drawing from [Lubow & D'Angelo \(2006\)](#).

## 6.2.2 Numerical simulations

### Procedure

We solve numerically for the 1D evolution of a viscously shearing disc (e.g., [Frank et al. 2002](#)) with a planetary mass sink. The governing equation for the surface density  $\Sigma(r, t)$  in cylindrical radius  $r$  and time  $t$  reads

$$\frac{\partial \Sigma}{\partial t} = \frac{3}{r} \frac{\partial}{\partial r} \left[ r^{1/2} \frac{\partial}{\partial r} \left( r^{1/2} \nu \Sigma \right) \right] - \frac{\dot{M}_{\text{p}}(t)}{2\pi r} \delta(r - r_{\text{p}}) \quad (6.20)$$

where  $\delta$  is the Dirac delta function and  $r_p$  is the radial position of the planet (held fixed). For the viscosity  $\nu$  we employ the [Shakura & Sunyaev \(1973\)](#)  $\alpha$ -prescription:

$$\nu = \alpha c_s^2 / \Omega = \alpha h^2 \Omega r^2 \quad (6.21)$$

where  $\Omega$  is the Keplerian orbital frequency around a  $1 M_\odot$  star,  $c_s = \sqrt{k_B T / \bar{m}}$ , the disc temperature is  $T = 200 \text{ K} (r/\text{au})^{-1/2}$ ,  $k_B$  is Boltzmann's constant,  $\bar{m} = 2m_H$  is the mean molecular mass,  $m_H$  is the mass of the hydrogen atom, and

$$h \equiv H/r = c_s / (\Omega r) \simeq 0.054 \left( \frac{r}{10 \text{ au}} \right)^{1/4}. \quad (6.22)$$

We fix  $\alpha = 10^{-3}$  for the results in this section. Given these inputs,  $\nu = \nu(r) \propto r^1$ .

Apart from the mass sink, equation (6.20), which combines the 1D mass and momentum equations, is identical to the diffusion equation governing an isolated viscous disc as derived by [Lynden-Bell & Pringle \(1974\)](#). What is missing is an explicit accounting for the repulsive Lindblad torque exerted by the planet. Many studies include the planetary torque by introducing, into the momentum equation, a term for the torque per unit radius that scales as  $\text{sgn}(x)/x^4$ , where  $x \equiv r - r_p$  (e.g., [Lin & Papaloizou 1986](#); [Lubow & D'Angelo 2006](#)). Compared against 2D hydrodynamical simulations, this  $1/x^4$  prescription has been shown in 1D studies to reproduce the azimuthally averaged surface density profiles of repulsive gaps near their peripheries (at  $x \gtrsim 4H$ ) but not near gap centers (at  $x \lesssim 4H$ ; [Fung et al. 2014](#), their section 4.3). In particular the 1D torque density prescription, which assumes angular momentum is deposited locally

and neglects wave propagation, fails to recover the flat bottoms of gaps and the surface densities there (cf. [Ginzburg & Sari 2018](#) who use the [Goodman & Rafikov 2001](#) wave steepening theory to lift these assumptions). This shortcoming of the  $1/x^4$  prescription means that it cannot be used to compute the planetary accretion rate  $\dot{M}_p$ , which depends on knowing the gas density in the planet’s immediate vicinity.

What we do instead to include the repulsive Lindblad torque when calculating planetary accretion is as follows. Within the radial grid cell at  $r = r_p$  of width  $\Delta r_p$ , the surface density is reduced after every timestep  $\Delta t$  according to

$$\Sigma(r_p, t + \Delta t) = \Sigma(r_p, t) - \frac{\dot{M}_p(t)\Delta t}{2\pi r_p \Delta r_p} \quad (\text{simulation}) \quad (6.23)$$

where the label “simulation” reminds us that this equation applies to the numerical simulation only and should not be used outside of that context. It is in evaluating  $\dot{M}_p$  that we include, in a “sub-grid” manner, the repulsive Lindblad gap:

$$\dot{M}_p(t) = A \times \frac{\Sigma(r_p, t)}{1 + B/\nu} \quad (\text{simulation}). \quad (6.24)$$

What equation (6.24) says is that the disc surface density the planet actually “sees” when consuming local gas is lower than the numerically computed “grid-level” surface density  $\Sigma(r_p, t)$ —lower by the Lindblad reduction factor  $1/(1+B/\nu)$  (equation 6.10). In other words, repulsion is encoded/enforced at a sub-grid level. We stress that equation (6.24) is used only in our numerical simulation to capture repulsion and should not be used outside of it; contrast (6.24) with, e.g., (6.14), and note that  $\Sigma(r_p, t)$  is notation

specific to the simulation and should not be confused with  $\Sigma_p$ , the actual surface density at the planet’s position.

Our numerical procedure captures the gap depth but not the gap width, as the sub-grid modification is restricted (for simplicity) to the grid cell containing the planet. We consider this crude scheme acceptable insofar as we are more interested in the gross magnitudes for  $\Sigma_p/\Sigma_+$  and  $\Sigma_p/\Sigma_-$  and less interested in the precise surface density gradients. An untested assumption underlying our numerical procedure—and in our steady-state analytics—is that material flows radially through the gap at whatever velocity  $u_r$  is needed to maintain continuity, i.e., to enforce  $\dot{M}_- = \dot{M}_+ - \dot{M}_p = -2\pi\Sigma_p r_p u_r$  (where  $u_r < 0$  for accretion toward the star). We cannot test this assumption as we do not resolve the flow dynamics inside the gap. We will call out this assumption in the results to follow (sections 6.3.1 and 6.4.4). Also, as a reminder, we note that while the surface density changes as a result of consumption, in this subsection we fix  $M_p$ , i.e., we do not update  $M_p$  using  $\dot{M}_p$  (this assumption is relaxed in section 6.3).

In evaluating the consumption and repulsion coefficients  $A$  and  $B$ , we make choices similar to those in our earlier order-of-magnitude analysis (section 6.2.1), except that now we include numerical pre-factors for greater precision:

$$A_{\text{Bondi}} = 0.5 \Omega r^2 \frac{m^2}{h^4} \quad \text{for sub-thermal } m \leq 3h^3 \quad (6.25)$$

$$A_{\text{Hill}} = 2.2 \Omega r^2 m^{2/3} \quad \text{for super-thermal } m > 3h^3 \quad (6.26)$$

$$B = 0.04 \Omega r^2 \frac{m^2}{h^3} \quad (6.27)$$

where all quantities are evaluated at  $r_p$ . The pre-factor of 0.5 in equation (6.25) is

calibrated using 3D simulation results for  $\dot{M}_p$  from D’Angelo et al. (2003; these are reprinted in fig. 1 of Tanigawa & Tanaka 2016). The coefficient of 2.2 in equation (6.26) follows from requiring that (6.25) match (6.26) at the thermal mass

$$M_{\text{thermal}} \equiv 3h^3 M_\star \simeq 0.5 \left( \frac{h}{0.054} \right)^3 M_J \quad (6.28)$$

defined by equating  $H$  with  $R_H = (m/3)^{1/3} r$ , with  $M_J$  the mass of Jupiter. Equation (6.27) is taken from the numerical 2D simulations of Kanagawa et al. (2015, see also Duffell & MacFadyen 2013 and Duffell 2015 who report similar results).

Note further that the expressions we used in section 6.2.1 for the steady disc accretion rates  $\dot{M}_+$  and  $\dot{M}_-$  should be amended with the numerical pre-factor  $3\pi$ , i.e.,  $\dot{M}_+ = 3\pi \Sigma_+ \nu$  and similarly for  $\dot{M}_-$  (e.g., Frank et al. 2002). This correction is already embedded in the diffusion equation (6.20). Including this pre-factor in equation (6.1) implies that  $A$  should be replaced with  $A/(3\pi)$  in equations (6.11)–(6.19). Putting it all together, we have

$$\frac{A_{\text{Bondi}}}{3\pi B} \simeq \frac{1.3}{h} > 1 \quad (6.29)$$

implying that consumption always dominates for sub-thermal masses. Furthermore,

$$\frac{A_{\text{Hill}}}{3\pi B} \simeq 5.5 m^{-4/3} h^3 \simeq 1.0 \left( \frac{m}{5 \times 10^{-3}} \right)^{-4/3} \left( \frac{h}{0.054} \right)^3 \quad (6.30)$$

implying that repulsion dominates for super-thermal masses exceeding a “repulsion mass”

$$\begin{aligned}
M_{\text{repulsion,visc}} &\simeq 3.6h^{9/4}M_{\star} \\
&\simeq 5.3M_{\text{J}} \left( \frac{h}{0.054} \right)^{9/4} \simeq 5.3M_{\text{J}} \left( \frac{r}{10 \text{ au}} \right)^{9/16} \\
&\simeq 1.2h^{-3/4}M_{\text{thermal}} \simeq 11 \left( \frac{0.054}{h} \right)^{3/4} M_{\text{thermal}}. \tag{6.31}
\end{aligned}$$

For  $M < M_{\text{repulsion,visc}}$ , consumption dominates and the planet accretes nearly all the disc gas that tries to diffuse past; for  $M > M_{\text{repulsion,visc}}$ , repulsion dominates and the planet’s accretion rate falls below the disc accretion rate. The above expression for  $M_{\text{repulsion,visc}}$  depends on our assumption that planetary accretion follows our Hill scaling  $A_{\text{Hill}} \propto m^{2/3}$  for super-thermal masses. As discussed in section 6.2.1, this assumption might not be correct. If instead of  $A_{\text{Hill}}$  we use  $A_{\text{TW}} = 0.29 \Omega r^2 m^{4/3}/h^2$  as found from the 2D numerical simulations of [Tanigawa & Watanabe \(2002\)](#), we would find  $A_{\text{TW}}/(3\pi B) \simeq 4 (M_{\text{p}}/M_{\text{J}})^{-2/3}(h/0.054)$ , in which case the mass above which repulsion dominates would change to  $M_{\text{repulsion,visc,TW}} \simeq 9 M_{\text{J}} [r/(10 \text{ au})]^{3/8}$ . This is nearly twice the value of  $M_{\text{repulsion,visc}}$  given by (6.31), and would imply a more extended consumption-dominated growth phase. Insofar as our nominal model adopts  $A_{\text{Hill}}$  which leads to a more limited consumption-dominated growth phase, the planet masses we compute for our viscous disc model are lower limits.

So far we have described how we compute the mass sink term, which includes the sub-grid Lindblad torque, in equation (6.20). The remaining diffusive term is solved in a standard way. We first change variables to  $z \equiv r^{1/2}\nu\Sigma$  and  $y \equiv 2r^{1/2}$  so that the

diffusive portion of equation (6.20) reads

$$\frac{\partial z}{\partial t} = \frac{12\nu}{y^2} \frac{\partial^2 z}{\partial y^2} \quad (6.32)$$

with non-constant diffusion coefficient  $12\nu/y^2$ . We solve equation (6.32) as an initial value problem using an implicit scheme (e.g., [Press et al. 2007](#)). Our computation grid extends from an inner boundary of  $r_{\text{in}} = 0.01$  au to an outer boundary of  $r_{\text{out}} = 500$  au, and is divided into 300 cells that are uniform in  $\Delta y$ . We fix the timestep  $\Delta t = 10^{-4} t_{\nu, \text{p}}$ , where  $t_{\nu, \text{p}} \equiv r_{\text{p}}^2/\nu(r_{\text{p}}) \simeq 1.7$  Myr is the viscous diffusion timescale at the planet's orbital radius of  $r_{\text{p}} = 10$  au (where  $h \simeq 0.054$ ). Recognizing that our transformed variable  $z$  is proportional to the viscous torque  $2\pi\nu\Sigma r^3 d\Omega/dr \propto r^{1/2}\nu\Sigma$ , we use a torque-free inner boundary condition,  $z(r_{\text{in}}) = 0$ , as would be the case if the disc were truncated by a co-rotating stellar magnetosphere (shearless boundary layer). At the outer boundary we assume the torque gradient  $\partial z/\partial r(r_{\text{out}}) = 0$ . Neither boundary condition is critical as we are interested in the flow near the planet, away from either boundary.

The surface density of the disc is initialized with the similarity solution for an isolated viscous accretion disc with  $\nu \propto r^1$  ([Lynden-Bell & Pringle 1974](#); [Hartmann et al. 1998](#)):

$$\Sigma(r, 0) = \frac{M_{\text{disc}}}{2\pi r_1^2} \frac{r_1}{r} e^{-r/r_1} \quad (\text{simulation}) \quad (6.33)$$

where  $M_{\text{disc}} = 15.5 M_{\text{J}} \simeq 0.015 M_{\odot}$  is the initial mass of the disc and  $r_1 = 30$  au is a characteristic disc radius (where the diffusion time is  $r_1^2/\nu \simeq 5$  Myr). We consider

two fixed planet masses,  $M_p = 0.3 M_J < M_{\text{thermal}}$  and  $M_p = 10 M_J > M_{\text{thermal}}$ . Planet masses that freely grow are modeled in section 6.3.

At every timestep, we first advance  $\Sigma(r, t) \rightarrow \Sigma(r, t + \Delta t)$  for all  $r$  according to (6.32) using the implicit solver, and then we advance  $\Sigma(r_p, t) \rightarrow \Sigma(r_p, t + \Delta t)$  using (6.23) and (6.24). This procedure is repeated until the disc is evolved for several  $t_{\nu, p}$ , long enough for the disc near the planet to achieve a quasi-steady state.

## Results

Figure 6.2 shows, for  $M_p = \{0.3, 10\}M_J$ , the numerically computed surface density profiles  $\Sigma(r)$  at  $t = 3t_{\nu, p} \simeq 5$  Myr. Overlaid for comparison is our numerical solution without a planet, which we have verified matches the analytic time-dependent similarity solution of Lynden-Bell & Pringle (1974). For the case with a planet, rather than plot at face value the numerically computed (grid-level)  $\Sigma(r_p, t)$ , we plot that value multiplied by the sub-grid reduction factor  $1/(1 + B/\nu)$ —this is the “true” value for  $\Sigma_p$  that incorporates the repulsive Lindblad torque. Since this sub-grid correction factor is applied to only a single grid point, we cannot resolve gap widths; our focus instead is on the gross gap contrasts  $\Sigma_p/\Sigma_+$  and  $\Sigma_p/\Sigma_-$ .

The surface density profiles shown in Figure 6.2 conform to the analytic considerations of section 6.2.1. For  $M_p = 0.3 M_J$  (top panel), conditions are consumption-limited:  $\Sigma_+/\Sigma_p \sim A_{\text{Bondi}}/(3\pi\nu)$  (equation 6.11 in the limit  $A_{\text{Bondi}}/(3\pi) > B > \nu$ ) and the surface density of the entire interior disc is depressed relative to the same disc without a planet by a factor of  $\Sigma_+/\Sigma_- \sim \dot{M}_+/\dot{M}_- \simeq A_{\text{Bondi}}/(3\pi B)$  (equations 6.15 and 6.17). By comparison, for  $M_p = 10 M_J$  (bottom panel), the gap is more nearly

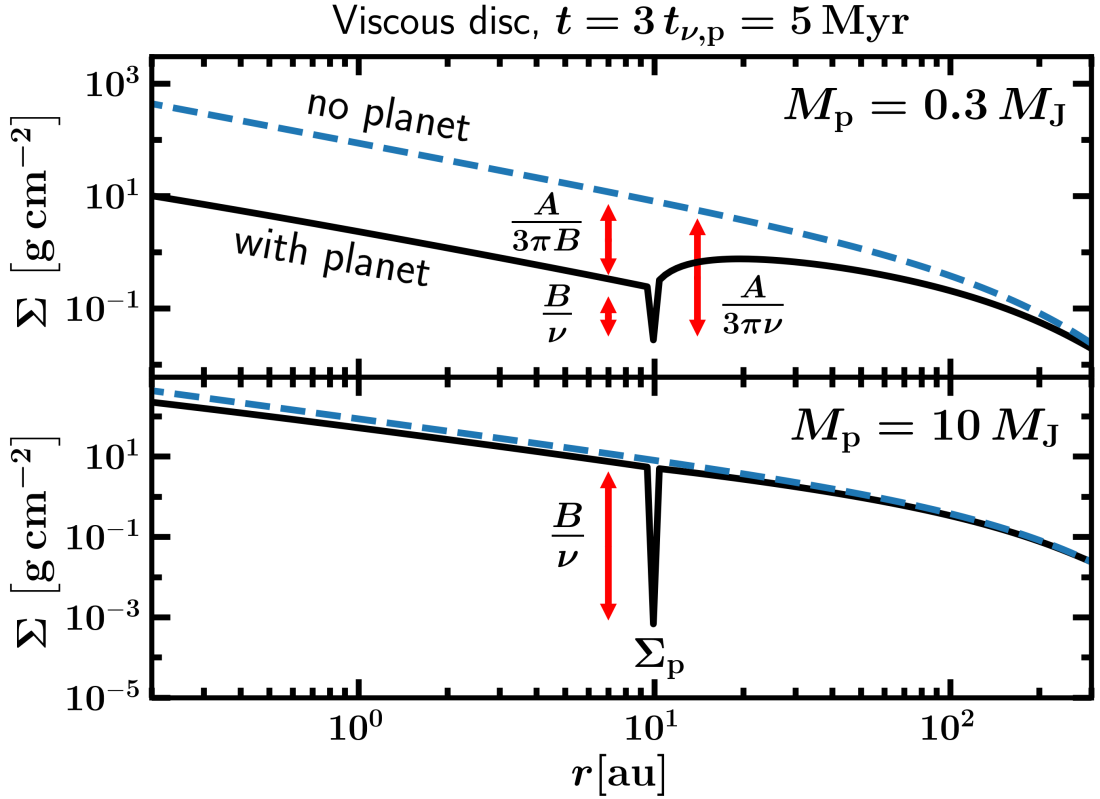


Figure 6.2: How the surface density profile of a viscous disc responds to a planet that both consumes disc gas, and repels gas away by Lindblad torques. Surface densities are calculated from our 1D numerical simulation of a planet of fixed mass, either  $M_p = 0.3 M_J$  (top panel) or  $M_p = 10 M_J$  (bottom panel), at  $t = 3t_{\nu,p}$  when the disc near the planet at  $r_p = 10 \text{ au}$  has viscously relaxed. When computing the planetary accretion rate  $\dot{M}_p$ , the gap is modeled as a single cell whose “true” surface density equals the grid-level  $\Sigma$  lowered by a factor of  $(1 + B/\nu) \simeq B/\nu$ ; plotted here are the true sub-grid values  $\Sigma_p$ . Accordingly, the planet’s gap is not spatially resolved and its width should not be taken literally from this figure. Red double-tipped arrows have lengths equal to their associated variables in dex, and demonstrate good agreement between numerics and analytics. The planet of mass  $M_p = 0.3 M_J$ , accreting at the Bondi rate, creates an asymmetric gap, with the inner disc surface density  $\Sigma_-$  lower than the outer  $\Sigma_+$  by  $A_{\text{Bondi}}/(3\pi B) > 1$ ; conditions are always consumption-dominated for Bondi accretion and  $B$  as given by (6.27). The planet of mass  $M_p = 10 M_J$ , accreting at the Hill rate, creates a symmetric gap where  $\Sigma_-/\Sigma_+ \sim 1$ ; conditions here are repulsion-dominated as  $M_p > M_{\text{repulsion,visc}}$  (equation 6.31).

symmetric,  $\Sigma_+/\Sigma_- \sim 1$  (equations 6.15 and 6.19), and deep and repulsion-dominated,  $\Sigma_+/\Sigma_p \sim B/\nu$  (equation 6.11 in the limit  $B > A_{\text{Hill}}/(3\pi) > \nu$ ).

So long as consumption is stronger than repulsion in the sense that  $A/(3\pi) > B$ —a condition that we have shown always obtains for sub-thermal masses accreting at the Bondi rate, and for sufficiently low-mass super-thermal masses accreting at the Hill rate ( $M < M_{\text{repulsion,visc}}$ )—repulsion does not much affect the gap surface density  $\Sigma_p$ . Figure 6.3 demonstrates that different choices for the repulsion coefficient  $B = \{10^{-2}, 10^{-3}, 10^{-4}\} \times A_{\text{Bondi}}$  all yield practically the same  $\Sigma_p$  (when corrected to the true sub-grid value) relative to  $\Sigma_+$ . What repulsion, in combination with consumption, affects instead is how much gas leaks past the planet into the inner disc: the three different values for  $B$  in Figure 6.3 yield three inner disc surface densities that, from equation (6.15), scale as  $\Sigma_-/\Sigma_+ \simeq (1 + B/\nu)/[1 + A_{\text{Bondi}}/(3\pi\nu)]$ . This factor scales as  $3\pi B/A_{\text{Bondi}}$  when  $A_{\text{Bondi}}/(3\pi) > B > \nu$  (dot-dashed and dotted lines), and as  $1/[1 + A_{\text{Bondi}}/(3\pi\nu)]$  when  $B < \nu$  (solid line; in this limit repulsion has no effect).

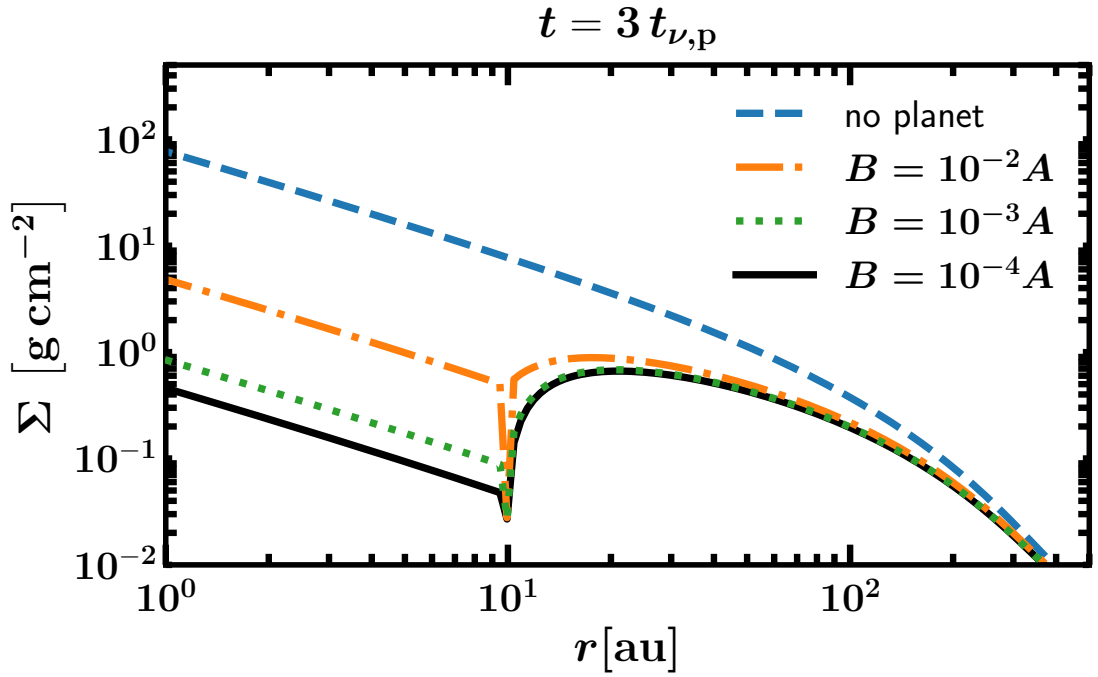


Figure 6.3: Same as Figure 6.2 for the case  $M_p = 0.3M_J$ , but for different choices of  $B$  scaled to  $A_{\text{Bondi}}$ . As long as  $A_{\text{Bondi}}/(3\pi) > B$ , the planet's gap is consumption-dominated and its surface density  $\Sigma_p$  is independent of the repulsion coefficient  $B$ . The depression of the inner disc relative to the outer disc is, however, sensitive to  $B$  for  $B > \nu$ ;  $\Sigma_-/\Sigma_+ \simeq (1 + B/\nu)/[A_{\text{Bondi}}/(3\pi\nu)]$ .

## 6.3 Viscous discs: Gas Giant Growth

### 6.3.1 Numerical calculation at $r_p = 10$ au

We now relax the assumption that the planet mass remains fixed, and at every timestep update  $M_p$  according to  $\dot{M}_p$  computed using equation (6.24). Our numerical procedure is unchanged from section 6.2.2 except that we initialize the planet mass at  $M_p(0) = 0.1 M_J$  and allow it to grow. For our nominal disc parameters ( $\alpha = 10^{-3}$ ,  $h = 0.054$  at  $r_p = 10$  au), a starting planet mass of  $0.1 M_J$  ( $m \simeq 0.95 \times 10^{-4}$ ) implies that, initially,  $A = A_{\text{Bondi}}$ ,  $A_{\text{Bondi}}/(3\pi B) \simeq 1.3/h \simeq 24$  (a consumption-dominated gap),  $A_{\text{Bondi}}/(3\pi\nu) \simeq 19$  (a strong outer gap contrast), and  $B/\nu \simeq 0.79$  (a weak inner gap contrast).

Figure 6.4 shows two snapshots in time of  $\Sigma(r)$  and the disc mass flow rate  $\dot{M}_{\text{disc}}(r) = -2\pi\Sigma r u_r$ , where

$$u_r = -\frac{3}{\Sigma r^{1/2}} \frac{\partial}{\partial r} \left( \nu \Sigma r^{1/2} \right) \quad (6.34)$$

is the gas radial velocity (e.g., [Frank et al. 2002](#)) evaluated numerically from our solution for  $\Sigma$  (omitting the single-point discontinuity at  $r = r_p$ ). Note that  $\dot{M}_{\text{disc}} > 0$  indicates inward mass transport, toward the star. The planet accretes predominantly from the outer disc, notwithstanding a small contribution from the inner disc before the disc has viscously relaxed; this early-time contribution can be seen at  $t = 0.3 t_{\nu,p}$  when  $\dot{M}_{\text{disc}} < 0$  from  $r \sim 3$  au to the planet’s orbit. The behaviour of  $\dot{M}_{\text{disc}}$  at  $r \sim 100$  au is characteristic of a viscous disc near its turn-around “transition radius” ([Lynden-Bell](#)

& Pringle 1974; Hartmann et al. 1998), outside of which the disc has not yet viscously relaxed; this outermost disc behaviour is not caused by the planet.

Embedded in Figure 6.4 is our assumption, first mentioned in section 6.2.2, that the disc flow inside the gap maintains continuity. At  $t = 3t_{\nu,p}$ ,  $\dot{M}_{\text{disc}}(r > r_p)$  is, to within a factor of 2, the same as  $\dot{M}_{\text{disc}}(r < r_p)$ . Because the gap surface density  $\Sigma_p$  at this time is about 4 orders of magnitude smaller than the surface densities  $\Sigma_+$  and  $\Sigma_-$  outside the gap, the radial velocity  $|u_r|$  within the gap must be 4 orders of magnitude larger than the radial velocities outside, to maintain the near-constancy of  $\dot{M}_{\text{disc}}$  across  $r_p$ . Since the radial accretion velocities away from the gap are of order  $r/t_\nu \sim \nu/r \sim \alpha h c_s \sim 2$  cm/s, we must have  $|u_r| \sim 0.2$  km/s within the gap. How such a radial velocity is achieved is not specified by our model, which does not resolve the gap spatially.

Figure 6.5 displays the planet's mass as a function of time. We identify a consumption-dominated phase during which the planet grows from  $0.1$  to  $5 M_J$  ( $M < M_{\text{repulsion,visc}}$ ; equation 6.31) and a slower repulsion-dominated phase between  $5$  and  $8 M_J$  ( $M > M_{\text{repulsion,visc}}$ ). During the first phase, accretion starts at the Bondi rate and switches to the Hill rate once  $M_p > M_{\text{thermal}} \simeq 0.5 M_J$  (equations 6.28 and 6.25–6.26). A consumption-dominated ( $A/(3\pi) > B$ ) and deep ( $A/(3\pi) > \nu$ ) gap implies from (6.14) that  $\dot{M}_p \simeq \dot{M}_+$ , i.e., the planet's accretion rate is about as large as it can be. During the final repulsion-limited phase, when  $M_p > 5 M_J$  and  $A_{\text{Hill}}/(3\pi) > B$ , consumption slows and the planet undergoes a last near-doubling in mass as the remainder of the disc diffuses away, onto the star.

### 6.3.2 Analytic estimates of the final planet mass

We can compare our numerical result for the final mass at  $r_p = 10$  au to the following analytic estimates, derived by neglecting the initial short-lived Bondi accretion phase and assuming that at all times the planet accretes at the Hill rate ( $A = A_{\text{Hill}}$ ) and has a large inner gap contrast ( $B > \nu$ ):

$$\begin{aligned} \dot{m} &= \frac{A_{\text{Hill}} \Sigma_p}{M_\star} \\ &= \frac{A_{\text{Hill}}}{M_\star} \frac{\Sigma_+ \nu}{A_{\text{Hill}}/(3\pi) + B} \end{aligned} \quad (6.35)$$

where we have used (6.11). At small orbital distances, final planet masses exceed  $M_{\text{repulsion,visc}}$  and so their final growth phase is repulsion-limited:

$$\begin{aligned} \dot{m} &= \frac{A_{\text{Hill}}}{B} \frac{\Sigma_+ \nu}{M_\star} \\ &= 55\alpha h^5 m^{-4/3} \frac{\Sigma_+ r_p^2}{M_\star} \Omega. \end{aligned} \quad (6.36)$$

We approximate  $\Sigma_+$  using the similarity solution for an isolated viscous disc with no planet and  $\nu \propto r^1$ :

$$\Sigma_+ \sim \frac{M_{\text{disc}}}{2\pi r_1^2} \left( \frac{r_1}{r_p} \right) T^{-3/2} e^{-(r_p/r_1)/T} \quad (6.37)$$

where  $T \equiv 1 + t/t_1$ ,  $t_1 \equiv r_1^2/[3\nu(r_1)]$ , and  $M_{\text{disc}}$  is the initial disc mass (Lynden-Bell & Pringle 1974; Hartmann et al. 1998). Integrating equation (6.36) from  $t = 0$  to  $t$  gives

$$m(t) \sim \left( \frac{385}{18\sqrt{\pi}} \frac{M_{\text{disc}}}{M_{\star}} \frac{h^5 r_1}{h_1^2 r_p} \right)^{3/7} \times \left[ \text{Erf} \left( \sqrt{\frac{r_p}{r_1}} \right) - \text{Erf} \left( \sqrt{\frac{r_p t_1}{r_1(t+t_1)}} \right) \right]^{3/7} \quad (\text{repulsion-limited}) \quad (6.38)$$

where  $h_1$  is the disc aspect ratio at  $r_1$ . As  $t \rightarrow \infty$ , equation (6.38) simplifies to

$$m_{\text{final,visc}} \sim \left[ \frac{385}{18\sqrt{\pi}} \frac{M_{\text{disc}}}{M_{\star}} \frac{h^5 r_1}{h_1^2 r_p} \text{Erf} \left( \sqrt{\frac{r_p}{r_1}} \right) \right]^{3/7} \quad (\text{repulsion-limited}) \quad (6.39)$$

which further simplifies in the limit  $r_p \ll r_1$  (away from the initial disc outer edge) to

$$M_{\text{final,visc}} \sim 10 M_J \left( \frac{M_{\text{disc}}}{15.5 M_J} \right)^{3/7} \left( \frac{r_p}{10 \text{ au}} \right)^{9/28} \quad (\text{repulsion-limited}) \quad (6.40)$$

for our fiducial parameters. Note that  $M_{\text{final,visc}}$  in these limits is independent of  $\alpha$  and  $r_1$ . Equation (6.40) may be reproduced to order-of-magnitude by multiplying  $\dot{m}$  (evaluated at  $t = t_1$ ) by  $t_1$ . In Figure 6.5 we plot equation (6.39) as the uppermost horizontal dashed line, labeled  $M_{\text{final,visc}}$ .

At the largest orbital distances, conditions tend to remain consumption-limited as  $M_p$  stays below  $M_{\text{repulsion,visc}}$ . Then the planet accretes nearly all of the disc gas that tries to diffuse past the planet—and diffusion can be in the outward direction ( $\dot{M}_{\text{disc}} < 0$ ) if the planet is located near or beyond the disc’s turn-around radius. Accordingly we

estimate the planet mass as

$$M_p(t) \sim \int_0^t |\dot{M}_{\text{disc}}| dt \quad (\text{consumption-limited}) \quad (6.41)$$

where  $\dot{M}_{\text{disc}}$  is approximated by the no-planet similarity solution (equation 35 of [Hartmann et al. 1998](#)). For  $r_p \leq r_1/2$ ,

$$M_p(t) \sim M_{\text{disc}} \left( e^{-r_p/r_1} - \frac{e^{-(r_p/r_1)/T}}{\sqrt{T}} \right) \quad (\text{consumption-limited}) \quad (6.42)$$

and for  $r_p > r_1/2$ ,

$$M_p(t) \sim M_{\text{disc}} \left( \sqrt{\frac{2r_1}{r_p}} e^{-1/2} - e^{-r_p/r_1} - \frac{e^{-(r_p/r_1)/T}}{\sqrt{T}} \right) \quad (\text{consumption-limited}). \quad (6.43)$$

We will make use of equations (6.38), (6.42), and (6.43) in section 6.5 when we discuss, in the context of observations, how the final planet mass depends on disc mass and orbital distance.

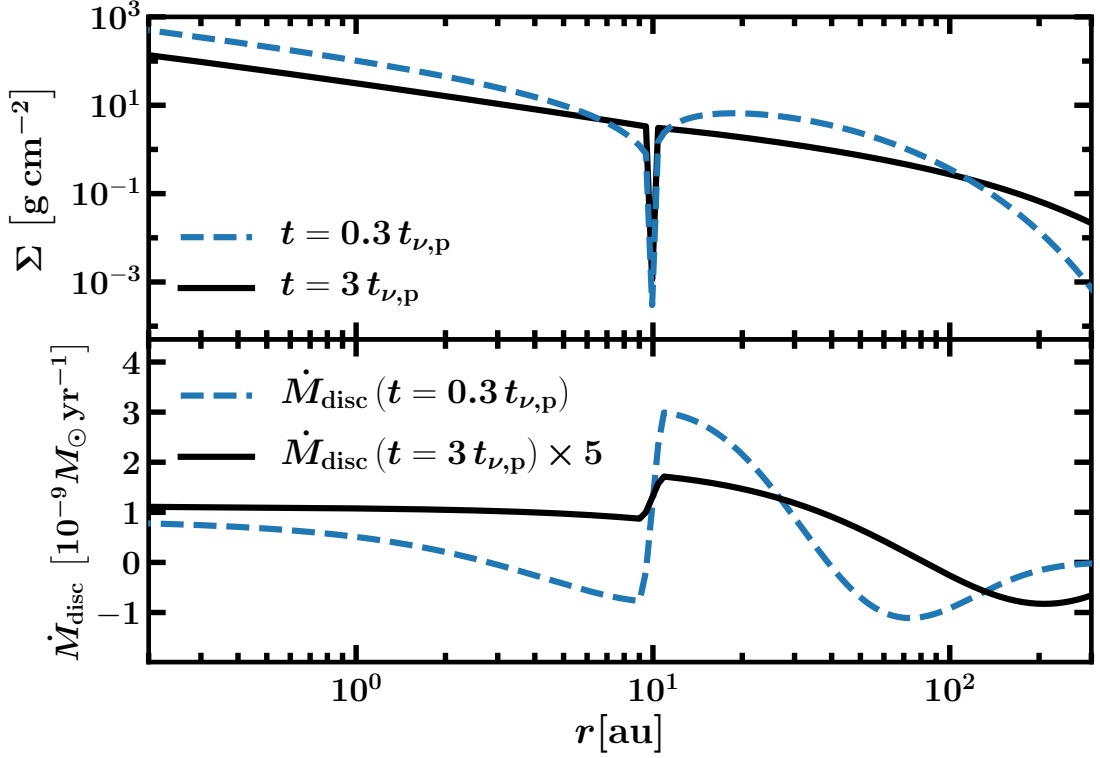


Figure 6.4: Snapshots of the surface density profile  $\Sigma(r)$  and disc accretion rate  $\dot{M}_{\text{disc}}(r) = -2\pi\Sigma u_r r$  ( $> 0$  for accretion toward the star) for a planet embedded at  $r_p = 10$  au in a viscous  $\alpha = 10^{-3}$  disc. The planet mass is allowed to freely grow starting from  $M_p(0) = 0.1M_J$ . At  $t = 0.3t_{\nu,p}$ , the planet resides in a consumption-dominated, asymmetric gap (top panel, dashed curve) and accretes from regions both exterior and interior to its orbit which have not yet viscously relaxed (bottom panel, dashed curve). At the later time  $t = 3t_{\nu,p}$ , the planet has grown sufficiently (see also Figure 6.5) that its gap is now repulsion-dominated and more symmetric (top panel, solid curve); the planet now accretes only from the outer disc, reducing the flow of mass into the inner disc by less than a factor of 2 (bottom panel, solid curve. At this time we have multiplied  $\dot{M}_{\text{disc}}$  by a factor of 5 for easier viewing).

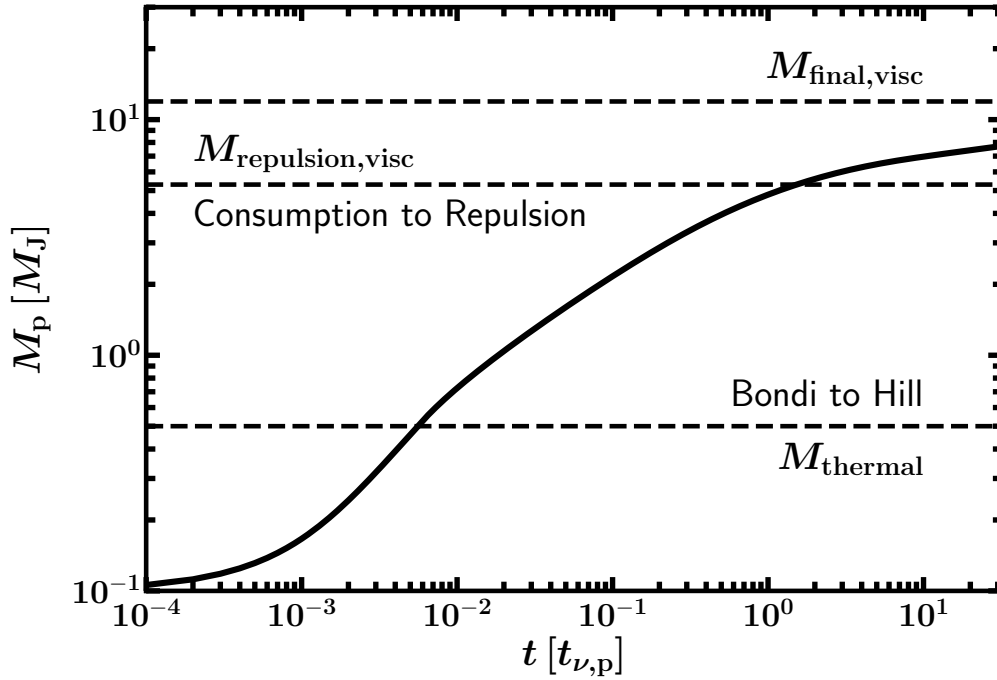


Figure 6.5: Accretion history of a planet of initial mass  $M_p(0) = 0.1M_J$  embedded at  $r_p = 10$  au (where  $h = 0.054$ ) in a viscous disc of initial mass  $M_{\text{disc}} = 15.5M_J$ . Transitions from Bondi accretion to Hill accretion ( $M_{\text{thermal}}$ , equations 6.25–6.26 and 6.28), and from consumption to repulsion-dominated gaps ( $M_{\text{repulsion,visc}}$ , equation 6.31), are indicated. An analytic estimate of the final planet mass is plotted as  $M_{\text{final,visc}}$  (equation 6.39), computed assuming repulsion-dominated conditions (at  $r_p = 10$  au for this disc mass, conditions are actually intermediate between the repulsion and consumption limits, and so plotting equation 6.42 which assumes consumption-dominated conditions would give a similar result as equation 6.39; see also Figure 6.9).

## 6.4 Planets in Inviscid Wind-Driven Discs

Motivated by recent ALMA observations that point to little or no turbulence in protoplanetary discs (e.g., [Pinte et al. 2016](#); [Flaherty et al. 2017](#)), and by theoretical work arguing that discs are, for the most part, laminar because they are too cold and dusty to support magnetorotational turbulence (e.g., [Gammie 1996](#); [Perez-Becker & Chiang 2011](#); [Bai 2011](#)), we here turn away from the  $\alpha$ -based picture of turbulent and diffusive discs, and consider instead inviscid (zero viscosity) discs that accrete by virtue of magnetized winds (e.g., [Bai et al. 2016](#); [Bai 2016](#)). We review how wind-driven discs work in section 6.4.1 and how planets open repulsive gaps in inviscid discs in section 6.4.2. We then study how repulsion combines with consumption to set gap depths and planetary accretion rates, analytically in section 6.4.3 and numerically in section 6.4.4.

### 6.4.1 Wind-driven accretion discs

Inviscid, wind-driven accretion discs do not behave diffusively. Instead they are governed by simple advection: at every radius  $r$ , material moves inward with a vertically-averaged radial speed  $u_r$  because it has lost angular momentum to a magnetized wind. The mass carried away by the wind itself is small compared to the mass advected inward through the disc (see Appendix B.2, in particular the discussion below equation B.16). Then from continuity, including our planetary mass sink,

$$\frac{\partial \Sigma}{\partial t} = \frac{1}{r} \frac{\partial}{\partial r} (\Sigma r u_r) - \frac{\dot{M}_p(t)}{2\pi r} \delta(r - r_p). \quad (6.44)$$

In Appendix B.2 we show how a wind-driven disc inspired by [Bai et al. \(2016\)](#) and [Bai \(2016\)](#) can have  $u_r$  approximately constant ( $< 0$  for accretion). We utilize here, for simplicity, a constant  $u_r \equiv c < 0$  model:

$$\frac{\partial \Sigma}{\partial t} = \frac{c}{r} \frac{\partial}{\partial r} (\Sigma r) - \frac{\dot{M}_p(t)}{2\pi r} \delta(r - r_p). \quad (6.45)$$

It is instructive to examine the solution to (6.45) when  $\dot{M}_p = 0$ . The no-planet solution is separable:

$$\Sigma(r, t) = f(r)g(t) = \frac{M_{\text{disc}}}{2\pi(ct_{\text{adv}})^2} \frac{|c|t_{\text{adv}}}{r} e^{-r/(|c|t_{\text{adv}})} e^{-t/t_{\text{adv}}} \quad (6.46)$$

for constants  $M_{\text{disc}}$  (the initial disc mass) and  $t_{\text{adv}}$ , which we interpret as a disc radial advection time or drain-out time. For  $c = -4$  cm/s (a value we relate to magnetic field parameters in Appendix B.2) and  $t_{\text{adv}} = 3$  Myr, the characteristic disc size is  $|c|t_{\text{adv}} \simeq 25$  AU, which seems reasonable. Equation (6.46) resembles the [Lynden-Bell & Pringle \(1974\)](#) solution for a viscous disc which gives, for  $\nu \propto r^1$ , a surface density profile that scales as  $r^{-1} \exp(-r/r_1)$  at fixed  $t$  (equation 6.37). This spatial resemblance is not surprising, as our viscous disc happens also to have an accretion velocity that is constant with radius:  $|u_r| \sim r/t_\nu \sim \nu/r = \text{constant}$ . However, the solutions differ in their time behaviours; at fixed  $r$ , the wind-driven surface density decays exponentially as  $\exp(-t/t_{\text{adv}})$ , whereas our viscous disc decays as a power law  $t^{-3/2}$  (within viscously relaxed regions at small radii; [Lynden-Bell & Pringle 1974](#); [Hartmann et al. 1998](#)). Viscous discs evolve more slowly because they conserve their total angular momentum;

they can only drain away on the inside by redistributing their angular momentum to the outside in a kind of zero-sum game. Wind-driven discs are not so constrained; they lose their angular momentum wholesale to a wind, and so can dissipate more quickly.

We emphasize that  $u_r = c$  is a vertically averaged, mass weighted, radial accretion velocity. In simulations by [Bai & Stone \(2013\)](#) of discs whose magneto-thermal winds are anchored at their electrically conductive surfaces, accretion actually occurs in a vertically thin, rarefied layer several scale heights above the midplane. The radial accretion velocity in this high-altitude layer is fast, on the order of the sound speed  $c_s$ . The bulk of the mass of the disc, below this layer, is inert (see fig. 10 of [Bai & Stone 2013](#)). It is with this static and inviscid gas, extending from the midplane to a couple scale heights above and below, that the planet interacts, as we now describe.

#### 6.4.2 Repulsion in inviscid discs

Without viscosity, disc gas in the vicinity of the planet depletes indefinitely, as it is repelled by the planetary Lindblad torque but cannot diffuse back. Under these conditions, [Ginzburg & Chiang \(2019a\)](#) derived how the gas density at the center of the planet's gap scales with elapsed time  $t$ , for a given planet-to-star mass ratio  $m = M_p/M_\star$  and disc aspect ratio  $h = H/r$  (see the inviscid branch of their equation 17, and also their appendix):

$$\frac{\Sigma_p}{\Sigma_-} \sim h^{549/49} m^{-4} (\Omega t)^{-39/49} \equiv \tilde{B}_{\text{inv}}^{-1} \quad (6.47)$$

where  $\Omega$  is the orbital frequency of the planet,  $\Sigma_p$  is the surface density within the gap, and  $\Sigma_-$  is the surface density downstream of the planet in the accretion flow (see Figure 6.1). By construction,  $t$  is the time over which the planet's mass is close to its given value  $m$  (say within a factor of 2). In practice, for inviscid discs where gaps deepen dramatically with increasing planet mass, the mass doubling time of a planet lengthens with each doubling, so  $t$  is of order the system age.

Equation (6.47) does not apply when  $\tilde{B}_{\text{inv}} < 1$ , i.e., when a repulsive gap has not yet been opened because not enough time has elapsed for a given planet mass. To account for this possibility, we generalize (6.47) using

$$\frac{\Sigma_p}{\Sigma_-} \sim \frac{1}{1 + \tilde{B}_{\text{inv}}} \quad (6.48)$$

by analogy with equation (6.10) for the viscous case. Note that  $\tilde{B}_{\text{inv}}$  is dimensionless while its viscous counterpart  $B$  has dimensions of viscosity.

### 6.4.3 Consumption and repulsion combined

We now assemble the physical ingredients laid out in sections 6.4.1 and 6.4.2 into a sketch of how consumption and repulsion combine in an inviscid, wind-driven disc. Following by analogy our analysis in section 6.2.1 for a viscous disc, we first write

down mass conservation (see equation 6.1 and Figure 6.1):

$$\begin{aligned}
\dot{M}_+ &= \dot{M}_- + \dot{M}_p \\
2\pi\Sigma_+r|c| &= 2\pi\Sigma_-r|c| + \dot{M}_p \\
&= 2\pi\Sigma_-r|c| + A\Sigma_p
\end{aligned} \tag{6.49}$$

where in lieu of the viscosity we now have  $r|c|$ . After replacing  $\Sigma_-$  in (6.49) using our momentum relation (6.48), we have

$$\Sigma_+ \sim (1 + \tilde{B}_{\text{inv}})\Sigma_p + \frac{A}{2\pi r|c|}\Sigma_p \tag{6.50}$$

which implies the outer gap contrast

$$\frac{\Sigma_p}{\Sigma_+} \sim \frac{1}{1 + A/(2\pi r|c|) + \tilde{B}_{\text{inv}}}. \tag{6.51}$$

As in the viscous case (equation 6.11), we see here that consumption ( $A/(2\pi r|c|)$ ) and repulsion ( $\tilde{B}_{\text{inv}}$ ) add. Taking  $A$  to be the Bondi value (equation 6.25) gives the ratio

$$\begin{aligned}
\frac{A_{\text{Bondi}}/(2\pi r|c|)}{\tilde{B}_{\text{inv}}} &\sim \frac{0.5}{2\pi} \frac{h^{353/49}}{m^2(\Omega t)^{39/49}} \frac{\Omega r_p}{|c|} \\
&\sim 0.04 \left(\frac{M_p}{0.1 M_J}\right)^{-2} \left(\frac{t}{3 \text{ Myr}}\right)^{-39/49} \times \\
&\quad \left(\frac{|c|}{4 \text{ cm/s}}\right)^{-1} \left(\frac{r_p}{10 \text{ au}}\right)^{489/196}
\end{aligned} \tag{6.52}$$

which informs us that repulsion dominates consumption ( $\tilde{B}_{\text{inv}} > A_{\text{Bondi}}/(2\pi r|c|)$ ) when

$$M_{\text{p}} > M_{\text{repulsion,inv}} \sim 0.02 M_{\text{J}} \left( \frac{t}{3 \text{ Myr}} \right)^{-39/98} \times \left( \frac{|c|}{4 \text{ cm/s}} \right)^{-1/2} \left( \frac{r_{\text{p}}}{10 \text{ au}} \right)^{489/392}. \quad (6.53)$$

That repulsion dominates consumption even for small masses is in contrast to the viscous case (see equation 6.31 for  $M_{\text{repulsion,visc}}$ ). Repulsion-dominated gaps are symmetric between the inner and outer discs (equations 6.48 and 6.51):

$$\begin{aligned} \Sigma_{\text{p}}/\Sigma_{-} &\sim \Sigma_{\text{p}}/\Sigma_{+} \sim 1/(1 + \tilde{B}_{\text{inv}}) \\ &\sim 2 \times 10^{-3} \left( \frac{h}{0.054} \right)^{549/49} \left( \frac{10^{-4}}{m} \right)^4 \left( \frac{3 \text{ Myr}}{t} \right)^{39/49} \end{aligned} \quad (6.54)$$

where for the last equality we have assumed that the gaps are deep ( $\tilde{B}_{\text{inv}} > 1$ ). Under these conditions, we may estimate a final accreted planet mass by time-integrating

$$\begin{aligned} \dot{M}_{\text{p}} &= A_{\text{Bondi}} \Sigma_{\text{p}} \\ &\sim A_{\text{Bondi}} \frac{\Sigma_{+}}{\tilde{B}_{\text{inv}}} \\ &\sim \frac{A_{\text{Bondi}}}{\tilde{B}_{\text{inv}}} \frac{M_{\text{disc}}}{2\pi(ct_{\text{adv}})^2} \frac{|c|t_{\text{adv}}}{r_{\text{p}}} e^{-r_{\text{p}}/(|c|t_{\text{adv}})} e^{-t/t_{\text{adv}}} \end{aligned} \quad (6.55)$$

from  $t = 0$  to  $\infty$ , where for  $\Sigma_{+}$  we have employed the no-planet solution (6.46). This last approximation is analogous to the one we made in (6.37) for a viscous disc. Equation

(6.55) integrates to yield

$$\begin{aligned}
M_{\text{final,inv}} &\sim \left[ \frac{1.5}{2\pi} \Gamma\left(\frac{10}{49}\right) \left(\frac{M_{\text{disc}}}{M_{\star}}\right) \left(\frac{r_{\text{p}}}{|c|t_{\text{adv}}}\right) \right. \\
&\quad \left. \times h^{353/49} (\Omega t_{\text{adv}})^{10/49} e^{-r_{\text{p}}/(|c|t_{\text{adv}})} \right]^{1/3} M_{\star} \\
&\sim 0.3 M_{\text{J}} \left(\frac{M_{\text{disc}}}{15.5 M_{\text{J}}}\right)^{1/3} \left(\frac{r_{\text{p}}}{10 \text{ au}}\right)^{163/196} e^{-r_{\text{p}}/(3|c|t_{\text{adv}})} \\
&\quad \text{(repulsion-limited)} \tag{6.56}
\end{aligned}$$

where  $\Gamma$  is the gamma function, and the numerical evaluation uses our fiducial parameters including  $|c| = 4 \text{ cm/s}$ ,  $t_{\text{adv}} = 3 \text{ Myr}$ , and  $M_{\star} = 1M_{\odot}$ . Our estimated final mass of  $0.3 M_{\text{J}}$  at  $r_{\text{p}} = 10 \text{ au}$  remains smaller than  $M_{\text{thermal}} \simeq 0.5M_{\text{J}}$  and so our use of  $A_{\text{Bondi}}$  is self-consistent.

Our expression (6.56) for  $M_{\text{final,inv}}$  resembles equation (19) of [Ginzburg & Chiang \(2019a\)](#); ours is an improvement as we have accounted explicitly for the transport properties of the disc through the radial velocity  $c$  (see the discussion of transport-limited accretion in their section 4.1).

#### 6.4.4 Numerical simulations

We test the ideas in section 6.4.3 by numerically solving the continuity equation (6.45) and the momentum equation (6.48). To model the planetary mass sink in equation (6.45), we utilize the same sub-grid procedure of section 6.2.2, replacing equation (6.24)

with

$$\dot{M}_p(t) = A \times \frac{\Sigma(r_p, t)}{1 + \tilde{B}_{\text{inv}}} \quad (\text{simulation}) \quad (6.57)$$

where  $\Sigma(r_p, t)$  is the grid-level surface density in the bin containing the planet, and  $A$  and  $\tilde{B}_{\text{inv}}$  are given by equations (6.25)–(6.26) and (6.47), respectively. The initial mass of the planet is set to  $M_p(0) = 0.1 M_J$  (we will see that using smaller initial masses hardly changes the outcome). We solve the advective portion of equation (6.45) with a first-order upwind scheme (e.g., [Press et al. 2007](#)) applied to a grid that extends from  $r_{\text{in}} = 0.01$  au to  $r_{\text{out}} = 500$  au across 300 cells uniformly spaced in  $\log r$ . We fix  $c = -4$  cm/s and initialize the grid using (6.46), with  $t_{\text{adv}} = 3$  Myr and  $M_{\text{disc}} = 15.5 M_J = 0.015 M_{\odot}$ , the same value chosen for our viscous disc calculations. Our timestep is set to  $\Delta t = 0.2 \Delta r_{\text{min}} / |c|$ , where  $\Delta r_{\text{min}} = 3 \times 10^{-3}$  au is our smallest bin width. Other disc properties such as  $h(r)$  and  $\Omega(r)$  are the same as before. For the outer boundary condition we impose a ghost cell just outside  $r_{\text{out}}$  where the surface density is fixed at 0.

Figure 6.6 (the inviscid counterpart to Figure 6.2) shows  $\Sigma(r)$  at  $t = t_{\text{adv}}$  when  $M_p$  has grown to  $0.3 M_J$ , illustrating many of the features anticipated from our analytic treatment. Without a planet, the surface density profile follows  $r^{-1} \exp[-r/(|c|t_{\text{adv}})]$  as expected from equation (6.46). With a planet, a gap is created that is nearly symmetric between the inner and outer discs, and whose depth is dominated by Lindblad repulsion (enforced by our sub-grid scheme), not consumption (equation 6.54). The inviscid gap is deep (scaling as  $m^{-4}$ ; [Ginzburg & Sari 2018](#); [Ginzburg & Chiang 2019a](#); see also [Duffell](#)

2020). Figure 6.7 (analogous to Figure 6.4) provides snapshots of  $\Sigma(r)$  and  $\dot{M}_{\text{disc}}(r)$  taken at different times, and Figure 6.8 (analogous to Figure 6.5) plots  $M_{\text{p}}(t)$ . Unlike in a viscous disc, our example planet in an inviscid disc does not consume most of the disc mass exterior to its orbit; the disc accretion rate profile  $\dot{M}_{\text{disc}}(r)$  is not much affected by the planet except during an initial transient phase at  $t < t_{\text{adv}}$ . We see a need for a high radial accretion velocity  $|u_r|$  within the gap (see also section 6.3.1): to ensure that  $\dot{M}_{\text{disc}}$  grades smoothly across the gap as shown in Figure 6.7,  $|u_r|$  must increase in proportion to the gap contrast  $\Sigma/\Sigma_{\text{p}}$ . Inviscid gap contrasts are on the order of  $10^5$ , and so  $|u_r| \sim 10^5 |c| \sim 4$  km/s, comparable to the orbital velocity. Note that simulations of planets in inviscid discs have not reproduced the deep gaps expected from our analytics, finding gap contrasts only up to a factor of  $\sim 10$  (e.g., [Fung & Chiang 2017](#); [McNally et al. 2019, 2020](#)). On the one hand the simulations are of limited duration and so their gaps may not have fully developed; on the other hand, the simulations allow for orbital migration and hydrodynamical instabilities, effects which may prevent gaps from becoming too deep in reality.

That the disc accretion flow proceeds largely unimpeded from outside to inside the planet’s orbit is a consequence of the gap being repulsion-dominated (equation 6.15, with  $\nu$  replaced by  $r|c|$ ). The planet diverts such a small fraction of the disc flow that it grows from  $0.1 M_{\text{J}}$  to only  $0.3 M_{\text{J}}$ ; most of the original  $15.5 M_{\text{J}}$  contained in the disc drains onto the star. Figure 6.8 also shows that reducing the initial seed mass to  $M_{\text{p}}(0) = 0.01 M_{\text{J}}$  hardly affect the final mass.

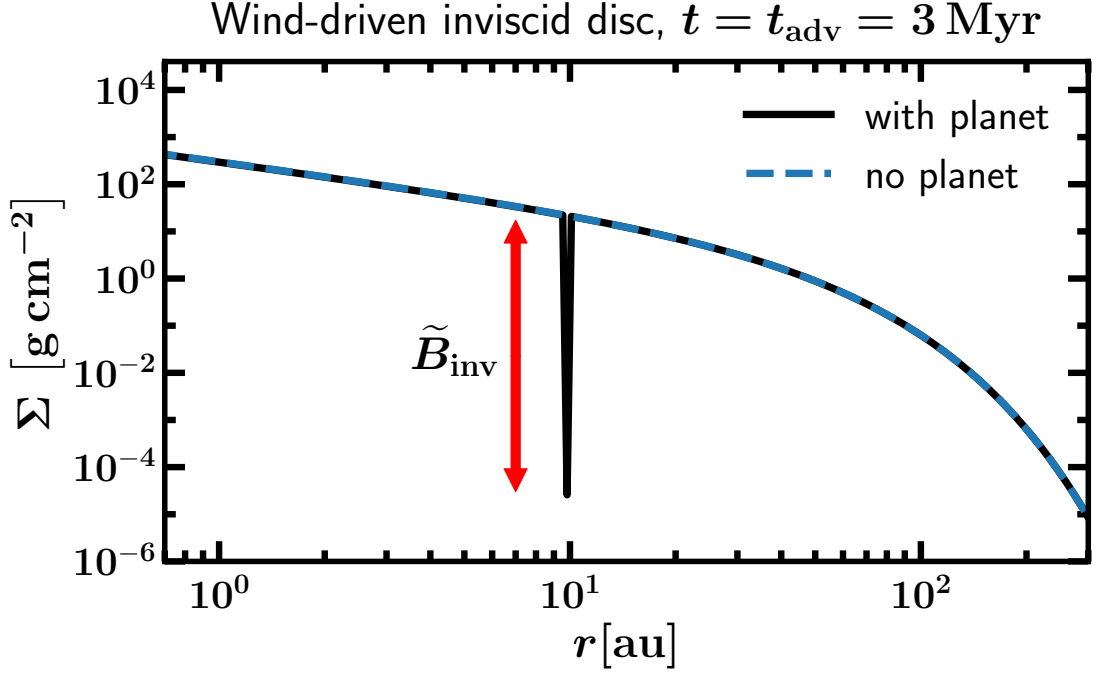


Figure 6.6: How the surface density profile of an inviscid disc responds to a planet that consumes disc gas and repels gas away by Lindblad torques. The planet, located at  $r_p = 10 \text{ au}$ , freely accretes starting from a seed mass of  $0.1M_J$ ; the  $\Sigma$  profile shown here is taken at a time  $t = t_{\text{adv}} = 3 \text{ Myr}$ , when the planet has grown to  $\sim 0.3M_J$  (see also Figure 6.8). As is the case throughout this paper, the planet’s gap is not spatially resolved, but is modeled as a single cell. The “true” surface density inside this cell equals the grid-level  $\Sigma$  lowered by a factor of  $\tilde{B}_{\text{inv}}$ , whose magnitude is given by the red double-tipped arrow. The gap is repulsion and not consumption dominated ( $\tilde{B}_{\text{inv}} > A/(2\pi r|c|)$ , equation 6.52); as such, the gap is symmetric in the sense that the surface density contrast with the outer disc is practically the same as with the inner disc. This figure is the inviscid counterpart to Figure 6.2 which was made for a viscous disc.

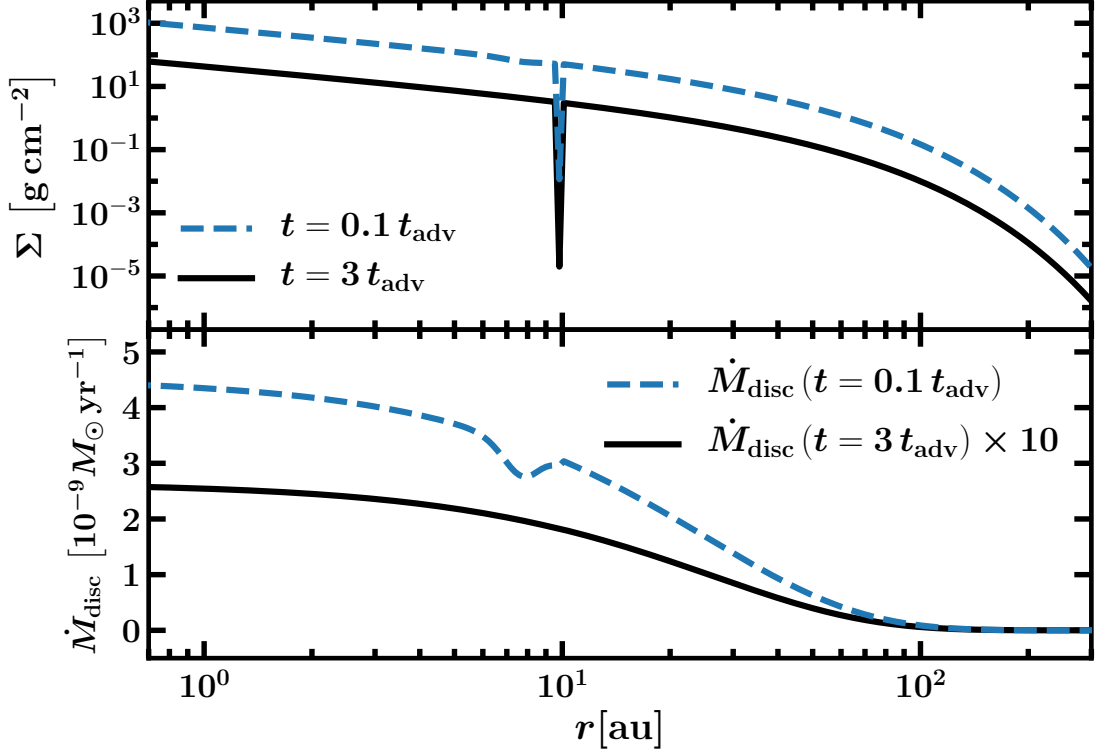


Figure 6.7: Snapshots of the surface density profile  $\Sigma(r)$  and disc accretion rate  $\dot{M}_{\text{disc}}(r) = -2\pi\Sigma u_r r$  ( $> 0$  for accretion toward the star) for a planet embedded in an inviscid, wind-driven disc. The planet mass is allowed to freely grow starting from  $M_p(0) = 0.1 M_J$ ; the masses corresponding to the plotted times are  $0.27 M_J$  ( $t = 0.1 t_{\text{adv}} = 0.3$  Myr) and  $0.34 M_J$  ( $t = 3 t_{\text{adv}} = 9$  Myr; see also Figure 6.8). At  $t = 3 t_{\text{adv}}$ , the disc has relaxed into a quasi-steady state in the presence of the planetary mass sink, and  $\dot{M}_{\text{disc}}(r)$  looks essentially the same as it would without the planet; the accretion rate onto the planet is negligible compared to the disc accretion rate—the gap is repulsion-dominated—and so the disc is not materially affected. Even at  $t = 0.1 t_{\text{adv}}$ , the interior surface density  $\Sigma_-$  and  $\dot{M}_{\text{disc}}$  depress by only  $\sim 15\%$  because of consumption.

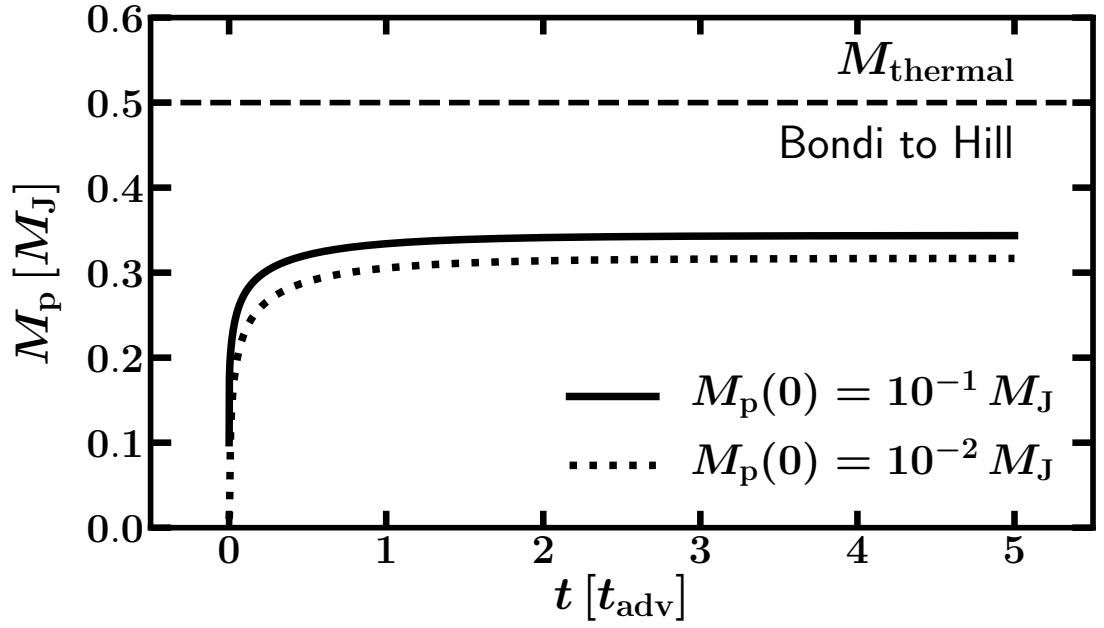


Figure 6.8: Mass evolution of a planet embedded at  $r_p = 10$  au in an inviscid but still accreting disc of initial mass  $M_{disc} = 15.5 M_J$ . Within  $\sim 1$  disc advection time  $t_{adv}$ , the planet, whose gap is repulsion-dominated ( $\tilde{B}_{inv} > A_{Bondi}/(2\pi r_p |c|)$ ), grows to a mass of  $\sim 0.35 M_J$ . The final planet mass varies by only  $\sim 10\%$  when the initial seed mass  $M_p(0)$  varies by a factor of 10. This figure is the inviscid counterpart to Figure 6.5 which was made for a viscous disc.

## 6.5 Summary and Discussion

Planets open gaps in circumstellar discs in two ways: by repelling material away via Lindblad torques, and by consuming local disc gas. Measured relative to the disc outside the planet’s orbit, the two effects are additive: both repulsion and consumption add to deepen the planet’s gap relative to the outer disc (see equation 6.11 or 6.51). Relative to the inner disc, downstream of the mass sink presented by the planet, the gap surface density contrast is set by repulsion only (see equation 6.10 or 6.48).

Many planet formation studies (e.g., [Tanigawa & Tanaka 2016](#); [Lee 2019](#)) take the planet’s hydrodynamically-limited accretion rate  $\dot{M}_p = \min(\dot{M}_{\text{hydro}}, \dot{M}_{\text{disc}})$ , where  $\dot{M}_{\text{hydro}}$  is the planetary accretion rate computed according to the hydrodynamics of flows in the immediate vicinity of the planet, and  $\dot{M}_{\text{disc}}$  is the local disc accretion rate (the mass crossing the planet’s orbital radius, per time). Prescribing the planet’s accretion rate in this way is equivalent to comparing consumption, as measured by the “consumption coefficient”  $A \equiv \dot{M}_p / \Sigma_p$ , where  $\Sigma_p$  is the surface density inside the gap, and repulsion, as measured by the “repulsion coefficient”  $B \equiv T / (\Sigma_p \Omega r^2)$ , where  $T$  is the repulsive planetary torque and  $\Omega r^2$  is the angular momentum per unit mass (see also [Tanigawa & Tanaka 2016](#) and [Tanaka et al. 2020](#) who use the same framework). Under consumption-limited conditions ( $A/(3\pi) > B$ ), the planet’s accretion rate saturates to nearly the disc’s accretion rate:  $\dot{M}_p = \min(\dot{M}_{\text{hydro}}, \dot{M}_{\text{disc}}) = \dot{M}_{\text{disc}}$ . Otherwise, under repulsion-limited conditions ( $A/(3\pi) < B$ ),  $\dot{M}_p = \min(\dot{M}_{\text{hydro}}, \dot{M}_{\text{disc}}) = \dot{M}_{\text{hydro}}$ .

### 6.5.1 Final planet masses

In conventional viscous discs with large enough  $\alpha$ -diffusivities<sup>22</sup> and our assumed parameters, planets begin their growth under consumption-dominated conditions and possibly continue their growth under repulsion-dominated conditions, arriving at final masses well in excess of a Jupiter. We show in Figure 6.9 the final mass of a planet embedded in an  $\alpha = 10^{-3}$  disc, as a function of the planet’s orbital distance  $r_p$ , computed using our numerical code of sections 6.2–6.3. Final planet masses increase gradually from  $4 M_J$  at 1 au, to  $8 M_J$  at 30 au, in a disc of initial mass  $M_{\text{disc}} = 15.5 M_J = 0.015 M_\odot$ . In a disc  $5\times$  more massive, the corresponding range of planet masses is  $9\text{--}20 M_J$ . The final masses are not sensitive to  $\alpha$  insofar as  $\alpha$  controls only the timescale over which the disc evolves (modulo disc dispersal by some other means, e.g., photoevaporation; see [Tanaka et al. 2020](#)). Final masses do depend on the initial mass of the disc, scaling as  $M_{\text{disc}}^{3/7}$  under repulsion-dominated conditions (equation 6.39) and  $M_{\text{disc}}^1$  under consumption-dominated conditions (equation 6.42 or 6.43). The trend of final planet mass with distance shown in Figure 6.9 follows, for the most part, the trend predicted for repulsion-limited conditions, except at large  $r_p$  where consumption dominates. The final mass profiles in Figure 6.9 recall those of the super-Jupiters in the HR 8799 system; the four planets, located between 15 and 70 AU of their host star, have practically the same mass, about  $6\text{--}7 M_J$  ([Wang et al. 2018](#)).

Initially and everywhere in a viscous disc, a planet, despite opening a gap, consumes practically all of the disc gas that tries to diffuse past its orbit (equation

---

<sup>22</sup>If the Shakura-Sunyaev  $\alpha \lesssim 10^{-4}$ , discs respond to planetary torques as if they were inviscid ([Ginzburg & Chiang 2019a](#), their fig. 1).

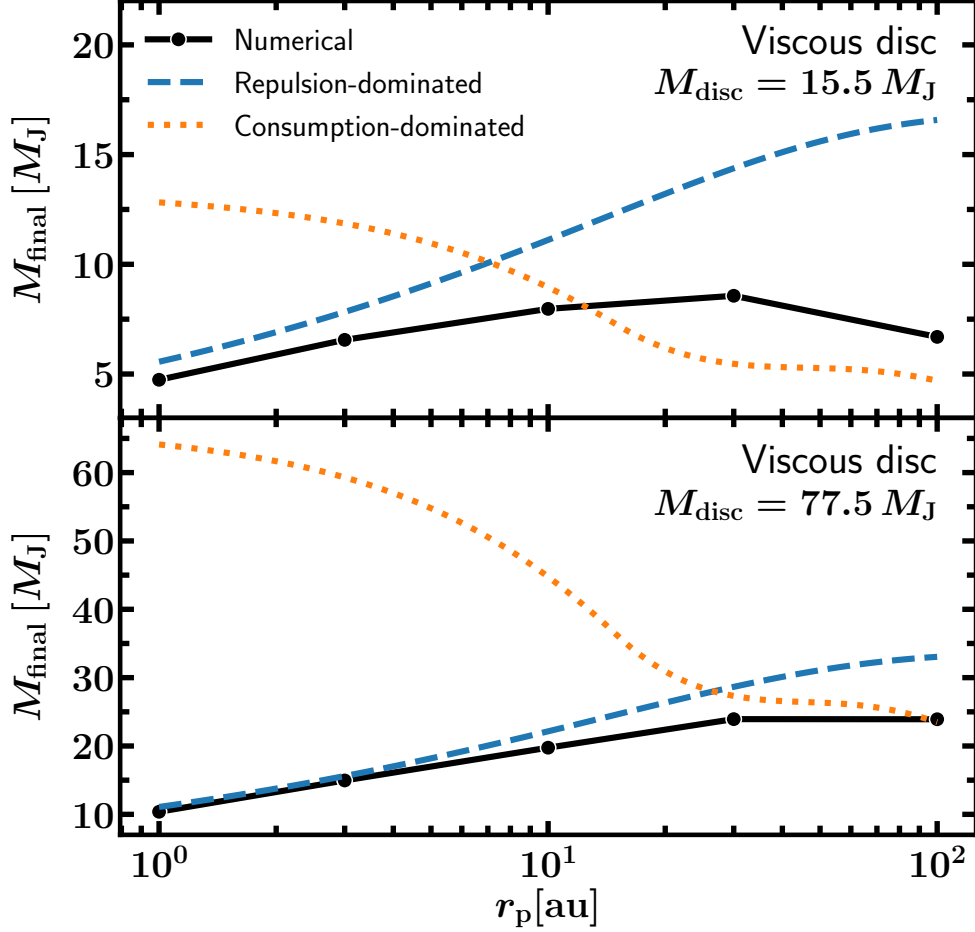


Figure 6.9: Final planet masses grown from viscous discs having  $\alpha = 10^{-3}$  and varying total mass (top vs. bottom panels). Planet masses are initialized at  $0.1 M_J$  and grown using the 1D numerical code of section 6.3, which utilizes the repulsive gap contrast of Kanagawa et al. (2015; see also Duffell & MacFadyen 2013 and Fung et al. 2014) and gas accretion that switches from Bondi to Hill at the thermal mass. Points are plotted at  $t = 50 t_1 = 85$  Myr, where  $t_1 = r_1^2 / [3\nu(r_1)]$  is the viscous diffusion time at  $r_1 = 30$  au. Analytic curves are given by equation (6.38) for the repulsion limit (dashed blue), and equations (6.42)–(6.43) for the consumption limit (dotted orange), also evaluated at  $t = 50 t_1$ . At most orbital distances, planet mass growth is limited by repulsion-dominated gaps; only at the largest distances, where the disc aspect ratio is large, are gaps relatively harder to open and conditions remain consumption-limited. The analytics, which are derived assuming the planet mass is small compared to the disc mass, are a better guide for the more massive disc in the bottom panel.

6.14 with  $A/(3\pi) > B > \nu$ , where  $\nu$  is the disc viscosity). This consumption-limited behaviour persists up to a repulsion mass  $M_{\text{repulsion,visc}} \simeq 5 M_{\text{J}} [r_{\text{p}}/(10 \text{ au})]^{9/16}$  (equation 6.31), above which repulsion dominates. The repulsion mass is not the thermal mass  $M_{\text{thermal}}$  (equation 6.28), but exceeds it by a factor of  $\sim h^{-3/4}$ , where  $h$  is the disc aspect ratio. Growth continues more slowly at  $M_{\text{p}} > M_{\text{repulsion,visc}}$ , with the planet mass increasing beyond  $M_{\text{repulsion,visc}}$  by up to a factor of  $\sim 4$  for our parameter choices.

Equation (6.38) gives an approximate analytic expression for the planet mass vs. time during this final repulsion-limited stage. It predicts that planet masses are of order  $10 M_{\text{J}}$  by the time the disc dissipates. This result is derived by assuming the planet accretes at a rate that scales as  $A_{\text{Hill}} = 2.2 \Omega r^2 m^{2/3}$ , where  $m$  is the planet-to-star mass ratio; this prescription is commonly adopted by hydrodynamical simulations of planet-disc interactions, and might be appropriate for super-thermal masses. If instead of  $A_{\text{Hill}}$  we use the empirical formula  $A_{\text{TW}} = 0.29 \Omega r^2 m^{4/3}/h^2$  drawn from 2D numerical simulations by [Tanigawa & Watanabe \(2002\)](#), then the mass above which repulsion dominates changes to  $M_{\text{repulsion,visc,TW}} \simeq 9 M_{\text{J}} [r/(10 \text{ au})]^{3/8}$ , nearly twice the value of  $M_{\text{repulsion,visc}}$  derived using the Hill scaling. Using  $A_{\text{TW}}$  leads to a more extended consumption-dominated growth phase, and final planet masses larger by order-unity factors compared to those of the solid curves in Figure 6.9. Overall, it appears that in viscous discs, planets accrete a not-small fraction of the disc mass, which can be many tens of Jupiter masses ([Tripathi et al. 2017](#), their fig. 10; see also [Powell et al. 2019](#)). This is in agreement with [Tanaka et al. \(2020\)](#), who limit giant planet growth by incorporating photoevaporative mass loss from the disc.

In inviscid discs, conditions tend to be repulsion-dominated even at low planet masses. Without viscosity or turbulent transport to compete against, planetary Lindblad torques carve deep gaps that are repulsion-dominated even for sub-thermal planets accreting at the Bondi rate (equation 6.52). Repulsion-dominated gaps are symmetric in the sense that gap contrasts between the outer and inner discs are the same; accordingly, disc accretion rates are nearly continuous across the gap (e.g., Figure 6.7), which means that most of the disc mass is not diverted onto the planet (in the language of [Tanigawa & Tanaka 2016](#),  $\dot{M}_p = \min(\dot{M}_{\text{hydro}}, \dot{M}_{\text{disc}}) = \dot{M}_{\text{hydro}}$ ). Maintaining the disc accretion rate across a gap demands that the radial accretion velocity within the gap be as large as the gap is deep. Whether such fast inflows are possible, and whether inviscid gaps can be as deep as expected from our analytics (cf. numerical simulations that find only shallow gaps; [Fung & Chiang 2017](#); [McNally et al. 2019, 2020](#)), are unresolved issues.

Figure 6.10, analogous to Figure 6.9, shows that final planet masses in our model inviscid discs range between  $\sim 0.05$  and  $1 M_J$ , more than an order-of-magnitude smaller than their viscous disc counterparts. For the most part, the masses computed for inviscid discs using our numerical 1D code are well reproduced by equation (6.56), derived in the repulsion limit. This formula, which predicts that final planet masses scale as  $M_{\text{disc}}^{1/3}$  and  $r_p^{163/196} \simeq r_p^{0.83}$ , is similar to that derived by [Ginzburg & Chiang \(2019a, their equation 19\)](#),<sup>23</sup> and improves upon it by accounting for the structure and transport properties of the parent disc—specifically how the disc may accrete by

---

<sup>23</sup>Our final planet masses are a factor of  $\sim 3$  lower than theirs, a consequence largely of their choice for  $h$  which is 50% larger.

shedding angular momentum through a magnetized surface wind (e.g., [Bai 2016](#)).

Orbital migration in viscous discs has been shown in numerical simulations to enhance  $\dot{M}_p$  relative to the migration-free case (e.g., [Dürmann & Kley 2017](#)). Including migration would only amplify our finding that final planet masses in viscous discs are large, approaching if not well within the regime of brown dwarfs. Accretion rates should also increase for planets migrating in inviscid, wind-driven discs; in 3D, strongly sub-thermal planets have been shown to migrate inward ([McNally et al. 2020](#)). We may need such enhancements in  $\dot{M}_p$  to explain, within an inviscid scenario, giant planets like our own Jupiter, i.e., to bring planet masses up to  $1M_J$  at distances of 1–10 au (Figure 6.10). On the other hand, sub-Jupiter masses, down to  $\sim 0.1 M_J$  in many cases, are inferred from ALMA observations of disc gaps ([Zhang et al. 2018](#)), and suggest that planets there are strongly repelling inviscid gas.

The asymmetric gap we computed for the viscous disc model in Figure 6.2 suggests a strong, mostly one-sided migration torque forcing the planet inward. However, this is misleading because our numerical procedure does not spatially resolve the gap, whose true radial width lies between  $H$  (the pressure scale height) and  $r_p$  ([Ginzburg & Sari 2018](#)). Most of the migration torque is exerted by disc gas on the bottoms of gaps, displaced radially from the planet by  $\sim \pm H$ , and here the actual surface density gradients, and of course the surface density itself, are small (see also [Kanagawa et al. 2018](#)).

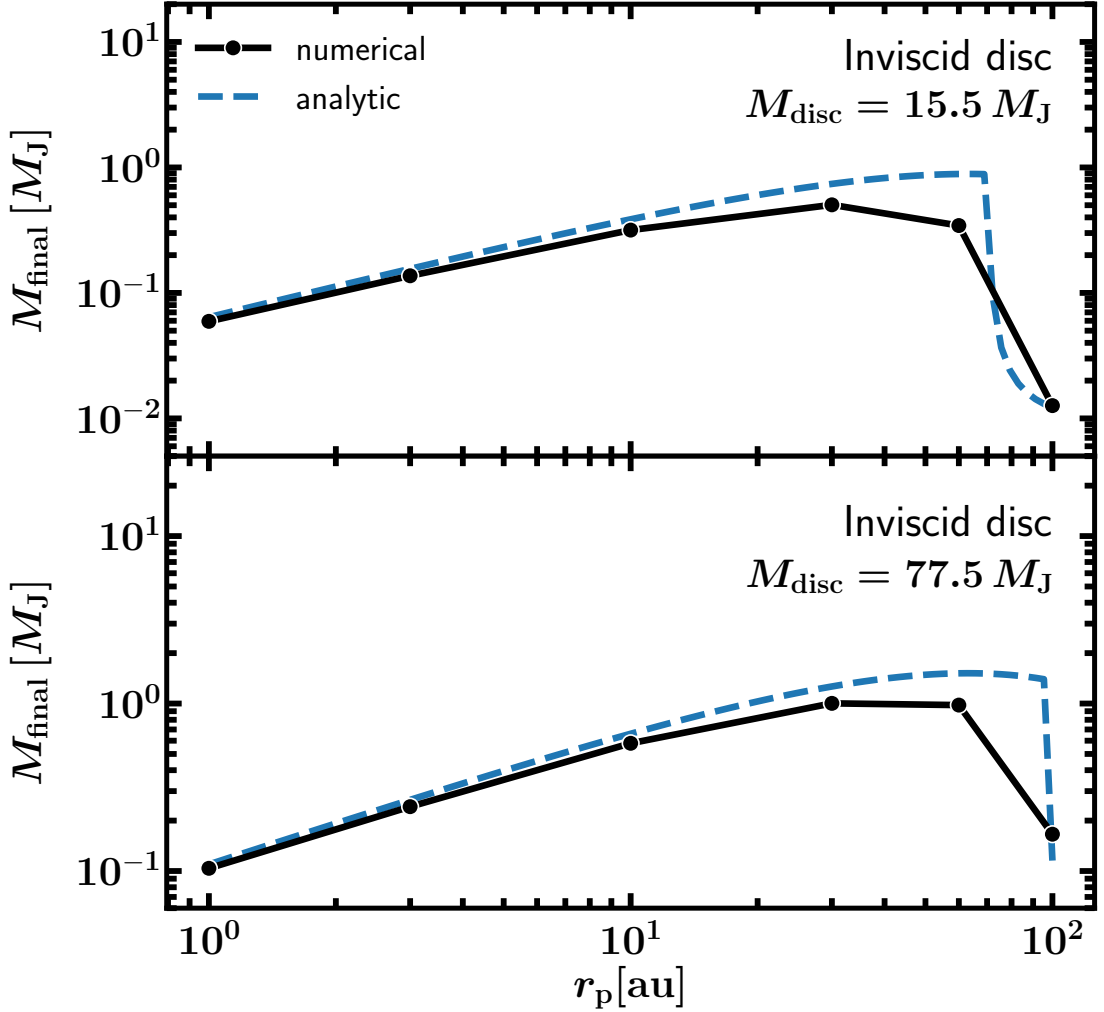


Figure 6.10: Final planet masses in an inviscid, wind-driven disc of varying mass (top vs. bottom panels). Planet masses are initialized at  $0.01M_J$  and grown using the 1D numerical code of section 6.4.4, which uses the time-dependent gap contrast of [Ginzburg & Chiang \(2019a\)](#) to model repulsion, in a purely advective disc whose height-averaged radial accretion velocity is  $c = -4$  cm/s and exponential drain-out time is  $t_{\text{adv}} = 3$  Myr. Points are plotted after  $5t_{\text{adv}} = 15$  Myr. They mostly respect equation (6.56), which gives final planet masses grown in repulsion-limited and deep ( $\tilde{B}_{\text{inv}} > 1$ ) gaps (dashed curve not including the drop-off at the largest distances). At  $r_p \sim 100$  au, the disc has such low density that the planet’s initial growth timescale  $M_p/\dot{M}_p$  is comparable to  $t_{\text{adv}}$ ; here there are not many doublings before the disc drains away. In this regime the planet does not open a substantial gap ( $\tilde{B}_{\text{inv}} < 1$ ) and its final mass can be estimated analytically by integrating  $\dot{M}_p = A_{\text{Bondi}}\Sigma$  with  $\Sigma$  given by the no-planet solution (6.46); the dashed curve is the minimum of the resulting expression (not shown) and (6.56).

### 6.5.2 Transitional discs

We have shown how a planet accreting from its parent disc can change the disc’s entire complexion. This make-over is most evident for a planet that siphons away most of the disc’s accretion flow—as it can in a viscously diffusing disc—carving out a consumption-limited gap that divides a gas-rich outer disc with surface density  $\Sigma_+$  from a gas-poor inner one with surface density  $\Sigma_-$ . Transitional discs have just such an outer/inner structure (e.g., [Espaillat et al. 2014](#); [Dong et al. 2017](#)), suggesting that they represent viscous discs whose inner regions are cleared by accreting planets (with dust filtration at the outer gap edge, and grain growth in the inner disc, enhancing the surface density contrast in dust over gas; [Dong et al. 2012](#); [Zhu et al. 2012](#)).

In a viscous disc, a single accreting planet suffices to deplete the entire disc interior to its orbit. The 2D single-planet simulations of [Zhu et al. \(2011\)](#) bear this out; they find an outer vs. inner disc contrast of  $\Sigma_+/\Sigma_- \sim 10$  for a  $1 M_J$  planet that accretes at the Hill rate from a disc of  $h \simeq 0.05$  (their fig. 1, model P1A1). This numerical result agrees with our analytic theory, which predicts according to equations (6.15) and (6.30) that

$$\frac{\Sigma_+}{\Sigma_-} \simeq \frac{A_{\text{Hill}}}{3\pi B} \simeq 7 \left( \frac{M_{\text{P}}}{M_{\text{J}}} \right)^{-4/3} \left( \frac{h}{0.05} \right)^3 \quad (6.58)$$

for a consumption-dominated and deep gap with  $A_{\text{Hill}}/(3\pi) > B > \nu$ , where  $\nu$  is the disc viscosity. In steady state,  $\Sigma_+/\Sigma_- = \dot{M}_+/\dot{M}_-$ , the ratio of outer-to-inner disc accretion rates. A value of  $\dot{M}_+/\dot{M}_- \sim 10$ , as we have found for the above parameters, accords with the observation that the median accretion rate for stars hosting transitional discs

is lower than that of stars hosting non-transitional discs by a factor of  $\sim 10$  (Najita et al. 2007; Kim et al. 2013). However, the corresponding factor-of-10 reduction in  $\Sigma$  seems too small to match observed gas depletions in transitional disc cavities. In the disc studied in CO by Dong et al. (2017), the gas surface density declines by  $\sim 10^3$  from  $r = 70$  au to 15 au. As recognized by Zhu et al. (2011; see also Owen 2016), it is a challenge to simultaneously explain how disc inner cavities can be strongly depleted in density while their central stars continue to accrete at near-normal rates.

This challenge seems more easily met in the repulsion limit, where deep gaps are carved by planets which alter the disc accretion flow only modestly—assuming radial accretion velocities within the gap are large enough to maintain mass transport rates across it.

The repulsion limit is attained in viscous discs by planets having  $M > M_{\text{rep,visc}} \simeq 5.3 M_{\text{J}} \left(\frac{r}{10 \text{ au}}\right)^{\frac{9}{16}}$ , or in inviscid discs by planets having  $M > M_{\text{rep,inv}} \simeq 0.02 M_{\text{J}} \left(\frac{r}{10 \text{ au}}\right)^{\frac{489}{392}}$ .

In both cases, multiple planets with adjoining gaps would be required to evacuate transition disc cavities spanning decades in radius—more planets in a viscous scenario where each gap has a radial width closer to  $H$ , and fewer in an inviscid scenario where each gap is of order  $r_{\text{p}} > H$  wide (Ginzburg & Sari 2018; note that widths are not captured by our single-grid-point treatment of gaps). The inviscid picture requires only super-Earth masses and appeals more, insofar as observations seem to have already ruled out transitional discs containing families of super-Jupiters as required in the viscous scenario. Inviscid discs can still accrete, either by virtue of magnetized winds (Bai 2016; Wang & Goodman 2017), or by the repulsive torques of their embedded planets (Goodman &

Rafikov 2001; Sari & Goldreich 2004; Fung & Chiang 2017).

## Chapter 7

# Measuring the Orbital

# Parameters of Radial Velocity

# Systems in Mean Motion

# Resonance—a Case Study of HD

# 200964

## 7.1 Introduction

A  $p:q$  mean-motion resonance (MMR) occurs when the ratio of the periods of two interacting planets is close to  $p/q$ . This commensurability allows planetary conjunctions to occur at consistent locations in the planets' orbits, leading to periodic

transfers of energy and angular momentum between the two bodies. Many examples of bodies in mean motion resonance are known in the solar system (for a review, see e.g. [Peale 1986](#)) and in exoplanetary systems (e.g. [Lissauer et al. 2011](#), [Izidoro et al. 2017](#)). In this paper, we restrict our focus to systems of giant planets in MMR. Mean motion resonance between Jupiter and Saturn has been suggested as a possible phenomenon early in the solar system’s history (e.g. [Morbidelli et al. 2007](#), [Walsh et al. 2011](#)). Several sets of giant planets in resonance have been identified directly (e.g., GJ 876, [Lee & Peale 2002](#); HD 5319, [Giguere et al. 2015](#); HD 33844, [Wittenmyer et al. 2016](#); HD 47366, [Marshall et al. 2019](#); HD 202696, [Trifonov et al. 2019](#); and TOI-216, [Kipping et al. 2019](#)) and resonance has been inferred due to stability constraints in the directly imaged system of giants HR 8799 (e.g., [Fabrycky & Murray-Clay 2010](#); [Wang et al. 2018](#)). Understanding the population of giant planets in MMRs is important for constraining the typical migration histories of giant planets, as convergent migration of giant planets in a gas disk is a commonly cited mechanism for formation of gas giants in MMR (e.g. [Lee & Peale 2002](#)).

Resonances often constitute stable regions in otherwise unstable parts of phase space. Because the interactions between planets in MMR can generate periodic oscillations of the system’s line of conjunctions, they can protect planets from close encounters. Thus, MMRs are often invoked to explain observed systems that initially appear to be unstable.

Unfortunately, the presence of MMRs greatly complicates analysis of RV systems. Strong planet-planet interactions cause the planets to deviate from pure Keplerian

motion even on the timescale of typical RV observations. This complicates the usual RV fitting process, where planets are often allowed to move on unperturbed Keplerian orbits. Furthermore, the additional frequencies introduced by these dynamical interactions can shift the peaks in a periodogram of the RV signal away from the true orbital periods of the planets. This difficulty in identifying the periods of the planets in turn means that, perhaps counterintuitively, the particular resonance that a system is in is not clear from the outset of fitting. Further exacerbating this issue is the fact that libration of the MMR’s resonant angle occurs on timescales that are generally longer than the timescale of the RV observations, meaning that our observations only capture part of the full libration. This sampling issue, along with error in the observations, means that the best-fit solutions to RV signals may lie far from solutions that actually exhibit long term stability.

Thus, fitting RV systems in MMR necessitates different methods than those traditionally used to fit radial velocity systems. Firstly, theoretical radial velocities must be generated through full numerical integration of the equations of motion of the system (e.g., [Tan et al. 2013](#), [Wittenmyer et al. 2014](#), [Nelson et al. 2014](#), [Trifonov et al. 2017](#), [Millholland et al. 2018](#)). Furthermore, while initial searches through parameter space can be performed without incorporating long term stability, the “true” posterior distribution of the planetary orbital parameters should not include points that are unstable on short timescales. In some cases “rejection sampling”, i.e. throwing out all points that do not exhibit stability, can produce posterior distributions conditioned on long-term stability. However, as will be seen in this work, it is often the case that the

fraction of stable points is so small that the posterior produced by rejection sampling does not adequately represent the underlying probability distribution. Thus, in order to find long-term stable posterior distributions it is often necessary to incorporate stability during the search through parameter space, though this is often not explicitly done. Incorporating long term stability makes exploring the parameter space difficult, as while regions close to particular MMRs will exhibit long term stability, intermediate regions will generally have no stable solutions, meaning that each proposed resonance must be investigated separately.

In this work, we illustrate these difficulties and ways they can be mitigated through the example of the planetary system orbiting the star HD 200964. HD 200964 is an intermediate mass subgiant (see Table 7.1 for a summary of the stellar parameters), which was reported by [Johnson et al. \(2011a\)](#) (hereafter [JPH11](#)) to host two massive ( $M_p \gtrsim M_J$ ) giant planets in a tight orbital configuration ( $P_c:P_b \sim 800:600$  days). [JPH11](#) gave a best-fit, long term ( $> 10^7$  years) stable solution that was close to a 4:3 MMR. In this work, we include additional observations from both the Keck telescope as well as the Automated Planet Finder (APF), which increase the length of time spanned by the RV data. In addition, we explicitly require stability in our search over parameter space, which greatly aids in finding regions of parameter space that both fit the data well and exhibit long term stability. We find that, in addition to the 4:3 solution identified by [JPH11](#), the system can be fit by both a 3:2 MMR and a 7:5 MMR, with the 7:5 providing the best fit to the measured radial velocity. The presence of multiple plausible MMRs highlights the general difficulty in pinning down MMR in observed

Table 7.1: Stellar parameters for HD 200964, taken from [Brewer et al. \(2016\)](#)

Parameter	Value
$V_{\text{mag}}$	6.48
Distance [pc]	72.2
$T_{\text{eff}}$	4982
$\log g$	3.22
[M/H]	-0.1
$\log L [L_{\odot}]$	1.13
$R_* [R_{\odot}]$	4.92
$M_* [M_{\odot}]$	1.45
Age [Gyr]	3.3

radial velocity systems. We also note that if the system is truly in a 3:2 MMR, this would mitigate difficulties in forming the system through convergent migration.

In Section 7.2, we discuss how our observations of HD 200964 were performed. In Section 7.3, we discuss the results of previous analyses of HD 200964. In Section 7.4 we discuss the various methods we employed to find best-fit, long-term stable solutions to the observed radial velocity. In Section 7.5 we analyze the MMRs that stabilize the best-fit solutions we find. In Section 7.6 we perform our methodology on the [JPH11](#) dataset and compare our results with theirs, and in Section 7.7 we discuss the possibility of a third planet in the system. Finally, in Section 7.8 we summarize our results and give our conclusions.

## 7.2 Observations

The radial velocity measurements of HD 200964 used in this analysis come from three different facilities: the Hamilton spectrometer ([Vogt 1987](#)) paired with the Shane 3 m or the 0.6 m Coude Auxiliary Telescope, the HIRES spectrometer ([Vogt et al. 1994](#)) on Keck I, and the Levy spectrometer on the Automated Planet Finder

(APF) telescope (Vogt et al. 2014). In all cases, the star’s Doppler shifts were measured by placing a cell of gaseous iodine in the converging beam of the telescope, imprinting the stellar spectrum with a dense forest of iodine lines from 5000-6200 Å (Butler et al. 1996). These iodine lines were used to generate a wavelength calibration that reflects any changes in temperature or pressure that the spectrometer undergoes, and enables the measurement of each spectrometer’s point spread function. Although each spectrometer covers a much broader wavelength range, 3400-9000 Å for the Hamilton and 3700-8000 Å for HIRES and the Levy, only the iodine rich 5000-6200 Å region was used for determining the observation’s RV shift. For each stellar spectrum, the iodine region was divided into  $\sim 700$  individual 2Å chunks. Each chunk produces an independent measure of the wavelength, point spread function, and Doppler shift. The final measured velocity is the weighted mean of the velocities of all the individual chunks. It is important to note that all RVs reported here have been corrected to the solar system barycenter, but are not tied to any absolute RV system. As such, they are “relative” velocities, with a zero point that is usually set simply to the mean of each dataset.

We make use of two previously published RV datasets, denoted here as the “Lick” and “Keck11” datasets, taken from Johnson et al. (2011b) which originally announced the detection of these planets in the context of their intermediate-mass subgiant host star survey (Johnson et al. 2006; Peek et al. 2009; Bowler et al. 2010; Johnson et al. 2010). The Lick data have SNR of  $\sim 120$  in the center of the iodine region ( $\lambda = 5500\text{Å}$ ) corresponding to an internal uncertainty value of  $4\text{-}5\text{m s}^{-1}$ , while the Keck11 have SNR  $\sim 180$  in the same area which brings the internal uncertainties down to  $1.5\text{-}2\text{m s}^{-1}$ . For

additional details on this data, see [Johnson et al. \(2011b\)](#). New to this paper are an additional 50 velocities taken with Keck HIRES and 36 velocities taken with the APF, all obtained as part of the long running LCES Doppler survey ([Butler et al. 2017](#)) and denoted as “Keck” and “APF”, respectively. For our HIRES observations the median SNR in the iodine region is 159, corresponding to an average internal uncertainty of  $1.4\text{m s}^{-1}$ . The APF observations have a median SNR of 101 in the iodine region, which produces an average internal uncertainty of  $1.5\text{m s}^{-1}$ . These internal uncertainties reflect only one term in the overall RV error budget, and result from a combination of systematic errors from things like properly characterizing the point spread function, detector imperfections, optical aberrations, and under sampling the iodine lines, among others.

The new Keck and APF radial velocities are given in Tables 7.2 and 7.2 respectively. Additionally, all four data sets, along with our maximum likelihood solution without stability taken into account (see Section 7.4.1), are plotted in Figure 7.1.

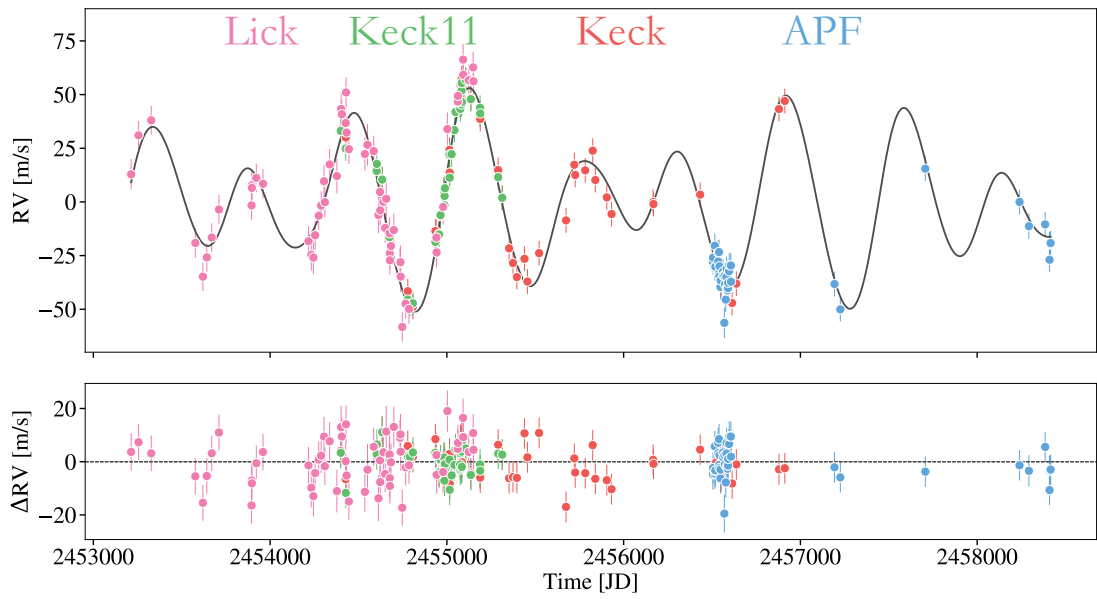


Figure 7.1: The four data sets for the radial velocity of HD 200964, along with the theoretical radial velocity curve obtained using the parameters given in Table 7.5. The data sets are: Lick (pink points), Keck11 (green points), Keck (red points), and APF (blue points). Note that, as discussed in Section 7.4.1, each data set has a constant offset that we fit separately. Furthermore, the jitter term given in Table 7.5 is added in quadrature to the quoted error bars to obtain the error bars shown in the figure. The residuals between the theoretical velocity and the data are shown in the bottom panel.

Table 7.2: Keck Radial Velocities for HD 200964

Julian Day	RV [m s <sup>-1</sup> ]	Uncertainty [m s <sup>-1</sup> ]
2454399.75186	23.56	1.54
2454427.75745	19.83	1.13
2454634.07880	0.38	1.57
2454674.91593	-24.76	1.46
2454778.80262	-51.78	1.54
2454807.78906	-59.08	1.62
2454935.13871	-23.75	1.21
2454956.09772	-25.09	1.39
2454964.11957	-16.80	1.39
2454984.06802	-4.39	1.36
2454985.09297	-5.21	1.52
2455014.96811	14.08	1.61
2455015.95302	3.45	1.56
2455075.07263	40.27	1.53
2455076.06215	35.78	1.65
2455077.05115	44.44	1.51
2455082.04172	35.42	1.50
2455083.04807	45.17	1.70
2455084.02263	47.35	1.48
2455084.99943	38.08	1.53
2455106.90692	46.40	1.32

Table 7.2 (cont'd): Keck Radial Velocities for HD 200964

Julian Day	RV [m s <sup>-1</sup> ]	Uncertainty [m s <sup>-1</sup> ]
2455135.75335	38.24	1.40
2455187.69803	30.50	1.63
2455188.69157	28.42	1.54
2455290.14918	4.66	1.47
2455313.13833	-8.29	1.12
2455352.08439	-31.80	1.38
2455374.11241	-38.66	1.51
2455395.95755	-45.18	1.38
2455439.01932	-36.70	1.38
2455455.73766	-47.27	1.42
2455521.79477	-34.05	1.39
2455674.14167	-18.79	1.47
2455720.97469	7.14	0.57
2455726.03586	2.36	1.28
2455782.84153	4.52	1.34
2455824.92332	13.68	1.23
2455839.82582	0.00	1.27
2455904.73172	-8.06	1.43
2455931.69116	-15.84	1.41
2456166.74440	-10.20	1.40
2456168.86382	-11.20	1.21

Table 7.2 (cont'd): Keck Radial Velocities for HD 200964

Julian Day	RV [ $\text{m s}^{-1}$ ]	Uncertainty [ $\text{m s}^{-1}$ ]
2456433.04139	-6.80	1.14
2456522.09346	-38.29	1.59
2456529.87766	-35.31	1.54
2456551.82347	-49.97	1.18
2456613.77979	-57.29	1.44
2456637.69903	-48.26	1.32
2456878.89942	33.07	1.56
2456911.71152	36.84	1.42

Table 7.3: APF Radial velocities for HD 200964

Julian Day	RV [ $\text{m s}^{-1}$ ]	Uncertainty [ $\text{m s}^{-1}$ ]
2456504.82513	0.54	1.26
2456505.93027	2.60	1.29
2456515.85262	8.11	1.20
2456516.89268	-2.40	1.27
2456517.78745	-1.66	1.23
2456518.81965	-1.70	1.25
2456534.80483	4.89	1.21
2456535.80156	0.75	1.28
2456539.79917	5.14	1.36
2456540.82230	-4.63	1.55
2456541.85331	-6.12	1.16
2456542.75722	-1.48	1.02
2456547.79837	-11.14	1.29
2456548.77462	-8.03	1.21
2456562.80405	-3.92	1.05
2456563.71147	-5.93	1.08
2456569.79719	-27.84	4.34
2456570.79627	-5.96	1.55
2456573.72675	-9.89	1.44
2456577.80143	-17.01	1.00
2456581.79176	-6.52	0.78
2456582.73480	-2.58	0.63
2456583.69447	-11.73	1.09
2456588.68050	-12.69	0.57
2456589.77159	-11.57	1.02
2456590.66789	-11.63	1.32
2456591.66285	-9.16	0.74
2456596.59997	-3.76	1.12
2456597.69329	-0.91	0.72
2456606.66048	-1.10	0.84
2456607.69387	-8.66	1.00
2457192.94571	-9.75	1.23
2457225.99709	-21.57	0.80
2457706.65722	43.99	1.23
2458239.99803	28.47	1.08
2458292.79881	17.20	1.81
2458384.63820	18.05	0.93
2458408.59895	8.73	0.79
2458409.59737	1.57	0.78
2458411.59738	9.05	0.90
2458413.59601	8.92	0.76
2458415.59282	9.33	0.80

### 7.3 Previous Analysis

The first analysis of the planetary system around HD 200964 was given by [JPH11](#), using the “Lick” and “Keck11” datasets. These authors first perform a Markov chain Monte Carlo (MCMC) analysis of the system assuming Keplerian orbits for both of the planets in the system, i.e. neglecting planet-planet interactions. They use the results of this Keplerian MCMC to initialize a Differential Evolution Markov Chain Monte Carlo (DEMCMC) algorithm. The theoretical radial velocity at a given time is calculated using an  $N$ -body integrator, with a constraint that the system must remain stable for 100 years. They then perform rejection sampling on their final posterior, throwing out points which are not stable for  $10^7$  years. Their best-fit, long term stable solution appears to have an RMS scatter of 28.1 m/s, which would indicate poor agreement between the model and the data. Furthermore, as also reported by [Tadeu dos Santos et al. \(2015\)](#), we find that the best fit solution reported by [JPH11](#) does not exhibit long-term stability, regardless of whether the reported orbital elements are taken to be astrometric or Jacobi. However, [JPH11](#) do not appear to specify the epoch at which the planets have the reported orbital elements. When planet-planet interactions are included, the orbital elements of the planets change as a function of time. Thus, in order to fully specify an orbit, the time at which the orbital elements are referenced must be stated in addition to the elements themselves. For example, for the parameters given by [JPH11](#), the period of the outer planet ranges from  $\sim 772$  to 857 days over the timescale of the radial velocity observations. Given the degree to which the orbital elements change over the timescale of the observations for the parameters reported by

JPH11, it is quite possible that the discrepancy we find between their best-fit solution and the data is because the epoch to which the elements are referenced is not specified.

The reported 4:3 MMR exhibited by the system is interesting, as it is quite difficult to capture planets of gas giant mass into this resonance through convergent migration alone, as discussed by Rein et al. (2012). Subsequent works have explored the stable regions of parameter space for the parameters reported by JPH11, (Wittenmyer et al. 2012), investigated in more detail the resonant behavior exhibited for the reported parameters (Mia & Kushvah 2016) and investigated other, more complex scenarios for the formation of HD 200964 (Emel’yanenko 2012, Tadeu dos Santos et al. 2015)

## 7.4 Methods

In this work, in addition to analyzing a baseline of data longer than that used in JPH11, we investigate the underlying posterior by explicitly conditioning our Markov chain Monte Carlo (MCMC) search on long-term stability. MCMC is a commonly used method to sample from a probability distribution (see e.g. Sharma 2017 for a review); in this context it used to sample from the posterior probability distributions for the orbital parameters of the planetary system (as well as the stellar jitter, see below). In this section we specify the methods employed to find these stable, best-fit solutions. We begin by investigating best-fit solutions including planet-planet interactions but neglecting stability (Section 7.4.1). After constructing the posterior distribution of orbital parameters without stability, we show that “rejection sampling”, i.e. discarding solutions that do not exhibit long-term stability, yields few long-term stable solutions

(Section 7.4.2). Thus, to improve our measurement of the long-term stable posterior distribution, we explore parameter space using a likelihood function that explicitly takes stability into account (Section 7.4.3). We find that this method does a much better job of fitting the posterior distribution, though we find the posterior is multi-modal (Section 7.4.4). Finally, we perform a Monte Carlo search to verify after the fact that we have identified all relevant stable regions of parameter space (Section 7.4.5).

### 7.4.1 Fits Incorporating Planet-Planet Interactions

We begin our analysis by searching for fits to the RV data without explicitly requiring our solutions to be stable. Firstly, we note that inspection of a usual generalized Lomb-Scargle periodogram (GLS, see e.g. [Zechmeister & Kürster 2009](#)), leads inexorably to the conclusion that the two planets in the system are closely packed. A GLS for the RV data shown in Figure 7.1 is plotted in Figure 7.2. The two largest peaks (note that we have omitted a peak at  $\sim 1$  day which is likely an alias of the sampling period of the data) of the GLS are near  $\sim 600$  and  $\sim 900$  days. While the actual periods of the planets we determine will be affected by planetary eccentricity and dynamical interaction between the planets, these close peaks nonetheless indicate that the system likely contains two closely packed planets.

Thus the gravitational interactions between the planets constitute an important component to the observed radial velocity of HD 200964, and cannot be neglected. Often, theoretical radial velocity values are calculated by advancing the planets along Keplerian orbits, in effect neglecting any perturbations between the planets. For non-closely packed systems this is generally a fine approximation, as perturbations between

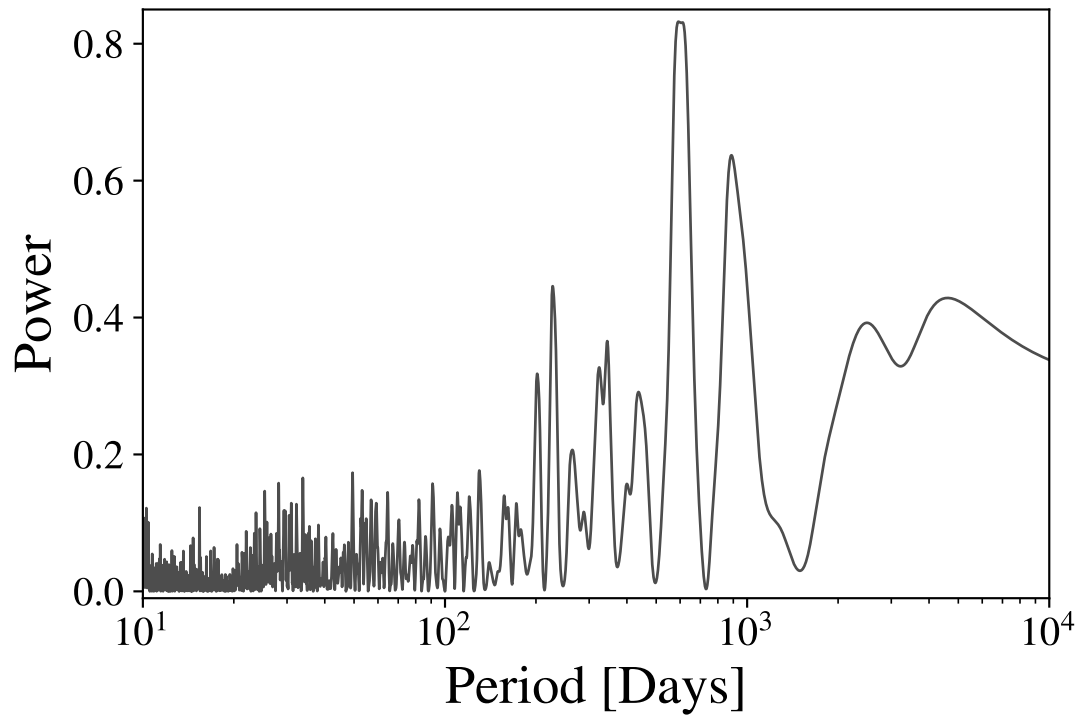


Figure 7.2: A generalized Lomb-Scargle periodogram for the RV data of HD 200964. Note the two strong peaks at  $\sim 600$  and  $\sim 900$  days, demonstrating that the system likely features two closely-packed planets. The full width at half maximum of each peak is indicated by the gray rectangle.

the planets are unimportant over the timescale of the RV observations. As illustrated in Figure 7.3, however, this is not the case for HD 200964. Figure 7.3 plots the radial velocity as a function of time determined by both using only Keplerian orbits, as well as a full  $N$ -body integration of the equations of motion. The difference between the two values is shown in the bottom panel. The orbital parameters used correspond to our best-fit, long-term stable solution (see Section 7.4.3).

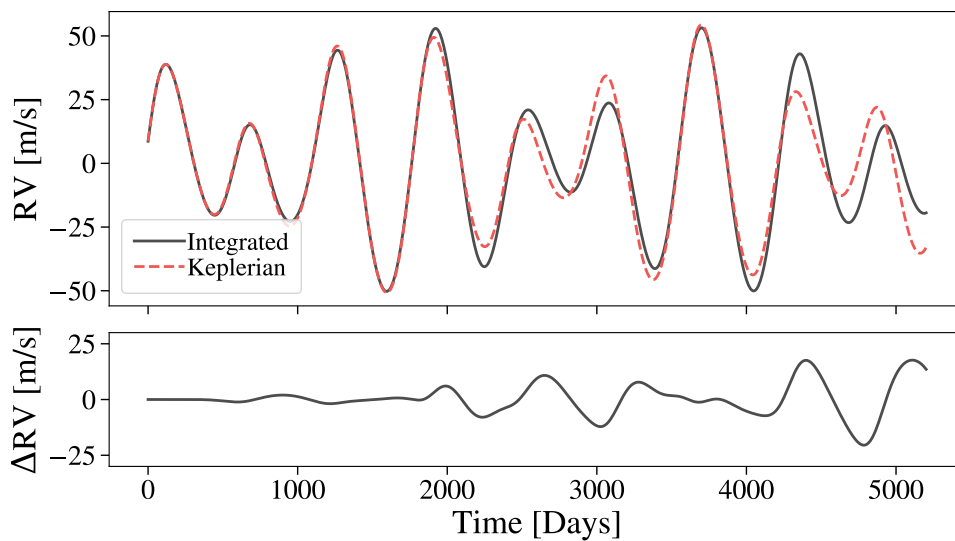


Figure 7.3: A comparison of the radial velocity determined by numerically integrating the motions of the planets and by advancing the planets forward on Keplerian orbits. The orbital parameters used are our best-fit long-term stable solution, as discussed in Section 7.4.3. The top panel shows the stellar radial velocity determined by the two methods, while the bottom shows the difference in the two curves. There is substantial disagreement between the integrated and Keplerian radial velocities due to the strong planet-planet interactions present.

Clearly, neglecting the planet-planet interactions is a poor approximation; in what follows all calculation of radial velocity values will be done by numerically integrating the star-planet system forward in time. In order to perform our numeric inte-

grations, both to calculate the theoretical radial velocity and to determine the lifetime of our planetary systems (see Sections 7.4.2 and 7.4.3), we use the  $N$ -body integration package REBOUND (Rein & Liu 2012).

For the purpose of computing the theoretical radial velocity for comparison with the observations, we use the IAS15 integrator (Rein & Spiegel 2015), which is a 15th order integrator with adaptive time stepping. All orbital elements provided in this paper are quoted relative to the primary star, i.e. they are astrometric coordinates, and are given at the epoch of the first data point, i.e. JD 2453213.895. Following Brewer et al. (2016), we take the central star to have mass  $M_* = 1.45M_\odot$ . We use a usual radial velocity coordinate system, such that the inclination  $i$  represents the angle between orbital plane and the plane of the sky, which we take to be the reference plane. The argument of periaapse,  $\omega$ , is the angle between the line of ascending nodes and the periaapse direction. The observer is taken to lie in the  $-\hat{z}$  direction relative to the reference plane; in keeping with convention velocities in this direction, i.e. towards the observer, are quoted as positive. For clarity, due to the strong planet-planet interactions we specify the mean longitudes of the two planets at epoch,  $\lambda$ , as opposed to the planets' time of periastron passage. In this work we fix  $i = 90^\circ$ , corresponding to edge on orbits, and fix the longitude of ascending node,  $\Omega = 0$ . We comment on the degeneracy between the system's inclination and the masses of the planets in Section 7.4.4.

Following other works (e.g Johnson et al. 2007, Cumming et al. 2008, JPH11), we introduce a “stellar jitter” term in our fitting, which is an additional error term that is added in quadrature to the “known” error, i.e. the error on each measurement

is taken to be  $\sqrt{\sigma_k^2 + \sigma_j^2}$ , where  $\sigma_k$  is the given error and  $\sigma_j$  is the proposed value of the stellar jitter term. We also note that we are using a single value to characterize the stellar jitter, meaning that we are neglecting variation in jitter between different instruments (Balbus 2009). We have checked that the inclusion of multiple jitters has no qualitative effect on the posterior distribution shown in Figure 7.4. However, fitting a different jitter for each data set (as is done in e.g. Nelson et al. 2016 or Millholland et al. 2018) would allow us to characterize the difference in instrumental noise between the various datasets.

We calculate the likelihood for a given set of orbital parameters by assuming that the radial velocity measurements are all independent and Gaussian distributed, with error given by  $\sigma_i = \sqrt{\sigma_k^2 + \sigma_j^2}$ , as discussed in the preceding paragraph. In this case, the log likelihood  $\mathcal{L}$  is given by

$$\mathcal{L} = - \sum_i \left[ \frac{(v_i - RV(t_i) - O_D)^2}{2\sigma_i^2} + \log(\sigma_i \sqrt{2\pi}) \right] \quad (7.1)$$

where  $v_i$  are the measured radial velocities and  $RV(t_i)$  are the model radial velocities. Here  $O_D$  refers to the constant offset to each dataset (see Section 7.2), which must also be fit, introducing 4 additional parameters into our fitting. Instead of including the 4 offsets as parameters in our MCMC search, the offsets are separately optimized for every proposed set of orbital parameters. That is, once the model radial velocities are known, it is straightforward to show that the constant offset to each dataset that maximizes the likelihood can be obtained by calculating the weighted mean of the difference between

the model and the data

$$O_D = \frac{1}{S} \sum_{i \in D} \frac{v_i - RV(t_i)}{\sigma_i^2} \quad (7.2)$$

where  $S \equiv \sum_i 1/\sigma_i^2$ . This simplifies our fitting algorithm, but does mean that we may miss degeneracies between the constant offsets and the orbital elements.

For our priors, we assume uniform probability in some specified domain for each parameter, except for the planetary eccentricities, where the priors are uniform in log space. For periods of each planet, the priors are uniform between 400 to 1000 days for planet b, and 500 to 1100 days for planet c. The prior on planetary mass is uniform between 0.1 and 10  $M_J$  for both planets. For the planetary eccentricity, the prior is uniform in log space between -4.5 and 0. For all the angles, the priors are taken to be uniform between  $-720^\circ$  and  $720^\circ$ . This is done to ensure that the arguments of pericenter do not diverge to arbitrarily large values when the planet's eccentricity is low. In practice the actual values of parameters in our searches are quite far from the limiting bounds, with the exception of planetary eccentricity and the corresponding argument of pericenter, where the bounds are important for cases of low eccentricity.

To explore the parameter space, we initially use the `scipy` minimizer to optimize the orbital parameters. We initially fix the orbital periods and masses of the planets, using the GLS and the amplitude of the RV signal to provide rough estimates of these parameters, and perform an optimization on the rest of the parameters, starting from random values. We chose five of these optimizations which both had high likelihood and different final parameters to initialize our MCMCs.

We used the software `emcee` (Foreman-Mackey et al. 2013) to perform our MCMC search. We initialized different MCMC searches from our converged optimizations. We let these MCMCs run for  $\sim 1000$  steps, and look at the regions of high likelihood. We found that all of these searches identify a single region as having the highest likelihood. We then reinitialized a final search in this region. We ran this MCMC for an initial burn in period, then discarded these walker positions and ran the MCMC to convergence. To assess convergence of our MCMC runs, we used the potential scale reduction factor (PSRF, Gelman & Rubin 1992). A common method to assess convergence is to run the MCMC until the PSRF for every parameter has a value  $< 1.1$  (Brooks & Gelman 1998). However, for our MCMC runs the PSRF for the two eccentricities and arguments of pericenter often do not fall below 1.1, likely because at low eccentricities the posterior probability is completely insensitive to these parameters. Thus, in practice we consider our MCMC converged if the PSRF for all parameters, except for the two eccentricities and two arguments of pericenter, is below 1.1.

A corner plot showing our best fit posterior distribution for the orbital parameters is shown in Appendix C (Figure C.1). The model radial velocity produced from our best-fit parameters (maximum likelihood) is shown in Figure 7.1, the median values of our posterior distribution are given in Table 7.4, and the maximum likelihood orbital parameters are given in Table 7.5.

The periods of the planets in our posterior distribution are much more constrained than the results obtained by JPH11. The median period ratio of the system has also moved to  $P_c/P_b \sim 7/5$ , whereas JPH11 found values much closer to  $4/3$ . This is

Table 7.4: Median orbital parameters, no long term stability

Parameter <sup>a</sup>	HD 200964 b	HD 200964 c
Orbital Period, $P$ [days],	$604.69^{+3.38}_{-3.10}$	$852.55^{+9.42}_{-8.30}$
Mass, $m$ [ $M_J$ ]	$1.72^{+0.05}_{-0.05}$	$1.20^{+0.06}_{-0.06}$
Mean longitude, $\lambda$ [deg]	$307.40^{+5.26}_{-5.06}$	$239.47^{+6.27}_{-6.42}$
Argument of periastron, $\omega$ [deg]	$294.48^{+21.08}_{-22.70}$	$259.32^{+57.71}_{-47.07}$
$\log_{10}$ Eccentricity, $e$	$-1.15^{+0.11}_{-0.15}$	$-1.49^{+0.55}_{-1.81}$
Stellar Jitter, $\sigma_j$ [m/s]	$6.05^{+0.46}_{-0.39}$	

<sup>a</sup>Values for orbital elements are in astrometric coordinates, are referenced to the epoch of the first data point, JD 2453213.895, and assume an inclination  $i = 90^\circ$ . The reported values are median values for the posterior distribution, and the reported error bars are 84% and 16% quantiles.

due to our observations spanning a longer timescale. To illustrate this point, in Figure 7.5 we plot the posterior for our new data along with the  $N$ -body integrated posterior distribution produced by analyzing just the [JPH11](#) data (see Section 7.6). This is consistent with the results of [Luhn et al. \(2019\)](#), who also report the period of planet c to be around 850 days based on a Keplerian fit to the data.

Interestingly, using  $N$ -body integration to determine the theoretical RV values broadens the posterior distribution of  $P_b$  and  $P_c$  compared to a purely Keplerian fit for the full dataset. For comparison with our  $N$ -body integrated fits, we repeat our analysis with the assumption of Keplerian orbits for both planets. The 2D histogram of a Keplerian fit to the data is plotted in red in Figure 7.4. In particular, it appears that the dynamical interaction between the planets allows for period ratios close to both 3:2 and 4:3 to fit the data, which are more strongly ruled out in a purely Keplerian fit.

Closer examination of our  $N$ -body integrated posterior distribution shows that many of the points, including our best fit solution, feature extremely close encounters between the two planets. An example from our best-fit parameters is shown in Figure

Table 7.5: Maximum likelihood orbital parameters, no long term stability

Parameter <sup>a</sup>	HD 200964 b	HD 200964 c
Orbital Period, $P$ [days],	607.7	845.3
Mass, $m$ [ $M_J$ ]	1.71	1.21
Mean longitude, $\lambda$ [deg]	312.5	233.7
Argument of periastron, $\omega$ [deg]	297.4	270.5
$\log_{10}$ Eccentricity, $e$	-1.13	-0.92
Stellar Jitter, $\sigma_j$ [m/s]	5.60	

<sup>a</sup>Values for orbital elements are in astrometric coordinates, are referenced to the epoch of the first data point, JD 2453213.895, and assume an inclination  $i = 90^\circ$ .

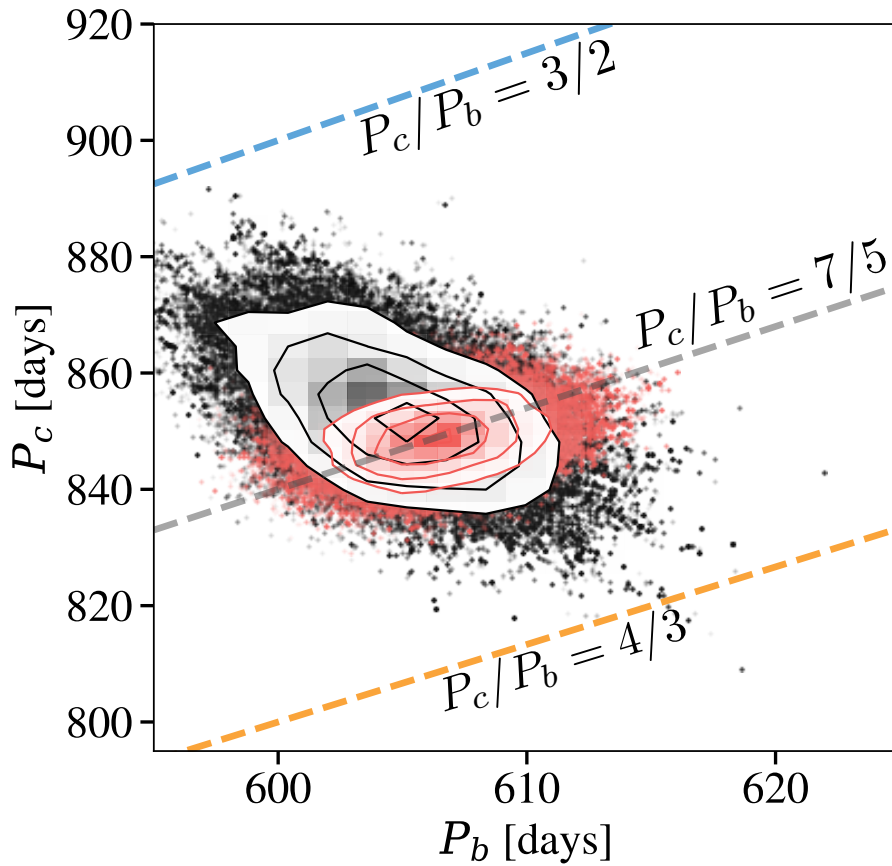


Figure 7.4: 2D histograms of the posterior distributions for the planets' periods, using  $N$ -body integration to calculate the radial velocity but without long-term stability (black points, see Section 7.4.1) and advancing the planets on Keplerian orbits (red points). Lines denoting exact ratios of  $P_c/P_b$  are shown for ratios of 3:2 (blue), 7:5 (gray) and 4:3 (orange).

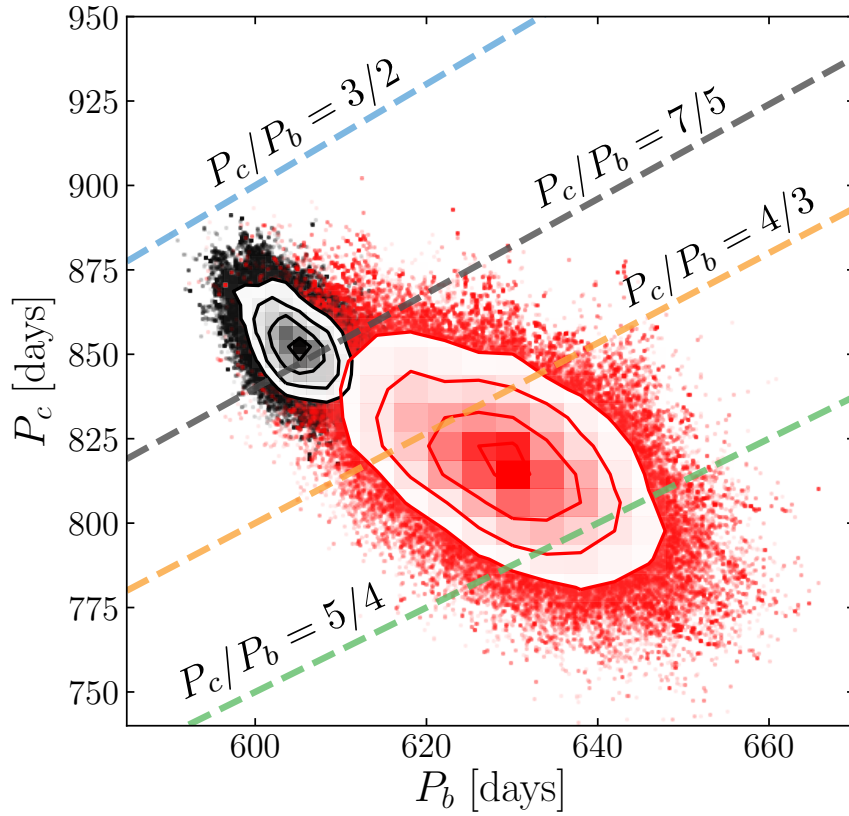


Figure 7.5: 2D histograms of the posterior distributions for the planets' periods, using  $N$ -body integration to calculate the radial velocity but without long-term stability. The black points show the posterior produced by using the full dataset, while the red points show the posterior obtained by analyzing only the [JPH11](#) data. Lines denoting exact ratios of  $P_c/P_b$  are shown for ratios of 3:2 (blue), 7:5 (gray), 4:3 (orange), and 5:4 (green).

7.6, which plots the distance between each planet and the central star as a function of time. While neither of the planets is ejected over this timescale, the two planets, particularly the outer planet, experience large amplitude fluctuations in distance from the central star. Thus, it is extremely unlikely, if the system were truly in this orbital configuration initially, that we would observe it before the configuration changed substantially. Furthermore, integration over long time scales indicates the outer planet is scattered out past 100 AU on  $10^5$  year timescales.

The majority of the solutions in Figure 7.4 do not exhibit long term stability.

#### 7.4.2 Rejection Sampling

In order to find long term stable solutions, we begin by using “rejection sampling” on the posterior distribution found in Section 7.4.1. Rejection sampling is less computationally intensive than doing a full search conditioned on stability, and has been employed in other works to find best fit orbital parameters for planetary systems which are also stable (e.g. [Wang et al. 2018](#)). In rejection sampling, we first construct a posterior distribution for the planetary system that does not take stability into account. Some fraction of the points (or, in our case, all of the points) in the posterior are chosen at random, and are then tested for long-term stability. All of the points in the posterior that pass the stability criteria then make up the new best-fit posterior which is conditioned on stability.

The converged posterior distribution shown in Figure 7.4 contains 287,296 points in parameter space. We then tested all of these points for stability for  $10^3$  orbital periods of planet c. We consider systems stable if both planets remained between 150%

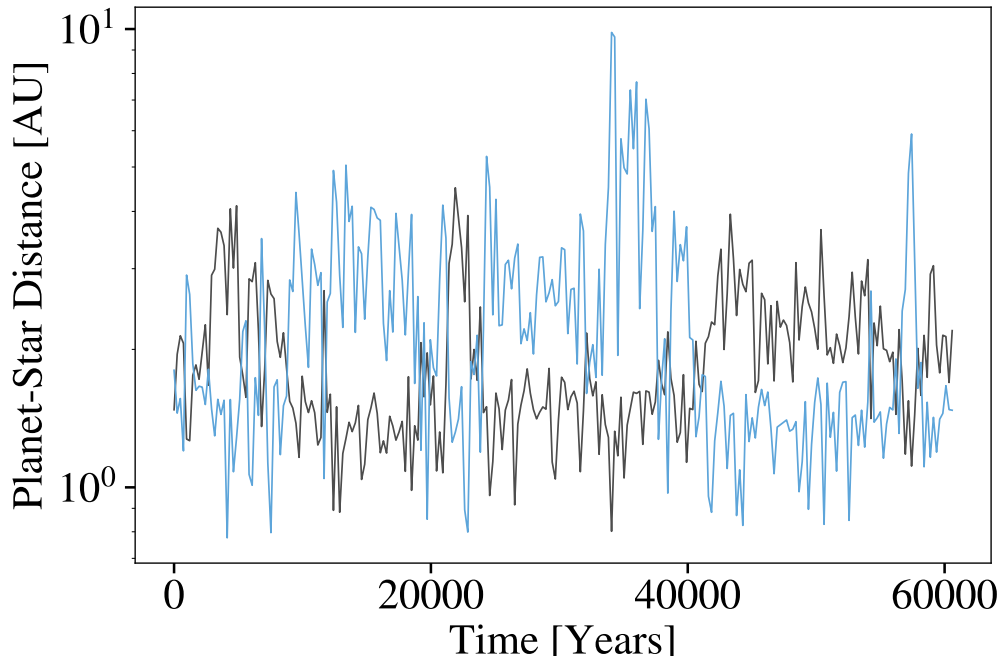


Figure 7.6: Distance between planet b (black line) and planet c (blue line), and the host star for our best-fit solution without long-term stability (see Section 7.4.1). The planets experience large, non-periodic fluctuations in distance from the star due to their strong mutual perturbations. The short timescale of these fluctuations relative to the age of the host star makes it unlikely, if the proposed best fit solution were correct, that the system would be observed in the original orbital configuration. Furthermore, these fluctuations are a strong indication that the system will become unstable on timescales much less than the age of the system. This is indeed the case—planet c is eventually scattered to a distance  $> 100$  AU on  $10^5$  year timescales.

of their initial periastron distance and 50% of their apastron distance from the central star during the course of the integration. We considered distance from the central star, as opposed to the semi-major axis of the planets, as many of our best fit solutions feature extremely close encounters between the planets, as discussed above. This can cause the semi-major axis of planet b to diverge as its velocity is temporarily excited to above the escape velocity from the system, despite the fact that the system remains stable after this close encounter. Though it is unlikely a system featuring such a close encounter will survive on long timescales, we did not want to prematurely discard these solutions without checking for long term stability. These integrations were again carried out using the IAS15 integrator.

Of the points in the initial posterior, 2,295, i.e.  $< 1\%$  of the systems survived for  $10^3$  orbital periods. We then tested these remaining points for longer term stability: each set of orbital parameters was integrated for  $10^7$  orbital periods of planet c. For these long term stability analyses we use the WHFAST integrator ([Rein & Tamayo 2015](#)), an implementation of the symplectic Wisdom-Holman integrator. Unless otherwise noted, we set the timestep for our integrations with WHFAST to be  $dt = P_{\min}/100$ , where  $P_{\min}$  is the shortest initial orbital period of the planets in the system. This is five times shorter than the orbital period recommended by [Duncan et al. \(1998\)](#), who recommend  $dt = P_{\min}/20$  for a second order symplectic integrator. Of the points tested, only 1,111 survive for  $10^7$  orbital periods. This is far too few points to construct a converged posterior for stable, best fit solutions to the data. We would require 1-2 orders of magnitude more points in our original, non-stable posterior, in order to retain

enough points in the rejection sampling to construct a converged stable posterior, which would be extremely computationally intensive. Though the posterior obtained through rejection sampling is clearly not converged, the points do appear to lie in the general region of parameter space identified in Section 7.4.3. With rejection sampling, we only identify stable fits near 7:5 period ratio (c.f. Figure 7.8, purple points), while the broader search described in Section 7.4.3 identifies other possible period ratios.

It is also interesting to note that when this exercise was carried out for fits on just the Keck and APF datasets (i.e. omitting the Lick and Keck11 datasets), *none* of the points in the initial posterior survived for  $10^7$  orbital periods. It is only when we have data spanning a longer timescale that we appear to be able to find *any* best-fit solutions that also exhibit stability. We suspect that this effect stems from the longer time baseline and better coverage of the RV signal that inclusion of the two later data sets provides. As more data is included the parameters of the planets in the system become better constrained, and our posterior distribution moves closer to the “true” parameters of the underlying system, which presumably does exhibit long term stability. Thus, with more data, we expect a greater likelihood that the posterior distribution we construct without explicitly including stability will overlap with stable regions of parameter space.

While rejection sampling is insufficient to construct a converged posterior distribution, some of these points are useful places to initialize MCMC searches with stability included, which we discuss in the next section.

### 7.4.3 Likelihood Function Conditioned on Stability

As rejection sampling is insufficient to produce a converged posterior distribution, we therefore try a different approach—we modify the likelihood function used in performing searches of parameter space by setting the likelihood function to be 0 if the system is not found to be stable for a predetermined period of time. We consider a planetary system to be stable if the semi-major axes of both planets remain between 50% and 150% of their initial values. This means that any samples in our final posterior distributions now exhibit long-term stability, but also means that our search has trouble exploring between stable regions of parameter space. If we were merely looking for maximum likelihood solutions, the stable solutions we found through rejection sampling would be sufficient for initializing our long-term stable MCMC searches. However, given the large upwards shift in period ratio that occurs when more data is included in the fitting when compared to the [JPH11](#) data (see Figure 7.5), we feel it is quite important to explore other possible modes near the best-fitting solutions, since it is quite possible, as we discuss below, that additional frequencies introduced by the dynamical interaction between the planets are obscuring the underlying period ratio. Due to this difficulty, we use several different methods and initializations for our search, which we discuss in detail below. We ultimately identify three peaks in our posterior distribution, which are discussed in Section 7.4.4. We do require multiple different initializations to find these various modes, which leaves open the question of whether other initialization methods might find additional modes in the posterior distribution. We return to this question in Section 7.4.5.

The simplest method of initialization, as well as the method that overall finds the best-fitting region of parameter space, is to simply initialize our MCMC near the best-fit solution found by rejection sampling. This method produces a peak near a 7:5 period commensurability, which is unsurprising given that this is where our non-stable posterior distribution is located. For another initialization, we use a genetic algorithm (GA) to explore the parameter space. As we suspect there may be multiple local maxima of our posterior distribution, a GA may be useful to identify these different maxima and ultimately identify the global maximum. We use the open-source optimization framework Pyevolve (Perone 2009). Our genetic algorithm calculates likelihood scores using the same criteria discussed above, i.e. log-likelihood derived from assuming the observations are Gaussian distributed and independent, conditioned on long-term stability. The negative of the log-likelihood is used as the “fitness” for the GA. For our GA runs we test for stability for  $10^6$  periods of planet c’s orbit. We find that allowing the algorithm to evolve until an average fitness score of at least 800 is reached, or until there is no significant increase in likelihood between sequential generations, is sufficient time for the algorithm to find useful starting points for the MCMC. We initialize the MCMC in a small Gaussian ball around the best fit parameters determined by the genetic algorithm, and allow the MCMC to run to convergence.

The GA strongly favors a region of stability similar to the parameters identified in Figure C.1, but with the period of the larger planet closer to  $\sim 900$  days, which places the system firmly in a 3:2 MMR, as discussed in Section 7.5. This region is extremely stable, making it easier for the GA to explore. The GA misses the stable region of

parameter space near  $P_c/P_b \sim 7/5$  identified by our rejection sampling in Section 7.4.2; this is likely because the search by the GA is *too* broad for this application, and the stable region near 7:5 is much more narrow than the region near 3:2.

We also begin a search starting from the orbital parameters identified by [Tadeu dos Santos et al. \(2015\)](#), who explored the formation and evolution of HD 200964 using the data of [JPH11](#), with a higher stellar mass of  $M_* = 1.57M_\odot$ , and gave long-term stable solutions in the 4:3 MMR. The specific parameters reported in this work do not match the data well according to our model, likely because of a disagreement between the coordinate systems used. Thus, beginning with their reported planetary masses (scaled by a factor  $M_p/M_*$ ) and eccentricities, we first optimize over angular parameters, before performing an optimization over all parameters and a subsequent MCMC search. This search does find stable solutions near a 4:3 period ratio that fit the data well, but the search also finds a smaller number of solutions near the 7:5. Though the walkers in our search spend more time near 4:3, solutions near 7:5 clearly have better posterior probability; it is likely the MCMC has difficulty moving between the two period ratios due to a dearth of stable solutions at period ratios intermediate between the two regions. We therefore initialize another MCMC at our best fit solution from the previous run. This MCMC converges to a region similar to the region identified by starting at the best-fit obtained through rejection sampling.

Thus, we have identified three peaks in our posterior distribution—one near a 3:2 period ratio, another near a 4:3 period ratio, and peak containing our best fit solution near a 7:5 period ratio. In the next section we discuss these peaks in more

detail.

#### 7.4.4 Final Posterior Distribution

We give median values of the orbital parameters from each mode of the posterior distribution in Table 7.8, and maximum likelihood parameters in Table 7.11. Since the 4:3 distribution joins on to the 7:5 distribution, we remove all points with  $P_c > 7/5 P_b$  before calculating the median or the errors. Theoretical radial velocity curves for the maximum likelihood parameters are shown in Figure 7.7. The full posterior distributions are plotted in Appendix C. We also stress that it is more meaningful to talk about overall stable regions of parameter space rather than particular orbital configurations. Long-term orbital integrations are inherently chaotic, and lifetimes of a given set of orbital parameters can vary by an order of magnitude depending on the machine used to carry out the integration.

All of our parameters discussed above are reported for  $i = 90^\circ$ . Though there are still strong degeneracies between  $M_p$  and  $i$  in our modeling, we note both the theoretical RV signal and the long-term stability of the system are directly sensitive to the planetary mass  $M_p$ , as opposed to just  $M_p \sin i$ , which is the relevant quantity when planets are allowed to move on purely Keplerian orbits. One extension of our work would be to directly constrain the masses of the planets by allowing the overall inclination of the system to vary, while still keeping the planets coplanar. We could also allow mutual inclinations between the planets, which would necessitate allowing  $\Omega$  to vary. This could improve our stability constraints, and allow us to further constrain  $M_p$ . We leave these investigations as avenues for future work.

Table 7.6: Median orbital parameters,  $10^6 P_c$  stability, 7:5 MMR

Parameter <sup>a</sup>	HD 200964 b, 7:5	HD 200964 c, 7:5
Orbital Period, $P$ [days]	$603.27^{+2.33}_{-2.17}$	$854.46^{+4.56}_{-4.39}$
Mass, $m$ [ $M_J$ ]	$1.72^{+0.05}_{-0.05}$	$1.16^{+0.05}_{-0.05}$
Mean longitude, $\lambda$ [deg]	$307.90^{+4.32}_{-4.04}$	$236.76^{+4.28}_{-4.50}$
Argument of periastron, $\omega$ [deg]	$325.762^{+13.16}_{-13.51}$	$252.58^{+112.94}_{-103.12}$
$\log_{10}$ Eccentricity, $e$	$-1.21^{+0.05}_{-0.05}$	$-3.10^{+0.90}_{-0.98}$
Stellar Jitter, $\sigma_j$ [m/s]	$6.27^{+0.42}_{-0.40}$	

<sup>a</sup>Values for orbital elements are in astrometric coordinates, are referenced to the epoch of the first data point, JD 2453213.895, and assume an inclination  $i = 90^\circ$ . The reported values are median values for the posterior distribution, and the reported error bars are 84% and 16% quantiles.

We also note that all three posterior distributions identified, that is, near period ratios of 3:2, 4:3, and 7:5, feature a long tail in the eccentricity of planet c consistent with planet c on a circular orbit. We therefore re-run our MCMC, now setting planet c to be circular, which eliminates two parameters from our fitting. The resultant searches identify very similar regions of parameter space to the solutions with eccentricity included, but none of the solutions are truly consistent with planet c being circular. Instead, planet c’s eccentricity is quickly excited by the companion, and, over longer timescales, both planets’ eccentricities oscillate, with average values that are both of order  $10^{-1}$ . We also comment that for two planets to be in MMR, the “test” particle must have some eccentricity. Thus, in what follows we use our orbital solutions with eccentricity included.

As previously discussed, all three of these posteriors represent different modes of the overall posterior distribution of orbital parameters. A 2D histogram of the posterior distribution of  $P_c$  vs.  $P_b$  is shown in Figure 7.8, overplotted with the non-stable 2D

Table 7.7: Median orbital parameters,  $10^6 P_c$  stability, 4:3 MMR

Parameter <sup>a</sup>	HD 200964 b, 4:3	HD 200964 c, 4:3
Orbital Period, $P$ [days]	$605.85^{+2.53}_{-2.48}$	$837.51^{+4.62}_{-6.12}$
Mass, $m$ [ $M_J$ ]	$1.74^{+0.05}_{-0.05}$	$1.13^{+0.05}_{-0.06}$
Mean longitude, $\lambda$ [deg]	$311.31^{+4.49}_{-4.46}$	$223.98^{+4.70}_{-4.91}$
Argument of periastron, $\omega$ [deg]	$293.97^{+14.15}_{-13.89}$	$273.05^{+96.72}_{-118.05}$
$\log_{10}$ Eccentricity, $e$	$-1.16^{+0.06}_{-0.05}$	$-2.99^{+1.02}_{-1.06}$
Stellar Jitter, $\sigma_j$ [m/s]	$6.57^{+0.47}_{-0.42}$	

<sup>a</sup>Values for orbital elements are in astrometric coordinates, are referenced to the epoch of the first data point, JD 2453213.895, and assume an inclination  $i = 90^\circ$ . The reported values are median values for the posterior distribution, and the reported error bars are 84% and 16% quantiles.

Table 7.8: Median orbital parameters,  $10^6 P_c$  stability, 3:2 MMR

Parameter <sup>a</sup>	HD 200964 b, 3:2	HD 200964 c, 3:2
Orbital Period, $P$ [days]	$598.70^{+2.79}_{-2.77}$	$881.11^{+7.62}_{-6.62}$
Mass, $m$ [ $M_J$ ]	$1.68^{+0.06}_{-0.06}$	$1.26^{+0.07}_{-0.07}$
Mean longitude, $\lambda$ [deg]	$287.17^{+6.15}_{-4.57}$	$269.31^{+5.52}_{-5.80}$
Argument of periastron, $\omega$ [deg]	$317.12^{+17.78}_{-19.11}$	$169.28^{+160.12}_{-35.34}$
$\log_{10}$ Eccentricity, $e$	$-1.12^{+0.14}_{-0.19}$	$-1.47^{+0.38}_{-1.91}$
Stellar Jitter, $\sigma_j$ [m/s]	$7.47^{+0.33}_{-0.49}$	

<sup>a</sup>Values for orbital elements are in astrometric coordinates, are referenced to the epoch of the first data point, JD 2453213.895, and assume an inclination  $i = 90^\circ$ . The reported values are median values for the posterior distribution, and the reported error bars are 84% and 16% quantiles.

Table 7.9: Maximum Likelihood orbital parameters,  $10^6 P_c$  stability, 7:5 MMR

Parameter <sup>a</sup>	HD 200964 b, 7:5	HD 200964 c, 7:5
Orbital Period, $P$ [days]	601.5	856.8
Mass, $m$ [ $M_J$ ]	1.75	1.18
Mean longitude, $\lambda$ [deg]	304.7	238.5
Argument of periastron, $\omega$ [deg]	327.1	246.2
$\log_{10}$ Eccentricity, $e$	-1.18	-2.02
Stellar Jitter, $\sigma_j$ [m/s]	6.1	

<sup>a</sup>Values for orbital elements are in astrometric coordinates, are referenced to the epoch of the first data point, JD 2453213.895, and assume an inclination  $i = 90^\circ$ .

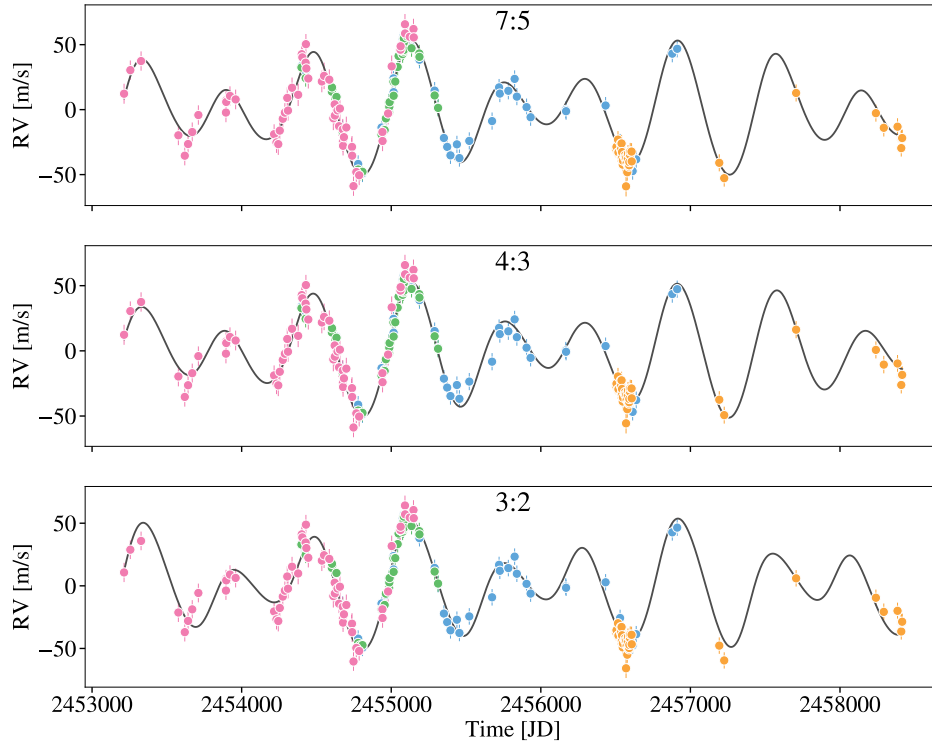


Figure 7.7: Comparison of the theoretical radial velocity curves for our best-fit, long-term stable solutions with different period ratios. *Top Panel:* Our overall maximum likelihood solution, which has  $P_c/P_b \sim 7/5$ . *Middle Panel:* An example solution which shows clear libration of the 4:3 resonant angle. *Bottom Panel:* Our maximum likelihood solution that also shows libration of the 3:2 resonant angle.

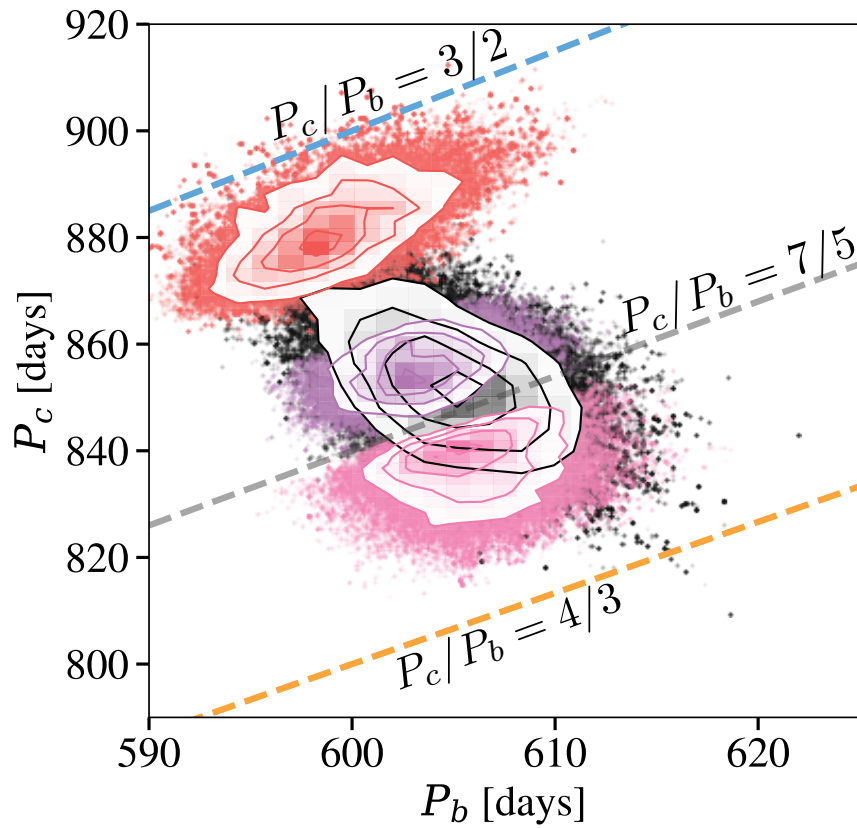


Figure 7.8: 2D histograms of the posterior distributions for the planets' periods without long-term stability (black points, see Section 7.4.1) and the three modes identified for fits conditioned on stability for  $10^6 P_c$  (pink, purple, and red points, see Section 7.4.3). Note that the plotted values refer to the periods at JD 2453213.895. Lines denoting exact ratios of  $P_c/P_b$  are shown for ratios of 3:2 (blue), 7:5 (gray) and 4:3 (orange).

Table 7.10: Maximum Likelihood orbital parameters,  $10^6 P_c$  stability, 4:3 MMR

Parameter <sup>a</sup>	HD 200964 b, 4:3	HD 200964 c, 4:3
Orbital Period, $P$ [days]	605.6	839.3
Mass, $m$ [ $M_J$ ]	1.77	1.16
Mean longitude, $\lambda$ [deg]	308.1	227.6
Argument of periastron, $\omega$ [deg]	304.1	293.8
$\log_{10}$ Eccentricity, $e$	-1.3	-3.36
Stellar Jitter, $\sigma_j$ [m/s]	6.4	

<sup>a</sup>Values for orbital elements are in astrometric coordinates, are referenced to the epoch of the first data point, JD 2453213.895, and assume an inclination  $i = 90^\circ$ .

Table 7.11: Maximum Likelihood orbital parameters,  $10^6 P_c$  stability, 3:2 MMR

Parameter <sup>a</sup>	HD 200964 b, 3:2	HD 200964 c, 3:2
Orbital Period, $P$ [days]	598.8	886.4
Mass, $m$ [ $M_J$ ]	1.72	1.33
Mean longitude, $\lambda$ [deg]	286.4	272.8
Argument of periastron, $\omega$ [deg]	304.1	181.1
$\log_{10}$ Eccentricity, $e$	-1.12	-1.08
Stellar Jitter, $\sigma_j$ [m/s]	7.2	

<sup>a</sup>Values for orbital elements are in astrometric coordinates, are referenced to the epoch of the first data point, JD 2453213.895, and assume an inclination  $i = 90^\circ$ .

histogram. We use this plot to give an idea of where each modes lies in  $P_c$  vs  $P_b$  space; we stress that each mode is pulled from a separate posterior distribution, meaning that the relative likelihood of the modes is not indicated by the density of points in each 2D histogram. Given where each mode lies relative to the non-stable histogram however, it is clear that the mode at period ratios slightly larger than 7:5 will have the overall highest likelihood. To further emphasize this point, in Figure 7.9 we plot  $P(D|\theta)$ , i.e. the likelihood, hexagonally binned in  $P_b$  vs.  $P_c$  space and averaged. Again, we stress that this is not a proper marginalization over the other parameters in our space; however, since it can be seen in Appendix C that the posterior distributions for the other parameters occupy similar regions of parameter space, this plot still gives a rough idea of the relative probability in each mode without being quantitatively rigorous.

Figure 7.9 makes it clear that the mode identified near 7:5 is by far the most likely – it is higher in likelihood than the 4:3 by a factor of  $\sim \exp(10 - 15)$ , and the 3:2 mode by a factor of  $\sim \exp(20 - 25)$ . If we were concerned only with agreement between the data and our model, this mode would constitute our full posterior distribution. However, given the large shift in period ratio seen when more data is added to the RV signal, it is important to identify possible modes near the best-fit solution, as these modes may prove to be the “true” solution when more data is added.

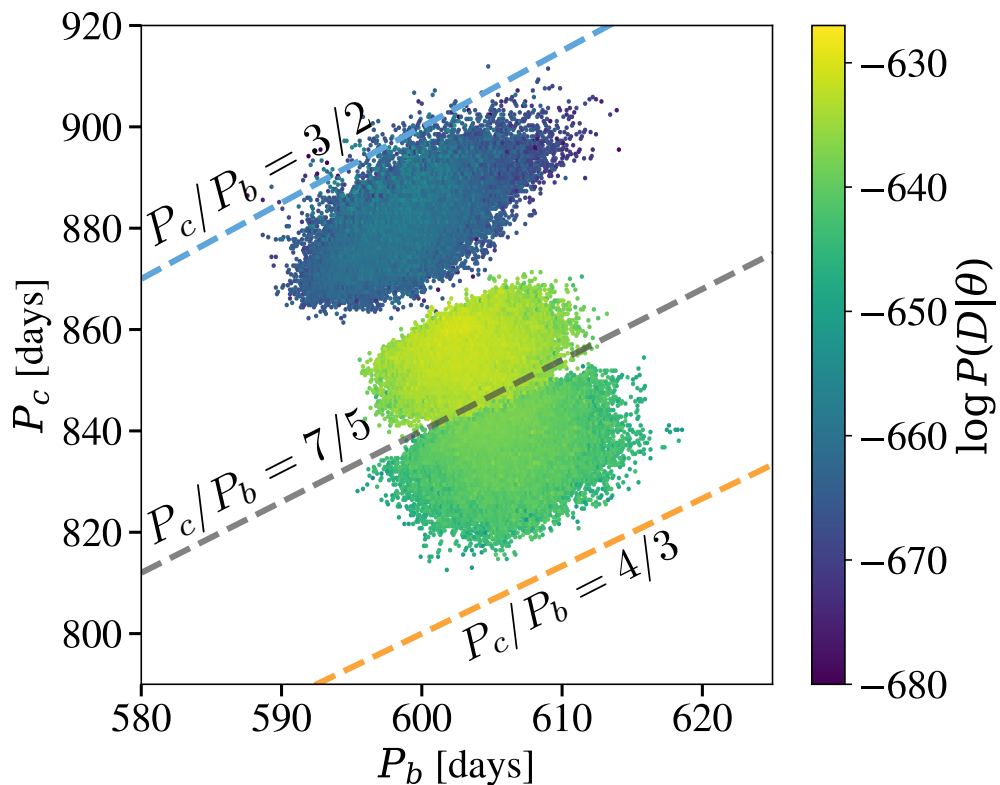


Figure 7.9: Posterior probability distributions shown in Figure 7.8, with the points hexagonally binned and averaged. The points are colored by  $\log P(D|\theta)$ . The plotted values refer to the periods at JD 2453213.895. Note that the probability has not been properly marginalized over the other parameters, and is only meant to give a rough idea of the relative probability between the peaks (see text). Lines denoting exact ratios of  $P_c/P_b$  are shown for ratios of 3:2 (blue), 7:5 (gray) and 4:3 (orange).

Though we have identified three different modes of our posterior distribution clustered around three different values of the period ratio, all of the periods discussed thus far refer to the periods of the two planets at epoch; over time, the periods of the two planets will oscillate due to their mutual perturbations. To get a better sense of mean values of period ratio for these three modes, and to give a sense of the likelihood in each mode, we randomly sample 1000 points from each of our posterior distributions. For each point, we numerically integrate the system for  $500 P_c$ , and compute the mean values of  $P_b$  and  $P_c$ . These values are plotted in Figure 7.10, along with  $P(D|\theta)$  for each point. Integrating out the solutions has little effect on the period ratios for points in the 4:3 posterior—these points remain at values slightly larger than a 4:3 period ratio. For the 7:5 posterior however, the average periods all lie much closer to an exact 7:5 ratio, or slightly below, whereas their initial ratios were generally above 7:5. For the 3:2 points the ratios all now lie above 3:2, while their initial period ratios were all below.

After this long term averaging over orbital elements, the period ratio distributions of our posterior modes lie even more clearly along or near lines of constant period ratio. This provides further support to the idea that these orbital configurations are stabilized by mean motion resonance. We explore this idea further in Section 7.5.

#### 7.4.5 Stable Regions of Period-Period Space

To check whether we have identified all of the possible modes, we perform a simple Monte Carlo simulation to analyze the stable regions near the planetary parameters we have identified. We initialize  $10^6$  planetary systems, randomly drawing all parameters, except for the planetary periods, from normal distributions centered on

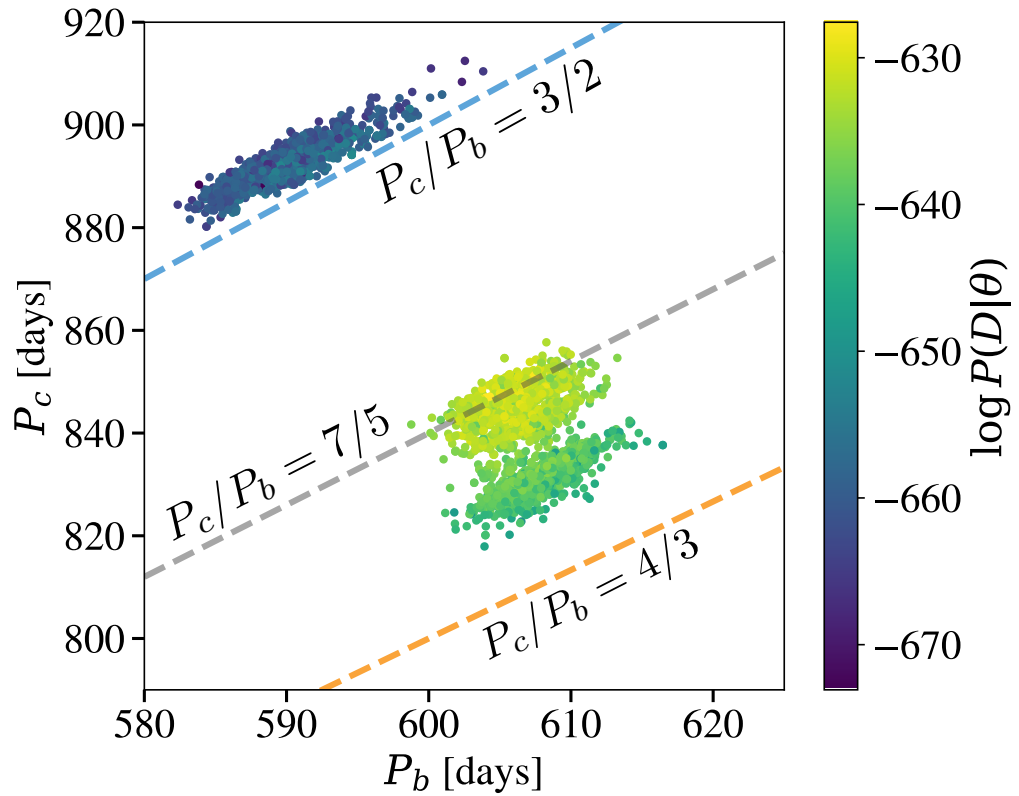


Figure 7.10: Osculating period values averaged over  $500P_c$  for 1000 draws from the three modes of the posterior distribution identified by our MCMC search. Each mode lies close to a different fixed value of  $P_c/P_b$ . Colors are the same as those in Figure 7.9. Lines denoting exact ratios of  $P_c/P_b$  are shown for ratios of 3:2 (blue), 7:5 (gray) and 4:3 (orange). See Section 7.4.4 for a discussion.

the values for the parameters identified from the other modes. We used the following parameters for the normal distributions, where  $\mu$  denotes the mean of the normal distribution and  $\sigma$  the standard deviation:  $\mu_{m_b} = 1.7M_J$ ,  $\sigma_{m_b} = 0.1$ ,  $\mu_{m_c} = 1.2M_J$ ,  $\sigma_{m_c} = 0.2$ ,  $\mu_{\lambda_b} = 300^\circ$ ,  $\sigma_{\lambda_b} = 20$ ,  $\mu_{\lambda_c} = 250^\circ$ ,  $\sigma_{\lambda_c} = 40$ ,  $\mu_{\log e_b} = -1.1$ ,  $\sigma_{\log e_b} = 0.2$ ,  $\mu_{\log e_c} = -1.5$ ,  $\sigma_{\log e_c} = 0.1$ ,  $\mu_{\omega_b} = 310^\circ$ ,  $\sigma_{\omega_b} = 100$ ,  $\mu_{\omega_c} = 200^\circ$ ,  $\sigma_{\omega_c} = 100$ . The periods of the two planets are drawn from uniform distributions in the range 575 to 635 for planet b, and 790 to 925 days for planet c. Each planetary system is tested for stability in the manner described above, and the stable systems are recorded. A 2D histogram of the stable solutions in period space, along with the 3 modes and the non-stable posterior, are shown in Figure 7.11.

Several features are apparent from Figure 7.11. Firstly, stable regions of parameter space lie along diagonals running from the lower lefthand side to the upper right, indicating that stable regions of parameter space lie along regions of constant period ratio. Secondly, there is an extremely stable region of parameter space near the 3:2 MMR, and another stable region at ratios slightly larger than 4:3. Interestingly, the 7:5 mode, which has the overall highest likelihood, lies between these two stable regions. This is likely because the 7:5 mode is second order, making it weaker than the first order 3:2 and 4:3 resonances it is adjacent to. The lack of stable regions of parameter space near the 7:5 emphasizes the need to account for stability when considering the posterior probability distribution of the orbital parameters. From Figure 7.11, it seems that if we are interested in additional possible stable modes, the only possibilities are the two regions near 3:2 and 4:3, which is precisely the other locations our search uncovered.

Since any possible modes cannot lie too far from the non-stable posterior, Figure 7.11 provides further evidence that we have identified all relevant modes of the long-term stable posterior distribution.

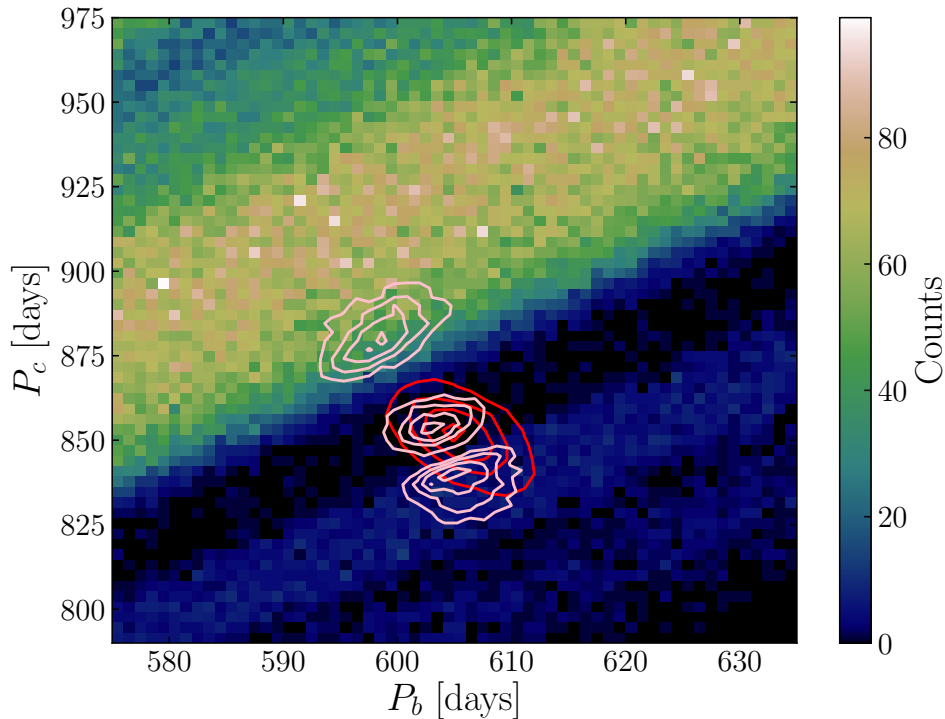


Figure 7.11: 2D histogram of results from a Monte Carlo simulation of stable planetary systems. Orbital parameters for the two planets are randomly drawn, and systems that pass the stability criteria described in the text are recorded. The non-stable posterior distribution of the planetary periods is shown in red, and the three long-term stable modes are shown in pink.

## 7.5 Analysis of Underlying Mean-Motion Resonance

As discussed in the last section, and demonstrated in Figure 7.10, the period ratios of the points in our posterior distribution lie near lines of constant period ratio, which supports the idea that these systems are in MMR. In order to investigate whether

our stable best fit solutions are truly in resonance, we track the evolution of the resonant angle,  $\phi$ , over time. A  $p/q$  MMR between a massive perturber and a massless test particle is characterized by libration of the angle

$$\phi = p\lambda_{\text{outer}} - q\lambda_{\text{inner}} - (p - q)\varpi_{\text{test}} \quad (7.3)$$

(see e.g. [Murray & Dermott 1998](#)). For a truly massless test particle, if the semi-major axis ratio and initial angles are perfectly tuned,  $\phi$  is constant; for values slightly off from this region,  $\phi$  oscillates sinusoidally. In the case of HD 200964, libration of the resonant angle will be complicated by the large masses of both planets—not only are both planets of comparable mass, but in addition both planets are relatively massive compared to the central star. Thus, we do not expect libration of the resonant angle to be particularly “clean.”

We begin by discussing our solutions near a 3:2 period ratio, as they most clearly exhibit libration. The resonant angles for the maximum likelihood 3:2 solution are plotted in Figure 7.12. The two resonant angles,  $\phi_{\text{inner}}$  and  $\phi_{\text{outer}}$ , obtained by considering the inner and outer planets to be the test particle in Equation (7.3), are shown. Both angles show clear libration, albeit with a large amplitude. Thus, it is straightforward to conclude that our long-term stable solutions near a 3:2 period ratio are in a 3:2 MMR.

For our 7:5 solutions however, the situation is more complex. The evolution of the 7:5 resonant angle for our maximum likelihood long term stable solution is shown

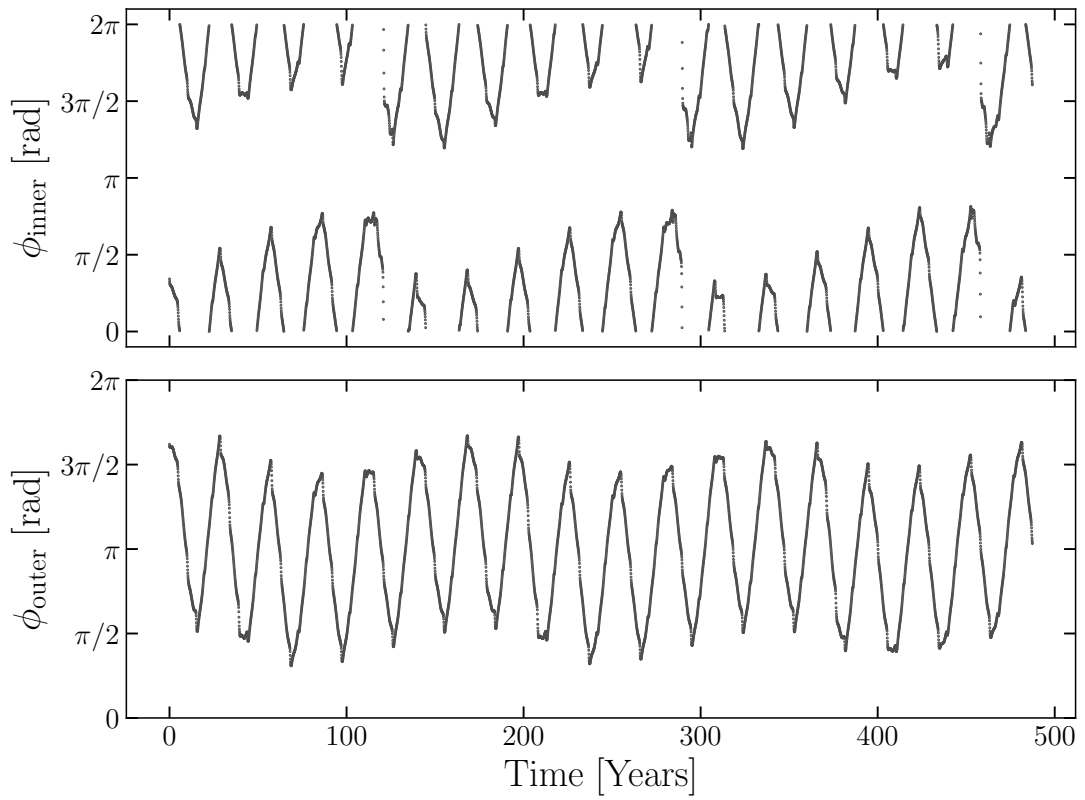


Figure 7.12: Value of the inner and outer 3:2 resonant angles for our best-fit 3:2 solution. Both angles clearly librate.

in Figure 7.13. The two resonant angles,  $\phi_{\text{inner}}$  and  $\phi_{\text{outer}}$  are again shown. As can be seen in the figure, there does appear to be periodic variation in the value of  $\phi$ , but it is complicated by the presence of several other effects, which we enumerate in Figure 7.14 by examining the evolution of  $\phi$  as both the masses and the mass ratio of the planets involved in the resonance are increased.

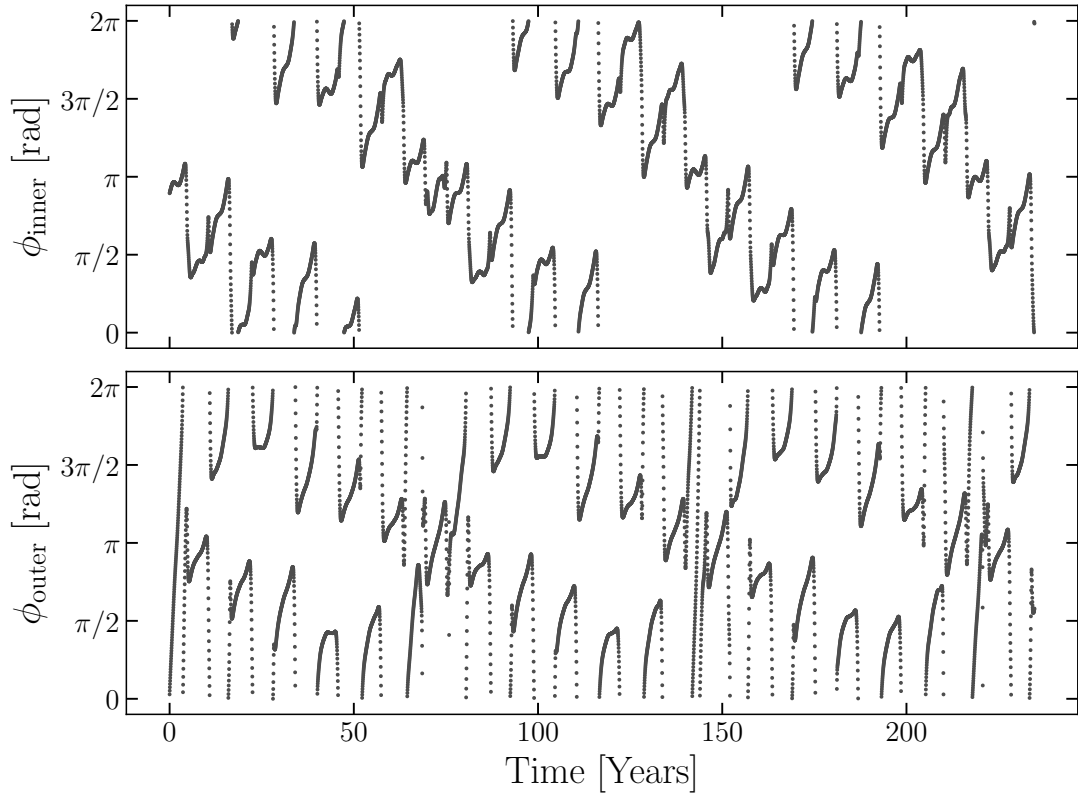


Figure 7.13: Value of the inner and outer 7:5 resonant angles for our best-fit solution, which are defined in Equation (7.3). The angles do appear to show libration, but the large masses of both planets involved in the resonance complicate the libration pattern, as discussed in the text and demonstrated in Figure 7.14

To begin, we plot the value of  $\phi_{\text{inner}}$  for two planets with  $M_c = 10^{-4}M_J$ , and  $M_b = 0$ . The angles of the planets are initialized such that the system begins perfectly

in resonance. The planet’s resonance angle is fixed at  $\phi = \pi$  over the integration. As we increase the mass of the outer planet, the center of the resonance shifts off of an exact 7:5 period ratio. This causes the system to be initialized off resonance, causing  $\phi$  to librate about  $\pi$ . Increasing the mass further to  $0.5M_J$  adds two new effects—firstly, the period of the libration of the resonant angle decreases dramatically, which is expected as the mass of the planets involved in the resonance increases. Secondly, there is now a much shorter period variation that has been introduced into  $\phi$ . This variation is caused by the outer planet perturbing the test particle during their closest approach, and therefore occurs on the synodic period of the planets. To illustrate this, we have noted conjunctions between the planets with dashed vertical lines. The strength of these synodic kicks makes the libration of the resonant angle less clear, though it can still be discerned by eye in this case.

If we now give both planets comparable mass, as seen in the righthand top panel, the fact that the “test” particle now has the same mass as the particle we are considering the “perturber” for calculating  $\phi$  causes the center of the libration to circulate as well, though the oscillation of  $\phi$  about this circulating center can be clearly discerned.

Finally, we increase the mass of both planets to  $0.5M_J$ . In this case, we see a combination of the two effects that were present previously— $\phi$  oscillates about a center that circulates, while the strong synodic kicks cause large oscillations of  $\phi$  on a synodic period.

These effects combine to produce the complicated behavior seen in the libration

of  $\phi_{\text{inner}}$  for our best fit solution—for such high mass planets, the synodic kicks are extremely strong, and are on top of the rapid circulation of the center of the resonance. For contrast, in Appendix C.2 we give analogous plots for the 3:2 resonant angle in Figure C.5. In this case, the strength of the 3:2 resonance causes much less significant aberration from test particle case, even when both planets are  $\sim M_J$ .

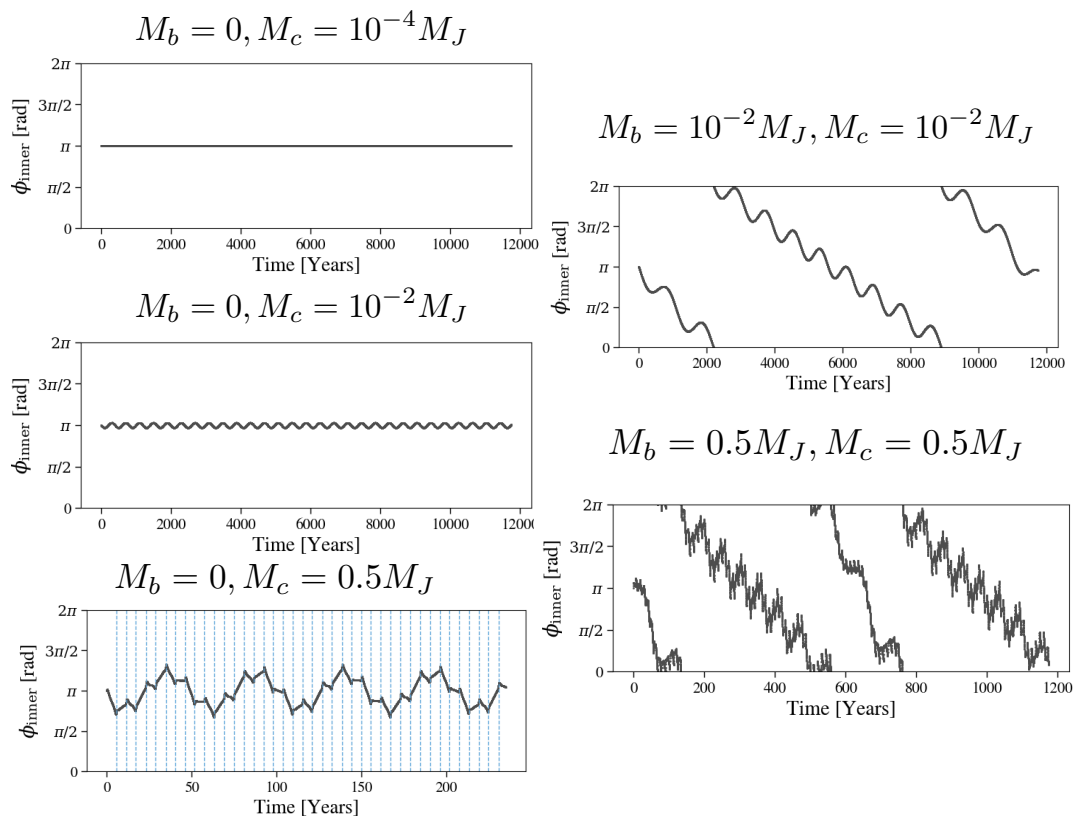


Figure 7.14: Evolution of  $\phi_{\text{inner}}$  for the 7:5 MMR as the masses of the planets involved in the resonance are increased. For low mass planets, libration of  $\phi_{\text{inner}}$  is easily discerned (middle left panel). As the mass of the perturbing planet is increased, kicks on a synodic timescale distort the libration pattern (bottom left panel; blue dashed lines denote conjunctions between the planets). If both planets have comparable mass, the center of the libration begins to circulate on the secular timescale (upper right panel). Finally, for large, comparably massive planets, both these effects serve to “wash out” the libration of  $\phi_{\text{inner}}$  (lower right panel).

For the 4:3, we can find orbital configurations that show clear libration even

for very massive planets. However, the orbital configurations that match the data well appear to be only marginally in the 4:3 resonance or not at all, since the complicated effects seen in  $\phi$  are not due to the massive planets involved in the resonance alone. To illustrate this, in Appendix C.2, Figure C.6, we plot the evolution of  $\phi$  in a manner analogous to the plots made for the 3:2 and 7:5 MMRs.

For the points in our posterior distribution, we only observed behavior similar to libration for the 4:3 resonance in  $\phi_{\text{outer}}$ . An illustration of this is shown in Figure 7.15, which plots the outer resonant angle for a solution that does appear to show libration, and for our best-fit solution, which shows circulation. There appears to be a continuous evolution in behavior as the period of planet c is increased: for lower values of period, the outer 4:3 resonant angle does appear to librate about  $\phi = \pi$ , which is expected for a 4:3 MMR, though with a complex structure. For the larger period ratio solutions we find, i.e. those near a period ratio of 7:5, the angle appears to circulate instead.

In summary, the 3:2 solutions we find are the only for which identification of the MMR through libration of the resonant angle is straightforward. For the 7:5 period ratio solutions,  $\phi$  does appear to show periodic behavior which is clearly distinct from circulation. Interpretation of this behavior is not straightforward, though it does appear that the behavior of  $\phi$  for the 7:5 MMR is consistent with libration for two Jupiter mass planets perturbing one another. For the 4:3 solutions, we see continuous behavior as the period ratio is increased, ranging from clear libration for period ratios closer to 4:3 to clear circulation for period ratios equal to or larger than 7:5.

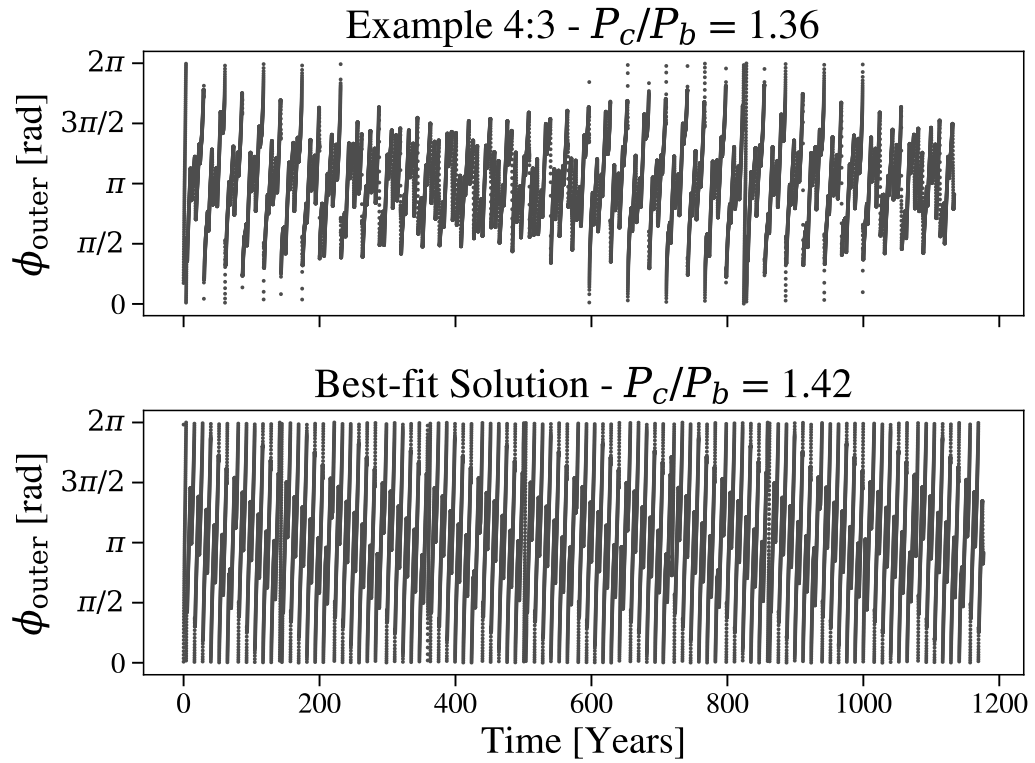


Figure 7.15: Value of the outer 4:3 resonant angle for two orbital configurations drawn from our posterior distribution. In the upper panel, we plot  $\phi_{\text{outer}}$  for a case where the period ratio of the planets is close to 4:3, and  $\phi_{\text{outer}}$  appears to librate. In the lower panel we plot the 4:3 outer resonant angle for our maximum solution; the angle appears to circulate in this case.

## 7.6 Reanalysis of Early Data

Having now found several viable period ratios for long-term stable fits to the data, this now raises the question of whether the multiple resonances we have identified could have been found with just the data published in [JPH11](#). We therefore apply our methodology to just the Lick and Keck11 datasets, and analyze what aspects of the results we have presented can be found from those data sets alone.

To begin, we use a methodology similar to that discussed in Section 7.4.3 to find a long term stable posterior distribution of orbital parameters. We perform initial optimization from several different locations in parameter space, including the parameters reported by [JPH11](#). We then run an initial  $N$ -body MCMC search from the best-fit obtained through optimization, without stability included, until we have a converged posterior distribution with  $\sim 10^6$  points. At this point we perform a  $10^6$  year rejection sample on our posterior, which leaves us with around 200 points in parameter space. This rejection sample identifies two clear regions of stability, one near a 4:3 period ratio and one near a 3:2. We follow up our rejection sampling with MCMC searches conditioned on stability starting in both of these regions.

The resulting posterior distribution is shown in Figure 7.16, along with the  $N$ -body integrated posterior without stability. As can be seen in the figure, the posterior distribution near 3:2 is quite similar to the one found for our longer dataset, while the 4:3 distribution is broader and at slightly larger values of  $P_b$ . It is notable here that the stable regions of parameter space are quite distant from the best-fitting region, which for the early data is at low values of period ratio. This result is in contrast to our

analysis of the full data set, for which the best-fitting and stable regions lie on top of one another. This means that stability analysis is even more important when the data set is not as complete.

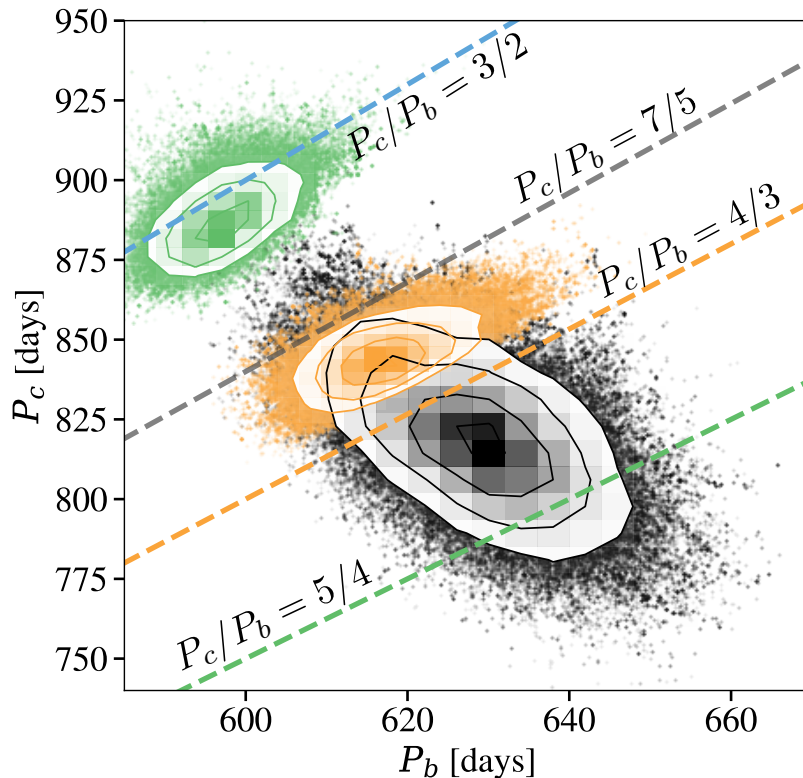


Figure 7.16: 2D histograms of the posterior distributions for our planetary parameters from analysis of just the datasets used in [JPH11](#). The black points show the distribution without long-term stability, while the orange and green points show our posterior conditioned on stability for  $10^6 P_c$ . Lines denoting exact ratios of  $P_c/P_b$  are shown for ratios of 3:2 (blue), 7:5 (gray), 4:3 (orange), and 5:4 (green).

Thus, in addition to the 4:3 solution, we can identify the 3:2 orbital solution from analysis of the early data alone. However, it is interesting to note that the 7:5 solutions are not identified by this early search; it is only with the inclusion of more data that the 7:5 is even identified as a solution.

## 7.7 Possibility of a Third Planet

Though the two planet configurations we have identified provide plausible long-term stable fits to the data, it is still possible there are other planets in the system. We briefly investigate this possibility by adding a third planet to our model and investigate the resulting change in our maximum likelihood.

We initialize our fitting of third planet by looking at a periodogram of the residuals of our data. We take the strongest peak identified by the periodogram, which is at  $\sim 7$  days, and use this orbital period as our starting point when adding the third planet. Given the low period, the residual could be due to a stellar signature. The rotation period of the star is likely to be too long to be causing this signature: [Jofré et al. \(2015\)](#) found a  $v \sin i$  value of  $1.88 \pm 0.23$  km/s. Even at the upper end of the error bar, a simple calculation of rotation period using the value  $R_* = 4.92 R_\odot$  gives  $P_{\text{rot}} = 2\pi R_*/v \sin i \approx 118$  days, which is clearly too long to give the  $\sim 7$  day planetary signal unless the star is rotating very close to pole on. On the other hand, the S-index values for HD 200964 do show some power at 8 days in the Keck data set, with a moderate correlation (Pearson correlation coefficient of 0.29), though this signal is not present in the APF data. Furthermore, there is significant power in both datasets around 26 days, which could likely be driving the correlation.

Because the GLS favors a lower period for the third planet, it is unlikely that planet-planet interactions are important for modeling this third body. An initial optimization over the third planet's parameters further reinforces this point, as the optimization favors the third planet having low mass compared to the other two, with

$M_d \sim 5 \times 10^{-2} M_J$ . To enforce long-term stability in the system, we therefore fix the orbital parameters of planets b and c, and fit only the parameters of planet d. This means we will miss any covariances between the parameters of the hypothetical third planet and the two outer planets, but this method also ensures that the resulting three planet system exhibits long term stability.

We perform an MCMC search over the third planet’s parameters, starting from the point identified by our optimization. The underlying parameter space is difficult to probe, with many of the solutions having log likelihoods that are comparable to the two-planet case. We do find orbital configurations that improve our log likelihood substantially enough that they may be significant. For a simple comparison we use a Bayesian information criterion (BIC) to compare our two models. We note, however, that the BIC is a surrogate for calculating the evidence, which is the more robust method (see e.g. [Liddle 2007](#) for a discussion). For a given model, the BIC is calculated via

$$\text{BIC} = k \log n - 2 \log \hat{L} \tag{7.4}$$

where  $\hat{L}$  is the maximum likelihood,  $n$  is the number of observations, and  $k$  is the number of model parameters (i.e. 15 for the 2 planet case and 20 for the 3 planet case). In order to compare different models we calculate the BIC for each model and select the model with the lowest BIC.

Our maximum likelihood third planet parameters are similar to those identified above: the planet is low mass ( $M_d = 4.22 \times 10^{-2} M_J$ ), in a short period ( $P_d = 7.89$  days), highly eccentric ( $e_d = 0.588$ ) orbit. The  $\Delta\text{BIC}$  for this model versus our two planet

model is  $\Delta\text{BIC} = 4.90$ . This means that the three planet model is preferred. The radial velocity signal for the third planet with the signals from planets b and c removed is plotted in Figure 7.17. Thus, while a three planet model does provide a smaller BIC, the BIC difference between the two models is not large, indicating that the three planet model is not strongly preferred over the two planet model.

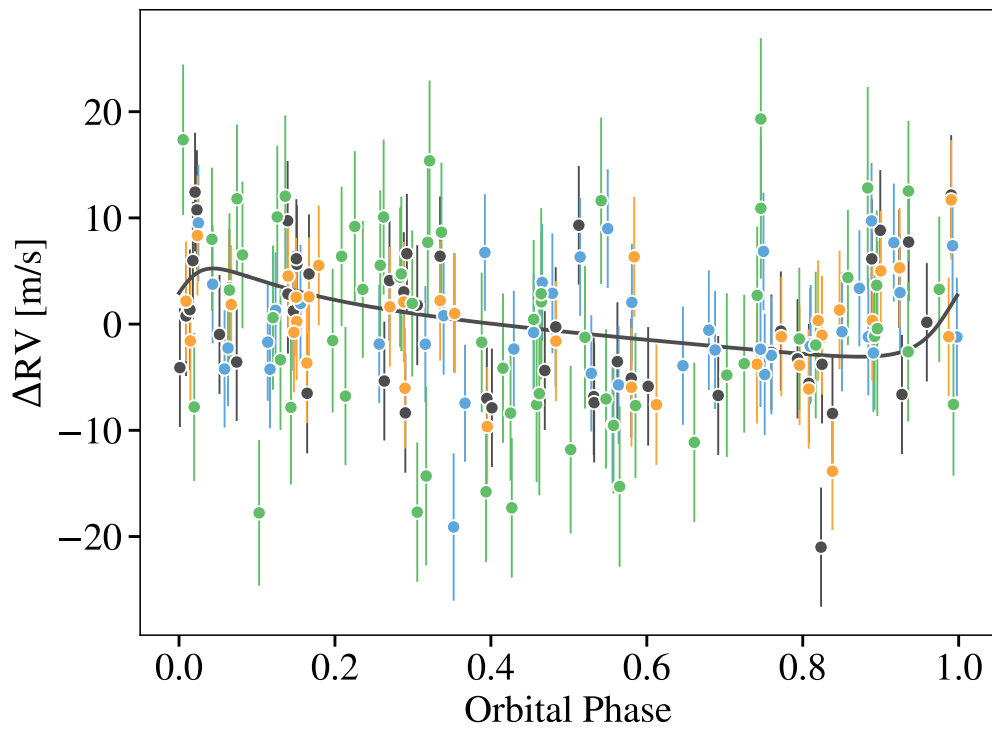


Figure 7.17: Radial velocity of the best-fitting third planet as a function of orbital phase. The radial velocity of planets b and c has been removed.

## 7.8 Summary and Conclusions

In this paper we have investigated the mean motion resonance between the two planets orbiting the star HD 200964. We find that the system is stabilized because it is in, or near, a mean motion resonance. However, which of three possible resonances the system is in (3:2, 4:3, or 7:5) remains unclear, as the full libration period of the system’s resonance angle ( $\sim 30$  years) is longer than the observational baseline ( $\sim 14$  years). We also find indications of a possible “low” mass ( $M_p \sim 0.05M_J$ ) third planet to the system on a short period ( $\sim 8$  day) orbit, though this third planet is not strongly preferred over our two planet model.

Previous analyses (JPH11) identified the system as being in a 4:3 resonance. By including stability in our searches we were able to identify additional long-term stable solutions near a 3:2 MMR, even using the same data analyzed in JPH11, though 4:3 solutions remain better fits to this data set. Furthermore, by using radial velocity data spanning a longer timescale than previous works, we found that the best fitting orbital configurations were not in the 3:2 or 4:3 MMR, but instead had period ratios much closer to 7:5.

The original identification of a 4:3 resonance was puzzling on theoretical grounds, as convergent migration of gas giants strongly prefers capture into the 3:2 rather than the 4:3 or 7:5. It is interesting to note that with the inclusion of more data the period ratio has gone up. We conclude that, this fact, along with the errors underlying the radial velocity measurements and the long timescale variation provided by libration of the resonant angle generate sufficient uncertainty in the period ratio that the 3:2 remains a

plausible solution to the observed signal.

If long period observations are not available, it is of paramount importance that long-term stability is included in fitting RV systems in MMR. For these shorter period solutions, the region of parameter space identified by simply finding the best-fit to the RV data can be a considerable distance from the regions of parameter space that exhibit long-term stability. Thus, requiring any proposed set of best-fit parameters to exhibit long-term stability is invaluable in identifying the the “true” values of the underlying planetary system, which may be obscured by the strong perturbations of the planets on one another.

# Bibliography

- Agnor, C. B., Canup, R. M., & Levison, H. F. 1999, *Icarus*, 142, 219
- Alcalá, J. M., Natta, A., Manara, C. F., et al. 2014, *A&A*, 561, A2
- Alibert, Y. 2017, ArXiv e-prints, arXiv:1705.06008
- Anderson, K. R., Lai, D., & Pu, B. 2020, *MNRAS*, 491, 1369
- Andrews, S. M. 2015, *PASP*, 127, 961
- . 2020, arXiv e-prints, arXiv:2001.05007
- Andrews, S. M., Rosenfeld, K. A., Kraus, A. L., & Wilner, D. J. 2013, *ApJ*, 771, 129
- Andrews, S. M., Wilner, D. J., Hughes, A. M., Qi, C., & Dullemond, C. P. 2009, *ApJ*, 700, 1502
- Armitage, P. J. 2011, *ARA&A*, 49, 195
- Bae, J., Nelson, R. P., & Hartmann, L. 2016, *ApJ*, 833, 126
- Bai, X.-N. 2011, *ApJ*, 739, 50
- . 2016, *ApJ*, 821, 80
- Bai, X.-N., & Stone, J. M. 2011, *ApJ*, 736, 144
- . 2013, *ApJ*, 769, 76
- Bai, X.-N., Ye, J., Goodman, J., & Yuan, F. 2016, *ApJ*, 818, 152

- Balbus, S. A. 2009, ArXiv e-prints, arXiv:0906.0854
- Batalha, N. M., Rowe, J. F., Bryson, S. T., et al. 2013, *ApJS*, 204, 24
- Batchelor, G. 2000,
- Benz, W., Slattery, W. L., & Cameron, A. G. W. 1988, *Icarus*, 74, 516
- Binney, J., & Tremaine, S. 2008, *Galactic Dynamics*
- Birnstiel, T., Dullemond, C. P., & Brauer, F. 2009, *A&A*, 503, L5
- . 2010, *A&A*, 513, A79
- Birnstiel, T., Klahr, H., & Ercolano, B. 2012, *A&A*, 539, A148
- Birnstiel, T., Ormel, C. W., & Dullemond, C. P. 2011, *A&A*, 525, A11
- Bitsch, B., Izidoro, A., Johansen, A., et al. 2019, *A&A*, 623, A88
- Bitsch, B., Lambrechts, M., & Johansen, A. 2015, *A&A*, 582, A112
- Bitsch, B., Morbidelli, A., Johansen, A., et al. 2018, *A&A*, 612, A30
- Blandford, R. D., & Payne, D. G. 1982, *MNRAS*, 199, 883
- Blum, J., & Wurm, G. 2008, *ARA&A*, 46, 21
- Borucki, W. J., Koch, D., Basri, G., et al. 2010, *Science*, 327, 977
- Boss, A. P. 1997, *Science*, 276, 1836
- Bottke, W. F., Vokrouhlický, D., Marchi, S., et al. 2015, *Science*, 348, 321
- Bowler, B. P. 2016, *PASP*, 128, 102001
- Bowler, B. P., Johnson, J. A., Marcy, G. W., et al. 2010, *ApJ*, 709, 396
- Brandt, T. D., McElwain, M. W., Turner, E. L., et al. 2014, *ApJ*, 794, 159
- Brauer, F., Dullemond, C. P., & Henning, T. 2008, *A&A*, 480, 859
- Brewer, J. M., Fischer, D. A., Valenti, J. A., & Piskunov, N. 2016, *ApJS*, 225, 32

- Brooks, S., & Gelman, A. 1998, *Journal of Computational and Graphical Statistics*, 7, 434
- Brügger, N., Alibert, Y., Ataiee, S., & Benz, W. 2018, *A&A*, 619, A174
- Bryan, M. L., Knutson, H. A., Lee, E. J., et al. 2019, *AJ*, 157, 52
- Butler, R. P., Marcy, G. W., Williams, E., et al. 1996, *PASP*, 108, 500
- Butler, R. P., Vogt, S. S., Laughlin, G., et al. 2017, *AJ*, 153, 208
- Cameron, A. G. W. 1973, *Icarus*, 18, 407
- Canup, R. M. 2012, *Science*, 338, 1052
- Carballido, A., Fromang, S., & Papaloizou, J. 2006, *MNRAS*, 373, 1633
- Chambers, J. E. 2014, *Icarus*, 233, 83
- . 2016, *ApJ*, 825, 63
- Chauvin, G., Vigan, A., Bonnefoy, M., et al. 2015, *A&A*, 573, A127
- Cheng, N. S. 2009, *Powder Technology*, 189, 395
- Chiang, E., & Youdin, A. N. 2010, *Annual Review of Earth and Planetary Sciences*, 38, 493
- Chiang, E. I., & Goldreich, P. 1997, *ApJ*, 490, 368
- Cimerman, N. P., Kuiper, R., & Ormel, C. W. 2017, *MNRAS*, 471, 4662
- Csanady, G. T. 1963, *Journal of Atmospheric Sciences*, 20, 201
- Cumming, A., Butler, R. P., Marcy, G. W., et al. 2008, *PASP*, 120, 531
- Cuzzi, J. N., Dobrovolskis, A. R., & Champney, J. M. 1993, *Icarus*, 106, 102
- Cuzzi, J. N., & Hogan, R. C. 2003, *Icarus*, 164, 127
- D'Alessio, P., Calvet, N., & Hartmann, L. 2001, *ApJ*, 553, 321

- D'Angelo, G., Kley, W., & Henning, T. 2003, *ApJ*, 586, 540
- Dawson, R. I., Lee, E. J., & Chiang, E. 2016, *ApJ*, 822, 54
- Dodson-Robinson, S. E., Veras, D., Ford, E. B., & Beichman, C. A. 2009, *ApJ*, 707, 79
- Dohnanyi, J. S. 1969, *J. Geophys. Res.*, 74, 2531
- Dones, L., & Tremaine, S. 1993, *Icarus*, 103, 67
- Dong, R., Rafikov, R., Zhu, Z., et al. 2012, *ApJ*, 750, 161
- Dong, R., van der Marel, N., Hashimoto, J., et al. 2017, *ApJ*, 836, 201
- Dubrulle, B., Morfill, G., & Sterzik, M. 1995, *Icarus*, 114, 237
- Duffell, P. C. 2015, *ApJ*, 807, L11
- . 2020, *ApJ*, 889, 16
- Duffell, P. C., & Chiang, E. 2015, *ApJ*, 812, 94
- Duffell, P. C., Haiman, Z., MacFadyen, A. I., D'Orazio, D. J., & Farris, B. D. 2014, *ApJ*, 792, L10
- Duffell, P. C., & MacFadyen, A. I. 2013, *ApJ*, 769, 41
- Duncan, M. J., Levison, H. F., & Lee, M. H. 1998, *AJ*, 116, 2067
- Dürmann, C., & Kley, W. 2015, *A&A*, 574, A52
- . 2017, *A&A*, 598, A80
- Emel'yanenko, V. V. 2012, *Solar System Research*, 46, 321
- Espaillet, C., Muzerolle, J., Najita, J., et al. 2014, in *Protostars and Planets VI*, ed. H. Beuther, R. S. Klessen, C. P. Dullemond, & T. Henning, 497
- Fabrycky, D. C., & Murray-Clay, R. A. 2010, *ApJ*, 710, 1408
- Flaherty, K. M., Hughes, A. M., Rose, S. C., et al. 2017, *ApJ*, 843, 150

- Flock, M., Nelson, R. P., Turner, N. J., et al. 2017, *ApJ*, 850, 131
- Foreman-Mackey, D., Hogg, D. W., Lang, D., & Goodman, J. 2013, *PASP*, 125, 306
- Frank, J., King, A., & Raine, D. J. 2002,
- Freikh, R., Jang, H., Murray-Clay, R. A., & Petrovich, C. 2019, *ApJ*, 884, L47
- Freikh, R., & Murray-Clay, R. A. 2017, *AJ*, 154, 98
- Fressin, F., Torres, G., Charbonneau, D., et al. 2013, *ApJ*, 766, 81
- Fung, J., Artymowicz, P., & Wu, Y. 2015, *ApJ*, 811, 101
- Fung, J., & Chiang, E. 2016, *ApJ*, 832, 105
- . 2017, *ApJ*, 839, 100
- Fung, J., Shi, J.-M., & Chiang, E. 2014, *ApJ*, 782, 88
- Fung, J., Zhu, Z., & Chiang, E. 2019, *ApJ*, 887, 152
- Galicher, R., Marois, C., Macintosh, B., et al. 2016, *A&A*, 594, A63
- Gammie, C. F. 1996, *ApJ*, 457, 355
- Gelman, A., & Rubin, D. B. 1992, *Statistical Science*, 7, 457
- Giguere, M. J., Fischer, D. A., Payne, M. J., et al. 2015, *ApJ*, 799, 89
- Ginzburg, S., & Chiang, E. 2019a, *MNRAS*, 487, 681
- . 2019b, *MNRAS*, 490, 4334
- Ginzburg, S., & Sari, R. 2018, *MNRAS*, 479, 1986
- Goldreich, P., Lithwick, Y., & Sari, R. 2002, *Nature*, 420, 643
- . 2004, *ARA&A*, 42, 549
- Goldreich, P., & Sari, R. 2003, *ApJ*, 585, 1024
- Goldreich, P., & Tremaine, S. 1980, *ApJ*, 241, 425

- . 1982, *ARA&A*, 20, 249
- Goldreich, P., & Ward, W. R. 1973, *ApJ*, 183, 1051
- Goodman, J., & Rafikov, R. R. 2001, *ApJ*, 552, 793
- Grishin, E., & Perets, H. B. 2015, *ApJ*, 811, 54
- . 2016, *ApJ*, 820, 106
- Guillot, T. 2005, *Annual Review of Earth and Planetary Sciences*, 33, 493
- Guillot, T., Ida, S., & Ormel, C. W. 2014, *A&A*, 572, A72
- Hartmann, L., Calvet, N., Gullbring, E., & D'Alessio, P. 1998, *ApJ*, 495, 385
- Hawley, J. F., Gammie, C. F., & Balbus, S. A. 1995, *ApJ*, 440, 742
- Hayashi, C. 1981, *Progress of Theoretical Physics Supplement*, 70, 35
- Hill, G. W. 1878, *American Journal of Mathematics*, 1, 5
- Homann, H., Guillot, T., Bec, J., et al. 2016, *A&A*, 589, A129
- Ida, S., Guillot, T., & Morbidelli, A. 2016, *A&A*, 591, A72
- Inaba, S., & Ikoma, M. 2003, *A&A*, 410, 711
- Izidoro, A., Bitsch, B., Raymond, S. N., et al. 2019, arXiv e-prints, arXiv:1902.08772
- Izidoro, A., Ogihara, M., Raymond, S. N., et al. 2017, *MNRAS*, 470, 1750
- Jofré, E., Petrucci, R., Saffe, C., et al. 2015, *A&A*, 574, A50
- Johansen, A., & Lacerda, P. 2010, *MNRAS*, 404, 475
- Johansen, A., & Lambrechts, M. 2017, *Annual Review of Earth and Planetary Sciences*, 45, 359
- Johnson, J. A., Marcy, G. W., Fischer, D. A., et al. 2006, *ApJ*, 652, 1724
- Johnson, J. A., Fischer, D. A., Marcy, G. W., et al. 2007, *ApJ*, 665, 785

Johnson, J. A., Bowler, B. P., Howard, A. W., et al. 2010, *ApJ*, 721, L153

Johnson, J. A., Payne, M., Howard, A. W., et al. 2011a, *AJ*, 141, 16

Johnson, J. A., Clanton, C., Howard, A. W., et al. 2011b, *ApJS*, 197, 26

Kanagawa, K. D., Muto, T., Tanaka, H., et al. 2015, *ApJ*, 806, L15

Kanagawa, K. D., Tanaka, H., & Szuszkiewicz, E. 2018, *ApJ*, 861, 140

Kant, I. 1755,

Kataoka, A., Tanaka, H., Okuzumi, S., & Wada, K. 2013, *A&A*, 557, L4

Kim, K. H., Watson, D. M., Manoj, P., et al. 2013, *ApJ*, 769, 149

Kimmig, C. N., Dullemond, C. P., & Kley, W. 2020, *A&A*, 633, A4

Kipping, D., Nesvorný, D., Hartman, J., et al. 2019, *MNRAS*, 486, 4980

Kleine, T., Touboul, M., Bourdon, B., et al. 2009, *Geochim. Cosmochim. Acta*, 73, 5150

Kley, W., & Dirksen, G. 2006, *A&A*, 447, 369

Kley, W., & Nelson, R. P. 2012, *ARA&A*, 50, 211

Kratter, K., & Lodato, G. 2016, *ARA&A*, 54, 271

Kratter, K. M., & Murray-Clay, R. A. 2011, *ApJ*, 740, 1

Kratter, K. M., Murray-Clay, R. A., & Youdin, A. N. 2010, *ApJ*, 710, 1375

Lambrechts, M., & Johansen, A. 2012, *A&A*, 544, A32

—. 2014, *A&A*, 572, A107

Lambrechts, M., Johansen, A., & Morbidelli, A. 2014, *A&A*, 572, A35

Lambrechts, M., & Lega, E. 2017, *A&A*, 606, A146

Lambrechts, M., Morbidelli, A., Jacobson, S. A., et al. 2019, *A&A*, 627, A83

Laplace, P. S. 1796, *Exposition du systeme du monde*

- Lee, A. T., Chiang, E., Asay-Davis, X., & Barranco, J. 2010, *ApJ*, 718, 1367
- Lee, E. J. 2019, *ApJ*, 878, 36
- Lee, E. J., & Chiang, E. 2015, *ApJ*, 811, 41
- . 2016, *ApJ*, 817, 90
- Lee, E. J., Chiang, E., & Ormel, C. W. 2014, *ApJ*, 797, 95
- Lee, M. H., & Peale, S. J. 2002, *ApJ*, 567, 596
- Leinhardt, Z. M., & Stewart, S. T. 2012, *ApJ*, 745, 79
- Levison, H. F., Kretke, K. A., & Duncan, M. J. 2015a, *Nature*, 524, 322
- Levison, H. F., Kretke, K. A., Walsh, K. J., & Bottke, W. F. 2015b, *Proceedings of the National Academy of Science*, 112, 14180
- Liddle, A. R. 2007, *MNRAS*, 377, L74
- Lin, D. N. C., & Papaloizou, J. 1986, *ApJ*, 309, 846
- Lin, D. N. C., & Papaloizou, J. C. B. 1993, in *Protostars and Planets III*, ed. E. H. Levy & J. I. Lunine, 749–835
- Lin, J. W., Lee, E. J., & Chiang, E. 2018, *ArXiv e-prints*, arXiv:1806.00487
- Lissauer, J. J. 1993, *ARA&A*, 31, 129
- Lissauer, J. J., Hubickyj, O., D’Angelo, G., & Bodenheimer, P. 2009, *Icarus*, 199, 338
- Lissauer, J. J., Fabrycky, D. C., Ford, E. B., et al. 2011, *Nature*, 470, 53
- Lubow, S. H., & D’Angelo, G. 2006, *ApJ*, 641, 526
- Luhn, J. K., Bastien, F. A., Wright, J. T., et al. 2019, *AJ*, 157, 149
- Lynden-Bell, D., & Pringle, J. E. 1974, *MNRAS*, 168, 603
- Lyra, W. 2014, *ApJ*, 789, 77

- Mamajek, E. E. 2009, in American Institute of Physics Conference Series, Vol. 1158, American Institute of Physics Conference Series, ed. T. Usuda, M. Tamura, & M. Ishii, 3–10
- Marcus, P. S., Pei, S., Jiang, C.-H., et al. 2015, *ApJ*, 808, 87
- Markiewicz, W. J., Mizuno, H., & Voelk, H. J. 1991, *A&A*, 242, 286
- Marois, C., Macintosh, B., Barman, T., et al. 2008, *Science*, 322, 1348
- Marois, C., Zuckerman, B., Konopacky, Q. M., Macintosh, B., & Barman, T. 2010, *Nature*, 468, 1080
- Marshall, J. P., Wittenmyer, R. A., Horner, J., et al. 2019, *AJ*, 157, 1
- McNally, C. P., Nelson, R. P., Paardekooper, S.-J., & Benítez-Llambay, P. 2019, *MNRAS*, 484, 728
- McNally, C. P., Nelson, R. P., Paardekooper, S.-J., Benítez-Llambay, P., & Gressel, O. 2020, *MNRAS*, 493, 4382
- Mia, R., & Kushvah, B. S. 2016, *MNRAS*, 457, 1089
- Millholland, S., Wang, S., & Laughlin, G. 2017, *ApJ*, 849, L33
- Millholland, S., Laughlin, G., Teske, J., et al. 2018, *AJ*, 155, 106
- Mizuno, H. 1980, *Progress of Theoretical Physics*, 64, 544
- Morbidelli, A., Lambrechts, M., Jacobson, S., & Bitsch, B. 2015, *Icarus*, 258, 418
- Morbidelli, A., Levison, H. F., & Gomes, R. 2008, *The Dynamical Structure of the Kuiper Belt and Its Primordial Origin*, ed. Barucci, M. A., Boehnhardt, H., Cruikshank, D. P., Morbidelli, A., & Dotson, R., 275–292
- Morbidelli, A., Szulágyi, J., Crida, A., et al. 2014, *Icarus*, 232, 266

- Morbidelli, A., Tsiganis, K., Crida, A., Levison, H. F., & Gomes, R. 2007, *AJ*, 134, 1790
- Muley, D., Fung, J., & van der Marel, N. 2019, *ApJ*, 879, L2
- Murray, C. D., & Dermott, S. F. 1998, *Solar System Dynamics*
- Muzerolle, J., Luhman, K. L., Briceño, C., Hartmann, L., & Calvet, N. 2005, *ApJ*, 625, 906
- Najita, J. R., Strom, S. E., & Muzerolle, J. 2007, *MNRAS*, 378, 369
- Nakagawa, Y., Sekiya, M., & Hayashi, C. 1986, *Icarus*, 67, 375
- Natta, A., Testi, L., & Randich, S. 2006, *A&A*, 452, 245
- Nelson, B. E., Ford, E. B., Wright, J. T., et al. 2014, *MNRAS*, 441, 442
- Nelson, B. E., Robertson, P. M., Payne, M. J., et al. 2016, *MNRAS*, 455, 2484
- Ogihara, M., Kokubo, E., Suzuki, T. K., & Morbidelli, A. 2018, *A&A*, 615, A63
- Oka, A., Nakamoto, T., & Ida, S. 2011, *ApJ*, 738, 141
- Ormel, C. W. 2013, *MNRAS*, 428, 3526
- Ormel, C. W., & Cuzzi, J. N. 2007, *A&A*, 466, 413
- Ormel, C. W., & Klahr, H. H. 2010, *A&A*, 520, A43
- Ormel, C. W., & Kobayashi, H. 2012, *ApJ*, 747, 115
- Ormel, C. W., Shi, J.-M., & Kuiper, R. 2015, *MNRAS*, 447, 3512
- Owen, J. E. 2016, *PASA*, 33, e005
- Papaloizou, J. C. B., Nelson, R. P., & Masset, F. 2001, *A&A*, 366, 263
- Pascucci, I., Testi, L., Herczeg, G. J., et al. 2016, *ApJ*, 831, 125
- Peale, S. J. 1986, *Orbital resonances, unusual configurations and exotic rotation states*

- among planetary satellites, ed. J. A. Burns & M. S. Matthews, 159–223
- Peek, K. M. G., Johnson, J. A., Fischer, D. A., et al. 2009, *PASP*, 121, 613
- Perets, H. B., & Murray-Clay, R. A. 2011, *ApJ*, 733, 56
- Perez-Becker, D., & Chiang, E. 2011, *ApJ*, 727, 2
- Perone, C. S. 2009, *SIGEVolution*, 4, 12
- Perri, F., & Cameron, A. G. W. 1974, *Icarus*, 22, 416
- Petit, J.-M., & Henon, M. 1986, *Icarus*, 66, 536
- Pinte, C., Dent, W. R. F., Ménard, F., et al. 2016, *ApJ*, 816, 25
- Piso, A.-M. A., Youdin, A. N., & Murray-Clay, R. A. 2015, *ApJ*, 800, 82
- Pollack, J. B., Hubickyj, O., Bodenheimer, P., et al. 1996, *Icarus*, 124, 62
- Powell, D., Murray-Clay, R., Pérez, L. M., Schlichting, H. E., & Rosenthal, M. 2019, *ApJ*, 878, 116
- Powell, D., Murray-Clay, R., & Schlichting, H. E. 2017, *ApJ*, 840, 93
- Preibisch, T., & Feigelson, E. D. 2005, *ApJS*, 160, 390
- Press, W. H., Teukolsky, S. A., Vetterling, W. T., & Flannery, B. P. 2007, *Numerical Recipes 3rd Edition: The Art of Scientific Computing*, 3rd edn.
- Rafikov, R. R. 2004, *AJ*, 128, 1348
- . 2006, *ApJ*, 648, 666
- Rein, H., & Liu, S.-F. 2012, *A&A*, 537, A128
- Rein, H., Payne, M. J., Veras, D., & Ford, E. B. 2012, *MNRAS*, 426, 187
- Rein, H., & Spiegel, D. S. 2015, *MNRAS*, 446, 1424
- Rein, H., & Tamayo, D. 2015, *MNRAS*, 452, 376

- Ribas, Á., Merín, B., Bouy, H., & Maud, L. T. 2014, *A&A*, 561, A54
- Rosenthal, M. M., Chiang, E. I., Ginzburg, S., & Murray-Clay, R. A. 2020, *MNRAS*,  
arXiv:2004.13720
- Rosenthal, M. M., & Murray-Clay, R. A. 2018, *ApJ*, 864, 66
- . 2019, arXiv e-prints, arXiv:1908.06991
- Rosenthal, M. M., Murray-Clay, R. A., Perets, H. B., & Wolansky, N. 2018, *ApJ*, 861,  
74
- Rosenthal, M. M., Jacobson-Galan, W., Nelson, B., et al. 2019, *AJ*, 158, 136
- Safronov, V. S. 1972,
- Sari, R., & Goldreich, P. 2004, *ApJ*, 606, L77
- Schlichting, H. E. 2014, *ApJ*, 795, L15
- Shakura, N. I., & Sunyaev, R. A. 1973, *A&A*, 24, 337
- Sharma, S. 2017, *ARA&A*, 55, 213
- Stewart, S. T., & Leinhardt, Z. M. 2009, *ApJ*, 691, L133
- Suzuki, T. K., Ogihara, M., Morbidelli, A., Crida, A., & Guillot, T. 2016, *A&A*, 596,  
A74
- Szulágyi, J., Morbidelli, A., Crida, A., & Masset, F. 2014, *ApJ*, 782, 65
- Tadeu dos Santos, M., Correa-Otto, J. A., Michtchenko, T. A., & Ferraz-Mello, S. 2015,  
*A&A*, 573, A94
- Tan, X., Payne, M. J., Lee, M. H., et al. 2013, *ApJ*, 777, 101
- Tanaka, H., Murase, K., & Tanigawa, T. 2020, *ApJ*, 891, 143
- Tanigawa, T., & Tanaka, H. 2016, *ApJ*, 823, 48

- Tanigawa, T., & Watanabe, S.-i. 2002, *ApJ*, 580, 506
- Tognelli, E., Prada Moroni, P. G., & Degl'Innocenti, S. 2011, *A&A*, 533, A109
- Trifonov, T., Kürster, M., Zechmeister, M., et al. 2017, *A&A*, 602, L8
- Trifonov, T., Stock, S., Henning, T., et al. 2019, *AJ*, 157, 93
- Tripathi, A., Andrews, S. M., Birnstiel, T., & Wilner, D. J. 2017, *ApJ*, 845, 44
- Visser, R. G., & Ormel, C. W. 2016, *A&A*, 586, A66
- Voelk, H. J., Jones, F. C., Morfill, G. E., & Roeser, S. 1980, *A&A*, 85, 316
- Vogt, S. S. 1987, *PASP*, 99, 1214
- Vogt, S. S., Allen, S. L., Bigelow, B. C., et al. 1994, in *Proc. SPIE, Vol. 2198, Instrumentation in Astronomy VIII*, ed. D. L. Crawford & E. R. Craine, 362
- Vogt, S. S., Radovan, M., Kibrick, R., et al. 2014, *PASP*, 126, 359
- Walsh, K. J., Morbidelli, A., Raymond, S. N., O'Brien, D. P., & Mandell, A. M. 2011, *Nature*, 475, 206
- Walter, F. M., Brown, A., Mathieu, R. D., Myers, P. C., & Vrba, F. J. 1988, *AJ*, 96, 297
- Wang, J. J., Graham, J. R., Dawson, R., et al. 2018, *AJ*, 156, 192
- Wang, L., & Goodman, J. J. 2017, *ApJ*, 835, 59
- Weidenschilling, S. J. 1977a, *MNRAS*, 180, 57
- . 1977b, *Ap&SS*, 51, 153
- Weiss, L. M., Marcy, G. W., Petigura, E. A., et al. 2018, *AJ*, 155, 48
- Windmark, F., Birnstiel, T., Ormel, C. W., & Dullemond, C. P. 2012, *A&A*, 544, L16
- Winston, E., Megeath, S. T., Wolk, S. J., et al. 2010, *AJ*, 140, 266

- Wittenmyer, R. A., Horner, J., & Tinney, C. G. 2012, *ApJ*, 761, 165
- Wittenmyer, R. A., Tan, X., Lee, M. H., et al. 2014, *ApJ*, 780, 140
- Wittenmyer, R. A., Johnson, J. A., Butler, R. P., et al. 2016, *ApJ*, 818, 35
- Wu, Y. 2019, *ApJ*, 874, 91
- Xu, Z., Bai, X.-N., & Murray-Clay, R. A. 2017, *ApJ*, 847, 52
- Yin, Q., Jacobsen, S. B., Yamashita, K., et al. 2002, *Nature*, 418, 949
- Youdin, A. N., & Goodman, J. 2005, *ApJ*, 620, 459
- Youdin, A. N., & Lithwick, Y. 2007, *Icarus*, 192, 588
- Zechmeister, M., & Kürster, M. 2009, *A&A*, 496, 577
- Zhang, S., Zhu, Z., Huang, J., et al. 2018, *ApJ*, 869, L47
- Zhu, W. 2019, arXiv e-prints, arXiv:1907.02074
- Zhu, W., & Wu, Y. 2018, *AJ*, 156, 92
- Zhu, Z., Nelson, R. P., Dong, R., Espaillat, C., & Hartmann, L. 2012, *ApJ*, 755, 6
- Zhu, Z., Nelson, R. P., Hartmann, L., Espaillat, C., & Calvet, N. 2011, *ApJ*, 729, 47

# Appendix A

## Calculation of Gas-Assisted Growth Timescale

### A.1 Summary of Calculation Algorithm

In this appendix, we summarize the recipe for calculating the growth timescale.

Our model takes in five input parameters:  $M_*$ ,  $a$ ,  $M$ ,  $r_s$ , and  $\alpha$ . Once these parameters are specified we can calculate the parameters of the protoplanetary disk at the given orbital separation (see Table 2.2). We then need to calculate the Stokes number of the small body  $St \equiv t_s \Omega$ . Particles with  $r_s < 9\lambda/4$  (which applies over most of parameter space) are in the Epstein regime, which allows us to immediately calculate their stopping time:

$$t_{s,\text{Eps}} = \frac{\rho_s}{\rho_g} \frac{r_s}{v_{th}} . \quad (\text{A.1})$$

For  $r_s > 9\lambda/4$  the stopping time is calculated numerically. We begin by setting  $v_{pg} = v_{\text{gas}} \equiv \sqrt{\alpha c_s^2 + \eta^2 v_k^2}$ . We then calculate the drag force on the particle using

$$F_D = \frac{1}{2} C_D(Re) \pi r_s^2 \rho_g v_{pg}^2, \quad (\text{A.2})$$

where

$$C_D(Re) = \frac{24}{Re} (1 + 0.27 Re)^{0.43} + 0.47 [1 - \exp(-0.04 Re^{0.38})], \quad (\text{A.3})$$

and  $Re = 4r_s v_{pg} / (v_{th} \lambda)$ . The stopping time is then given by

$$t_s = \frac{m v_{pg}}{F_D}, \quad (\text{A.4})$$

where  $m$  is the mass of the small body. Using this stopping time we can recalculate  $v_{pg}$ .

The relevant equations are

$$v_{pg,\ell} = \eta v_k St \frac{\sqrt{4 + St^2}}{1 + St^2}, \quad (\text{A.5})$$

and

$$v_{pg,t} = \begin{cases} \sqrt{\alpha} c_s \left( \frac{St'^2 (1 - Re_t^{-1/2})}{(St' + 1) (St' + Re_t^{-1/2})} \right)^{1/2}, & St' < 10 \\ \sqrt{\alpha} c_s \sqrt{\frac{St'}{1 + St'}}, & St' \geq 10 \end{cases} \quad (\text{A.6})$$

Here  $Re_t \equiv \alpha c_s H_g / (v_{th} \lambda)$  and  $St' \equiv t_s / t'_{\text{eddy}}$ , where

$$t'_{\text{eddy}} = \frac{\Omega^{-1}}{\sqrt{1 + \left(\frac{v_{pg,\ell}}{\sqrt{\alpha} c_s}\right)^2}}. \quad (\text{A.7})$$

The total velocity relative to the gas is

$$v_{pg} = \sqrt{v_{pg,\ell}^2 + v_{pg,t}^2}. \quad (\text{A.8})$$

Using this new velocity we can recalculate  $F_D$  and obtain a new value of  $t_s$ . We then iterate this process until we obtain the desired accuracy for  $St$ .

Once  $St$  is known, we calculate the length scales needed to determine the growth timescale. We first calculate  $R_{\text{stab}}$ :

$$R_{\text{stab}} = \min(R_{WS}, R_{\text{shear}}, R_H) \quad (\text{A.9})$$

Here  $R_H$  is the planet's Hill radius:

$$R_H = a \left( \frac{M}{3M_*} \right)^{1/3}. \quad (\text{A.10})$$

$R_{WS}$  is the planet's WISH radius:

$$R_{WS} = \sqrt{\frac{GMm}{F_D(v_{\text{gas}})}}. \quad (\text{A.11})$$

For a particle in a linear drag regime, there is a simple analytic expression for  $R_{WS}$ :

$$R_{WS} = R_H \sqrt{3St \left( \frac{v_H}{v_{\text{gas}}} \right)}. \quad (\text{A.12})$$

$R_{\text{shear}}$  is the shearing radius, which is the solution to the equation

$$R_{\text{shear}} = \sqrt{\frac{GMm}{F_D(R_{\text{shear}}\Omega)}}. \quad (\text{A.13})$$

In non-linear drag regimes, we solve this equation numerically. For a particle in a linear drag regime, the above equation has the analytic solution

$$R_{\text{shear}} = R_H (3St)^{1/3}. \quad (\text{A.14})$$

Using  $R_H$  and the planet's Bondi radius

$$R_b = \frac{GM}{c_s^2} \quad (\text{A.15})$$

we calculate  $R_{\text{atm}}$ :

$$R_{\text{atm}} = \min(R_b, R_H), \quad (\text{A.16})$$

which in turn tells us the impact parameter for accretion:

$$R_{\text{acc}} = \max(R_{\text{stab}}, R_{\text{atm}}). \quad (\text{A.17})$$

The scale height of the small bodies is determined by the Kelvin-Helmholtz scale height

$$H_{KH} = \frac{2\eta v_k}{\Omega} \min(1, St^{-1/2}) , \quad (\text{A.18})$$

and turbulent scale height

$$H_t = H_g \min\left(\sqrt{\frac{\alpha}{St}}, 1\right) . \quad (\text{A.19})$$

We take  $H_p$  to be:

$$H_p = \max(H_t, H_{KH}) . \quad (\text{A.20})$$

Using  $R_{\text{acc}}$  and  $H_p$  we can determine  $H_{\text{acc}}$ :

$$H_{\text{acc}} = \min(R_{\text{acc}}, H_p) . \quad (\text{A.21})$$

We now calculate the approach velocity of the small bodies,  $v_\infty$ . The laminar and turbulent components of the velocity due the particle's interactions with the gas are given by

$$v_{pk,\ell} = \eta v_k \frac{\sqrt{1 + 4St^2}}{1 + St^2} , \quad (\text{A.22})$$

and

$$v_{pk,t} = \begin{cases} \sqrt{\alpha} c_s \left( 1 - \frac{St'^2 (1 - Re_t^{-1/2})}{(St' + 1)(St' + Re_t^{-1/2})} \right)^{1/2}, & St' < 10 \\ \sqrt{\alpha} c_s \sqrt{\frac{1}{1 + St'}}, & St' \geq 10 \end{cases} \quad (\text{A.23})$$

where again  $St' \equiv t_s/t'_{\text{eddy}}$ , with  $t'_{\text{eddy}}$  given by Equation (A.7). The total velocity is again given by

$$v_{pk} = \sqrt{v_{pk,\ell}^2 + v_{pk,t}^2}, \quad (\text{A.24})$$

The value of  $v_\infty$  is then given by

$$v_\infty = \max(v_{pk}, v_{\text{shear}}), \quad (\text{A.25})$$

where  $v_{\text{shear}} = R_{\text{acc}}\Omega$ .

We now have enough information to calculate the growth timescale  $t_{\text{grow}}$ :

$$t_{\text{grow}} = \frac{MH_p}{2f_s \Sigma v_\infty R_{\text{acc}} H_{\text{acc}}}. \quad (\text{A.26})$$

In order to determine whether a particle can accrete, we calculate its incoming kinetic energy

$$KE = \frac{1}{2} m v_\infty^2, \quad (\text{A.27})$$

and the work done by gas drag

$$W = 2F_D(v_{\text{enc}})R_{\text{acc}} . \quad (\text{A.28})$$

Here  $v_{\text{enc}}$  is the velocity of the particle during its interaction with the core

$$v_{\text{enc}} = \begin{cases} \max(v_{\text{orbit}}, v_{pg}), & v_{\infty} < v_{\text{orbit}} \\ \max(v_{\text{kick}}, v_{pg}), & v_{\infty} > v_{\text{orbit}} \end{cases} \quad (\text{A.29})$$

where  $v_{\text{orbit}} = \sqrt{GM/R_{\text{acc}}}$ , and  $v_{\text{kick}} = GM/(R_{\text{acc}}v_{\infty})$ . Particles can accrete if

1.  $R_{\text{stab}} > R_b$  and  $W > KE$

2.  $R_{\text{stab}} < R_b$  and  $W < KE$

3.  $R_{\text{stab}} = R_H$  and  $v_{\infty} = v_H$

If the particle does not fall into any of these regimes then we set  $t_{\text{grow}} = \infty$ . In case 3 the growth timescale is given by

$$t_{\text{grow}} = \frac{t'_{\text{grow}}}{\min(1, W/KE)} . \quad (\text{A.30})$$

where  $t'_{\text{grow}}$  is given by Equation (A.26).

## A.2 Derivation of Velocity Formulae in Different Frames

In this appendix we give detailed derivations of the equations given in Section 2.3.4. In what follows we assume that the turbulence is ergodic, i.e. that time averaging the system is equivalent to ensemble averaging, and that the turbulence is a stationary

process.

The methods for calculating turbulent velocity in e.g. [Voelk et al. \(1980\)](#) begin by decomposing the total velocity  $\mathbf{v}$  into time averaged and fluctuating components, a technique known as “Reynolds averaging.” (See [Cuzzi et al. 1993](#), Appendix A). That is, we take  $\mathbf{v} = \bar{\mathbf{v}} + \delta\mathbf{v}$ , such that  $\langle \delta\mathbf{v} \rangle = 0$ , where  $\langle \dots \rangle$  denotes ensemble averaging.  $\bar{\mathbf{v}}$  is associated with the laminar component of velocity while  $\delta\mathbf{v}$  is associated with the turbulent velocity. We can use this same decomposition to determine how to combine the laminar and turbulent components as well as how to compute the velocity after changing reference frames.

We first note that decomposing the velocity as above, taking the dot product of each side of the equation and time averaging gives

$$\langle \mathbf{v} \cdot \mathbf{v} \rangle = \bar{v}^2 + \langle \delta v^2 \rangle + 2 \langle \bar{\mathbf{v}} \cdot \delta\mathbf{v} \rangle \quad (\text{A.31})$$

$$v^2 = \bar{v}^2 + \langle \delta v^2 \rangle , \quad (\text{A.32})$$

which is the same as Equation (2.25), and is used to combine the turbulent and laminar components of the velocity, which are calculated separately.

For the purposes of this problem, we are concerned with velocities relative to two frames: velocities relative to the total gas velocity are needed for the calculation of drag forces, while velocities relative to the local Keplerian velocity are needed to determine the rate that small bodies encounter large ones. If the subscripts  $p, g$ , and  $k$  denoted the velocity of the small bodies, the gas, and the Keplerian velocity respectively, then we may write

$$\mathbf{v}_{pk} = \mathbf{v}_{pg} + \mathbf{v}_{gk} . \quad (\text{A.33})$$

Reynolds averaging (A.33) gives

$$\bar{\mathbf{v}}_{pk} = \bar{\mathbf{v}}_{pg} + \bar{\mathbf{v}}_{gk} . \quad (\text{A.34})$$

So the laminar component of the particle's velocity can be changed from one frame to another in the usual manner independent of the turbulent velocity, as is done in the main text (c.f. Equation 2.26).

To compute how the turbulent velocity changes between frames, we require the equation of motion for the grains. Following [Voelk et al. \(1980\)](#), for a particle in a linear drag regime ( $F_D \propto v$ ) we can write

$$\frac{d\mathbf{v}_{pk}}{dt} = \mathbf{a}_g - \frac{\mathbf{v}_{pg}}{t_s} , \quad (\text{A.35})$$

where  $\mathbf{a}_g$  is the acceleration due to forces other than gas drag, such as gravity. Reynolds averaging and subtracting the result from (A.35) gives

$$\frac{d}{dt} (\delta\mathbf{v}_{pk}) = -\frac{\delta\mathbf{v}_{pg}}{t_s} , \quad (\text{A.36})$$

where we've assumed that  $\mathbf{a}_g$  only varies on large spatial scales, so  $\langle \mathbf{a}_g \rangle = 0$ . Now

subtracting equation (A.34) from Equation (A.33) and rearranging slightly gives

$$\delta \mathbf{v}_{gk} = \delta \mathbf{v}_{pk} - \delta \mathbf{v}_{pg} . \quad (\text{A.37})$$

Taking the dot product and time averaging gives

$$\langle \delta v_{gk}^2 \rangle = \langle \delta v_{pk}^2 \rangle + \langle \delta v_{pg}^2 \rangle - 2 \langle \delta \mathbf{v}_{pk} \cdot \delta \mathbf{v}_{pg} \rangle . \quad (\text{A.38})$$

Plugging in Equation (A.36) into the last term on the righthand side gives

$$\langle \delta v_{gk}^2 \rangle = \langle \delta v_{pk}^2 \rangle + \langle \delta v_{pg}^2 \rangle + 2t_s \left\langle \delta \mathbf{v}_{pk} \cdot \frac{d}{dt} (\delta \mathbf{v}_{pk}) \right\rangle \quad (\text{A.39})$$

$$= \langle \delta v_{pk}^2 \rangle + \langle \delta v_{pg}^2 \rangle + t_s \frac{d}{dt} \langle \delta v_{pk}^2 \rangle . \quad (\text{A.40})$$

For a stationary process the last term will be zero, so we have

$$\langle \delta v_{gk}^2 \rangle = \langle \delta v_{pk}^2 \rangle + \langle \delta v_{pg}^2 \rangle , \quad (\text{A.41})$$

which is used in our model to convert the turbulent component of the velocity from the frame relative to the gas to the frame relative to Keplerian (c.f. Equation 2.27).

### A.3 Canonical Core Accretion Timescale

In this appendix we give a short summary of how growth proceeds for cores accreting particles for which the gas drag force is negligible. See [Goldreich et al. \(2004\)](#)

for a more in depth review of these processes. Since small bodies in this regime cannot dissipate their kinetic energy through gas drag, in order for the accretion to occur the impact parameter of the incoming particle must be small enough that it collides with the core. The maximum impact parameter at which a particle will be gravitationally focused into a collision with the core is given by

$$R_{\text{focus}} = R \left( 1 + \frac{v_{\text{esc}}^2}{v_{\infty}^2} \right)^{1/2}, \quad (\text{A.42})$$

where  $R$  is the radius of the core, and  $v_{\text{esc}} = \sqrt{2GM/R}$  is the escape velocity from the core. The scale height of small bodies is given by the vertical component of their velocity dispersion –  $H_p \sim v_z/\Omega$ .

While there are a number of gas free growth regimes, and therefore timescales, we confine our attention to the regime where the velocity of dispersion of the small bodies is approximately the Hill velocity,  $v_H = R_H\Omega$ . Here  $R_H$  is the core's Hill radius (see Section 2.4), and  $\Omega$  is the local Keplerian orbital frequency. This regime gives the highest possible growth rate without invoking some external mechanism to bring the velocity dispersion below the Hill velocity, since interactions with the core will drive bodies up to the Hill velocity. In this regime the core can accrete over the entirety of  $R_{\text{focus}}$  in the vertical direction, so  $\sigma \approx 4R_{\text{focus}}^2$ . If we set  $v_{\infty} \approx v_z \approx v_H$ , and note that  $v_{\text{esc}}/v_H \sim (R_H/R)^{1/2}$ , then we see that  $t_{GF}$  is of order

$$t_{GF,v=v_H} \sim \frac{M}{2f_s \Sigma R_H^2 \Omega} \left( \frac{R_H}{R} \right), \quad (\text{A.43})$$

Scaled to our fiducial values (see Section 2.5.1), the timescale is given by

$$t_{GF} \approx 7 \times 10^5 \left( \frac{a}{\text{AU}} \right)^{3/2} \left( \frac{M}{M_\oplus} \right)^{1/3} \text{ years}. \quad (\text{A.44})$$

If there are  $\sim$  km sized objects available, then cores may grow by gravitational focusing in addition to gas-assisted growth. Furthermore, if for a given set of parameters, the gravitational focusing timescale is shorter than the gas-assisted growth timescale, then gravitational focusing will be the dominant mechanism of growth, which can cause cores to still grow in regimes where gas-assisted growth is slow.

## A.4 Details of Turbulent Velocity Calculation

In this appendix we describe some of the more minor details of the calculation of the velocity of small bodies due to turbulence.

The results of [Voelk et al. \(1980\)](#) and all work derived from these results, in particular Equation (2.22), rest on the assumption that there is a well-defined stopping time for the particle, independent of the particle's velocity. Thus Equation (2.22) may not hold when the particle enters the Ram pressure gas drag regime. However, Equation (2.21) holds whenever the particle's stopping time is large enough that it receives many

“kicks” from the largest scale eddies before a stopping time has elapsed. In other words, Equation (2.21) holds when  $St \gg 1$ . Since for  $Re \gg 1$  the particle will be in the Ram pressure regime, which is quadratic in velocity, we need only be concerned about the validity of our approximation if we have  $Re \gg 1$  before  $St \gg 1$ . Figure A.1 shows a plot of the Reynolds number of particles as a function of semi-major axis and Stokes number. We have restricted the figure to show  $St < 1$ , since for larger values of  $St$  we expect Equation (2.21) to hold to reasonable accuracy. In the plot we indicate the region where  $Re > 25$ , which we take as the approximate region where accuracy of our model is in question. The plot is for  $\alpha = 10^{-1}$ , which is the most restrictive case; for lower values of  $\alpha$  the region where  $St < 1$  and  $Re > 25$  shrinks.

The laminar velocity affects the turbulent velocity of the particle as well. This effect can be qualitatively understood by considering the fact that a laminar component to the particle’s velocity decreases the amount of time that the particle interacts with a turbulent eddy of a given wave number  $k$ . The original [Voelk et al. \(1980\)](#) result is dependent on the value of what they call  $k^*$ , which is the divide between eddies which are large enough that the particle comes into equilibrium with the eddy, and eddies which either decay or are traversed by the particle before they have a substantial frictional effect. To order of magnitude, the relative velocity between the particle and the gas is simply equal to the velocity of the eddy that the particle is marginally coupled to, i.e. the velocity of the eddy with wavenumber  $k_*$ . Since the presence of a laminar component to the velocity will affect which eddies the small bodies can drift through over a stopping time, introducing a laminar velocity will change the value of  $k^*$ , which in

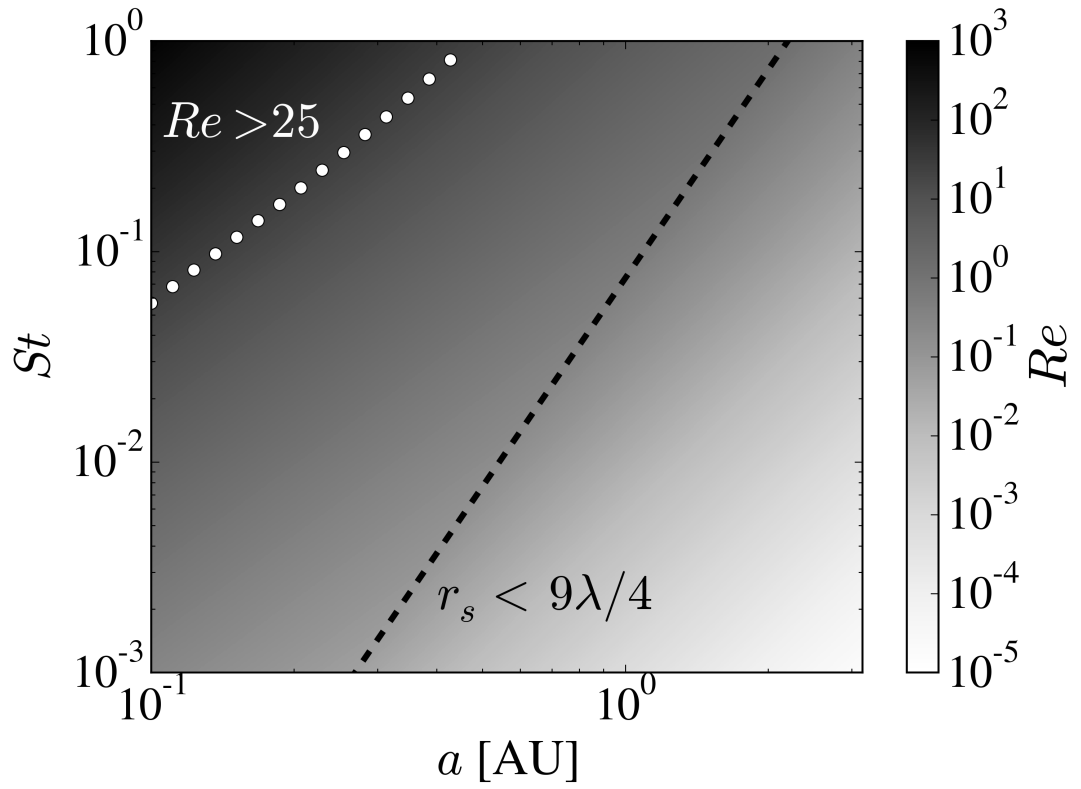


Figure A.1: The Reynolds number of a small body as a function of Stokes number and semi-major axis, for the case  $\alpha = 10^{-1}$ . The region where  $Re > 25$  and the assumptions made in our model begin to be violated is indicated, as is the region where  $r_s < 9\lambda/4$  and the particle enters the diffuse regime. For lower values of  $\alpha$  the region where  $Re > 25$  shrinks rapidly.

turn has important effects on the RMS turbulent velocity as a function of particle size. OC07 therefore refer to the effects of a laminar component of velocity as “eddy-crossing effects.”

OC07 neglect the effect of a laminar component on the particle velocity, noting that it is only important in the weakly turbulent regime for small Stokes numbers. As we are interested here in varying the strength of turbulence and determining its effect of planetary growth rates, the weakly turbulent regime is of interest to us.

[Youdin & Lithwick \(2007\)](#) note that, in the regime where eddy crossing effects are non-negligible, we can approximate these effects by using an effective large eddy turnover time,  $t'_{\text{eddy}}$ , given by

$$t'_{\text{eddy}} = \frac{t_L}{\sqrt{1 + (v_{pg,\ell}/v_t)^2}}, \quad (\text{A.45})$$

where  $v_{pg,\ell}$  is the laminar component of the particle’s velocity, measured relative to the RMS gas velocity.

In conclusion, we calculate the turbulent component of the small body’s velocity by combining equations (2.21) and (2.22), with the large eddy turnover time  $t_{\text{eddy}}$  modified by equation (A.45).

## Appendix B

# Appendices for Consumption Calculation

### B.1 Analytic Steady-State Solution for $\Sigma$ and $\dot{M}$ For Viscous Disc with Planet

In this appendix we provide an analytic expression for the surface density profile of a disc with an embedded planet. Our derivation here is more careful than our order-of-magnitude sketch in section 6.2.1, and similar to that presented in Lubow & D'Angelo (2006, their section 2.4), with a couple of differences: we reduce the surface density at the planet's location by a factor  $1 + B/\nu$  to account for repulsive Lindblad torques (see section 6.2.1), and we express our solution in terms of the surface density at infinity as opposed to the surface density at the planet's location.

Using the same notation as in section 6.2.1, and neglecting for the moment

the Lindblad torque, the equations of mass and angular momentum conservation with a mass sink at  $r = r_p$  read

$$\frac{1}{r} \frac{d(\mu u_r r / \nu)}{dr} = -\frac{\dot{M}_p}{2\pi r} \delta(r - r_p) \quad (\text{B.1})$$

$$\frac{r^2 \Omega \mu u_r}{\nu} = -\frac{d}{dr} (3\mu \Omega r^2) \quad (\text{B.2})$$

where  $u_r$  is the radial velocity and  $\mu \equiv \Sigma \nu$ . Equation (B.1) indicates that the mass flow rate  $\dot{M}_+ = -2\pi \mu_+ u_r r / \nu$  is spatially constant in regions exterior to the planet's orbit (the outer disc), and likewise for  $\dot{M}_-$  in regions interior to the planet's orbit (the inner disc):

$$\dot{M}_- = \dot{M}_+ - A \frac{\mu_p}{\nu_p} \quad (\text{B.3})$$

where we have used  $\dot{M}_p = A \mu_p / \nu_p$  and  $\nu_p \equiv \nu(r_p)$ . Since  $\dot{M}_-$  and  $\dot{M}_+$  are constants, equation (B.2) can be solved to yield

$$3\pi \mu_{\pm}(r) = \dot{M}_{\pm} + \frac{C_{\pm}}{\sqrt{r}} \quad (\text{B.4})$$

where  $C_{\pm}$  are integration constants. For the inner disc we use the boundary condition  $\mu_-(r_*) = 0$ , whence

$$3\pi \mu_-(r) = \dot{M}_- \left( 1 - \sqrt{\frac{r_*}{r}} \right). \quad (\text{B.5})$$

Following our treatment in the main text, we encode the planetary gap caused by

Lindblad torques at a sub-grid level, i.e., we force the surface density at the planet's location to be depleted relative to the surface density just interior to the planet according to

$$\mu_p = \mu_-(r_p) (1 + B/\nu_p)^{-1} \quad (\text{B.6})$$

where subscript  $p$  denotes the planet's location. For the outer disc, we fix the surface density at infinity,  $\mu(\infty) = \mu_\infty$ , so that

$$\dot{M}_+ = 3\pi\mu_\infty. \quad (\text{B.7})$$

Then from equations (B.3), (B.5), and (B.6) we have

$$\frac{\mu_p}{\mu_\infty} = \frac{1}{\frac{1}{1-\sqrt{r_*/r_p}} + \left(\frac{A}{3\pi} + \frac{B}{1-\sqrt{r_*/r_p}}\right)/\nu_p} \quad (\text{B.8})$$

which can be compared to equation (6.11). We may also solve for

$$\frac{\dot{M}_p}{\dot{M}_+} = \frac{A/(3\pi\nu_p)}{\frac{1}{1-\sqrt{r_*/r_p}} + \left(\frac{A}{3\pi} + \frac{B}{1-\sqrt{r_*/r_p}}\right)/\nu_p} \quad (\text{B.9})$$

$$\frac{\dot{M}_-}{\dot{M}_+} = \frac{1 + B/\nu_p}{1 + \left[\frac{A}{3\pi} \left(1 - \sqrt{\frac{r_*}{r_p}}\right) + B\right]/\nu_p} \quad (\text{B.10})$$

which can be compared to equations (6.14) and (6.15). Finally, stitching the outer disc

solution to the inner disc solution implies  $\mu_+(r_p) = \mu_-(r_p) = \mu_p(1 + B/\nu_p)$  and

$$3\pi\mu_+(r) = 3\pi\mu_\infty \left[ 1 - \sqrt{\frac{r_p}{r}} \left( 1 - \frac{\mu_p(1 + B/\nu_p)}{\mu_\infty} \right) \right]. \quad (\text{B.11})$$

The equations above mirror the results in section 6.2.1, with the addition of a factor of  $3\pi$  (see section 6.2.2) and the factor of  $1 - \sqrt{r_*/r_p}$  which accounts for the star's ability to divert material from the planet.

In Figure B.1 we plot equations (B.5), (B.6) and (B.11), adopting parameters as close as possible to those used in the top panel of Figure 6.2 so that we may compare the numerical result there to the analytic result here (see caption to Figure B.1 for details).

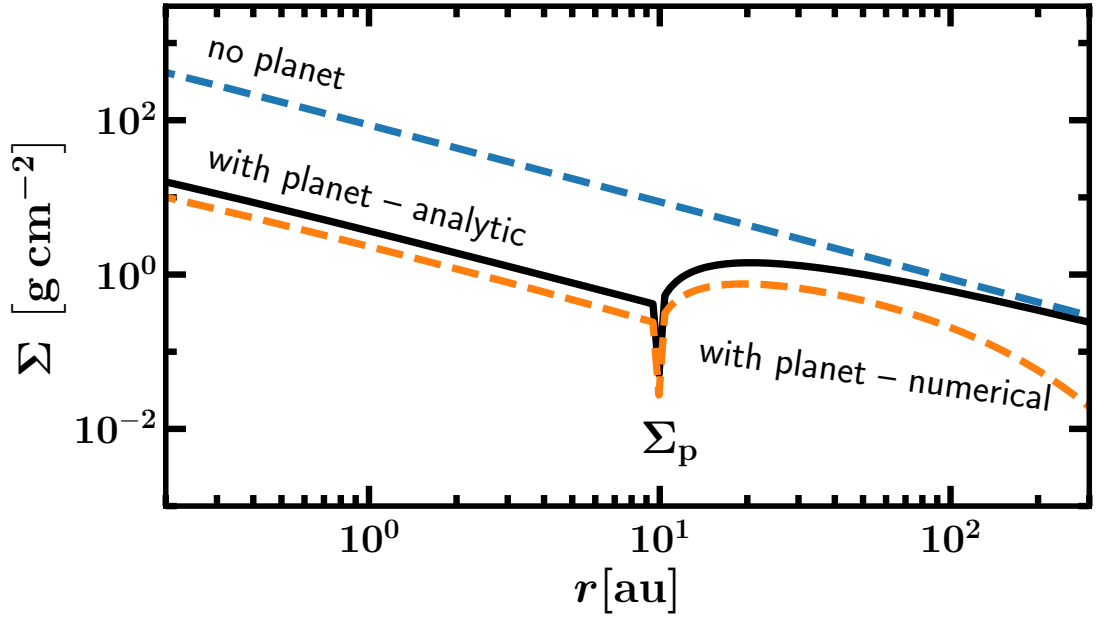


Figure B.1: Analytic solution (black solid curve) for the surface density profile of a viscous disc perturbed by a planet, as given by equations (B.5), (B.6) and (B.11), using parameters as close as possible to those used in the top panel of Figure 6.2, whose numerical result is overlaid here for comparison (orange dashed curve). For our analytic unperturbed “no planet” disc (blue dashed curve) we use a power law of slope -1 and normalization at 1 au equal to the corresponding “no planet” curve in Figure 6.2. The  $A$  and  $B$  coefficients are taken from equations (6.25) and (6.27) for  $M_p = 0.3 M_J$ . The differences between the analytic and numeric curves mainly arise from the behaviour of the outermost disc near the turn-around “transition radius” (Lynden-Bell & Pringle 1974; Hartmann et al. 1998). This transition radius, which varies with time, does not appear in our steady-state solution.

## B.2 Magnetized winds and disc accretion

We motivate here our simple, constant accretion velocity model for a wind-driven disc using the numerical simulations of Bai and collaborators. From continuity (equations 1, 6, and 9 of [Bai 2016](#)),

$$\begin{aligned}\frac{\partial \Sigma}{\partial t} &= +\frac{1}{2\pi r} \frac{\partial \dot{M}_{\text{disc}}}{\partial r} - \frac{1}{2\pi r} \frac{\partial \dot{M}_{\text{wind}}}{\partial r} \\ &= +\frac{1}{2\pi r} \frac{\partial}{\partial r} \left[ 2(\lambda - 1)r \frac{\partial \dot{M}_{\text{wind}}}{\partial r} \right] - \frac{1}{2\pi r} \frac{\partial \dot{M}_{\text{wind}}}{\partial r}\end{aligned}\quad (\text{B.12})$$

where

$$\dot{M}_{\text{wind}}(r) = \int^r \frac{\partial \dot{M}_{\text{wind}}}{\partial r} dr \quad (\text{B.13})$$

is the cumulative rate at which mass is carried to infinity by the wind (integrated over the disc within  $r$ ). From equation (20) of [Bai et al. \(2016\)](#),

$$\frac{\partial \dot{M}_{\text{wind}}}{\partial r} = 2\pi r \rho_0 u_{\text{p}0} \quad (\text{B.14})$$

where  $\rho_0$  and  $u_{\text{p}0}$  are the volumetric mass density and poloidal velocity of the wind where it is launched, near the disc surface. All quantities subscripted with 0 are evaluated at the wind base  $(r_0, z_0)$ .

The disc accretion rate

$$\dot{M}_{\text{disc}} \equiv -2\pi \Sigma r u_r = 2(\lambda - 1)r \frac{\partial \dot{M}_{\text{wind}}}{\partial r} \quad (\text{B.15})$$

for surface density  $\Sigma$  and radial velocity  $u_r$  is identical in definition to the variable  $\dot{M}_{\text{disc}}$  used throughout our paper. Unlike  $\dot{M}_{\text{wind}}$ ,  $\dot{M}_{\text{disc}}$  is not a cumulative quantity, but measures the mass crossing a circle of radius  $r$  per unit time, and uses a sign convention such that  $\dot{M}_{\text{disc}} > 0$  for  $u_r < 0$ .

Disc accretion by a wind hinges on the “magnetic lever arm”

$$\lambda = (r_A/r_0)^2 \tag{B.16}$$

where  $r_A$  is the Alfvén radius for the wind streamline running through  $r_0$ . A lever arm  $\lambda > 1$  enables  $\dot{M}_{\text{disc}} > 0$  by having the wind carry away more specific angular momentum than the Keplerian disc has at  $r_0$ . The fiducial wind model of Bai (2016, their fig. 2) has  $(\lambda - 1)$  ranging from  $\sim 30$  at  $r = 0.3$  AU to  $\sim 2$  at 30 AU; therefore the first term in (B.12) dominates the second term by a factor of order  $2(\lambda - 1) \sim 4\text{--}60$ . Only the first term is modeled in our paper.

Bai (2016) and the magnetized disc wind literature dating back to Blandford & Payne (1982) parameterize the wind mass-loss rate in terms of the dimensionless mass loading parameter

$$\mu = \frac{\omega r_0}{B_{p0}} \times k = \frac{\omega r_0}{B_{p0}} \times \frac{4\pi\rho u_p}{B_p} \tag{B.17}$$

where  $k$  is the ratio of poloidal mass flux to poloidal field strength  $B_p$  ( $k$  is constant along a magnetic field line), and  $\omega$  is the angular velocity of a field line, approximately equal to the Keplerian frequency  $\Omega_K$  at  $r_0$ . Note that  $\mu$  (not to be confused with  $\mu$  in Appendix B.1) varies with  $r$  from field line to field line. Evaluating  $\mu$  at the wind base,

we rewrite (B.14) as

$$\frac{\partial \dot{M}_{\text{wind}}}{\partial r} = \frac{\mu B_{\text{p0}}^2}{2\omega} \quad (\text{B.18})$$

(Bai et al. 2016, equation 21). Now parameterize  $B_{\text{p0}}$  in terms of the midplane plasma beta:

$$\beta_0 = \frac{8\pi}{B_{\text{p0}}^2} \frac{\Sigma k_{\text{B}} T}{\sqrt{2\pi\bar{m}}H} \quad (\text{B.19})$$

where  $k_{\text{B}}$  is Boltzmann's constant,  $T$  is the disc temperature,  $H = c_{\text{s}}/\Omega_{\text{K}}$  is the disc scale height,  $c_{\text{s}} = \sqrt{k_{\text{B}}T/\bar{m}}$  is the gas sound speed, and  $\bar{m}$  is the mean molecular weight.

Then

$$\frac{\partial \dot{M}_{\text{wind}}}{\partial r} = \frac{\sqrt{8\pi k_{\text{B}}} T}{\beta_0 \bar{m}} \frac{\mu \Sigma}{H \omega} = \frac{\sqrt{8\pi k_{\text{B}}} T^{1/2} \mu \Sigma}{\sqrt{\bar{m}} \beta_0}. \quad (\text{B.20})$$

Combine (B.20) and (B.15) to find

$$u_r = -\sqrt{\frac{8}{\pi}} \frac{\sqrt{k_{\text{B}}}}{\sqrt{\bar{m}} \beta_0} T^{1/2} \mu (\lambda - 1) \sim -\frac{\mu (\lambda - 1)}{\beta_0} c_{\text{s}}. \quad (\text{B.21})$$

In the fiducial model of Bai (2016, see their fig. 2),  $\mu$  increases from  $\sim 0.06$  at  $r = 0.3$  AU to  $\sim 4$  at 30 AU, and  $(\lambda - 1)$  decreases from  $\sim 30$  to  $\sim 2$  over the same range; therefore the product  $\mu(\lambda - 1)$  increases from  $\sim 2$  to  $\sim 8$ , scaling roughly as  $r^{0.3}$ . Their model temperature scales as  $T \propto r^{-1/2}$ ; therefore the combination  $T^{1/2} \mu(\lambda - 1)$  is nearly constant with  $r$ . Assuming it to be constant implies from (B.21) that  $u_r$  is similarly constant (cf. Kimmig et al. 2020), if  $\beta_0$  is constant:

$$u_r \sim -4 \left( \frac{10^5}{\beta_0} \right) \text{cm/s}. \quad (\text{B.22})$$

Taking  $\beta_0$  to be a strict constant corresponds to a model intermediate between the conserved-flux model of [Bai \(2016\)](#) (dashed line in the right panel of their fig. 5) and their flux-proportional-to-mass model (solid line). Using their initial fiducial  $\beta_0 = 10^5$  implies the disc at  $r = 30$  AU drains out in  $r/|u_r| \simeq 3$  Myr.

## Appendix C

# Additional Plots for analysis of the planetary system around HD 200964

### C.1 Full Posterior Distributions

In this section we provide the full posterior distributions the solutions discussed in the text. Our best-fit posterior distribution without stability taken into account is given in Figure C.1. Our best-fit posterior distribution conditioned on stability for  $10^6 P_c$  is given in Figure C.2, and our best-fit posteriors near a 3:2 and 4:3 period ratio are given in Figures C.3 and C.4.

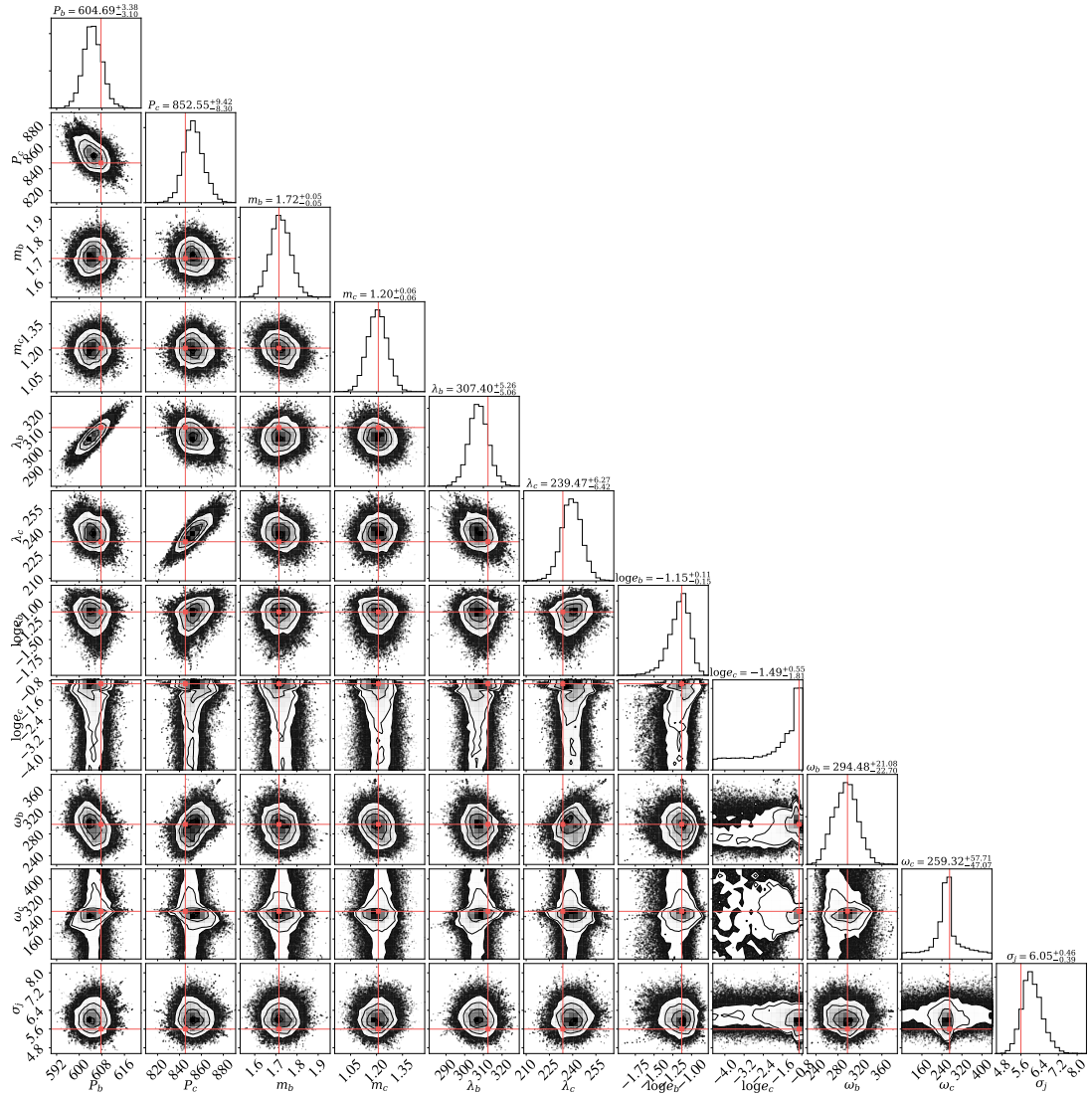


Figure C.1: A corner plot showing the posterior distribution of the planetary parameters for the two planets orbiting HD 200964, without long term stability taken into account. All values for the orbital elements refer to the values at JD 2453213.895. The red lines indicate the location of the maximum likelihood parameters.

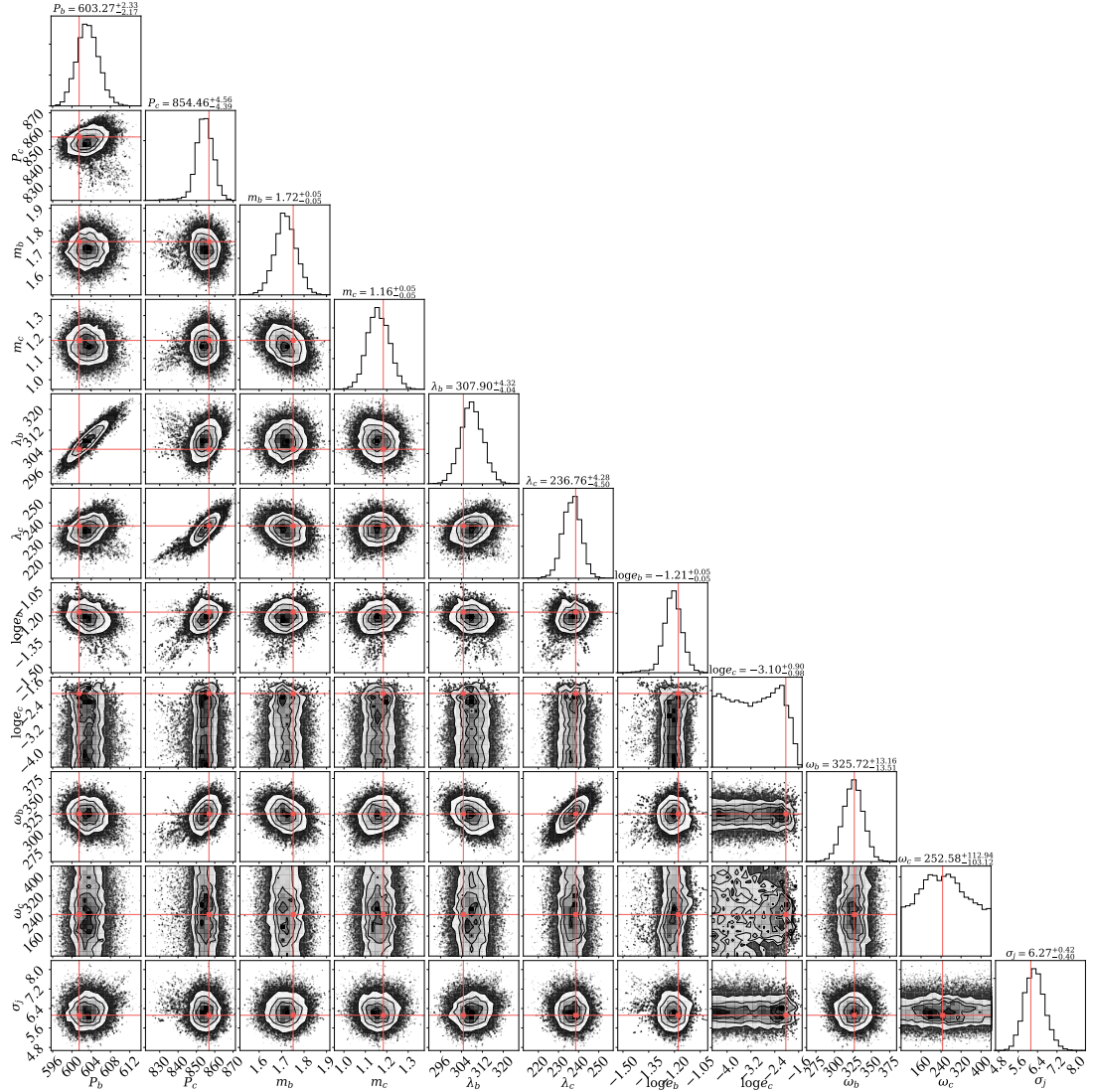


Figure C.2: Corner plot showing the posterior distribution of parameters obtained by conditioning the likelihood function on stability for  $10^6 P_c$ . This posterior contains our best-fit, long-term stable solution. All values for the orbital elements refer to the values at JD 2453213.895. The red lines indicate the location of the maximum likelihood parameters.

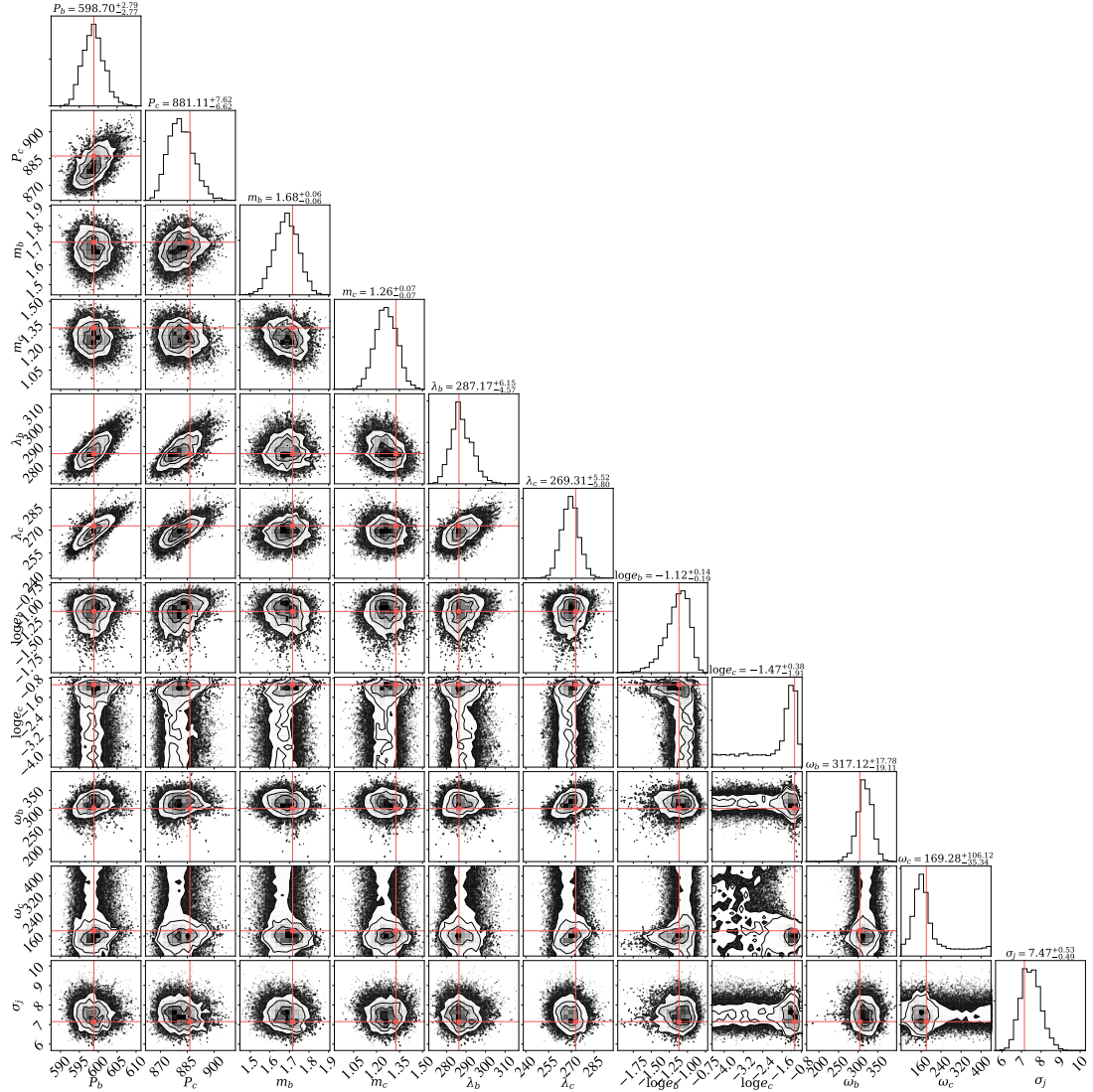


Figure C.3: Corner plot showing the posterior distribution of parameters for period ratios  $P_c/P_b \sim 3/2$ , obtained by conditioning the likelihood function on stability for  $10^6 P_c$ . This posterior was obtained by initializing the search close to the 3:2 MMR. As can be seen in Figure 7.9, the points in this posterior have an overall lower value of log likelihood than the posterior distribution shown in Figure C.2.

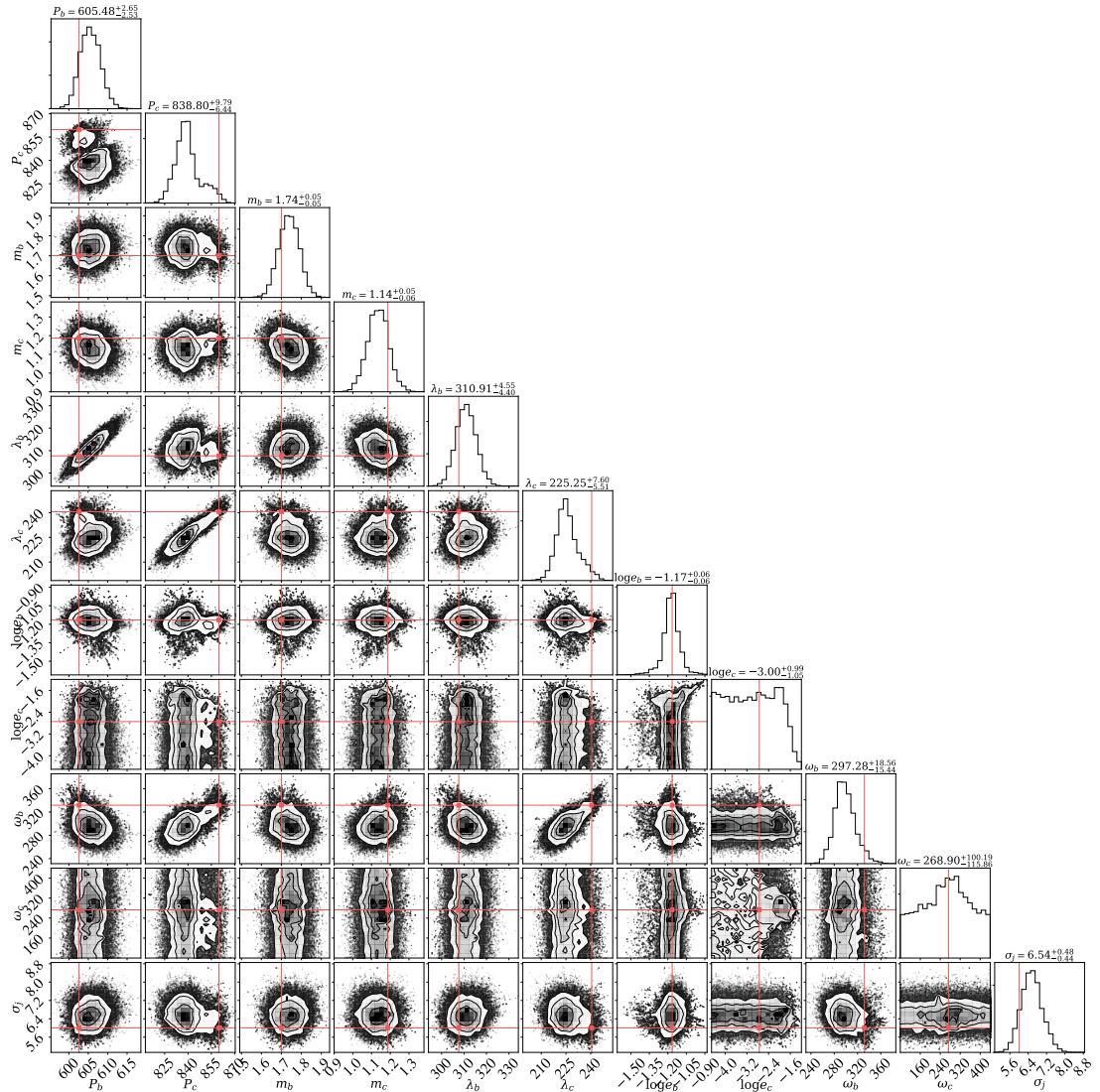


Figure C.4: Corner plot showing the posterior distribution of parameters for period ratios  $P_c/P_b \sim 4/3$ , obtained by conditioning the likelihood function on stability for  $10^6 P_c$ . This posterior was obtained by initializing the search near previously published orbital solutions. This search identifies two clear modes in  $P_c$  vs.  $P_b$ . Though the walkers spend more time at the lower period ratio mode, reinitializing the search at the higher period mode reveals that these solutions are a better fit to the data. See Section 7.4.3 for more detail.

## C.2 Plots of the evolution of $\phi$ for the 3:2 and 4:3 MMR

In this section we make plots for the evolution of the resonant angle for the 3:2 and 4:3 MMR which are analogous to the ones plotted in Figure 7.14. The evolution of the 3:2 MMR is shown in Figure C.5, and the evolution of the 4:3 MMR is shown in Figure C.6.

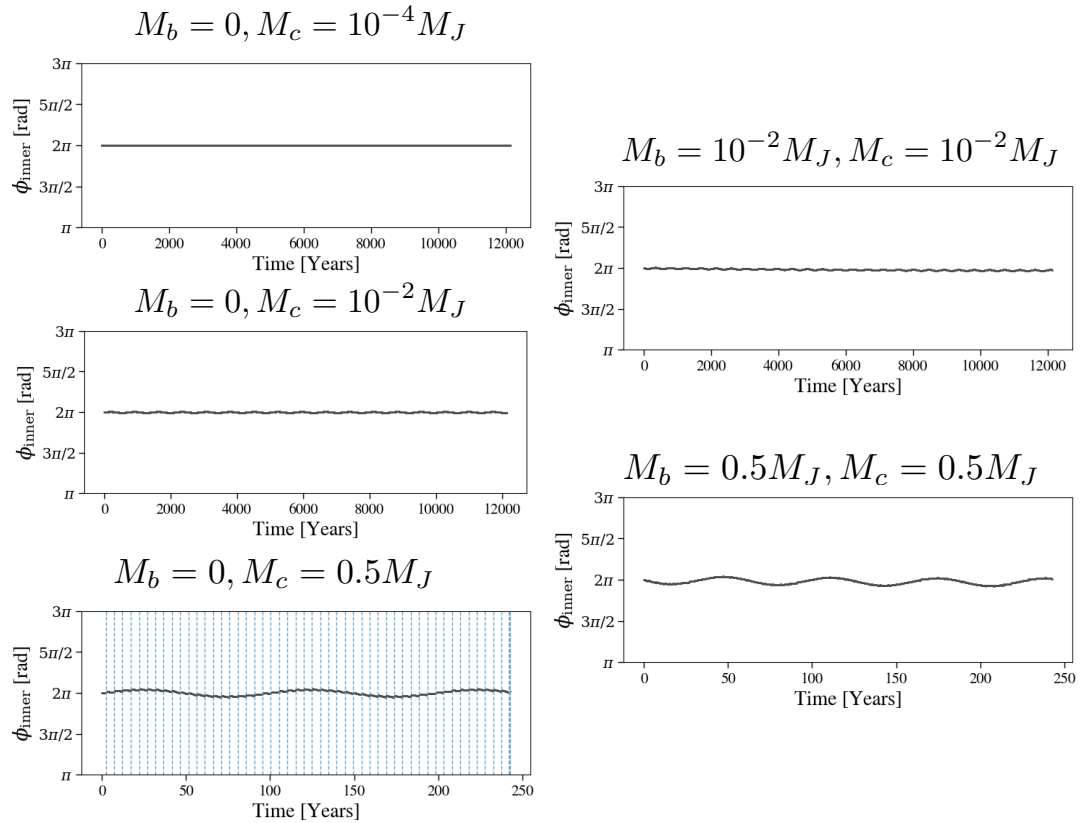


Figure C.5: Evolution of  $\phi_{\text{inner}}$  for the 3:2 MMR as the masses of the planets involved in the resonance are increased. The panels are analogous to Figure 7.14

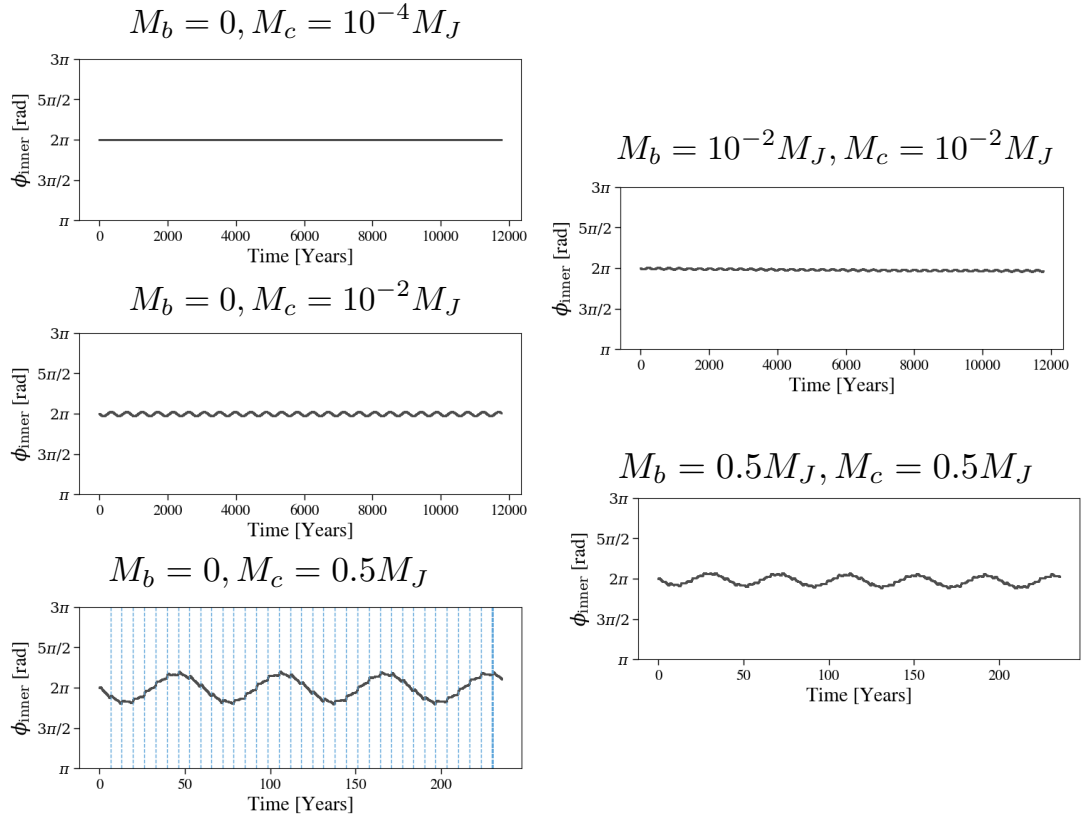


Figure C.6: Evolution of  $\phi_{\text{inner}}$  for the 4:3 MMR as the masses of the planets involved in the resonance are increased. The panels are analogous to Figure 7.14